Multiscale description of the laser-plasma interaction : application to the physics of shock ignition in inertial confinement fusion

Arnaud Colaitis

université de BORDEAUX

Thesis

Submitted in partial fulfillment of the requirements for the degree of

Doctor of Philosophy in Plasma Physics

Université de Bordeaux, Ecole doctorale des sciences et de l'ingénieur,
Section: Astrophysique, Plasmas, Nucléaire

Multiscale Description of the Laser-Plasma Interaction, Application to the Physics of Shock Ignition in Inertial Confinement Fusion

---

by

Arnaud Colaïtis

supervised by

V. Tikhonchuk

G. Duchateau

Ph. Nicolaï

Defended the 10th of November (2015) in Talence (France)
Board of examiners:

Riconda, C.	Associate Professor, UPMC, LULI (France)	**Reviewer**
Michel, P.	Staff Scientist, LLNL (United States)	**Reviewer**
Labaune, C.	Research Director, CNRS, LULI (France)	**Head of the Jury**
Hüller, S.	Research Director, CNRS, CPHT (France)	**Examiner**
Bonnaud, G.	Professor, CEA-DSM, INSTN (France)	**Examiner**
Tikhonchuk, V.	Professor, Université de Bordeaux, CELIA (France)	**Examiner**
Duchateau, G.	Research Engineer, CEA-DAM, CELIA (France)	**Examiner**
Nicolaï, Ph.	Research Engineer, CEA-DAM, CELIA (France)	**Examiner**
Masson-Laborde, P.-E.	Research Engineer, CEA-DAM, DCSA (France)	**Invited**

Communications related to this thesis

Several parts of this work have been communicated to the scientific community. We give here a list of the publications in peer-reviewed journals, alongside a list of presentations in conferences and graduate summer schools.

List of publications:

1. A. Colaïtis, G. Duchateau, P. Nicolaï, and V. Tikhonchuk. "Towards modeling of nonlinear laser-plasma interactions with hydrocodes: The thick-ray approach". In: *Physical Review E*, 89:033101, Mar 2014. doi:10.1103/PhysRevE.89.033101. URL: http://link.aps.org/doi/10.1103/PhysRevE.89.033101.

2. A. Colaïtis, G. Duchateau, X. Ribeyre, and V. Tikhonchuk. "Modeling of the cross beam energy transfer with realistic ICF beams in a large-scale hydrocode". In: *Physical Review E*, 91:013102, Jan 2015. doi:10.1103/PhysRevE.91.013102. URL: http://link.aps.org/doi/10.1103/PhysRevE.91.013102.

3. A. Colaïtis, G. Duchateau, X. Ribeyre, Y. Maheut, G. Boutoux, L. Antonelli, Ph. Nicolaï, D. Batani, and V. Tikhonchuk. "A multiscale hydrodynamic model for the laser-plasma interaction". In: *Physical Review E - Rapid Communication*, 92:041101, Oct 2015. doi:10.1103/PhysRevE.92.041101. URL: http://link.aps.org/doi/10.1103/PhysRevE.92.041101.

4. A. Colaïtis, S. Hüller, G. Duchateau, D. Pesme, V. Tikhonchuk. "Crossed Beam Energy Transfer (CBET): assessment of the Paraxial Complex Geometrical Optics approach versus a time-dependent paraxial description and experimental results". In: *to be submitted to Physics of Plasmas*

5. V. T. Tikhonchuk, A. Colaïtis, A. Vallet, E. Llor Aisa, G. Duchateau, Ph. Nicolaï, X. Ribeyre. "Physics of Laser-Plasma Interaction and Shock Ignition of Fusion Reactions". In: *Plasma Physics and Controlled Fusion*, 58:014018, Nov 2015. doi:10.1088/0741-3335/58/1/014018. URL: http://iopscience.iop.org/article/10.1088/0741-3335/58/1/014018

List of first author presentations at conferences:

1. Oral presentation at *Atelier* ILPHYGERIE *2013*, Paris. "Trajectographie laser pour l'attaque directe : introduction des faisceaux épais".

2. Oral presentation at *Anomalous Absorption Conference 2014*, Estes Park, CO. "Modeling of Cross Beam Energy Transfer in Direct-Drive Implosions".

3. Poster presentation at *Anomalous Absorption Conference 2014*, Estes Park, CO. "Modeling of Laser-Plasma Interactions and Realistic ICF beams with Hydrocodes: the Thick Rays Approach".

4. Poster presentation at *European Conference on Laser Interaction with Matter*, Paris. "Modeling of Laser-Plasma Interactions and Realistic ICF beams with Hydrocodes: the Thick Rays Approach".

5. Oral presentation at *Workhsop Physique Théorique 2015*, Bordeaux. "Propagation et interactions non linéaires de faisceaux lasers dans des plasmas de fusion".

6. Oral presentation at *Atelier* ILPHYGERIE *2015*, Paris. "Propagation et interactions non linéaires de faisceaux lasers dans les plasmas de fusion".

7. Oral presentation at *Forum Institut Laser Plasma 2015*, Porquerolles. "Modélisation des interactions laser-plasma non linéaires aux échelles hydrodynamiques : application á l'échange d'énergie par croisement de faisceaux".

List of presentations associated to this work:

1. Plenary presentation by V. TIKHONCHUK at *48^{n}d EPS Conference on Plasma Physics, 2015*, Lisbon. "Physics of laser-plasma interactions and Shock Ignition of fusion reactions".

2. Oral presentation by D. BATANI at *Inertial Fusion Sciences and Applications 2015*, Seattle. " ".

3. Invited presentation by V. TIKHONCHUK at *Inertial Fusion Sciences and Applications 2015*, Seattle. "Multi-Scale Models of Laser-Plasma Interaction for the Shock Ignition Scheme".

4. Oral presentation by S. HÜLLER at *Inertial Fusion Sciences and Applications 2015*, Seattle. "Modeling of crossed laser beam energy transfer (CBET): comparison between a paraxial geometrical optics approach and a paraxial description with smoothed laser beams".

Acknowledgments

Tout d'abord, merci à P. Balcou, directeur du laboratoire, pour m'avoir permis d'effectuer ma thèse au CELIA dans le groupe Fusion (IFCIA). C'était un plaisir de travailler au sein de ce laboratoire. J'ai ainsi eu l'occasion de rencontrer des gens ouverts, enthousiastes et d'un très haut niveau scientifique et technique.

Ensuite, je souhaite remercier Vladimir Tikhonchuk, directeur de ma thèse. Il a toujours su m'indiquer la direction générale à suivre tout en me laissant de la liberté et de l'autonomie. Ses connaissances de l'électrodynamique et de l'interaction laser-plasma ont été une aide inestimable dans l'aboutissement de mon travail. Je garde précieusement les produits de nos nombreuses réunions : ces petites feuilles griffonnées de notes et d'idées au stylo vert.

Un grand merci également à mes deux autres directeurs de thèse : Guillaume Duchateau et Philippe Nicolaï. Je vous remercie de m'avoir fait confiance en me laissant la liberté d'explorer ce sujet de thèse. Bien plus, je vous voudrais vous remercier pour chaque conseil prodigué, chaque critique pertinente, chaque encouragement. Votre soutien m'a permis de garder confiance en moi.

Je remercie mes rapporteurs de thèse ; Caterina Riconda et Pierre Michel, d'avoir accepté d'évaluer mon travail. Je n'aurais pas pu espérer meilleures personnes pour ce rôle et je suis honoré de votre bienveillance. Mes remerciements vont aussi aux membres du jury ; Guy Bonnaud, Paul-Edouard Masson-Laborde, Stefan Hüller, et à la présidente du jury Christine Labaune. C'était un privilège que de vous présenter mon travail et je vous suis reconnaissant pour vos commentaires constructifs, qui m'encouragent à continuer dans cette voie.

Je remercie aussi Stefan Hüller et Denis Pesme pour leur collaboration dans le cadre de la comparaison avec le code Harmony. De nombreuses fois, j'ai été amené à échanger avec Stefan lors des derniers mois de ma thèse et cela a été un réel plaisir de travailler avec une personne aussi intéressée, ouverte d'esprit, scientifiquement pointue, toujours disponible et enthousiaste.

Je remercie encore une fois le CELIA et le groupe Fusion et tout particulièrement Xavier Ribeyre que j'ai sollicité à de nombreuses reprises sur tout ce qui touchait à l'optique et à la FCI. Merci pour son soutien et son intérêt pour mon travail. Merci notamment de m'avoir m'avoir laissé établir une place forte sur sa machine pendant une bonne partie de ma thèse. Un grand merci également à Edouard Le Bel pour sa patience et sa pédagogie concernant les questions de FCI, ainsi que pour ses nombreux encouragements. J'adresse aussi mes remerciements à Jérôme Breil qui a répondu à mes nombreuses interrogations techniques sur le code Chic, qui n'a jamais hésité à m'aider pour me sortir du pétrin numérique, et qui a su me faire confiance pour mes développements du code. Merci également à Jean-Luc Feugas pour son aide avec le code M_1 et pour les discussions sur les modèles de transport électroniques. Je remercie de même Rachel Nuter pour son aide sur les simulations PICs avec Ocean, ainsi que sur les questions liées au Raman. Enfin, je remercie Dimitri Batani de l'intérêt porté à mon travail et de sa disponibilité vis à vis de l'interprétation de l'expérience sur Pals.

De plus, je voudrais remercier Gilles Riazuelo de m'avoir reçu à Bruyères-Le-Chatel pour me former au code Parax. Même si, je n'ai au final pas utilisé ces résultats, nos discussions m'ont été très utiles pour comprendre les méthodes de lissage optique employées en FCI. Merci aussi à Claude Gouédard qui m'a permis de mieux comprendre où je me dirigeais avec la méthode des faisceaux épais en l'espace de quelques minutes seulement en début de thèse !

Merci aussi à Elodie Beziat et Loïc Baucher pour leur grande patience face à mon expansionnisme frénétique sur les disques locaux des stations de la moitié du groupe et pour avoir répondu positivement à mes demandes de sudo apt-get farfelues. Merci aussi à Emmanuelle Lesage et Céline Oum pour leur aide administrative tout au long de la thèse. Je remercie plus particulièrement Emmanuelle pour son soutien moral pendant cette troisième année si particulière.

Un grand merci aux doctorants et post-doctorants, pour la compagnie et l'ambiance, mais aussi pour les discussions de physique. En particulier, merci à Dario Del Sorbo pour sa bonne humeur, pour m'avoir appris à parler un italien parfait, pour m'avoir expliqué le non-local et la différence entre "marron" et "marrant", à Basil Deschaud pour être Basil, pour son côté bifide, pour les excursions avec Josianne, et pour les discussions sur les matrices creuses, à Pierre Forestier-Colleoni pour sa clémence vis à vis de notre incompétence totale au donjon, pour les sandwichs, pour les innombrables divertissements nécessaires pour rester sain d'esprit (i.e. "petits jeux"), et pour m'avoir appris que l'on pouvait respirer le plombs et lécher le béryllium (mais pas l'inverse). Je remercie également Yohan Maheut de m'avoir tenu au courant des "hot news", de son aide vis à vis de la manip PALS et de sa grande patience face à mes nombreuses questions, à Sebastien Guisset pour son enthousiasme permanent et contagieux et Julien Moreau pour son talent d'acteur ("oui, c'est ca"). Merci enfin, à mes co-bureaux; Yohan Maheut, Gabriel Georges et Ludovic Barilleau de m'avoir supporté pendant ces trois ans, pendant les hauts et les bas de la thèse. Notamment, merci à Gabriel pour sa générosité de temps CPU, je lui dois la moitié de mes simulations !

Je remercie également Aymeric Spiga, François Forget et Ehouarn Millour pour les excellents moments que j'ai passés au Laboratoire de Météorologie Dynamique. Merci pour toutes les opportunités que vous m'avez offertes, et merci de m'avoir fait confiance. Travailler à vos côtés m'a définitivement convaincu que je voulais me lancer dans la recherche, et m'a poussé à faire un doctorat.

Merci aussi aux personnes qui m'ont fait basculer vers la physique, à l'Imperial College London ; Sergey Lebedev et Adam J. Harvey-Thompson pour l'excellent stage sur MAGPIE. Un grand merci également à Seto Ballian, William Ockell, Martin Pichler et Hassan Tahini pour tout le temps que nous avons passé ensemble à Londres, je ne me serais sans doute pas dirigé dans cette voie sans vous.

Merci à mes amis de plus longue date, qui sont toujours restés à mes côtés malgré la distance ; Kiki (kick host), Bibi, Coco, Lilou, Fratchy (=pro)... et tous les autres ! Merci aussi à Vincent (scout !) pour les nombreuses soirées jeux et l'excellente compagnie ! En particulier, un grand merci à Nicolas Buret et Mélissa Steward (Buret !), c'est toujours un immense plaisir de se voir et de se revoir ! Merci pour le soutien psychologique longue distance, il fût précieux !

Enfin, un grand merci à mes parents, à qui je dois tout, et en particulier de m'avoir donné le goût des sciences qui m'a finalement amené ici. Merci de m'avoir toujours soutenu dans mes projets. Merci à mon frère d'avoir veillé sur moi avec son œil de grand frère, et à ma belle-sœur d'avoir supporté mon babillage incessant sur les plasmas. Merci aussi à mon grand-père Jean, je suis très fier qu'il ait assisté à ma soutenance de thèse. Merci également à ma belle famille, d'avoir supporté mon humeur de thésard grincheux et de m'avoir permis de me reposer à maintes reprises. Enfin, merci à tout les membres de ma famille; grands-parents, cousin(e)s, petit(e)s-cousin(e)s,

oncles et tantes, etc... ca a toujours été un grand plaisir de se voir au cours de la thèse. Une pensée particulière pour ma cousine Sophie et ma grand-mère Jeanne, qui n'étaient pas à mes côtés physiquement mais qui sont bien présentes dans mon cœur.

Pour terminer, je voudrais remercier ma femme Laureline, qui m'a toujours soutenu au cours de ces trois années, pendant les hauts et les bas de la thèse. Elle a toujours cru en moi et m'a constamment poussé à donner le meilleur de moi-même, tout en veillant à ce que je ne m'épuise pas en cours de route. Je n'aurais sans doute pas terminé cette course sans elle et je lui dois tant. Enfin, merci à mon fils Maël, pour ses grands sourires, ses grands yeux ouverts et curieux, et tout simplement pour être là.

Contents

Chapter 0

Introduction

0.1 Multiscale description of the laser-plasma interaction

Interaction of laser beams with plasmas entails a wide range of physical processes, from heating and acceleration of charged particles to excitation of plasma waves, generation and saturation of laser-plasma instabilities. Understanding of the laser-plasma coupling as a whole involves various physical fields, including the description of the plasma's electromagnetic response, the theory of wave-particle interaction and instabilities, and the theory of linear and nonlinear plasma waves. Although numerous wave-plasma couplings have been observed in experiments, many arduous problems that remain to be understood arise from the variety of interaction processes at play. Indeed, a rich combination of coupling processes occur in the underdense plasma, that depend on the laser intensity and quality, local plasma parameters such as the temperature and gradient scale length, and the plasma composition. In turn, the plasma parameters depend on the coupling processes. In addition, these couplings interact with each other, thus creating additional competition or feedback processes. Understanding this nonlinear and coupled problem is the motivation for numerous theoretical, numerical and experimental works and collaborations. Notable examples are: the identification of density profile steepening [1, 2], measurements of intense laser light absorption [3, 4, 5, 6, 7, 8], experimental evidence of heated electrons characterized by at least two temperatures [9, 10, 11, 12], identification of the Brillouin [13, 14, 15, 16] and Raman [17, 18, 19, 20, 21] parametric instabilities, and the evaluation of the wavelength-scaling of coupling processes [22, 23, 24, 25]. The development of modern numerical tools allows for more comprehensive theoretical studies of these processes, and as such, better interpretation of experiments and the investigation of various physical fields. As we will see, the main motivation of this work lies in the description of these nonlinear and coupled processes at the scales of the target's dynamics.

We consider Laser-Plasma Interactions (LPIs) using laser pulses of durations of the order of $[0.1, 10]$ ns, and for which the so-called *interaction parameter* $I\lambda_L^2$ is in the range $[10^{13}\text{-}10^{17}]$ Wμm^2/cm^2 (I is the laser vacuum intensity and λ_L its vacuum wavelength). Such laser parameters are commonly realized in High Energy Density Physics experiments, notably in applications to Laboratory Astrophysics and Inertial Confinement Fusion (ICF) science. The dynamics of targets subject to such pulse durations and intensities occur on spatial and temporal scales of the order

	Spatial scales (m)	Temporal scales (s)
Hydrodynamics	10^{-3} - coronal plasma 10^{-5} - in-flight shell 10^{-7} - hydrodynamic shocks	
Laser	10^{-4} - focal spot 10^{-6} - laser inhomogeneities	10^{-8} - pulse duration 10^{-12} - smoothing (SSD)
Hydro. resolution	$10^{-7}/10^{-4}$ Lagrangian method $\rightarrow$ variable step	$10^{-15}/10^{-12}$ numerical stability condition $\rightarrow$ variable step
Maxwell's Eqs. in plasma	$10^{-8}/10^{-7}$ Debye length/wavelength $\rightarrow$ in all plasmas	10^{-16} $\frac{1}{\omega}$/laser period $\rightarrow$ in all plasmas

Table 1 – *Spatial and temporal scales involved in the hydrodynamic description of laser-target processes for the laser intensities of interest to this study.*

of a millimeter and of several nanoseconds. On the one hand, theoretical descriptions of plasma flows on the entirety of these scales rely on fluid approaches, using so-called *hydrodynamic models* which allow to study large plasma volumes on long durations. On the other hand, nonlinear laser-plasma interactions are appropriately studied at the microscopic and mesoscopic scales, typically using kinetic (*particle-in-cell* and *Fokker-Planck*) and *paraxial electromagnetic* models. The range of scales that arises from the necessity to describe the whole target evolution including fine scale LPI processes is illustrated in Tab. 1.

The state-of-the-art description of laser propagation on large scales relies on reduced approaches compatible with the performances of modern computers. The most common one is the *Ray-Tracing* model [26], that describes laser beams by bundles of needle-like rays following the *Geometrical Optics* (GO) propagation laws and characterized by a power density. In situations where collective effects and nonlinear couplings are unimportant ($I\lambda_L^2 \lesssim 5 \times 10^{13}$ Wμm^2/cm^2), GO-based models are sufficiently precise and computationally efficient. They describe the laser refraction and plasma heating due to collisional energy absorption. Conversely, LPI modeling at higher interaction parameters requires knowledge of quantities such as the electric field amplitude and direction of the wavefront, which are not readily described by GO. Note that although the notion of GO ray direction exists, that of wavefront direction does not. The physics of linear and nonlinear LPIs at these scales is usually addressed by using limitations of the maximum electron thermal flux or by adjusting the energy deposition of laser beams so as to reproduce experimental results. Such approaches hinder the understanding of the physical processes at play and limit the predictive capability of existing numerical tools. From these assessments, recent efforts have been made in describing nonlinear LPIs at hydrodynamic scales, notably in the case of inline solvers for the energy exchange between crossed laser beams [27, 28]. Those have notably allowed to better interpret and design ICF experiments [29] and can be applied to assess more complicated laser-target configurations such as the Polar Direct Drive scheme [30]. Similarly, the effects of high energy electrons generated by nonlinear LPIs on the plasma dynamics are of particular

importance for ICF studies [31, 32], Double Ablation Front experiments at high intensities, or for the design and interpretation of ns-scale laser target experiments in general [33].

Considering the large variety of laser-target configurations involving these processes, there is an evident need for a multiscale model that can account for linear and nonlinear LPIs in hydrodynamic codes, as well as the interwoven couplings between the laser propagation in plasmas, Hot Electron (HE) sources created by nonlinear LPIs, HE beams propagation and plasma dynamics. Modeling nonlinear LPIs and the laser-plasma-electron coupling on hydrodynamic scales poses severe difficulties related to (i) the accurate description of the laser intensity in plasmas, (ii) the consistent description of HE sources from the laser propagation model and (iii) the transport of HE beams in plasma. The first two limitations are related to the standard use of geometrical optics, which does not allow for robust evaluations of laser intensity in plasmas [34] while the third is related to the scarcity of accurate and CPU-efficient HE propagation models coupled to hydrocodes. The object of this work is to address these difficulties in order to formulate a multiscale model that describes the hydrodynamic laser-plasma interaction, including its coupling with the generation of high energy electron populations.

Applications of this novel formulation are conducted in the framework of Inertial Confinement Fusion. More precisely, the Shock Ignition scheme is thought to be particularly vulnerable to LPIs, as it involves a ∼500 ps duration high intensity laser pulse. We present in the following section the context of ICF, and the position of nonlinear LPIs on its operating framework. This provides the basis for the formulation of goals and objectives of this thesis.

0.2 The laser-plasma interaction in the framework of Inertial Confinement Fusion

0.2.0.1 Thermonuclear Fusion

Achieving a fusion reaction consists in bringing two positively charged light nuclei sufficiently close to each other for them to bind through the attractive strong force, which typical range is of the order of a few fermi, i.e. a few 10^{-15}m. Approaching the nuclei to such distances requires to overcome the long-range Coulomb repulsion of the charged nuclei. Although the corresponding kinetic energies are of the order of 300 keV (for Deuterium-Tritium reactions), quantum tunneling effects [35] make these reactions possible at lower energies. The cross-sections σ of fusion reactions for various nuclei are shown in Fig. 0-1 [left]. The 'easiest' (i.e. most probable) fusion reaction at low temperature is that of D-T fusion, which cross-section at 10 keV is up to two orders of magnitude higher than for other reactants. This particular reaction reads:

$$ {}^{2}_{1}\mathrm{D} + {}^{3}_{1}\mathrm{T} \rightarrow {}^{4}_{2}\mathrm{He} + \mathrm{n} + 17.6\ \mathrm{MeV}\ , \tag{1} $$

where the 17.6 MeV of kinetic energy liberated in the fusion process is shared between the α particle (3.56 MeV) and the neutron (14.03 MeV).

In the so-called *Gamow* region below ∼ 100 keV, the D-T fusion reaction cross-section increases monotonously with the kinetic energy of the projectiles. At such temperatures, the fuel becomes a plasma of electrons and two species of ions. Considering a plasma at thermal equilibrium

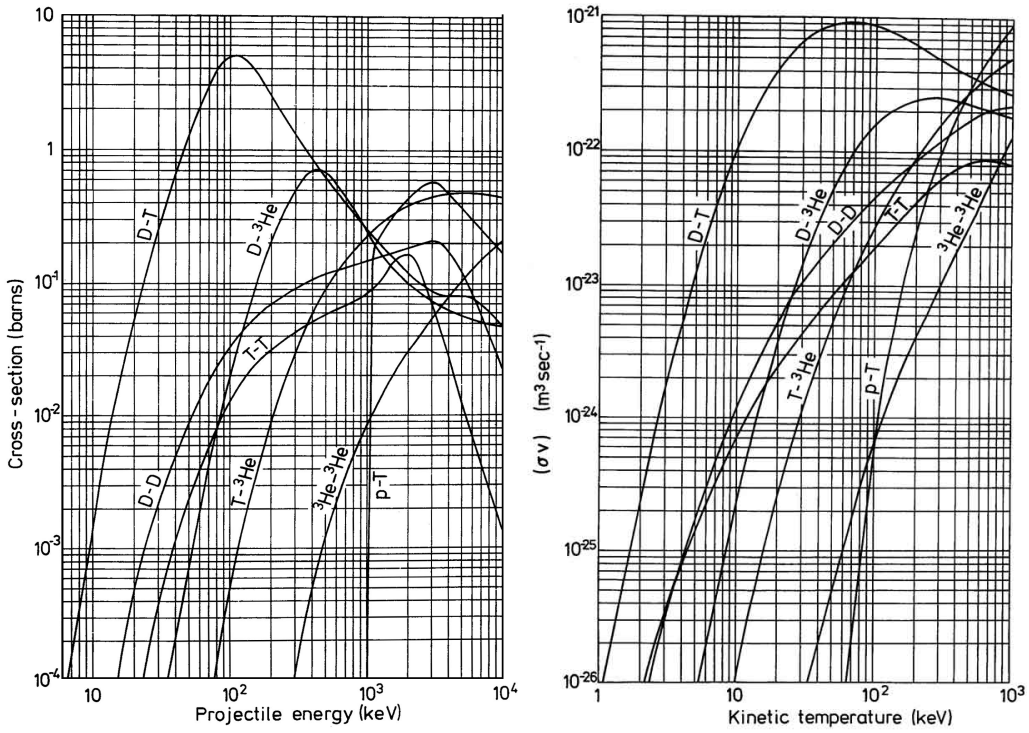

Figure 0-1 – *[left] fusion reaction cross-sections (in barns, i.e. $10^{-28}m^2$) as a function of the relative mean kinetic energy between nucleons in keV, and [right] thermal reactivity for the fusion reactions (in m^3/s) as a function of the kinetic temperature in keV. Figures from* http://www.kayelaby.npl.co.uk.

and characterized by a Maxwellian distribution function of mean temperature $T \simeq 10$ keV, the ions in the high-energy tail of the distribution function lie close to the maximum of the fusion cross-section. Integrating over the Maxwellian distribution, one can compute the average thermal reactivity $\langle \sigma v \rangle$ of a fusion plasma as a function of its average temperature T, as shown in Fig. 0-1 [right]. Heating of the plasma allows to compensate for the energy losses in elastic ion-ion collisions, which have a much higher cross-section. This approach where fusion reactions are obtained through the high energy ions in the tail of the distribution function of a hot plasma is termed *thermonuclear fusion*. It is the approach of choice for producing large amounts of nuclear fusion energy.

0.2.0.2 Burning of the D-T fuel

At the aforementioned temperature of 10 keV, the plasma cannot be contained in any solid container; the latter would be quickly deteriorated, thus polluting and cooling the fuel. As such, these plasmas must be confined in a vacuum. However, because high temperatures also imply high pressures, the plasma will naturally tend to expand and cool down. In effect, the plasma must be confined in a given volume for a sufficiently long time so that most of the D-T fuel has time to burn. For an initially equimolar mix of D-T and assuming a constant temperature

throughout the confinement, the fraction of burnt fuel F_{DT} reads [36, 37]:

$$F_{\mathrm{DT}} = \frac{\langle\sigma v\rangle n_0\tau/2}{\langle\sigma v\rangle n_0\tau/2 + 1} \ , \tag{2}$$

where τ is the confinement time and n_0 the initial ion number density. This simple formula highlights the two main parameters in thermonuclear fusion ; the temperature T (contained in $\langle\sigma v\rangle$) and the product $n_0\tau$. In order to burn half of the fuel, Eq. (2) shows that $n_0\tau$ must be of the order of $2\langle\sigma v\rangle^{-1}$. Given the difficulty to simultaneously maximize n_0 and τ, the fusion problem can be approached by using short confinement times and high density plasmas, or large confinement times and low density plasmas (the latter being the case of the Magnetic Confinement Fusion approach).

0.2.1 Inertial Confinement Fusion

With invention of the laser, the possibility to focus high amounts of energy in small volumes was considered as a mean to ignite the fusion reactions. Early experiments suggested that the optimal configuration was to irradiate a solid spherical target, thus heating it to high temperatures while confining the plasma on very short timescales by its own inertia, which gave birth to the term of *Inertial Confinement Fusion* (ICF) [38].

0.2.1.1 Hot-Spot ignition of the fuel

By considering a sphere uniformly irradiated by laser beams, it can be shown that the burnt fuel fraction reads [36, 37]:

$$F_{\mathrm{DT}}^{\mathrm{ICF}} = \frac{\rho r}{\rho r + (8\sqrt{\overline{m}_{\mathrm{DT}}\gamma k_{\mathrm{B}}T})/\langle\sigma v\rangle} \ , \tag{3}$$

with γ the heat capacity ratio, k_{B} the Boltzmann constant, $\overline{m}_{\mathrm{DT}}$ the average mass of D and T nuclei and ρr the *areal density* of the fuel, related to the previously defined $n_0\tau$ product by $\rho r = 4\sqrt{\overline{m}_{\mathrm{DT}}\gamma k_{\mathrm{B}}T}n_0\tau$. This equation highlights that obtaining high burnt fractions requires to increase the areal density of a spherical target. Given that the areal density of a sphere of a mass M and a radius R scales as $\rho R = (3/(4\pi))^{1/3}M^{1/3}\rho^{2/3}$, one concludes that (i) any attempt to increase the areal density at a constant mass requires an increase in the density ρ above the solid density, and (ii) for a given areal density (i.e. for a fixed burnt fraction), increasing the density implies that a smaller fuel mass is required, and thus less laser energy is needed to heat it to the desired temperature.

The current approaches to ICF consider bringing a small mass of combustible at high densities with the desired thermodynamic properties, while maintaining the symmetry of compression and using low enough laser energies so that the overall fusion energy far exceeds the invested energy for compression and heating of the combustible. Toward this objective, heating the entire mass of a D-T sphere is inefficient because the required invested energy is too large. The historical and standard approach to ICF is that of *hot-spot ignition*, where only a small mass of the target is brought to the required conditions for the initiation of nuclear reactions. In this framework, targets are constituted of a spherical D-T shell containing a low density D-T gas. Once fusion reaction are ignited in the hot-spot, the generated α particles deposit their energy in the dense

cold shell surrounding the hot-spot and ignite it. The hotspot heating is achieved by the $P\mathrm{d}V$ work communicated from a dense imploding shell. Obtaining the required hotspot parameters for the ignition of fusion reactions and of the target shell requires to compress the target to very high densities, i.e. to obtain high convergence ratios of the order of 30-40.

0.2.1.2 Target compression using lasers

The capsule acceleration and compression originate from the expulsion of shell material ablated by the laser at the outer target surface.The laser ablation produces a pressure $\mathcal{P}_\mathrm{A}$ that scales like, in the absence of anomalous laser absorption processes:

$$\mathcal{P}_\mathrm{A} = 57(\eta_\mathrm{abs} I_{15,\mathrm{W/cm^2}}/\lambda_{L,\mu m})^{2/3} \text{ Mbar} , \tag{4}$$

where η_abs is the laser energy absorption fraction, $I_{15,\mathrm{W/cm^2}}$ is the vacuum laser intensity in units of 10^{15} W/cm^2, and $\lambda_{L,\mu m}$ is the laser vacuum wavelength in μm. The ablation pressure is approximately equal to the pressure at the critical density ρ_c, where the laser light is reflected and the flow velocity equals the acoustic velocity c_s, so that $\mathcal{P}_\mathrm{A} \approx \dot{m}_a c_s \approx \rho_c c_s^2 \propto (I/\lambda_L)^{2/3}$, where $\dot{m}_a$ is the ablated mass rate. These estimates show that increasing the ablation pressure and the ablated mass rate require an increase in the laser intensity.

The velocity of the shell during its free-flight (so-called *implosion velocity*) can be related to the ablation mass rate by $U_\mathrm{imp} \approx \dot{m}_a \mathcal{A}/\rho$, where $\mathcal{A}$ is the shell in flight *aspect ratio* (radius over thickness of the shell $R/\Delta R$) and ρ is the in-flight shell density. Finally, the convergence ratio can be expressed as:

$$C = \frac{U_\mathrm{imp}}{\rho^{1/3}(\alpha A_F \mathcal{A})^{1/2}} = \frac{\dot{m}_a \mathcal{A}^{1/2}}{\rho^{4/3}(\alpha A_F)^{1/2}} , \tag{5}$$

where α is the *adiabat* of the shell, defined as the ratio of its pressure over the Fermi pressure $p_F = A_F \rho_s^{5/3} = 2.16\rho_s^{5/3}$ Mbar. From Eq. (5), one readily sees that for a given initial target density, obtaining high convergence ratios requires (i) high implosion velocities, obtained through a high ablation mass rate, that is, a high ablation pressure and a high laser intensity (Eq. (4)), (ii) a low shell adiabat, that is, the shell must remain cold during the implosion, i.e. the compression must be as isentropic as possible, and (iii) a high aspect ratio. The fulfillment of these points as a mean to achieve high convergence ratios is not necessarily straightforward. Firstly, high laser intensities are detrimental to the capsule implosion because of the development of nonlinear laser plasma interactions that can lead to the shell preheat (raising α) or to asymmetries in the irradiation field. Secondly, the implosion of the capsule is sensitive to hydrodynamic instabilities (such as the Rayleigh Taylor instability (RTI)), which growth is related to the acceleration of the ablation front, and is seeded by capsule non-uniformities or irradiation asymmetries. The RTI modulates the density profile, which may cause a rupture of the shell for deformation wavelengths larger than the capsule thickness. As a result, the RTI limits the maximum shell acceleration and thus puts a higher limit on the implosion velocity. Additionally, increasing the aspect ratio leads to a capsule that is susceptible to a larger range of deformation wavelengths, and thus is more fragile from the standpoint of the RTI. In order to lower the sensitivity of the capsule implosion to hydrodynamic instabilities and to increase the energy gain, alternative ignition schemes have

been developed.

0.2.1.3 Alternative Ignition schemes

Hotspot ignition relies on the subsequent assembly of the fuel and ignition of the hotspot, solely through the target's compression with one shaped laser pulse. For low adiabat implosions (α being of the order of 2), the energy required for the compression of the shell is of the same order as the energy required for the heating of the hotspot. The working principle of various alternative ignition schemes is to separate the implosion and ignition phases, that is, (i) use a dedicated low energy laser pulse for the compression of the shell only, in which case the slower $P\mathrm{d}V$ work communicated to the target center is not sufficient anymore to bring the fuel to its ignition temperature and (ii) communicate the additional energy required for the ignition of the hotspot by a different laser pulse. The main idea behind these schemes is to reduce the laser energy and to increase the target robustness, through a better control of each phase of the whole process.

In the *Fast Ignition* [39, 40, 41] scheme, the additional energy is brought in the form of a high energy electron or ion beam created by the interaction of a high power high energy laser beam with a specially prepared target. Given the inherent technical complexity of fast ignition, other alternatives were developed, and notably the *Shock Ignition* [42, 31] scheme. The latter consists in using a high intensity laser spike near the end of the compression phase to launch a strong shock into the target, thus raising the hotspot pressure and temperature above the ignition threshold when the cold shell is assembled. The attractiveness of this ignition scheme notably relies on its effective simplicity: the required pulse shapes being available on the current generation of high power laser facilities and the required targets being of the same order of complexity than direct-drive hotspot scheme targets [43]. By decoupling the compression and the heating phase, much lower laser energies are required (of the order of 500 kJ) for the obtention of similar target gains, thus making it potentially easier to implement. However, using an intense laser spike raises new physical issues related to the generation and amplification of strong shocks and fluxes of energetic electrons.

0.2.2 Interaction regime

It is traditionally considered that the optimal laser-plasma interaction regime for ICF is that of collisional absorption, where the electrons oscillating in the laser field heat the plasma through collisions with the ions. This mechanism is preferred because (i) it allows to transfer the laser energy to the thermal population of plasma and (ii) it does not involve so-called *anomalous* absorption processes that may be detrimental to the compression efficiency (those are detailed below). The fraction of laser energy transmitted to the plasma by collisional absorption is a function of the electron-ion collision frequency, dependent on the average charge state of the ions Z and on the density n_e. Considering that high-Z materials have a low hydrodynamic efficiency (they require higher energies to ionize and tend to re-emit X-rays which preheat the target), the optimal interaction domain for ICF is that of medium-Z ablator, typically plastic, carbon or beryllium. The energy from the collisional absorption of the laser is mostly deposited at a critical density $n_c \propto \lambda_L^{-2}$ that defines the location of the electromagnetic wave reflection. In order to

maximize the coupling to the solid target, the critical density must be as close as possible to the solid density.

Considering the importance of (i) coupling the laser energy from collisional absorption as efficiently as possible to the solid target and (ii) the issues raised by nonlinear LPIs, which thresholds scale in $I\lambda_L^2$, the technology of choice for ICF is that of short wavelength (and high power) lasers. The lasers used in fusion science are based on Neodymium-doped glass (Nd:Glass) amplifiers at the fundamental wavelength of 1054 nm (for phosphate glasses). The laser light is frequency tripled prior to its interaction with the target, to a wavelength of 351 nm. The frequency tripling process allows to increase the critical density by a factor of 9 and increase the absorption efficiency, the ablation pressure (4) and the intensity threshold for nonlinear LPIs. However, the overall laser efficiency is rather poor, of the order of a few %.

When the interaction parameter $I\lambda_L^2$ crosses the threshold of $\sim 10^{14}$ Wμm^2/cm^2, the laser plasma interaction becomes prone to numerous couplings between electromagnetic and plasma waves [20, 44, 45]. Most of these additional processes, summarized in Fig. 0-2, have nonlinear behaviors and are in general nefarious to the implosion [46, 47]. The most prominent mechanisms are the coupling of the laser light to local plasma modes, the *Electron Plasma Waves* (EPW) (processes of *Stimulated Raman Scattering* (SRS) and *Two-Plasmon Decay* (TPD)) and *Ion Acoustic Waves* (IAW) (process of *Stimulated Brillouin Scattering* (SBS)). Considering the laser intensities used in ICF, the non-linear LPIs can be categorized according to their potentially detrimental effects for the capsule implosion:

- Symmetry breaking hazards;
  - The overlap of laser beams in plasma produces ion acoustic waves (IAW) due to the ponderomotive force that can lead to energy exchange between the beams through the diffraction process. This particular case of the three-wave interaction is also referred to as *Cross-Beam Energy Transfer* (CBET). Early theoretical work [48] showed that resonantly excited IAWs can be driven in the framework of the baseline National Ignition Facility (NIF) configuration [49], and indeed CBET is now used to tune the symmetry irradiation in indirect drive ICF [29]. Direct-drive configurations have also been found to be prone to the CBET instability [27, 50], affecting both the symmetry of the implosion and the laser-target coupling.
  - Similarly, any instability that induces some degree of scattered light may lead to variations in the irradiation symmetry. Notably, the SBS and SRS instabilities can scatter large portions of laser light. Considering that an irradiation uniformity of the order of 1% must be kept in order to reach the required compression factors of hotspot ignition, these processes are significant.
- Pre-heat hazards;
  - Any LPI that drives electron plasma waves to sufficiently high phase velocities may accelerate electrons to high energies. Most notably, the SRS and TPD instabilities can drive electrons to energies of up to several hundred of keV, which may raise the adiabat of the shell and decrease the hydrodynamic efficiency of the implosion.

  - In addition to the shell preheat, high energy electron populations generated by nonlinear LPIs directly affect the plasma dynamics [31, 32] by altering the shock propagation and strength. This is of particular importance for the Shock Ignition scheme, for which the effect of hot electrons is uncertain [51].

- Coupling losses;

  - In addition to the geometry breaking effects, the parametric instabilities amplify the scattered waves thus deteriorating the coupling losses. Notably, in direct-drive configurations, CBET shifts energy from incoming beams to outgoing beams and thus, laser energy is taken away from the critical density, which in turns decreases the laser-target coupling.
  - More generally, large volumes of an underdense plasma lead to significant amounts of backscattered light thus decreasing the laser-target coupling.

- Other;

  - Laser *filamentation*, which results from the laser beam refraction in local density inhomogeneities amplified thermally and ponderomotively by the focused beam, leads to strong and localized electric fields and density modulations that may amplify other instabilities.
  - *Resonant Absorption* (RA), that is the absorption of laser light due to the resonant excitation of the electron plasma wave at the critical density. It can lead to significant absorption fractions in the early stages of the interaction when the density profile is sufficiently steep. However, it is commonly considered that hot electrons accelerated by EPWs driven by the resonantly excited electric field are in general too cold to cause a significant preheat [36].

The development of nonlinear processes is controlled on some degree by the use of temporal and spatial beam smoothing techniques, which work by altering the intensity fluctuations and coherence properties of laser beams in their focal plane. These optical methods are crucial to the reduction of nonlinear LPI growth and the mitigation of hydrodynamic instabilities. More generally, optical smoothing techniques are widely used in high power laser systems in order to control the properties of laser beams. As such, these are an integral part of the description of the laser-plasma interaction.

Considering the vacuum laser wavelength of $\lambda_L = 351$nm, the typical laser intensity is $\sim 5 \times 10^{14}$ W/cm^2 during the compression phase of shock ignition and $\sim 5 \times 10^{15}$ W/cm^2 during the spike. Both stages are prone to nonlinear LPIs, although in different regimes. While the compression phase is less sensible to HE preheat and symmetry breaking issues than the standard hotspot scheme because of a lower laser intensity, the laser spike employed for the generation of the strong shock lies in a strongly nonlinear interaction regime. Considering typical spike durations of ~ 500 ps at peak intensity, nonlinear LPIs have ample time to develop and (i) drive copious amounts of high energy supra-thermal electrons, and (ii) significantly reduce the laser-target coupling for the strong shock generation through CBET. Although the shock ignition scheme

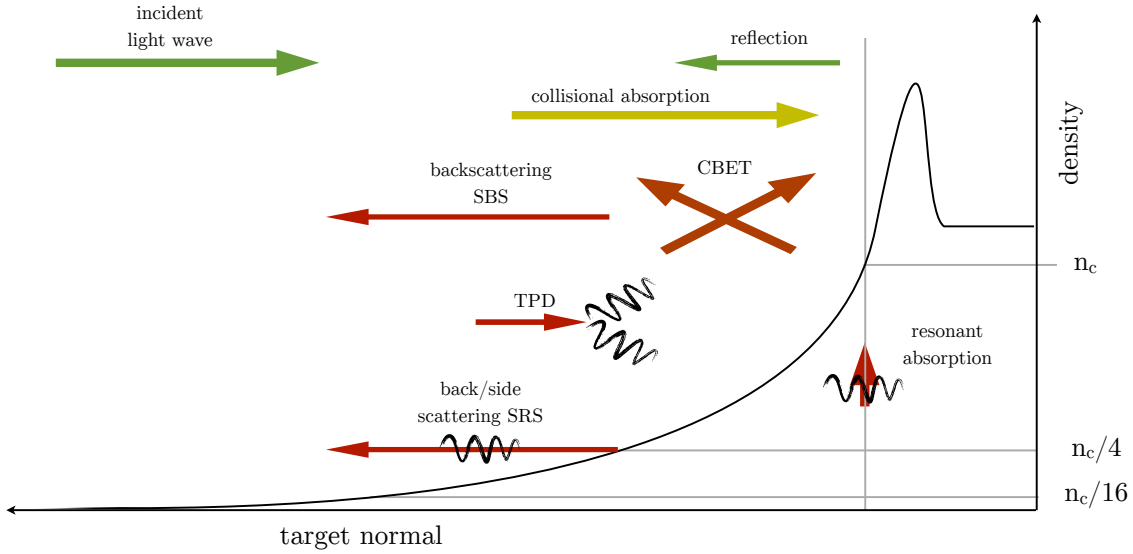

Figure 0-2 – *(color) Schematic diagram of some of the LPI processes involved in Inertial Confinement Fusion, as a function of the coronal plasma density profile along the normal of the target. The color code indicates linear LPI processes in yellow and nonlinear processes in red. Black curly lines indicate the excitation of Electron Plasma Waves.*

promises higher gains and better robustness than the conventional hotspot ignition scheme, the physics of the laser-plasma interaction must be carefully investigated, especially during the laser spike.

0.3 Objective of this work

The subject of this work is: *Multiscale Description of the Laser-Plasma Interaction, Application to the Physics of Shock Ignition in Inertial Confinement Fusion.* It is separated in two parts. The first part is dedicated to the description of the LPI coupling processes at the scales of a target's hydrodynamics. Such a description is motivated by the interpretation and design of laser-based HEDP experiments in general, be it of Laboratory Astrophysics or Inertial Confinement Fusion. The second part of this work is dedicated to the study on large hydrodynamic scales of the typical highly nonlinear LPIs representative of the final phase of shock ignition ICF. The objectives of the thesis are formulated as follows.

- Given the scale discrepancy that arises from the description of both; the target dynamics and the rich variety of processes at play in the Laser-Plasma-Interaction, we wish to propose a suitable laser model that can describe the laser propagation as well as linear and nonlinear processes at hydrodynamic scales. This laser model must: (i) be well adapted for the computation of nonlinear LPIs, (ii) be CPU-efficient at the large-scales at play and (iii) reproduce the main characteristics of laser beams used in high power laser systems, including the effects of smoothing techniques.

- Given the interaction regime of $I\lambda_L^2 \in [10^{13}\text{-}10^{17}]$ Wμm^2/cm^2, the description of the nonlinear LPIs must account for: (i) acceleration and transport of high energy electrons by parametric instabilities and resonant absorption, (ii) scattering of laser energy by nonlinear processes, particularly by Cross-Beam Energy Transfer and (iii) competition between LPI processes. With the aim of an implementation in a hydrodynamic code, this model must be implemented in an inline-approach, i.e. fully-coupled to the hydrodynamics.

- Given two of the main issues related to nonlinear-LPIs in Shock Ignition ICF, that are the irradiation field symmetry-breaking from CBET, and the target pre-heating from parametric instabilities, the study of the SI scheme is conducted in two steps: (i) the study of the CBET and how it affects the hydrodynamics of an imploding spherical target and (ii) the study of the effect of high-energy electron beams on shock dynamics, and how they affect the ignition conditions of the target.

0.4 Organization of the manuscript

The description of the multiscale laser-plasma interaction model and its application to LPI and ICF problems is divided in 6 Chapters.

Chapter I We present in Ch. 1 the linear theory of Electromagnetic (EM) wave propagation in plasmas. We derive the monochromatic wave equation, base framework of the description of laser beams in plasmas, from Maxwell's equations. The basic theory of the electromagnetic response of the plasma, used throughout this work, is introduced. In order to assess the physical behavior of EM waves propagation in plasmas, we describe various standard solutions of the wave equation, relevant to various sections of this document. Particularly, we define the framework of the scalar wave equation, that is the starting point of most reduced laser propagation models used at hydrodynamic scales.

Chapter II The most widespread approach to the modeling of the laser propagation at hydrodynamic scales, that is the GO-based Ray-Tracing method, is introduced in Ch. 2. After an assessment of the limits of the RT model for the purpose of describing nonlinear LPIs, we propose an adaptation to collisional plasmas and to the framework of a Lagrangian hydrodynamic code of Ray-based Paraxial Complex Geometrical Optics [52] (PCGO). PCGO is an alternate method for describing scalar wavefields that replaces the needle-like rays of GO by Gaussian optical beamlets. We illustrate its usefulness in modeling nonlinear LPIs in the case of the ponderomotive self-focusing instability.

Chapter III The PCGO framework, usually limited to the description of Gaussian beams, is expanded further in Ch. 3. High-power laser beams employ Phase Plates (PP), optical elements used to control the spatial shape of their intensity profile. Making use of the properties of PP-smoothed beams, we present a method that can be employed to reproduce realistic beams using PCGO beamlets. Additional reduced models are presented, that allow to account for various smoothing techniques within the PCGO framework.

Chapter IV Building on the technique of Gaussian optical beamlets, we treat separately two branches of nonlinear LPI problems. First, we propose in Ch. 4 an inline PCGO-based approach to the modeling of CBET in large-scale hydrocodes. The latter model is validated against theoretical works, cross-validated with a paraxial wave solver, and compared to experimental data. It is used in an academic study of direct-drive ICF subject to CBET.

Chapter V An inline model to treat the laser/plasma/hot-electron coupling is presented in Ch 5. We propose a supra-thermal electron transport model, and present its validation against a reference solution. Various reduced models are then proposed in order to relate the RA, SRS and TPD mechanisms to HE fluxes and temperatures. The resulting multiscale model fully couples the description of laser propagation, the definition of HE sources, and the propagation of HE beams.

Chapter VI Finally, we present in Ch. 6 a validation of the LPI-HE model against several experiments in various geometries. Given a good agreement observed with the experimental data, the physics of coupling LPI-generated HEs to the target dynamics is investigated. It is notably found that LPI-generated HEs significantly affect the properties of shock propagating in the target. Lastly, the multiscale LPI-HE model is applied to a Shock Ignition configuration, in order to assess the influence of LPIs generated during the final laser spike onto the implosion dynamics.

Conclusions of this work are presented in Ch 7.

Chapter 1

Linear theory of electromagnetic waves in plasmas

We present in this chapter the linear theory of electromagnetic wave propagation and interaction with plasmas. Starting from the microscopic Maxwell's equations in Sec. 1.1, we derive the monochromatic wave equation in an inhomogeneous plasma, base framework of the description of laser-plasma interactions. This notably requires to examine the microscopic structure of the plasma to determine its electromagnetic response, from kinetic theory. Solutions of the wave equation for a homogeneous plasma are used to illustrate the base properties of transverse electromagnetic wave propagation and collisional absorption, in Sec. 1.2. The framework of light wave propagation is extended to inhomogeneous plasmas in Sec. 1.3, using various standard approaches and highlighting the particular processes of collisional and resonant absorption. The scalar wave equation, basis of the large-scale description of wave-fields, is also derived. Longitudinal plasma waves, which constitute eigenmodes of the plasma, are briefly described in Sec. 1.4. Finally, parametric instabilities are presented in Sec. 1.5 with the objective of highlighting the most unstable configurations encountered in inhomogeneous plasmas.

1.1 Maxwell's equations in plasmas

1.1.1 Macroscopic Maxwell's equations

The description of the temporal and spatial evolution of magnetic and electric fields, as well as their interaction with each other and with local charges and currents, was first proposed by J. C. Maxwell [53]. It consisted of a set of 20 equations with 20 variables, that were put together in a more "modern" form by O. Heaviside [54] in 1891 (concurrently with J. W. Gibbs and H. Hertz) in 4 equations of 4 variables in vector notations. The latter *Hertz-Heaviside* and *Maxwell-Hertz* restatement of the original equations is referred to as the *Maxwell's equations* in the modern literature, and reads:

$$\textit{Gauss' law} \; ; \quad \nabla.\boldsymbol{E} = \frac{\rho}{\epsilon_0} \; ,$$
$$\textit{Gauss' law for magnetism} \; ; \quad \nabla.\boldsymbol{B} = 0 \; ,$$

$$\begin{aligned} &\textit{Maxwell-Faraday} \ ; \quad \nabla \times \boldsymbol{E} = -\frac{\partial \boldsymbol{B}}{\partial t} \ , \\ &\textit{Maxwell-Ampere} \ ; \quad \nabla \times \boldsymbol{B} = \mu_0 \boldsymbol{J} + \mu_0 \epsilon_0 \frac{\partial \boldsymbol{E}}{\partial t} \ , \end{aligned} \tag{1.1}$$

where $\boldsymbol{E}$ and $\boldsymbol{B}$ are the electric and magnetic fields, ϵ_0 and μ_0 are the vacuum electric and magnetic permittivities, $\boldsymbol{J}$ is the electric current density and ρ is the charge density. The charge and current densities are related by the *continuity equation*:

$$\frac{\partial \rho}{\partial t} + \nabla . \boldsymbol{J} = 0 \ , \tag{1.2}$$

and the current density is related to the electric field by the conductivity tensor, which contains all the information on the dielectric properties of the medium. The set of Eqs. (1.1) constitute the basis of the classical theory of ElectroMagnetic (EM) fields. In this form, it describes the evolution of EM fields with respect to punctual charges and currents. Applying Maxwell's equations to continuous media requires the introduction of additional fields that include the macroscopic properties of the medium.

Considering a large-scale environment composed of n microscopic sources of currents and charges, the microscopic fields $\boldsymbol{e}$ and $\boldsymbol{b}$ created by the n microscopic sources are solutions of n systems of Eqs. (1.1). Considering (i) a very large number n, that for solid matter is of the order of 10^{23} per cubic centimeter, and (ii) that the dynamics of the microscopic sources is by definition governed by quantum effects, an averaged description of the field on classical length scales is required. As such, we define averaged magnetic and electric fields $\boldsymbol{E} = \langle \boldsymbol{e} \rangle$ and $\boldsymbol{B} = \langle \boldsymbol{b} \rangle$, which obey the Maxwell's and continuity equations with the averaged current and charge densities $\langle \boldsymbol{J} \rangle$ and $\langle \rho \rangle$. The averaging process for the sources requires to account for the detailed atomic structure of the medium, thus allowing to formulate the Maxwell's equation for continuous media.

The average charge density $\langle \rho(\mathbf{r}, t) \rangle$ as a function of the spatial and temporal coordinates $\mathbf{r}$ and t can be estimated by [55]:

$$\langle \rho(\mathbf{r}, t) \rangle \simeq \rho(\mathbf{r}, t) - \nabla . \boldsymbol{P}(\mathbf{r}, t) \ , \tag{1.3}$$

with ρ the *net average charge density* and $\boldsymbol{P}$ the *polarization density*, defined by:

$$\rho(\mathbf{r}, t) = \left\langle \sum_m q_m \delta(\mathbf{r} - \mathbf{r}_m(t)) + q_e \sum_i \delta(\mathbf{r} - \mathbf{r}_i(t)) \right\rangle \ , \tag{1.4}$$

$$\boldsymbol{P} = \left\langle \sum_m \delta(\mathbf{r} - \mathbf{r}_m(t)) \mathbf{d}_m(t)) \right\rangle \ , \tag{1.5}$$

where q_m and $\mathbf{d}_m(t)$ are the total charge and dipole moment of the m-th molecular component located at position $\mathbf{r}_m(t)$, $\mathbf{r}_i(t)$ is the position of the i-th free conduction electron of charge q_e. The polarization density $\boldsymbol{P}$ is a measure of the density of the dipole moments carried by the molecules in the system. In general, a finite polarization $\boldsymbol{P}$ comes from the presence of an electric field $\boldsymbol{E}$. This field-induced polarization results from (i) the displacement of electronic clouds in the electric field and (ii) changes in spatial alignments of molecules that carry an intrinsic dipole moment. The other term in Eq. (1.3), that is the net average charge density ρ, is in general zero

unless *external charges* ρ_{ext} are present in the system.

In a similar fashion, the averaged current density can be estimated by [55]:

$$\langle \boldsymbol{J}(\mathbf{r},t)\rangle \simeq \boldsymbol{J}(\mathbf{r},t) + \frac{\partial \boldsymbol{P}}{\partial t} + \nabla \times \boldsymbol{M} \ , \tag{1.6}$$

with $\boldsymbol{J}$ the *net average current* and $\boldsymbol{M}$ the *magnetization*, defined by:

$$\boldsymbol{J}(\mathbf{r},t) = \left\langle q_e \sum_i \frac{\partial \mathbf{r}_i}{\partial t}\delta(\mathbf{r}-\mathbf{r}_i)\right\rangle + \left\langle \sum_m q_m \frac{\partial \mathbf{r}_m}{\partial t}\delta(\mathbf{r}-\mathbf{r}_m)\right\rangle \ . \tag{1.7}$$

The net average current density $\boldsymbol{J}$ is the current carried by free charge carriers and molecules in the system, while the magnetization $\boldsymbol{M}$ represents the average density of magnetic dipole moments in the system. The magnetization fields are created by externally imposed macroscopic current distributions, so that $\boldsymbol{M}$ depends on $\boldsymbol{H}$. Similarly to ρ, the net average current density $\boldsymbol{J}$ is in general zero unless *external currents* $\boldsymbol{J}_{\text{ext}}$ are present.

The form of the field equations obtained by substituting the average charge and current densities (1.3) and (1.6) into the Maxwell's equation suggests the introduction of *auxiliary fields* $\boldsymbol{D}$ and $\boldsymbol{H}$, defined as:

$$\begin{aligned} \boldsymbol{D} &= \epsilon_0 \boldsymbol{E} + \boldsymbol{P} \ , \\ \boldsymbol{H} &= \frac{1}{\mu_0}\boldsymbol{B} - \boldsymbol{M} \ , \end{aligned} \tag{1.8}$$

where $\boldsymbol{D}$ is called the *electric displacement field* and $\boldsymbol{H}$ the *magnetizing field*. Given that $\boldsymbol{P}$ is a function of $\boldsymbol{E}$, and that $\boldsymbol{M}$ is a function of $\boldsymbol{H}$, the polarization and magnetization densities are usually approximated by *linear functionals*, with the following general form:

$$\boldsymbol{P}(\mathbf{r},t) = \int \mathrm{d}^3\mathbf{r}' \int_{-\infty}^{t} \mathrm{d}t' \chi_e(\mathbf{r}-\mathbf{r}', t-t')\epsilon_0 \boldsymbol{E}(\mathbf{r}',t') \ , \tag{1.9}$$

$$\boldsymbol{M}(\mathbf{r},t) = \int \mathrm{d}^3\mathbf{r}' \int_{-\infty}^{t} \mathrm{d}t' \chi_m(\mathbf{r}-\mathbf{r}', t-t')\boldsymbol{H}(\mathbf{r}',t') \ , \tag{1.10}$$

where χ_e and χ_m are the *dielectric susceptibility* and *magnetic susceptibility*, respectively. These expressions may also be written as a tensorial convolution product in order to account for anisotropic responses of the material, and the dielectric and magnetic susceptibilities may also depend on the fields $\boldsymbol{E}$ and $\boldsymbol{H}$ in the case of *nonlinear materials*. In the present form, we see that the medium can exhibit the property of spatial and temporal dispersion. The auxiliary fields obey the equations:

$$\nabla.\boldsymbol{D} = \rho \ , \tag{1.11}$$

$$\nabla \times \boldsymbol{H} = \boldsymbol{J} + \frac{\partial \boldsymbol{D}}{\partial t} \ , \tag{1.12}$$

where the $\partial \boldsymbol{D}/\partial t$ term, also noted $\boldsymbol{J}_{\text{pol}}$, has a meaning of the current density induced by the wave. In the linear electromagnetic theory, the materials are characterized on macroscopic scales

by the *constitutive relations*:

$$\boldsymbol{D} = \hat{\epsilon}\boldsymbol{E} \ , \tag{1.13}$$

$$\boldsymbol{H} = \frac{1}{\hat{\mu}}\boldsymbol{B} \ , \tag{1.14}$$

where $\hat{\epsilon}$ and $\hat{\mu}$ are the *dielectric permittivity* and *magnetic permittivity*, that depend on the physical characteristics of the medium. Those may represent anisotropic materials (i.e. $(\hat{\epsilon}, \hat{\mu})$ are tensors), inhomogenous materials (i.e. $(\hat{\epsilon}, \hat{\mu})$ vary in space) and absorptive or dispersive materials (i.e. $(\hat{\epsilon}, \hat{\mu})$ are frequency dependent and complex).

Finally, the *macroscopic Maxwell's equations* read:

$$\nabla.\boldsymbol{D} = \rho_{\text{ext}} \ , \tag{1.15}$$

$$\nabla.\boldsymbol{B} = 0 \ , \tag{1.16}$$

$$\nabla \times \boldsymbol{E} = -\frac{\partial \boldsymbol{B}}{\partial t} \ , \tag{1.17}$$

$$\nabla \times \boldsymbol{H} = \boldsymbol{J}_{\text{ext}} + \frac{\partial \boldsymbol{D}}{\partial t} \ , \tag{1.18}$$

where we have assumed that the non zero contributions to the net average charge and currents originate from the external sources. In this form, the macroscopic behavior of the material is factorized into the auxiliary fields through the constitutive relations. This set of equations, which is more convenient for the macroscopic description of light wave propagation in materials, is also referred to as *Maxwell's equations in matter*.

1.1.2 Electromagnetic response of plasma: kinetic theory

Plasmas are gases constituted of charged particles, electrons and ions, which interact collectively through electromagnetic forces. In order to resolve Maxwell's equations in plasma, we must determine the form of constitutive relations (1.13) and (1.14), which are, in general, non-stationary and nonlocal. First, we restrict the constitutive relations to the framework of interest to this work and then use kinetic theory to determine the electromagnetic response of the plasma.

1.1.2.1 Constitutive relations

From now on and in the rest of this work, we consider the case of monochromatic waves of frequency ω, such that the fields are proportional to $\exp[-\imath\omega t]$. Furthermore, we assume that there are no external charges or currents in the system, so that $\rho_{\text{ext}} = 0$ and $\boldsymbol{J}_{\text{ext}} = 0$. Finally, we consider plasmas with weak magnetic fields, which implies $\boldsymbol{M} = 0$. This is a good approximation for typical ICF plasmas, where the electron gyration frequency around magnetic field lines is much smaller than the typical collision frequency.

Assuming the plasma is a linear material (i.e. ϵ does not depend on $\boldsymbol{E}$ and $\boldsymbol{B}$), the constitutive relations read, in the Fourier space:

$$\boldsymbol{D} = \epsilon\boldsymbol{E} = \epsilon_0\boldsymbol{E} + \boldsymbol{P} = \epsilon_0(1+\chi_e)\boldsymbol{E} \ , \tag{1.19}$$

$$\boldsymbol{H} = \boldsymbol{B}/\mu_0 \ , \tag{1.20}$$

where the dielectric susceptibility χ_e remains to be expressed. The Maxwell-Ampere equation (1.18) now reads $\nabla \times \boldsymbol{B} = \mu_0 \boldsymbol{J}_{\text{pol}} = -\mu_0 \imath\omega \boldsymbol{D} = -\imath c^2(1+\chi_e)\boldsymbol{E}$, so that χ_e can be determined by relating the current in the plasma to the electric field. This relation also defines the plasma conductivity σ, with $\boldsymbol{J}_{\text{pol}} = \sigma \boldsymbol{E}$.

1.1.2.2 Vlasov-Fokker-Planck equation

The most accurate classical microscopic description of a plasma consists in characterizing each particle by its position $\mathbf{r}$ and momentum $\mathbf{p}$ as a function of time. The forces acting on the particles can be decomposed in two components; the *external* forces applied to the plasma, and the *internal* forces arising from the mutual interactions between particles. The internal force is responsible for the collective behavior of the system. This force fluctuates rapidly in both space and time, whereas global external forces applied to the plasma vary on a macroscopic scale. It is advantageous to consider a description of the plasma that is averaged on small elementary volumes in order to obtain a continuous-like description. This procedure requires the hypothesis of *weak correlations* between particles: their separation must be large enough so that their trajectories are mainly determined by average forces (internal or external), i.e. the microscopic fluctuations created by the local influence of other particles are relatively small. In this framework, the ion and electron distribution functions f_i and f_e (noted f_α), averaged over microscopic volumes, obey the kinetic equation:

$$\frac{\partial f_\alpha}{\partial t} + \mathbf{v}.\nabla_{\mathbf{r}} f_\alpha + \mathbf{F}_\alpha.\nabla_{\mathbf{p}} f_\alpha = 0 \ , \tag{1.21}$$

where $\mathbf{v} = \mathbf{p}/(m_\alpha \gamma)$ is the velocity variable, γ is the particle relativistic factor and $\mathbf{F}_\alpha$ is the self-consistent force. In the case of a plasma, $\mathbf{F}_\alpha$ is the Lorentz force arising from the self-consistent electric and magnetic fields $\boldsymbol{E}$ and $\boldsymbol{B}$: $\mathbf{F}_\alpha = (q_\alpha/m_\alpha)(\boldsymbol{E} + \mathbf{v} \times \boldsymbol{B})$ with q_α the particle charge. In that case, the kinetic equation is called *Vlasov equation*. This formalism is valid for length scales larger than or comparable to the Debye length, Eq. (1.34). This corresponds to the collisionless limit.

The correlations between particle motion are taken into account with a *collision integral*: an additional term on the right hand side of Eq. (1.21). Considering perturbations of up to the order 2 in the correlation term between particles, the *Vlasov-Fokker-Planck equation* reads:

$$\frac{\partial f_\alpha}{\partial t} + \mathbf{v}.\nabla_{\mathbf{r}} f_\alpha + \mathbf{F}_\alpha.\nabla_{\mathbf{p}} f_\alpha = \sum_\beta C_{\alpha\beta} \ , \tag{1.22}$$

where $\sum_\beta C_{\alpha\beta}$ is the collision integral, describing the binary collisions of charged particles due to their Coulomb interaction in a plasma.

1.1.2.3 Collision integral

In the general case of a collisional plasma, the current density can be estimated from the Vlasov-Fokker-Planck equation (1.22) with a simplified collision term, the *Krook operator*, that represents

a relaxation towards a local thermal equilibrium:

$$\sum_\beta C_{\alpha\beta} = -\sum_\beta \nu_{\alpha\beta}(f_\alpha - f^M_{\alpha\beta}) \ , \tag{1.23}$$

where f_α is the distribution function of species α and $f^M_{\alpha\beta}$ is a Maxwellian distribution function that depends on mean temperatures $T_{\alpha\beta}$ and velocities $\mathbf{u}_{\alpha\beta}$ defined by the conservation of density, momentum and energy in the binary interaction of the α and β species:

$$f^M_{\alpha\beta} = \left(\frac{m_\alpha}{2\pi k_\mathrm{B} T_{\alpha\beta}}\right)^{3/2} \exp\left[-\frac{m_\alpha(\mathbf{v}-\mathbf{u}_{\alpha\beta})^2}{2k_\mathrm{B}T_{\alpha\beta}}\right] \ , \tag{1.24}$$

$$n_\alpha = \int f_\alpha \mathrm{d}^3 v \ , \tag{1.25}$$

$$(n_\alpha m_\alpha + n_\beta m_\beta)\mathbf{u}_{\alpha\beta} = \int \mathbf{v}(m_\alpha f_\alpha + m_\beta f_\beta)\mathrm{d}^3 v \ , \tag{1.26}$$

$$\frac{3}{2}(n_\alpha + n_\beta)k_\mathrm{B}T_{\alpha\beta} = \frac{1}{2}\int (\mathbf{v}-\mathbf{u}_{\alpha\beta})^2(m_\alpha f_\alpha + m_\beta f_\beta)\mathrm{d}^3 v \ . \tag{1.27}$$

We now consider that the species are close to Maxwellian distributions f^M_α, such that $f_\alpha = f^M_\alpha + f^1_\alpha$ with f^1_α a small perturbation. The Maxwellian distribution f^M_α is characterized by a temperature T_α and reads:

$$f^M_\alpha = \left(\frac{m_\alpha}{2\pi k_\mathrm{B} T_\alpha}\right)^{3/2} n^0_\alpha \exp\left[-\frac{m_\alpha v^2}{2k_\mathrm{B}T_\alpha}\right] \ . \tag{1.28}$$

In order to linearize the Krook operator, we develop $f^M_{\alpha\beta}$ in series around $u_{\alpha\beta} = 0$ and $T_{\alpha\beta} = T_\alpha$:

$$\overline{f^M_{\alpha\beta}} = f^M_\alpha + \delta\mathbf{u}_{\alpha\beta}.\left(\frac{\partial f^M_{\alpha\beta}}{\partial \mathbf{v}}\right)_{u_{\alpha\beta}=0, T_{\alpha\beta}=T_\alpha} + \delta T_{\alpha\beta}\left(\frac{\partial f^M_{\alpha\beta}}{\partial T_{\alpha\beta}}\right)_{u_{\alpha\beta}=0, T_{\alpha\beta}=T_\alpha} \ , \tag{1.29}$$

where

$$(n^0_\alpha m_\alpha + n^0_\beta m_\beta)\delta\mathbf{u}_{\alpha\beta} = \int \mathbf{v}(m_\alpha f^1_\alpha + m_\beta f^1_\beta)\mathrm{d}^3 v \ , \tag{1.30}$$

$$\frac{3}{2}(n^0_\alpha + n^0_\beta)k_\mathrm{B}\delta T_{\alpha\beta} = \frac{1}{2}\int (\mathbf{v})^2(m_\alpha f^1_\alpha + m_\beta f^1_\beta)\mathrm{d}^3 v \ , \tag{1.31}$$

$$n^0_\alpha = \int f^0_\alpha \mathrm{d}^3 v \ , \tag{1.32}$$

so that the linearized Krook operator using $\overline{f^M_{\alpha\beta}}$ finally reads:

$$\overline{\sum_\beta C_{\alpha\beta}} = -\sum_\beta \nu_{\alpha\beta}\left[f^1_\alpha - \frac{m_\alpha \mathbf{v}.\delta\mathbf{u}_{\alpha\beta}}{k_\mathrm{B}T_\alpha} f^M_\alpha\right] \ , \tag{1.33}$$

where we have simplified the expression by considering that temperature variations are of second order compared to velocity variations. The linearized Krook operator involves various collision frequencies that must be explicitly defined in order to estimate the plasma conductivity.

1.1.2.4 Collision frequencies

The momentum transfer between two colliding charged particles can be described by a collision cross-section that presents the particularity of (i) diverging for long-range interactions, because of the infinite range of the Coulomb potential, and (ii) involving quantum effects for interactions at a distance less than the De Broglie length. In plasmas, electrons quickly react to any excess positive charge and move to compensate it. This process acts to shield the electrostatic potential created by charge carriers, so that the collision cross-section remains finite for long-range interactions. The electrostatic potential decreases exponentially over a characteristic length scale, called the *Debye length*:

$$\lambda_D = \left[\sum_{j=e,i} \frac{q_j^2 n_j}{\epsilon_0 k_\mathrm{B} T_j} \right]^{-1/2} . \tag{1.34}$$

Considering a particle of species α, with a velocity v_α, colliding with a distribution of particles β of number density n_β, the average collision frequency reads [36]:

$$\nu_{\alpha\beta} = 4\pi \left\langle \frac{n_\beta (q_\alpha q_\beta)^2}{(4\pi\epsilon_0)^2 \mu^2 v_\alpha^3} \ln\Lambda \right\rangle , \tag{1.35}$$

where $\mu = m_\alpha m_\beta/(m_\alpha + m_\beta)$, q_i is the charge of particle i, and $\ln\Lambda$ is the *Coulomb logarithm* that accounts for the short-range and long-range processes at play in the collision. The average in (1.35) is taken over the velocity distributions of particles α and β. Assuming that the Coulomb logarithm vary weakly with the velocity, and considering the distribution functions of the particles to be Maxwellian, the average collision frequency reads [56]:

$$\nu_{\alpha\beta} = \frac{4}{3}\sqrt{2\pi}\langle n_\beta\rangle \frac{\langle q_\alpha q_\beta\rangle^2}{(4\pi\epsilon_0)^2 \mu^2 \left(\langle v_\alpha^2\rangle/3\right)^{3/2}} \ln\Lambda . \tag{1.36}$$

Applying this formula to electron-electron collisions ($\mu = m_e/2$), electron-ion collisions ($\mu \approx m_e$) and ion-ion collisions ($\mu = m_i/2$), we obtain:

$$\nu_{ee} = \frac{1}{6\sqrt{2}\pi^{3/2}} \frac{\sqrt{2} n_e e^4 \ln\Lambda_{ee}}{\epsilon_0^2 m_e^2 v_{T,e}^3} , \tag{1.37}$$

$$\nu_{ei} = \frac{1}{6\sqrt{2}\pi^{3/2}} \frac{\langle Z^2\rangle}{\langle Z\rangle} \frac{n_e e^4 \ln\Lambda_{ei}}{\epsilon_0^2 m_e^2 v_{T,e}^3} , \tag{1.38}$$

$$\nu_{ii} = \frac{1}{6\sqrt{2}\pi^{3/2}} \frac{\langle Z^4\rangle}{\langle Z\rangle} \frac{\sqrt{2} n_e e^4 \ln\Lambda_{ii}}{\epsilon_0^2 m_i^2 v_{T,i}^3} . \tag{1.39}$$

In the case of multiple ion species, more collision frequencies could be introduced. A simplified description is often considered where all ion species are represented by a single *average ion*. Then, the expression for ν_{ei} motivates the definition of an *effective charge state* $Z_\mathrm{eff} = \langle Z^2\rangle/\langle Z\rangle$, where the average is taken over the ion species concentration. In a non-magnetized plasma, each free plasma mode (longitudinal and transverse waves, see Secs. 1.2 and 1.4) is damped according to these collisional rates, and eventually with additional Landau damping terms. Note that in general, the electron-electron coefficient can be neglected compared to the electron-ion coefficient

for $Z \geq 4$.

1.1.2.5 Dielectric susceptibility of the plasma

We now consider the case of electrons accelerated in a homogeneous electric field oscillating at a frequency ω. The ions of a charge Z are supposed to be at a thermal equilibrium, described by a Maxwellian distribution f_i^M (and $f_i^1 = 0$). We define the electron distribution function $f_e = f_e^M + f_e^1$ with f_e^1 a small perturbation. Assuming that the phase velocity of the wave is much larger than the electron thermal velocity, the linearized kinetic equation reads [36]:

$$\frac{\partial f_e^1}{\partial t} - \frac{e}{m_e}\boldsymbol{E}.\nabla_{\mathbf{p}} f_e^M = -\sum_{\beta\in\{e,i\}} \nu_{e\beta}\left[f_e^1 - \frac{m_e \mathbf{v}.\delta\mathbf{u}_{e\beta}}{k_{\mathrm{B}}T_e} f_e^M\right] , \tag{1.40}$$

where the right hand side is the linearized Krook operator and we have used the time independence of the equilibrium function f_e^M. Because of momentum conservation, the electron-electron collisions do not contribute to the damping of the wave and we can neglect the terms $\propto \nu_{ee}$. Furthermore, considering the low electron to ion mass ratio, the term proportional to the mean velocity perturbation $\delta\mathbf{u}_{ei}$ can be neglected compared to f_e^1. Finally, Eq. (1.40) reads, in Fourier space:

$$-\imath\omega f_e^1 + \frac{e}{k_{\mathrm{B}}T_e}\boldsymbol{E}.\mathbf{v} f_e^M = -\nu_{ei} f_e^1 , \tag{1.41}$$

where we have used the property of the Maxwellian distribution $\nabla_p f_e^M = -\mathbf{v} f_e^M/(k_{\mathrm{B}}T_e)$. Multiplying both sides in Eq. (1.41) by $-e\mathbf{v}$ and integrating in momentum space, we obtain the current density $\boldsymbol{J}_{\mathrm{pol}}$ induced by the oscillating electric field:

$$-\imath\omega\boldsymbol{J}_{\mathrm{pol}} - \frac{e^2}{m_e} n_e^0 \boldsymbol{E} = -\nu_{ei}\boldsymbol{J}_{\mathrm{pol}} , \tag{1.42}$$

where we have used:

$$\boldsymbol{J}_{\mathrm{pol}} = e\int \mathbf{v} f_e^1 \mathrm{d}^3\mathbf{v} . \tag{1.43}$$

Recalling that the current is related to the polarization density by $\boldsymbol{J}_{\mathrm{pol}} = \imath\omega\boldsymbol{P}$ and using $\boldsymbol{P} = \epsilon_0\chi_e\boldsymbol{E}$ we obtain an expression for the conductivity σ:

$$\boldsymbol{J}_{\mathrm{pol}} = \sigma\boldsymbol{E} = -\imath\omega\epsilon_0\chi_e\boldsymbol{E} = -\frac{n_e^0 e^2}{m_e(\imath\omega - \nu_{ei})}\boldsymbol{E} . \tag{1.44}$$

The imaginary part of the polarization current implies that electrons accelerated in the electric field of the laser decelerate through electron-ion collisions, thus transferring energy from the wave to plasma. This process of collisional absorption is called the *inverse Bremsstrahlung*. A more detailed analysis accounting for ion density fluctuations [57, 36] yields a formulation of the current with a modified Coulomb logarithm $\nu_{\mathrm{IB}} = \nu_{\mathrm{ei}} \ln\Lambda_{\mathrm{IB}}/\ln\Lambda_{ei}$. The latter is termed *inverse Bremsstrahlung collision frequency* and involves a Coulomb logarithm Λ_{IB} that is dependent on the wave frequency ω. Additional corrections are usually made to Λ_{IB}, accounting for quantum mechanical effects related to multi-photon and electron-photon interactions [58, 59, 60]. The expressions for the Coulomb logarithms used in this work are given in App. A.5.

Finally, the dielectric susceptibility χ_e (1.9) and relative permittivity ϵ (1.13) read:

$$\begin{aligned}\chi_e(\omega) &= -\frac{\omega_{\rm pe}^2}{\omega(\omega+\imath\nu_{\rm IB})}\ ,\\ \epsilon(\omega) &= 1-\frac{\omega_{\rm pe}^2}{\omega(\omega+\imath\nu_{\rm IB})}\ ,\end{aligned} \tag{1.45}$$

where $\omega_{\rm pe}$ is the electron plasma frequency, $\omega_{\rm pe}=\sqrt{n_e e^2/(m_e\epsilon_0)}$.

The relative permittivity $\epsilon(\omega)$ can be decomposed into a real and an imaginary part as $\epsilon=\epsilon'+\imath\epsilon''$:

$$\epsilon' = 1-\frac{(\omega_{\rm pe}/\omega)^2}{1+(\nu_{\rm IB}/\omega)^2} \approx 1-\left(\frac{\omega_{\rm pe}}{\omega}\right)^2\ , \tag{1.46}$$

$$\epsilon'' = \frac{\nu_{\rm IB}}{\omega}\frac{(\omega_{\rm pe}/\omega)^2}{1+(\nu_{\rm IB}/\omega)^2} \approx \frac{\nu_{\rm IB}}{\omega}\left(\frac{\omega_{\rm pe}}{\omega}\right)^2\ , \tag{1.47}$$

where we have assumed $\nu_{\rm IB}\ll\omega$ in the right-hand-side of the equations and only retained the term linear on $\nu_{\rm IB}$. The frequency dependence of the dielectric permittivity is a consequence of the dispersive property of plasmas. Having determined ϵ, we can now apply the macroscopic Maxwell's equations to plasmas.

1.2 Base properties of light wave propagation in plasmas

1.2.1 Wave equation

We consider the case of a monochromatic electromagnetic wave propagating in a inhomogeneous, isotropic, dispersive and non-magnetic material. In that framework, fields are proportional to $\exp[-\imath\omega t]$ and the dielectric and magnetic permittivities read $\hat{\epsilon}=\epsilon(\omega,\mathbf{r})$ and $\hat{\mu}=\mu_0$, so that the macroscopic Maxwell's equations read, in the frequency domain:

$$\begin{aligned}\nabla.\boldsymbol{E} &= -(1/\epsilon)\nabla\epsilon.\boldsymbol{E}\ ,\\ \nabla.\boldsymbol{B} &= 0\ ,\\ \nabla\times\boldsymbol{E} &= \imath\omega\boldsymbol{B}\ ,\\ \nabla\times\boldsymbol{B} &= -\imath\omega c^2\epsilon\boldsymbol{E}\ ,\end{aligned} \tag{1.48}$$

which can be expressed as:

$$\begin{aligned}\nabla\times\boldsymbol{E}-\imath\omega\boldsymbol{B} &= 0\ ,\\ \nabla\times\boldsymbol{B}+\imath(\omega/c^2)\epsilon(\omega,\boldsymbol{r})\boldsymbol{E} &= 0\ ,\end{aligned} \tag{1.49}$$

where $\epsilon(\omega,\boldsymbol{r})$ is the complex-valued, inhomogeneous and scalar (i.e. isotropic) dielectric permittivity.

Taking the curl of the first equation in (1.49) and eliminating for $\boldsymbol{B}$ yields:

$$\triangle\boldsymbol{E}+\nabla(\nabla\ln\epsilon.\boldsymbol{E})+(\omega/c)^2\epsilon(\omega,\boldsymbol{r})\boldsymbol{E}=0\ , \tag{1.50}$$

where we have used the vector identity $\nabla \times \nabla \times \boldsymbol{A} = \nabla(\nabla.\boldsymbol{A}) - \triangle \boldsymbol{A}$. We refer to this equation as the wave equation for the electric field. The expression for the magnetic field is derived similarly, by taking the curl of the second equation in (1.49) and eliminating for $\boldsymbol{E}$:

$$\nabla(\nabla.\boldsymbol{B}) - \triangle \boldsymbol{B} + \imath(\omega/c)\nabla \times (\epsilon(\omega, \boldsymbol{r})\boldsymbol{E}) = 0 \ . \tag{1.51}$$

Since $\nabla \times (\epsilon(\omega, \boldsymbol{r})\boldsymbol{E}) = \epsilon(\omega, \boldsymbol{r})\nabla \times \boldsymbol{E} + \nabla\epsilon(\omega, \boldsymbol{r}) \times \boldsymbol{E}$, we get the wave equation for the magnetic field:

$$\triangle \boldsymbol{B} + (\omega/c)^2\epsilon(\omega, \boldsymbol{r})\boldsymbol{B} + \frac{1}{\epsilon(\omega, \boldsymbol{r})}\nabla\epsilon(\omega, \boldsymbol{r}) \times \nabla \times \boldsymbol{B} = 0 \ , \tag{1.52}$$

where we have used $\nabla.\boldsymbol{B} = 0$.

1.2.2 Dispersion relation

The propagation of light waves in homogeneous plasmas of uniform density is now considered. In that case, $\nabla\epsilon(\omega, \boldsymbol{r}) = 0$ and $\nabla.\boldsymbol{E} = 0$, so that Eqs. (1.50) and (1.52) become identical and read:

$$\triangle \boldsymbol{E} + \frac{\omega^2}{c^2}\epsilon(\omega)\boldsymbol{E} = 0 \ , \tag{1.53}$$

$$\triangle \boldsymbol{B} + \frac{\omega^2}{c^2}\epsilon(\omega)\boldsymbol{B} = 0 \ . \tag{1.54}$$

The various components of the electric and magnetic fields in these equations are uncoupled, e.g. the evolution of E_x does not depend on the evolution of E_y. Consequently, their resolution reduces to a set of *scalar wave equations* in the form of *homogeneous scalar Helmholtz equations*:

$$\triangle u(\omega, \boldsymbol{r}) + \frac{\omega^2}{c^2}\epsilon(\omega)u(\omega, \boldsymbol{r}) = 0 \ , \tag{1.55}$$

where $u(\omega, \boldsymbol{r})$ is the scalar wave amplitude, written in the frequency domain, that represents any component of the electric or magnetic field. Assuming u is of the form $u_0 \exp[-\imath \mathbf{k}.\mathbf{r}]$ and taking the spatial Fourier transform of this equation, we obtain the dispersion relation for the EM waves:

$$-k^2 + \frac{\omega^2}{c^2}\epsilon(\omega) = 0 \ . \tag{1.56}$$

It is worth mentioning that this form of the dispersion relation also holds for inhomogeneous plasmas as long as the $\nabla(\nabla \ln \epsilon.\boldsymbol{E})$ term can be neglected compared to the other terms in Eq. (1.50). As it is discussed further in Secs. (1.3.2) and (1.3.4), this depends on the wave polarization.

1.2.3 Wave reflection: the critical density

Considering a collisionless media, with $\epsilon = \epsilon'$, the dispersion relation (1.56) becomes:

$$k^2c^2 = \omega^2 - \omega_{\mathrm{pe}}^2 \ . \tag{1.57}$$

This equation implies that wave propagation can occur only for $\omega > \omega_{\mathrm{pe}}$, in which case the wavevector k is real. For $\omega < \omega_{\mathrm{pe}}$, the plasma electrons react instantaneously to the electric field

modulations of frequency ω, thus shielding the field of the light wave. Note that in vacuum, $\omega_{\rm pe} = 0$ so that the free-space wavenumber of the EM wave is $k_{\rm FS} = \omega/c$. The equality $\omega = \omega_{\rm pe}$ defines the *critical density* beyond which a light wave does not propagate:

$$n_c = \frac{\epsilon_0 \omega^2 m_e}{e^2} \ , \tag{1.58}$$

where ϵ_0 is the vacuum dielectric permittivity and e the electron charge. Plasma regions where the electron density $n_e > n_c$ are called over-dense or super-critical regions, and regions where $n_e < n_c$ are called under-dense or sub-critical regions.

1.2.4 Wave velocity and refraction

The *group velocity* characterizes the rate at which the energy of the wave propagates in space. It is defined as $\mathbf{v}_g = \partial\omega/\partial\mathbf{k}$. Taking the derivative of Eq. (1.57) with respect to k yields $2kc^2 = 2\omega\partial\omega/\partial k$, thus:

$$v_g(\omega) = c\sqrt{1 - \frac{\omega_{\rm pe}^2}{\omega^2}} = c\sqrt{1 - \frac{n_e}{n_c(\omega)}} \ , \tag{1.59}$$

where $v_g = |\mathbf{v}_g|$. This relation indicates that the group velocity of the wave is c in vacuum, and less than c in the plasma. The *phase velocity*, rate at which the phase of the wave propagates in space, is defined as $\mathbf{v}_{\rm ph} = \omega\mathbf{k}/k^2$. Noting that $kc^2 = \omega v_g$, the phase velocity reads:

$$v_{\rm ph}(\omega) = \frac{c}{\sqrt{1 - \omega_{\rm pe}^2/\omega^2}} = \frac{c}{\sqrt{1 - n_e/n_c(\omega)}} \ , \tag{1.60}$$

and we have $v_g v_{\rm ph} = c$. The difference between the phase and group velocities indicates that plasmas are dispersive materials, the light wave refracts at a different rate depending on the frequency. The *refractive index* $n' = c/v_{\rm ph}$ describes how light is refracted by the medium:

$$n'(\omega) = \sqrt{1 - \frac{n_e}{n_c(\omega)}} = \sqrt{\epsilon'(\omega)} \ , \tag{1.61}$$

which is less than 1 in under-dense plasmas. It is interesting to note that this is contrary to light wave propagation in solid materials (such as glass), where the index of refraction is ≥ 1. More generally, the refractive index in optical components increases with the density of the glass, so that light waves tend to bend toward higher densities. On the contrary, the refractive index of plasmas decreases for higher densities, so that light waves tend to bend toward lower densities. Note that the above definitions for the group velocity and phase velocity are unchanged in the case of a dissipative media, whereas the index of refraction acquires an imaginary part and is defined as:

$$n^2 = \epsilon = \epsilon' + \imath\epsilon'' \ . \tag{1.62}$$

1.2.5 Effects of a complex dielectric permittivity

We now extend the previous analysis to the case of a dissipative media characterized by $\epsilon = \epsilon' + \imath\epsilon''$.

1.2.5.1 Wave energy

In the general case of a collisional plasma and for a *transverse wave* (where $\boldsymbol{E}$, $\boldsymbol{B}$ and $\mathbf{k}$ form an orthonormal set), the averaged energy density of the electric field $\bar{W}_\mathrm{E}$, magnetic field $\bar{W}_\mathrm{B}$ and averaged energy flux $\bar{\boldsymbol{S}} = \langle \boldsymbol{E} \times \boldsymbol{H} \rangle$ (so-called *Poynting vector*) read:

$$\bar{W}_\mathrm{E} = \frac{\epsilon_0}{4}\frac{\partial}{\partial\omega}(\omega\Re(\epsilon))|E|^2 = \frac{\epsilon_0}{4}\left(1+\frac{\omega_\mathrm{pe}^2}{\omega^2}\right)|E|^2 \ , \tag{1.63}$$

$$\bar{W}_\mathrm{B} = \frac{\langle(\mathbf{k}\times\boldsymbol{E})^2\rangle}{2\mu_0\omega^2} = \frac{\epsilon_0}{4}\left(1-\frac{\omega_\mathrm{pe}^2}{\omega^2}\right)|E|^2 \ , \tag{1.64}$$

$$\bar{\boldsymbol{S}} = \frac{1}{2}\epsilon_0\frac{\mathbf{k}c^2}{\omega}|E|^2 = \frac{1}{2}\epsilon_0\frac{\mathbf{k}}{k}cn'|E|^2 \ . \tag{1.65}$$

It follows from these equations that $\bar{\boldsymbol{S}} = \mathbf{v}_g\bar{W}$, with $\bar{W} = \bar{W}_\mathrm{E} + \bar{W}_\mathrm{B}$. The latter relation shows that despite the dissipation of electromagnetic energy into the medium, the group velocity can still be interpreted as the rate of wave energy propagation in space. Consequently, the electromagnetic energy density propagating at the group velocity of the wave per unit area reads:

$$I = |\mathbf{v}_g\bar{W}| = cn'\epsilon_0E_0^2/2 \ . \tag{1.66}$$

This quantity is the wave *intensity*, a key definition used in the description of laser-plasma interactions.

1.2.5.2 Complex refractive index

Assuming a complex dielectric permittivity, the refractive index can be decomposed in a real part and imaginary part $n = n' + n'' = \sqrt{\epsilon}$ and $n^2 = n'^2 - n''^2 + 2\imath n'n''$. Far from the critical density surface, $n' \gg n''$ so that $n'^2 \approx \epsilon'$, as in the collisionless case. Using the full formulation for ϵ, Eq. (1.45), $n' = \Re(\sqrt{\epsilon})$ and $n'' = \Im(\sqrt{\epsilon})$ read:

$$n' = \frac{1}{\sqrt{2}\sqrt{1+(\nu_\mathrm{IB}^2/\omega^2)}}\left[N^2+\frac{\nu_\mathrm{IB}^2}{\omega^2}+\left[\left(1+\frac{\nu_\mathrm{IB}^2}{\omega^2}\right)\left(N^4+\frac{\nu_\mathrm{IB}^2}{\omega^2}\right)\right]^{1/2}\right]^{1/2} \ , \tag{1.67}$$

$$n'' = \frac{(\omega_\mathrm{pe}^2\nu_\mathrm{IB}/\omega^3)}{\sqrt{2}\sqrt{1+(\nu_\mathrm{IB}^2/\omega^2)}}\left[N^2+\frac{\nu_\mathrm{IB}^2}{\omega^2}+\left[\left(1+\frac{\nu_\mathrm{IB}^2}{\omega^2}\right)\left(N^4+\frac{\nu_\mathrm{IB}^2}{\omega^2}\right)\right]^{1/2}\right]^{-1/2} \ , \tag{1.68}$$

where N is the refractive index in collisionless plasmas $N = \sqrt{1-n_e/n_c}$. Taylor expanding at the lowest order in ν_IB/ω around 0 yields:

$$n'_{\nu_\mathrm{IB}\ll\omega} = N + O\left(\frac{\nu_\mathrm{IB}^2}{\omega^2}\right) \ , \tag{1.69}$$

$$n''_{\nu_\mathrm{IB}\ll\omega} = \frac{(\omega_\mathrm{pe}^2\nu_\mathrm{IB}/\omega^3)}{2N} + O\left(\frac{\nu_\mathrm{IB}^2}{\omega^2}\right) \ . \tag{1.70}$$

In practice, the expression (1.69) is used for n' for the computation of electromagnetic wave refraction in plasmas. However it only holds at high temperatures where the collision frequency

is small compared to the light wave frequency (see the discussion in Sec. 1.2.6).

1.2.5.3 Collisional absorption

Starting from the dispersion relation, we relate the imaginary part of the wavevector to the wave damping due to collisions. The dispersion relation (1.56) in a collisional media reads:

$$k^2c^2 = \omega^2 - \frac{\omega_{\rm pe}^2\omega}{\omega + \imath\nu_{\rm IB}} \approx \omega^2 - \omega_{\rm pe}^2\left(1 - \frac{\imath\nu_{\rm IB}}{\omega}\right) = \omega^2\left[N^2 - \imath\frac{\omega_{\rm pe}\nu_{\rm IB}}{\omega^3}\right] \ , \tag{1.71}$$

where it was assumed in the right hand side that $\nu_{\rm IB} \ll \omega$. Similarly to the refractive index, we can express $k = k' + \imath k''$, so that $k^2 = k'^2 - k''^2 + 2\imath k'k''$. Assuming $\nu_{\rm IB} \ll \omega$ we obtain:

$$k'_{\nu_{\rm IB}\ll\omega} = \frac{\omega}{c}\sqrt{1 - \left(\frac{\omega_{\rm pe}}{\omega}\right)^2} = \frac{\omega}{c}N \ , \tag{1.72}$$

$$k''_{\nu_{\rm IB}\ll\omega} = \frac{\omega_{\rm pe}^2\nu_{\rm IB}}{2\omega c\sqrt{\omega^2 - \omega_{\rm pe}^2}} = \frac{\omega_{\rm pe}^2\nu_{\rm IB}}{2\omega^2 cN} \ . \tag{1.73}$$

Considering a plane wave propagating in the z direction, its electric field $\boldsymbol{E} = E\mathbf{e}_x$ can be expressed as $E = E_0\mathrm{e}^{\imath(kz-\omega t)} = E_0\mathrm{e}^{\imath k'z}\mathrm{e}^{-\imath\omega t}\mathrm{e}^{-k''z}$ which gives $|E| = |E_0|\mathrm{e}^{-k''z}$, i.e. the light wave is damped due to the electron-ion collisions. The energy conservation of the wave can be expressed as:

$$\frac{\partial\bar{W}}{\partial t} + \nabla.\bar{\boldsymbol{S}} = -U_s \ , \tag{1.74}$$

where the right-hand-side U_s represents the energy sink due to collisions. The rate of energy loss can be estimated in steady-state from the energy conservation equation (1.74):

$$-\frac{\nabla.\bar{\boldsymbol{S}}}{\bar{W}} = \frac{U_s}{\bar{W}} = \nu^{\rm EM} = 2k''v_g \ , \tag{1.75}$$

where we have defined the damping rate $\nu^{\rm EM}$. As such, $\nu^{\rm EM}\bar{W}$ represents the power density transferred from the wave to the medium due to the dissipation of the polarization current by the electron-ion collisions. Assuming a homogeneous media and using the complete expression of $k'' = \Im(\sqrt{k^2}) = n''k_{\rm FS}$, the electromagnetic wave damping rate reads:

$$\nu^{\rm EM} = \frac{\sqrt{2}N(\omega_{\rm pe}^2\nu_{\rm IB}/\omega^2)}{\sqrt{1 + (\nu_{\rm IB}^2/\omega^2)}}\left[N^2 + \frac{\nu_{\rm IB}^2}{\omega^2} + \sqrt{\left(1 + \frac{\nu_{\rm IB}^2}{\omega^2}\right)\left(N^4 + \frac{\nu_{\rm IB}^2}{\omega^2}\right)}\right]^{-1/2} \ . \tag{1.76}$$

Taylor-expanding this expression at the order 1 in series of $(\nu_{\rm IB}/\omega)$ gives:

$$\nu^{\rm EM}_{\nu_{\rm IB}\ll\omega} = \nu_{\rm IB}\frac{\omega_{\rm pe}^2}{\omega^2} = \nu_{\rm IB}\frac{n_e}{n_c} \ . \tag{1.77}$$

This expression is the standard definition used for the computation of electromagnetic wave absorption in plasmas. As for the refractive index, it only holds at high temperatures and high frequencies (see the discussion in Sec. 1.2.6), whereas the expression given in Eq. (1.76) is also valid when $\nu_{\rm IB} \geq \omega$.

1.2.6 Common assumptions

Several assumptions have been introduced in this section, namely $\nu_{ei} \ll \omega$ and $\epsilon'' \ll \epsilon'$. We briefly discuss their validity domain.

The first assumption can be assessed in the framework of typical laser-plasma interaction regimes considered in this work. Given that $\nu_{\mathrm{IB}} \propto n_e T_e^{-3/2} \ln \Lambda_{\mathrm{IB}} Z_{\mathrm{eff}}$ and neglecting a weak dependence of $\ln \Lambda_{\mathrm{IB}}$ on the temperature, the assumption $\nu_{ei} \ll \omega$ holds along the trajectory of EM wave propagation if it holds at the critical density. Using typical values of $\ln \Lambda_{\mathrm{IB}} = 8$, $Z_{\mathrm{eff}} = 5$ (that corresponds to a medium Z ablator), $\lambda_L = 351$ nm and $n_e = n_c$, the temperatures above which $\nu_{\mathrm{IB}} > \omega/10$ and $\nu_{\mathrm{IB}} > \omega/100$ are $T_e \sim 160$ eV and $T_e \sim 720$ eV, respectively. Hence, early in the interaction when the laser intensity is low and the plasma is cold, the above assumption may not hold. Rapidly, as the coronal plasma heats up, it enters its validity domain and holds for the rest of the interaction duration.

The second assumption, $\epsilon'' \ll \epsilon'$, is commonly used in hydrodynamic codes because it is necessary to the validity of the Ray-Tracing approach (see Sec. 2.2). It is worth mentioning that this assumption is more restrictive than $\nu_{\mathrm{IB}} \ll \omega$, the latter authorizing $\epsilon'' \geq \epsilon'$ near the critical density (where $\omega \to \omega_{\mathrm{pe}}$). Similarly, the complete expression for ϵ' given in Eq. (1.46) allows to consider plasmas at the critical density (for $\omega = \omega_{\mathrm{pe}}$), which is also of importance for the validity of the reduced models presented in the following chapter. For these reasons, when possible, the assumption of $\nu_{ei} \ll \omega$ should be preferred over that of $\epsilon'' \ll \epsilon'$.

1.3 Electromagnetic wave propagation in inhomogeneous plasmas

We now consider the wave propagation in inhomogeneous plasmas, where the density depends of the spatial coordinates. Several approaches to resolving the wave equation are presented, with the aim of highlighting the main properties of the light wave linear interaction with inhomogeneous plasmas, and of assessing the validity domain of typical approaches.

1.3.1 The WKB approximation for collisionless plasma

Assuming that the density inhomogeneity is in the same direction as the wave propagation direction (e.g. the z direction), the electric field is of the form $\boldsymbol{E} = E_x(z)\mathbf{e}_x + E_y(z)\mathbf{e}_y + E_z(z)\mathbf{e}_z$ and the wave equation (1.50) reads, in Cartesian coordinates:

$$\begin{aligned} \frac{\mathrm{d}^2 E_{x,y}}{\mathrm{d}z^2} + \frac{\omega^2}{c^2}\epsilon E_{x,y} = 0 \ , \\ \frac{\omega^2}{c^2}\epsilon E_z = 0 \ , \end{aligned} \tag{1.78}$$

which yields $E_z = 0$, for the transverse wave, and the equation for E_x and E_y are in the form of the scalar wave equation (1.55). In the framework of the WKB approximation (after the name of

the physicists who developed it; Wentzel-Kramers-Brillouin), we seek for solutions of the form:

$$E_x(z) = E_{x,0}(z) \exp\left[\imath k_{\mathrm{FS}} \int_0^z \Psi(z')\mathrm{d}z'\right] , \tag{1.79}$$

where the $E_{x,0}$ and Ψ functions are written in the *Slowly Varying Envelope Approximation* (SVEA), e.g. it is assumed that they vary slowly on a wavelength scale:

$$\left|\frac{\mathrm{d}^2 E_{x,0}(z)}{\mathrm{d}z^2}\right| \ll \left|k_{\mathrm{FS}}\Psi(z)\frac{\mathrm{d}E_{x,0}(z)}{\mathrm{d}z}\right| , \tag{1.80}$$

$$\left|\frac{\mathrm{d}^2 \Psi(z)}{\mathrm{d}z^2}\right| \ll \left|k_{\mathrm{FS}}\Psi(z)\frac{\mathrm{d}\Psi(z)}{\mathrm{d}z}\right| , \tag{1.81}$$

where we have used $k(z) = k_{\mathrm{FS}}\Psi(z)$ (that can be noted from Eq. (1.79)). Substituting for $E_x(z)$ (1.79) in the scalar wave equation (1.55) yields:

$$E''_{x,0} + 2\imath k_{\mathrm{FS}} E'_{x,0}\Psi + \imath k_{\mathrm{FS}} E_{x,0}\Psi' - k_{\mathrm{FS}}^2 E_{x,0}\Psi^2 + k_{\mathrm{FS}}^2 \epsilon(\omega, z) E_{x,0} = 0 , \tag{1.82}$$

where the prime notation designates a derivative with respect to z. At the order 0 in $\mathrm{d}/\mathrm{d}z$, we get:

$$\Psi = \sqrt{\epsilon(\omega, z)} . \tag{1.83}$$

By taking the terms in Eq. (1.82) at the order 1 in $\mathrm{d}/\mathrm{d}z$, we obtain:

$$2E'_{x,0}\Psi + E_{x,0}\Psi' = 0 . \tag{1.84}$$

This differential equation admits a solution:

$$E_{x,0} = C/\sqrt{\Psi} , \tag{1.85}$$

where C is a constant factor. The second order term in Eq. (1.82) is neglected according to the SVEA hypothesis. Injecting Eqs. (1.83) and (1.85) in (1.79) yields:

$$E_x(z) = (E_{\mathrm{FS}}/\epsilon(\omega, z)^{1/4}) \exp\left[\imath k_{\mathrm{FS}} \int_0^z \sqrt{\epsilon(\omega, z')}\mathrm{d}z'\right] , \tag{1.86}$$

where the constant factor C has been set to the free space electric field E_{FS}. This result highlights that the amplitude of the electric field increases as $E_{\mathrm{FS}}\epsilon^{-1/4}$ as the wave propagates toward the critical density. Simultaneously, by conservation of the electromagnetic energy, the magnetic field amplitude decreases as $B_{\mathrm{FS}}\epsilon^{1/4}$.

It was assumed in the derivation of Eq. (1.86) that $E''_{x,0} \ll 2\imath k_{\mathrm{FS}} E'_{x,0}\Psi + \imath k_{\mathrm{FS}} E_{x,0}\Psi'$. A sufficient condition for this assumption to be valid can be written as:

$$\left|E'_{x,0}\right| \ll |k(z)E_{x,0}| . \tag{1.87}$$

Substituting the solution for $E_{x,0}$ yields:

$$\frac{1}{\epsilon}\left|\frac{\mathrm{d}\epsilon}{\mathrm{d}z}\right| \ll \frac{8\pi}{\lambda(z)} \ , \tag{1.88}$$

that is, the fractional change in the plasma dielectric function must be small on the scale of the local wavelength. This condition shows that the WKB approximation breaks down for steep density gradients and near the critical density, where $\epsilon \to 0$ and $\lambda \to \infty$, i.e. it is only valid for a weakly inhomogeneous plasma and sufficiently far from the critical density.

1.3.2 Laser absorption in inhomogeneous plasmas

We now consider the case of collisional absorption of a light wave propagating in the (y, z) plane and incident at an initial angle θ on a plasma with a linear density profile such that $N^2(z) = 1 - z/L = 1 - n_e(z)/n_c$. Depending on the polarization of the wave, two cases must be distinguished. If its electric field lies out the plane of incidence, i.e. $\boldsymbol{E} = E_x(y, z)\mathbf{e}_x$, the wave is termed *s-polarized*. Conversely, if the electric field of the wave lies in the plane of incidence, i.e. $\boldsymbol{E} = E_y(y, z)\mathbf{e}_y + E_z(y, z)\mathbf{e}_z$, the wave is termed *p-polarized*. Depending on the polarization, the wave equation takes a different form and an additional absorption process appears, that is the *Resonant Absorption*. We present the collisional laser absorption fraction in inhomogeneous plasmas in the case of *s*-polarized wave, and describe the mechanism of resonant absorption in the *p*-polarized case.

1.3.2.1 Absorption fraction of *s*-polarized waves

We consider a *s*-polarized wave with an electric field $\boldsymbol{E} = E_x(y, z)\mathbf{e}_x$. The wave equation reads:

$$\frac{\partial^2 E_x}{\partial y^2} + \frac{\partial^2 E_x}{\partial z^2} + k_{\mathrm{FS}}^2 \epsilon(z) E_x = 0 \ . \tag{1.89}$$

Because ϵ only depends on z, k_y is a constant and equal to its value at $z = 0$. Geometrically, we have $k_y^{z=0} = (\omega/c)\sin\theta$ and $k_z^{z=0} = (\omega/c)\cos\theta$. Assuming a plane-wave solution with a spatial dependence for $\boldsymbol{E}$ of the form $\exp(\imath \mathbf{k}.\mathbf{r})$:

$$E_x(y, z) = E(z)\exp(\imath k_y y) = E(z)\exp(\imath(\omega/c)\sin\theta y) \ . \tag{1.90}$$

Substituting this expression for E_x in Eq. (1.89) yields:

$$E(z)\frac{\omega^2}{c^2}\left(\epsilon(z) - \sin^2\theta\right) + \frac{\mathrm{d}^2 E(z)}{\mathrm{dz}^2} = 0 \ . \tag{1.91}$$

Using the WKB approximation in this case:

$$E_x(y, z) \propto \exp\left[\imath k_{\mathrm{FS}} \sin\theta y \int_0^z k_z(z')dz'\right] \ , \tag{1.92}$$

we find:

$$k_z^2(z) = k_{\mathrm{FS}}^2(\epsilon - \sin^2\theta) \ . \tag{1.93}$$

Consequently, the wave propagation zone is limited to $\epsilon > \sin^2\theta$. Reflection of the light wave occurs for $\epsilon(z) = \sin^2\theta$. Substituting ϵ by the definition given in Eq. (1.45) yields:

$$k_z^2(z) = k_{\mathrm{FS}}^2\left(\cos^2\theta - \frac{\omega_{\mathrm{pe}}^2}{\omega(\omega + \imath\nu_{\mathrm{IB}})}\right) . \tag{1.94}$$

As a representative example, let us consider an isothermal plasma with a linear density profile $n_e = n_c z/L$. Considering $\ln\Lambda_{\mathrm{IB}}$ a constant we have $\nu_{\mathrm{IB}}(z) \approx \nu_{\mathrm{IB}}^\star n_e(z)/n_c = \nu_{\mathrm{IB}}^\star z/L$ with $\nu_{\mathrm{IB}}^\star$ the inverse Bremsstrahlung collision frequency at the critical density, so that:

$$k_z^2 c^2 = \omega^2\left(\cos^2\theta - \frac{z/L}{1 + \imath(\nu_{\mathrm{IB}}^\star/\omega)(z/L)}\right) . \tag{1.95}$$

The fractional energy loss can then be obtained from the squared modulus of the field:

$$|E_x(y,z)|^2 = |E_x(y,0)|^2 \exp\left[-2\int_0^z \Im(k_z(z'))\mathrm{d}z'\right] . \tag{1.96}$$

Substituting k_z by its expression in Eq. (1.95), assuming $\nu_{\mathrm{IB}} \ll \omega$ and considering a wave that propagates up to the turning point $z_{\mathrm{T}} = L\cos^2\theta$ and back to the vacuum, the fractional absorption f_A^{col} reads:

$$f_A^{\mathrm{col}} = 1 - \exp\left[-4\int_0^{L\cos^2\theta} \Im(k_z(z'))\mathrm{d}z'\right] = 1 - \exp\left[-\frac{32\nu_{\mathrm{IB}}^\star}{15c} L\cos^5\theta\right] , \tag{1.97}$$

which shows that in order to maximize collisional absorption, normal laser incidence (i.e. $\theta \simeq 0$) and long scale-length plasmas are preferred. The angle dependence is a consequence of the wave traveling less deep into the plasma and thus encountering less plasma, in regions further from the maximum value of ν_{IB}. Typical plasma profiles in ICF are rather exponential than linear. Considering a profile of the form $\epsilon(z) = 1 - \exp(z/L)$, the turning point of the wave is now $z_{\mathrm{T}} = L\ln(\cos^2\theta)$. Substituting the (z/L) terms in Eq. (1.95) by $\exp(z/L)$, the fractional absorption reads [61]:

$$f_A^{\mathrm{col}} = 1 - \exp\left[-4\int_{-\infty}^{L\ln(\cos^2\theta)} \Im(k_z(z'))\mathrm{d}z'\right] = 1 - \exp\left[-\frac{8\nu_{\mathrm{IB}}^\star}{3c} L\cos^3\theta\right] , \tag{1.98}$$

which is a lower absorption fraction than in the linear case for any incidence angle.

1.3.2.2 Resonant Absorption of p-polarized waves

For a p-polarized wave, the electric field reads $\boldsymbol{E}(y,z) = E_y(y,z)\mathbf{e}_y + E_z(y,z)\mathbf{e}_z$. It is convenient here to work with the magnetic field of the wave $\boldsymbol{B}(y,z) = B_x(y,z)\mathbf{e}_x$. Similarly to Eq. (1.89), the magnetic field wave equation for an EM wave in a plasma (1.52) projected on $\mathbf{e}_x$ reads:

$$\frac{\partial^2 B_x}{\partial y^2} + \frac{\partial^2 B_x}{\partial z^2} + \frac{\omega^2}{c^2}\epsilon(z)B_x = \frac{\partial B_x}{\partial z}\frac{\partial \ln\epsilon}{\partial z} . \tag{1.99}$$

Similarly to Eq. (1.90), $B_x(y,z)$ is expressed as:

$$B_x(y,z) = B(z)\exp(\imath k_y y) = B(z)\exp(\imath\omega/c\sin\theta y) \ . \tag{1.100}$$

Substituting this expression for B_x in the $\mathbf{e}_z$ component of Ampere's law yields:

$$-\frac{\partial B_x(y,z)}{\partial y} = -\imath\frac{\omega}{c}\epsilon(z)E_z(y,z) \ . \tag{1.101}$$

After differentiation and assuming $E_z(y,z) = E_z(z)\exp(\imath\omega/c\sin\theta y)$, an expression for $E_z(z)$ is obtained:

$$E_z(z) = \sin\theta B_x(z)/\epsilon(z) \ . \tag{1.102}$$

Recalling that $\epsilon(z)$ is minimum for $n_e = n_c$, where it is proportional to $\imath\nu_{\mathrm{IB}}/\omega$ (that is in general $\ll 1$), this equation illustrates that the component of the electric field parallel to the density gradient can reach very large values at the critical density. The resonantly excited field is damped by electron-ion collisions and leads to an additional absorption fraction, derived in App. C.1, that is most prominent for plasmas with strong density gradients. Additionally, the resonantly excited field can drive EPWs parallel to the density gradient direction, which in turn may accelerate electrons (see Sec. 1.4.1).

1.3.3 Paraxial Wave Equation

The Paraxial Wave Equation (PWE), first invented in [62, 63], is a class of solutions that relies on the existence of a principal propagation direction for the wave. To illustrate its principle, we consider a monochromatic wave of the form $E = E_0\exp[-\imath\omega t + \imath\mathbf{k}.\mathbf{r}]$ propagating in a plasma where $n_e/n_c \ll 1$ and $\nu_{ei} \ll \omega$. Under such conditions, the wave is transverse and obeys the scalar Helmholtz equation for its field E_0. The wave equation written in the time domain reads:

$$\left[\frac{\partial^2}{\partial t^2} + \omega_{\mathrm{pe}}^2 + \nu_{\nu_{\mathrm{IB}}\ll\omega}^{\mathrm{EM}}\frac{\partial}{\partial t} - c^2\triangle\right]E_0 = 0 \ , \tag{1.103}$$

where it was assumed that the density field is homogeneous. Considering that the plasma density n is perturbed around an equilibrium value n_0, Eq. (1.103) takes the form:

$$\left[\frac{\partial^2}{\partial t^2} + \omega_{\mathrm{pe},0}^2 + \nu_{\nu_{\mathrm{IB}}\ll\omega}^{\mathrm{EM}}\frac{\partial}{\partial t} - c^2\triangle\right]E_0 = -\frac{\omega^2}{n_c}(n-n_0)E_0 \ , \tag{1.104}$$

where the left-hand-side contains the damping term $\nu\partial_t$, and the remaining terms are called a *propagator*. The right-hand-side accounts for the refraction of the wave on density inhomogeneities. This equation is very costly to resolve on spatial and temporal scales large compared to the wavelength and period. Therefore, it is commonly simplified by making additional assumptions, that are (i) the temporal slowly varying envelope approximation:

$$\left|\frac{\partial^2 E_0}{\partial t^2}\right| \ll \left|2\omega\frac{\partial E_0}{\partial t}\right| \ , \tag{1.105}$$

(ii) the wavenumber k satisfies the dispersion relation (1.56) for the non-perturbed density n_0, and (iii) $\mathbf{k}$ is a privileged propagation direction (z-axis, without loss of generality), so that:

$$|\triangle_{\parallel} E_0| \ll \left|2k_{\mathrm{FS}}\frac{\partial E_0}{\partial z}\right| \ , \ |\triangle_{\perp} E_0| \ , \tag{1.106}$$

where $\triangle_{\perp} = \frac{\partial^2}{\partial x^2} + \frac{\partial^2}{\partial y^2}$ and $\triangle_{\parallel} = \frac{\partial^2}{\partial z^2}$ designate the transverse and parallel components of the Laplace operator, respectively. Using assumptions (1.105) and (1.106), Eq. (1.104) now reads:

$$\left[\frac{\partial}{\partial t} + \mathbf{v}_g.\nabla + 2\nu^{\mathrm{EM}}_{\nu_{\mathrm{IB}}\ll\omega} - \imath\frac{c^2}{2\omega}\triangle_{\perp}\right] E_0 = -\imath\frac{\omega}{2n_c}\delta n E_0 \ , \tag{1.107}$$

where $\delta n = n - n_0$ represents the long-wavelength density modifications around the equilibrium density n_0, and the group velocity $\mathbf{v}_g = \mathbf{k}c^2/\omega$ is defined according to the dispersion relation (1.56). This type of paraxial wave equation is widely used for nonlinear LPI modeling. It is further discussed in Secs. 3.3.1 and 4.3. The term proportional to $\mathbf{v}_g$ accounts for the wave propagation, whereas the term in $\triangle_{\perp}$ accounts for its transverse diffraction.

The validity domain of PWE (1.106) depends on the deviation of the wave with respect to the paraxial direction (z), that arises e.g. from the refraction. The error arising from the refraction process can be evaluated by considering a plasma with a linear density profile of the form $n_e/n_c = z/L$, as in Sec. 1.3.2. In that case, the wave amplitude can be described in a WKB approximation:

$$E(x,y,z) = E_0(x,y,z)\exp\left[\imath\int_0^z k_z(z')\mathrm{d}z' + \imath k_{\mathrm{FS}}\sin\theta y - \imath\omega t\right] \ . \tag{1.108}$$

Injecting this form into the Helmholtz equation (1.55) gives:

$$\triangle E_0 + 2\imath\left(k_z\frac{\partial E_0}{\partial z} + k_{\mathrm{FS}}\sin\theta\frac{\partial E_0}{\partial y}\right) - \imath k_{\mathrm{FS}}^2\frac{E_0}{2k_z L} = 0 \ , \tag{1.109}$$

where we have used the dispersion relation (1.93) and supposed a stationary propagation. In order to neglect the parallel component of the Laplace operator and describe this wave-field in the paraxial approximation, the assumptions equivalent to Eqs. (1.106) that must be met read:

$$\left|\frac{\partial^2 E_0}{\partial z^2}\right| \ll \left|2(k_z - k_{\mathrm{FS}}\sin\theta)\frac{\partial E_0}{\partial z}\right| \ , \ \left|\frac{\partial^2 E_0}{\partial y^2}\right| \ , \ \left|\frac{\partial^2 E_0}{\partial x^2}\right| \ , \tag{1.110}$$

where we have used $\nabla.\boldsymbol{E} = 0$, that is valid far from the critical density (see Sec. 1.3.4) or for a s-polarized wave. We can estimate the validity of the first inequality by assuming that $\partial^2 E_0/\partial z^2 = O(E_0 k^2)$ and $\partial E_0/\partial z = O(E_0 k)$, with the local wavenumber $k(z) = k_{\mathrm{FS}}\sqrt{\epsilon(z)}$, so that it now reads:

$$1 \ll 4\pi\frac{\sqrt{\cos^2\theta - z/L} - \sin\theta}{\sqrt{1 - z/L}} \ . \tag{1.111}$$

Evaluating the coordinate z at which the right-hand-side of Eq. (1.111) is equal to 10 (for $\theta \neq 0$), and injecting this value into the expression for the local wave angle at z with respect to the z-axis; $\varphi(z) = \arctan(k_y/k_z(z))$, we find that the paraxial approximation breaks down when the wave

propagates at an angle of $\sim 10°$ with respect to the paraxial axis. Even though formulations that extend the validity domain of the PWE exist (such as the *wide-angle* PWE [64, 65]), its use is usually limited to maximum wave angles of $\sim 30°$. Such angles are bound to occur in plasmas with linear (or exponential) density profiles obtained when considering laser interactions with solid targets. Furthermore, the paraxial wave equation remains numerically costly when considering large plasma volumes and long temporal duration. Consequently, the paraxial approximation is not the method of choice for the description of laser beam propagation at hydrodynamic scales[1].

1.3.4 The scalar wave equation in inhomogeneous and collisional plasma

In the general case of wave propagation in a collisional plasma, at any angle with density inhomogeneities, and up to the critical density, the approaches presented in the previous sections are not always valid. Specifically, the wave equation involves an additional term $(\nabla(\nabla \ln \epsilon.\boldsymbol{E}))$ that couples the various components of the vector field. The latter is often neglected or omitted, thus reducing the problem to a scalar wave equation, because (i) this additional term is difficult to treat and (ii) the literature is rich with methods and solutions for dealing with scalar waves. As an example, the homogeneous scalar Helmholtz equation is the basis of the widespread Geometrical Optics method, and also of Complex Geometrical Optics (these are presented in the following Chapter).

Assuming that the typical length scale variation of the electric field is λ, we can write $\triangle \boldsymbol{E} = O(E/\lambda^2)$, $k_{\mathrm{FS}}^2 \epsilon \boldsymbol{E} = O((2\pi)^2 E/\lambda^2)$ and $\nabla(\nabla \ln \epsilon.\boldsymbol{E}) = O((E/\lambda)(\nabla\epsilon/\epsilon))$. The $\nabla(\nabla \ln \epsilon.\boldsymbol{E})$ term can be neglected compared to the others if the dielectric permittivity of the medium vary slowly compared to the length over which the electric field vary in space. A necessary (but not sufficient) condition can be expressed as:

$$\left|\frac{\nabla\epsilon}{\epsilon}\right| \ll \frac{8\pi}{\lambda} \ , \tag{1.112}$$

which is similar to the restriction used in the WKB approximation (1.88). Considering a medium with a linear density variation, as presented in Sec. 1.3.2 and assuming $\nu_{\mathrm{IB}} \ll \omega$, it can be shown that this assumption is valid at the turning point of the wave, but not close to the critical density (in cases where $\theta = 0$).

In the framework of the Paraxial Complex Geometrical Optics method presented in the following Chapter, the plasma parameters are considered to depend on the (y, z) coordinates, and to be invariant in the x-direction. An explicit form of the $\nabla(\nabla \ln \epsilon.\boldsymbol{E})$ term in the Cartesian coordinates reads:

$$\begin{aligned}\nabla(\nabla \ln \epsilon.\boldsymbol{E}) = &\frac{\partial}{\partial x}\left[\left(E_x\frac{\partial}{\partial x} + E_y\frac{\partial}{\partial y} + E_z\frac{\partial}{\partial z}\right)\ln\epsilon\right] \\ &+ \frac{\partial}{\partial y}\left[\left(E_x\frac{\partial}{\partial x} + E_y\frac{\partial}{\partial y} + E_z\frac{\partial}{\partial z}\right)\ln\epsilon\right] \\ &+ \frac{\partial}{\partial z}\left[\left(E_x\frac{\partial}{\partial x} + E_y\frac{\partial}{\partial y} + E_z\frac{\partial}{\partial z}\right)\ln\epsilon\right] \ .\end{aligned} \tag{1.113}$$

[1] A notable exception is the modeling of the LPI in indirect-drive geometries, where the laser beams are co-propagating at the laser entrance hole. The use of modern super-computers allows to model such interactions with a PWE approach.

Considering a dielectric function depending on 2 coordinates $\epsilon(y,z)$, an electromagnetic wave incident on the plasma with no $\mathbf{k}$-vector component in the x direction stays confined in the (y,z) plane. Assuming that the wave is s-polarized, i.e. its electric field reads $\boldsymbol{E} = E_x(y,z)\mathbf{e}_x$, and substituting for $\boldsymbol{E}$ and the dielectric function in Eq. (1.113), it is straightforward to see that $\nabla(\nabla \ln \epsilon.\boldsymbol{E}) = 0$. Consequently, the wave equation for the electric field can be reduced to a scalar Helmholtz equation. In that context, the scalar wave approximation is valid anywhere in the plasma (for $n_e \leq n_c$). Note that in the case of p-polarized waves, the condition for validity of the scalar wave equation is more complex, related to necessary conditions such as Eq. (1.112) that break down near the critical density. As such, reduced propagation models based on the Hemholtz equation are unable to describe p-polarized waves. In the framework of PCGO, presented in Ch. 2, this shortcoming is addressed by using a dedicated resonant absorption model described in Sec. 5.3 and validated in Sec. 6.1.

1.4 Longitudinal waves in plasmas

The presence of free charge carriers in the plasma allows the existence and propagation of so-called *longitudinal waves*; electrostatic perturbations that only involve the electric field component longitudinal to their propagation direction. These waves exclusively exist inside the plasma and are either excited from instabilities or from their coupling with external electromagnetic waves. In general, the associated longitudinal dielectric permittivity depends on the contribution from the species α in the plasma; $\epsilon_L = 1 + \sum_\alpha \delta\epsilon_{L,\alpha}$ [66], and according to (1.78), the dispersion relation of the wave reads $\epsilon_L = 0$. We briefly detail in this section the characteristics of Electron Plasma Waves (EPWs) and Ion Acoustic Waves (IAWs), plasma eigenmodes involved in parametric instabilities.

1.4.1 Electron Plasma Waves

EPWs, also called Langmuir waves, correspond to the high frequency response of the plasma to the longitudinal field. Considering that ions respond slowly to high frequency modulations of the electric field, due to their high mass, their contribution to the local charge density can be neglected and the ions are considered as a stationary and homogeneous fluid. Formally, the high frequency assumption allows to define $m_i \to \infty$, so that $\delta\epsilon_{L,i} = 0$, and to assume that the phase velocity of the wave ω/k is much larger than the electron thermal velocity $v_{T,e}$ (where as usual, ω is the frequency of the wave and $k = |\mathbf{k}|$ its wavenumber). According to Eq. (1.78) this wave has a longitudinal polarization and its electrostatic field obeys the Gauss law for the charge density:

$$\nabla.\boldsymbol{E} = -\frac{e}{\epsilon_0}\int f_e^1 \mathrm{d}^3 v \ , \tag{1.114}$$

where f_e^1 is a perturbation to the Maxwellian distribution function, as defined in Sec. 1.1.2. Assuming that the plasma is close to thermal equilibrium, ϵ_L can be estimated in Fourier space from Eq. (1.114) and from the linearized Vlasov-Fokker-Planck equation [66]:

$$\epsilon_L(\mathrm{k},\omega) = 1 + \frac{e^2}{k^2\epsilon_0}\left(1 + \imath\frac{\nu_{ei}}{\omega}\right)\int \frac{\mathbf{k}.\nabla_{\mathbf{p}} f_e^M}{\omega + \imath\nu_{ei} - \mathbf{k}.\mathbf{v}}\mathrm{d}\mathbf{p} \ . \tag{1.115}$$

Expanding this expression in Taylor series around $kv_{T,e}/\omega \ll 1$ and $\nu_{ei}/\omega \ll 1$, we obtain:

$$\epsilon_L(\mathrm{k},\omega) = 1 + \delta\epsilon_{L,e} = 1 - \frac{\omega_{\mathrm{pe}}^2}{\omega^2}\left(1 + 3\frac{k^2 v_{T,e}^2}{\omega^2} - \imath\frac{\nu_{ei}}{\omega}\right) . \tag{1.116}$$

The dependence on k of ϵ_L implies that the plasma is spatially dispersive for the EPWs. Noting that this dependence vanishes for a cold fluid with $v_{T,e} = 0$, we see that this is a purely kinetic effect arising from the thermal motion of electrons. The dispersion relation is then obtained by solving $\epsilon_L = 0$, which gives:

$$\omega_{\mathrm{EPW}}(k) = \pm\omega_{\mathrm{pe}}\left(1 + \frac{3}{2}k^2\lambda_{De}^2\right) - \frac{\imath}{2}\nu_{ei} , \tag{1.117}$$

with $\lambda_{De} = v_{T,e}/\omega_{\mathrm{pe}}$ is the electron Debye length and the $\pm$ sign corresponds to two waves propagating along $\pm\mathbf{k}$. The EPWs are damped due to the electron-ion collisions with a rate $\nu_{\mathrm{EPW},c} = \nu_{ei}/2$. In addition, wave damping also occurs in collisionless media with a damping rate [36]:

$$\frac{\nu_{\mathrm{EPW},L}}{\Re(\omega_{\mathrm{EPW}})} = -\sqrt{\pi}\frac{\Re(\omega_{\mathrm{EPW}})^3}{k^3}\left(\frac{m_e}{2k_{\mathrm{B}}T_e}\right)^{3/2}\exp\left[-\frac{\Re(\omega_{\mathrm{EPW}})^2 m_e}{2k^2 k_{\mathrm{B}}T_e}\right] , \tag{1.118}$$

that is the so-called *Landau damping*, that arises from a wave interaction with the resonant particles of velocity close to the phase velocity of the wave. The Landau damping dominates for waves with a relatively small phase velocity $\omega/k \sim$ (3-5)$v_{T,e}$, while the collisional damping dominates for $\omega/k \geq 10v_{T,e}$. Additionally, the Landau damping prevents the waves to exist for $\omega/k \leq v_{T,e}$.

As the phase velocity of the plasma waves is smaller than c, electrons can be trapped in the EPW and be accelerated. They acquire an energy that roughly corresponds to the kinetic energy associated with the wave's phase velocity, $m_\alpha v_{\mathrm{ph}}^2/2$. Considering the condition for the existence of EPWs, that is $\omega/k > v_{T,e}$, trapped particles can reach energies much higher than the plasma temperature. As such, these electrons are termed *supra-thermal*. In certain conditions, the EPW can cease to exist due to so-called *wave-breaking* processes, thus liberating in the plasma the supra-thermal electrons. For that reason, any LPI process that excites EPWs can potentially drive supra-thermal electrons in the plasma and is considered as a pre-heat concern in ICF, typical supra-thermal energies ranging from the keV to a few hundred keVs.

1.4.2 Ion Acoustic Waves

Contrary to EPWs, IAWs are low frequency waves with $\omega \ll \omega_{\mathrm{pe}}$. In general, these waves exist in the interval of phase velocities $v_{T,e} \gg \omega/k \gg v_{T,i}$, so that both the ion and the electron susceptibilities contribute in the expression of the dielectric permittivity. The ion contribution to the dielectric permittivity, $\delta\epsilon_{i,L}$, can be computed similarly to $\delta\epsilon_{L,e}$ in the case of EPWs because $\omega/k \gg v_{T,i}$. The latter thus reads:

$$\delta\epsilon_{L,i} = -\frac{\omega_{\mathrm{pi}}^2}{\omega^2}\left(1 + 3\frac{k^2 v_{T,i}^2}{\omega^2}\right) , \tag{1.119}$$

where $\omega_{\rm pi} = \sqrt{Z^2e^2n_i^0/m_i\epsilon_0}$ is the ion plasma frequency. Given that $\omega/k \ll v_{T,e}$, the dependence on ω can be neglected in the expression for $\delta\epsilon_{L,e}$ and Eq. (1.115) gives:

$$\delta\epsilon_{L,e} \approx \frac{m_e e^2}{k^2 k_{\rm B} T_e \epsilon_0} \int f_e^M \mathrm{d}^3 v = \frac{1}{k^2\lambda_{De}^2} \ , \tag{1.120}$$

so that the dispersion relation $\epsilon_L = 0$ for the IAWs reads:

$$1 + \frac{1}{k^2\lambda_{De}^2} - \frac{\omega_{\rm pi}^2}{\omega^2}\left(1 + 3\frac{k^2 v_{T,i}^2}{\omega^2}\right) = 0 \ , \tag{1.121}$$

for which a solution is:

$$\omega_{\rm IAW}^2(k) = \frac{k^2 c_s^2}{1 + k^2\lambda_{De}^2} + 3k^2 v_{T,i}^2 \ , \tag{1.122}$$

with $c_s = \sqrt{Zk_{\rm B}T_e/m_i}$ the ion acoustic velocity. This dispersion relation behaves differently depending on the value of $k^2\lambda_{De}^2$. For $k^2\lambda_{De}^2 \ll 1$, the dispersion of the IAW is weak and the phase velocity of the wave is close to its group velocity $\omega/k \approx c_s$. The IAW in this limit corresponds to quasi-neutral oscillations of the plasma density, associated with a weak electric field. These waves can only exist in a plasma where $ZT_e \gg 3T_i$. For $k\lambda_{De} \gg 1$, the waves are termed Ion Plasma Waves and correspond to charge oscillations associated to the ions.

The damping of IAWs originates from ion-ion collisions $\nu_{{\rm IAW},c}$ and from Landau damping $\nu_{{\rm IAW},L}$ on electrons and ions. When the ion-ion collision frequency is small, i.e. $\nu_{ii} \ll \omega_{\rm IAW}$, the damping rates read:

$$\nu_{{\rm IAW},c} = \frac{v_{T,i}^2\nu_{ii}}{2c_s^2} \ , \tag{1.123}$$

$$\nu_{{\rm IAW},L} = \sqrt{\frac{\pi}{8}} k v_s \left[\frac{\omega_{\rm pi}}{\omega_{\rm pe}} + \left(\frac{v_s}{v_{T,i}}\right)^3 \exp[-v_s^2/2v_{T,i}^2]\right] \ , \tag{1.124}$$

where $v_s = \sqrt{c_s^2 + 3v_{T,i}^2}$ and the Landau damping is constituted of contributions from the electrons and the ions. For $ZT_e/3T_i < 10$, one must also consider the electron-ion collisions in the expression for the collisional damping rate (in the case where $T_e \simeq T_i$, the wave is simply a *neutral* accoustic wave and not an IAW). Note that considering the domain of existence of the IAWs, that is $v_{T,e} \gg \omega/k \gg v_{T,i}$, the latter cannot accelerate electrons to supra-thermal velocities and as such, parametric instabilities that couples exclusively with IAWs (such as SBS) do not constitute a preheat concern in ICF.

1.5 Parametric Instabilities in plasmas

The theory of electromagnetic waves in plasmas presented in Secs. 1.2 and 1.2 is focused on the linear phenomena of wave propagation and collisional absorption. As mentioned in the introduction, nonlinear wave-plasma couplings appear at high values of the interaction parameter $I\lambda^2$, most prominently the so-called parametric instabilities.

In classical mechanics, parametric instabilities designate a class of instabilities provoked by

the periodic perturbation in time of the parameters defining the eigenmodes of a stable system that is described around its equilibrium state in the approximation of small perturbations. In plasmas, the parameters of the system depend not only on the time but also on the space, which leads to the existence of two main classes of parametric instabilities; *decay parametric instabilities* and *modulation parametric instabilities*. The former is a resonant instability where a wave decays into two eigenmodes of the system, while the latter is a non-resonant instability that couples two waves through plasma density modulations.

In the context of laser plasma interactions, the decay parametric instabilities notably include the processes of Stimulated Raman Scattering (SRS), Stimulated Brillouin Scattering (SBS) and Two Plasmon Decay (TPD), while modulation parametric instabilities are at the origin of the filamentation and self-focusing instabilities. In the shock-ignition ICF scheme, as well as in ICF in general, SRS, SBS and TPD are primary sources of disruption of the implosion. Notably, SRS and TPD are potential pre-heat concerns, while SBS affects the laser drive symmetry. We describe in this section the basic principles of parametric systems in continuous media, restricted to the decay parametric instabilities, with the aim of giving some hints about the principal regimes under which SRS, SBS and TPD operate in ICF. Those principles are applied to the derivation and validation of PCGO-based CBET in Secs. 4.2 and 4.1, and to the definition of hot electron sources from SRS and TPD instabilities in Sec. 5.4.

1.5.1 Generalities on decay parametric instabilities

Decay parametric instabilities are a class of parametric instabilities that resonantly couple three waves through the wavenumber and frequency matching conditions:

$$\begin{aligned} \omega_0 &= \omega_1 + \omega_2 \ , \\ \mathbf{k}_0 &= \mathbf{k}_1 + \mathbf{k}_2 \ , \end{aligned} \tag{1.125}$$

where ω is a frequency and $\mathbf{k}$ a wavenumber, the 0 subscript indicates the *mother wave* and the 1 and 2 subscripts the *daughter waves*. In addition, each wave α satisfies its own dispersion relation $D_\alpha(\omega_\alpha, \mathbf{k}_\alpha) = 0$. Here $D = \epsilon_L$ in the case of longitudinal plasma waves and $D = k^2 - \omega^2\epsilon/c^2$ in the case of transverse electromagnetic waves. It can be shown that a necessary condition for the three-wave coupling to produce unstable solutions is $\Im\omega_{1,2} > 0$, which implies that $\omega_0 > \omega_{1,2}$. That is the frequency of a mother wave is higher than the frequencies of daughter waves. In general, the mother wave corresponds to an electromagnetic wave, and the daughter waves are either electromagnetic or plasma waves. The waves are assumed to be of the form:

$$A_\alpha(\mathbf{r}, t) = a_\alpha(\mathbf{r}, t) \exp\left(\imath \mathbf{k}_\alpha.\mathbf{r} - \imath\omega'_\alpha(\mathbf{k}_0)t\right) + c.c. \ , \tag{1.126}$$

where ω'_α designates the real part of the solution in ω of $D_\alpha(\omega, \mathbf{k}_\alpha) = 0$, and the a_α amplitudes are described in the Slowly Varying Envelope Approximation in time and space. The evolution equation for the slowly varying amplitudes read [36]:

$$\left(\frac{\partial}{\partial t} + \mathbf{V}_{g0}.\nabla + \nu_0\right) a_0(\mathbf{r}, t) = -\gamma_0 a_1 a_2 \ ,$$

$$\left(\frac{\partial}{\partial t} + \mathbf{V}_{g1}.\nabla + \nu_1\right) a_1(\mathbf{r},t) = \gamma_0 a_0 a_2^\star \ ,$$
$$\left(\frac{\partial}{\partial t} + \mathbf{V}_{g2}.\nabla + \nu_2\right) a_2(\mathbf{r},t) = \gamma_0 a_0 a_1^\star \ , \tag{1.127}$$

where $\mathbf{V}_{g\alpha}$ and ν_α are the group velocity and linear damping rate of wave α, and γ_0 is the *coupling contant*. In this system of equations, the daughter waves describe the eigenmodes of the plasma when no mother wave is present, while the mother wave modulates the plasma parameters.

The temporal SVEA can be expressed as:

$$\left|\frac{1}{a_\alpha}\frac{\partial a_\alpha}{\partial t}\right| \ll \min(\omega_1, \omega_2) \ . \tag{1.128}$$

It is satisfied if $\gamma_0 \ll \min(\omega_1, \omega_2)$. Moreover, much less stringent conditions can be obtained when the group velocity of one of the daughter waves is very small, e.g. $|V_{g1}| \ll |V_{g2}|$. The regime of parametric instability where the SVEA is valid is called the *weak coupling* regime, while it is otherwise referred to as the *strong coupling* regime. For simplicity, we limit ourselves to the weak coupling regime.

The solutions described by the system of equations (1.127) can be regrouped in three categories depending on their stability.

- (I) The system is unstable if it possesses at least one unstable eigenmode (i.e. with a positive imaginary part), in which case the initial plasma perturbations grow exponentially in time as $\approx \exp \gamma t$ (with γ being a temporal growth rate). This is the *absolute* regime of the instability.

- (II) The system is stable in the sense that it does not possess any unstable eigenmode. However, the initial perturbations can grow along their propagation direction, in which case the system is said to present spatial amplification and the daughter waves amplitudes grow as $\approx \exp Kx$ (with K being a spatial growth rate). This is the *convective* regime of the instability.

- (III) The system does not present any unstable eigenmode and does not have the property of spatial amplification, in which case it is stable.

Depending on the strength of the coupling constant γ_0, there are several sets of conditions for the parametric system to respect in order to present convective or absolute instability, which principally stem from (i) inhomogeneity of the medium, (ii) finite length of the interaction zone and (iii) laser incoherence. We first discuss the convective and absolute instabilities in an infinite homogeneous plasma, and then adress the first two conditions. The mathematical results presented in the subsequent sections are described in more details in [67, 68, 69, 70, 71, 72, 73, 74].

In both cases of convective and absolute instabilities, the exponential growth of the instability (in time or in space) can be limited by nonlinear saturation mechanisms which act to stop the growth of the daughter waves amplitudes. Amongst these saturation mechanisms we note: (i) the *pump depletion*, that is simply a decrease of the mother wave amplitude as it communicates its

energy to the daughter waves and (ii) kinetic effects that increase nonlinearly the damping rates ν_α or destroy the resonance conditions (1.125). These saturation mechanisms are subject of the *nonlinear theory* of parametric instabilities. The aim of this section being to give an introduction to parametric instabilities, we limit our description to the linear theory and to phenomena of wave de-phasing.

1.5.1.1 Interaction in a homogeneous medium

The analysis of instabilities in a homogeneous medium was done by Bers and Briggs [75], who derived a general criteria for an instability. The parametric instabilities in the convective or absolute regimes are described in Refs. [36, 67, 68, 76, 77, 78, 79, 80]. The principal results are:

- In an infinite medium, the system is stable in the sense of (III) if it satisfies the inequality:

$$\gamma_0 < \gamma_{\rm th} = \sqrt{\nu_1 \nu_2} \ . \tag{1.129}$$

- The system is unstable in the absolute sense if:

$$V_{g1} V_{g2} < 0 \ , \tag{1.130}$$

$$\gamma_0 > \gamma_{\rm th}^{\rm abs} = \frac{\sqrt{|V_{g1} V_{g2}|}}{2} \left(\frac{\nu_1}{|V_{g1}|} + \frac{\nu_2}{|V_{g2}|} \right) \ , \tag{1.131}$$

  where in this 1D analysis (along the x axis), the group velocities are defined by $V_{g,i} = \mathbf{V}_{g,i}.\mathbf{e}_x$. These conditions define the *weak damping* limit.

- In the $\gamma_{\rm th} < \gamma_0 < \gamma_{\rm th}^{\rm abs}$ domain with $V_{g1} V_{g2} < 0$, the instability is in the convective regime. These inequalities define the *strong damping* limit. Furthermore, for parametric systems with $V_{g1} V_{g2} > 0$ and $\gamma_{\rm th} < \gamma_0$ the instability is in the convective regime in the entire domain.

1.5.1.2 Interaction in an inhomogeneous medium

The resonance conditions for a given pair of daughter waves can be fulfilled in one point, in which case the instability is localized in space. This can notably occur when the plasma parameters (density, temperature...) vary in space, so that the resonance conditions (1.125) may be satisfied only on a fraction of the system length (keeping in mind that in that case the local dispersion relations $D_\alpha(\omega_\alpha, k_\alpha(x))$ also depend on the spatial variable).

It is convenient to write the amplitudes (in 1D):

$$a_\alpha = \hat{a}_\alpha \exp\left(\imath \int_{x_r}^{x} k_\alpha(x') \mathrm{d}x' \right) \ , \tag{1.132}$$

so that the parametric system reads:

$$\left(\frac{\partial}{\partial t} + V_{g0} \frac{\partial}{\partial x} + \nu_0 \right) \hat{a}_0(x,t) = -\gamma_0 \hat{a}_1 \hat{a}_2 \exp\left(-\imath \int_0^x \Delta k(x') \mathrm{d}x' \right) \ ,$$

$$\left(\frac{\partial}{\partial t} + V_{g1} \frac{\partial}{\partial x} + \nu_1 \right) \hat{a}_1(x,t) = \gamma_0 \hat{a}_0 \hat{a}_2^\star \exp\left(\imath \int_0^x \Delta k(x') \mathrm{d}x' \right) \ ,$$

$$\left(\frac{\partial}{\partial t}+V_{g2}\frac{\partial}{\partial x}+\nu_2\right)\hat{a}_2(x,t)=\gamma_0\hat{a}_0\hat{a}_1^\star\exp\left(\imath\int_0^x\Delta k(x')\mathrm{d}x'\right)\ , \tag{1.133}$$

where the phase matching parameter $\Delta k(x)=k_0(x)-k_1(x)-k_2(x)$ and it was assumed that the resonance point $\Delta k(x_r)=0$ is at $x_r=0$. The phase matching parameter can be expanded as a power series around the resonance point $x_r=0$:

$$\Delta k(x)=\sum_{n=1}\frac{x^n}{n!}\left(\frac{\partial^{(n)}\Delta k(x)}{\partial x^{(n)}}\right)_{x=0}\ . \tag{1.134}$$

Two typical types of phase matching profiles are considered: a linear profile where this expansion is kept at the order 1, and a parabolic profile, where the expansion is kept at the order 2 and the first order term $\Delta k'$ is zero. Main ideas of parametric instabilities in linear and parabolic profiles were first formulated by M. N. Rosenbluth [76] based on preliminary works from Refs. [81, 82].

Assuming that the coupling equations can be satisfied onto the resonance width Δk_r, the condition $|\Delta k(x)|\leq\Delta k_r$ defines a length L_{inh} on which the coupling relations are satisfied. It can be shown, through a temporal Laplace transform of the system of equations (1.133) that in the weak and strong damping limits, respectively:

$$\Delta k_r^{\mathrm{abs}}\simeq\frac{2\gamma_0}{\sqrt{|V_{g1}V_{g2}|}}\ , \tag{1.135}$$

$$\Delta k_r^{\mathrm{conv}}\simeq\max\left(\frac{\nu_i}{|V_{gi}|}\right)\ , \tag{1.136}$$

where it was assumed in $\Delta k_r^{\mathrm{conv}}$ that the system is far from the convective threshold, $\gamma_{\mathrm{th}}^{\mathrm{abs}}\ll\gamma_0<\gamma_{\mathrm{th}}^{\mathrm{abs}}$. Using these expressions, it can be shown that the length onto which the resonance is satisfied reads (for a linear phase matching profile):

$$\begin{aligned}L_{\mathrm{inh,lin}}^{\mathrm{abs}}&\simeq\frac{4\gamma_0}{\sqrt{|V_{g1}V_{g2}|}}\left[\left(\frac{\partial\Delta k(x)}{\partial x}\right)_{x=0}\right]^{-1}\ ,\\ L_{\mathrm{inh,lin}}^{\mathrm{conv}}&\simeq 2\max\left(\frac{\nu_i}{|V_{gi}|}\right)\left[\left(\frac{\partial\Delta k(x)}{\partial x}\right)_{x=0}\right]^{-1}\ .\end{aligned} \tag{1.137}$$

In this regime, there is not absolute parametric instability for any value of γ_0 and any sign of $V_{g1}V_{g2}$. In contrast, the spatial amplification is allowed for $\gamma_0>\gamma_{\mathrm{th}}$. In the weak damping limit, the spatial growth rate is $|K_{\max}|=\gamma_0/\sqrt{|V_{g1}V_{g2}|}$ over a length scale $L_{\mathrm{inh,lin}}^{\mathrm{abs}}$. In the strong damping limit and far from the threshold, the spatial growth rate is $|K_{\max}|=\gamma_0^2/|V_{g1}V_{g2}\max(\nu_i/|V_{gi}|)|$ over a length scale $L_{\mathrm{inh,lin}}^{\mathrm{conv}}$.

1.5.1.3 Finite length interaction in an inhomogeneous medium

Combining the effects of inhomogeneities to a finite length of the interaction L, it can be shown that [83]:

- (I) The absolute instability can exist only if (i) $V_{g1}V_{g2}<0$ and $\gamma_0>\gamma_{\mathrm{th}}^{\mathrm{abs}}$, and (ii) $L_{\mathrm{eff}}^{\mathrm{abs}}=\min(L,L_{\mathrm{inh}}^{\mathrm{abs}})>\pi\sqrt{|V_{g1}V_{g2}|}/(2\gamma_0)$, where it is assumed that the phase matching profile exhibits a local extremum.

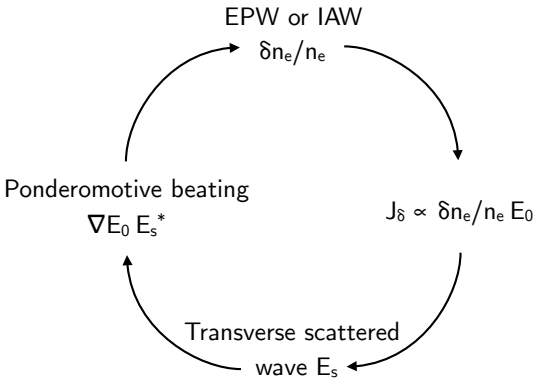

Figure 1-1 – *Nonlinear couplings at the origin of the SBS (for the IAW) and SRS (for the EPW) instabilities.*

- (II) The parametric system presents a spatial growth when it is not unstable with respect to (I), and $\gamma_0 > \gamma_{\text{th}}$. The amplitude of the daughter waves grow in $\exp G$ with $G \simeq |K_{\max}| L_{\text{eff}}$. In the convective regime in the weak damping limit ($\gamma_0 > \gamma_{\text{th}}^{\text{abs}}$ and $V_{g1}V_{g2} > 0$):

$$K_{\max} = \gamma_0 / \sqrt{|V_{g1}V_{g2}|} \ , \tag{1.138}$$

$$L_{\text{eff}} = L_{\text{eff}}^{\text{abs}} \ , \tag{1.139}$$

  and in the convective regime in the strong damping limit and far from the threshold ($\gamma_{\text{th}}^{\text{abs}} > \gamma_0 \gg \gamma_{\text{th}}$):

$$K_{\max} = \frac{\gamma_0^2}{|V_{g1}V_{g2}| \max(\nu_i/|V_{gi}|)} \ , \tag{1.140}$$

$$L_{\text{eff}} = L_{\text{eff}}^{\text{conv}} = \min(L, L_{\text{inh}}^{\text{conv}}) \ . \tag{1.141}$$

1.5.2 Most unstable modes of the principal instabilities

1.5.2.1 Stimulated Raman Scattering

The Stimulated Raman Scattering (SRS) is a parametric instability resulting from a resonant coupling of a high amplitude light wave with an Electron Plasma Wave (EPW) and a scattered light wave. The coupling relations (1.125) read:

$$\omega_0 = \omega_1 + \omega_{\text{EPW}} \ , \tag{1.142}$$

$$\mathbf{k}_0 = \mathbf{k}_1 + \mathbf{k}_{\text{EPW}} \ , \tag{1.143}$$

where the 1 subscript indicates the scattered light wave. Given that the minimum frequency of an EM wave in a plasma is ω_{pe} (1.57), it is straightforward to see that Eq. (1.142) implies $\omega_0 \geq 2\omega_{\text{pe}}$, that is $n_e \leq n_c/4$: the SRS instability can only occur below (or at) the quarter critical density.

The physical mechanism of the SRS instability coupling is summarized in Fig. 1-1. A high amplitude transverse EM wave propagating in a plasma where there is an electron density perturbation $\delta n/n_0$ originating from an EPW produces a non linear current $\boldsymbol{J}_\delta$. This effect can

be seen by considering a density of the form $n_e = n_0(1 + \delta n/n_0)$ when expressing the plasma dielectric susceptibility, through the computation of the polarization current, Eq. (1.44). Adding this non linear current as a source term in the Maxwell's equations produces a transverse electric field $\boldsymbol{E}_1$ at the shift frequency $\omega_1 = \omega_0 - \omega_{\rm pe}$. The beating of the two EM waves $\boldsymbol{E}_0$ and $\boldsymbol{E}_1$ contributes to the local *ponderomotive force*, proportional to $\nabla E_0 E_1^\star$, which expels electrons from regions of high intensity gradients. The ponderomotive beating of the mother wave and the daughter wave oscillates at the plasma frequency and reinforces the initial density perturbation $\delta n/n_0$ if the coupling relations (1.142) and (1.143) are satisfied.

The scattered wave may be excited in any directions with respect to the mother wave, although the sidescattering modes quickly escape from the interaction zone in inhomogeneous media. Considering the most unstable configuration, with the polarization vector of the incident wave orthogonal to the plane $(\mathbf{k}_0, \mathbf{k}_{\rm EPW})$ and $n_e \ll n_c$, the coupling coefficients for the forward and backward scattering modes read [36]:

$$\gamma_{0,\rm SRS}^{\rm forward} \approx \frac{\omega_0}{2}\left(\frac{n_e}{n_c}\right)^{3/4}\left(\frac{v_{\rm osc}}{c}\right) , \tag{1.144}$$

$$\gamma_{0,\rm SRS}^{\rm backward} \approx \omega_0\left(\frac{n_e}{n_c}\right)^{1/4}\left(\frac{v_{\rm osc}}{c}\right) , \tag{1.145}$$

where $v_{\rm osc}$ is the quiver velocity of the electrons in the mother wave electric field, written in the Fourier convention (with our notations: $v_{\rm osc} = eE_0/(2m_e\omega_0)$). According to these relations, the backward SRS can be anticipated to be faster growing than the forward SRS, as the former has a higher coupling constant.

The damping of the scattered wave depends on electron-ion collisions, and is related to the collisional absorption coefficient derived in Sec. 1.2.5 by $2\nu_1 = \nu_1^{\rm EM} \approx \nu_{\rm IB}\omega_{\rm pe}^2/\omega_1^2$, where the frequency of the scattered wave depends on the resonance density and is given by $\omega_1^2 = \omega_0^2(1 - \sqrt{n_e/n_c})^2$. As detailed in Sec. 1.4.1, the damping rate of the EPW $\nu_{\rm EPW}$ is the sum of a contribution from collisional damping $\nu_{{\rm EPW},c} = \nu_{ei}/2$ and a contribution from Landau damping $\nu_{{\rm EPW},L}$. For densities and temperatures of the order of $n_e/n_c \simeq 1/10$, $T_e \simeq 1$ keV, the EPW wave number is $k_2\lambda_D < 0.25$ and the collisional damping is larger than the Landau damping. This corresponds to the *collisional regime*. Using these expressions and the above values of the coupling constant, we can obtain the intensity thresholds for the most unstable configuration for the convective forward and backward SRS instability in the collisional regime and for $n_e \ll n_c$ [36]:

$$(I_{14,\rm W/cm^2}\lambda_{0,\mu m}^2)_{\rm th,SRS}^{\rm forward} = 1.61\times10^{-4}\left(\frac{n_e}{n_c}\right)^{3/2}\frac{\sqrt{1-n_e/n_c}\ln\Lambda_{\rm IB}\ln\Lambda_{ei}Z_{\rm eff}}{\lambda_{0,\mu m}T_{e,\rm keV}^3} , \tag{1.146}$$

$$(I_{14,\rm W/cm^2}\lambda_{0,\mu m}^2)_{\rm th,SRS}^{\rm backward} = 4.1\times10^{-5}\left(\frac{n_e}{n_c}\right)^{5/2}\frac{\sqrt{1-n_e/n_c}\ln\Lambda_{\rm IB}\ln\Lambda_{ei}Z_{\rm eff}^2}{\lambda_{0,\mu m}^2T_{e,\rm keV}^3(1-\sqrt{n_e/n_c})^2} . \tag{1.147}$$

For moderate Z plasmas, 351 nm wavelength lasers, and for densities well below the quarter critical density, the threshold for backward scattering is lower than that for forward scattering.

The above intensity thresholds are given for a homogeneous plasma and are valid well below the quarter-critical density, point at which the SVEA breaks down as the scattered wave is

excited close to its own critical density. Consequently, the effect of the inhomogeneity was studied separately in the two subdomains of $n_e < n_c/4$ and in the vicinity of the quarter critical density.

- (i) Assuming the density profile in the region below the quarter critical density is monotonous (as is the case in ICF), we have seen in Sec. 1.5.1.2 that the absolute SRS instability cannot exist. However, a coupling between forward and backward SRS through a common EPW can lead to the existence of an absolute instability (for both modes) [84, 85].

- (ii) In the vicinity of the quarter critical density, the absolute threshold for the SRS instability is [86, 87, 88]:

$$\frac{v_{\rm osc}}{c} > \frac{1}{2}(k_0 L_{n_c/4})^{-2/3} \ . \tag{1.148}$$

  It can be presented in terms of the local laser intensity as:

$$\begin{aligned}(I_{\rm PW/cm^2})^{\rm inh,n_c/4}_{\rm abs,SRS} &= \left[10^{-7}\frac{N_{n_c/4}\epsilon_0 c^5 m_e^2 (2\pi)^{2/3}}{2e^2}\right](\lambda_{0,\mu m} L^2_{n_c/4,\mu m})^{2/3} \\ &\simeq 102(\lambda_{0,\mu m} L^2_{n_c/4,\mu m})^{-2/3} \ ,\end{aligned} \tag{1.149}$$

  with the gradient scale length defined as $L_{n_c/4,\mu m} = [(1/n){\rm d}n/{\rm d}x]_{n=n_c/4}$. The inhomogeneous threshold for the absolute SRS instability at the quarter critical density for typical laser plasma interaction parameters is $2.6\times10^{14}{\rm W/cm^2}$, considering a typical gradient scale length of 150 μm and λ_0=351 nm.

Comparing the thresholds for the convective SRS sidescattering below $n_c/4$, the absolute SRS below $n_c/4$ and absolute SRS at the quarter critical density, it can be shown that for long scale length plasmas (that corresponds to the case of ICF) it is the latter that possesses the lower threshold [69, 89]. Furthermore, experimental studies of the angular distribution of the scattered wave have shown that it is mainly the backward SRS that dominates over the other scattering directions [90, 91, 92], in accordance with the theory.

1.5.2.2 Stimulated Brillouin Scattering

The Stimulated Brillouin Scattering (SBS) instability is conceptually similar to the SRS instability, but the coupling of the incident and scattered light waves operates through an Ion Accoustic Wave (IAW) instead of an EPW. The coupling relations (Eqs. (1.125)) read:

$$\omega_0 = \omega_1 + \omega_{\rm IAW} \ , \tag{1.150}$$

$$\mathbf{k}_0 = \mathbf{k}_1 + \mathbf{k}_{\rm IAW} \ . \tag{1.151}$$

The light waves are still coupled to an electron density fluctuations, although the latter corresponds to a low frequency IAW. Contrary to the SRS instability, since the frequency of the IAW $\omega \ll \omega_0$, SBS can occur at any point below the critical density. This also implies that the scattered light frequency is very close to the incident light wave frequency.

The coupling of the incident and scattered EM waves is most strong when their electric fields are parallel and orthogonal to the scattering plane $(\mathbf{k}_0, \mathbf{k}_{\rm IAW})$. The group velocities of the

daughter waves are given by:

$$V_{g1} = k_1 c^2/\omega_1 \simeq V_{g0} = N_0 c \ , \tag{1.152}$$

$$V_{g2} = \frac{3v_{T,i}^2 + (\lambda_D^2\omega_{pi}^2/(1+k_{\mathrm{IAW}}^2\lambda_{De}^2)^2)}{\sqrt{3v_{T,i}^2 + (\lambda_D^2\omega_{pi}^2/(1+k_{\mathrm{IAW}}^2\lambda_{De}^2))}} \approx \sqrt{(ZT_e+3T_i)/m_i} \ , \tag{1.153}$$

where we assumed $k_{\mathrm{IAW}}\lambda_{De} \ll 1$ in the right-hand-side of Eq. (1.153), N_0 is the plasma index of refraction N seen by the mother wave, $k_{\mathrm{IAW}} = |\mathbf{k_0} - \mathbf{k}_1| \simeq 2k_0 \sin\theta$ with θ the angle between $\mathbf{k}_0$ and $\mathbf{k}_1$, and $v_{T,i}$ is the ion thermal velocity. In the limit $|k_2\lambda_D| \ll 1$, V_{g2} is close to the ion acoustic velocity $c_s = \sqrt{(ZT_e+3T_i)/m_i}$.

Finally, the coupling constant for the SBS instability in the most unstable case and for $|k_2\lambda_D| \ll 1$ reads [93, 94, 78, 69, 88, 95, 79, 96]:

$$\gamma_{0,\mathrm{SBS}}^2 = \omega_{pi}^2 \frac{V_{g0}}{2c_s}\left(\frac{v_{\mathrm{osc}}}{c}\right)^2 \ . \tag{1.154}$$

The damping rate of the daughter EM wave is related to the collisional absorption coefficient derived in Sec. 1.2.5; $2\nu_1 = \nu_{\mathrm{IB}}$. As is detailed in Sec. 1.4.2, the damping rate of the daughter IAW is the sum of contributions from the collisional and Landau damping. Considering the variety of damping regimes, it is useful to describe the results as a function of the normalized damping $\hat{\nu}_{\mathrm{IAW}} = \nu_{\mathrm{IAW}}/\omega_{\mathrm{IAW}}$, this quantity being of the order of 10^{-2} for a cold plasma and 10^{-1} for a typical coronal plasma.

Recalling that the convective threshold is given by $\gamma_0^2 > \nu_1\nu_2$, a criterion can be derived on the interaction parameter $I_{14}\lambda^2$, that yield in practical units:

$$(I_{14,\mathrm{W/cm^2}}\lambda_{0,\mu m}^2)_{\mathrm{th,SBS}} = 1.17\times10^{-2}\sqrt{1-n_e/n_c}\frac{n_e}{n_c}\frac{\ln\Lambda_{\mathrm{IB}} Z_{\mathrm{eff}}\hat{\nu}_{\mathrm{IAW}}}{\lambda_{0,\mu m}\sqrt{T_{e,\mathrm{keV}}}}\left(1+\frac{3T_i}{ZT_e}\right) \ . \tag{1.155}$$

For a $T_e = ZT_i = 1$ keV coronal plasma with $Z = 6$, $n_e = 0.1n_c$, $\hat{\nu}_{\mathrm{IAW}} = 0.1$ and $\ln\Lambda_{\mathrm{IB}} = 10$, the threshold is of 1.9×10^{13} W/cm^2 for $\lambda_0 = 351$ nm, which is rather low for current laser standards. Experiments at 351 nm in 1 ns pulses at 1×10^{15} W/cm^2 have demonstrated integrated backscattered levels from SBS of the order of $5-10\%$ [97, 98]. These relatively low values are explained by the role of nonlinear saturation mechanisms, and competition with other instabilities.

Although the SBS instability is rather insensitive to inhomogeneities of the plasma density and temperature [36], it is not the case for velocity gradients. The plasma flow shifts the frequencies of the mother and daughter EM waves by the Doppler effect. The particular case of SBS in presence of a constant velocity gradient (in the framework of CBET) is studied in Sec. 4.2.

1.5.2.3 Two Plasmon Decay

The Two Plasmon Decay (TPD) instability results from the coupling of an incident transverse wave with two EPWs (or plasmons). The coupling relations (Eqs. (1.125)) read:

$$\omega_0 = \omega_{\mathrm{EPW},1} + \omega_{\mathrm{EPW},2} \ , \tag{1.156}$$

$$\mathbf{k}_0 = \mathbf{k}_{\mathrm{EPW},1} + \mathbf{k}_{\mathrm{EPW},2} \ , \tag{1.157}$$

which notably implies $\omega_0 \simeq 2\omega_{pe}$, i.e. the instability is localized in the vicinity of the quarter critical density. The coupling constant for the TPD can be obtained by linearizing the dispersion relations in the vicinity of their resonance:

$$\gamma_0^2 = \frac{(\mathbf{k}_{\mathrm{EPW},2}.\mathbf{e}_0)^2}{4}\left[\frac{k_{\mathrm{EPW},1}^2 - k_{\mathrm{EPW},2}^2}{k_{\mathrm{EPW},1}k_{\mathrm{EPW},2}}\right]^2 v_{\mathrm{osc}}^2 \ , \tag{1.158}$$

where $\mathbf{e}_0$ is the polarization vector of the transverse mother wave. It can be shown that the most favorable configuration is that in which $\mathbf{k}_1$ and $\mathbf{k}_2$ lie in the $(\mathbf{e}_0, \mathbf{k}_0)$ plane. In that configuration, the most unstable geometry (assuming $|\mathbf{k}_{\mathrm{EPW}}| \gg |\mathbf{k}_0|$) is that where $\mathbf{k}_{\mathrm{EPW},1}$ is at an angle of $\pi/4$ with respect to $\mathbf{k}_0$ and $\mathbf{k}_{\mathrm{EPW},2}$ at an angle of $3\pi/4$ with respect to $\mathbf{k}_0$. In that case the coupling constant reads [99, 100, 77]:

$$\gamma_{0,\mathrm{TPD}}^2 = \frac{\sqrt{3}\omega_0}{4}\frac{v_{\mathrm{osc}}}{c} \ . \tag{1.159}$$

Using the Landau and collisional EPW damping rates $\nu_{\mathrm{IAW},L}$ and $\nu_{\mathrm{IAW},c}$ expressed in Eqs. (1.117) and (1.118), the convective threshold for the TPD reads:

$$(I_{14,\mathrm{W/cm^2}}\lambda_{0,\mu m}^2)_{\mathrm{th,TPD}} = 1.212\times10^{-5}\left(\frac{\ln\Lambda_{ei}Z_{\mathrm{eff}}}{\lambda_{0,\mu m}T_{e,\mathrm{keV}}^{3/2}}\right)^2\left(1+\frac{\nu_{\mathrm{IAW},1L}}{\nu_{\mathrm{IAW},1c}}\right)\left(1+\frac{\nu_{\mathrm{IAW},2L}}{\nu_{\mathrm{IAW},2c}}\right) \ . \tag{1.160}$$

In the collisional regime, and for typical ICF conditions ($Z = 6$, $\ln\Lambda_{ei} = 10$, $\lambda_0 = 351$ nm, $T_e = 1$ keV), the threshold is 3×10^{14} W/cm^2, which can be easily exceeded with current laser systems.

The TPD takes place at $n_c/4$, region at which the plasma density is rarely homogeneous in laser-solid interactions, and thus the effects of inhomogeneities must be accounted for. A relatively accurate value for the inhomogeneous and absolute threshold reads [77]:

$$\left(\frac{v_{\mathrm{osc}}}{v_{T,e}}\right)^2 k_0 L_{n_c/4} > 3 \ . \tag{1.161}$$

In terms of the local laser intensity the TPD threshold reads:

$$\begin{aligned}(I_{\mathrm{PW/cm^2}})_{\mathrm{th,TPD}}^{\mathrm{inh}} &= \left[\frac{10^{-4}12\pi N m_e c^3\epsilon_0}{e}\right]\frac{T_{e,\mathrm{keV}}}{\lambda_{0,\mu m}L_{n_c/4,\mu m}} \\ &\simeq 4.43\frac{T_{e,\mathrm{keV}}}{\lambda_{0,\mu m}L_{n_c/4,\mu m}} \ .\end{aligned} \tag{1.162}$$

It was shown in [77, 101] that the exact threshold depends also on the parameter $\beta = 1.41NT_e/(I_{14,\mathrm{W/cm^2}}\lambda_{0,\mu m}^2)$, the former being lower for $\beta < 1$ and higher for $\beta > 1$. Considering the typical laser systems employed in ICF, the parameter β is typically $\sim$ 3-4, that corresponds to the right-hand-side in Eq. (1.161) close to the asymptotic value of 4.1. In that case, the intensity threshold in the so-called *high β regime* becomes:

$$(I_{\mathrm{PW/cm^2}})_{\mathrm{th,TPD}}^{\mathrm{inh}} \simeq 6.05\frac{T_{e,\mathrm{keV}}}{\lambda_{0,\mu m}L_{n_c/4,\mu m}} \ . \tag{1.163}$$

Considering the above laser and plasma parameters, the intensity threshold is of 1.2×10^{14}W/cm^2,

which is rather similar to the absolute SRS threshold at the quarter critical density.

1.5.2.4 Competition between nonlinear LPI processes

Given various spatial locations where the processes presented above occur, there is a geometrical competition for the mother wave energy between parametric instabilities. As such, because SRS can grow convectively before $n_c/4$, it reduces the mother wave energy before the latter can couple to EPWs at the quarter-critical density and drive the TPD instability. Consequently, for a light wave incident on a plasma and initially above the TPD threshold, the SRS below the quarter-critical density can prevent TPD from occurring altogether. Similarly, SBS can occur at various locations in the plasma depending on local phase matching conditions, and may decrease the strength of the mother wave needed for excitation of other instabilities. This is also valid in the case of laser light absorbed by Resonant Absorption, which is geometrically affected by nonlinear couplings occurring prior to the wave's turning point.

1.5.2.5 Role of optical smoothing on parametric instabilities

The light intensity profiles produced by high power laser systems are deformed wavefront aberrations and nonlinear processes in amplifiers that cause statistical variations of the intensity in the laser's focal plane. These intensity fluctuations may exceed up to ~ 5 times the mean laser intensity. As such, parametric instabilities can develop in these regions even though the mean beam intensity may be below their thresholds. Furthermore these laser intensity fluctuations are not reproducible from shot to shot, partly because they are caused by the thermal noise in laser amplifiers. Naturally, these intensity fluctuations are also detrimental for the symmetry of target irradiation, seeding perturbations of the ablation front that may be amplified by the ablative Rayleigh-Taylor instability during the acceleration and deceleration phases of the capsule implosion [102, 103, 104, 105, 106, 107, 108], and reducing the yield of fusion reactions [109, 110, 46].

The occurrence of parametric instabilities in these high intensity regions can be amplified by additional processes of laser *self-focusing* and *filamentation*. In the interaction regime of interest here, self-focusing arises from a nonlinear modification of the local refractive index of the plasma due to thermal and ponderomotive effects. As an example, the collisional absorption, proportional to the laser intensity, heats the plasma on the beam axis more rapidly than on its low intensity wings, thus increasing the on-axis plasma pressure and creating a local density depletion. The beam then focuses on this axis as it would in a lens, thus increasing the local laser intensity and hence the collisional absorption, and so on. When local self-focusing structures appear along the propagation of a beam, stemming e.g. from local density inhomogeneities or from laser intensity fluctuations, the beam undergoes the so-called filamentation process.

Considering the problematic of nonlinear LPI reduction and control of the focal spot intensity profile, dedicated optical smoothing techniques have been developed. They aim at reducing the size of characteristic intensity fluctuations (*speckles*) and moving them across the focal spot. Controlling the vacuum intensity fluctuations is commonly achieved using Phase Plates [111] and Polarization smoothing. These techniques allow to decrease the occurrence of high intensity spikes by spatially de-phasing portions of the laser field in the focusing volume, thus creating small-scale

interference patterns in the focal plane, and by superposing de-correlated interference patterns. The resulting small-scale intensity statistics, termed *speckle pattern*, is well controlled and its average intensity envelope is reproducible from shot to shot. Decreasing the growth rate of the filamentation process and increasing the smoothness of the average intensity profile is achieved by temporal smoothing techniques such as the temporal Smoothing by Spectral Dispersion and Longitudinal Smoothing, which allow to move the speckle pattern in time. These techniques, detailed in Sec. 3.1, decrease the growth rate of nonlinear LPIs by reducing and shifting in time the high intensity regions of the beam, thus preventing these processes to reach a steady state. Notably, the effect of SSD on the production of supra-thermal electrons by parametric instabilities has been demonstrated in experiments presented in Refs. [112, 113]. This problem is studied in Sec. 6.3.

1.6 Conclusions

We have presented the linear theory of electromagnetic waves in plasmas, highlighting the main mechanisms of the linear laser-plasma interaction and using the kinetic theory to estimate the plasma response. Several widespread methods for resolving the wave equation in inhomogeneous plasmas were introduced, considering in particular the processes of collisional and resonant absorption. The framework of the scalar Helmholtz equation has been introduced. The latter is valid for arbitrary plasma configurations in the case of s-polarized waves. Considering its relative simplicity compared to the full wave equation, it constitutes the starting point for reduced propagation models used in large-scale hydrodynamic codes. Finally, we have presented the longitudinal plasma modes and nonlinear couplings leading to parametric instabilities. Notably, we introduced the most unstable modes of SRS, SBS and TPD using both theoretical considerations and experimental observations.

Chapter 2

Laser-plasma interaction modeling in radiative hydrocodes

The description of laser beam propagation in a plasma in large-scale hydrodynamic codes relies on reduced models compatible with the scales at play. This chapter is dedicated to the description of such models and their implementation into the radiative hydrodynamic code Chic developed at Celia. After recalling the governing equations resolved in radiative hydrodynamic codes and briefly detailing the Chic code in Sec. 2.1, the derivation of the Geometrical Optics equations, which constitute the background of the widespread Ray-Tracing (RT) method, is presented in Sec. 2.2. Given the inherent difficulties in estimating nonlinear LPIs using GOs, evoked in Sec. 2.2.4, we present in Sec. 2.3 an adaptation to collisional plasmas and to a Lagrangian framework of a beam-tracing method based on the Paraxial Complex Geometrical Optics (PCGO) equations. The latter readily describes the intensity of Gaussian wave-fields and is employed throughout this work. The PCGO and RT approaches are compared for the modeling of a nonlinear LPI, the ponderomotive self-focusing, in Sec. 2.3.5.3.

2.1 Hydrodynamic description of plasmas

2.1.1 From kinetic theory to the fluid approximation

The kinetic theory of plasmas introduced in Sec. 1.1.2 allows to describe fine-scale phenomena with a sufficient accuracy and is rather complete. However, it is costly in terms of numerical computation. In general, it is only used for small plasma volumes and assuming a reduced number of dimensions (in space and velocity). The complexity of the problem can be reduced by considering situations where the mean free path of particles λ_{mfp} is much smaller than the characteristic length scales of the plasma L_{ch}, and the time between subsequent collisions ν^{-1} is small compared to the characteristic time of the studied phenomena t^{-1}. The kinetic timescale ν^{-1} can be approached by the average electron-ion collision frequency ν_{ei} presented in Sec. 1.1.2, while the characteristic length scale depends on the electron mean free path $\lambda_{\text{mfp},e} = v_{T,e}/\nu_{ei}$. These assumptions are valid for many processes at play in the physics of Inertial Confinement Fusion, although there are specific cases where so-called *non-local* effects are important, notably in terms of electron heat transport from the laser-plasma interaction and α-particle kinetics for

the ignition and combustion of the hotspot fuel.

Under the conditions $\lambda_{\text{mfp},e} \ll L_{\text{ch}}$ and $\nu_{ei}^{-1} \ll t$, the plasma can be treated in a fluid approach as a *quasi-neutral* gas. Although it is constituted of charged particles, the assumption of quasi-neutrality is a good approximation because of the plasma screening effect presented in Sec. 1.1.2: for length scales longer than the Debye length and outside of boundary regions, plasmas respond collectively to imposed electric fields or charge perturbations. This process is efficient only if there are enough charges in the sphere of radius λ_D around the charge carrier. This can be expressed as a condition on the number of electrons within the *Debye sphere*:

$$N_D = n_e \frac{4}{3}\pi\lambda_D^3 \gg 1 \ , \tag{2.1}$$

where N_D is called the *plasma parameter*. This will always be the case in the interaction conditions considered here. Considering a gas of ions and electrons, the quasi-neutral assumption yields a relation between the average ion and electron number densities:

$$Q = 0 = n_e - Z n_i \ . \tag{2.2}$$

The framework of hydrodynamic models applied to plasmas is that of scales $\lambda_{\text{mfp},e} \ll L_{\text{ch}}$ and $\nu_{ei}^{-1} \ll t$, with $N_D \gg 1$ and thus deviations from quasi-neutrality are small, i.e. $\delta Q/n_e \ll 1$. This allows to describe plasmas as a single fluid with two species of particles characterized by Maxwellian distribution functions; electrons and ions, verifying the condition (2.2) but having different temperatures.

2.1.2 Radiative Hydrodynamics

The *single fluid*, *two temperature* model is the basic framework for the study of ICF. It is complemented with the radiative effects and laser-plasma coupling. Here we present the basic elements of ICF radiative hydrodynamic codes by taking as an example the Chic code developed at Celia. This code is used for the implementation of a new laser-plasma interaction model presented in this thesis.

2.1.2.1 The Chic code

The plasma in the Chic code is treated as a quasi-neutral mixture of electrons and N_i ion species obeying the fluid equations, and described by two different temperatures. The basic averaged macroscopic quantities are defined as:

$$\begin{aligned}
n_i m_i &= \sum_{k=1}^{N_i} n_k m_k \ , \\
\rho_m &= n_e m_e + n_i m_i \ , \\
\rho_m \mathbf{u}_m &= n_e m_e \mathbf{u}_e + n_i m_i \mathbf{u}_i \ , \\
n_e &= Z_{\text{eff}} n_i \ , \\
\mathbf{j} &= e n_e (\mathbf{u}_i - \mathbf{u}_e) \ ,
\end{aligned}$$

$$
\begin{aligned}
P_m &= P_e + P_i \ , \\
\epsilon_m &= \epsilon_e + \epsilon_i \ , \\
\mathbf{q}_m &= \mathbf{q}_e + \mathbf{q}_i \ ,
\end{aligned} \tag{2.3}
$$

where the i, e and m subscripts indicate ion species, electron species and mean species, respectively. ρ is the mass density, $\mathbf{u}$ is the velocity, $\mathbf{j}$ is the current density, P is the plasma pressure, ϵ is the specific internal energy, $\mathbf{q}$ is the heat flux and it is assumed that $|\mathbf{u}_i - \mathbf{u}_e| \ll c$. The mean fluid obeys the Euler equations, originating from the conditions of mass and momentum conservation:

$$
\frac{\partial \rho_m}{\partial t} + \nabla.(\rho_m \mathbf{u}_m) = 0 \ , \tag{2.4}
$$

$$
\rho_m \left(\frac{\partial}{\partial t} + \mathbf{u}_m.\nabla \right) \mathbf{u}_m = -\nabla P_m + F_{\text{ext}} \ , \tag{2.5}
$$

where F_{ext} represents external forces. Although the plasma is considered as a single fluid, ion and electrons are treated separately in terms of energy balance, with separate temperatures T_i and T_e because the time of energy equilibration is comparable with the characteristic hydrodynamic time of ICF conditions. In this two temperature approach, the equations expressing the energy conservation read:

$$
\begin{aligned}
\rho_m \left(\frac{\partial}{\partial t} + \mathbf{u}_m.\nabla \right) \epsilon_e + \nabla.\mathbf{q}_e &= -P_e \nabla.\mathbf{u}_m - 2\alpha \frac{m_e}{m_i} C_{V,e} \nu_{ei} (T_e - T_i) + \mathcal{W}_{\text{ext}} \ , \\
\rho_m \left(\frac{\partial}{\partial t} + \mathbf{u}_m.\nabla \right) \epsilon_i + \nabla.\mathbf{q}_i &= -P_i \nabla.\mathbf{u}_m + 2\alpha \frac{m_e}{m_i} C_{V,e} \nu_{ei} (T_e - T_i) \ ,
\end{aligned} \tag{2.6}
$$

where $C_{V,e} = (3/2) n_e k_{\text{B}}$ is the electron heat capacity, the latter species being treated as an ideal gas, $\mathcal{W}_{\text{ext}}$ represents the external electron power density source (or sink) term, and $\alpha \in [0; 1]$ is a free parameter for the electron-ion coupling. The electron and ion heat fluxes q_e and q_i are calculated from the *Spitzer* theory [114].

The external source term $\mathcal{W}_{\text{ext}}$ and external force term F_{ext} are computed by additional packages that are specific to the processes meant to be studied. *Radiative Hydrodynamic codes* resolve the fluid equations coupled with radiative transport modules. Those are completed with Local Thermal Equilibrium (LTE) opacity tables and the hydrodynamic equations are closed using tabulated Equation Of States (EOS) designed for various plasma regimes. In the particular case of laser fusion studies, additional packages are often used, including the effects of magnetic fields on electron thermal transport limitation or non-local models, thermonuclear burn and laser propagation models. The structure of the Radiative Hydrodynamic code of the Celia laboratory, Chic, is shown in Fig. 2-1.

These equations are resolved in a Lagrangian formalism, i.e. in a frame that is co-moving with the fluid. In this description, collisional fluids are described by individual fluid parcels, which spatial evolution is followed through time. Mathematically, this is equivalent to considering the evolution of a field $\mathbf{Q}$ through its material derivative $\mathrm{D}\mathbf{Q}/\mathrm{D}t$, defined in an Eulerian formalism by $\mathrm{D}\mathbf{Q}/\mathrm{D}t = \partial\mathbf{Q}/\partial t + (\mathbf{u}.\nabla)\mathbf{Q}$. This approach simplifies the fluid equations and allows to correctly describe flow discontinuities such as shocks, although it renders more complex the numerical implementation of codes resolving these equations. Notably, in order to preserve the topology of

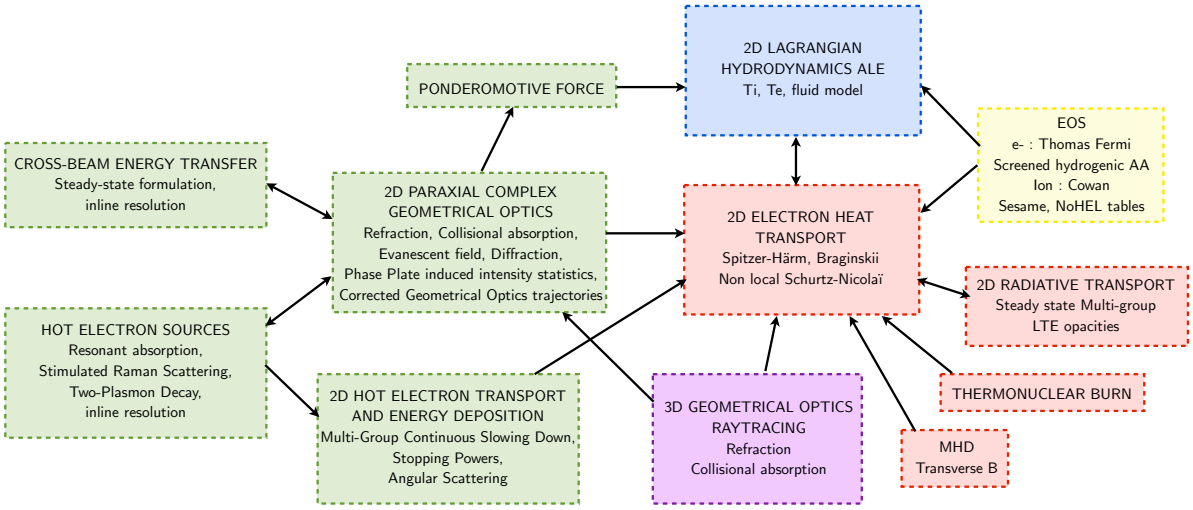

Figure 2-1 – *Main structure of the* Chic *code (adapted from [115]). The Ray-Tracing package (purple) is the historical optical module implemented in the* Chic *code. The green packages, related to the use of Complex Geometrical Optics, were added and developed during the thesis work and are detailed in this document.*

Lagrangian fluid meshes, the use of remapping and rezoning techniques are often required, such as the Arbitrary Lagrangian Eulerian method, implemented in Chic. The mesh in the Chic code is *irregular* and *unstructured*. The first term implies that neighborhood relations between cells are not defined by storage arrangement in the computer memory (e.g. in vector or matrix form), but defined by an irregular connectivity that requires the explicit storage of neighborhood information. The second term means that the shape of mesh cells and the distance between neighbors change with respect to time. It is important to note that in addition to the scale problems mentioned earlier, the framework of unstructured and irregular meshes limits the description of the laser propagation to the most basic formulations.

In radiative hydrodynamic codes, the external source term is usually decomposed between various contributions:

$$\mathcal{W}_{\text{ext}} = \mathcal{W}_{\text{rad}} + \mathcal{W}_{\text{fus}} + \mathcal{W}_{\text{LPI}} \ , \tag{2.7}$$

with $\mathcal{W}_{\text{rad}}$ the contribution from radiative transfer, $\mathcal{W}_{\text{fus}}$ the contribution from fusion reactions and $\mathcal{W}_{\text{LPI}}$ the source term from the laser-plasma interaction. The most widespread approach to modeling the laser plasma interaction in hydrocodes is the Ray-Tracing model, based on Geometrical Optics. The Ray-Tracing interfaces with the fluid equations via the collisional absorption term $\mathcal{W}_{\text{col}}$ such that $\mathcal{W}_{\text{LPI}} = \mathcal{W}_{\text{col}}$. The latter inverse Bremsstrahlung absorption term modeled with Geometrical Optics is described in Sec. 2.2.2. The state of the modules implemented in the Chic code at the beginning of this thesis is shown in Fig. 2-1, as red, yellow, blue and purple insets. At this point, the external force term in Chic did not include any contributions, so that $F_{\text{ext}} = 0$, and the LPI module was a standard 3D Ray-Tracing package, indicated in purple in Fig. 2-1. The latter describes the 3D laser propagation onto the 2D-axisymmetric or 2D-planar mesh and includes the processes of refraction and inverse Bremsstrahlung.

2.1.2.2 Addtional terms presented in this work

The work presented in this thesis concerns the addition of new physical LPI processes at the hydrodynamic scale. As such, those are interfaced with the fluid equations through the source terms $\mathcal{W}_{\rm LPI}$ and $F_{\rm ext} = F_{\rm ext,LPI}$. The various additional processes we present in this work are decomposed as:

$$F_{\rm ext,LPI} = F_{\rm Pond} \ , \tag{2.8}$$

$$\mathcal{W}_{\rm LPI} = \mathcal{W}_{\rm col} + \mathcal{W}_{\rm RA} + \mathcal{W}_{\rm HE} \ , \tag{2.9}$$

$$\mathcal{W}_{\rm HE} = \mathcal{W}_{\rm HE}^{\rm TPD} + \mathcal{W}_{\rm HE}^{\rm SRS} + \mathcal{W}_{\rm HE}^{\rm RA} \ , \tag{2.10}$$

where $F_{\rm Pond}$ is the ponderomotive force (see Sec. 2.4.1), $\mathcal{W}_{\rm col}$ is the inverse Bremsstrahlung laser absorption (described here with the Paraxial Complex Geometrical Optics, as presented in 2.3.3.2) and $\mathcal{W}_{\rm RA}$ is the contribution from the resonant absorption that does not accelerate hot electrons (see Sec. 5.3). In addition to these processes, we account for the energy deposited by high energy electron beams propagating in the plasma in $\mathcal{W}_{\rm HE}$ (see Sec. 5.1 for the propagation model). This term is decomposed according to the laser-plasma interaction that generates the supra-thermal electrons; $\mathcal{W}_{\rm HE}^{\rm TPD}$ for the Two Plasmon Decay (see Sec. 5.4), $\mathcal{W}_{\rm HE}^{\rm SRS}$ for the Stimulated Raman Scattering (see also Sec. 5.4) and $\mathcal{W}_{\rm HE}^{\rm RA}$ for the Resonant Absorption (see Sec. 5.3). It is important to note that $\mathcal{W}_{\rm LPI}$ also contains information on instabilities that redistribute the laser energy. This is notably the case of Cross Beam Energy Transfer and the backscattered energy flux from SRS, that dynamically modify the intensity distribution. Those particular processes are presented in Secs. 4.1 and 5.4.2, respectively. A summary of the physical processes we have added is given in Fig. 2-1 as green insets.

2.2 Geometrical Optics-based Ray Tracing

2.2.1 Eikonal equation: the ray trajectory

The Ray-Tracing method relies on Geometrical Optics (GO) principles. The starting point of GO is the Helmholtz equation written for a monochromatic laser wave and presented in Secs. 1.2.2 and 1.3.4:

$$\triangle u(\omega, \boldsymbol{r}) + k_{\rm FS}^2 \epsilon(\omega, \boldsymbol{r}) u(\omega, \boldsymbol{r}) = 0 \ , \tag{2.11}$$

where the wave dispersion and absorption are described via the frequency dependent relative permittivity $\epsilon(\omega, \boldsymbol{r})$, composed of a real and imaginary part and modeled by:

$$\epsilon(\omega, \boldsymbol{r}) = \epsilon'(\omega, \boldsymbol{r}) + \imath \epsilon''(\omega, \boldsymbol{r}) \approx 1 - \frac{n_e}{n_c}\left(1 + \imath \frac{\nu_{\rm IB}}{\omega}\right) \ , \tag{2.12}$$

where n_c is the critical density, $\epsilon'(\omega, \boldsymbol{r})$ is the real part and $\epsilon''(\omega, \boldsymbol{r})$ the imaginary part of the relative permittivity, and the right-hand-side approximation was obtained by assuming $\nu_{\rm IB} \ll \omega$.

In the most basic case of a homogeneous medium $\epsilon = \epsilon(\omega)$, the Helmholtz equation admits

solutions in the form of a *plane wave*:

$$u(\boldsymbol{r}) = A \exp[\imath \boldsymbol{k}.\boldsymbol{r}] \ , \tag{2.13}$$

where A is an amplitude. Building on this idea, the GO method relies on the description of waves in smooth inhomogeneous media in the Slowly Varying Envelope Approximation (SVEA). Assuming that the field amplitude varies slowly compared to the wave frequency, solutions to the Helmholtz equation can be sought as *almost-plane waves*:

$$u(\boldsymbol{r}) = A(\boldsymbol{r}) \exp[\imath k_{\mathrm{FS}} \psi'(\boldsymbol{r})] \ , \tag{2.14}$$

where $A(\boldsymbol{r})$ is an amplitude and $\psi'(\boldsymbol{r})$ is the eikonal, or optical path (with respect to the notations employed in Sec. 1.3.1, we have $\psi \equiv \int \Psi \mathrm{d}l$). Because the Geometrical Optics deals with real-valued fields and trajectories, it is intrinsically assumed that A and ψ' are real valued (hence the notation for ψ', to contrast with the case of the Complex Geometrical Optics developed in Sec. 2.3.2.2 that involves an imaginary part ψ''). The validity of the SVEA requires that the field amplitude $A(\boldsymbol{r})$ and the eikonal ψ' vary slowly over the wavelength $\lambda_L/(2\pi n') = c/\omega$. In the framework of an almost-plane homogeneous wave, this is equivalent to:

$$|\nabla A| \ll k_{\mathrm{FS}} |A| \ , \tag{2.15}$$

$$|\nabla k_j| \ll k_{\mathrm{FS}} |k_j| \ , \tag{2.16}$$

$$|\nabla n| \ll k_{\mathrm{FS}} |n| \ , \tag{2.17}$$

$$n'' \ll n' \tag{2.18}$$

with k_j the j-th component of the wavevector $\boldsymbol{k} = k_{\mathrm{FS}} \nabla \psi'$, and the last assumption is equivalent to considering weakly dissipative media in order to avoid rapid amplitude variations, as the field attenuates in $A \propto A_0 \exp[-k_{\mathrm{FS}} \int n'' \mathrm{d}l]$ (see Secs. 1.2.5 and 1.3.2). Given the expressions for the refractive indices in plasmas (Eqs. (1.67) and (1.68)), the assumption (2.18) does not hold in the vicinity of the critical density surface, which is a strong handicap for the GO formulation.

In the general approach, the field amplitude A is expanded as a sum of A_m field amplitudes proportional to inverse powers of the dimensional parameter $\imath k_{\mathrm{FS}}$. For the purpose of this demonstration and following Sec. 1.3, we only keep the 0-th order term A_0, noted A for simplicity. Substituting the model of Eq. (2.14) into the Helmholtz equation yields an equation at various orders in $\imath k_{\mathrm{FS}}$:

$$A \left[(\nabla \psi)^2 - \epsilon' \right] + \frac{1}{\imath k_{\mathrm{FS}}} \left[2 \nabla \psi . \nabla A + A \triangle \psi + k_{\mathrm{FS}} \epsilon'' A \right] + \frac{1}{(\imath k_{\mathrm{FS}})^2} \triangle A = 0 \ . \tag{2.19}$$

By identifying the various terms in powers of $(\imath k_{\mathrm{FS}})^{-1}$ we obtain three equations:

$$(\nabla \psi)^2 = \epsilon'(\boldsymbol{r}) \ , \tag{2.20}$$

$$2 \nabla \psi . \nabla A + A \triangle \psi + k_{\mathrm{FS}} \epsilon'' A = 0 \ , \tag{2.21}$$

$$\triangle A = 0 \ , \tag{2.22}$$

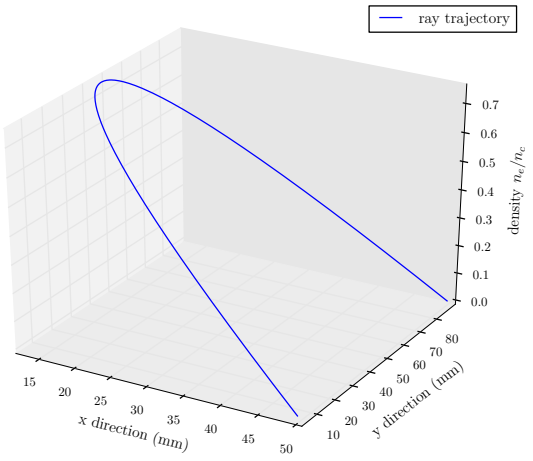

Figure 2-2 – *Geometrical Optics ray propagating in a plasma with a linear density profile along the x direction, and constant density in the y direction.*

where it was assumed that $\epsilon'' \ll \epsilon'$, in agreement with the SVEA. Equation (2.20) is called *eikonal equation* and Eq. (2.21) is the *zeroth-order transport equation*. The eikonal equation (2.20) is a nonlinear partial differential equation of the first order and belongs to the Hamilton-Jacobi variety. Using the characteristics technique yields the Hamiltonian $\mathcal{H}$ of the system, consisting of a particle of a unit mass moving in the potential $\frac{1}{2}\epsilon'(\mathbf{r})$:

$$\mathcal{H} = \frac{1}{2}\left[\boldsymbol{p}^2 - c^2\epsilon'(\boldsymbol{r})\right] = 0 \ , \tag{2.23}$$

where $\boldsymbol{p} = c\nabla\psi'$ is identified as the momentum of the ray. The characteristic system can be written in a vector form in Cartesian coordinates:

$$\begin{aligned} \frac{\mathrm{d}\boldsymbol{r}}{\mathrm{d}\tau'} &= \frac{\partial\mathcal{H}}{\partial(\boldsymbol{p})} \ , \\ \frac{\mathrm{d}(\boldsymbol{p})}{\mathrm{d}\tau'} &= -\frac{\partial\mathcal{H}}{\partial\boldsymbol{r}} \ , \end{aligned} \tag{2.24}$$

where τ' is the parametric variable of the system of a dimension of time. Using Eq. (2.23) yields the *ray equations in Hamiltonian form*:

$$\begin{aligned} \frac{d\boldsymbol{r}}{d\tau'} &= \boldsymbol{p} \ , \\ \frac{d\boldsymbol{p}}{d\tau'} &= \frac{c^2}{2}\nabla\epsilon'(\boldsymbol{r}) \ . \end{aligned} \tag{2.25}$$

The parametric ray coordinate τ' is related to the elementary arclength $\mathrm{d}s$ by $\mathrm{d}\tau' = \mathrm{d}s/(c\sqrt{\epsilon'})$, where $c\sqrt{\epsilon'}$ is the group velocity. This set of equations, that describes the trajectory of a ray, constitutes the base framework of the RT method. Figure 2-2 illustrates the trajectory of a ray propagating in a linear density gradient of the form $\epsilon(x) = 1 - x/L$ with a non-zero initial velocity in the y direction. Injecting this form of ϵ in the ray trajectory equation (2.25) and resolving for

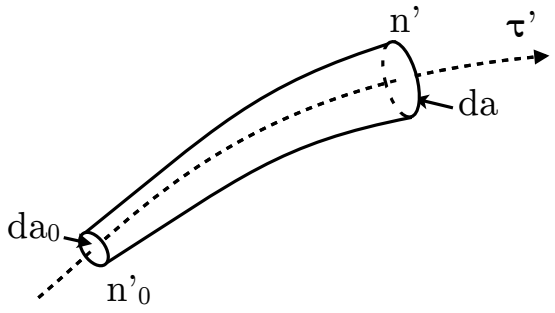

Figure 2-3 – *Illustration of the ray tube; a bundle of rays of infinitesimal initial cross-section da_0 that propagates from τ'_0 to τ', in a medium with a varying index from n'_0 to n'.*

the ray position r_x and r_y gives:

$$r_x(\tau) = -\frac{c^2}{4L}\tau^2 + v_{x0}\tau + r_{x0} \ , \tag{2.26}$$

$$r_y(\tau) = v_{y0}\tau + r_{y0} \ , \tag{2.27}$$

with r_{x0} and r_{y0} the initial ray position and v_{x0} and v_{y0} its initial velocity. This equation is a parametric form of a parabola.

Finally, the phase of the ray reads:

$$\psi' = \psi'_0 + \int_{\tau'_0}^{\tau'} \left[\epsilon'(\mathbf{r}(\tilde{\tau}'))\right]^{\frac{1}{2}} \mathrm{d}\tilde{\tau}' \ , \tag{2.28}$$

where ψ'_0 is an initial phase and τ'_0 is the initial parametric coordinate.

The numerical methods and algorithms employed for the resolution of the GOs equations in the triangularized mesh cells of the Lagrangian hydrodynamic code Chic are detailed in App. A.1.

2.2.2 Energy flux, ray tube and collisional damping

We have seen in the previous section that the trajectory of the ray is described by the eikonal equation. Similarly, the evolution of the field amplitude is described by the zeroth-order transport equation (2.21). It can be shown that the solution to this equation, expressed as a function of the ray parametric coordinate τ', reads [116]:

$$A(\tau') = A(\tau'_0)/\sqrt{\mathcal{J}} \exp\left[-\frac{k_{\mathrm{FS}}}{2}\int_{\tau'_0}^{\tau'} \epsilon'' \mathrm{d}\tilde{\tau}'\right] \ , \tag{2.29}$$

where the quantity $\mathcal{J} = n'\mathrm{d}a/(n'_0\mathrm{d}a_0)$ is the *ray divergence*. The geometrical meaning of the ray divergence $\mathcal{J}$ is related to the change in cross-section $\mathrm{d}a$ of an infinitely narrow bundle of rays, from τ'_0 to τ'. This narrow bundle of rays is termed a *ray tube* (see Fig. 2-3), its divergence being

caused by the refraction of the medium, so that $\mathcal{J}$ ultimately describes the decrease in intensity due to the wave refraction. Although Eq. (2.29) describes the energy conservation inside of a ray tube, it is important to note that it does not describe diffraction effects, nor does it define any notion of ray width. We define the power P associated with the ray as:

$$P(\tau') = \frac{1}{2} c\epsilon_0 \int_{\mathcal{S}(\tau')} A^2(\tau') n'(\tau') \mathrm{d}a \ , \tag{2.30}$$

where $\mathcal{S}(\tau')$ is the cross-section of the ray tube at τ' (see Fig. 2-3). Integrating Eq. (2.29) over $\mathrm{d}a(\tau')$ and differentiating with respect to the ray parameter τ' yields the conservation of power along the ray trajectory:

$$\frac{\mathrm{d}P}{\mathrm{d}\tau'} = -\nu^{\mathrm{EM}}_{\nu_{\mathrm{IB}} \ll \omega} P \ , \tag{2.31}$$

where we have used $\epsilon'' \ll \epsilon'$ and the EM wave damping rate is expressed by its formulation far from the critical density (1.77). The right-hand-side term in the power conservation equation represents the collisional absorption of laser beam energy by the process of inverse Bremsstrahlung (IB). Note that this formulation of the damping is similar to what was derived in the WKB approximation in Sec. 1.3.2. In order to model large aperture laser beams using Geometrical Optics, bundles of rays are given an initial power distribution depending on the spatial power profile that is aimed to be reproduced. The amount of energy absorbed by the plasma is the integral of $\mathrm{d}P/\mathrm{d}\tau'$ over the trajectories of the rays in each mesh cell.

2.2.3 Summary of the Geometrical Optics framework

We have demonstrated several features of the Geometrical Optics formulation. Ray-Tracing models implemented in hydrocodes are based on GO, and as such they possess the following capabilities and limitations;

- they describe a refraction of the wave field,
- account for a weak collisional absorption by the inverse Bremsstrahlung,
- are limited to weakly absorptive media $\epsilon' \gg \epsilon''$, in order to (i) retain the validity of the SVEA and (ii) keep the eikonal equation (2.20) real-valued,
- do not describe wave diffraction[1],
- do not describe the evolution of the transverse amplitude profile, i.e. there is no notion of the beam width,
- are not well suited to model temporal and spatial laser smoothing, because the needle-like description cannot model realistic intensity distributions,
- the needle-like nature of RT rays is incompatible with the notion of ray intensity, as the wavefront surface does not exist. Similarly, because the trajectory of different RT rays

[1] Although the diffraction process can be mimicked by spreading the initial conditions for the ray trajectories, as is done in many hydrodynamic codes using the RT model, we show in Sec. 2.3.5.3 that this approach mis-estimates the diffraction process in inhomogeneous media.

are independent, estimating in plasma the local direction of the Poynting vector from bundles of ray trajectories is not straightforward and requires potentially complex numerical algorithms.

The RT method, without any notion of beam intensity, is relatively well suited for describing the linear inverse Bremsstrahlung absorption at moderate laser intensity regimes and for interactions with warm targets. This is not the case for other laser-plasma interactions, i.e. nonlinear LPIs, for which knowledge of the laser intensity is the key factor.

2.2.4 Estimation of the intensity field

There are several ways of estimating the intensity field in the RT method, which are mainly: (i) reconstructing a local beam width by considering the distance between adjacent rays, and thus estimating an intensity from the ray power, and (ii) reconstructing the intensity from the collisional absorption field, as is described below. Each of these methods pose severe challenges and require numerous and cumbersome numerical procedures to yield physical estimates. As an example, in the case of the first method, neighboring rays intersect close to the critical density so that the reconstructed beam width reaches zero and the intensity diverges.

In order to provide a clear comparison of RT-based intensity estimates versus the intensity described by the PCGO model (presented in Sec. 2.3.5.3), we describe here the intensity reconstruction method. The intensity associated with a distribution of needle-like rays can be expressed from the conservation equation for the laser energy (1.74):

$$\frac{\partial \bar{W}}{\partial t} + \nabla.\bar{\boldsymbol{S}} = -\nu_{\mathrm{IB}} \frac{n_e}{n_c} \bar{W} \ . \tag{2.32}$$

At a given hydrodynamic timestep, the laser propagation is stationary so that the first term can be neglected. Integrating over a cell k by assuming a constant inverse Bremsstrahlung collision frequency, a constant EM wave energy density, a constant plasma density and using the *Stokes* formula, equation (2.32) reads:

$$\iint \mathrm{dS_k} \nabla.\bar{\boldsymbol{S}} = \int \bar{\boldsymbol{S}}.\mathbf{dl} = -\Delta P^k_{\mathrm{abs}} = -\nu_{\mathrm{IB}} \frac{n_e}{n_c} \frac{\epsilon_0}{2} |E|^2 \Delta \mathrm{S_k} \ , \tag{2.33}$$

with $\Delta P^k_{\mathrm{abs}}$ being the total power absorbed in the cell k and ΔS_k the area of this cell. Rearranging, the beam intensity in the triangle k reads:

$$I_k = \frac{c\sqrt{\epsilon'}\Delta P^k_{\mathrm{abs}}}{\Delta S_k \nu_{\mathrm{IB}} n_e/n_c} \ . \tag{2.34}$$

This formulation for the reconstructed intensity has four main limitations:

- it is inversely proportional to the density. As such, it diverges at low densities and the intensity cannot be described in vacuum,
- it looses precision near the critical density, where the assumption made on $\epsilon'' \ll \epsilon'$ of GO does not hold,

- it does not hold information on macroscopic beam quantities such as direction and width (although the notion of ray direction exists), which are crucial for some LPI processes, notably regarding the direction of light scattering and the Doppler shifts by plasma flows,

- the spatial resolution of the intensity field estimated by this method is entirely dependent on the size of the hydrodynamic mesh and not on the location of intensity gradients. For the process of plasma heating by IB absorption, this is unimportant because the thermal conductivity of the plasma smoothes temperature gradients efficiently. However, finer processes of LPI require a detailed knowledge of the intensity, especially because of their nonlinear nature. This could be addressed by subgrid refinement of mesh cells with an Adaptive Mesh Refinement (AMR) method based on IB absorption gradients, which is both numerically complex and costly in terms of memory and CPU usage.

These points underline that in the present form, the Geometrical Optics based Ray-Tracing models are not well suited for the description of intensity fields in plasmas and hence the description of nonlinear LPIs. From this point on, we present an alternative description of the wave-field at hydrodynamic scales, based on the Paraxial Complex Geometrical Optics. This model has been developed in this thesis and is the base framework of all other processes described in the following chapters.

2.3 Adaptation of Ray-Based Paraxial Complex Geometrical Optics to collisional plasmas and to a Lagrangian Hydrodynamic code

An alternative class of solutions to the Helmholtz equation, that considers thick-rays instead of needle-like rays, is presented in this section. The so-called *Paraxial Complex Geometrical Optics* method is a paraxial-eikonal based form of the Complex Geometrical Optics (CGO) [117], that deals with the problem of Gaussian beam diffraction in inhomogeneous media [52, 118, 119, 120]. We present its formulation for collisional plasmas and a method of numerical resolution of equations on an unstructured irregular mesh. This model, that we implemented in Chic, is used throughout this work.

2.3.1 Motivation

As it was emphasized in Sec. 2.2.4, the key quantity for the modeling of nonlinear LPIs is the intensity field. Given that in the most basic approach of GO, the ray power is known, it is sufficient to describe the evolution of the beam width in order to compute its intensity. On the one hand, the Geometrical Optics describes a field with the amplitude $A(\tau)$ only depending on the curvilinear ray coordinate, i.e. there is no knowledge of the beam envelope and width. However, the GO is an attractive method because it relies on the resolution of Ordinary Differential Equations. On the other hand, the paraxial approximation presented in Sec. 1.3.3 describes the full wave envelope $A(x, y, z)$ along a privileged direction. The corresponding Paraxial Wave Equation, even described within the Slowly Varying Envelope Approximation, is difficult to resolve because it

belongs to Partial Differential Equations. Furthermore, we have seen that the validity condition of the paraxial approximation is difficult to satisfy for typical plasmas created from laser-solid interactions.

PCGO is built on both approaches, taking (i) the numerical efficiency of GO, which allows to implement it in a hydrocode, and (ii) the notion of beam envelope described by the paraxial approximation. The core principle of PCGO is to consider a particular class of wave-fields in the paraxial approximation, that is the *fundamental Gaussian mode*. As such, it can be considered less precise than the Paraxial Wave Equation, which is not limited to this particular field ansatz. In the case of Gaussian beams, the equations of PCGO are reduced to a set of Ordinary Differential Equations that describe the wavefront curvature of a Gaussian beam, including the effects of diffraction, as was first shown in [121]. Consequently, while being a paraxial approach, PCGO retains the CPU-efficiency of GO. We introduce in Sec. 2.3.2.1 the basics of Gaussian beam optics, and notably show that the Gaussian wave-field described in the paraxial approximation is characterized by a complex wavefront and curvature, as was first demonstrated by [118] and [122]. As such, there are two justifications for the use of the Complex Geometrical Optics over GO: (i) the Gaussian mode being described by complex parameters, the operating framework must be complex as well, and (ii) in the case of strongly absorptive media for which $\epsilon'' \geq \epsilon'$, the GO approach is not valid as the latter deals with real-valued rays. We present in Sec. 2.3.2.2 the idea behind the Complex Geometrical Optics, and make the distinction between the *eikonal-based* form of CGO, compared to the *ray-based* form.

As we will see, the wave front curvature equation of PCGO ultimately consists of a non-linear Riccati-type equation that is conceptually similar to those obtained with other asymptotic methods from various fields of physics, as it is illustrated in Fig. 2-4. As an example, while CGO belongs to the field of optics and electrodynamics, the Dynamic Ray Tracing (DRT) method [123] was proposed for the elastic wave theory (e.g. see Refs. [124, 125]). Its extension to the complex plane (so-called complex-DRT) [126, 127] yields equations equivalent to that of PCGO. Equivalent equations were also found in the study of the problem of Gaussian beam diffraction, using WKB theory and the paraxial approximation, as was first demonstrated in [128]. More generally, the problem of Gaussian beam diffraction in inhomogeneous media is of interest in optics, geophysics, acoustics, radio physics and plasma physics (see [129, 130] for applications to magnetized non-collisional plasmas).

2.3.2 Gaussian Beams and Complex GO

Paraxial Complex Geometrical Optics are a branch of the Complex Geometrical Optics that considers *Gaussian* wave-fields described in the *eikonal form* with a *paraxial approximation*. In order to clearly define the working principles of PCGO, we introduce in the following section the basic properties of Gaussian beams, and give an introduction to the Complex Geometrical Optics.

2.3.2.1 Optics of Gaussian Beams

For simplicity, we derive the Gaussian beam equations in the case of a vacuum, i.e. for $\epsilon = 1$. Considering solutions for the field of the form $E(x, y, z) = E_0(x, y, z) \exp[-\imath k z]$, with $k = \sqrt{\epsilon'} k_{\mathrm{FS}}$,

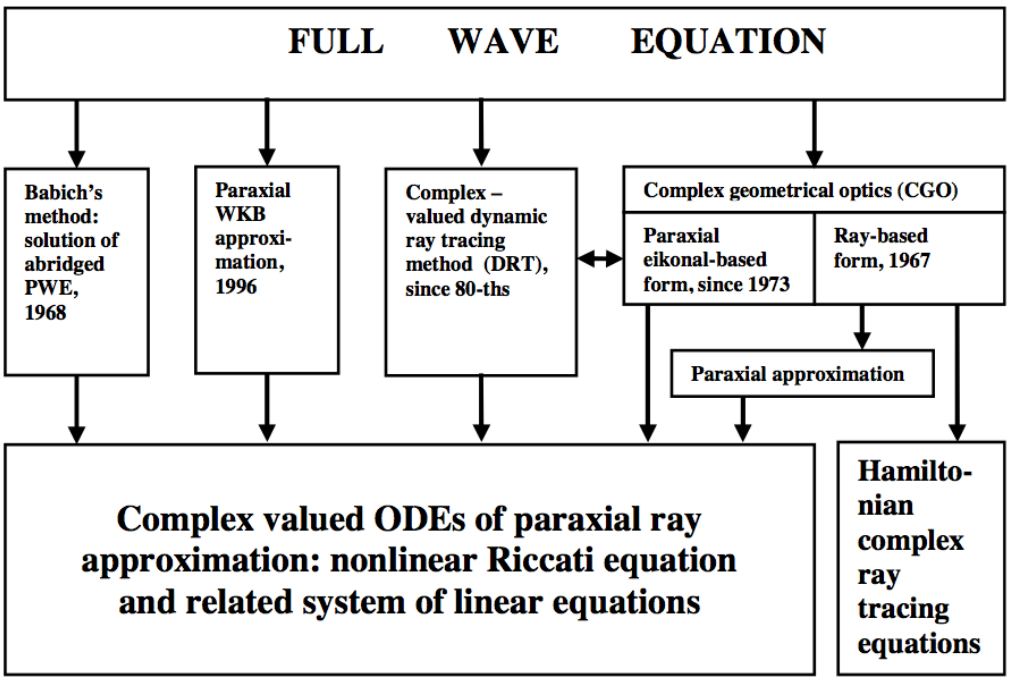

Figure 2-4 – *The problem of Gaussian beam diffraction in inhomogeneous media from various methods and physical fields (reproduced from [131]).*

the Helmholtz equation (1.55) transforms into a Paraxial Wave Equation (1.107):

$$\frac{\partial^2 E_0}{\partial x^2} + \frac{\partial^2 E_0}{\partial y^2} - 2\imath k \frac{\partial E_0}{\partial z} = 0 \ , \tag{2.35}$$

where the second order derivative in the axis of propagation z is neglected. We seek a solution that depends on the propagation coordinate z and that is cylindrically symmetric around z:

$$E_0(x, y, z) = A_0 \exp\left[-\imath\left(\varphi(z) + \frac{k}{2q(z)} r^2\right)\right] \ , \tag{2.36}$$

with $r^2 = x^2 + y^2$, $\varphi(z)$ is a phase shift factor, A_0 is a constant amplitude and $q(z)$ is the so-called *beam parameter*. Substituting (2.36) into (2.35) we obtain:

$$2k\left(\frac{\mathrm{d}\varphi}{\mathrm{d}z} + \frac{\imath}{q(z)}\right) + r^2 \frac{k^2}{q^2(z)}\left(1 - \frac{\mathrm{d}q}{\mathrm{d}z}\right) = 0 \ . \tag{2.37}$$

Given that this quadratic equation must hold for any value of r, the coefficients of the polynomial must be zero and we get:

$$\begin{aligned} \frac{\mathrm{d}q}{\mathrm{d}z} &= 1 \ , \\ \frac{\mathrm{d}\varphi}{\mathrm{d}z} &= -\frac{\imath}{q(z)} \ . \end{aligned} \tag{2.38}$$

Integrating these equations between 0 and z gives:

$$q(z) = q_0 + z \ , \tag{2.39}$$

$$\varphi(z) = -\imath \ln(1 + z/q_0) \ , \tag{2.40}$$

where $q_0 = q(0)$. The wave's electric field now reads:

$$E(x, y, z) = A_0 \exp\left[-\ln\left(1 + \frac{z}{q(z) - z}\right) - \imath \frac{k}{2q(z)} r^2\right] \exp\left[-\imath k z\right] \ . \tag{2.41}$$

We now identify the physical meaning of the beam parameter q. Setting $1/q = 1/q' - \imath/q''$, the beam intensity reads:

$$E E^\star = \frac{A_0^2}{(1 + z/q_0)^2} \exp\left[-\frac{k r^2}{q''(z)}\right] \ . \tag{2.42}$$

This equation shows that the transverse intensity profile is a Gaussian function, of a radius at the half maximum $w(z) = \sqrt{2q''(z)/k}$, which defines $q''(z) = \pi w^2(z)/\lambda$ (where $\lambda = 2\pi/k$ is the local wavelength). At the focal position $z = 0$, we have $1/q_0 = -\imath\lambda/(\pi w_f^2)$, where $w_f = w(0)$ is called the *beam waist*. The real part of q defines the beam curvature radius $R(z)$. Indeed, by using (2.39) we obtain the relationship between z, q' and q'':

$$w^2(z) = w_f^2 \left[1 + \left(\frac{\lambda z}{\pi w_f^2}\right)^2\right] \ , \tag{2.43}$$

$$R(z) = q'(z) = z \left[1 + \left(\frac{z\lambda}{\pi w_f^2}\right)^{-2}\right] \ . \tag{2.44}$$

The characteristic distance of beam divergence $z_R = \pi w_f^2/\lambda$ is called the *Rayleigh length*. Equation (2.43) illustrates that the beam waist attains its minimum at the focal position. The surfaces of constant phase in the field form of (2.41) read:

$$-kz - \Im\left(\ln\left(1 + \frac{z}{q(z) - z}\right)\right) - \frac{k r^2}{2q'(z)} = \text{constant} \ . \tag{2.45}$$

Using $\ln(a + \imath b) = (\ln(a^2 + b^2))/2 + \imath \tan^{-1}(b/a)$, we get:

$$k\left(z + \frac{r^2}{2q'(z)}\right) + \tan^{-1}\left(\frac{1}{1 - z/q'(z)} \frac{\frac{z\lambda}{\pi w_f^2}}{\left[1 + \left(\frac{\lambda z}{\pi w_f^2}\right)\right]}\right) = \text{constant} \ . \tag{2.46}$$

For $z \gg \pi w_f^2/\lambda$, and using Eq. (2.44), we see that the $\tan^{-1}$ factor is constant. Re-arranging, we obtain:

$$z = \frac{\text{constant}}{k} - \frac{r^2}{2q'(z)} \ . \tag{2.47}$$

This equation describes a parabola, that approaches a spherical surface of radius $R(z) = q'(z)$ for $r^2 \ll z^2$. For that reason, $q'(z)$ is identified as the curvature radius of the wavefront and we have:

$$\frac{1}{q(z)} = \frac{1}{R(z)} - \imath \frac{\lambda}{\pi w^2(z)} \ , \tag{2.48}$$

where $w(z)$ and $R(z)$ obey Eqs. (2.43) and (2.44), respectively. Note that for $z = 0$, $R \to \infty$, so that the wavefront is flat at the waist of the beam. Finally, the electric field and the beam intensity read:

$$E(r,z) = A_0 \frac{w_f}{w(z)} \exp\left[-\imath k \left(z - \frac{1}{2R(z)} - \Phi\right) - \frac{r^2}{w^2(z)}\right] \ , \tag{2.49}$$

$$I(r) = I_0 \exp\left[-\frac{2r^2}{w^2(z)}\right] \ , \tag{2.50}$$

where we have used $\ln[1 + z/q_0] = \ln[w/w_f] + \imath \tan^{-1}[\lambda z/(\pi w_f^2)]$ and we have defined the phase shift factor $\Phi = \tan^{-1}[\lambda z/(\pi w_f^2)]$. This field distribution is called the fundamental Gaussian mode.

2.3.2.2 Complex Geometrical Optics

Complex Geometrical Optics is centered around the notion of complex rays, which are the complex-equivalent of rays in GO. Gaussian beam diffraction aside, CGO is commonly used to describe wave-fields in the vicinity of caustics, radio wave propagation through the ionosphere, wave penetration into a caustic, space-time diffraction of Gaussian pulses in dispersive media, and propagation of surface waves (see Ref. [116] for a review).

CGO deals with *plane inhomogeneous waves*, described by a complex wavevector:

$$\mathbf{k} = \mathbf{k}' + \imath \mathbf{k}'' \ , \tag{2.51}$$

so that the wave-field $u = \exp[\imath \mathbf{k}.\mathbf{r}]$ contains an oscillating component $\exp[\imath \mathbf{k}'.\mathbf{r}]$ and a decaying factor $\exp[-\mathbf{k}''.\mathbf{r}]$. In this formulation, the field modulus $|E| \propto \exp[-\mathbf{k}''.\mathbf{r}]$ is not necessarily constant on a surface of constant wavefront $\mathbf{k}'.\mathbf{r}$, that is why these waves are termed inhomogeneous waves.

The SVEA in the framework of CGO translates in a slow variation of ϵ', A, $\boldsymbol{k}'$ and $\boldsymbol{k}''$ over the scale of the vacuum wavelength λ_L. Contrary to the SVEA approximations of GO (2.18), there is no related assumption on the variation of the field modulus $|E| = |A| \exp[-k_{\mathrm{FS}} \psi'']$ over the wavelength scale, so that CGO is valid in strongly dispersive media, e.g. in the vicinity of the critical density surface in the case of plasmas. This extended validity domain is related to the description of inhomogeneous waves, which is consistent with the local wave field structure in these regions.

Ray-based CGO The notion of complex ray was first introduced in [117], as the continuity in 6-dimensional complex space $(x', x'', y', y'', z', z'')$ of the GO ray equations. Introducing the GO form of the wave (2.14) with a complex-valued eikonal $\psi = \psi' + \imath \psi''$, a complex-valued amplitude

$A = A' + \imath A''$ and for a complex media $\epsilon = \epsilon' + \imath\epsilon''$, the same equations are obtained for the eikonal equation (2.20) (with a complex ϵ), and the zero-th order transport equation (2.21) reads:

$$u(\mathbf{r}) = \frac{u(\mathbf{r}_0)}{\mathcal{J}} \exp\left[\imath k_{\mathrm{FS}} \int_{\tau_0}^{\tau} \epsilon(\mathbf{r}(\tau))\mathrm{d}\tilde{\tau}\right] , \tag{2.52}$$

where the ray parameter $\tau = \mathrm{d}s/(c\sqrt{\epsilon})$ is also complex-valued and $\mathbf{r}_0$ is the initial ray position. Applying the characteristics technique once again yields the trajectory equation in so-called *Hamiltonian form* or *ray-based form*, with complex-valued solutions for the ray position $\mathbf{r}$ and momentum $\mathbf{p}$.

The idea behind ray-based CGO is to reconstruct the field amplitude at a point $\mathbf{r}'$ in the real-space by summation of the amplitudes of all rays passing by $\mathbf{r}'$. This requires an iterative method to find the distribution of initial positions $(x_0', x_0'', y_0', y_0'', z_0', z_0'')$ for which ray trajectories intersect with $\mathbf{r}'$. This is a difficult procedure that requires heavy numerical algorithms. These algorithms are similar to those used in GO-based Ray-Tracing methods (in real space) in the field of computer graphics.

Eikonal-based CGO The eikonal-form of CGO deals with the resolution of the eikonal and transport equation directly, where the unknown variables are $\nabla\psi'$ and $\nabla\psi''$. The physical meaning of these quantities is comparable to that in GO; the propagation direction of the wave in CGO being given by $\nabla\psi'$, while the direction of the Poynting vector gradient is given by $\nabla\psi''$ [116]. Writing the eikonal equation (2.20) and identifying the real and imaginary parts we obtain:

$$(\nabla\psi')^2 - (\nabla\psi'')^2 = \epsilon' , \tag{2.53}$$

$$2\nabla\psi'.\nabla\psi'' = \epsilon'' , \tag{2.54}$$

which implies that in lossy media, the direction of energy propagation and of Poynting vector gradient are not orthogonal. Identifying the real and imaginary parts, the transport equations (2.21) read:

$$2(\nabla\psi'.\nabla A' - \nabla\psi''.\nabla A'') + A'\triangle\psi' - A''\triangle\psi'' = 0 , \tag{2.55}$$

$$2(\nabla\psi''.\nabla A' + \nabla\psi'.\nabla A'') + A'\triangle\psi'' + A''\triangle\psi' = 0 . \tag{2.56}$$

Analytical solution of these equations is rather complex, even for homogeneous media. A numerical resolution was proposed by [132] in the case of Gaussian beams in inhomogeneous media, notably showing that these equations do model the physical process of beam diffraction. The PCGO method presented below belongs to the eikonal-based form because it deals with the computation of the eikonal ψ directly, instead of relying on a summation of infinitely narrow complex rays. It also belongs to beam-tracing methods [129] because the central axis of the wave in PCGO is described by a GO ray.

2.3.3 Paraxial Complex Geometrical Optics in dissipative media

The physical idea of PCGO is to represent a Gaussian beamlet, which symmetry axis follows the laws of Geometrical Optics. As such, the method consists in (i) projecting the eikonal and transport equations of CGO along a GO ray trajectory, and (ii) formulating a phase model for ψ that describes a Gaussian mode in the paraxial approximation. As mentioned earlier, this method is qualified as Complex because it involves Gaussian beams, which are described by complex parameters, and the medium dielectric permittivity which is also complex.

2.3.3.1 Eikonal and transport equations in the ray-centered coordinate system

As in CGO, PCGO is based on solutions of the Helmholtz equation (2.11) in the form of an almost-plane inhomogeneous waves, that is:

$$u(\boldsymbol{r}) = A(\boldsymbol{r}) \exp[\imath k_{\mathrm{FS}} \psi(\boldsymbol{r})] \ , \tag{2.57}$$

where $A(\boldsymbol{r})$ and $\psi(\boldsymbol{r})$ are complex-valued. This model is paraxial because it describes a principal propagation direction for the wave (given by the curvilinear trajectory $\nabla\psi'(\boldsymbol{r})$), and that deviations from this main axis must be small (this results from the SVEA, detailed below). Substituting this model into the Helmholtz equation, we retrieve the complex-valued eikonal and zeroth-order transport equations of CGO (see Sec. 2.3.2.2).

The validity domain of these equations is related to the SVEA validity of CGO. Sufficient conditions for PCGO are discussed in Sec. 2.3.3.3.

Let us project the eikonal and transport equations onto a GO ray trajectory. To this end, we define a new coordinate system $\{q_1, q_2, \tau\}$, where the vector $\mathbf{q} = \{q_1, q_2\}$ is orthogonal to the ray and τ is tangent to it. In a 3D framework, this new coordinate system must account for torsion and curvature of the ray in order to constitute a rotationless orthogonal basis, providing parallel transport along the ray. This is not an issue in the 2D framework presented here so that we do not consider this problem. Note that such a basis in 3D is proposed in Ref. [133] (and referred to as Popov's ray-centered coordinate system). The eikonal equation written in the central ray coordinate system reads:

$$\begin{aligned} \frac{1}{h^2}\left(\frac{\partial\psi}{c\partial\tau}\right)^2 + \left(\frac{\partial\psi}{\partial q_1}\right)^2 + \left(\frac{\partial\psi}{\partial q_2}\right)^2 = \\ \epsilon(\boldsymbol{r}_c) + (\boldsymbol{q}\cdot\nabla)\epsilon(\boldsymbol{r}_c) + \frac{1}{2}(\boldsymbol{q}\cdot\nabla)^2\epsilon(\boldsymbol{r}_c) + \dots \ , \end{aligned} \tag{2.58}$$

where $h = \sqrt{\epsilon(\boldsymbol{r}_c,\tau)} - (\boldsymbol{q}\cdot\nabla)\sqrt{\epsilon(\boldsymbol{r}_c,\tau)}$ is the Lamé coefficient, $\boldsymbol{r}_c$ refers to the central ray position and the relative permittivity $\epsilon(\boldsymbol{r}) = \epsilon(\boldsymbol{r}_c + \boldsymbol{q})$ has been expanded in the Taylor series of $\boldsymbol{q} = \boldsymbol{r} - \boldsymbol{r}_c$. The transport equation in the new coordinate system reads:

$$\frac{2}{c^2h^2}\frac{\partial\psi}{\partial\tau}\frac{\partial A}{\partial\tau} + \left[\frac{1}{ch}\frac{\partial}{\partial\tau}\left(\frac{1}{ch}\frac{\partial\psi}{\partial\tau} + \frac{\partial^2\psi}{\partial q_1^2} + \frac{\partial^2\psi}{\partial q_2^2}\right)\right] A = 0 \ , \tag{2.59}$$

which expresses the conservation of EM energy along the ray propagation. Note that the imaginary part of the dielectric permittivity ϵ'' is not present in this equation because it is accounted for in

the eikonal equation.

2.3.3.2 Formulation in absorptive media

Phase model for PCGO beamlets The phase of a PCGO ray contains informations on the central ray trajectory and on phase deviations around the central ray. We decompose the phase of the wave-field in two contributions on the ray and the envelop:

$$\psi(q_1,q_2,\tau) = \overbrace{\psi_c(\tau)}^{\text{Trajectory}} + \overbrace{\tilde{\psi}(q_1,q_2,\tau)}^{\text{Envelop}} , \tag{2.60}$$

where $\psi_c = \psi_c'(\tau) + \imath\psi_c''(\tau)$ is a complex function. This model adds two terms to the central ray phase ψ_c'. First, $\tilde{\psi}(q_1,q_2,\tau)$ is the phase of the wave around the central ray that we relate to its thickness and curvature. As in the standard PCGO, it is assumed to vary in a quadratic way with q:

$$\tilde{\psi}(q_1,q_2,\tau) = \frac{1}{2}B_{ij}(\tau)q_iq_j \ . \tag{2.61}$$

Secondly, $\imath\psi_c''(\tau)$ is a purely imaginary phase term that accounts for absorption or gain induced by the medium where the wave propagates, for which no assumption on ϵ''/ϵ' is made.

Wave front curvature equation The wave front curvature of a PCGO ray is derived by resolving the eikonal equation (as in Sec. 2.3.2.2) at various orders in the transverse coordinate $\mathbf{q}$ and by separating the real and imaginary parts. For the sake of simplicity, it is now assumed that the geometry is 2D planar, so that there is only one component in $\mathbf{q}$ and there is no torsion on the central ray (see Fig. 2-5 for the central ray coordinate system). The following analysis can be readily extended in 3D, as it is explained in the monograph [116] with more details on 3D PCGO in general. Introducing equation (2.60) in the eikonal equation (2.58) yields:

$$\begin{aligned} &\frac{1}{c^2h^2}\left[\left(\frac{\mathrm{d}\psi_c}{\mathrm{d}\tau}\right)^2 + \frac{\mathrm{d}\psi_c}{\mathrm{d}\tau}\frac{\mathrm{d}B}{\mathrm{d}\tau}q^2 + \left(\frac{1}{2}\frac{\mathrm{d}B}{\mathrm{d}\tau}q^2\right)^2\right] \\ &+(Bq)^2 = \epsilon_c' + \imath\epsilon_c'' + q\frac{\partial(\epsilon_c'+\imath\epsilon_c'')}{\partial q} + \frac{q^2}{2}\frac{\partial^2(\epsilon_c'+\imath\epsilon_c'')}{\partial q^2} \ , \end{aligned} \tag{2.62}$$

where the notation $\epsilon_c = \epsilon(\boldsymbol{r}_c)$ was introduced and the Lamé parameter reads:

$$h^2 = |\boldsymbol{h}.\boldsymbol{h}| = \epsilon_c - (\boldsymbol{q}\cdot\nabla)\epsilon_c + \frac{1}{4\epsilon_c}((\boldsymbol{q}\cdot\nabla)\epsilon_c)^2 \ . \tag{2.63}$$

At the order 0 in q, Eq. (2.62) reads:

$$\left[\frac{\mathrm{d}\psi_c'}{\mathrm{d}\tau'} - \frac{n''}{n'}\frac{\mathrm{d}\psi_c''}{\mathrm{d}\tau'}\right] + \imath\left[\frac{\mathrm{d}\psi_c''}{\mathrm{d}\tau'} + \frac{n''}{n'}\frac{\mathrm{d}\psi_c'}{\mathrm{d}\tau'}\right] = c(\epsilon_c' + \imath\epsilon_c'') \ , \tag{2.64}$$

where we have expressed the derivative as a function of the real-valued ray parameter using:

$$\frac{\mathrm{d}\tau'}{\mathrm{d}\tau} = 1 + \imath\frac{n''}{n'} \ . \tag{2.65}$$

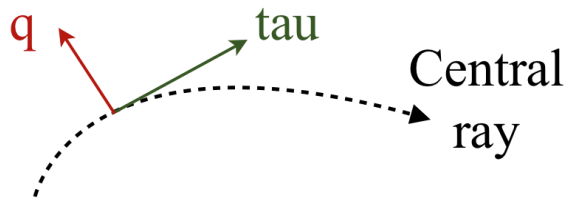

Figure 2-5 – *Schematic illustration of the central ray coordinate system in 2D configuration. The central GO ray is shown as a dashed black line, the (q,τ) coordinate system at a given point of the trajectory as red and green vectors, respectively.*

Equating the real and imaginary parts in (2.64) yields:

$$\frac{\mathrm{d}\psi_c'}{\mathrm{d}\tau'} = c\epsilon_c' \left(1 + \frac{n''}{n'}\frac{\epsilon_c''}{\epsilon_c'}\right)\left[1 + \left(\frac{n''}{n'}\right)^2\right]^{-1} \approx c\epsilon_c' + O\left(\frac{\nu_{\mathrm{IB}}}{\omega}\right)^2 , \tag{2.66}$$

$$\frac{\mathrm{d}\psi_c''}{\mathrm{d}\tau'} = c\epsilon_c'' \left(1 - \frac{n''}{n'}\frac{\epsilon_c'}{\epsilon_c''}\right)\left[1 + \left(\frac{n''}{n'}\right)^2\right]^{-1} = \frac{c\epsilon_c''}{2} , \tag{2.67}$$

where the expression in the right-hand-side of Eq. (2.66) was obtained by a Taylor expansion in series of ν_{IB}/ω, which is valid for $\nu_{\mathrm{IB}} \ll \omega$. Equation (2.66) [right] is a standard equation for the central ray phase in PCGO for weakly dissipative media, while Eq. (2.67) relates the complex phase perturbation to the imaginary part of the relative permittivity, i.e. to the absorption or gain of the medium.

Using Eqs. (2.66) and (2.67), one can show that the terms of order 1 in q in (2.62) are cancelled. At the order 2 and using Eqs. (2.66) and (2.67), one obtains:

$$\frac{1}{c}\frac{\mathrm{d}B}{\mathrm{d}\tau} + B^2 = -\frac{3}{4\epsilon_c}\left(\frac{\partial\epsilon_c}{\partial q}\right)^2 + \frac{1}{2}\frac{\partial^2\epsilon_c}{\partial q^2} . \tag{2.68}$$

This is a nonlinear Riccati-type equation describing the wave front curvature. Re-arranging, we obtain:

$$B^2 + \frac{1}{c}\frac{\mathrm{d}B}{\mathrm{d}\tau} = \alpha_{\Re}(\tau') + \imath\alpha_{\Im}(\tau') , \tag{2.69}$$

$$\alpha_{\Re}(\tau') = -\frac{3}{4\epsilon_c'}\left[\frac{\left(\frac{\partial\epsilon_c'}{\partial q}\right)^2 + \frac{\partial\epsilon_c''}{\partial q}\left(\frac{2\epsilon_c''}{\epsilon_c'}\frac{\partial\epsilon_c'}{\partial q} - \frac{\partial\epsilon_c''}{\partial q}\right)}{1 + \frac{\epsilon_c''^2}{\epsilon_c'^2}}\right] + \frac{1}{2}\frac{\partial^2\epsilon_c'}{\partial q^2}$$

$$\approx -\frac{3}{4\epsilon_c'}\left(\frac{\partial\epsilon_c'}{\partial q}\right)^2 + \frac{1}{2}\frac{\partial^2\epsilon_c'}{\partial q^2} , \tag{2.70}$$

$$\alpha_{\Im}(\tau') = -\frac{3\epsilon_c''}{4\epsilon_c'^2}\left[\frac{-\left(\frac{\partial\epsilon_c'}{\partial q}\right)^2 + \frac{\partial\epsilon_c''}{\partial q}\left(\frac{2\epsilon_c'}{\epsilon_c''}\frac{\partial\epsilon_c'}{\partial q} + \frac{\partial\epsilon_c''}{\partial q}\right)}{1 + \frac{\epsilon_c''^2}{\epsilon_c'^2}}\right] + \frac{1}{2}\frac{\partial^2\epsilon_c''}{\partial q^2}$$

$$\approx -\frac{3\epsilon_c''}{4\epsilon_c'^2}\left[\frac{\partial\epsilon_c'}{\partial q}\left(\frac{\partial\epsilon_c''}{\partial q}\frac{2\epsilon_c'}{\epsilon_c''}-\frac{\partial\epsilon_c'}{\partial q}\right)\right] , \tag{2.71}$$

where expressions in the right-hand-side of $\alpha_\Re$ and $\alpha_\Im$ have been obtained by assuming $\nu_{\mathrm{IB}} \ll \omega$ and limiting the Taylor series at the order 1. The standard nonlinear Riccati-type equation of PCGO is obtained by making the additional assumption of weakly dissipative media $\epsilon'' \ll \epsilon'$:

$$B^2 + \frac{1}{c}\frac{\mathrm{d}B}{\mathrm{d}\tau'} = -\frac{3}{4\epsilon_c'}\left(\frac{\partial\epsilon_c'}{\partial q}\right)^2 + \frac{1}{2}\frac{\partial^2\epsilon_c'}{\partial q^2} , \tag{2.72}$$

where it should be noted that the curvature matrix B is complex because of the initial condition $B(0)$. This can be seen by noting that B is related to the complex beam parameter of Gaussian beams derived in Sec. 2.3.2.1.

The contribution from $\alpha_\Im$ to the ray curvature and width has been assessed and is seen to be rather small in general, except in regions close to the critical density surface, where the assumption $\epsilon'' \ll \epsilon'$ breaks down. Even then, the contribution from $\alpha_\Im$ is seen to be rather limited, so that finally it is Eq. (2.72) that is used, where α is computed with $\epsilon' = 1 - (\omega_{\mathrm{pe}}/\omega)^2/(1 + (\nu_{\mathrm{IB}}/\omega)^2)$.

Form of the electric field The energy conservation equation for the amplitude (Eq. (2.59)) can be rewritten in terms of $\tilde{A}(\tau) = (\epsilon_c'(\tau))^{1/4}A(\tau)$, in the 2D planar geometry:

$$\frac{1}{c}\frac{\partial\tilde{A}}{\partial\tau} + \frac{1}{2}B(\tau)\tilde{A} = 0 , \tag{2.73}$$

for which a straightforward solution is $\tilde{A} = \tilde{A}(0)\exp[-\int cB(\tau)\mathrm{d}\tau/2]$. Taking the modulus of the solution and assuming $n'' \ll n'$ yields the energy flux conservation:

$$|\tilde{A}(\tau')| = |\tilde{A}(0)|\left[\frac{\Im(B)}{\Im(B(0))}\right]^{1/4} , \tag{2.74}$$

where we have used $\Re(B) = -(1/2)\mathrm{d}\ln\Im(B)/\mathrm{d}\tau'$, that can be obtained from the imaginary part of the wave front equation (where the contribution from $\alpha_\Im$ has been neglected). The full form of the electric field given by the model is then:

$$\begin{aligned} u(q,\tau') = {} & \frac{\tilde{A}(\tau')}{(\epsilon_c'(\tau'))^{1/4}} \\ & \times \exp\left[\imath k_{\mathrm{FS}}\left(\frac{\Re(B)}{2}q^2 - \int_0^{\tau'} c\epsilon_c'(\tilde{\tau}')d\tilde{\tau}'\right)\right] \\ & \times \exp\left[-k_{\mathrm{FS}}\left(\frac{\Im(B)}{2}q^2 + \int_0^{\tau'}\frac{c\epsilon_c''(\tilde{\tau}')}{2}d\tilde{\tau}'\right)\right] . \end{aligned} \tag{2.75}$$

This equation highlights the decaying factor in the electric field modeled with the contribution of ϵ_c''. Identifying the real and imaginary part of the scalar curvature B with the expression for the fundamental Gaussian mode (given by Eq. (2.49) in App. 2.3.2.1) yields the PCGO ray thickness

w and curvature radius R:

$$\Re(B) = \frac{\sqrt{\epsilon'}}{R} \ , \tag{2.76}$$

$$\Im(B) = \frac{2}{w^2 k_{\mathrm{FS}}} \ , \tag{2.77}$$

so that the field modulus finally reads:

$$|u(q,\tau')| = \frac{|\tilde{A}(0)|}{(\epsilon_c'(\tau'))^{1/4}} \sqrt{\frac{w}{w_0}} \exp\left[-k_{\mathrm{FS}} \int_0^{\tau'} \frac{c\epsilon_c''(\tilde{\tau}')}{2} d\tilde{\tau}'\right] \exp\left[\frac{-q^2}{w^2}\right] \ , \tag{2.78}$$

where w_0 is the initial Gaussian beam thickness. Note that compared to the formulation of Eq. (2.49), the pre-factor in Eq. (2.78) vary as $\sqrt{w_0/w}$. This is a consequence of the 2D-planar description of the wave-field, compared to the cylindrically-symmetric form given in the Appendix. The same difference can be noted in the derivation of the Gaussian beam ponderomotive self-focusing distances in Sec. 2.4.2.1 and Eq. (2.97). Finally, the intensity of the PCGO ray reads:

$$I(\tau') = I_0(\tau') \exp\left[\frac{-2q^2}{w^2}\right] \ , \tag{2.79}$$

$$I_0(\tau') = \frac{c\sqrt{\epsilon_c'}\epsilon_0}{2} |u(0,\tau')|^2 = \frac{c\epsilon_0}{2} |\tilde{A}(0)|^2 \left(\frac{w_0}{w}\right) \exp\left(-k_{\mathrm{FS}} \int_0^{\tau'} c\epsilon_c'' d\tilde{\tau}'\right) \ , \tag{2.80}$$

where I_0 is the on-axis intensity. Alongside the intensity, width and radius of curvature transported along a PCGO ray, the local beam frequency can be readily computed from the Doppler shift induced by plasma velocities described by the hydrodynamic core. In this 2D planar framework, the PCGO beamlet power P is defined by considering that the plasma is a slab of a unit height in the direction of invariance, so that:

$$P(\tau') = \sqrt{\frac{\pi}{2}} I_0(\tau') w(\tau') h \ . \tag{2.81}$$

In numerical simulations, we always set the beamlet power so as to reproduce the desired real (i.e. 3D) laser intensity. For that reason, the beamlet power P is not representative of the real laser power. This approach is consistent with the fact that computing linear and non-linear LPIs relies on the knowledge of the intensity field.

The initial condition $B(0)$ of the PCGO ray is given by the initial beam width w_0 and its initial curvature $R(0)$:

$$B(0) = \frac{\sqrt{\epsilon'}}{R(0)} + \imath \frac{2}{w_0^2 k_{\mathrm{FS}}} \ , \tag{2.82}$$

which is comparable to the complex beam parameter q^{-1} for Gaussian beams in vacuum, derived in Sec. 2.3.2.1. The initial curvature radius of the beam can notably be set to a specific value in order to control the location of the beamlet focus, as is used in Ch. 3 and shown in App. B.1.2.

2.3.3.3 Validity domain

The PCGO framework relies on the validity of the SVEA for CGO and of a Taylor expansion of the dielectric permittivity around the central ray. We describe sufficient conditions for the validity of PCGO.

The first condition, common to all GO methods (and Complex GO), states that the wavelength should be small compared to the characteristic scale L_{ch} of the plasma density inhomogeneities:

$$\frac{\lambda}{L_{\mathrm{ch}}} \ll 1 \ . \tag{2.83}$$

For ICF applications, the typical wavelength is 0.35 μm and the characteristic scale of inhomogeneities ~ 10 μm, so that this assumption generally holds in large scale hydrocodes. The second condition relates to the small angle paraxial-wave approximation:

$$\frac{\lambda}{w} \ll 1 \ . \tag{2.84}$$

Typical ICF beams have a radius at the focal plane of $\simeq 500$ μm, with imposed small scale modulations $\sim 2-3$ μm, which are well over λ. Although it appears to be an easily respected condition, it actually limits other parameters related to the reproducion of speckle patterns, as is shown in Sec. 3.2. The third condition is the most restrictive one and is related to the preservation of the Gaussian profile along the propagation:

$$\frac{w}{L_{\mathrm{ch}}} \ll 1 \ . \tag{2.85}$$

This assumption is incorrect for a large $\simeq 500$ μm beam in a typical ICF plasma, however it is satisfied if one considers the transverse radius of the small-scale intensity modulations. Although this limitation forbids the modeling of a whole ICF beam by a single thick ray, one may think to describe a whole laser beam as a composition of an ensemble of small beamlets with an envelop representing a whole beam. The idea to combine several Gaussian beamlets to reproduce super-Gaussian beams was first suggested in [134]. It was later shown in [135] that a superposition of 3 Gaussian beams does reproduce the diffraction behavior of one super-Gaussian beam of order 4, with an accuracy of 1 %. In our framework, superposing PCGO beamlets possesses the advantage of enabling to describe randomized laser beams smoothed by Phase Plates, where the whole beam is split in small beamlets with different phases. Thus, the PCGO method is providing an opportunity for the description of realistic smoothed beams and their associated intensity statistics. This approach is presented in details in Chapter 3.

The last assumption used in this model is $\epsilon'' \ll \epsilon'$ in the derivation of the wavefront equation (2.72). Contrary to GO, which formally breaks down when this assumption is not met, PCGO remains operational but the beamlet curvature radius and width are misestimated. This shortcoming is partially addressed by considering the evanescent field of the wave at the critical density, which allows to compute the absorption on the plasma skin depth for $n_e \geq n_c$, as presented in App. A.3.5.

2.3.4 Numerical implementation

We have implemented the PCGO model derived here in the Chic code. In order to compute the beamlet intensity field (2.80), the core equations resolved by the model are the GO equations (2.25), the collisional absorption equation (2.67) and the wave front equation (2.72). Despite its apparent simplicity, the implementation of PCGO in a Lagrangian hydrodynamic code is highly challenging and requires innovative algorithms and methods. In particular, it poses major difficulties related to;

- the width of the beamlets: because the PCGO ray has a thickness, it drives LPIs (such as inverse Bremsstrahlung) at a distance from its central axis, whereas GO only interacts with the plasma on its axis (because it has no width). Consequently, when the central ray is in a given mesh cell, one must also compute the interaction of the beamlet in neighborhood mesh cells (this neighborhood potentially constitutes the whole mesh). In general, the envelope of the PCGO beamlet can be seen as a smooth Gaussian field with a curved axis and decreasing maxima (due to absorption), as illustrated in Fig. 2-6. Difficulties related to this projection problem are addressed in App. A, notably detailing:
  - the definition of a selection criterion to find the intersection between the beam envelop and the mesh (in App. A.3.1),
  - the precise and efficient computation of integrals onto triangularized mesh cells of an unstructured and irregular mesh grid (in App. A.3.2),
  - the correction of projection algorithms to account for transverse plasma inhomogeneities (in App. A.3.3),
  - the definition of efficient search algorithms for finding cells in the neighborhood of a central ray located at an arbitrary position (in App. A.3.4),
  - the interaction of the beam envelop, defined from a central-ray in a sub-critical mesh cell, with the critical density surface, thus defining the notion of electric field decay on the skin depth (in App.A.3.5),
  - the issue of energy conservation, that arises from the various methods used in the field projection onto the Lagrangian mesh and that must account for the transverse inhomogeneities and the presence of a critical density surface (in App. A.4),
- the integration of the wave front curvature equation: because of its non-linear nature (due to the presence of the B^2 term) and the sub-grid definition of the ray trajectory, it requires various specific resolution methods that we detail in App. A, with notably:
  - the insufficient precision of GO trajectories predicted with usual Runge Kutta algorithms, which requires to couple analytical and numerical methods to reconstruct the correct ray timings in mesh cells (in App. A.1),
  - the reduction of the wave front equation to coupled linear Ordinary Differential Equations, in A.2,

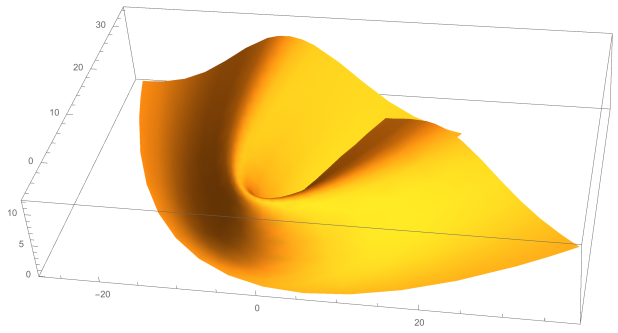

Figure 2-6 – *Illustration of arbitrary intensity fields predicted by PCGO: the central axis of the beam envelope is curved and follows geometrical optics laws, while the thickness and intensity of the beam changes with its propagation.*

- the computation of the source term $\alpha_{\Re}$, which requires to compute continuous and smooth first-order and second-order derivatives of the permittivity at arbitrary coordinates in the plasma, from a discrete density field defined on an unstructured grid (also in App. A.2),
- the numerical resolution of the nonlinear Riccati equation on a ray trajectory with a different step than for the integration of the trajectory equations, and on sub-discretized ray arcs in order to simplify the projection algorithms described above (in Apps. A.3.1 and A.3.2).

The PCGO model has been implemented in the Chic code. We discuss in what follows its validation and various applications.

2.3.5 Academic validation

Straightforward validations of the PCGO model implemented in Chic against theoretical solutions for Gaussian beams in vacuum and weakly dissipative constant density media have been conducted (not shown here for conciseness). We show here the cases of beam propagation in a plasma with a linear density profile and in a waveguide (the plasma is considered collisionless).

2.3.5.1 Propagation in a plasma with a linear density profile

The case of a thick ray incident at $\theta_0 = 30°$ with respect to the normal of a linear density ramp of the form $\epsilon = 1 - z/L$ is considered. The beam is initially parallel, of initial thickness $w_0 = 10\lambda_L$ and the gradient scale length is $L = 1000\pi\lambda_L$. The evolution of the beam thickness as a function of the central ray coordinate is presented in Fig. 2-7 [left]. On the ascending trajectory, diffraction competes against refraction, broadening the beam until refraction prevails before the turning point. The beam starts focusing on the descending trajectory, reaching a beam waist smaller

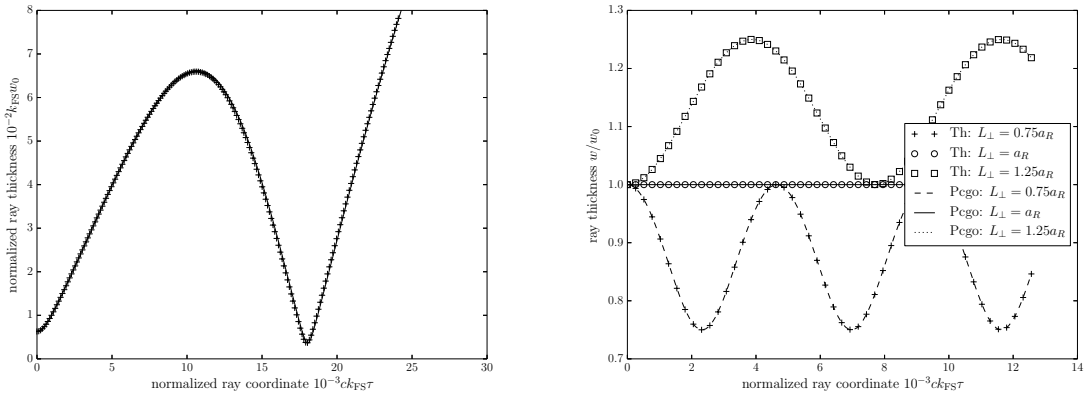

Figure 2-7 – *[left] Radius of a thick ray incident at $\theta_0 = 30°$ on a linear density ramp, as a function of the central ray coordinate. The thick-ray radius and τ coordinate are normalized to $10^2/k_{FS}$ and $10^3/(ck_{FS})$, respectively. Results from PCGO in* Chic *is showed as a plain line, and numerical integration of the wave front equation using the analytical form for $\alpha_\Re$ is shown as crosses. [right] Radius of a thick ray propagating along the axis of a waveguide as a function of the central ray coordinate, for different values of the characteristic length $L_\perp$. The thick-ray radius and τ coordinate are normalized to $10^2/k_{FS}$ and $10^3/(ck_{FS})$, respectively Theoretical solutions are shown as symbols and results from the PCGO model in* Chic *as lines (see legend on Figure).*

than the initial beam width. After the focus, the beam width starts increasing again. These results are compared to a numerical integration of the wave front equation, using the analytical expression for $\alpha_\Re$. The latter can be found by combining the expression of the ray trajectory in the linear density profile (that is a parabola, see Sec. 2.2.1), with the expression of the dielectric permittivity given above. The resulting expression for $\alpha_\Re$ given by Eq. (2.70) reads:

$$\alpha_\Re(\tau) = -\frac{12\sin^2\theta_0}{((c\tau)^2 - 4c\tau L\cos\theta_0 + 4L^2)^2} \ . \tag{2.86}$$

PCGO is found to be in perfect agreement with the theoretical solution, thus validating the computation of $\alpha_\Re$ performed in the model. Similar tests were conducted for other laser beam parameters confirming the validity of the PCGO model.

2.3.5.2 Propagation in a waveguide

For a beam with a plane initial wavefront, propagating along the axis of a waveguide medium with a parabolic density profile $\epsilon = \epsilon_0 - z^2/L^2$, one can solve analytically the wave front equation (2.72) for B [116]:

$$B_{\text{th}}^{\text{WG}} = \frac{1}{L_\perp}\frac{\imath\frac{L_\perp}{a_R} - \tan\frac{c\tau}{L_\perp}}{\imath\frac{L_\perp}{a_R}\tan\frac{c\tau}{L_\perp} + 1} \ , \tag{2.87}$$

where $L_\perp = L/\epsilon_0^{1/4}$ and a_R is the Rayleigh length. We consider a beam of wavelength $\lambda_L = 100\mu$m with an initial radius $w_0 = 10\lambda_L$, so that the Rayleigh length is $a_R = 100\pi\lambda_L$. Figure 2-7 [right] shows the thickness of such a ray, as computed by our model in Chic. Simulations are conducted for three values of the characteristic length $L_\perp$, for which the beam width oscillates when $L_\perp \neq a_R$,

or is constant when $L_\perp = a_R$ (i.e. diffraction is exactly compensated by the waveguide). PCGO results from Chic are found to be in perfect agreement with the theoretical solution of the wave front equation.

2.3.5.3 Diffraction modeling and collisional absorption: GO vs PCGO

As expected, comparisons of RT and PCGO in weakly dissipative constant density media yield a similar beam profile and a similar total power deposited by the beam in a plasma at distances smaller than the Rayleigh length. However, significant differences naturally arise between initially parallel RT rays and a PCGO thick ray at larger propagation distances. The difference is larger for beams that are narrow and have a small Rayleigh range with respect to the total simulation domain size. RT models commonly compensate for this flaw by using a spread in the rays initial k-vectors to locally model diffraction of the beam. Rays arranged in such a configuration reproduce the global envelope of a beam as well as its intensity profile. Using this technique, similar results for the spatial beam profile between PCGO and RT can be obtained. It is worth mentioning that modeling diffraction of a Gaussian beam in RT codes requires a significant number of rays (we have checked that in that case, about 5000 rays are necessary) whereas the PCGO model only requires one thick ray. In general, ICF beams are large and so is their Rayleigh length. However, nonlinear LPI effects crucially depend on diffraction modeling as a mechanism that acts against or with refraction to change the beam width and intensity. It is important to note that this method of reproducing diffraction using an initial condition on the k-vectors of the rays is exact only for vacuum conditions (or a constant density plasma). Any departure from these conditions will not be reflected with a change in diffraction strength for the beam modeled with RT. Because rays are independent, RT-based diffraction remains that of the initial condition, i.e. that of a beam in a vacuum. This difference is highlighted in what follows with an example of an inhomogeneous plasma.

The energy deposited in a linear density ramp of the form $n_e/n_c = 1 - z/L$ where $L = 0.5$ mm is considered. The simulation domain is 100×100 grid points in a box of 0.5 mm $\times$ 0.5 mm for an incident beam at an angle $\theta_0 = 0°$ and 0.5 mm $\times$ 1.0 mm for $\theta_0 = 50°$. The beam initial thickness is $w_0 = 21$ μm. The RT model is initialized so as to reproduce the caustic of the beam, with a focal length $f = 4$ m and diameter at lens of $D = 12.7$ cm. 10000 rays are used for the RT model. The beam initial power is $P_0 = 1.209 \times 10^{13}$ W/cm. According to results shown in Sec. 1.3.2, the power deposited in the plasma by a beam normal to the density gradient at $\theta_0 = 0°$ reads:

$$P_{\text{abs}}^{\text{th}} = P_0 \left(1 - \exp\left[\frac{-32\nu_{\text{IB}}^\star L}{15c}\right]\right) \ , \tag{2.88}$$

where the electron-ion collision frequency for these conditions is $\nu_{\text{IB}}^\star = \nu_{\text{IB}}(n_c) = 4.578 \times 10^{11}\text{s}^{-1}$ (the plasma is fully ionized Helium with $T_e = 5T_i = 2$ keV, and $\lambda_0 = 1.05$ μm). Using $L = 500$ μm yields a theoretical absorption coefficient $\eta_{\text{abs}}^{\text{th}} = P_{\text{abs}}^{\text{th}}/P_0 = 80.4\%$.

The upper row in Fig. 2-8 shows the simulation results for $\theta_0 = 0°$. The total power deposited with both models yields an absorption coefficient identical and conform to the theory, i.e. $\eta_{\text{abs}} = 80.4\%$. The discretized nature of the RT model [top-left] leads to a slightly sharper energy deposition and underestimation of the spatial distribution of the beam. The PCGO ray

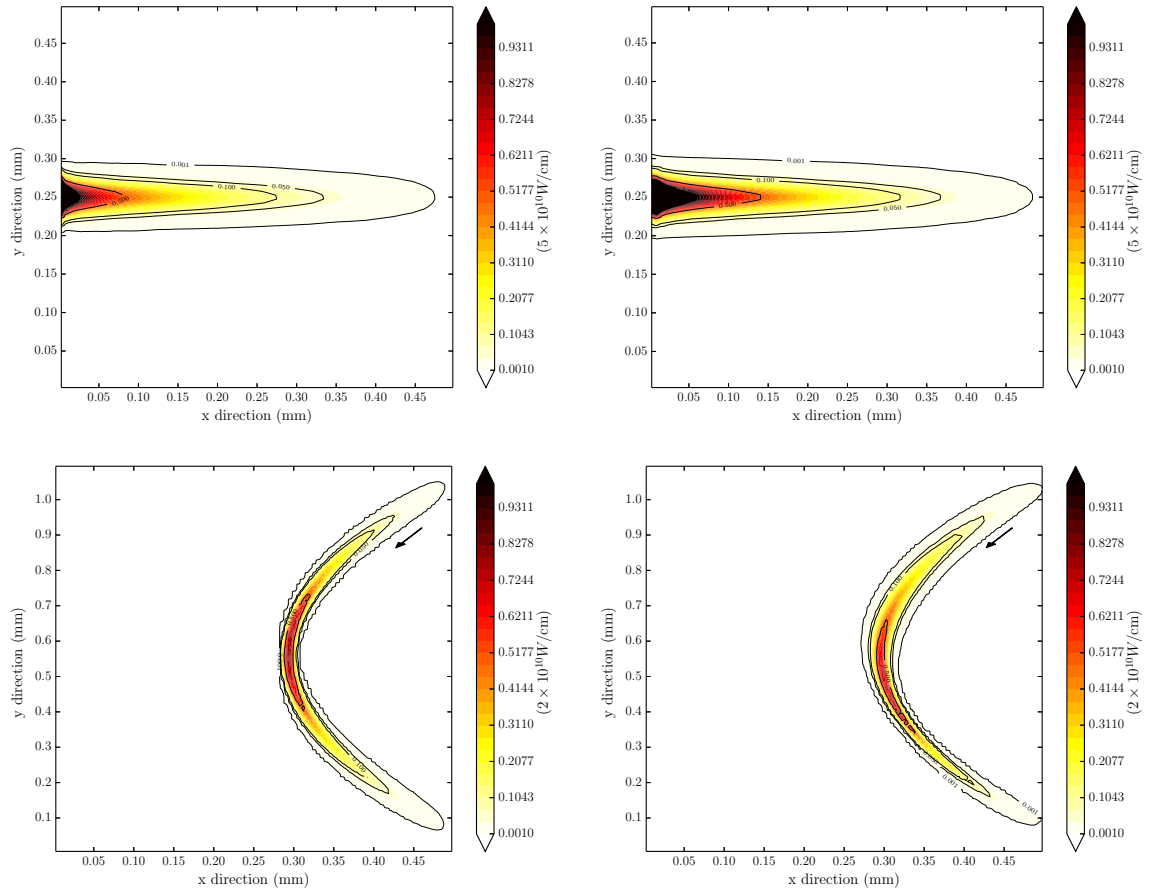

Figure 2-8 – *(Color) Power absorbed by Inverse Bremsstrahlung on a linear density ramp* $n_e/n_c = 1 - x/L$ *with* $L = (0.5\text{ mm})$. *The initial beam width is* $w = 21\mu$m *with zero curvature at the vacuum-plasma boundary. The beam is incident from the right on the density ramp at* $\theta_0 = 0°$ *[top] (the beam travels up to the critical density) and* $\theta_0 = 50°$ *[bottom] (the beam travels up to* $n_e/n_c \simeq 0.4$*) - see arrows for the beam direction. Results shown on the [left] panels are from a standard Ray Tracing model and on the [right] panels from the PCGO model.*

thickness, corresponding to theoretical solutions, is shown in Fig. 2-9 [left]. Diffraction effects broaden the beam and the spatial distribution of deposited power is larger for PCGO (Fig. 2-8 [top-right]).

The bottom row in Fig. 2-8 shows the simulation results for $\theta_0 = 50°$. The total absorption coefficient with both codes is identical: $\eta_{\text{abs}} = 16.4\%$. Results from the PCGO model [bottom-right], conform to the theory (see Sec. 2.3.5.1), show a peak power offset from the maximum density with $P_{\text{max}}^{\text{PCGO}} \simeq 1.52 \times 10^{10}$ W/cm (see Fig. 2-9 [right]). This shift is the consequence of modeling refraction and diffraction of a single Gaussian beam, compared to many needle-like independent rays. In the RT model [bottom-left], all rays converge to a same $\hat{x}$ coordinate, leading to a beam waist at maximum n_e/n_c (minimum $\hat{x}$). The RT model produces an artificial beam waist following from the geometrical configuration of the rays and does not reproduce the shifted waist of the beam. Peak deposited power in RT is overestimated, with $P_{\text{max}}^{\text{RT}} \simeq 1.66 \times 10^{10}$ W/cm, due to the discretized nature of the rays. Diffraction modeling in RT models is exact only

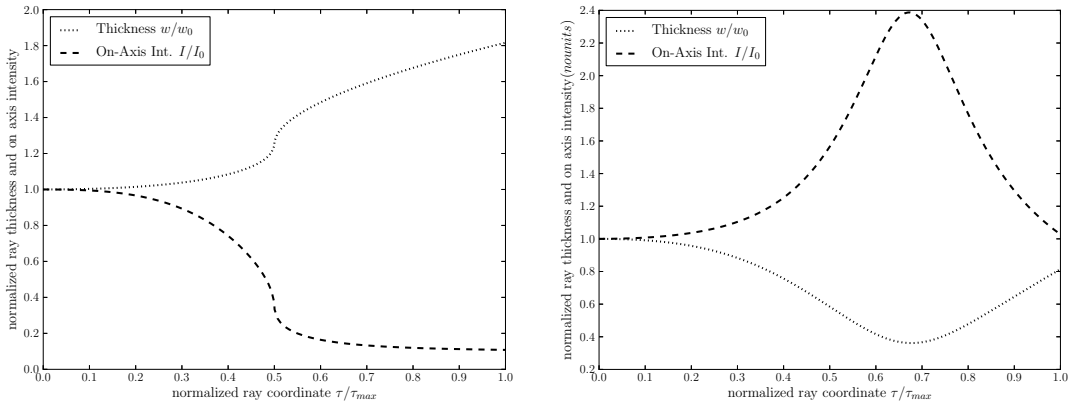

Figure 2-9 – *PCGO ray normalized radius (dotted lines) and normalized on-axis intensity (dashed lines), normalization with respect to initial values), for the linear density ramp with [left] $\theta_0 = 0°$ and [right] $\theta_0 = 50°$. Ray coordinate τ is normalized with respect to the maximum τ, where the ray leaves the plasma. τ/τ_{max}=0.5 corresponds respectively to the reflection [left] and turning point [right] of the ray.*

for a constant density media. Once variations appear in the density profile, because each ray independently follows its trajectory, diffraction may be locally underestimated or overestimated. Although the PCGO model corresponds to the exact solution in this specific case, the peak deposited power between RT and PCGO is different by only 9%. From the energy deposition standpoint only, the difference between RT and PCGO is relatively minor and likely to be smoothed by other physical processes. The underlying intensity difference and the lack of exact diffraction modeling more strongly impact nonlinear LPI modeling, as it is shown in the following section.

2.4 Nonlinear LPI modeling: the ponderomotive self-focusing

Self-focusing is a nonlinear LPI process where spatial gradients of dielectric permittivity induced by the wave-field lead to the beam refraction [136]. There are two contributions to self-focusing: thermal and ponderomotive. Both processes stem from the laser intensity non-uniformities. In thermal self-focusing, the enhanced laser energy deposition on the beam-axis leads to temperature gradients between the beam center and its wings, creating a thermally-induced pressure gradient. The plasma motion under the pressure gradient leads to the on-axis density depletion, which causes a refractive index gradient and consequently the on-axis beam focusing. In ponderomotive self-focusing, the on-axis density depletion is caused by the ponderomotive force expelling the electrons radially and creating a similar gradient of the refraction index.

The case of ponderomotive self-focusing is studied with the RT and PCGO approaches. In order to estimate the laser intensity in RT models, it is common to use the power absorbed by the inverse Bremsstrahlung as a proxy, alongside the cells surface area (see Sec. 2.2.4). This technique allows to evaluate the laser intensity distribution in plasma and is used in RT-based hydrocodes which include nonlinear LPI effects. The RT intensity reconstruction method presented in Sec. 2.2.4 is implemented in Chic for a comparison with the PCGO model. This section presents the

implementation of the ponderomotive force directly based on the electric field modeled by the PCGO technique and a comparison to the ponderomotive force estimated from the RT intensity reconstruction.

2.4.1 Ponderomotive potential

In an hydrodynamic approach, the ponderomotive force $F_P = -\nabla U$ acting on the electron fluid can be expressed as a gradient of the ponderomotive potential U [80]:

$$U = \frac{n_e e^2}{4 m_e \omega^2} |u|^2 \ , \tag{2.89}$$

with $|E|$ the electric field modulus. In this form, the ponderomotive force can be modeled in a hydrocode as an additional pressure term U in the plasma equation of motion. The mean ponderomotive potential U_q in cell q is computed separately for each sub-cell, defined by a triangularization of cell q. For a quadrangle q decomposed in two triangles:

$$\langle U_q \rangle = \frac{S_{q_1} \langle U \rangle_{q_1} + S_{q_2} \langle U \rangle_{q_2}}{S_{q_1} + S_{q_2}} \ , \tag{2.90}$$

where $\langle U \rangle_{q_1}$ and $\langle U \rangle_{q_2}$ are mean values corresponding to each triangle in cell q. The ponderomotive potential in the triangle i of cell q reads:

$$\langle U \rangle_{q_i} = \frac{n_e e^2}{4 m_e \omega^2} \frac{1}{S_{q_i}} \iint_{S_{q_i}} |E|^2 \mathrm{dS} \ , \tag{2.91}$$

where the integral over the triangle i is computed in the same way as for Eqs. (A.15) and (A.17) (see App. A.3.2), and assuming ϵ'' to be constant within a cell.

2.4.2 Gaussian beam self-focusing in a 2D geometry

The commonly used criteria for ponderomotive self-focusing are derived in a 3D or 2D-axisymetric framework. For the particular case of 2D planar configurations, these criteria must be adapted with the appropriate mathematical form for the electric field. In this subsection we derive the equations describing the ponderomotive self-focusing of a Gaussian beam propagating in an initially homogeneous plasma. Such a model was presented for Gaussian beams in cylindrical coordinates (so-called *2D-axisymetric*) in [137, 138, 139].

2.4.2.1 Beam width equation

Starting from the wave equation for the electric field as shown in [137], the electron density on the beam axis is depleted according to:

$$n = n_0 \exp\left[-\beta |E|^2\right] \ , \tag{2.92}$$

where $\beta = e^2/(4 m_e \omega^2 (T_e + T_i))$, n_0 is the initial electron density and $|E|$ is the electric field modulus. This formalism holds for length scales L such as $L \gg \lambda_D$ and timescales long compared

to L/c_s, where λ_D is the Debye length and c_s is the sound speed. For a plane wave and assuming $n_e/n_c \ll 1$ so that absorption can be neglected, one can derive the following equation for the complex field amplitude E in the paraxial approximation [138] (see Sec. 1.3.3):

$$-2\imath k_{\mathrm{FS}} c^2 \frac{\partial E}{\partial z} + c^2 \triangle_\perp E - \Gamma^2 E + \omega_{\mathrm{pe},0}^2 E(1 - \exp\left[-\beta |E|^2\right]) = 0 \ , \tag{2.93}$$

where $\omega_{\mathrm{pe},0}^2$ is the unperturbed plasma frequency, $\Gamma^2 = k_{\mathrm{FS}}^2 c^2 - \omega^2 + \omega_{\mathrm{pe},0}^2$ represents the nonlinear wavenumber shift due to the density depression on the beam-axis caused by the ponderomotive force and z is the propagation axis. E is written in term of amplitude A and eikonal ψ:

$$E = A(r,z) \exp\left[\imath k_{\mathrm{FS}} \psi(r,z)\right] \ , \tag{2.94}$$

where r is the transverse direction of the paraxial wave. Introducing Eq. (2.94) in (2.93) and assuming a 2D geometry yields:

$$2\left(\frac{\partial A}{\partial z} - \frac{\partial \psi}{\partial r}\frac{\partial A}{\partial r}\right) - A\frac{\partial^2 \psi}{\partial r^2} = 0 \ , \tag{2.95}$$

$$c^2 \frac{\partial^2 A}{\partial r^2} - k_{\mathrm{FS}}^2 c^2 A \left(-2\frac{\partial \psi}{\partial z} + \left(\frac{\partial \psi}{\partial r}\right)^2\right) - \Gamma^2 A + \omega_{\mathrm{pe},0}^2 A(1 - \exp\left[-\beta A^2\right]) = 0 \ , \tag{2.96}$$

which is similar to Eqs. (7) and (8) in [138], except for the missing cylindrical components of the Laplacian. We now assume a 2D Gaussian profile for the electric field amplitude E (see Sec. 2.3.2.1):

$$A(r,z) = (A_0/\sqrt{f}) \exp[-r^2/w_0^2 f^2] \ , \tag{2.97}$$

$$\psi(r,z) = -\frac{r^2}{2}\frac{1}{f}\frac{df}{dz} - \phi \ , \tag{2.98}$$

where $\phi(z)$ is the phase and $f(z)$ is the Gaussian beam shape factor, $f(z) = w(z)/w_0$. Note that for a cylindrically symmetric Gaussian beam, $\sqrt{f}$ is replaced by f in the expression of A. The consistency of this model can be verified by checking that Eqs. (2.97) and (2.98) always satisfy (2.95). Substitution of these expressions for A and ψ in Eq. (2.96) yields, at the order 0 in $r/(w_0 f)$:

$$f^2\Big[-2c^2 k_{\mathrm{FS}}^2 \phi' - \Gamma^2 - \omega_{\mathrm{pe},0}^2 \exp[-\beta A_0^2/f] + \omega_{\mathrm{pe},0}^2\Big] - \frac{2c^2}{w_0^2} = 0 \ . \tag{2.99}$$

The next order in the expansion is the order 2 in $r/(w_0 f)$:

$$f\Big[\left(f\left(c^2 k_{\mathrm{FS}}^2\left(2\phi' - w_0^2 f f''\right) + \Gamma^2 - \omega_{\mathrm{pe},0}^2\right) + \omega_{\mathrm{pe},0}^2 \exp[-\beta A_0^2/f]\left(f - 2\beta A_0^2\right)\right] + \frac{6c^2}{w_0^2} = 0 \ . \tag{2.100}$$

Equation (2.99) describes the phase of the wave, similar to Eq. (12) in [138] to a factor 1/2 for the first term in the right hand side:

$$\phi' = -\frac{1}{w_0^2 k_{\mathrm{FS}}^2 f^2} + \frac{\omega_{\mathrm{pe},0}^2 - \Gamma^2}{2c^2 k_{\mathrm{FS}}^2} - \frac{\omega_{\mathrm{pe},0}^2 \exp[-\beta A_0^2/f]}{2c^2 k_{\mathrm{FS}}^2} \ . \tag{2.101}$$

Injecting the above solution for the phase in Eq. (2.100) yields the shape factor equation:

$$f'' = \frac{4}{w_0^4 k_{\mathrm{FS}}^2 f^3} - \frac{2\beta A_0^2 \omega_{\mathrm{pe},0}^2 \exp[-\beta A_0^2/f]}{w_0^2 c^2 k_{\mathrm{FS}}^2 f^2} \ . \tag{2.102}$$

Equation (2.102) differs from the cylindrically symmetric case by a factor f in the second term of the right hand side and in the exponential term. These changes reflect the fact that the total power of the beam in a 2-dimensional framework varies with $1/f$ and not $1/f^2$. This equation can be solved numerically to find the self-focusing distance z_{sf} of a 2D Gaussian beam propagating in an initially constant density plasma, as well as the intensity amplification ratio $I_0/I_0(\tau = 0) = 1/f(z_{sf})$.

2.4.2.2 Critical power

An expression for the critical power above which a Gaussian beam propagating in an initially constant density media will undergo self-focusing can be derived from Eq. (2.102). This threshold corresponds to the power for which the diffraction of the beam is exactly compensated by the refraction due to the density waveguide created by the ponderomotive expelling of electrons from the wave-field. Such an equilibrium is obtained for $f = 1$ and $df/dz = d^2f/dz^2 = 0$. It is straightforward to find the expression for the equilibrium radius w_E using Eq. (2.102):

$$w_E = \sqrt{2}\frac{c}{\omega_{\mathrm{pe},0}} \frac{\exp\left[\beta A_0^2/2\right]}{\sqrt{\beta A_0^2}} \ . \tag{2.103}$$

A similar expression is obtained in [138] for a cylindrically symmetric Gaussian beam. Solutions of this non-linear equation for A_0 can be written in the form:

$$A_0 = \pm\imath \sqrt{\mathscr{W}\left(\frac{-2c^2}{w_0^2\omega_{\mathrm{pe},0}^2}\right)/\beta} \ ,$$

where $\mathscr{W}(z)$ is the real-valued Lambert W function, i.e. the real solution v such as $v\exp(v) = z$. Using $A_0^2 = 2I_0/(c\epsilon_0 N)$, replacing β by its expression and solving for I_0 yields the critical intensity $I_0^{C;w_0}$ of a beam with an initially plane wavefront (e.g. at its focus) and width w_0:

$$I_0^{C;w_0} = -2cn_cN(T_e + T_i)w_0\mathscr{W}\left(\frac{-2c^2}{w_0^2\omega_{\mathrm{pe},0}^2}\right) \ . \tag{2.104}$$

The total power carried by a Gaussian beam is $P^{\mathrm{3D}} = \int_0^\infty 2\pi r I_0 \exp[-2r/w_0] = (\pi/2)I_0 w_0^2$ in the cylindrically symmetric case and $P^{\mathrm{2D}} = \int_{-\infty}^{\infty} I_0 h \exp[-2r/w_0] = \sqrt{\pi/2} I_0 w_0 h$ in the case of a 2D planar geometry and considering a unit length $h = 1$ cm in the direction of the third dimension. The equivalent 3D critical power reads:

$$P_C^{\mathrm{3D}} = -cn_cN\pi(T_e + T_i)w_0^2\mathscr{W}\left(\frac{-2c^2}{w_0^2\omega_{\mathrm{pe},0}^2}\right) \ . \tag{2.105}$$

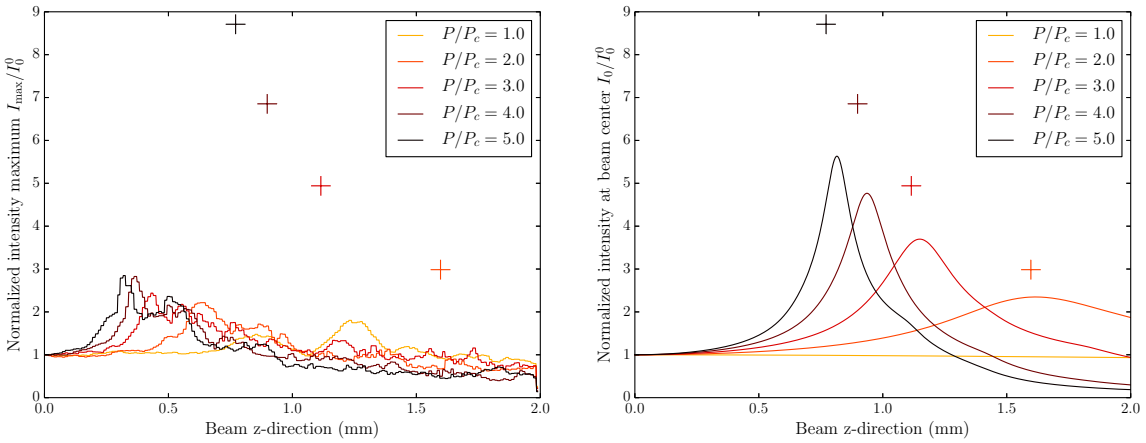

Figure 2-10 – *(Color) [Left] RT-based reconstructed maximum intensity, [right] PCGO central ray intensity, as a function of the beam propagation direction z, after 200 ps of simulation for the 5 cases. Intensities are normalized to the initial central ray intensity $I_0(\tau = 0)$. Theoretical values for intensity amplification and self-focusing distance are super-imposed as colored crosses.*

Adaptations that can be made in order to use PCGO in axisymmetric geometries from the 2D planar framework are presented in App. B.3.

2.4.3 Comparisons of GO and PCGO results for Gaussian beams

The ponderomotive self-focusing of a 2D planar Gaussian beam with a focal spot size $w_0 = 20\lambda_L$ and $\lambda_L = 1.05$ μm in a hydrogen plasma is now considered. In such a configuration, the initial diffraction of the beam is relatively weak, as it would be for an ICF beam. The hydrogen plasma with $T_e = 10T_i = 5$ keV and $n_e/n_c = 0.1$ is described by a 180×180 grid points in a box of 2 mm $\times$ 0.2 mm size. The simulation is run for 200 ps, time when the self-focusing has reached a steady-state. Under these conditions, the critical power for a purely ponderomotive self-focusing is $P_C = P_C^{3D} = 445.3$ MW. 5 cases are considered, where $P/P_C \in [1; 2; 3; 4; 5]$. RT runs are conducted with 10000 rays and diffraction modeling. Simulations yield similar results using 5000 rays, suggesting weak dependence on the number of rays above 5000.

2.4.3.1 Intensity profiles

Figure 2-10 [left] illustrates the RT maximum intensity in the transverse direction as a function of propagation direction z, at $t = 200$ ps. Although there is no clear intensity peak, partial self-focusing occurs for all cases. The self-focusing distance decreases when power increases for simulations ranging from $P/P_C = 1$ to $P/P_C = 3$, and remains similar at higher powers. The intensity amplification peak is also similar for all cases with $P/P_C \geq 2$. Theoretical values for intensity amplification and self-focusing distance are super-imposed as colored crosses. Theoretical values show a clear dependence the intensity amplification ratio and self-focusing distance on the beam power that the RT-based model does not reproduce. The RT intensity reconstruction requires a large number of rays per cell. Even when this condition is fulfilled, as each ray propagates independently, rays tend to get trapped in density channels thus creating local

waveguides. The thickness of these waveguides is determined by the mesh resolution. Although this phenomenon resembles filamentation, RT is not expected to model that process and it is a numerical artifact related to the discreteness of the mesh. Furthermore, once RT-filamentation has started, rays tend to stay trapped because there is no more energy deposition outside of the channels. Because of these limitations, the ponderomotive force from intensity reconstruction presents spatial modulations and large inaccuracies, leading to the observed discrepancies in self-focusing length and intensity amplification.

Results using PCGO are illustrated in Fig. 2-10 [right], showing normalized central ray intensity I_0/I_0^0 as a function of propagation direction z at $t = 200$ ps. For $P/P_C = 1$, the beam intensity is constant, corresponding to an equilibrium between diffraction and refraction from the waveguide created by the ponderomotive force. It is found that self-focusing distances are well reproduced with thick rays, and intensity amplification ratios are under-estimated. Because the ponderomotive force acts along the whole beam thickness, the width of the created waveguide is of the same order. Consequently, the assumption of a small beam thickness compared to plasma inhomogeneity ($w \ll L_{\text{ch}}$) is less accurate. This leads to an underestimation of the density curvature in the waveguide and of the refraction process. Although intensity amplification is underestimated, it follows the same tendency of higher amplification for higher powers as predicted by the theory. Furthermore, a departure from $w \ll L_{\text{ch}}$ due to the ponderomotive force is unlikely for realistic ICF beams modeled with PCGO, as the latter contain spatial intensity modulations and are constructed from smaller thick rays (see Sec. 3.2). It is worth mentioning that in simulations using paraxial electromagnetic codes (see for ex. [140]) the beam structure after focusing is strongly distorted, whereas the assumption in PCGO is made that beams always remain of Gaussian shape. Nevertheless, the focusing length and the intensity amplification are in agreement with our model.

2.4.3.2 Density channel

In the setup described above, the ionization state $Z = 1$ and the modulation length of transverse acoustic waves is much greater than the Debye length, so that it is a regime of weak ion acoustic wave damping. For a non isothermal plasma ($T_e \gg T_i$) with a weak ion damping, one transverse direction and no thermal effects, the paraxial wave equation possesses an analytical solution for the density perturbation caused by the ponderomotive force [141]:

$$\delta n(t,x) = \frac{1}{2cn_cT_e}\left[-I(x) + \frac{1}{2}[I(x+c_st) + I(x-c_st)]\right] \ ,$$

where $\delta n(t,x) = n_e(t,x)/n_e(0) - 1$. Hence, the ponderomotive force causes a central channel formation with a depletion factor of $-0.5I_0/(cn_cT_e)$ and two positive density perturbations propagating away from the beam axis with a factor $0.25I(x+c_st)/(cn_cT_e)$. Figure 2-11 [right] illustrates the density perturbation along the transverse direction of a PCGO ray for $z = 0.3$ mm, normalized to cn_cT_e/I_0. The density perturbation is in good agreement with the theory for all cases. Figure 2-11 [left] shows corresponding results using the RT model. Although results are similar to the theory for $P/P_C = 1$, increasing beam power leads to the formation of local waveguides modulated by the mesh size. Rays are trapped in the minima for δn and self-focusing

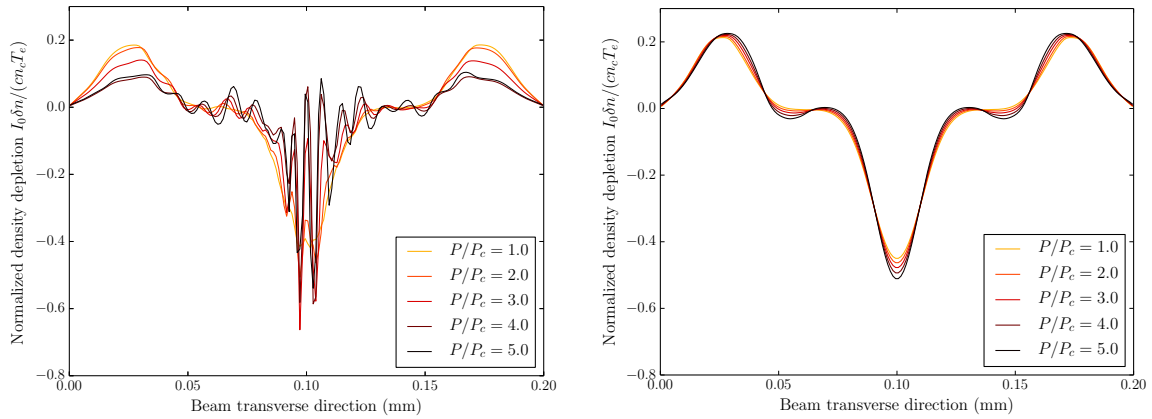

Figure 2-11 – *(Color) Density perturbation* $\delta n(t,x) = (n_e(t,x)/n_c - 0.1)/0.1$ *along the transverse to the beam, normalized to* cn_cT_e/I_0*, at* $z = 0.3$ *mm, after 100 ps. Results from the RT model [left] and PCGO model [right]. Density anomaly in the RT case is normalized to the maximum intensity, as there is no central ray intensity. Initial beam power with respect to* P_C *ranges from 1 to 5.*

does not occur at the beam scale.

Both the RT and PCGO models predict similar density depletions at a low power, but the RT model quickly grows unstable with respect to the numerical self-focusing instability. Intensity profiles modeled using PCGO are smooth and remain Gaussian, which allows for a better code robustness. In this purely ponderomotive case, the spiked profile produced by the RT method is a direct consequence of the spiked reconstructed intensity, which is the key quantity for LPI modeling. Consequently, nonlinear LPI effects modeled with RT codes are potentially subject to the same kind of instabilities and spatial modulations, which constitute a strong motivation for the development of alternatives such as PCGO.

2.5 Conclusions

The Paraxial Complex Geometrical Optics method has been adapted to the description of laser propagation in plasmas in two steps. First, the model has been extended to include the collisional absorption by the process of Inverse Bremsstrahlung, in a framework that is valid up to and at the critical density. Second, by neglecting the effect of the imaginary part of the dielectric permittivity on the optical beam thickness, it is found that the wave front equation is unchanged compared to the standard PCGO approach. Various specific algorithms and methods have been developed for the implementation of PCGO in the Lagrangian hydrodynamic code Chic in a 2D planar framework (see App. A), most of which are compatible with the Eulerian formalism of MHD codes, or with a 3D framework in general. This model allows to evaluate the beam intensity, radius of curvature and thickness at all points in the plasma. It consistently takes into account diffraction and absorption by the inverse Bremsstrahlung and is validated against several comprehensive test cases.

Compared to PCGO and to the theoretical solution of Gaussian beam propagation in inhomogeneous plasmas, the RT model is found to under-estimate the spatial location of the peak energy

transferred to the plasma by process of collisional absorption. This is notably a consequence of the RT vacuum diffraction model being inconsistent with respect to density gradients. Moreover, the knowledge of the wave electric field in PCGO allows to account for the laser absorption on the skin depth, which is of importance for the interaction of lasers with solid targets or for laser-target interactions in configurations at a quasi-normal incidence.

Application to the modeling of nonlinear LPIs is illustrated with the particular case of ponderomotive self-focusing, both in the RT and PCGO frameworks. A pressure term corresponding to the ponderomotive potential is added in the hydrodynamic core, computed from the RT reconstructed intensity or from the PCGO intensity field directly. It is found that PCGO yields the correct ponderomotive self-focusing critical power, self-focusing distance, transverse density depletion and approaches correctly the intensity amplification. Compared to the standard intensity reconstruction techniques used in RT codes, the needle-like nature of RT rays leads to artificial filamentation of the beam inside local waveguides with a size defined by the mesh discretization. This prevents the correct modeling of self-focusing distances and beam intensity amplifications. The vacuum diffraction modeled in the RT model breaks down for the non-constant refractive index in the density waveguide and fails to compensate the ponderomotive self-focusing effect. The difficulty to correctly estimate the laser beam intensity, direction and width is a major obstacle to nonlinear LPI modeling using RT models.

The model, results and comparisons presented in this Chapter were conducted using a single PCGO Gaussian beam. Given the stringent validity conditions of PCGO, and the fact that realistic laser beams employed in high power laser systems are rarely Gaussian, this framework must be extended to the modeling of non-Gaussian beams of arbitrary size and intensity profile. This is the object of the following Chapter.

Chapter 3

Realistic beam modeling using PCGO beamlets

In the previous chapter, the standard RT model used for computing laser propagation and collisional absorption in plasmas was presented. The PCGO model was introduced as an alternative method that allows for finer descriptions of the intensity field of Gaussian beamlets, when certain approximations on its width are met. In this Chapter, we describe how these elementary beamlets can be used to accurately model typical beams encountered in high power laser systems. Contrary to PCGO beamlets, the intensity field of such beams is not smooth, and their profile is rarely Gaussian. Moreover, their width in the focal plane can vary from ~ 1 cm to a few tens of μm, thus lying outside of the assumptions made in Sec. 2.3.3.3.

In standard RT-based approaches, the envelope of laser beams is modeled by bundles of needle-like rays, spatially arranged so as to reproduce the caustic of the beam by a spread in the rays initial k-vectors and powers. This approach, although straightforward, models perfectly smoothed beams which are not representative of realistic ones, notably regarding the rapidly varying intensity fluctuations inherent to high-power laser systems. Contrary to the RT approach, using a superposition of PCGO beamlets to reproduce a large beam does not lead to a smooth intensity distribution because the width and intensity of each beamlet obeys its own refraction and diffraction laws. As we will see, this property can be advantageously used to reproduce the full intensity statistic of real laser beams.

The statistics of intensity fluctuations notably depend on the smoothing techniques used to control laser beam characteristics. A precise modeling of nonlinear LPI requires, by definition of its nonlinear nature, to take into account the beam intensity statistics arising from the speckle pattern, and particularly the intensities higher than the average that are major contributions to nonlinear effects. The most common and relevant (to our study) beam forming techniques are presented in Sec. 3.1. Using the focal spot characteristics induced by those smoothing techniques, we present in Sec. 3.2 a method for reproducing the far-field intensity envelope and statistics of super-Gaussian beams smoothed by phase plates, using a superposition of PCGO beamlets. The high-intensity statistics produced by this method is shown to be comparable to reference calculations made with the paraxial electromagnetic code Miró in Sec. 3.3. Finally, we present in Sec. 3.4 reduced models based on the PCGO description of beams, that account for direct

effects of smoothing techniques on nonlinear LPIs.

3.1 Principal beam shaping techniques used in high power laser systems

The reduction of Rayleigh-Taylor Instabilities and nonlinear LPI growth requires to produce intensity profiles which envelop and intensity statistics are well defined and controlled. The statistical distribution of intensity non-uniformities can be quantified through the contrast, defined as:

$$C = \sqrt{\frac{\langle I^2 \rangle - \langle I \rangle^2}{\langle I \rangle^2}} \ , \tag{3.1}$$

which quantifies the importance of speckles with respect to the global beam envelope. A contrast of 0 % represents a perfectly smooth beam, while a contrast of 100 %, called a *pure speckle pattern*, represents a beam constituted of speckles only. Temporal and spatial laser smoothing in ICF aims at (i) controlling the intensity distribution in the focal plane $P(I)$ and (ii) achieving the lowest contrast possible C. This is achieved by various techniques which alter the phase of the laser field before its focusing in the target chamber. The typical methods employed in high-power laser systems can be summarized by decomposing the near-field (i.e. at the focusing optic) electric field of the laser $\mathbf{E}(x, y, t)$ as:

$$\begin{aligned} \mathbf{E}(x, y, t) = E_0(x, y, t) \exp[\imath\psi_{\mathrm{PP}}(x, y)] \exp[\imath\psi_{\mathrm{SSD}}(x, y, t)] \\ \exp[\imath\psi_{\mathrm{B}}(x, y, t)](\mathbf{x} + \mathbf{y} \exp[\imath\psi_{\mathrm{PS}}(y)]) \ , \end{aligned} \tag{3.2}$$

where x and y are coordinates along the $\mathbf{x}$ and $\mathbf{y}$ directions transverse to the beam propagation, $E_0(x, y, t)$ is the electric field of the beam envelope, $\psi_{\mathrm{PP}}(x, y)$ is the static phase contribution from Phase Plates, $\psi_{\mathrm{SSD}}(x, y, t)$ is the phase contribution from temporal smoothing (Smoothing by Spectral Dispersion), $\psi_{\mathrm{B}}(x, y, t)$ is the phase contribution from the B-integral [142] and $\psi_{\mathrm{PS}}(y)$ is the phase contribution from Polarization Smoothing (PS).

We present in this section the optical elements and techniques introduced in Eq. (3.2). Phase Plates are presented in Sec. 3.1.1. The physical interpretation of the structure of PP-smoothed beams allows to formulate the beam-splitting technique presented in Sec. 3.2. Polarization Smoothing is presented in Sec. 3.1.2 and its effect is accounted for in the PCGO formalism in Sec. 3.4.1. Finally, Smoothing by Spectral Dispersion is presented in Sec. 3.1.3 and its modeling with PCGO is described in Sec. 3.4.2. The contribution ψ_{B} from the B-integral comes from self-focusing in laser optical elements. It is in general neglected [143], and is not in the scope of this work.

3.1.1 Phase Plates

Phase Plates (PP), in conjunction with focusing optics, are optical elements used to alter and control the intensity distribution of laser beams in their focal plane. They are designed to shape the focal spot into highly reproducible envelope profiles, for which the small-scale intensity statistics is also well-defined. PPs work by altering the phase of a beam in the near field (at

the focusing optics), thus producing the desired intensity profile in the far field (i.e. in the focal plane). They are generally designed by the process of Iterative Fourier Transform Algorithms (IFTA) (see the Gershberg-Saxton algorithm [144]): an input beam with a known input intensity profile and a best-guess phase profile in the near-field is Fourier Transformed to the far-field. The resulting focal-plane intensity is discarded and replaced by the desired intensity profile, while the phase is kept. These are then Inverse Fourier Transformed back to the near-field, where the intensity is discarded and replaced by the known input intensity, while the phase is kept for the next iteration. Once convergence is obtained, the near-field phase profile is binarized and glass slabs are engraved. Various technologies of PPs exist, depending on the manufacturing process. Amongst the most common ones, *Random Phase Plates* (RPP) reproduce the phase profile using discrete square elements that induce a 0 or π phase shift. More recent methods have allowed to manufacture PPs with continuous phase-shifting profiles. These so-called *Kinoform Phase Plates* (KPP) are widely used in high-power laser facilities, and especially in the ICF domain.

Although PPs generate reliable and reproducible beam profiles in their focal plane, those present a highly contrasted intensity statistics (see Fig. 3-2 [right] in Sec. 3.3.2 for an example). As an illustration, the probability density $P(I)$ to find a hotspot with an intensity I for a beam smoothed by a RPP follows an exponential law [145]:

$$P(I) \propto \frac{1}{\langle I \rangle} \exp\left[-\frac{I}{\langle I \rangle}\right] . \tag{3.3}$$

Note that the distribution caused by a KPP is somewhat similar and also involves an exponentially decreasing factor [146]. The presence of small-scale intensity variations, or speckles, implies that localized regions of the plasma are eventually exposed to intensities several times above the average. For a purely RPP-smoothed speckle-pattern, according to Eq. (3.3), $C = 100\%$ (this is also true of a KPP-smoothed speckle pattern). Reducing the contrast is achieved by other smoothing techniques, including the simple overlap of laser beams.

3.1.2 Polarization smoothing

Reducing the instantaneous contrast of a beam can be achieved by means of Polarization Smoothing (PS). PS consists in splitting a beam into two equally intense beams of opposite polarization states before the focusing optics, e.g. by using birefringent wedges as is done on the OMEGA laser system. The two beams are focused simultaneously in the plasma, thus overlapping two identical but uncorrelated speckle patterns that combines trough their intensities instead of their electric fields. This technique instantaneously reduces the contrast by a factor of $\sqrt{2}$ [147]. The phase contribution from PS, that is typically effective in one transverse direction only, reads:

$$\psi_{\mathrm{PS}}(y) = k_{\mathrm{FS}} y \sin \Delta\theta_{\mathrm{PS}} , \tag{3.4}$$

where k_{FS} is the wavenumber at the birefringent wedge and $\Delta\theta_{\mathrm{PS}}$ is the angular separation of the beams induced by the wedge. A typical value for the OMEGA laser system is $\Delta\theta_{\mathrm{PS}} = 47\mu$rad.

3.1.3 Temporal smoothing

The development of temporal smoothing techniques stems from the observation that: (i) inhomogeneities in the laser field drive hydrodynamic instabilities only if they are sustained for long enough, and (ii) nonlinear LPIs efficiently grow in high intensity speckles only if those rest on the same place longer than the instability growth rate. Temporal smoothing is achieved in conjunction with PPs, by producing time-varying uncorrelated speckle patterns while keeping a controlled beam envelope profile. Consequently, it is more relevant to define beam smoothness using the notion of integrated contrast $\hat{C}$ (instead of C), computed from the time-integrated focal spot intensity field. Integrated contrasts (over a few hundred ps) of the order of 1% must be achieved in order to successfully drive a high-compression target in a direct drive ICF configuration [147].

Producing time-varying uncorrelated speckle patterns can be achieved by means of Smoothing by Spectral Dispersion. The base idea is to use frequency modulators in conjunction with gratings to add both a spatial and a temporal frequency variation to the beam. The most efficient SSD techniques employed in high power laser systems are implemented in 2D [147, 148, 149, 143], that is a different frequency modulation is imposed in the **x** and **y** directions in the plane perpendicular to the beam propagation directions. Because the beam position in the focal plane depends on the wavelength, the speckle pattern effectively moves and cycles with the frequency modulation imposed by SSD. In practice, SSD induces a spatial phase variation across the beam width so that a spectrum of frequencies is simultaneoulsy mixed in plasma. The number of times the same color appears in the wavefront at the final focusing optic (at a given time) is called the *number of colors* N_c. Many configurations of SSD exist, depending on the choice of N_c in each dimension, the modulator technology and settings, or parameters from the laser system itself such as the beam maximum angular spread and the nature of the final focusing optic. For simplicity, we restrict ourselves to the SSD system in use at the Omega laser facility, that is 2D-SSD (in the transverse directions of the beam) using sinusoidal modulators, with $N_c = 1 \times 1$. The PCGO-based SSD model presented in Sec. 3.4.2 is based on the 2D-SSD technique, but is readily applicable to other technologies such as the *Longitudinal SSD* [149, 150], which consists in displacing the speckle pattern along the propagation axis of the beam. Longitudinal SSD will notably be implemented on the *Laser Mégajoule* in France.

The near-field phase contribution of the 2D-SSD reads:

$$\psi_{\text{2DSSD}}(x, y, t) = n\delta_x \sin(2\pi\nu_x(t + \xi_x x)) + n\delta_y \sin(2\pi\nu_y(t + \xi_y y)) \ , \tag{3.5}$$

where $n = 3$ for a frequency-tripled beam (the modulator being located before the frequency tripling crystals), ν_x and ν_y are the *modulation frequencies* along the respective x and y directions, ξ_x and ξ_y are the phase variations induced by angular dispersion from the gratings and the *modulation depth* δ_x and δ_y represent the amplitude of the phase modulation. For a laser beam with an initial focal spot contrast C_0, an asymptotic integrated contrast $\hat{C}_a$, and smoothed by a SSD system of bandwidth $\Delta\nu = 2n\delta\nu$, the time evolution of the integrated contrast reads [143]:

$$\hat{C}(t) = \sqrt{C_0^2 \frac{1}{1 + \Delta\nu t} + \hat{C}_a^2} \ . \tag{3.6}$$

More complete formulations for the time evolution of the contrast of 2D-SSD smoothed beam are discussed in [151]. Typical 2D-SSD parameters used on the OMEGA laser facility are modulation frequencies of $\nu_x^{\mathrm{IR}} = 10.3$ GHz and $\nu_y^{\mathrm{IR}} = 3.3$ GHz, and modulation depths of $\delta_x = 3.897$ and $\delta_y = 6.145$ rad. The corresponding maximum wavelength shifts on target (in the UV) are of $\delta\lambda_x = 0.98$Å and $\delta\lambda_y = 0.5$Å. This frequency broadening, although small, is of importance when computing frequency detuning for the CBET process. As an example, identical frequency beams crossing in a stationary plasma cannot exchange energy through CBET. However, a frequency broadening as small as 1Å is sufficient to widen the resonance region to parts of the plasma of zero velocity, thus potentially inducing CBET.

Cumulating the techniques of KPPs, 2D SSD with 1THz UV bandwidth and 1 ps coherence time, PS, and beam overlap, asymptotic integrated contrasts of the order of 2% were reported on OMEGA [152], thus creating focal spots which intensity envelope are well defined, and sufficiently smooth with respect to hydrodynamic processes.

3.2 Modeling of realistic super-Gaussian beams using PCGO beamlets

In the framework of PCGO, each ray has a Gaussian intensity profile and its thickness must be larger than a few wavelengths and smaller than characteristic plasma inhomogeneities [52] (see Sec. 2.3.3.3). In order to ensure the validity of the aforementioned assumptions on the Gaussian ray thickness, it is necessary to model a large beam by a combination of smaller beamlets. Contrary to the analogous method used in the RT approach, overlapping PCGO beamlets leads to perturbed intensity fields, because of their Gaussian intensity profiles. Doing so, there is an additional degree of freedom, that is the focus location of each beamlet, which can be used to control these perturbations. The idea is then to use bundles of thick-rays in order to reproduce simultaneously the global beam characteristics and the overall intensity fluctuation statistics of a larger PP-smoothed beam. Figure 3-1 provides a general illustration of the method, that is detailed below. We note that the method presented here utilizes the framework of KPPs, and can be applied in a similar way to the modeling of RPP-smoothed beams, which is not presented here for conciseness.

3.2.1 Beam characteristics in the far field

The Rayleigh range of a Gaussian beam with a wavelength λ_L and a radius at the focal spot w_f is $z_R = \pi w_f^2/\lambda_L$. The smaller beamlets that constitute a split beam have significantly shorter Rayleigh ranges than the main beam. Such beamlets will rapidly focus and diverge, thus limiting the applicability of PCGO-based beam-splitting to relatively small regions. To that extent, a beam is subdivided in beamlets only in the far-field region, whereby far-field we mean close to the target plasma, i.e. close to the region considered in hydrodynamic simulations. As is illustrated in Fig. 3-1, we define a virtual circle in 2D (or virtual sphere in 3D) that encircles the plasma at all times. It must be large enough to account for the plasma expansion during the simulation. As an example, a circle of radius 0.8 cm centered on the capsule contains the plasma expansion of a standard direct drive implosion. From an averaged focal spot intensity

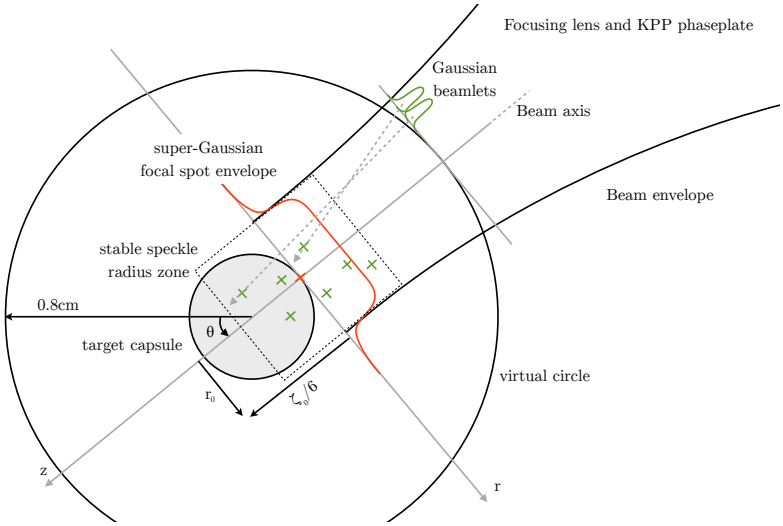

Figure 3-1 – *Diagram of the virtual circle defined for an ICF direct drive configuration. The capsule is represented as a grey-filled circle. Beam parameters are computed at a virtual circle of 8 mm radius from the focal spot intensity profile (red), the KPP phase plate and the focusing lens parameters. The overall intensity profile at the virtual circle is combined from Gaussian beamlets (green) individually focused pseudo-randomly in a region around the focal spot in which the speckle radius is stable (black dotted-lines box). z and r denote the local coordinate system respectively in the direction of propagation and transverse to the beam.*

distribution, given e.g. by experimental measurements of the focal spot of the laser system in vacuum, we compute the corresponding intensity profile at the virtual circle accounting for the specific characteristics of speckled beam propagation (this is detailed below). The resulting intensity profile at the virtual circle is split in a sum of elementary Gaussian PCGO beamlets. At each hydrodynamic timestep, the beamlets are propagated in vacuum from the virtual circle to the edge of the hydrodynamic mesh using the formulation for Gaussian beam propagation presented in Sec. 2.3.2.1. The propagation of each beamlet and interaction in the plasma is then resolved according to the standard hydrocode-based PCGO method presented in Ch. 2.

We consider an ICF beam equipped with a KPP phase plate. The beam is characterized at the focal spot by a width r_f and a correlation radius $\varrho_f = \lambda_L f/\phi$ (i.e. mean radius of the speckles), where f is the focal length of the final focusing lens and ϕ is the beam diameter at the focusing lens. The super-Gaussian beam envelope intensity $I_f(r)$ reads:

$$I_f(r) = I_0 \exp(-|r/r_f|^n) \ , \tag{3.7}$$

with I_0 the central intensity at focal spot, r the transverse coordinate and n the order of the Gaussian beam. The overall beam envelope intensity of a partially coherent order-n Gaussian beam can be computed at a distance z using [153]:

$$I(z,r) = \left[I_0 e^{-\left|\frac{r}{r_f}\right|^n} \right] * \left[\pi^{-3} \left(\frac{z}{z_0}\right)^{-2} \chi_{B(0,\pi z/z_0)} \left(\frac{r}{r_f}\right) \right] \ , \tag{3.8}$$

where $z = 0$ at the focal plane, $z_0 = k_{\mathrm{FS}} \varrho_f r_f$ is the equivalent Rayleigh length of the speckled

beam, $\chi_{B(a,b)}(r)$ represents a Heavyside distribution centered on a and of radius b and the symbol $*$ is a convolution product. The left-hand-side of Eq. (3.8) is the focal spot intensity profile. It is convoluted to a propagator on the right-hand-side of (3.8) in order to obtain the intensity distribution at a distance z from the focal plane. The intensity distribution at the virtual circle $I_v(r) = I(z = d_{f,v}, r)$, with $d_{f,v}$ the distance between the focus position and the virtual sphere along the beam axis, is computed from Eq. (3.8) by means of the Fast Fourier Transform (FFT) algorithm.

3.2.2 Beam-splitting

The beam envelope intensity at the virtual circle I_v must be divided in smaller beamlets in such a way that the composition of the beamlets intensities reproduces that of the whole beam. In practice, such a splitting is easier to implement for super-Gaussian beams, so that an order-n super-Gaussian distribution function is fit to I_v using a nonlinear least squares method. The resulting fitted intensity profile is characterized by a central intensity I_{0v}, thickness r_v and order n_v, defined at the virtual circle. Although I_v is not exactly of super-Gaussian shape, we note little difference between the fit (about 2%) and the requested profile. Moreover, energy conservation is ensured by renormalization so that the super-Gaussian beam carries the same power as the real beam computed by resolution of Eq. (3.8). The splitting of a super-Gaussian distribution into a finite sum of Gaussian distributions can be expressed as:

$$I_{0v} \exp\left[-\left|\frac{r}{r_v}\right|^{n_v}\right] = \sum_{k=1}^{N_B} I_{0v}^k \exp\left[-2\left(\frac{r-\mu_v^k}{w_v^k}\right)^2\right] , \tag{3.9}$$

where N_B is the number of beamlets, k is the beamlet index and I_{0v}^k, w_v^k, μ_v^k are the central beamlet intensity, beamlet width and offset from the main beam centroid, respectively. The curvature radius and propagation vector of each beamlet are left off this expression, as these are set separately so as to control the beamlets focal points (see Sec. 3.2.3). For N_B beamlets, there are $3N_B$ degrees of freedom in Eq. (3.9). Although a nonlinear least square fit could provide these $3N_B$ parameters, this procedure is delicate for large values of N_B. The problem is simplified by assuming that the beamlets defined at the virtual circle have the same width $\hat{w_v}$ and are equally spaced in μ_k. The values of I_{0v}^k are then computed using an analytical formula described in Appendix B.1 and by ensuring energy conservation. These values are functions of two parameters only: $\mathcal{R} = \hat{w_v^0}/\varrho_f$ and N_B, where ϱ_f is the correlation radius of a real speckle pattern and $\hat{w_v^0}$ is the beamlet radius at its focal spot. Both parameters control the pseudo-speckle pattern, as described in the next section.

3.2.3 Beamlet focusing

The longitudinal large scale variation of a speckle pattern defined by a beam envelope radius r_f and a correlation radius ϱ_f is characterized by the length scale $z_0 = k_{\mathrm{FS}} \varrho_f r_f$ [153]. The speckle radius of such a beam is approximately constant along the distance $\zeta_0 = z_0/\pi$ from the focal plane. The transverse scale of the beam at the focal plane is determined by the radius r_f, often available from experimental data. The parameters ζ_0 and r_f define a box around the focal spot where the

speckle pattern varies slowly. The N_B beamlets defined at the virtual circle are randomly focused in this box by setting accordingly their radii of curvature and k-vectors (see App. B.1.2). The focal spots of the beamlets are scattered by assuming a binormal distribution centered on the focal spot $(z_f; r_f)$ of the beam. The corresponding probability density function $\mathcal{F}$ reads:

$$\mathcal{F} = \frac{1}{2\pi\sigma_1\sigma_2} \exp\left[-\frac{(z-z_f)^2}{2\sigma_1^2} - \frac{(r-r_f)^2}{2\sigma_2^2}\right] \chi_{B(0,\sigma_2)}(r) \ , \tag{3.10}$$

where we have chosen a diagonal covariance matrix and σ_1 and σ_2 are the standard deviations along the z and r directions, where the z-coordinate is along the beam direction and the r-coordinate is in the focal plane (see Fig. 3-1). The Heavyside distribution on the right of (3.10) allows to discard unrealistic focal spot positions picked outside of the beam caustic in the r direction. This implies that the 2D distribution is not strictly binormal. We define σ_1 so that 99,7% of the focal points are located in the $[-\zeta_0/2, \zeta_0/2]$ interval and 68% are located in the $[-\zeta_0/6, \zeta_0/6]$ interval, i.e. $\sigma_1 = \zeta_0/6$. We define $\sigma_2 = 2r_f$.

3.2.4 Free parameters

The remaining degrees of freedom N_B and $\mathcal{R}$ are set by comparing the intensity map produced by the beamlets to the laser propagation code Miró in vacuum or in transparent materials [154, 155, 156]. The latter code is a paraxial wave solver that allows to model the effect of various optical elements, including Phase Plates (see Sec. 3.3.1). As a rule of thumb, N_B can be taken as the ratio of the radius of the whole beam at the focal spot to the speckle radius. Considering as an example the Omega experimental setup, for the super-Gaussian beam of the order 4 (SG4) at the wavelength of 351 nm equipped with KPP, $\varrho_f \simeq 2.33$ μm and $r_f = 352$ μm, giving $N_B = 151$. In practice, the size of the hydrodynamic grid is much larger than the speckle width so that several speckles can be found in the same cells, which spatially smoothes the intensity distribution and the corresponding coupling terms in the hydrodynamic equations. Consequently, instead of reproducing the exact beam speckle pattern at the focal spot, large pseudo-speckles are modeled, typically 3 to 10 times larger in radius than the real speckles. This is set through the $\mathcal{R}$ parameter, which controls the beamlet radius at the virtual circle. Because the pseudo-speckles are large, the number of beamlets N_B can be chosen smaller, typically by a factor of 2. The parameters N_B and $\mathcal{R}$ indirectly control the contrast of the beam and the 2D pseudo-speckle pattern. It is important to set these two parameters by comparing the generated 2D intensity field to a reference solution, e.g. a numerical resolution of the paraxial wave equation for the electric field in vacuum or in a homogeneous plasma.

3.3 Validation of the PP-smoothed PCGO beam model

The superposition of PCGO beamlets constructed according to the method presented in Sec. 3.2 produces a focal spot with a specific intensity envelope and statistics that aims to reproduce those of realistic beams. The performance of the superposition algorithm is evaluated by comparison of the intensity field with a reference solution obtained with Miró in a vacuum. The Miró code is a paraxial electromagnetic solver that computes the propagation of an EM wave in the laser

chain from the near-field, including the effect of focusing optics, Phase Plates, mirrors, and other optical devices used in high power laser system, up to the far-field in the target chamber.

3.3.1 Numerical modeling of the propagation of a wavefield through focusing optics: the MIRÓ code

Similarly as in the assumptions of the PCGO model, we initialize the MIRÓ code with a quasi-plane wave of principal wavevector $\mathbf{k}$. Contrary to PCGO, the wave is considered to be quasi-monochromatic of central frequency ω and spectral width $\Delta\omega$, assuming that $\Delta k = \Delta\omega/c \ll |\mathbf{k}|$ and $\Delta\omega \ll \omega$, where Δk and $\Delta\omega$ are the spatial and spectral dispersions, respectively. The electric field created by the overlap of N monochromatic components takes the form:

$$\mathbf{E}(x,y,z,t) = \sum_{l=1}^{N_B} \left(\frac{\mathbf{E}_l(x,y,t)}{\sqrt{2\sqrt{\epsilon'(\omega_l)}c\epsilon_0}} \exp \imath(\omega_l t - k_l z) + \text{c.c.} \right) , \tag{3.11}$$

where $\mathbf{E}_l$ is a complex vector, normalized so that the modulus of $\mathbf{E}$ is the intensity. In those notations, the z component is the propagation direction and x and y are transverse directions. The z component in $\mathbf{E}_l$ is small and has been neglected. The so-called *Fresnel diffraction* formulation that models the propagation of the EM wave in optical elements reads:

$$-2\imath k_l \frac{\partial \mathbf{E}_l}{\partial z} + \triangle_\perp \mathbf{E}_l = 0 , \tag{3.12}$$

which is a standard Paraxial Wave Equation. In the derivation of this formulation, the dispersion of the group velocity v_g has been neglected, it was assumed that the waves do not interact with each other, that the phase velocities and group velocities are collinear and that the group velocity is the same for all harmonics. Phase Plates are modeled by multiplying $\mathbf{E}$ by a phase term $\exp \imath\phi(x,y)$, where ϕ is a phase mask given by experimental data. The description of numerical algorithms employed in the resolution of Eq. (3.12) can be found in [157].

3.3.2 Comparison of the envelope intensity, speckle and pseudo-speckle patterns

We consider a setup similar to the OMEGA facility [158], where the laser beams at the wavelength of 351 nm are equipped with the KPP plates and have at the focal spot a super-Gaussian distribution (3.7) with $n^{\text{SG4}} = 4.1$ and $r_f^{\text{SG4}} = 352$ μm. The lens diameter is $\phi^{\text{SG4}} = 0.27$ m and focal length is $f^{\text{SG4}} = 1.80$ m. The focal spot intensity computed by MIRÓ is illustrated in Fig. 3-2 [left]. Figure 3-2 [right] shows a profile taken in the center of the focal spot, illustrating the highly contrasted nature of the beam. Results for the 2D intensity field $I_{\text{Miró}}(x,z)$ as computed by MIRÓ using the same SG4 KPP phase plate data are shown in Fig. 3-3 [top-left]. In order to compare MIRÓ to PCGO in CHIC in the same conditions, the results from MIRÓ are convolved with the hydrodynamic mesh resolution used for the simulations (see Fig. 3-3 [top-right]), using:

$$I_{\text{Miró}}^{\text{smoothed}}(x,z) = \frac{1}{d_x d_y} (I_{\text{Miró}} * \chi_{B\{(0,d_x),(0,d_z)\}})(x,z) , \tag{3.13}$$

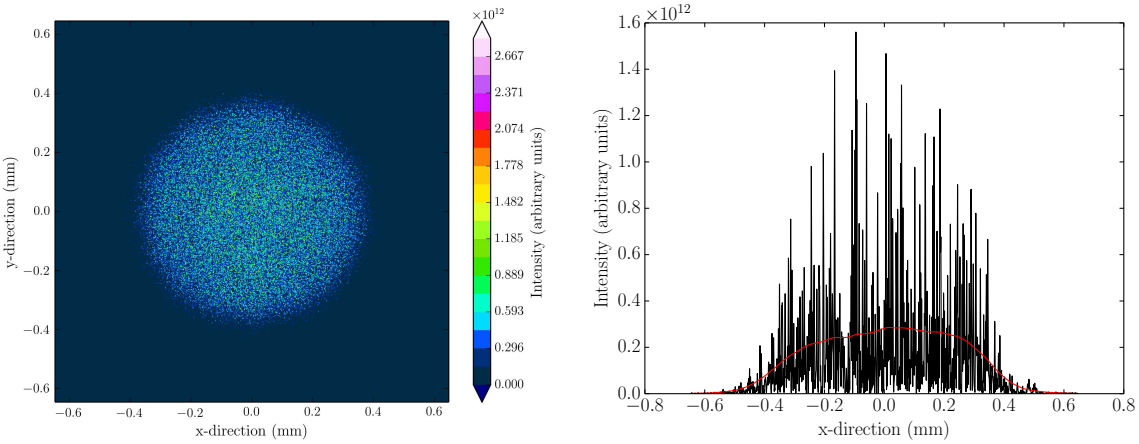

Figure 3-2 – *[left] Vacuum focal spot intensity of a KPP-smoothed beam using the characteristics of a beamline of the* Omega *laser facility, with the SG4 Phase Plate, computed with* Miró*. [right] Corresponding intensity profile in the focal spot for $y = 0$. The average intensity, that is the beam envelope, is shown as a red solid line.*

where $I_{\text{Miró}}^{\text{smoothed}}(x, z)$ is the smoothed Miró data, x and z are the transverse and longitudinal directions (here $y = 0$, as in Fig. 3-2), and the convolution kernel is a bi-dimensional Heavyside distribution of width d_x and d_z along the x and z directions, respectively, where d_x and d_z are the size of the regular mesh grid used here, that is $d_x = 1.2/180$ mm and $d_z = 4/180$ mm. Figure 3-3 [bottom] shows the 2D intensity field obtained using the PCGO splitting algorithm for $N_B = 100$ and $\mathcal{R} = 7$, in a simulation domain of 180×180 grid points in a box of 4 mm $\times 1.2$ mm.

Although the realizations presented in Fig. 3-3 look different, the splitting algorithm described in Sec. 3.2 reproduces accurately the intensity statistics for normalized intensities $I/\langle I \rangle > 0.09$ (see Fig. 3-4 [top-left]), where $\langle I \rangle$ is the mean intensity. The statistics for lower intensity values is less accurately reproduced, owing to a large width of the pseudo-speckles. This is acceptable when studying nonlinear LPI, where it is the higher intensities that are of interest. Decreasing N_B at a constant $\mathcal{R}$ would effectively reduce this discrepancy but would degrade the contrast away from the beam's focal spot. Similarly, decreasing $\mathcal{R}$ at a constant N_B would also increase the low intensity statistics. However, low values of $\mathcal{R}$ lead to shorter Rayleigh ranges for the beamlets, which limits the applicability of the splitting method to smaller plasmas. Comparing intensity slices at the focal spot shows overall agreement (see Fig. 3-4 [top-right]). The fractional encircled energy of the PCGO beam is rather close to the convolved Miró data (Fig. 3-4 [bottom]), with a slightly steeper cutoff in the wings of the beam. This difference is acceptable in the case of direct drive configurations where there is no laser entrance hole to fit in and the wing intensity information will be lost as many beams overlap over the target in 2D or 3D configuration. Both profiles have similar contrasts, with $C_{\text{PCGO}} \simeq C_{\text{MIRO}} = 0.66$ (with $C_{\text{MIRO}} \neq 1$ because of the convolution with the hydrodynamic mesh). We note that the contrast of the un-convolved Miró data is $C = 1$, which is consistent with a pure speckle pattern.

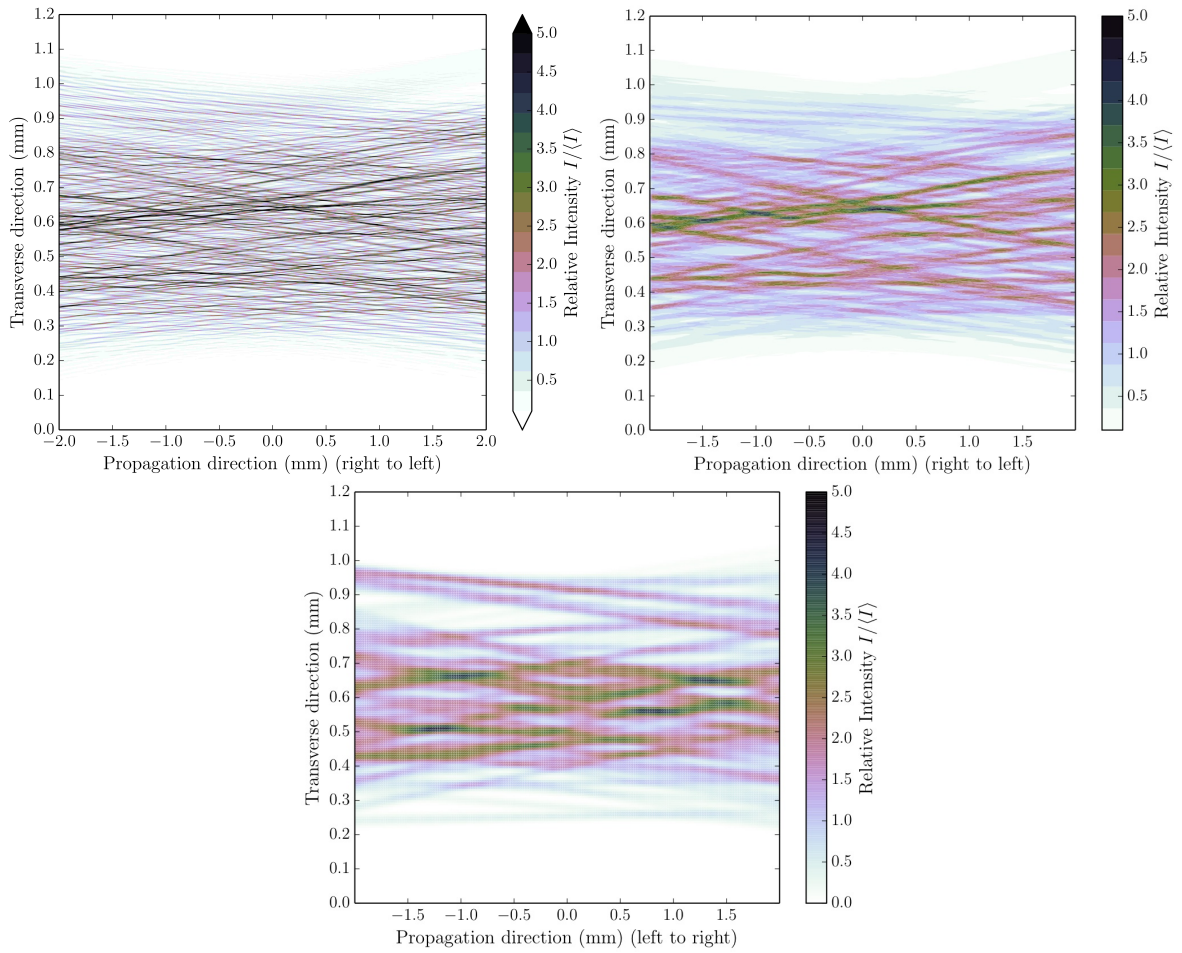

Figure 3-3 – *2D intensity field as computed by* Miró *for the* Omega *beam configuration with SG4 KPP phase plate, with [top-right] and without [top-left] 2D convolution to the mesh resolution used for the comparison with PCGO, i.e. dx=22 µm and dy=6.7 µm. [Bottom] corresponding results using the splitting algorithm and PCGO, projected onto the hydrodynamic mesh. Intensity is normalized to the average intensity of the un-convolved* Miró *data* $\langle I\rangle = 1.87 \times 10^{11}$ *W/cm.*

3.3.3 Hydrodynamic relevance of the pseudo-speckle pattern

The intensity statistics of the pseudo-speckle pattern produced by the method presented in Sec. 3.2 is accurate enough for the modeling of collisional absorption and nonlinear LPIs. However, it can be argued that the hydrodynamic asymmetries created by pseudo speckles may not be correct when compared to that of the real speckle pattern, thus introducing a bias in the simulations. This remark can be adressed by a consideration on the typical mesh resolution employed in simulations of full-scale ICF implosions. To fully appreciate the impact of discrete pseudo speckles on the hydrodynamics, one would require a spatial resolution of about 5 points per pseudo speckle width. For a pseudo speckle of 23 μm in diameter ($\mathcal{R} = 10$ and beam parameters of an Omega beamline with the SG4 KPPs), this represents a transverse resolution of 4.6 μm. Such resolutions across the whole diameter of the beam(s) are costly. In general, simulations are conducted on grids for which the finer (on the laser axis) transverse mesh resolution is of the order of 10-15 μm, so that the pseudo speckle pattern has little consequences on the hydrodynamics. This

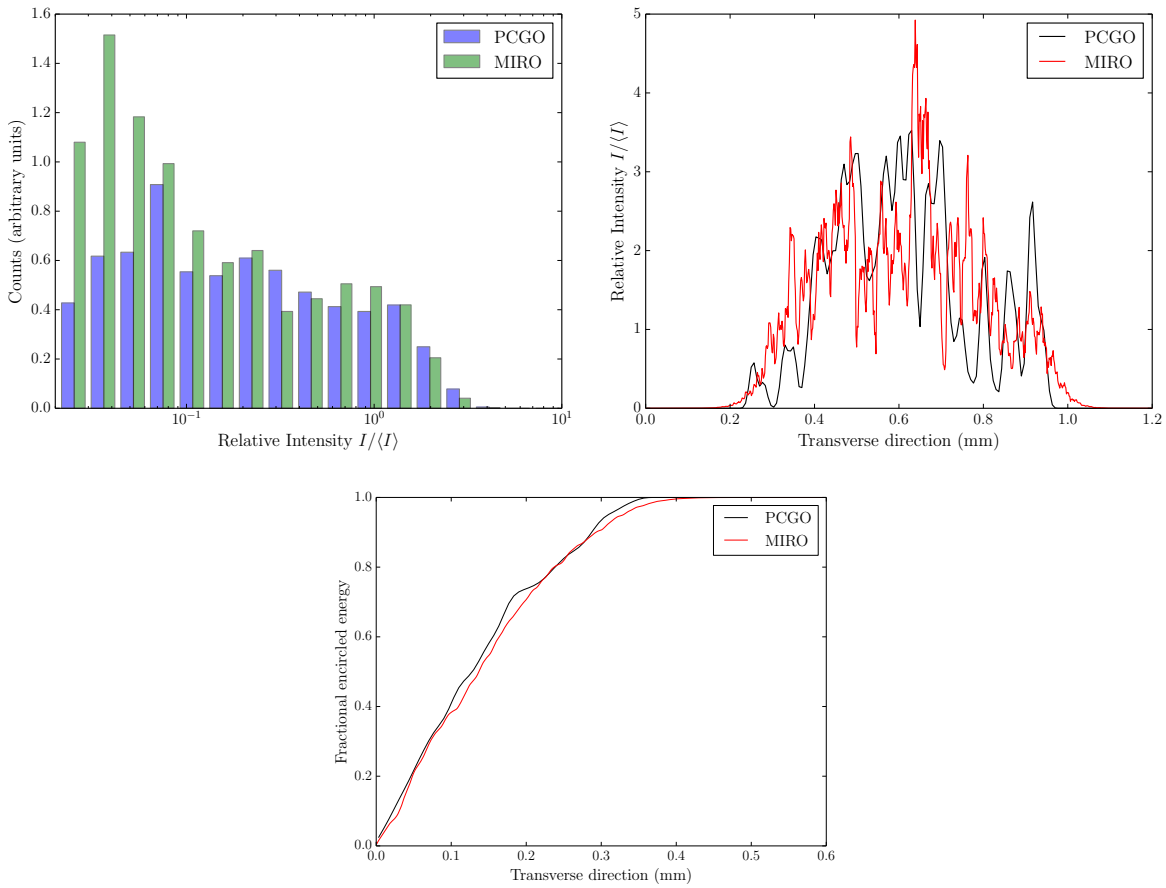

Figure 3-4 – *[Top-left] histogram of the 2D intensity field illustrated in Fig. 3-3 for the convolved* Miró *data in green (lighter grey) and for PCGO in blue (darker grey). [Top-right] intensity profile at focal spot from convolved* Miró *data in red (grey) and PCGO in black. Intensity is normalized to the average intensity of the convolved* Miró *data* $\langle I\rangle = 2.00 \times 10^{11}$ *W/cm. [Bottom] Fractional encircled energy as a function of radius, in the focal plane, for the convolved* Miró *data in red (grey) and PCGO in black.*

means that in simulations with standard mesh resolutions, hydrodynamic processes driven by collisional-absorption are not sensitive to small-scale laser inhomogeneities of high contrast beams. Finally, considering the case of beams smoothed by PS and 2D-SSD, the contrast in the focal spot reaches value below 5%, which greatly reduce any impact of the pseudo-speckle pattern on the hydrodynamics, even for mesh resolutions below 5 μm.

3.4 Modeling of laser smoothing techniques relevant to nonlinear LPIs with PCGO

Methods employed for laser smoothing can be of importance to the correct description of the laser-plasma interaction. Particularly, SSD and PS have significant influence on nonlinear LPIs, and those must be adequately described.

3.4.1 Reduced PS model

As discussed in Sec. 3.1.2, Polarization Smoothing instantaneously reduces the contrast of laser beams to 70.7% [147] when considering a PP smoothed beam. Modeling the contrast reduction from PS with PCGO is not relevant, as the pseudo-speckle pattern generated by PCGO beamlets overlap does not have a 100% contrast, for several reasons. Firstly, pseudo-speckles are at least 5 to 10 times larger than the real speckles, as a direct consequence of assumptions made in the PCGO model (see Sec. 2.3.3.3). Secondly, as shown in Sec. 3.3.2, the low-intensity statistics is not well reproduced by the beamlet overlap method, thus leading to a lower initial contrast. Both these issues are due to the pseudo-speckles being larger and less numerous than real speckles, and to the typical grid size of the mesh in hydrodynamic simulations that smoothes the intensity field seen by the hydrodynamics (through collisional absorption). For the SG4 KPP presented in Sec. 3.3.2, the instantaneous contrast of the beam is of about 66%, which is close to the contrast achieved with PS. In a sense, the beamlet overlap method models beams as if those were smoothed by PS. This is not an issue, as the typical mesh resolution employed in radiative hydrocodes cannot resolve the hydrodynamic effects of a 100% contrast beam.

Among the nonlinear LPIs modeled in the following chapters, we consider the effect of PS on the resonant absorption and CBET only. For the resonant absorption, only the p-polarized light can tunnel to the critical density and resonantly excite an EPW. Hence, the absorption fraction f_A (see Sec. 5.3) from resonant absorption is multiplied by a factor $\xi_P = P_p/(P_p + P_s)$ to account for polarization mixing, where P_p and P_s are the partial powers of the corresponding polarizations. For the CBET process, the ion acoustic wave is created by the beating of the EM waves, through the ponderomotive force. The beat wave being created by the spatial interference of the two electric fields, the polarization of the waves directly affects the amplitude of the ion acoustic wave. We consider a linear approach, that is we linearly relate the difference in polarization angles χ between the two waves to the CBET power transfer (see Sec. 4.1) by multiplying it by a factor $\xi_P = \cos\chi$. In the case of PS, each beam is composed of mixed orthogonal polarizations, so that there are as much interactions between waves of aligned polarization and waves of orthogonal polarization. Statistically, this is equivalent to setting a value of $\xi_P = 1/2$ for all interactions between the two beams smoothed with PS. This reduction of CBET gain by a factor of 2 with PS was derived in [159] for cases where the CBET gain is small (i.e. there is no pump depletion) and for intersections at small angles. When accounting for the numerous processes that can rotate the polarizations of the beams in plasma, the actual polarization of laser light in plasma (with PS) is uniformly distributed. In that case, the polarization factor reads $\xi_P = (1 + \cos^2\theta)/4$ [160], where here θ is the arbitrary angle between the intersecting beams.

3.4.2 Reduced SSD model

The framework of Complex Geometrical Optics does not account for the detailed phase shift induced by temporal smoothing according to Eq. (3.5), notably because the electric field in the PCGO model does not include the corresponding phase information and the characteristic smoothing time is comparable to the hydrodynamic timestep. However, as for the case of KPP smoothing, some effects of SSD on LPIs and laser beam intensity statistics can be approached. As

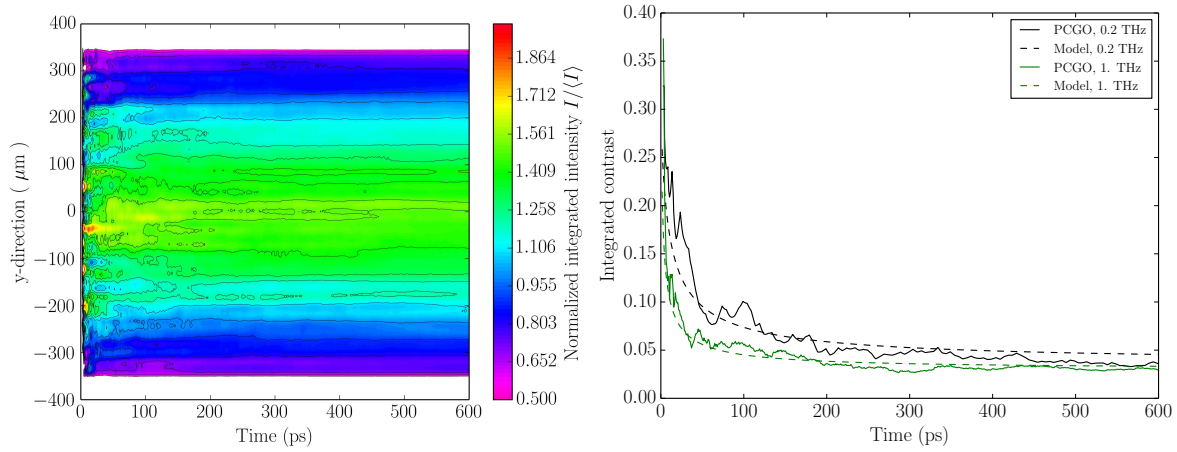

Figure 3-5 – *[Left] Time-integrated focal spot transverse intensity for the $\Delta\nu = 1\,THz$ case, illustrating the contrast reduction from the successive overlap of uncorrelated pseudo-speckle patterns. [Right] Time evolution of the integrated contrast reproduced by mimicking the SSD-induced speckle pattern variation (solid lines) for two bandwidth values. The expected smoothing rate is shown as a dashed lines.*

such, we only aim to reproduce the spatial speckle pattern variation and the increase in spectral width.

For a SSD-smoothed beam with an effective (on-target) bandwidth of $\Delta\nu$, the coherence time $\tau_c = 1/\Delta\nu$ describes the lifetime of the speckle pattern. Statistically, speckle patterns generated by SSD smoothed beams can be considered uncorrelated when separated by τ_c. This effect is approached in the PCGO framework by generating a new pseudo-speckle pattern each τ_c, through a random generation of new beamlet focal points (see Sec. 3.2.3). For a SSD system using a sinusoidal random phase modulation with a modulator frequency ν and a modulation depth δ (see Sec. 3.1.3), the contrast of the SSD-smoothed beam reaches its asymptotic value when many independent speckle patterns have been cycled, for integration times longer than $\delta/\nu \gg \tau_c$ [151]. This is transcribed in our model by using a cyclic set of random focal points that is repeated every δ/ν. The integrated intensity distribution produced by this method in the case of the OMEGA SG4 beam is illustrated in Fig. 3-5 [left], for a SSD-smoothed beam with the modulator frequency $\nu_x = 10.4$GHz, modulator depth after frequency tripling $\delta_{x,\mathrm{UV}} = 3\delta_x = 42.9$ and two values of the bandwidth after frequency tripling; $\Delta\nu_{x,\mathrm{UV}} = 0.2$ THz and $\Delta\nu_{x,\mathrm{UV}} = 1$ THz. We use 120 PCGO beamlets. This reduced SSD model based on PCGO reproduces correctly the time dependence of the smoothed beam contrast, as indicated in Fig. 3-5 by a comparison with theoretical estimates (Eq. (3.6)), which has been observed to agree with experimental data [143] for 2D-SSD sinusoidal modulators. The asymptotic contrast reached in this case is around $\hat{C}_a = 3\%$, in general agreement with theoretical values.

Spectral broadening is accounted for by changing the frequency of PCGO beamlets. For a beam of central frequency ω, beamlet frequencies are randomly set in the $[\omega - \delta\omega/2; \omega + \delta\omega/2]$ interval using a uniform statistical distribution, where $\delta\omega$ is the on-target spectral broadening. Because $\delta\lambda_L = (\lambda_L/\omega)\delta\omega \ll \lambda_L/2$ (typically a fraction of Å), it is considered that the frequency of those beamlets is ω for the computation of n_c and central ray trajectories.

3.5 Conclusions

Laser beams employed in high-power laser systems are shaped using various optical elements, producing beams with specific intensity statistics and often non-Gaussian transverse intensity envelopes. Phase plates effectively split beams in beamlets by inducing spatial variations in the phase of the beam in the near-field. Taking advantage of their use, we have presented adaptations that can be made in order to use several PCGO beamlets to model one large speckled beam, thus reproducing the intensity statistics and envelope induced by the use of a KPP or RPP. This adaptation has been validated against results obtained with the paraxial electromagnetic solver Miró in the case of the SG4 Phase Plates on the Omega laser facility. The method we have presented allows to model the correct intensity statistics (for $I > \langle I \rangle/10$), beam envelope profile and caustic induced by the use of Phase Plates, as well as the integrated beam contrast from SSD (with sinusoidal phase modulators) and the effects of Polarization Smoothing on the intensity distribution in plasma. The reduced SSD model accounts for the effect of the beam spectral broadening on CBET. Additionally, a reduced model that describes the effects of mixed beam polarizations on CBET and resonant absorption has been proposed. These adaptations are key to the use of PCGO in laser-target simulations and for the interpretation and design of experiments.

Chapter 4

Modeling and study of the Cross Beam Energy Transfer: the EYEBOLT model

We present in this Chapter a model of energy transfer between crossed laser beams in plasmas (CBET), based on the PCGO framework. In essence, modeling CBET requires to describe the interaction of two electromagnetic waves through the ponderomotive excitation of an ion acoustic wave, in an a-priori inhomogenous and expanding plasma. This is a complex nonlinear and non-stationary process that has been studied in details by using theoretical approaches [161, 162, 163, 164] and paraxial electromagnetic codes at mesoscopic scales of a few tens of hundreds microns [165, 166, 167, 168, 169, 170, 171, 172, 173, 174]. In hydrocodes, which involve scales larger by at least an order of magnitude, the beam wavefields and plasma waves are not readily described. Development of CBET models in this framework is challenging and relies on necessary simplifying assumptions. Simplified CBET models require, in addition to the intensity field and plasma parameters, quantities that are not readily described by RT models, such as the beam width and propagation direction[1], or being able to update the intensity filed downstream of the interaction region. Despite those difficulties, inline RT-based CBET models have been developed in the past, based on the method of intensity reconstruction [27, 175, 50] (see also Sec. 2.2.4). However, given the inherent difficulty of knowing the intensity distribution within the GO approach, these models have proven to be difficult to implement. As such, they require significant numerical developments in order to achieve convergence, including renormalization of the beams energy or arbitrary limitation of the IAW amplitudes.

Taking advantage of the PCGO formalism, a steady-state model of CBET based on elementary interactions between Gaussian beamlets is developed and presented in Sec. 4.1. The EYEBOLT model (for EnergY Exchange Between OpticaL Thick-rays) is validated against several known cases. First, we derive analytical formulations for the rate of energy transfer between two laser beams interacting in homogeneous and inhomogeneous plasmas, and compare it to results from EYEBOLT in Sec. 4.2. Second, the model is compared to a time-dependent paraxial solver for EM waves, embedded in a nonlinear small-scale hydrodynamics model, in Sec. 4.3. Finally, we present the numerical results and their interpretation concerning a reference experiment that was

[1] Although the notion of ray direction exists, the notion of beam direction does not because ray trajectories are independent.

conducted on the NOVA laser facility [176] in Sec. 4.4. The EYEBOLT model is then applied to the academic case of a direct-drive capsule implosion in the OMEGA beam configuration [177], in two-dimensional (2D) planar geometry and using the phase plates.

4.1 EYEBOLT, an inline CBET model for large-scale hydrocodes using PCGO beamlets

4.1.1 Elementary transfer formulation

4.1.1.1 General framework

We consider an energy exchange between two EM waves propagating in a plasma. The waves exchange energy through diffraction on a commonly excited Ion Acoustic Wave-driven electron density perturbation. The energy exchange is the most efficient in the resonant case where the beat frequency of the two interacting waves is equal to the IAW frequency. This corresponds to the process of Stimulated Brillouin Scattering, that was introduced in more details in Sec. 1.5.2.2. The two waves of wavevectors $\mathbf{k}_1$ and $\mathbf{k}_2$ and frequencies ω_1 and ω_2 intersect at an angle θ and excite an ion acoustic wave of wavevector $\mathbf{k}_s = \mathbf{k}_1 - \mathbf{k}_2$ and frequency ω_s. We define the *frequency shift* Ω, that includes the effect of Doppler shift due to the plasma flow, as:

$$\Omega = \omega_1 - \omega_2 - (\mathbf{k}_1 - \mathbf{k}_2).\mathbf{V}_p \ , \tag{4.1}$$

where $\mathbf{V}_p$ is the plasma velocity. The *frequency detuning* is then defined as $\Omega - \omega_s$, that is zero at resonance. Without loss of generality, we assume $\Omega > 0$, i.e. the wave labelled as 1 is the high frequency (pump) beam, the Doppler shift included. The wave 2 is called the probe beam. Using these notations, the coupled equations describing the evolution of the wave intensities in the slowly-varying envelope approximation read [36] (see also Sec. 1.5.2.2):

$$\begin{aligned}
(\partial_t + 2\nu_1 + \mathbf{V}_{g1}.\nabla)|a_1|^2 &= \omega_1 \frac{n_e}{n_c} \Im\left(\frac{\Gamma_s}{\mathscr{D}_s}\right) |a_1|^2 |a_2|^2 \ , \\
(\partial_t + 2\nu_2 + \mathbf{V}_{g2}.\nabla)|a_2|^2 &= -\omega_2 \frac{n_e}{n_c} \Im\left(\frac{\Gamma_s}{\mathscr{D}_s}\right) |a_1|^2 |a_2|^2 \ , \\
\mathbf{k_1} &= k_1 \mathbf{e}_\xi \ , \\
\mathbf{k_2} &= k_2 \mathbf{e}_\eta \ ,
\end{aligned} \tag{4.2}$$

where $\Gamma_s \equiv (e/m_e v_{T,e})^2 k_s^2 c_{\text{se}}^2/(1 + k_s^2 \lambda_{De}^2)^2$ denotes the coupling coefficient ($c_{\text{se}}^2 = ZT_e/m_i$ is the contribution of the electrons to the sound velocity), $|a_i|^2$ designates the squared transverse amplitude of wave i, $\mathbf{V}_{gi} = c^2 \mathbf{k_i}/\omega_i$ is the group velocity of wave i, ν_i is the damping rate of wave i, $\mathbf{e}_\xi$ and $\mathbf{e}_\eta$ are the unit vectors for the wave directions in the (ξ, η) coordinate system (illustrated in Fig. 4-1) and $\mathscr{D}_s = \Omega^2 - \omega_s^2 + 2i\omega_s\nu_s$ is the resonance denominator, with ν_s being the ion acoustic wave damping rate. Assuming steady-state, small detuning $\omega_1 - \omega_2 \ll \omega_1, \omega_2$, and neglecting the transverse EM damping rates ν_i, Eqs. (4.2) reads, along the respective wave

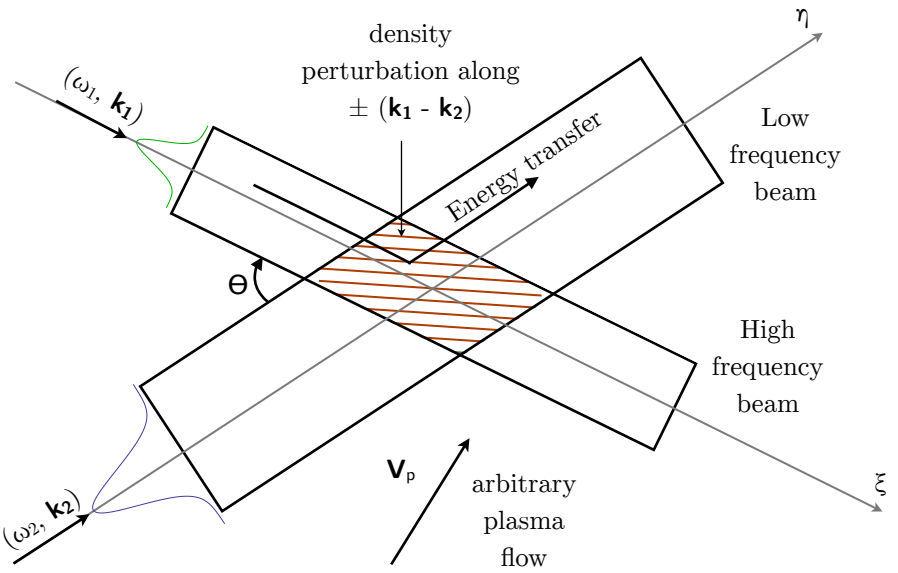

Figure 4-1 – *Schematic representation of the CBET configuration considered. The high frequency beam 1 propagates along the ξ axis and the low frequency beam 2 along the η axis. The plasma parameters; density, temperature, velocity, are a-priori arbitrary in the interaction region, and the upstream intensity profiles of the waves are also arbitrary.*

directions ξ and η:

$$\begin{aligned} \partial_\xi \mathcal{I}_1 &= -2\beta(\xi,\eta)\mathcal{I}_1\mathcal{I}_2 \ , \\ \partial_\eta \mathcal{I}_2 &= 2\beta(\xi,\eta)\mathcal{I}_1\mathcal{I}_2 \ , \end{aligned} \tag{4.3}$$

where $\mathcal{I}_i = |a_i|^2/\langle|a_1|^2_{\rm in}\rangle$ is the normalized intensity of beam i, $\langle|a_1|^2_{\rm in}\rangle$ is the initial mean intensity of wave 1, and β is a coupling coefficient defined below. With our notations, the normalization factor, corresponding to the input intensity of the first wave (pump beam) entering the interaction region, $\langle|a_1|^2_{\rm in}\rangle$ reads:

$$\langle|a_1|^2_{\rm in}\rangle = \frac{c^2_{\rm se} v^2_{{\rm osc},1}}{c^2_{\rm seff}(1+k_s^2\lambda_D^2)v^2_{T,e}} \approx \frac{v^2_{{\rm osc},1}}{v^2_{T,e}} = \frac{9.34\times10^{-3}}{N_1 T_{e,{\rm keV}}}\frac{I_1\lambda_1^2}{10^{14}{\rm W}\mu{\rm m}^2/{\rm cm}^2} \ , \tag{4.4}$$

where $v_{{\rm osc},1}$ is the oscillation velocity of the electrons in the field of wave 1 written in the Fourrier convention, N_1 is the plasma refractive index seen by wave 1, λ_1 the vacuum wavelength of wave 1, and $c^2_{\rm seff}/c^2_{\rm se} = 1 + 3T_i(1+k_s^2\lambda_D^2)/(ZT_e)$ is a correction factor close to unity. The expressions in the right-hand-side were obtained by assuming that $k_s\lambda_D \ll 1$ and $ZT_e \gg 3T_i$.

To a factor of $\langle|a_1|^2_{\rm in}\rangle$, the nonlinear coupling coefficient β in Eq. (4.3) is the imaginary part of the ion-acoustic response to the ponderomotive force [164], and reads:

$$\beta(\xi,\eta) = \langle|a_1|^2_{\rm in}\rangle \frac{\omega^2_{\rm pe}\omega_s^2\nu_s\Omega}{\omega_2 V_{g,2}[(\omega_s^2-\Omega^2)^2+4\nu_s^2\Omega^2]} \ , \tag{4.5}$$

where $\omega_s = V_{gs}|\mathbf{k}_s|$ is the ion-acoustic frequency at the beat wave wavenumber with V_{gs} the group

velocity of the ion acoustic wave defined in Sec. 1.5.2.2 (with $V_{gs} \approx c_s = \sqrt{ZT_e + 3T_i/m_i}$ for $k\lambda_{De} \ll 1$). The quantities involved in the coupling coefficient are functions of the local plasma parameters $\{T_e, n_e, \mathbf{V}_p\}$ inside the interaction region, so that in general β is a function of the spatial coordinates (ξ, η).

We define the fractional beam power $\hat{P}_i(\eta, \xi)$ as:

$$\begin{aligned} \hat{P}_1(\eta, \xi) &= \int_{-\infty}^{\eta} \mathcal{I}_1(\eta', \xi) \mathrm{d}\eta' \ , \\ \hat{P}_2(\eta, \xi) &= \int_{-\infty}^{\xi} \mathcal{I}_2(\eta, \xi') \mathrm{d}\xi' \ , \end{aligned} \tag{4.6}$$

so that $\mathcal{P}_i^{\text{out}} = \hat{P}_i(\infty, \infty)$ is the total power downstream of the intersection for beam i, and $\mathcal{P}_1^{\text{in}} = \hat{P}_1(-\infty, \infty)$ and $\mathcal{P}_2^{\text{in}} = \hat{P}_2(\infty, -\infty)$ are the total power upstream of the intersection for beams 1 and 2, respectively. Note that with our notations, what we have termed beam power are in units of m^{-1}, because the intensities $\mathcal{I}$ are normalized. Summing the two equations in (4.3) and integrating over the interaction region gives:

$$\int_{-\infty}^{\xi} \int_{-\infty}^{\eta} (\partial'_\xi \mathcal{I}_1 + \partial'_\eta \mathcal{I}_2) \mathrm{d}\eta' \mathrm{d}\xi' = \hat{P}_1(\eta, \xi) - \hat{P}_1(\eta, -\infty) + \hat{P}_2(\eta, \xi) - \hat{P}_2(-\infty, \xi) = 0 \ . \tag{4.7}$$

Setting $\eta \to \infty$ and $\xi \to \infty$ we obtain the power transfer equation:

$$\mathcal{P}_1^{\text{in}} - \mathcal{P}_1^{\text{out}} = \mathcal{P}_2^{\text{out}} - \mathcal{P}_2^{\text{in}} = \mathcal{P}_T \ , \tag{4.8}$$

where $\mathcal{P}_T$ is the total power transfer (also in units of m^{-1}). We now present the formulation of $\mathcal{P}_T$ for elementary energy transfers between PCGO beamlets.

4.1.1.2 Elementary energy exchange between beamlets

Each elementary energy transfer between PCGO beamlet is based on the formulation presented above, with an additional layer of simplifying assumptions. In order to integrate the coupled equations for the waves intensities (4.3), we simplify the formulation for the coupling parameter β by assuming that the plasma parameters, namely the density, temperature and flow velocity direction and amplitude, are constant in the interaction region. These quantities are set to the plasma parameters at the coordinate of the intersection between the centroids of the beamlets, interpolated from the mesh grid of the hydrodynamic code. The resulting constant coupling coefficient is noted $\overline{\beta}$ and with respect to the definition of Eq. (4.5) we have $\overline{\beta} = \beta(0, 0)$. When not specified otherwise, the damping coefficient ν_s/ω_s is computed using empirical formulas such as those presented in Ref. [178], that account for both the collisional and the Landau damping. For a constant $\overline{\beta}$, Eq. (4.3) can be integrated for arbitrary upstream intensity profiles $\mathcal{J}_i$ by defining the normalized beam widths [179]:

$$\begin{aligned} \hat{w}_1(\eta) &= 2\overline{\beta} \int_{-\infty}^{\eta} \mathcal{J}_1(\eta') \mathrm{d}\eta' \ , \\ \hat{w}_2(\xi) &= 2\overline{\beta} \int_{-\infty}^{\xi} \mathcal{J}_2(\xi') \mathrm{d}\xi' \ . \end{aligned} \tag{4.9}$$

In that framework, integration of Eq. (4.3) yields the intensity of the beams in the intersection region:

$$\begin{aligned}\mathcal{I}_1(\eta,\xi) &= \mathcal{J}_1(\eta)\frac{\exp\left[-\hat{w}_1(\eta)\right]}{\exp\left[\hat{w}_2(\xi)\right]-1+\exp\left[-\hat{w}_1(\eta)\right]}\ ,\\ \mathcal{I}_2(\eta,\xi) &= \mathcal{J}_2(\xi)\frac{\exp\left[\hat{w}_2(\xi)\right]}{\exp\left[\hat{w}_2(\xi)\right]-1+\exp\left[-\hat{w}_1(\eta)\right]}\ .\end{aligned} \tag{4.10}$$

In PCGO, beamlets are defined with a transverse intensity profile (see Sec. 2.3.3.2):

$$I_i = I_{0,i}\exp\left[-2\left(\frac{r_i}{w_{0,i}}\right)^2\right]\ , \tag{4.11}$$

where r_i is the transverse coordinate to beamlet i, $I_{0,i}$ is its on-axis intensity and $w_{0,i}$ its width. In this framework, the normalized upstream intensity profiles $\mathcal{J}$ in the (η,ξ) coordinate system read:

$$\mathcal{J}_1(\eta) = \exp[-2(\eta\sin\theta/w_{0,1})^2]\ ;\quad \mathcal{J}_2(\xi) = \mathcal{R}_\mathrm{I}\exp[-2(\xi\sin\theta/w_{0,2})^2]\ , \tag{4.12}$$

where $\mathcal{R}_\mathrm{I} = I_{0,2}/I_{0,1}$ is the upstream probe-to-pump on-axis intensity ratio. We compute the associated power transfer $\mathcal{P}_T$ between the higher-frequency wave 1 and lower-frequency beam 2 by combining and integrating Eqs. (4.6), (4.10) and (4.12):

$$\mathcal{P}_T = \frac{\mathcal{R}_\mathrm{I}\xi_P}{2\overline{\beta}}\log\left[\exp(-\hat{w}_2(\infty))+\exp(\hat{w}_1(\infty))(1-\exp(-\hat{w}_2(\infty)))\right]\ , \tag{4.13}$$

where we have introduced the polarization coefficient ξ_P defined in Sec. 3.4.1. The normalized beam width downstream of the interaction region and for the Gaussian intensity profiles read:

$$\begin{aligned}\hat{w}_1(\infty) &= (2\pi)^{1/2}\overline{\beta}w_{0,1}/|\sin\theta|\ ,\\ \hat{w}_2(\infty) &= (2\pi)^{1/2}\mathcal{R}_\mathrm{I}\overline{\beta}w_{0,2}/|\sin\theta|\ .\end{aligned} \tag{4.14}$$

Note that these formulations diverge for $\sin\theta = 0$. In that configuration, the two beams share one centroid, thus creating an infinite interaction region, leading to maximum gain, i.e. pump depletion. In practice, intersection of beamlet centroids at $\theta = 0°$ or $\theta = 180°$ are excluded in our simulations. Finally, the probe-beam amplification, defined as $T_\mathrm{probe} = (\mathcal{P}_2^\mathrm{in}+\mathcal{P}_T)/\mathcal{P}_2^\mathrm{in}$, reads:

$$T_\mathrm{probe} = 1+\xi_P\left[\frac{1}{\mathcal{R}_\mathrm{I}G_2}\log\left[1+\exp(G_1)\left(\exp(\mathcal{R}_\mathrm{I}G_2)-1\right)\right]-1\right]\ , \tag{4.15}$$

where we have defined the gain values $G_1 = \hat{w}_1(\infty)$ and $G_2 = G_1(w_{0,2}/w_{0,1})$.

Given two PCGO beamlets in the 2D planar framework, which parameters upstream of their intersection are a power $P_i^\mathrm{in} = \sqrt{\pi/2}hw_{0,i}I_{0,i}$ with a width $w_{0,i}$ and on-axis intensity $I_{0,i}$ (h is a unit height, see Sec. 2.3.3.2), their downstream power are computed as:

$$\begin{aligned}P_1^\mathrm{out} = T_\mathrm{pump}P_1^\mathrm{in} &= (1-\mathcal{R}_\mathrm{P}(T_\mathrm{probe}-1))P_1^\mathrm{in}\ ,\\ P_2^\mathrm{out} &= T_\mathrm{probe}P_2^\mathrm{in}\ ,\end{aligned} \tag{4.16}$$

where $T_{\text{pump}} \leq 1$ is the *pump depletion ratio* and $\mathcal{R}_{\text{P}} = (w_{0,2}/w_{0,1})\mathcal{R}_{\text{I}}$ is the upstream power ratio for the beamlets. The maximum power transfer occurs for $T_{\text{pump}} = 0$, that is $T_{\text{probe}} = (1+\mathcal{R}_{\text{P}})/\mathcal{R}_{\text{P}}$.

4.1.2 From elementary to large-scale energy transfers

Equation (4.15) describes an idealized case of a steady-state interaction between two Gaussian beamlets. In order to extend the energy transfer between whole beams including many elementary transfers between PCGO beamlets, a number of simplifying assumptions are made.

- The spatial configuration of the CBET causes the two beams to have different intensity distributions after the transfer, i.e. they do not remain Gaussian [164] (this can also be seen from Eqs. (4.10)). In general, the output intensity profile can exhibit more than one intensity peak and be deviated (skewed). In order to fulfill the limitations of the thick-ray model, we assume the intensity distribution of a beam after an energy transfer remains Gaussian, with the same width as before the energy exchange. Consequently, the amount of power transferred between beams is only impacted on their intensity. This assumption is reasonable as for these deformations to be significant in terms of influence on the small scale hydrodynamics, a high mesh resolution would be required. Moreover these deviations from the Gaussian profile are observed only in the case of high energy transfer, while the energy exchange between beamlets is kept at a low level because of small beamlet sizes.

- We neglect changes in centroids directions of the crossed beams [164]. This phase distortion due to CBET is relatively small and is close to zero when the energy exchange is maximum (i.e. when $\overline{\beta}$ is maximum). Although the PCGO model is well suited to take into account this second order effect, it is not accounted for in the present version.

- We make the further approximation that the energy transfer region is point-like, i.e. we do not project intensity variations inside the transfer region onto the hydrodynamic mesh and beam parameters are modified at the point where the centroids cross each other. This is reasonable considering the typical thickness of PCGO rays compared to the size of mesh cells. Furthermore, given that many beamlets overlap in plasma, such effects are negligible.

- Finally, because the transfer regions are modeled as being point-like, we consider intersections between only two thick-rays at a time, i.e. overlapping energy transfer regions are treated separately and in a chronological order.

Once the energy transfer between two beams has been computed and their downstream intensities are found, the beamlet propagation is recomputed from the point of crossing along the central rays by re-integrating the wave front equations (2.72). Resolving the stack of CBET intersections in a chronological and consistent order requires specific algorithms of intersection sorting, ordering and identification of loops, which are described in App. B.2. Simplification of this stack can be achieved by neglecting CBET interactions with small coupling coefficients. In applications, we chose to neglect crossings with $\overline{\beta} < 5 \times 10^{-4}\overline{\beta}_{\text{max}}$. The cut-off value for $\overline{\beta}$ has been chosen so as to consider the maximum number of beamlet intersections as possible. Lower cut-off values do not yield different results.

The power exchange being known analytically and all intersections being solved in a chronological order, the energy is naturally conserved in the present CBET model, as it is conserved in each elementary process according to Eq. (4.8). It is also worth mentioning that the beamlet-related quantities required to compute an energy transfer (i.e. width and intensity) are always well defined by PCGO, even for normally incident beamlets on the critical density and at turning points. This property that the intensity and width of PCGO beamlets do not diverge near or at the critical density (as shown in Sec. 2.3.5.3 and Fig. 2-9 [left]) is a strong motivation for its use for CBET computations and nonlinear LPIs in general.

4.2 Theoretical validation of the CBET model: comparison to academic cases

The theoretical validation of the EYEBOLT model is based on two points.

- First, an assessment of the *quadratic decomposition* approach, e.g. the discretization of the CBET between two large beams by $(N_{B1} \times N_{B2})$ local CBETs between PCGO beamlets, is conducted in Sec. 4.2.1. This comparison is conducted in the framework of steady-state energy transfer at the resonance and in homogeneous media.
- Second, a comparison of CBET linear gains for beams crossing in an inhomogeneous plasma is presented in Sec. 4.2.2, in the case of (i) large pump-to-probe intensity ratios, and (ii) similar pump-to-probe intensity ratios.

Throughout this section and in the numerical comparison with the paraxial solver (in Sec. 4.3), the plasma is considered to be non-collisional. Note that this is a good approximation at the low densities considered here.

4.2.1 Quadratic decomposition approach

The EYEBOLT model relies on the description of the CBET between whole beams by many elementary energy transfers between Gaussian beamlets. Considering two lasers beams modeled with PCGO with N_{B1} and N_{B2} beamlets, respectively, the global Cross-Beam Energy Transfer is modeled by $N_{B1} \times N_{B2}$ elementary energy exchanges, as illustrated in Fig. 4-2. The validity of this approach can be assessed in the framework of a plasma of constant density, temperature and flow velocity, as was presented in Sec. 4.1.1.2.

We consider the energy exchange between two nearly flat-top beams with aligned polarizations ($\xi_P = 1$), which intensity profile upstream of the intersection region are:

$$\mathcal{J}_1(\eta) = \frac{1}{1+\mathcal{R}_\mathrm{I}} \exp\left[-\left|\frac{\eta \sin\theta}{\mathcal{D}}\right|^8\right] \quad ; \quad \mathcal{J}_2(\xi) = \frac{\mathcal{R}_\mathrm{I}}{1+\mathcal{R}_\mathrm{I}} \exp\left[-\left|\frac{\xi \sin\theta}{\mathcal{D}}\right|^8\right] \quad , \tag{4.17}$$

where $\mathcal{D}$ is the beam diameter, θ is the angle at which the waves intersect, and similarly to Sec. 4.1.1.2, $\mathcal{R}_\mathrm{I}$ is the upstream probe-to-pump intensity ratio of the two waves (here $\mathcal{R}_\mathrm{I} = \mathcal{R}_\mathrm{P}$. The normalization used in this formulation is such that the *overlapped intensity* in the focal plane of the wave is equal to $\langle |a_0|^2_\mathrm{in} \rangle$. We designate by $I^\Sigma_\mathrm{FS}\lambda^2_L$ the overlapped vacuum interaction parameter

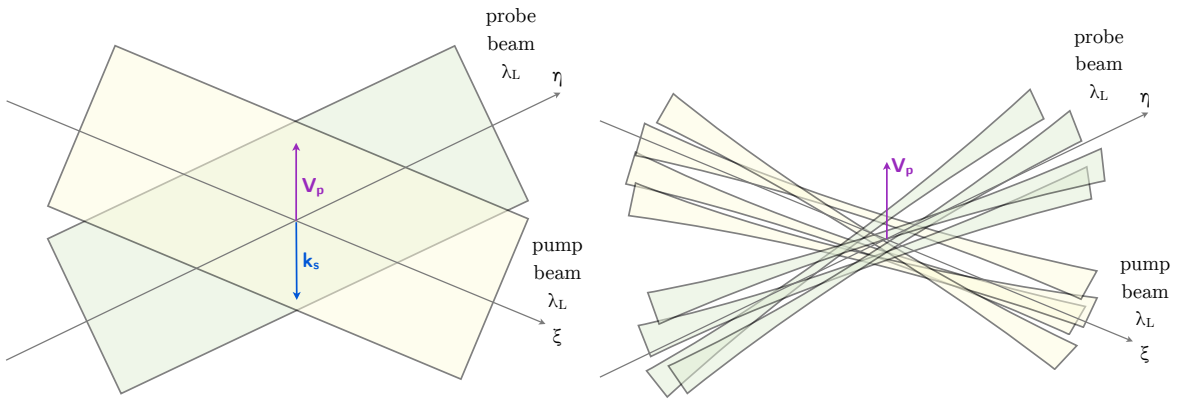

Figure 4-2 – *Illustration of the quadratic decomposition of [left] the CBET between two beams by [right] $N_{B1} \times N_{B2}$ elementary energy exchanges between PCGO beamlets. The flow velocity $\mathbf{V}_p$ is in the direction of $-\mathbf{k}_s$ and $|\mathbf{V}_p| = c_s$. Note that $-\mathbf{k}_s$ in this schematic refers to the beat wavenumber of the waves shown on the [left] panel, i.e. the whole laser beams. Given that PCGO beamlets are pseudo-randomly focused in our model, as illustrated in the [right] panel (see also Sec. 3.2), each elementary energy exchange sees a local $\mathbf{k}_s$ that is not exactly collinear with the plasma velocity $\mathbf{V}_p$.*

inside the CBET region. This notation will also be used in the comparison with the paraxial solver in Sec. 4.3.

The frequencies of the beams are identical, $\omega_1 = \omega_2$, and the plasma flow velocity is such that $\mathbf{V}_p = -\mathbf{k}_s$ and $|\mathbf{V}_p| \approx c_s$ (here $k_s \lambda_D \ll 1$), so that $\Omega = k_s c_s = \omega_s$, i.e. we are at resonance and $\overline{\beta}$ is maximum. Similarly as in Sec. 4.1.1.2, integration of Eqs. (4.6) and (4.10) using the flat-top upstream intensity profiles given by Eq. (4.17) gives the probe beam power amplification $T_{\text{probe}}^{\text{flat}}$ downstream of the transfer region:

$$T_{\text{probe}}^{\text{flat}} = (\mathcal{R}_{\text{I}} \overline{G})^{-1} \log \left[1 + \exp \overline{G}(1 + \mathcal{R}_{\text{I}}) - \exp \overline{G} \right] , \tag{4.18}$$

$$\overline{G} = \frac{4\mathcal{D}\overline{\beta}(\Omega = \omega_s)\Gamma[9/8]}{(1 + \mathcal{R}_{\text{I}})|\sin\theta|} , \tag{4.19}$$

where Γ is the Euler Gamma function.

We consider beams with a vacuum wavelength $\lambda_L = 1.05$ μm, intersecting at an angle $\theta \in \{20°, 60°\}$ in a fully ionized hydrogen plasma with $T_e = 3$ keV, $T_i \ll Z T_e$, $n_e = n_c/10$, $\nu_s/\omega_s = 1/10$ (that is a rather standard value for laser-ablator interaction in ICF). Using the left-hand-side of Eq. (4.4), the relation between the vacuum interaction parameter $I_{\text{FS}}^{\Sigma} \lambda_L^2$ (in units of 10^{14} Wμm^2/cm^2) and $\langle |a_0| \rangle^2$ is obtained, so that $\overline{G}$ reads:

$$\overline{G} = \frac{1.45 (I_{\text{FS}}^{\Sigma} \lambda_L^2)(1 + 0.21 \sin(\theta/2)^2)}{|\sin\theta|(1 + \mathcal{R}_{\text{I}})(1 + 0.003(1 + 0.21 \sin(\theta/2)^2))} , \tag{4.20}$$

where, considering that the plasma is non-collisional, we have used $I_{\text{FS}}^{\Sigma} \lambda_L^2 = I^{\Sigma} \lambda_L^2 / N$, with N the refraction index and I the in-plasma intensity used in Eq. (4.4). This formulation for $\overline{G}$ is injected in (4.18) to obtain the amplification $T_{\text{probe}}^{\text{flat}}(\theta, I_{\text{FS}}^{\Sigma} \lambda_L^2, \mathcal{R}_{\text{I}})$. Note that for a fixed angle θ, the term $\overline{G}(1 + \mathcal{R}_{\text{I}})$ in Eq. (4.18) is proportional to $I_{\text{FS}}^{\Sigma} \lambda_L^2$.

This theoretical formulation is compared to simulations using 30 beamlets for each beam

(the beam splitting algorithm in that case does not allow to use less beamlets, see App. B.1.1). Resulting probe beam amplifications are shown in Fig. 4-3 for $\theta = 20°$. Considering a range of parameters $\mathcal{R}_\mathrm{I} \in [10^{-3}, 10^2]$, $I_\mathrm{FS}^\Sigma \lambda_L^2 \in [10^{-3}, 10^2] \times 10^{14}$ Wμm^2/cm^2 and $\theta \in \{20°, 60°\}$, the maximum relative error arising from the quadratic decomposition of the CBET region with PCGO beamlet is 2.1%, across an interval for $\overline{G} \in [4 \times 10^{-5}; 4 \times 10^2]$. Note that results are not sensitive to the number of beamlets past the minimum of 30 we have used here. The error is maximum in a region where $1 + \mathcal{R} \approx 1$ and $\overline{G} \approx 10$. It can be seen from Eq. (4.18) that the system is particularly stiff in this region, where the two exponential factor almost cancel out.

The low error observed across the wide range of parameters is a strong result of the quadratic decomposition approach, especially when considering the nonlinear nature of CBET, illustrated by the exponential factor in Eq. (4.18). It may be explained by the fact that for a beam i of intensity I_i, modeled by N_{Bi} beamlets, the intensityI_{ik} of beamlet k is not I_i/N_{Bi}. In fact, following the beam-splitting algorithm presented in Sec. 3.2.2, the beamlet intensity is of the same order of magnitude as $I_i/2$, so that the PCGO-based CBET approach we have presented is not a linear discretization of CBET in the sense of the factors $I_\mathrm{FS}^\Sigma \lambda_L^2$ and $\overline{G}$. An analytical formulation of the energy transfer of $N_{B1} \times N_{B2}$ energy exchanges between Gaussian optical beamlets would highlight the key parameters in minimizing the error from the quadratic decomposition. That error is likely to arise from the free parameters of the beam splitting model exposed in Sec. 3.2.2 and App. B.1.1; elementary width of the beamlets compared to the speckle radius, elementary intensity, number of beamlets used, etc...

These results are a validation of the approach considered in the Eyebolt model, of representing the intersection between beams by many elementary intersections between beamlets. These results are now extended to the case of CBET in an expanding plasma.

4.2.2 Steady-state CBET in an expanding plasma

4.2.3 Theoretical framework

We now consider the energy exchange between two EM waves propagating in a plasma with a linear velocity profile, constant density and constant temperature. In the vicinity of the resonance, point where $\Omega \approx \omega_s$, $\mathscr{D}_s$ can be approximated by:

$$\mathscr{D}_s \approx 2\omega_s(\Omega - \omega_s + i\nu_s) \ , \tag{4.21}$$

where we have used $\Omega^2 - \omega_s^2 \approx 2\omega_s(\Omega - \omega_s)$. In that case, the non-linear coupling coefficient given in Eq. (4.5) reads:

$$\beta(\xi, \eta) = \frac{\beta_0}{1 + \left[\frac{\Omega - \omega_s}{\nu_s}\right]^2} \ , \tag{4.22}$$

where we have introduced $\beta_0 = \beta(\Omega = \omega_s)$:

$$\beta_0 = \langle |a_1|_\mathrm{in}^2 \rangle \frac{\omega_\mathrm{pe}^2 \omega_s}{4\omega_2 V_{g,2} \nu_s} = \frac{\gamma_0^2}{\nu_s V_{g,2}} \ , \tag{4.23}$$

which we have related to the SBS coupling constant γ_0 introduced in Sec. 1.5.2.2.

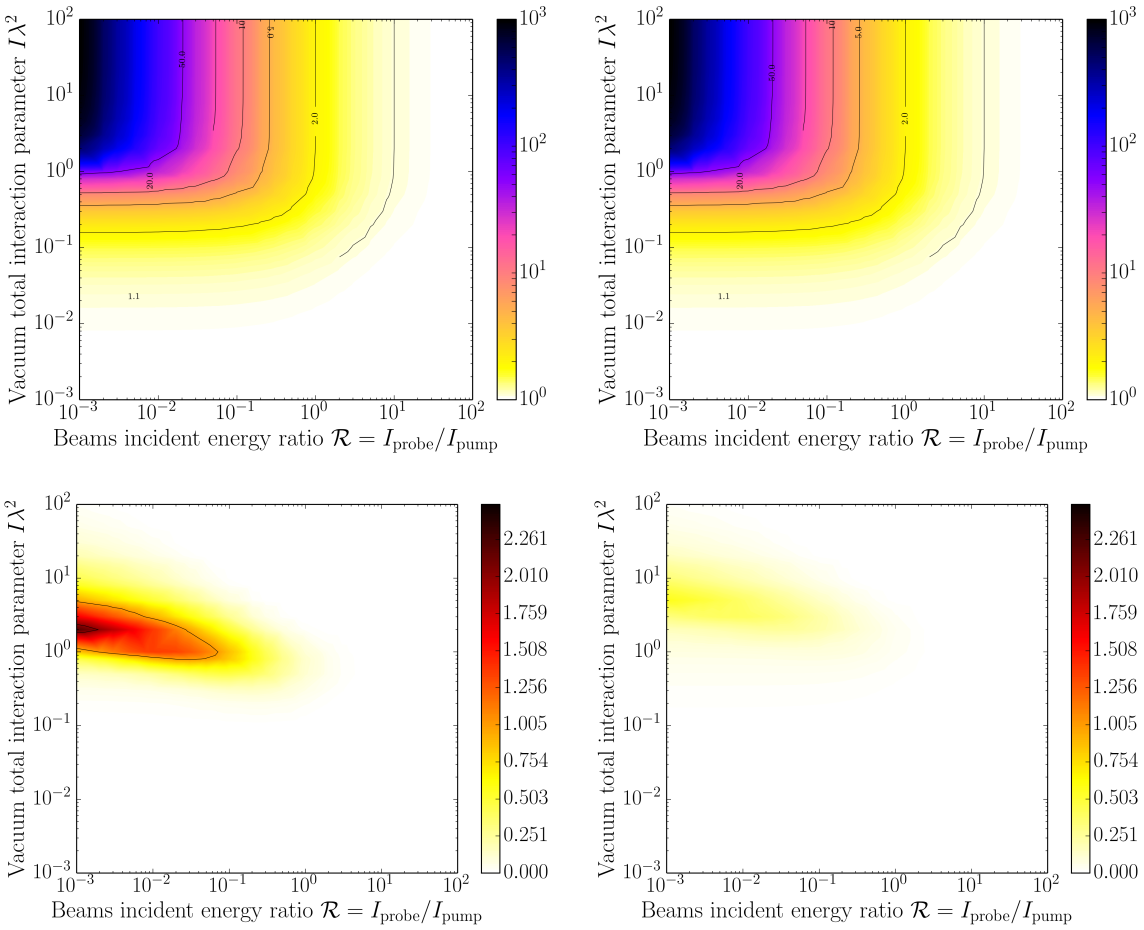

Figure 4-3 – *Probe beam amplification downstream of the transfer region, [top-left] results from the* EYEBOLT *model* $T^{\text{PCGO}}_{\text{probe}}$*, [top-right] theoretical formulation for* $T^{\text{flat}}_{\text{probe}}(\theta, I_0\lambda_L^2, \mathcal{R}_1)$*, and [bottom] relative error* $|T^{\text{flat}}_{\text{probe}} - T^{\text{PCGO}}_{\text{probe}}|/T^{\text{flat}}_{\text{probe}}$ *in percent. The angle between the beams is* $\theta = 20°$*, except for [bottom-right] for which* $\theta = 60°$*. Similar results are obtained for* $\theta = 140°$*. The overlapped vacuum interaction parameter is in units of* 10^{14} $W\mu m^2/cm^2$*.*

We consider a plasma with a linear velocity profile of the form $\mathbf{V}_p(y) = [V_{p,0} + yc_s/L_\perp]\mathbf{e_y}$, with $y = \eta \mathbf{e_y}.\mathbf{e}_\eta + \xi \mathbf{e_y}.\mathbf{e}_\xi$ the coordinate in the direction of the velocity vector $\mathbf{e_y}$, c_s is the sound speed defined as $c_s^2 = (ZT_e + 3T_i)/m_i$ (with m_i the ion mass), $V_{p,0}$ is the plasma velocity at the origin of the (ξ, η) coordinate system, and $L_\perp$ is the velocity gradient defined as: $L_\perp = c_s/\mathrm{d_y}V|_{y=0}$. We denote as ϕ the angle between $\mathbf{k}_s$ and $\mathbf{V}_p$, so that $\mathbf{e_y}.\mathbf{e}_\xi = -\sin(\phi + \theta/2)$ and $\mathbf{e_y}.\mathbf{e}_\eta = -\sin(\phi - \theta/2)$. In that configuration, $\beta(\xi, \eta)$ reads:

$$\beta(\xi,\eta) = \frac{\frac{\gamma_0^2}{\nu_s V_{g,1}}}{1 + \frac{k_s^2 c_s^2}{\nu_s^2}\left[\mathcal{Q}_0 - \mathcal{Q}(\xi,\eta)\right]^2} \ , \tag{4.24}$$

with

$$\mathcal{Q}(\xi,\eta) = \left| \frac{V_{p,0}}{c_s} - \frac{\eta \sin(\phi - \theta/2) + \xi \sin(\phi + \theta/2)}{L_\perp} \right| \cos\phi \ ,$$

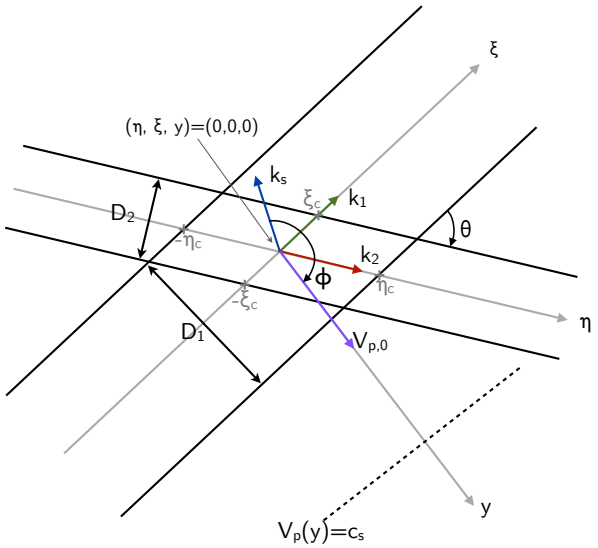

Figure 4-4 – *(color) Schematic representation of the CBET configuration. The high frequency beam 1 propagates along the ξ axis and the low frequency beam 2 along the η axis. The plasma flow velocity is in the y direction with value $V_{p,0}$ at the intersection between the beams centroids. The line of constant $V_p = c_s$ is located at an arbitrary location, indicated here with a dashed line.*

$$\mathcal{Q}_0 = \frac{\omega_1 - \omega_2}{k_s c_s} - \frac{c_{s\text{eff}}}{c_s\sqrt{1 + k_s^2\lambda_D^2}} \approx \frac{\omega_1 - \omega_2}{k_s c_s} - 1 \ , \tag{4.25}$$

where we have assumed $k_s\lambda_D \ll 1$ on the right-hand-side of $\mathcal{Q}_0$. Considering the energy transfer between two beams of constant diameters $\mathcal{D}_1$ and $\mathcal{D}_2$ throughout the interaction region (see Fig. 4-4), we define the linear gain G of the energy transfer from the probe power amplification:

$$\exp G = T_{\text{probe}} = \int_{-\xi_c}^{\xi_c} \mathcal{I}_2^{\text{out}}(\xi)\mathrm{d}\xi \Big/ \int_{-\xi_c}^{\xi_c} \mathcal{I}_2^{\text{in}}(\xi)\mathrm{d}\xi \ , \tag{4.26}$$

where $\xi_c = \mathcal{D}_1/(2\sin\theta)$, $\mathcal{I}_2^{\text{out}}(\xi) = \mathcal{I}_2(\xi, \eta_c)$, $\mathcal{I}_2^{\text{in}}(\xi) = \mathcal{I}_2(\xi, -\eta_c)$ and $\eta_c = \mathcal{D}_2/(2\sin\theta)$.

4.2.3.1 Theoretical gains and comparison with EYEBOLT

Infinitesimal probe-to-pump intensity ratio We consider the case of a probe intensity I_2 much lower than the pump intensity I_1, i.e. $I_2 \ll I_1$. In that case, I_1 can be considered constant throughout the interaction region. We construct a spatial phase-matching variation between the beams by considering a plasma with a constant velocity gradient (that is often the case in ICF plasmas). Assuming an initially constant transverse profile for the beams, i.e. $\mathcal{I}_1^{\text{in}}(\xi) = \mathcal{I}_1^{\text{in}} = 1$ and $\mathcal{I}_2^{\text{in}}(\eta) = \mathcal{I}_2^{\text{in}} = 1$, it is straightforward to show that Eq. (4.3) yields:

$$\mathcal{I}_2^{\text{out}}(\xi) = \mathcal{I}_2^{\text{in}} \exp \int_{-\eta_c}^{\eta_c} 2\beta(\xi, \eta')\mathrm{d}\eta' \ , \tag{4.27}$$

so that Eq. (4.26) for the gain reads:

$$T_{\text{probe}}^{I_2\ll I_1} \equiv \exp G_{\text{inh}}^{I_2\ll I_1} = \frac{1}{2\xi_c}\int_{-\xi_c}^{\xi_c} \exp\left[\int_{-\eta_c}^{\eta_c} 2\beta(\xi,\eta)\mathrm{d}\eta\right]\mathrm{d}\xi \ . \tag{4.28}$$

We note that analytical integration of β in this equation requires splitting the integral in two separate sub-domains to account for the absolute value of the velocity in Eq. (4.25). These domains are delimited by the line where the plasma velocity is zero, defined by $\eta\sin(\phi-\theta/2)+\xi\sin(\phi+\theta/2) = L_\perp V_{p,0}/c_s$. The formulation for $G_{\text{inh}}^{I_2\ll I_1}$ in Eq. (4.28) accounts for the local plasma parameters in the interaction region, along the directions ξ and η. As we have shown in Sec. 1.5.1.3, for a finite-length interaction in an inhomogeneous medium, $G_{\text{inh}}^{I_2\ll I_1}$ can be estimated by $G_{\max}$:

$$G_{\max} = \frac{2\gamma_0^2}{\nu_s V_{g,1}}\min\left\{L_{\text{int}}, L_{\text{inh}}\right\} \ , \tag{4.29}$$

where L_{inh} is the characteristic scale of the inhomogeneity and L_{int} the characteristic scale of the finite-length interaction. Note that the gain associated with L_{inh} is the so-called *Rosenbluth gain* [76], written for the intensity; $G_{\text{ros}} = (2\gamma_0^2/(\nu_s V_{g,1}))L_{\text{inh}}$. Here, the characteristic scales read:

$$L_{\text{int}} = \frac{\mathcal{D}_1}{2\sin\theta} \ , \tag{4.30}$$

$$L_{\text{inh}} = \pi\frac{L_\perp \nu_s/\omega_s}{\cos\phi\sin(\phi+\theta/2)} \ . \tag{4.31}$$

The gain $G_{\max}$ is an estimation of the gain that is a-priori a maximum value for the interaction, so that $G_{\max} \geq G_{\text{inh}}^{I_2\ll I_1}$.

For the case presented here, we choose the following parameters for the plasma: $\nu_s/\omega_s = 1/10$, $n_e/n_c = 1/10$, $T_e = 3$ keV, $Z = 2.5$, $ZT_e \gg T_i$ and $A = 4.252$ (where A is the mass number). The beam parameters are the following; a free-space interaction parameter for the pump beam $I_{\text{FS},1}\lambda_L^2 = 0.9\times10^{14}$ Wμm^2/cm^2, a probe-beam intensity $I_2 \ll I_1$, equal beam diameters $\mathcal{D}_1 = \mathcal{D}_2 = \mathcal{D} = 600\lambda$, the f-number $f_\# = 7$ and interaction at an angle $\theta = 20°$. The beams intersect in their focal plane and the initial flat-top transverse intensity profiles are approximated by super-Gaussian profiles of an order 8. The latter are more comparable with the averaged intensity profiles obtained when using Phase Plates and correspond to profiles that can be reproduced with PCGO:

$$\mathcal{J}_1(\eta) = \exp\left[-\left|\frac{\eta\sin\theta}{\mathcal{D}}\right|^8\right] \ ; \quad \mathcal{J}_2(\xi) = \mathcal{R}_\text{I}\exp\left[-\left|\frac{\xi\sin\theta}{\mathcal{D}}\right|^8\right] \ , \tag{4.32}$$

which are similar to Eq. (4.17) with $\mathcal{R}_\text{I} \to 0$. Given those parameters, the beams widths can be considered constant throughout the interaction region, in accordance with the assumptions made in Sec. 4.2.2. A linear plasma velocity profile with $L_\perp = 500\lambda$, $V_{p,0} = c_s$ and $\phi = \pi$ is imposed. The resulting nonlinear coupling coefficient is illustrated in Fig. 4-5. The corresponding theoretical gain $G_{\text{inh}}^{I_2\ll I_1}$ is computed by numerical integration of Eq. (4.26). We find a probe power amplification $T_{\text{probe}}^{I_2\ll I_1} = 685$, so that the gain is $G_{\text{inh}}^{I_2\ll I_1} = 6.53$. Note that in this configuration $G_{\max} = 8.51$.

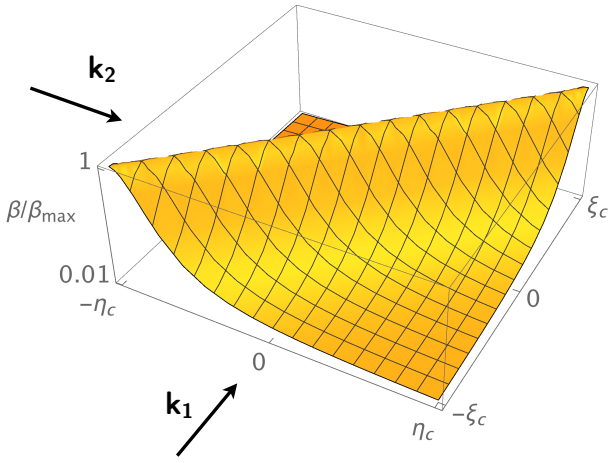

Figure 4-5 – *Illustration of the resonance function considered here, normalized to its maximum value. The two waves are input on the upper-left and bottom-left boundaries of the domain, indicated by arrows. Note that the ξ and η axis are shown to be orthogonal, but these are in reality at an acute angle of $\theta = 20°$.*

This theoretical configuration is reproduced with PCGO, modeling each super-Gaussian beam by $N_B = 100$ PCGO Gaussian beamlets using the method described in Ch. 3.2 for beams smoothed by Kinoform Phase Plates (KPP). In order to be consistent with the theory described here, the EM wave absorption was turned off. The CBET gain $G^{I_2 \ll I_1}_{\text{inh,PCGO}}$ is computed as a discrete version of Eq. (4.26), where the summation spans over beamlets from the probe beam:

$$\exp G^{I_2 \ll I_1}_{\text{inh,PCGO}} = \frac{\sum_{k=1}^{N_B} I_k^{\text{out}} w_k^{\text{out}}}{\sum_{k=1}^{N_B} I_k^{\text{in}} w_k^{\text{out}}} , \tag{4.33}$$

where I_k and w_k designate the intensity and width of a beamlet k, respectively. The EYEBOLT model yields $G^{I_2 \ll I_1}_{\text{inh,PCGO}} = 6.55$, corresponding to $T^{\text{ros}}_{\text{PCGO}} = 700$. Simulation results are in excellent agreement with the theory in that case and for various values of $L_\perp$, θ, ϕ, n_e/n_c for which the assumptions made in the theory presented in Sec. 4.2.2 are valid, the main constraint being the validity of Eq. (4.21), which limits the range of $L_\perp$ we can explore, depending on θ and ϕ.

For two beams modeled by $N_B = 100$ beamlets each, the large-scale resonance function is discretized by 10^4 beamlets intersections. Energy transfers between those pairs are resolved with a constant value of β determined by the coordinates of their centroids intersection (defined as $(\eta, \xi) = (0, 0)$). The accuracy of this method is naturally related to the width of each elementary beamlet intersection region compared to the width of the resonance function. In practice, the Gaussian beamlets used in PCGO are small compared to the characteristic inhomegeneities encountered in typical CBET configurations. As an example, for a typical direct-drive ICF configuration, CBET occurs near the resonance region (for which $V_{p,0} = c_s$), where the gradient scale length of the density, temperature and velocity are much larger than the typical beamlet width of 10-30 λ_L. In configurations in which this assumption would not be correct, we note that the precision of the EYEBOLT model may be enhanced by replacing $\beta(0, 0)$ by the average

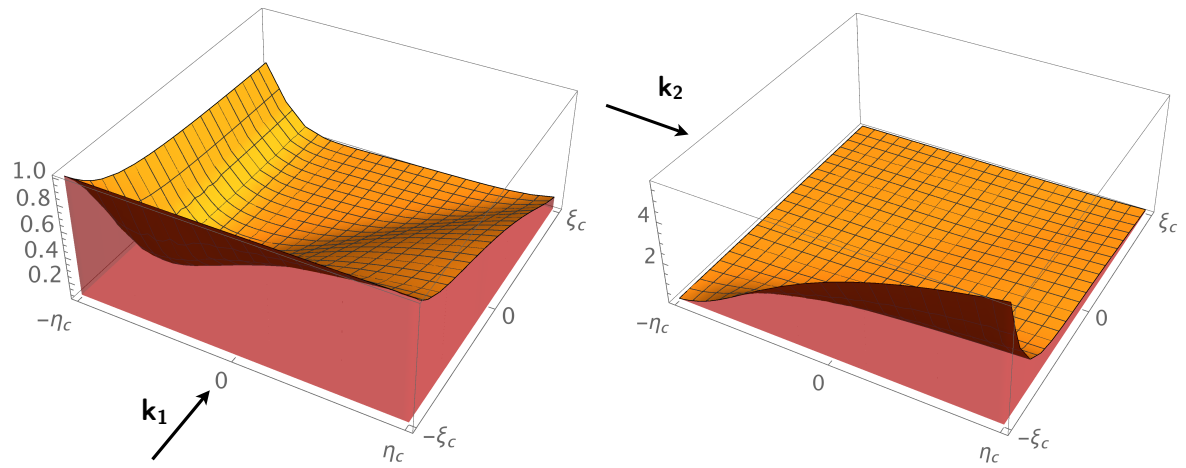

Figure 4-6 – *Map of the normalized intensity field $\mathcal{I}$, for the [left] pump beam 1 and [right] probe beam 2, for the particular case of $\mathcal{R}_\mathrm{I} = 1/8$. The input directions of the waves are indicated by arrows. Note that the ξ and η axis are shown to be orthogonal, but these are in reality at an acute angle of $\theta = 20°$.*

value of the nonlinear coupling coefficient in the interaction zone $\int\int \beta(\xi,\eta)\mathrm{d}\xi\mathrm{d}\eta/(4\xi_c\eta_c)$, for each elementary energy transfer between beamlets.

Interaction between beams of similar intensities We now consider the case where $\mathcal{R}_\mathrm{I} = \mathcal{I}_2^\mathrm{in}/\mathcal{I}_1^\mathrm{in}$ is closer to unity. For inhomogeneous plasmas, the estimation of the gain in such cases requires direct numerical resolution of Eq. (4.3). This numerical integration is most efficiently achieved by taking the crossed derivatives in Eqs. (4.3):

$$\begin{aligned} \partial_\eta\partial_\xi\mathcal{I}_1 &= -2\partial_\eta(\beta(\xi,\eta)\mathcal{I}_1\mathcal{I}_2) \ , \\ \partial_\xi\partial_\eta\mathcal{I}_2 &= 2\partial_\xi(\beta(\xi,\eta)\mathcal{I}_1\mathcal{I}_2) \ . \end{aligned} \tag{4.34}$$

This system is integrated using the Implicit Differential-Algebraic solver [180, 181, 182]. The initial conditions are defined on the input boundaries of the interaction region for both beams, i.e. there are four initial conditions to specify; $\mathcal{I}_1(-\xi_c,\eta)$, $\mathcal{I}_1(\xi,-\eta_c)$, $\mathcal{I}_2(\xi,-\eta_c)$ and $\mathcal{I}_2(-\xi_c,\eta)$. Two of these are the initial intensity profiles of the beams, $\mathcal{J}_1(\eta) = \mathcal{I}_1(-\xi_c,\eta)$ and $\mathcal{J}_2 = \mathcal{I}_2(\xi,-\eta_c)$, defined by:

$$\mathcal{J}_1(\eta) = \exp\left[-\left|\frac{\eta\sin\theta}{\mathcal{D}}\right|^8\right] \ ; \quad \mathcal{J}_2(\xi) = \mathcal{R}_\mathrm{I}\exp\left[-\left|\frac{\xi\sin\theta}{\mathcal{D}}\right|^8\right] \ . \tag{4.35}$$

The other two initial intensities are noted $\mathcal{G}_1(\xi) = \mathcal{I}_1(\xi,-\eta_c)$ and $\mathcal{G}_2(\eta) = \mathcal{I}_2(-\xi_c,\eta)$, and are solutions of the partial differential equations (4.3) for the intersection region edges:

$$\begin{aligned} \partial_\xi\mathcal{G}_1(\xi) &= -2\beta(\xi,-\eta_c)\mathcal{G}_1(\xi)\mathcal{J}_2(\xi) \ , \\ \partial_\eta\mathcal{G}_2(\eta) &= 2\beta(-\xi_c,\eta)\mathcal{G}_2(\eta)\mathcal{J}_1(\eta) \ , \end{aligned} \tag{4.36}$$

where the initial conditions for these equations are $\mathcal{G}_1(-\xi_c) = \mathcal{J}_2(-\xi_c) = \mathcal{R}_\mathrm{I}\exp(-1)$ and $\mathcal{G}_2(-\eta_c) = \mathcal{J}_1(-\eta_c) = \exp(-1)$.

We integrate Eqs. (4.34) and (4.36) for two values of $\mathcal{R}_\mathrm{I}$; $\mathcal{R}_\mathrm{I} = 1$ and $\mathcal{R}_\mathrm{I} = 1/8$. Other

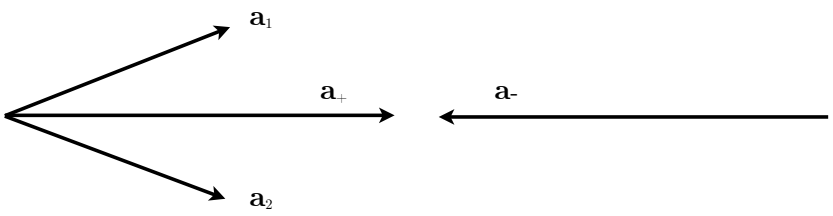

Figure 4-7 – *Illustration of the EM waves described in* HARMONY. *The code is formulated for the propagation and interaction of counter-propagating waves a_- and a_+. In our case, the a_- component is set to 0, and the a_+ term is decomposed in two co-propagating waves.*

plasma and beam parameters are the same as in Sec. 4.2.3.1. The resulting intensity map in the interaction region is illustrated in Fig. 4-6 for the case $\mathcal{R}_\mathrm{I} = 1/8$. The theoretical gains computed from the probe beam power amplification are, for the two cases, $G^{1:8}_\mathrm{inh} = 2.061$ and $G^{1:1}_\mathrm{inh} = 0.692$. Simulations using the EYEBOLT model and super-Gaussian of order 8 intensity profiles yield gain values of $G^{1:8}_\mathrm{inh,PCGO} = 2.056$ and $G^{1:1}_\mathrm{inh,PCGO} = 0.692$, which are in excellent agreement with the theory. Furthermore, a comparison of the output intensity profiles between the numerical solution and PCGO also shows excellent agreement, PCGO being able to accurately reproduce the regions of pump depletion and probe amplification. This is discussed further in Sec. 4.3.2.2 in the case of the comparison with the paraxial solver.

4.3 Comparison to a paraxial solver

Results from the steady-state EYEBOLT model are now compared to a time-dependent numerical resolution of the CBET. For the interaction of two electromagnetic beams, a system of partial differential equations using paraxial operators has to be solved with source terms for the coupling between the different modes [169, 170, 173]. Instead of the system of equations for the wave intensities (4.2), a system of equations for the corresponding complex-valued amplitudes is solved. This comparison aims at assessing (i) the validity of a CBET model in which the phase information has been discarded, and (ii) the assumption of steady-state CBET. A 2D planar geometry in Cartesian coordinates is considered, the main propagation axis being taken along the x coordinate.

4.3.1 Formalism of the HARMONY code

The code HARMONY [169, 170, 173] describes the coupling between two electromagnetic waves with amplitudes a_+ and a_- propagating in opposite directions (see Fig. 4-7). Coupling of these two waves is mediated by IAW with the complex-valued amplitude a_s:

$$\begin{aligned} \mathcal{L}_\mathrm{par}(a_+) &= -i(\omega_1/2n_{c,+})\,[a_s a_- + \delta n a_+] \ , \\ \mathcal{L}_\mathrm{par}(a_-) &= -i(\omega_2/2n_{c,-})\,[a_s^* a_+ + \delta n a_-] \ , \end{aligned} \tag{4.37}$$

where the paraxial operator $\mathcal{L}_\mathrm{par}(a_\pm) = [\partial_t + V_{g,\pm}\partial_x + \nu_\pm - i(c^2/2\omega_\pm)\triangle_\perp]a_\pm$, $V_{g,+}$ and $V_{g,-} \equiv -V_{g,+}$ stand for the group velocity of the forward and backward propagating waves, respectively, $\nu_\pm$ denotes the damping of these waves (see Sec. 1.3.3), and $\delta n = (n - n_\mathrm{eq})$ is the density

perturbation with n_{eq} the equilibrium density. In this general formulation, the right-hand-side terms in Eqs. (4.37) account for (i) the resonant 3-wave interaction of the incident wave a_+ and the backscattered wave a_- with the fundamental IAW component a_s, and for (ii) the refraction of the waves a_+ and a_- on the long-wavelength density modifications δn around the equilibrium density n_{eq}. In this approach, short-wavelength IAWs generated by the coupling between two laser beams with opposite wave vectors, $2|\mathbf{k}_+| \geq |\mathbf{k}_+ - \mathbf{k}_-| > |\mathbf{k}_+|$, are described by a nonlinear ion acoustic equation which takes into account high harmonics generation via hydrodynamic nonlinearity.

The ponderomotive modifications of the plasma density by each EM wave are described by a system of (nonlinear) fluid equations:

$$\partial_t n + \nabla n\mathbf{v}_0 = 0 \ , \tag{4.38}$$

$$\partial_t \left(n\mathbf{v}_0\right) + \nabla \left(n\mathbf{v}_0\mathbf{v}_0\right) + c_{\mathrm{seff}}^2 \nabla n + \hat{\nu}_k n\mathbf{v}_0 = -nc_{\mathrm{se}}^2 \nabla U_0 \ , \tag{4.39}$$

where $\hat{\nu}_k$ is a wavelength-dependent operator accounting for collisional and Landau damping. These equations describe the IAW in the specific case of the interaction between co-propagating EM waves. For an interaction between contra-propagating EM waves, an additional equation would be necessary. The right-hand-side term in Eq. (4.39) accounts for the ponderomotive force given by:

$$\nabla U_0 = (V_{\mathrm{osc}}^2/c_{\mathrm{se}}^2)\nabla(|a_+|^2 + |a_-|^2) \ . \tag{4.40}$$

The momentum transfer between the long- and short-wavelength IAWs is neglected [170], because it is of minor importance in this case.

The case of crossed laser beams with angles $< 45°$ is considered, so that the generated IAWs (i) propagate perpendicular to the axis in between the crossed beams, and (ii) are long-wavelength waves, so that the coupling is described via the term $\sim \delta n a_+$. In that case, the counter-propagating field a_- is set to zero and the field a_+ used in Eqs. (4.37) is split in two components separated by an angle θ (see Fig. 4-7) so that:

$$a_+ \equiv a_1 e^{i\mathbf{k}_{1,\perp}\cdot\mathbf{y}} + a_2 e^{i\mathbf{k}_{2,\perp}\cdot\mathbf{y}} \ , \tag{4.41}$$

$$a_- \equiv 0 \ , \tag{4.42}$$

with the propagation along the axis x and the common wave vector component $\mathbf{k}_{1,\parallel} = \mathbf{k}_{2,\parallel} = \mathbf{k}_1 \cos\theta/2$, while $\mathbf{k}_{1,\perp} = -\mathbf{k}_{2,\perp} = \mathbf{k}_1 \sin\theta/2$. In this framework, the equation for the fields read:

$$\mathcal{L}_{\mathrm{par}}(a_+) = -i\frac{\omega_1}{2n_{c,+}}\delta n(a_1 e^{i\mathbf{k}_{1,\perp}\cdot\mathbf{y}} + a_2 e^{i\mathbf{k}_{2,\perp}\cdot\mathbf{y}}) \ . \tag{4.43}$$

The EM field a_+ is generated by considering two separate beam elements which do not overlap in the near field, i.e. the width in Δk of each beam is smaller than their separation $2\mathbf{k}_1 \sin\vartheta/2$. Note that the ponderomotive force acting on the plasma fluid following Eqs. (4.39), $\propto \nabla U_0$, takes into account both the coupling between the components a_1 and a_2 of a_+, namely $(\nabla U_0)_{\mathrm{CBET}} \propto \nabla a_1 a_2^* \exp(i2|\mathbf{k}_1|y\sin\theta/2)$, but also the square terms $(\nabla U_0)_{\mathrm{self}} \propto \nabla(|a_1|^2 + |a_2|^2)$, responsible for self-focusing.

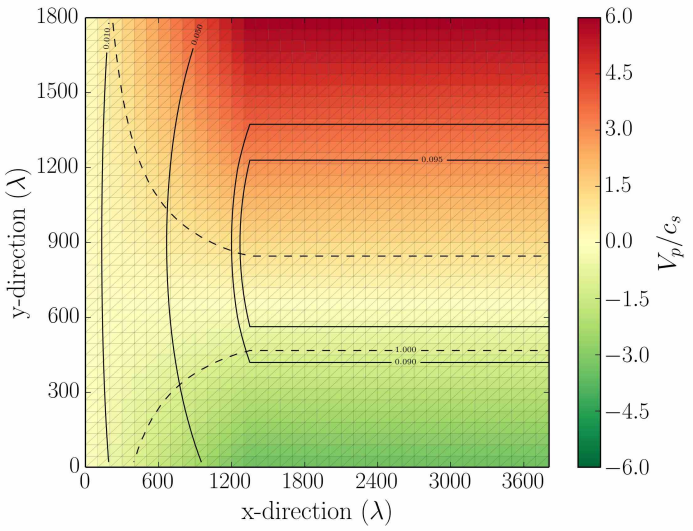

Figure 4-8 – *(color) Initial plasma parameters of the simulations. The color background indicates the plasma velocity* $\mathbf{V}_p.\mathbf{e}_y$ *in units of* c_s*. Negative values mean that the flow is directed along the unit vector* $-\mathbf{e}_y$*. Contours of constant density are shown in black plain lines, for* $n_e/n_c \in \{0.01, 0.05, 0.09, 0.095\}$*, and contours of constant velocity are shown in black dashed lines for* $\mathbf{V}_p.\mathbf{e}_y = \pm c_s$*.*

4.3.2 Comparison between PCGO and HARMONY simulations

The steady-state EYEBOLT approach and the time-dependent paraxial approach HARMONY are compared in several cases of various probe to pump intensity ratios $\mathcal{R}_\mathrm{I}$ and overlapped intensities $I_\mathrm{FS}^\Sigma \lambda_L^2$. The 2D simulation setup is a box of 4000 λ_L in length and 1800 λ_L in width in the $(\hat{x}, \hat{y})$ coordinate system (expressed in units of the vacuum wavelength λ_L). The chosen velocity and density profiles mimic that of a thin-foil experiment; with a quadratic density profile and a linear expansion velocity. For $\hat{x} \in [1300, 4000]$, the velocity is along the $\hat{y}$ direction and described by:

$$V_p(\hat{y})/c_s = (\hat{y} - 657)/200 \ , \tag{4.44}$$

and the density is described by

$$n_e(\hat{y})/n_c = 0.0995 - [(\hat{y} - 900)/1580]^2 \ , \tag{4.45}$$

with $\hat{y} \in [0, 1800]$. Note that the line of $V_p = 0$ does not correspond to the density maximum, as in a thin-foil experiment for which only one side of the foil is irradiated by laser beams. These profiles are linearly extended to zero velocity and zero density in the $\hat{x} \in [0, 1300]$ interval in order to avoid spurious couplings of edge modes to plasma waves. The resulting initial plasma conditions are illustrated in Fig. 4-8

The plasma is fully ionized hydrogen (i.e. $Z = 1$ and $A = 1$) and the damping rate is set to $\nu_s/\omega_s = 1/10$. With those parameters, the plasma velocity at the center of the interaction region is $V_{p,0} = 1.2c_s$ in the direction of increasing $\hat{y}$ and the density is $n_e = n_c/10$. The position of the resonance can be obtained by equating $\mathcal{Q}(\eta, \xi)$ and $\mathcal{Q}_0$ (Eq. (4.25)), which yields the optimal plasma velocity $V_{p,\mathrm{opt}} = \mathcal{Q}_0/\cos(\phi) = c_s$, i.e. at $\hat{y} \approx 860$. The mean intensity profiles (envelop)

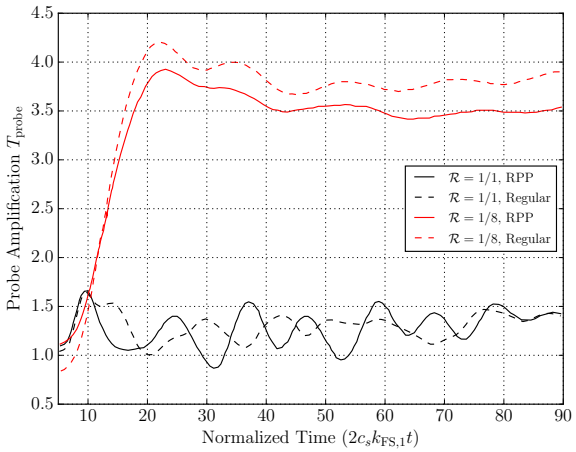

Figure 4-9 – *(color) Time history of the probe amplification from* HARMONY *simulations. Results at* $I_{FS}^{\Sigma}\lambda_L^2 = 0.9 \times 10^{14}$ $W\mu m^2/cm^2$ *for* $\mathcal{R}_I = 1/8$ *and* $\mathcal{R}_I = 1/1$ *are indicated with red (grey) lines and black lines, respectively. The cases of RPP smoothed beams (with speckles) are shown with plain lines and the cases of 'regular' beams (without speckles) at equivalent average beam intensities are shown with dashed lines. In the configuration considered here,* $2c_s k_{FS,1} t \sim 30$ *corresponds to* $t \sim 5$ *ps.*

of the beams are as follow:

$$\langle \mathcal{J}_1(\eta) \rangle = \frac{1}{1+\mathcal{R}_I} \exp\left[-\left| \frac{\eta \sin\theta}{\mathcal{D}} \right|^8 \right] \quad ; \quad \langle \mathcal{J}_2(\xi) \rangle = \frac{\mathcal{R}_I}{1+\mathcal{R}_I} \exp\left[-\left| \frac{\xi \sin\theta}{\mathcal{D}} \right|^8 \right] \quad , \tag{4.46}$$

with $\mathcal{D} = 600\lambda$ and the f-number $f_{\#} = 7$. The beams intersect in their focal plane in a region centered near the resonance line, at $\hat{x} = 2650$ and $\hat{y} = 900$. The beam crossing geometry in our simulations is simplified with respect to the scheme presented in Fig. 4-4, as the plasma flow velocity is parallel to k_s (i.e $\phi = 0$ or $\phi = \pi$).

The comparison relies on two sets of observables. First, a systematic study of the asymptotic power transfer between the beams for different values of the beam intensity ratio $\mathcal{R}_I = \mathcal{I}_2^{in}/\mathcal{I}_1^{in}$, namely $\mathcal{R}_I = \{1, 1/8, 1/64\}$, measured in terms of $\mathcal{P}_2^{out}/\mathcal{P}_2^{in} = \int \mathcal{I}_2^{out} d\xi / \int \mathcal{I}_2^{in} d\xi$, as a function of the interaction parameter $I_{FS}^{\Sigma}\lambda_L^2$. Second, a comparison of the spatial pattern of the CBET, including; the location and amplitude of the IAWs excited by the interaction of both beams, the intensity pattern of the beams in the simulation volume and the deviation of the beams after the transfer region.

Two series of simulations with HARMONY and PCGO have been carried out using two types of beams, namely; (i) optically 'smoothed' beams generated by phase plates in the near field, thus producing a speckle pattern for each beam in the interaction region (using Random Phase Plates (RPP) for HARMONY and Kinoform Phase Plates (KPP) for PCGO), and (ii) 'regular' beams of the same width and the same intensity envelope as the 'smoothed' beam, but without speckles. In both cases, the width in the interaction volume is controlled by applying a super-Gaussian envelope to the beams. The smoothed beams simulations constitute realistic cases, while the regular beams simulations are used to assess the spatial patterns arising in the transfer region. Note that the fractional power transfer between simulations with regular and smoothed beams

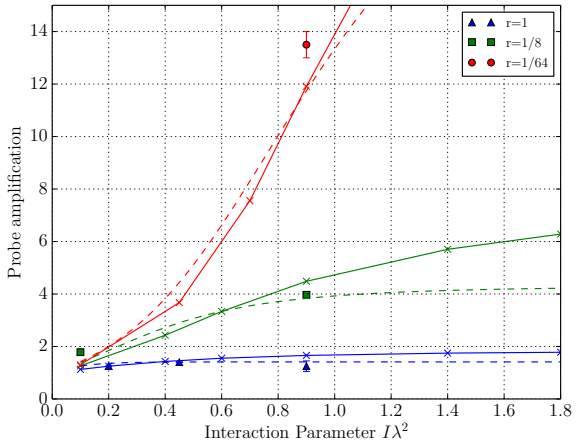

Figure 4-10 – *(color) Probe amplification as a function of the interaction parameter* $I_{\mathrm{FS}}^{\Sigma}\lambda_L^2$ *in* 10^{14} $W\mu m^2/cm^2$ *for various values of the upstream intensity ratio* $\mathcal{R}_{\mathrm{I}}$*. Results obtained with the* Eyebolt *model are shown as solid lines and results from* Harmony *as symbols. Results in both codes are based on a speckle pattern seed. The estimate from Eq. (4.15) with the gain values given in Sec. 4.3.2.1 are shown as dashed lines.*

are seen to be comparable, as illustrated in Fig. 4-9. The time of steady-state observed in the simulations vary depending on the interaction parameters. The duration of the transient period, defined as the time its takes for the power transfer to reach its final value (be it asymptotically or with small oscillations around a mean value), is in general of the order of $\sim 30(2c_s k_{\mathrm{FS},1} t)$, that is $t \sim 5$ ps here.

4.3.2.1 Asymptotic power transfer

The asymptotic power transfers obtained with both models are summarized in Fig. 4-10. PCGO and Harmony produce results in good agreement, for a wide range of intensity ratios and overlapped intensities. This is a strong result for the Eyebolt model, for which the computation time is of the order of 1 s, while the paraxial approach requires several hours (note that the latter must simulate ~ 30 ps while Eyebolt only estimates the steady-state value). While the agreement is best for $I_{\mathrm{FS}}^{\Sigma}\lambda_L^2 \leq 0.45 \times 10^{14}$ Wμm^2/cm^2, the agreement between the results at higher intensities decreases. The results shown here have been obtained for one set of simulations using the same random speckle patterns. Averaged results over many simulations with different random speckle patterns are presented in Fig. 4-11 [left] for Harmony. The averaged asymptotic power transfers are similar to those presented above in Fig. 4-10. This statistical analysis is also conducted by varying the random pseudo-speckle pattern in the PCGO model. The dispersion of the results from Harmony and Eyebolt is shown in Fig. 4-11 [right] for the $\mathcal{R}_{\mathrm{I}} = 1/8$ case. Accounting for the statistics, both models are in agreement up to $I_{\mathrm{FS}}^{\Sigma}\lambda_L^2 \leq 0.9 \times 10^{14}$ Wμm^2/cm^2. A possible explanation for the discrepancy at higher intensities is highlighted in Fig. 4-12: because the splitting algorithm employed in PCGO does not cover the wings of the beams as much as in Harmony, the inverse transfer resonance region is much less covered in the Eyebolt simulation, thus leading to an overestimation of the power transfer. Note that this is not an issue inherent to the PCGO model but to its current implementation in Chic for KPP

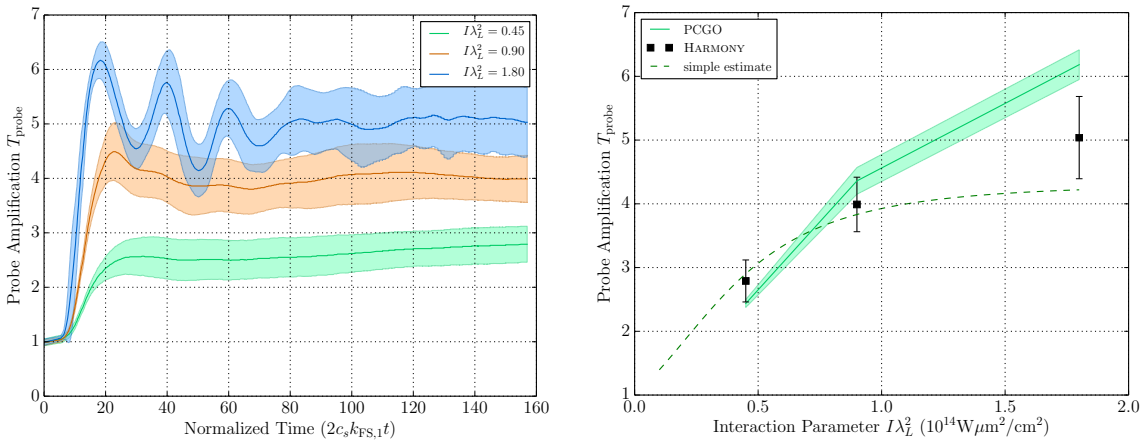

Figure 4-11 – *Probe amplification in the $\mathcal{R}_I = 1/8$ case, accounting for the statistical variance due to different random speckle patterns. [left] Time-history results from* HARMONY. *The central solid line represents the average value and the envelop is the $\pm$ 1 standard deviation region. [right] Results from* HARMONY *in black and results from* EYEBOLT *in light green. The envelops and error bars correspond to $\pm$ 1 standard deviation. The dashed green line corresponds to the estimate from Eq. (4.15). For both codes, results at a given $I_{FS}^{\Sigma}\lambda_L^2$ are averaged over 16 simulations. The interaction parameters is in units of 10^{14} $W\mu m^2/cm^2$.*

smoothed beams (see Sec. 3.2.2 and App. B.1.1). Finally, it must be noted that HARMONY simulations at high intensities and for $\mathcal{R}_I = 1$ do not reach a steady-state regime: the power transfer does not converge to the single value seen in the PCGO simulation ($\mathcal{P}_2^{out}/\mathcal{P}_2^{in} \sim 1.66$), but oscillates between two values $1.1 < \mathcal{P}_2^{out}/\mathcal{P}_2^{in} < 1.4$. In this case, mutual exchange between the beams occurs, due to the fact that the resonance zone of the inverse transfer is not too far. Although no clear steady-state regime is attained, it could be expected that the steady state power transfer predicted with EYEBOLT be between the aforementioned values. This discrepancy is also thought to be related to the modeling of the wings in PCGO.

In the region $I_{FS}^{\Sigma}\lambda_L^2 < 10^{14}$ Wμm^2/cm^2, the curves and points from the simulations shown in Fig. 4-10 are also in good agreement with the analytic expression for the fractional power transfer derived for a homogeneous plasma (Eq. (4.15)). For an inhomogeneous plasma, as in the cases we discuss here, under the condition that the resonant zone is well confined inside the zone of the overlapping beams, one can take for G_1 in good approximation the Rosenbluth gain G_{ros} given by Eq. (4.31) and for G_2 the gain value associated with the beam width given by Eq. (4.30). This simple model is not able to reproduce the transfer values predicted by HARMONY for $I_{FS}^{\Sigma}\lambda_L^2 > 10^{14}$ Wμm^2/cm^2.

4.3.2.2 Spatial characterization

As evoked earlier, two resonance lines are present in the interaction region, defined here by $\mathbf{V}_p.\mathbf{e}_y = \pm c_s$. The asymptotic value of energy transferred between beams depends on the balance between power transfer from the downward beam to the upward beam in the region where $\mathbf{V}_p.\mathbf{e}_y > 0$, and power transfer from the upward beam to the downward beam in the region where $\mathbf{V}_p.\mathbf{e}_y < 0$. Given the input velocity profiles, these lines are located at $\hat{y}_{c_s,+} = 860$ and

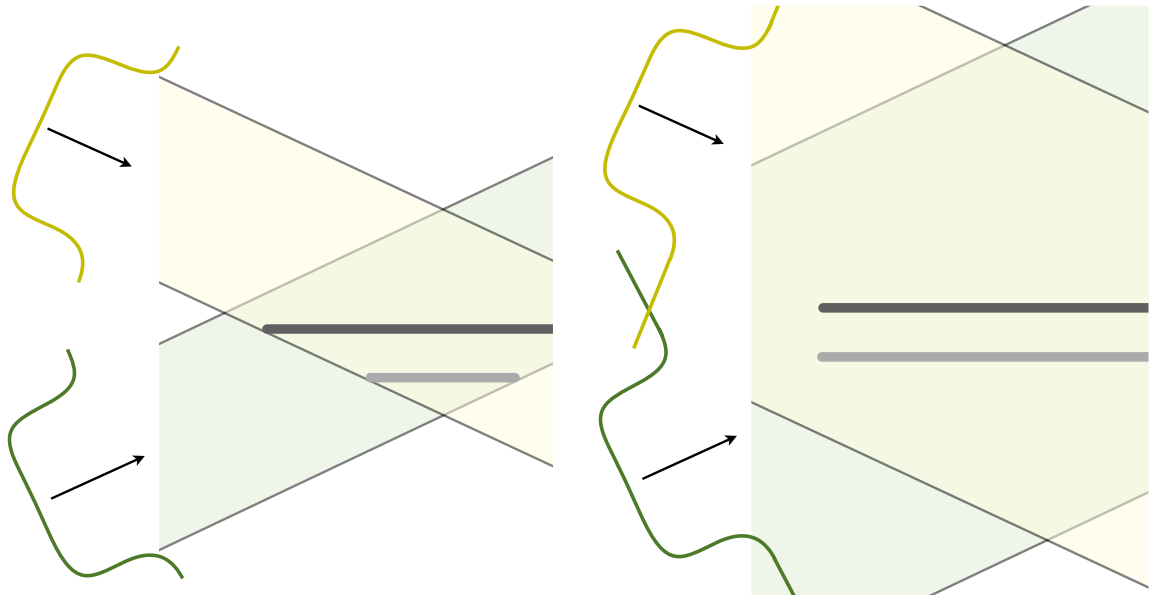

Figure 4-12 – *(color) Illustration of the position of the resonance zones and their coverage by the envelop of the beams. The direct resonance line that causes energy transfer from the downward beam to the upward beam is shown in black. The inverse resonance line that causes energy transfer from the upward beam to the downward beam is shown in light grey. Both these resonance lines are located at* $\mathbf{V}_p.\mathbf{e}_y = \pm c_s$*, as shown in Fig. 4-8. The [left] panel illustrates the beam envelop covered in the PCGO approach. Taking the beam 1 as an example, the upstream envelop intensity profile* $\langle \mathcal{J}_1(\eta) \rangle$ *given in Eq. (4.46) is described in PCGO with* $\eta \in [-\mathcal{D}, \mathcal{D}]$*. On the contrary, in the* HARMONY *code, the wings of the beam are modeled on the whole domain, as illustrated on the [right] panel. Consequently, the inverse transfer resonance zone, shown in light gray, is more amply covered by the beams in* HARMONY *than in the PCGO approach.*

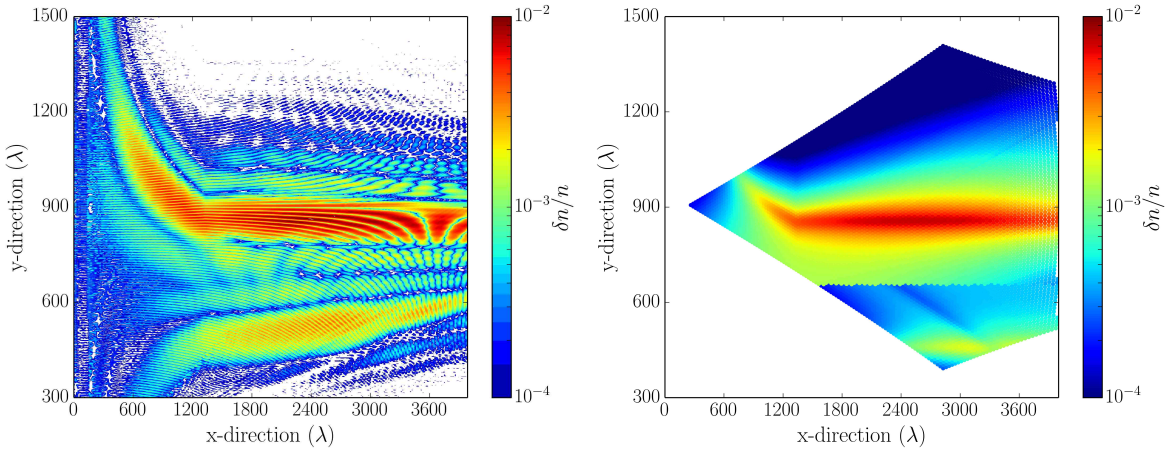

Figure 4-13 – *(color) Amplitude of the density perturbations* $\delta n/n$ *in* HARMONY *[left] and PCGO [right]. Each dot in the [bottom] figure represents the intersection between two PCGO beamlets. Simulation results are obtained for* $\mathcal{R}_\mathrm{I} = 1/1$ *and* $I^{\Sigma}_{\mathrm{FS}}\lambda_L^2 = 0.45 \times 10^{14}$ $W\mu m^2/cm^2$*.*

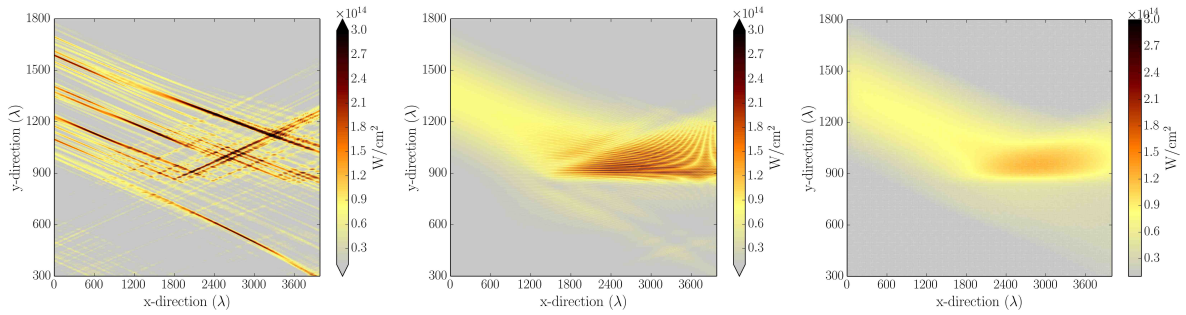

Figure 4-14 – *(color) Snapshots of the intensity pattern in the region where both beams overlap, for* $\mathcal{R}_{\rm I} = 1/8$ *and for* $I^{\Sigma}_{\rm FS}\lambda_{\rm L}^2 = 0.9\times10^{14}$ $W\mu m^2/cm^2$. *Input intensity profiles are PP-smoothed in the [left] panel, and flat-top (so-called 'regular' beams) in the [middle] and [right] panels. Results shown are from* HARMONY *[left,middle] and the* EYEBOLT *model [right].*

$\hat{y}_{c_s,-} = 460$. Those two locations are the expected regions of maximum IAW amplitude. The relative density perturbation $\delta n/n_{\rm eq}$ (with $n_{\rm eq}$ the unperturbed density) is obtained in HARMONY from the resolution of the nonlinear fluid equations (4.39). In the EYEBOLT model, this amplitude can be estimated in the framework presented in Sec. 4.2.2 writing the evolution equation for the ion density perturbation in steady-state. Before simplification, the latter reads:

$$[\partial_t^2 + 2(\nu_s - \imath\Omega)\partial_t - (\Omega^2 - \omega_s^2 + 2\imath\nu_s\Omega)]\frac{\delta n}{n_{\rm eq}} = -\omega_s^2 a_1 a_2^\star \ , \tag{4.47}$$

where it was assumed that $V_{g,s} \ll V_{g,1}, V_{g,2}$. The steady-state density perturbation predicted by EYEBOLT is then:

$$\frac{\delta n}{n_{\rm eq}} = \left|\frac{\omega_s^2 a_1 a_2^\star}{\Omega^2 - \omega_s^2 + 2\imath\nu_s\Omega}\right| \ . \tag{4.48}$$

This expression for the density perturbation is computed a-posteriori from the global intensity field, accounting for the contribution of all beamlets to the $a_1 a_2^\star$ term. The resulting density perturbation map is compared to results from HARMONY in Fig. 4-13. Both the average and maximum values of the perturbations in the main resonance region (where $V > 0$, $\hat{y} = 860$) are in good agreement between models, with $(\delta n/n_{\rm eq})_{\rm mean} \simeq 5\times10^{-3}$ and $(\delta n/n_{\rm eq})_{\rm max} \simeq 1\times10^{-2}$, respectively. It is not surprising to see that the IAWs amplitude in the downward velocity quadrant is slightly underestimated in PCGO, as the $V < 0$ resonance region covered by the PCGO beamlets is underestimated. Finally, we note that the spatial location of maximum IAW amplitudes for both models is in agreement with the theoretical values of $\hat{y}_{c_s,+}$ and $\hat{y}_{c_s,-}$.

The spatial pattern of the beams intensity inside the CBET region is now compared. Because PPs produce random speckle patterns, this comparison has been performed for the simulations with regular beams. The intensity field obtained inside the transfer region for RPP smoothed beams (Fig. 4-14 [left]) is of the same order of magnitude as for regular beams (Fig. 4-14 [middle]) but much finer structured. The regions where the pump beam is depleted are also rather similar between the smooth beam and the regular beam approaches. Figure 4-14 [right] illustrates the corresponding intensity field obtained with PCGO for regular beams. The regions where the pump beam has been depleted and where the probe beam has been preferentially amplified clearly cover

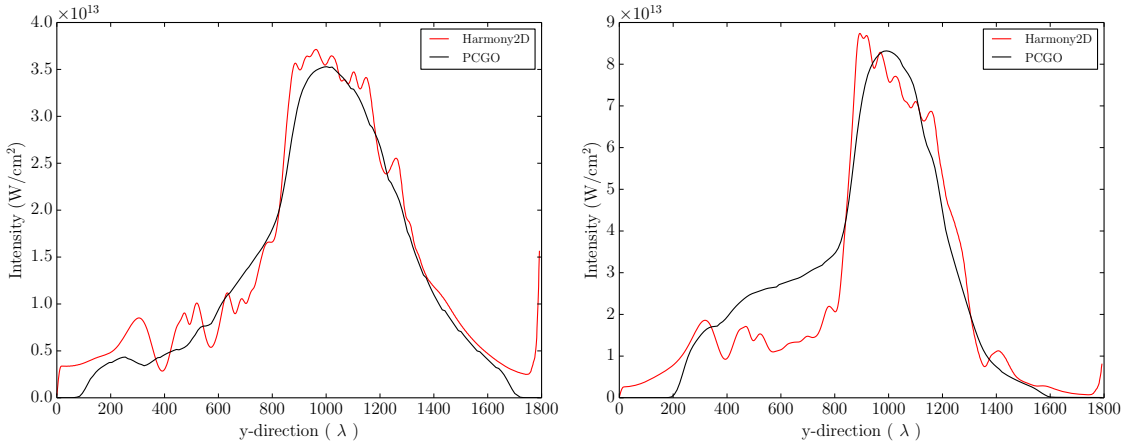

Figure 4-15 – *(color) Intensity profiles after the beam overlap region, taken at* $\hat{x} = 4000$*, for [left]* $\{\mathcal{R}_\mathrm{I} = 1,\ I^{\Sigma}_{\mathrm{FS}}\lambda_L^2 = 0.45\}$ *and [right]* $\{\mathcal{R}_\mathrm{I} = 1/8,\ I^{\Sigma}_{\mathrm{FS}}\lambda_L^2 = 0.9\times10^{14}\ W\mu m^2/cm^2\}$*. Results from* HARMONY *are shown in red (grey) and from the* EYEBOLT *model with regular beams in black.*

the same parts of the beams in both type of simulations. The small-scale structure seen inside the interaction region in Fig. 4-14 [middle] arises from the spatial and temporal interference of the beams and is not reproduced by PCGO, that can, by design, only model constructive spatial interference between beamlets. However, the average value of the intensity in that region is well reproduced by the PCGO model. The intensity profiles obtained after the CBET interaction, at $\hat{y} = 4000$, are illustrated in Fig. 4-15 for two particular cases and show good agreement between PCGO and HARMONY. Note that the downstream intensities from HARMONY shown in this figure have been smoothed using a finite impulse response filter in order to retrieve the envelope of the intensity field and remove the small-scale variations due to the beams interference.

It is interesting to extend this comparison of the global intensity field to that of the intensity per beam, so as to assess the deviation induced by CBET on each beam separately. The upward and downward EM waves modeled in HARMONY (a_1 and a_2 in a_+) are separated depending on the direction of their **k**-vectors. The resulting upward and downward transmission profiles after the intersection are compared between models in Fig. 4-16, showing good agreement for the steady-state transmissions per beam. Particularly, PCGO is able to capture the pump beam deviation caused by the interaction geometry, which causes a displacement of the barycenter of its energy density. It is also able to reproduce the narrowing of the transmitted beams, that is a consequence of the particular configuration of the beam with respect to the spatial profile of the resonance region.

4.4 Experimental validation of the CBET model

We now consider experimental measurements of CBET gains for crossed laser beams in weakly inhomogeneous plasmas, conducted on the NOVA laser facility [176]. A spherical polyamide shell of 1.3 mm radius containing 1 atmosphere of C_5H_{12} gas is heated by eight beams of wavelength $\lambda = 351$ nm with a 1 ns square pulse. Two additional beams intersect close to the plasma center, at an angle $\theta = 53°$ with each other. The frequency of the probe pulse is varied between shots, so

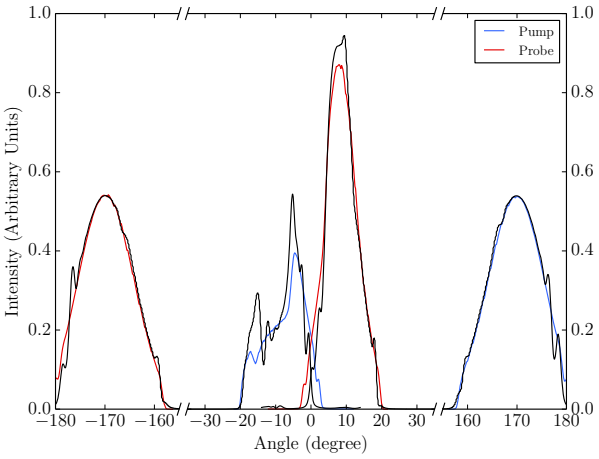

Figure 4-16 – *(color) Intensity profiles of the beams upstream and downstream of the transfer region, as a function of the angle with the $\hat{x}$ axis. The input beams are centered at $-170°$ and $+170°$ and the output beams are centered at $-10°$ and $+10°$. Results from* HARMONY *are shown as black lines and results from PCGO with colored lines. The blue (light grey) and red (dark grey) curves indicate the pump and the probe beams, respectively. The results from* HARMONY *are taken past the transient period.*

as to explore the resonant exchange of energy between the probe and pump beams. The probe pulse starts at the same time as the heater beams and lasts 2 ns, whereas the pump pulse starts 400 ps after the heater beams and lasts 1 ns. The pump beam average intensity is $\langle I_\mathrm{p} \rangle = 10^{15}$ W/cm^2 while the probe beam intensity is varied from $0.06\langle I_\mathrm{p} \rangle$ to $0.32\langle I_\mathrm{p} \rangle$, with a wavelength shift $\Delta\lambda$ of up to 7.3 Å. The probe beam amplification $\mathcal{A}$ is defined as the probe beam transmitted energy divided by the same quantity in shots without the pump beam. Simulations of this experiment are conducted using the CHIC hydrocode [115], modeling the laser-plasma interaction with the PCGO laser propagation and absorption model presented in previous chapters and using the EYEBOLT model.

During the 1 ns when the interacting beams are on, the hydrodynamic simulation predicts a relatively constant plasma density in the interaction region ($\sim n_e/n_c = 0.1$), with an electron temperature T_e varying between 1 and 2.5 keV. The mean ionization state $\langle Z \rangle$ of the plasma, computed using a Thomas-Fermi model [183, 184], varies between 0 and 2.5. The plasma expansion is rather symmetric and plasma flows in the interaction region are of the order of $0.01c_s$. Such low values are explained by the symmetry of the irradiation geometry, the close proximity (400 μm) of the interaction region to the center of the target and the early timing of the pump beam compared to the plasma expansion. The probe-beam transmission without pump beams is of $\sim 50\%$, similar to results presented in [176].

The only free parameter in the EYEBOLT model is the damping coefficient ν_s/ω_s. According to Ref. [185], the damping rate in CH plasmas depends on the parameters $\mu = k_s\lambda_D$ and $\tau = T_i/T_e$. The hydrodynamic simulations show these parameters in the interaction region vary from 0.13 to 0.235 and 0.145 to 0.58, respectively. We resolve numerically the kinetic dispersion relation given in [185] for a C_5H_{12} plasma in this range of parameters. An additional margin of 30% is added to this range, in order to account for an eventual spatial dispersion of $[\mu, \tau]$ in the vicinity of the interaction region. There are two ion modes corresponding to two ion species. We

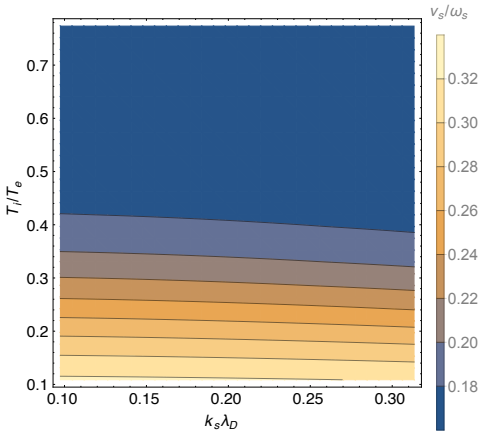

Figure 4-17 – *Slow mode IAW damping rate for C_5H_{12} as a function of $k_s\lambda_D$ and T_i/T_e for a range of parameters relevant to the experiment, computed from the kinetic dispersion relation.*

consider here only the slow mode, which has a smaller damping. Figure 4-17 shows the resulting slow mode damping rate as a function of $[\mu, \tau]$. This surface is fit to a 6th order polynomial for $\mu \in [0.10; 0.31]$ and $\tau \in [0.1, 0.8]$:

$$\frac{\nu_s}{\omega_s} = 0.31 + 0.038\mu + 0.85\tau - 0.23\mu\tau - 0.16\mu^2 - 9.69\tau^2 + 0.25\mu\tau^2 + 0.26\tau\mu^2 + 30.12\tau^3 - 44.26\tau^4 + 31.98\tau^5 - 9.17\tau^6 \ . \quad (4.49)$$

This approximation is accurate to within 0.2% in average, with a maximum error of 0.9%. Subsequent simulations using the EYEBOLT model are conducted using the polynomial fit for ν_s/ω_s.

Simulation results are compared to experimental data in Fig. 4-18. Far from resonance, the probe beam amplification is rather well reproduced by the model. Energy transfer at $\Delta\lambda = 0$ is low in the simulation, in agreement with the weak plasma flows in the interaction region. Experimental probe amplification for $\Delta\lambda = 0$ is slightly higher and may indicate that those plasma flows are underestimated, although the extent of the error bar does not allow to affirm it from this measurement only. Energy transfer for $\Delta\lambda > 0.55$ are also well reproduced within error bars. Simulation results in the $\Delta\lambda \in [0.3; 0.52]$ range yield a larger probe amplifications than in the experimental data. The EYEBOLT model predicts CBET linear gains[2] of the order of 1-1.3, while the maximum experimental gain is of the order of 1. Although the gains are overestimated, the order of magnitude is correct. These results consist a significant improvement over other prediction of linear gains for this experiment, of ~ 20 in Ref. [176], of ~ 7 in Ref. [48] and of $\sim$3-4 (in unpublished Ref. [17] of [176]). Our results are consistent with results from the Paraxial solver KOLIBRI of $\sim$1-1.3, presented in Ref. [186]. The overestimate of the energy transfer gains may be indicative of some form of backscattering in the experiment, that could have reduced the local intensity in the interaction region.

The most important discrepancy is found in the position of the resonance peak, located around

[2]We recall that here the linear gain is defined from the ratio of the probe beam transmitted power without and with the pump beam turned on, i.e. $\ln \mathcal{A}$

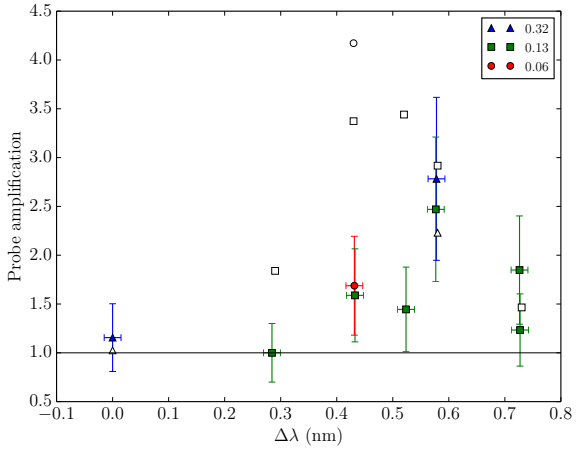

Figure 4-18 – *(color) Probe amplifications as a function of frequency detuning, for various probe to pump intensity ratios of 0.32 (triangles), 0.13 (squares) and 0.06 (circles). The probe beam transmission being reproducible to ±15% [176], the error in the energy ratio between experiments is estimated at ±30%. Simulation results are superimposed as empty symbols.*

$\Delta\lambda_{\text{sim}}^{\text{peak}} \sim 0.48$ nm (for $\mathcal{R}_{\text{I}} = 0.13$) in the simulations and $\Delta\lambda_{\text{exp}}^{\text{peak}} \sim 0.6$ nm (for $\mathcal{R}_{\text{I}} = 0.13$) in the experiment. This discrepancy is discussed further in what follows, alongside with the width of the resonance.

The experimental results are now analyzed in the theoretical framework derived in Sec. 4.2.2. In order to analyze the dependence with $\Delta\lambda$ of the results shown in Fig. 4-18, the following assumptions are made; the plasma parameters are (i) constant across the interaction region, (ii) constant during the beams interaction, (iii) constant for shots with different values of $\Delta\lambda$, (iv) constant for shots without the pump beam and (v) that the lasers upstream intensity is stable from shot to shot. Then the probe beam amplification $\mathcal{A}$ can be assimilated to the linear gain $\exp(G)$ and its dependence with the frequency detuning between the beams can be estimated from Eq. (4.24):

$$G(\Delta\lambda) \propto G_0 \left(1 + \left[\frac{\omega_p}{(\nu_s(1 + \lambda_p/(\Delta\lambda - \Delta\lambda^{\text{peak}}))}\right]^2\right)^{-1}, \tag{4.50}$$

where G_0 is the maximum gain obtained at resonance for $\Delta\lambda = \Delta\lambda^{\text{peak}}$. The experimental data and simulation results (for $\mathcal{R}_{\text{I}} = 0.13$) are fit to the gain function defined above using nonlinear least squares. Although this approach is qualitative, it allows to compare estimates for the width of the resonance, function of the temporally- and spatially-averaged damping rate $\bar{\nu_s}$, and to discuss the position of the resonance. As illustrated in Fig. 4-19, the averaged damping rates are similar in the simulation and in the experiment, with $\bar{\nu_s}^{\text{exp}} = 1.93 \times 10^{12}$ s^{-1} and $\bar{\nu_s}^{\text{sim}} = 2.67 \times 10^{12}$ s^{-1}. Accounting for temporal and spatial variations of the sound speed and of ν_s/ω_s, the damping rate in the simulations $\nu_s \in [9.7 \times 10^{11}; 5.3 \times 10^{12}]$ s^{-1}, which brackets the value estimated from the gain curves.

The difference between the positions of resonance peaks observed in experiments and in

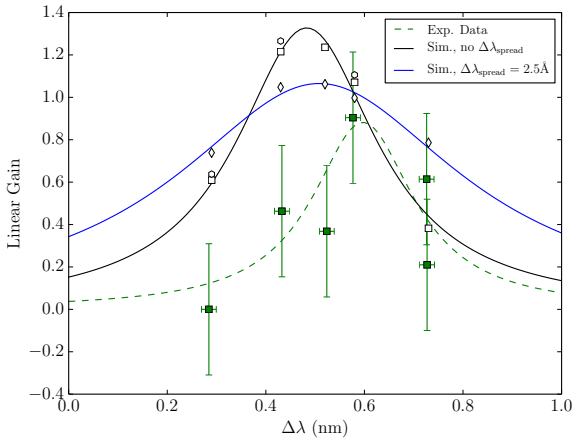

Figure 4-19 – *(color) Linear gain curves as a function of the frequency detuning between the beams. Simulation results are presented as black open symbols and experimental data points as green squares. For simulation results, squares indicate* SESAME *EOS and hexagons Ideal Gas law. Diamonds correspond to simulation results where a broad frequency spectrum of* $\Delta\lambda_{\text{spread}} = 2.5$Å *was assumed for the laser beams. The corresponding fits to a Lorentzian gain function are presented as solid lines.*

simulations is of 1.2 Å. The resonance peak position uniquely depend on the Doppler shift, which in turn is a function of the local sound speed velocity and of the irradiation symmetry. We assess the various contributions that may explain the observed difference in resonance position. In order to estimate the uncertainty on the sound velocity, several simulations were conducted using Ideal Gas law instead of SESAME Equation of States (see Fig. 4-19), without significant difference on the result. Assuming that the plasma flow is aligned with k_s, the plasma velocity required to shift the resonance by 1.2 Å is of $\sim 0.25c_s$. The simulations predict that the velocity vector is directed outward from the center of target, so that $\phi \sim 98°$. Considering that angle, the plasma flow velocity needed to Doppler shift the resonance is $\sim 1.2c_s$, a significant and unlikely value for the central region of a gas bag target. This indicates that if velocity fluctuations shifted the resonance, those probably did not arise purely from the plasma expansion but from hydrodynamic asymmetries that shifted the velocity vector in the k_s direction. Considering the angle and the intensity of the probe beam, a sufficiently strong ponderomotive force could shift the velocity vector in the right direction. However, simulations using the ponderomotive force module based on PCGO (see Sec. 2.4.1) suggest that this effect is not significant here. Another possibility that is investigated is the effect of the laser spectral spread on the energy transfer. Assuming a wavelength spread $\Delta\lambda_{\text{spread}}$ of the laser around its central wavelength λ (and around the central wavelength of the probe beam $\lambda + \Delta\lambda$), the width of the resonance region is expected to increase. It is assumed that the plasma parameters are characterized by a constant gradient in the interaction region. In that case, the plasma parameters are non symmetric with respect to the center of the interaction region and a uniform spectral broadening may shift the optimum resonance position. This is illustrated in Fig. 4-19. Assuming $\Delta\lambda_{\text{spread}} = 2.5$Å, the spectral broadening displaces the resonance peak by +0.25Å. Although the resonance width with spectral broadening appears wider than in the experiment, a lower value of the gain G_0 obtained in the simulation agrees with all experimental points and error bars.

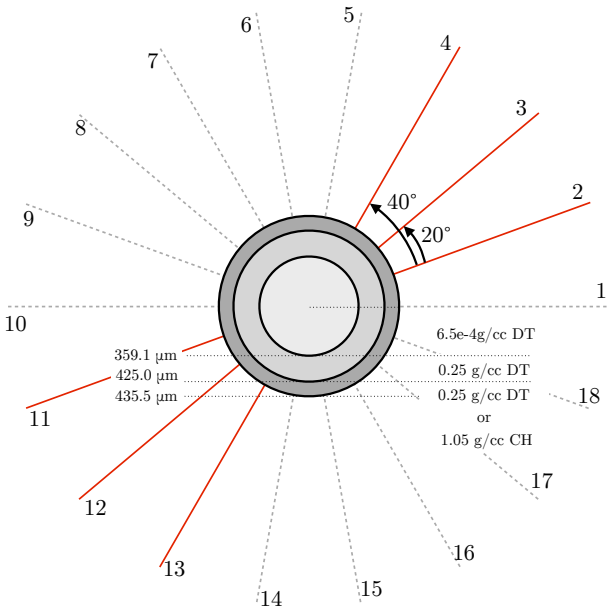

Figure 4-20 – *(color) Diagram of the capsule and beam configuration: 18 beams separated by intervals of 20°, focused on the exterior surface of the ablator and following the SG4 phase plate configuration of* $n^{\mathrm{SG4}} = 4.1$, $r_0^{\mathrm{SG4}} = 352\ \mu m$, $\lambda_L = 0.354\ \mu m$, $\phi^{\mathrm{SG4}} = 0.27\ m$ *and* $F^{\mathrm{SG4}} = 1.80\ m$. *Beam centroids are represented as numbered lines (beamlets are not shown). Dashed grey lines represent beams that do not interact through CBET. Red (dark grey) plain lines represent beams that can interact with each other by groups of 4, as detailed in Tab. 4.1*

4.5 Study of CBET in direct-drive implosions with various ablator materials

The CBET is of particular importance for the implosion symmetry of ICF targets. In both direct-drive and indirect-drive configurations, this nonlinear LPI effect causes dynamic modifications of the irradiation field that may lead to drive asymmetries and capsule deformations. We assess in this section the influence of CBET in a simplified direct-drive configuration that is relevant to the beam configuration of the OMEGA laser facility.

4.5.1 Numerical setup

4.5.1.1 The OMEGA chamber geometry and its transcription to a 2D CBET configuration

The OMEGA laser facility at the Laboratory for Laser Energetics, Rochester University, can use up to 8 rings of beams arranged at constant latitudes, for a total of 60 beams. The EYEBOLT model being 2D, we look for configurations where beams are co-planar in a plane passing by the capsule center. The latter planes can be visualized in an azimuth/elevation diagram, where these angles are defined in Fig. 4-21 [left]. Figure 4-21 [right] illustrates the beam positions with respect to their azimuthal angle and elevation angle. At a given azimuthal angle, beams are co-planar and the corresponding plane passes through the capsule center. These planes can be used as 2D simulation configuration for the PCGO model. At a given longitude (or azimuth),

Case	Interacting Beams	CBET main angles
Ref. Case	None	None
A	2 ; 3 ; 11 ; 12	20° ; 160° ; 180°
B	2 ; 4 ; 11 ; 13	40° ; 140° ; 180°

Table 4.1 – *Three simulated cases, summarizing the interacting beam numbers and CBET angles of the beams centroids. Each case is conducted twice, with a DT and a CH ablator.*

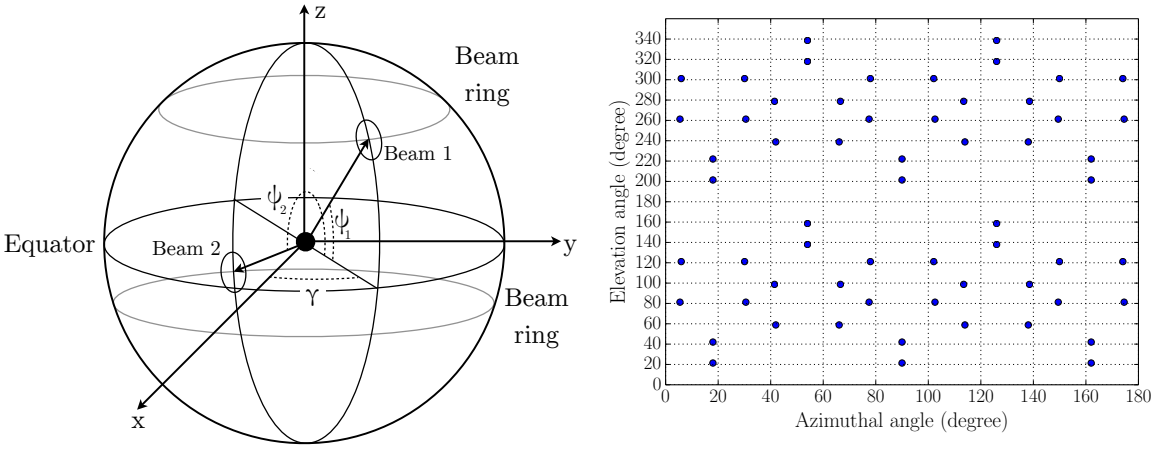

Figure 4-21 – *[left] Definition of the azimuthal angle γ and elevation angle ψ. The entire sphere can be characterized with $\gamma \in [0;180]°$ and $\psi \in [0;360]°$. In this example, beams 1 and 2 are on the same azimuthal plane and at different elevation angles ψ_1 and ψ_2. [right] Configuration of the 60 OMEGA beam ports in azimuthal/elevation angular coordinates. At a fixed γ, adjacent beams are separated by 20° or 40°. By considering adjacent γ planes, we could consider 2D interactions between beams with higher angular separations.*

beams are co-planar by bundles of 4, with two beams separated by angles of at least 20° or 40° and the other two beams in symmetric positions with respect to the capsule.

We consider a direct-drive capsule implosion in a 2D planar geometry. In order to reflect the 20° angular separation of the OMEGA beams in a given constant azimuth plane, the capsule is irradiated using equally spaced beams separated by 20°, i.e. 18 beams (see Fig. 4-20). Each beam is split in beamlets with $\mathcal{R} = 10$ and N_B=60, focused randomly so as to reproduce a pseudo-speckle pattern consistent with the intensity statistics of the KPP SG4 phase plate near the focal plane, smoothed with the hydrodynamic mesh resolution. Each beam has a different set of random generator seeds, so each of them produces a different pseudo-speckle pattern with a similar statistics, leading to a non-symmetric laser irradiation. Consequently, the simulation domain englobes the 360° of the cylinder, without assuming any hydrodynamic symmetries. Although it is numerically costly, this approach of a full cylinder modeling possesses the advantage of not cutting out any modes in the irradiation profile. An additional simulation without CBET is conducted, hereafter referred to as reference case, in order to provide a baseline for the capsule compression. Note that these simulations were not conducted with the SSD model presented in Sec. 3.4.2 (it was not implemented at the time), so that the global irradiation symmetry is not entirely uniform and some deformations are expected in the reference simulation. The interaction conditions are shown in Tab. 4.1.

We consider two CBET cases where the energy transfer is allowed only between 4 sets of beams, in order to model co-planar intersections of the real 3D OMEGA configuration (See Tab. 4.1). The remaining beams that do not interact via CBET provide the global irradiation symmetry needed to implode the target. For simplicity, beamlets from the same beams are not allowed to interact with each other: their intersection angle being small enough implies small gains. CBET computations are enabled after 100 ps of simulation so that a coronal plasma in which the beams interact is properly formed. All cases are conducted with the same random seeds so that the set of 18 random pseudo-speckle pattern is the same from one simulation to the other. The damping rate of the IAWs ν_s/ω_s is computed using empirical formulas based on Ref. [178], that account for Landau and collisional damping.

4.5.1.2 Cryogenic target and laser pulse profile definition

The beam splitting parameters $N_B = 60$ and $\mathcal{R} = 10$ are set by comparing the near-field intensity constructed by PCGO to Miró outputs using the OMEGA SG4 KPP phase plate data. We use a typical OMEGA 1 ns square pulse profile with 200 ps of rise time and a peak power around 25 TW, comprising a total energy of $E_{\text{tot}}^{\text{SG4}} = 25.7$ kJ. The total energy used in our 2D planar cases is scaled by κ in order to match the drive intensity of the 3D spherical case. The ratio κ of the average on-target intensity on the 2D cylinder $\langle I^{2D} \rangle$ to that of the average intensity on the 3D spherical capsule $\langle I^{3D} \rangle$ is:

$$\kappa = \frac{\langle I^{2D} \rangle}{\langle I^{3D} \rangle} = h/(2r_a) \ , \tag{4.51}$$

where $h = 1$ cm and r_a is the capsule outer radius. For the capsule configuration presented in Fig. 4-20, $\kappa = 11.481$. The target is composed of a 66 μm-thick cryogenic DT shell and is filled with a gaseous DT at 6.5×10^{-4}g/cm^3. Two sets of simulations are conducted with different ablators, using a 10 μm-thick plastic (CH) ablator or a 10 μm-thick cryogenic DT ablator. The Lagrangian mesh is initially cylindrical, organized with 140 cells in the radial direction and 200 in the angular direction, with a radial refinement in the ablator and shell regions. The intensity gradients imposed by the pseudo-speckle patterns require the use of ALE rezoning and remapping at each hydrodynamic timestep.

4.5.2 Results and analysis

4.5.2.1 Modification of collisional absorption by the CBET instability

Figure 4-22 illustrates the volumic power absorbed in plasma by the inverse Bremsstrahlung for cases A and B and different ablators. The absorption is naturally higher in targets with a CH ablator, owing to a higher ionization Z of the species.

We distinguish two main regions of beamlet overlap in the configurations A and B (see Tab. 4.1 and Fig. 4-22). The first region covers adjacent interacting beams (for example beams 11 and 12) and can extend from the median angle between them up to slightly beyond the edge of each beam. The second region is constituted by the overlap of nearly opposed beams (for example 2 and 11). The latter interaction regions are not visible in Fig. 4-22 and only occur late

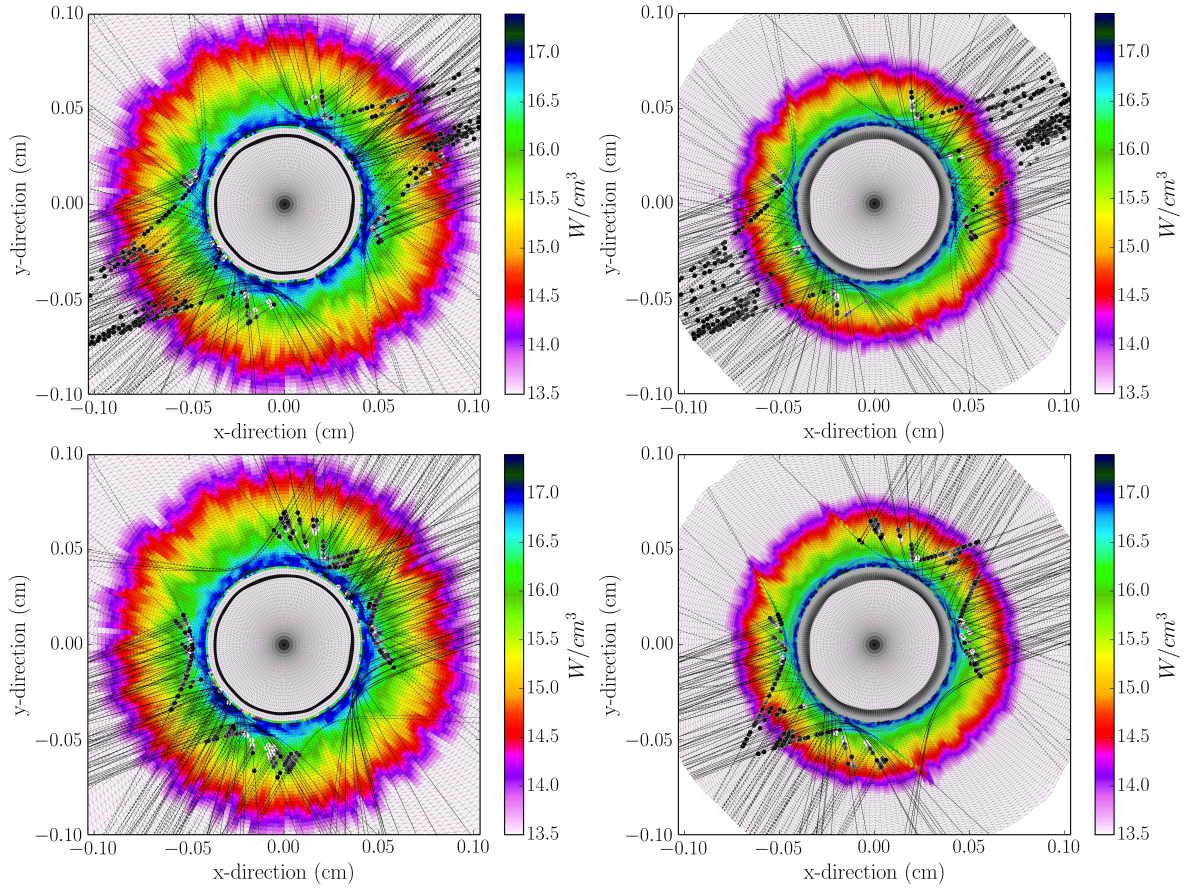

Figure 4-22 – *(color) Volumic power absorbed in plasma by the inverse Bremsstrahlung at about half of the laser pulse duration, i.e. after* 600 *ps of simulation, on a logarithmic scale. Volumic values are computed assuming a unit height of 1cm. Figures on the [top] lines are from cases A and on the [bottom] line from cases B. Figures on the [left] column present results using a CH ablator and on the [right] column with a DT ablator. Beamlet centroids for beams 2 and 11 are shown in solid black lines for all cases. Beamlets centroids for beams 3 and 12 for [top] figures and 4 and 13 for [bottom] figures are shown in dashed black lines (see Fig. 4-20 for beam numbering). Valid ray intersections for which CBET has been computed are indicated with grey-shaded dots, ranging from a probe gain of 1.5 in white to a probe gain of 1.01 in black.*

in the capsule implosion, when the plasma is sufficiently expanded to facilitate the intersection of beamlets from opposed beams. These regions are far from the critical density and between beamlets leaving the plasma, at similar angles with respect to the plasma flow so that there is little difference in the beams' Doppler shifts. In the geometry considered here, these intersections have negligible coupling efficiency β and have little or no influence on the laser irradiation symmetry.

In the setup presented in Fig. 4-22, beamlets intersections occur up to the critical density in extended regions where the plasma velocity extends from Mach 4.5 down to Mach 1 in the DT ablator case and Mach 0.5 in the CH ablator case. For a plasma flow at a velocity $\mathbf{V}_p$, the CBET phase matching condition for beams of the same frequency reads:

$$|\mathbf{k_2} - \mathbf{k_1}|c_s + (\mathbf{k_2} - \mathbf{k_1}).\mathbf{V}_p = 0 \ . \tag{4.52}$$

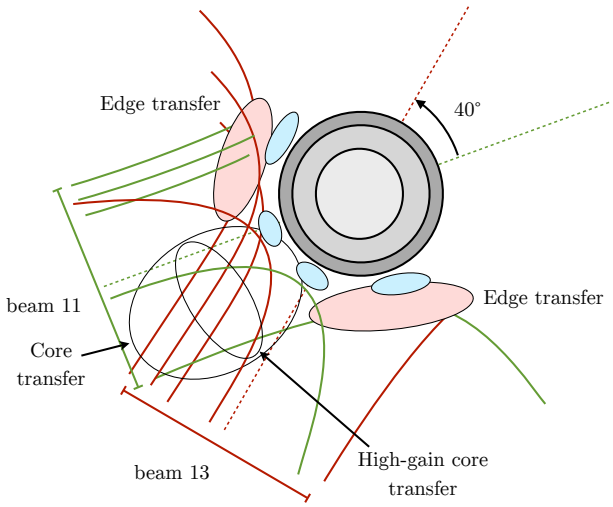

Figure 4-23 – *(color) Schematic illustration of the core and edge transfers for the case B. Beams 11 and 13 are shown as green (grey) and red (dark grey) lines, respectively. Increased absorption regions are shown in light red (large light grey zones) and decreased absorption regions in light blue (small light grey zones).*

Depending on the spatial configuration and propagation of the rays in plasma, there are many possible couples of Doppler-shifted **k**-vectors and plasma velocities that yield non-negligible CBET gains. In general, the larger the angle between the plasma flow and the vector $\mathbf{k_2} - \mathbf{k_1}$ is, the higher the plasma flow velocity must be in order to satisfy the phase-matching. This condition on the Mach number is relaxed since energy transfers between non-zero values of the frequency *detuning parameter* $\delta = \Omega - \omega_s$ are taken into account (see Eq. (4.5)). The spread in plasma flow velocities that can yield significant energy exchanges is only limited by the spatial configurations of the beamlet **k**-vectors. We identify several patterns to the energy exchanges that we refer to as the edge transfer and the core transfer (see Fig. 4-23). In both cases, we consider a given couple of adjacent interacting beams, i.e. separated by 20° for case A or 40° for case B.

The core transfer refers to the CBETs taking place near and in-between the beams' centroids, as illustrated in Fig. 4-23. These exchanges occur between beamlets that are incoming on the capsule at angles with the plasma flow that are slightly different. In that region, $(\mathbf{k_2} - \mathbf{k_1}).\mathbf{V}_p$ is small so that small frequency detuning can only occur for large values of the Mach number, i.e. away from the critical density. However, the CBET gain decreases for lower values of the plasma density and electron temperature. Consequently, there is an optimum spatial location, so-called high-gain core region, in which the density, temperature and Mach number are not too low for higher CBET energy exchanges to occur. This region is identified by larger probe gains in Fig. 4-22 at about 500 μm and 300 μm from the critical density for cases A and B respectively. CBET in this region is numerous and peaks at probe gains of 1.2, without privileged direction, thus creating a noisy absorption pattern of one to two shadow regions organized around the median angle between the adjacent beams.

In the edge transfer, the left edge of the leftmost beam is intercepted by the left edge of the rightmost beam. Conversely, the right edge of the rightmost beam is intercepted by the right edge of the leftmost beam. We distinguish two types of energy exchanges: intersections between ingoing beamlets and intersections between outgoing and ingoing beamlets. The Doppler-shift dictates

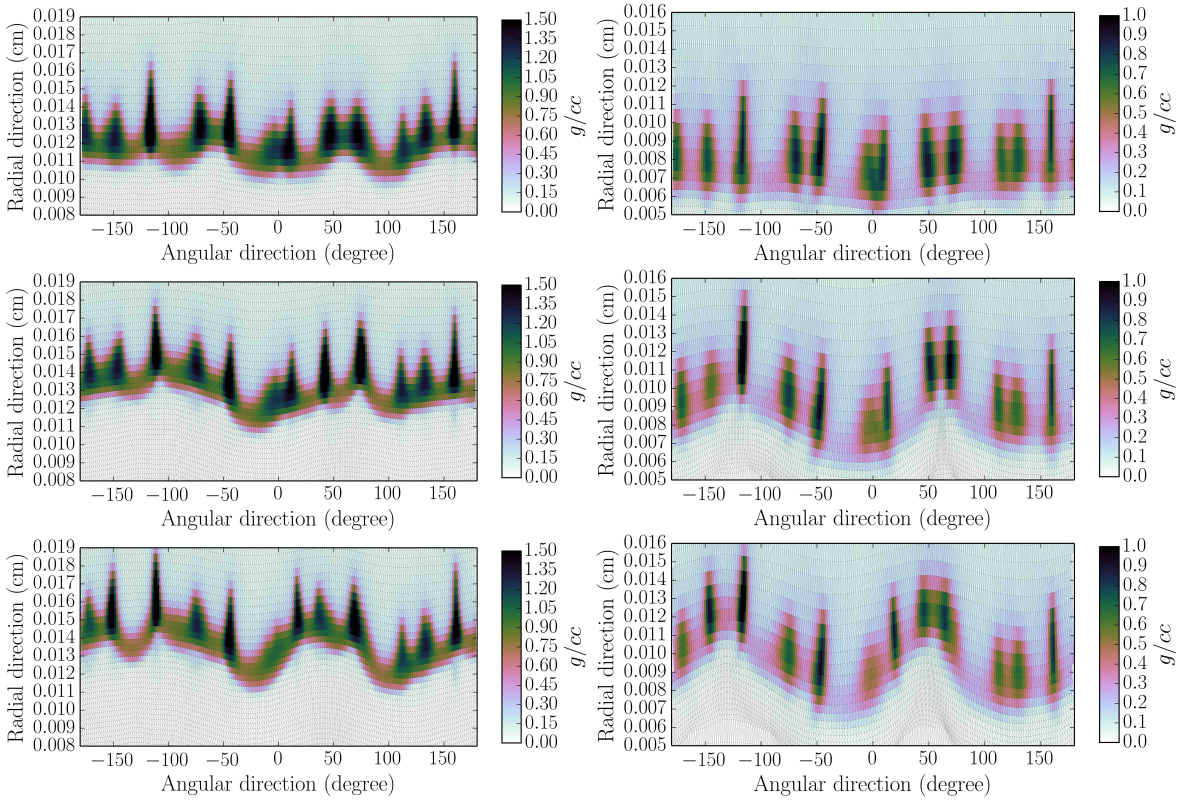

Figure 4-24 – *(color) Close-up of the density field near stagnation, represented in the r-θ plane, with θ = 0 for beam 1 (see Fig. 4-20). [Top] figures are from the reference case and correspond to deformations purely arising from the pseudo-speckle pattern of the lasers. [Middle] figures are from case A and [bottom] are from case B. Figures on the [left] column are obtained using a CH ablator and on the [right] column using a DT ablator. The internal shell interface, reported in Fig. 4-27, is the transition between the target interior (white field, below the mean shell position) and the imploding shell. Note that for a given ablator, the y-axis and color scales are the same.*

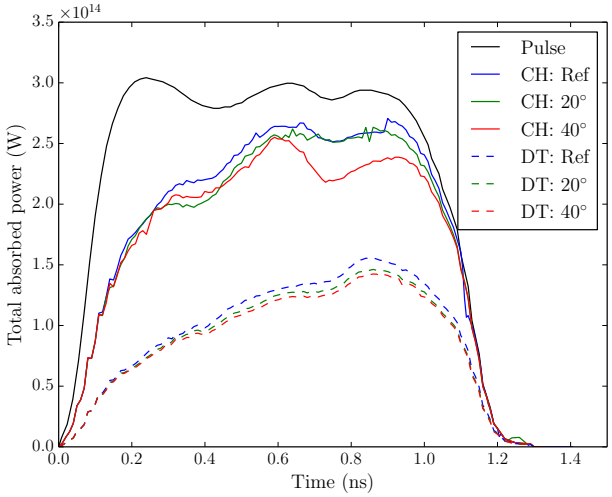

Figure 4-25 – *(color) Power absorbed by the plasma by inverse Bremsstrahlung as a function of time as blue (grey) lines for the reference case, as green (light grey) lines for case A and as red (lighter grey) lines for case B. Results are shown as plain lines for CH ablator simulations and as dashed lines for DT ablator simulations. The drive pulse is shown as a black plain line. 2D power is scaled by κ (see Sec. 4.5.1.2).*

Compression ratios	CH ablator	DT ablator
Ref. Case	3.54	5.57
A	3.17	4.55
B	3.04	4.2

Table 4.2 – *Convergence ratios at stagnation for all cases simulated, taking the initial outer shell radius as a reference.*

the energy exchange configuration. In the first case, the energy transfer occurs from the beamlet with a narrower angle to the beamlet with a broader angle (with respect to the plasma flow). In the second case, the outgoing beamlet is always amplified by the ingoing beamlet. Most power transfers observed in cases A and B completely deplete the pump beamlets. This is a consequence of the probe beamlets being amplified along their path prior to these CBETs. Most probe gain values in the edge transfer are less than 1.5 (see Fig. 4-22). Amplified probe beamlets create large scale modulations in the absorption field, thus decreasing the irradiation symmetry. Moreover, interactions between outgoing and ingoing beamlets lead to a direct decrease of the coupling between the laser beam and the capsule. Laser-plasma coupling losses are a geometrical feature that are more prominent for higher convergence ratios and in the 40 ° cases, as is illustrated in Fig. 4-25. Although the net loss in total absorption induced by CBET appears moderate, edge transfer also displaces absorbed power away from the critical density, thus reducing the laser-capsule coupling further. The coupling loss is in agreement with the decreased capsule convergence in the cases with CBET enabled, as can be observed by the mean position of the shell in Fig. 4-24.

4.5.2.2 Degradation of the shell profile at stagnation

The laser pulse driving the cylindrical capsule ends at $t = 1.28$ ns. Stagnation of the capsule occurs around $t = 1.31$ ns for the CH ablator case and around $t = 1.33$ ns for the DT ablator. At that point, modulations in the capsule density profile constitute a time and space-integrated proxy of the laser illumination modulations arising from the pseudo-speckle pattern and CBET. Simulations are analyzed at stagnation, i.e. around $t = 1.31$ ns.

Figure 4-24 shows the shell density profile in the r-θ plane for the reference case [top], case A [middle] and case B [bottom]. Because these simulations were not conducted with the SSD model presented in Sec. 3.4.2, the contrast of the individual beams is rather high, of the order of 10 %. More importantly, the overlap of the 18 beams does not produce a symmetrical irradiation pattern, which is the reason for the hydrodynamic instabilities that can be observed in the density profiles without CBET enabled [top]. Each simulation is conducted with the same irradiation profile, so that this bias is effectively removed when comparing the relative difference between results with and without CBET. The DT ablator targets [right] achieve higher convergence ratios than the CH ablator ones [left], straight consequence of them being lighter and subject to the same laser intensity. 2D convergence ratios computed from the target's initial radius of the outer shell, i.e. $r_s = 425$ μm, are shown in Table 4.2. CBET decreases the convergence ratio with respect to the reference case, by up to 14% for the CH ablator target and 25% for the DT ablator target. As evoked above, the edge transfers between outgoing and ingoing portions of the beams

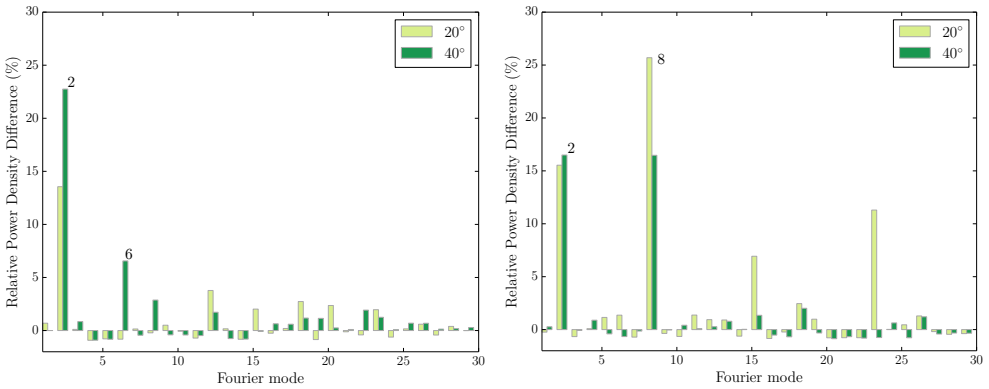

Figure 4-26 – *(color) Relative power density histograms of the inner shell interface Fourier modes, for the CH ablator case [left] and the DT ablator case [right], near stagnation. Relative power densities $\hat{p}$ are computed as $\hat{p} = (p_{\text{ref}} - p)/p_{\text{ref}}$ where p_{ref} and p are modes power densities of the reference case and corresponding case, respectively. Case A is shown in light green (light grey) and case B in dark green (dark grey). The mode 0 is not shown.*

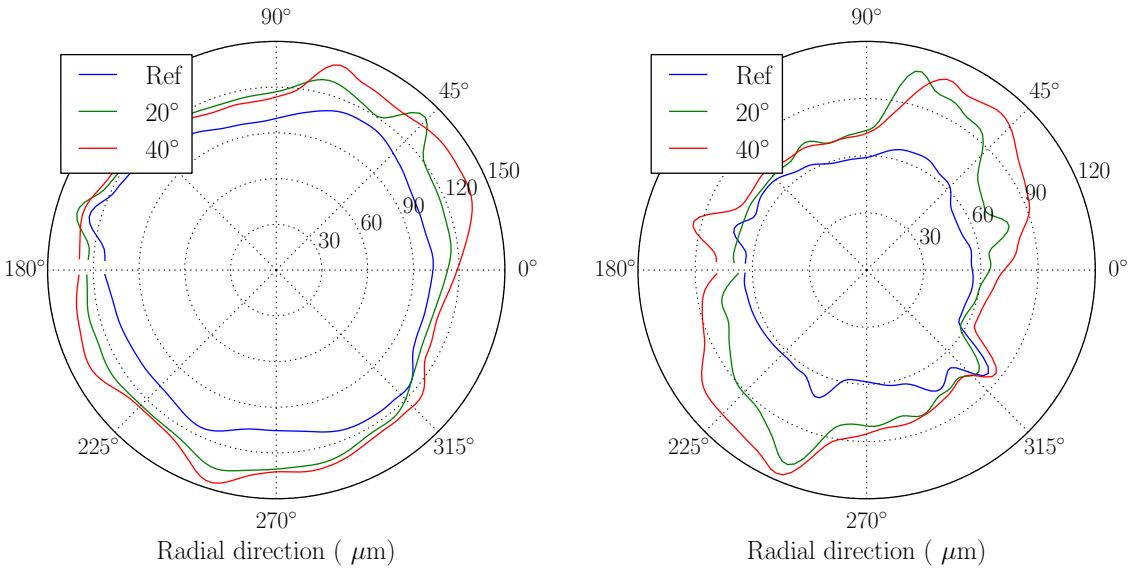

Figure 4-27 – *(color) Internal interface of the capsule near stagnation for the CH ablator case [left] and the DT ablator case [right]. Reference simulations are shown as blue lines (grey), case A simulations as green lines (light grey) and case B simulations as red lines (lighter grey).*

take energy away from the capsule, thus decreasing the laser-capsule coupling efficiency and consequently, the convergence ratio. This is consistent with the decrease in integrated absorption noted in Fig. 4-25. The convergence of the DT ablator target is more severely reduced as a result of the highly deformed shell that implodes with a lesser hydrodynamic efficiency, in addition to the decrease in laser-target energy transfer.

In order to conduct a Fourier decomposition of the shell modes, we identify the internal (resp. external) interfaces at a given angular coordinate θ as the positive (resp. negative) maximum of the derivative of the density in the r direction. Assuming that at least 6 points in θ are needed

in order to correctly describe a Fourier mode, the higher mode that can be characterized in our simulations with 200 angular points is mode 33. Internal and external interface profiles are smoothed using a finite impulse response filter of 6 points in length and fit using least squares to Fourier modes up to order 33. The resulting internal interface modes amplitudes with respect to the reference are shown in Fig. 4-26 (mode 0 is not shown).

The CH ablator target in the reference case (Fig. 4-24 [top-left]) presents small scale modulations on the external interface, corresponding to lumps of high density regions resembling fingers. Because the simulations are 2D planar and the convergence ratios rather low, the high amplitude of the deformations and the lumps of matter do not lead to the shell breakdown. High frequency modulations are smoothed out when reaching the internal interface, greatly reducing the power density of Fourier modes higher than 5. Significant long wavelength deformations are present at the internal interface, corresponding to modes 1, 3 and 4. The highest deformation present in the internal interface is of about 10% relative amplitude, measured as a half peak-to-peak amplitude (see Fig. 4-27). These modulations can be seen as the imprint of the beam configuration, including the effect of the pseudo-speckle pattern. In order to dissociate the effects of CBET to that of the pseudo-speckle pattern, the Fourier modes are compared to the reference case.

The Fourier analysis of the internal interface shows that CBET amplifies low modes 2 and 8 (CH ablator case). This can be seen in Fig. 4-27 as an oblate deformation of the inner interface of the shell, reaching a relative amplitude of about 13.5% for case A and 15% for case B. The dominant presence of mode 2 is a consequence of the higher absorption regions from the amplified edges of the beams, regions which are nearly symmetric with respect to those of the opposed beams. Although these could also lead to mode 4 deformations, the use of non-interacting beams to provide the cylindrical ablation pressure effectively smoothes those modes (e.g. beams 6, 7, 16, 17), which would not be the case in a 3D configuration.

The DT ablator targets (Fig. 4-24 [right]) also feature patterns of lumps of density arranged in fingers, but to a point where there is almost no more shell mass between those, and the capsule can be considered as punctured or broken. Cases A and B show a significant shell deformation of low modes 2 and 8. This case being more sensitive to energy exchanges due to a lower Z of the plasma, the effects of CBET are exacerbated and the mode 2 is highly prominent. The inner interface of the target reaches a maximum deformation of a relative amplitude of 24% in the reference case, 34% in case A and 31% in case B. Modes 6 and 8 present in DT and CH ablator cases are created by the 6 or 8 shadow regions from the edge and core transfer, this number depending on the CBET geometries created by the core transfer.

4.5.2.3 3D reconstruction of the shell deformation modes

The Omega chamber beam ports configuration can be decomposed in 8 adjacent constant azimuth planes, between which the co-planar interacting beams median angle is offset by an elevation of 20° to 80° depending on the azimuthal angle. It is thus expected that the mode 2 deformation imposed by CBET in the planar configuration creates higher order modes in a full 3D configuration. This can be estimated by making a linear combination of planar simulation results so as to reproduce the 3D Omega sphere configuration. Simulation results for the internal shell

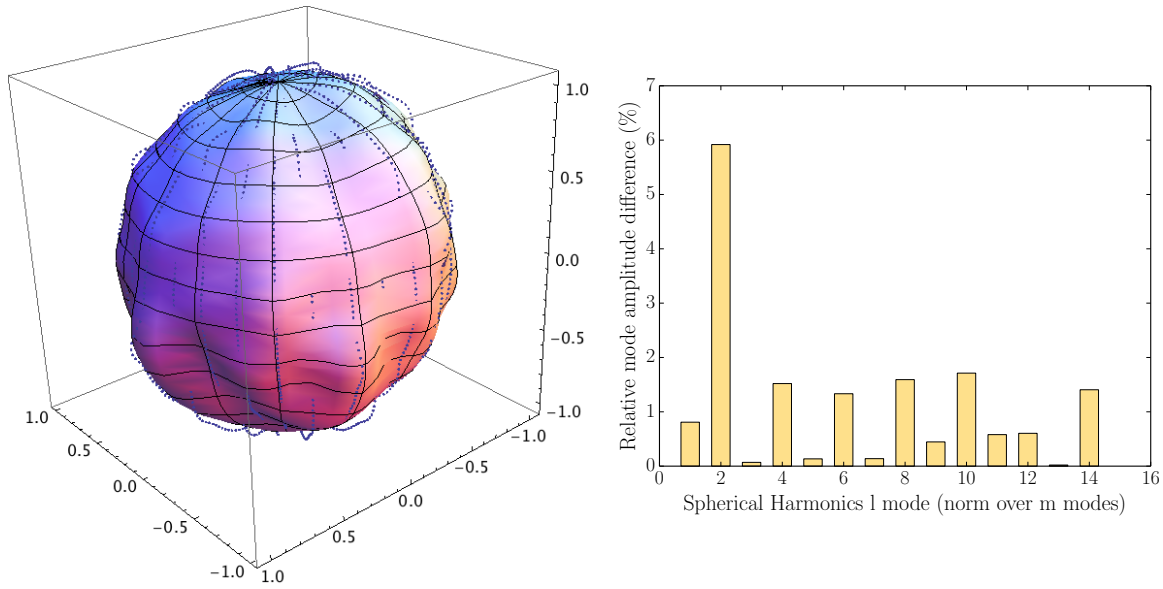

Figure 4-28 – *(color) [left] 3D internal shell surface perturbation near the stagnation for the CBET case, constructed as a linear combination of several 2D planar simulations. Simulation results are shown as blue (light grey) dots and the corresponding spherical harmonics fit is superimposed as a colored (greyscale) surface. [right] Relative mode amplitude difference* $\hat{a}_l = |a_l^{\text{ref}} - a_l|/a_l^{\text{ref}}$*, where* a_l^{ref} *and* a_l *are l-modes amplitudes for the reference case and CBET case, respectively.* a_l *modes are computed by taking the* L_2 *norm over the corresponding* $m-$*modes. Mode 0 is not represented.*

interface at stagnation are combined using one set of results per discrete azimuthal increment (see OMEGA beam configuration in Fig. 4-21 [right]), which corresponds to either the 20 or 40° CBET case, shifted by the corresponding elevation angle value. The combined dataset reproduces a spherical capsule from a linear combination of 2D planar simulations. We decompose this shell in the spherical harmonics Y_l^m up to $l = 14$ for all values of m. This is done using the simulation results with and without CBET. The difference in mode amplitudes is shown in Fig. 4-28, alongside with the combined dataset for the CBET case and its spherical harmonics fit. This linear analysis shows that CBET amplifies the spherical mode $l = 2$ similarly as in the planar case because of a combination of Y_2^{-2} and Y_2^0. Although even and odd modes are equally present in the intensity distribution on the capsule, only even modes are amplified by CBET, while the odd modes remain unchanged. Mode $l = 4$, which was not excited by CBET in the 2D simulations, contributes more significantly to the overall 3D shell deformation, mainly through Y_4^3. We retrieve excitation of modes $l = 6$ and $l = 8$, as well as higher order even modes. Although this linear combination of results does not include any interaction between azimuthal planes, it provides a rough estimate of potentially excited modes by CBET, arising only from the beam port configuration.

4.6 Conclusions

We have proposed a model to compute the macroscopic steady-state CBET between laser beams using many local power transfers between Gaussian beamlets described by Paraxial Complex

Geometrical Optics. It is shown to reproduce the linear gains and beam deviations given by the theory of steady-state energy transfer in inhomogeneous media. Furthermore, the comparison to the time-dependent paraxial solver HARMONY confirmed that the PCGO-based approach is able to reproduce correct linear gains on a large range of parameters $\mathcal{R}_\mathrm{I}$ and $I\lambda_L^2$, past a transient phase and in conditions where a steady-state regime exists. In the latter situations, it is seen that (i) the PCGO-based model reproduces a correct spatial repartition of the intensity field inside the CBET region and provides a correct estimation of the beams deviations, and (ii) can be used to estimate the location and value of the amplitude of IAWs excited by beating of electromagnetic interacting waves. In situations where a steady-state does not exist, the PCGO-based model yields estimates of the linear CBET gain that lie close to the reference solution. We note that the non-stationary situations reported here, caused by the presence of two resonance regions in the interaction volume with opposite energy transfer directions, are a priori unlikely to be encountered in ICF configurations. Finally, a good agreement with the experiment was found, with linear gains slightly overestimated and close to the measured ones, in a significantly better agreement than previous estimates conducted for this experiment. The model was not able to reproduce the location of the resonance that was observed in the experiment. The possible explanations of that fact include; (i) it is unlikely that this discrepancy originated from a Doppler shift effect, unless a major source of velocity asymmetries was present in every shot, and (ii) assuming the linear gain given by the PCGO-based model were indeed overestimated, accounting for the spectral width of the laser gives a gain function that could agree with all of the experimental error-bars. In that case, the observed maximum gain location in the experiment would not be that of the resonance, but results from statistical fluctuations of the shots in the experiment.

The EYEBOLT model being validated, we conducted full 360° simulations of a capsule implosion in which certain beams were allowed to interact through CBET, following the relevant co-planar beam angles of 20°, 40°, 140° and 160°, characteristic of the OMEGA chamber. The influence of the ablator material is assessed by repeating these simulations in a CH and a DT ablator case. The influence of modeling a pseudo-speckle pattern on the power deposition field and capsule implosion symmetry is studied as a reference case for comparisons with simulations with the same pseudo-speckle patterns but with CBET enabled. In the reference case without CBET, the power deposition profile exhibits a pseudo-speckle pattern being relatively smoothed out by the overlap of the beams. The internal shell interface is deformed by low amplitude long wavelength Fourier modes from 1 to 4. A variety of high frequency modes up to mode 33 are observed and greatly smoothed out when reaching the internal shell interface. Simulations with main CBET angles at 20° and 40° show that in those configurations CBET tend to create a pattern of high and low absorption regions through specific regimes of core and edge power transfers, significantly amplifying modes 2, 6 and 8 of the internal shell interface. A reconstruction of the shell based on a linear combination of planar results suggests that mode 4 is also likely to be excited by CBET in a full 3D configuration. Because the linear reconstruction does not account for CBET between non-coplanar beams, it is suspected that the mode 2 is here over-estimated. The choice of the ablator material is seen to be critical in terms of CBET, with lower Z materials presenting more efficient energy exchanges and thus higher shell deformations. We observe relative deformations of the inner shell interface at stagnation of up to 15% in the CH ablator case and 34% in the

DT ablator case. CBET is also seen to have an effect on the global laser-plasma coupling, by reducing the total amount of energy transferred to the plasma. 2D convergence ratios are lower when enabling CBET by up to 14% for the CH ablator case and 25% for the DT ablator case.

The results presented in this Chapter provide a solid validation of the PCGO-based approach as a mean to model CBET at large scales, and highlight the importance of modeling CBET in large scale hydrocodes for the design of laser-target experiments in ICF.

Chapter 5

Multiscale model for coupled laser propagation and hot electron generation and propagation: the Thetis model

The effect of high energy electron beams on the plasma dynamics is of particular importance for Shock Ignition (SI) studies [31, 187], laboratory astrophysics, double ablation front experiments [188] at high intensity, or for the design and interpretation of ns-scale laser target experiments [33]. In these conditions, only a multiscale model can resolve, at hydrodynamic scales, the interwoven couplings between the laser propagation in plasma, Hot Electron (HE) sources created by parametric instabilities, HE beams propagation and plasma dynamics.

The modeling of laser-plasma-electron couplings at hydrodynamic scales poses several difficulties, related to (i) an accurate description of the laser intensity in plasmas, (ii) a consistent characterization of HE sources using the laser propagation model and (iii) a description of HE beam propagation and energy deposition. While the first problem was addressed in Chs. 2 and 3, the other two are the object of this Chapter. Note that HE transport models are often included in large-scale hydrocodes, usually using Monte Carlo approaches, but they rely on ad-hoc electron sources.

We present in this chapter a reduced HE transport model based on the *Angular Scattering Approximation* (ASA) [189], adapted to 2D, transversally Gaussian, multigroup HE beams. Its derivation is presented in Sec. 5.1 and its validation in Sec. 5.2. Secondly, the coupling of PCGO beamlets to HE sources is presented in Secs. 5.3 and 5.4 for the cases of Resonant Absorption, Stimulated Raman Scattering and Two-Plasmon Decay. This model for hot electron generation from LPI processes calculated from Gaussian optical beamlets, beamlet-based hot electron propagation and energy deposition is referred to as the Two-dimensional Hot Electron Transport and emIssion Sources Thetis model. Similarly as for the PCGO model, the Thetis model can be adapted to particular 2D-axisymmetric configurations, as presented in App. B.3.

5.1 Reduced model for electron beam transport and plasma heating

5.1.1 1D and 2D models

5.1.1.1 Continuous Slowing Down Approximation

A simple and widespread description of electron propagation in matter is that of the *Continuous Slowing Down Approximation* (CSDA). Here, the energy ε of a mono-energetic and mono-directional electron beam continuously decreases due to collisions with plasma particles (ions and/or electrons):

$$\frac{d\varepsilon}{dz} = -S(\varepsilon, z) \ , \tag{5.1}$$

where $S(\varepsilon, z)$ is a *stopping power* that may include various contributions and correction factors. This 1D equation for the electron energy is similar to the laser beam energy loss used in hydrodynamic codes relying on the Ray-Tracing model. This discrete, ray-based formulation is easy to transfer from GO algorithms to electron beams. The spatial profile of hot electron sources can be reproduced by using spatial distributions of discrete electron rays. This approach is similar to the way GO rays are used in the RT model to reproduce spatial power profiles of laser sources. Although the CSDA model is simple to implement and numerically robust, it does not account for angular scattering on electrons and ions of the plasma, which is a severe approximation in the regimes of ICF [189].

5.1.1.2 Angular Scattering Approximation

The effect of angular scattering on the HE propagation is described by the kinetic Vlasov-Fokker-Planck equation by considering the electron-ion and electron-electron collisions. Because of the small value of the electron to ion mass ratio, it is assumed that ions conserve their energy throughout the collision. As such, the ion distribution function is approximated by a Dirac delta function and the electron-ion collision integral reduces to a *diffusion operator*. The resulting diffusion equation, written in terms of the electron energy ε and curvilinear coordinate $s = vdt$, reads:

$$\frac{\partial f}{\partial s} + \mathbf{\Omega}.\nabla f = n_i \int [f(\varepsilon, \mathbf{\Omega}', s) - f(\varepsilon, \mathbf{\Omega}, s)] \frac{d\sigma}{d\Omega}(|\mathbf{\Omega} - \mathbf{\Omega}'|) \mathrm{d}\mathbf{\Omega}' \ , \tag{5.2}$$

where f is the Electron Distribution Function, n_i is the ion density, $\mathbf{\Omega} = \mathbf{p}/p$ is the direction of electron propagation and $\frac{d\sigma}{d\Omega}$ is the differential angular cross-section given by the Rutherford formula [66]. Solutions of Eq. (5.2) are sought in cylindrical coordinates by assuming that n_i varies only along the propagation direction of the beam s and that the diffusion cross-section has an azimuthal symmetry. f is decomposed on the basis of spherical harmonics Y_{lm} and Eq. (5.2) is integrated over $\mathbf{\Omega}'$ and s to obtain the angular distribution $f(\theta, s)$ [190, 191]:

$$f(\theta, s) = \frac{1}{4\pi} \sum_{l=0}^{\infty} (2l+1) P_l(\cos\theta) \exp\left[- \int_0^s k_l(s') ds' \right] \ , \tag{5.3}$$

where the $P_l(\cos\theta)$ are the Legendre polynomials and k_l is the l-th moment of the differential angular cross section. Limiting the angular momentum expansion at the order 1 (in l), f reads:

$$f(\theta, s) = \frac{1}{4\pi} P_0 + \frac{3}{4\pi} P_1(\cos\theta) \exp\left[-\int_0^s k_1 ds\right] \ , \tag{5.4}$$

where the first moment of the differential angular cross section reads:

$$k_1 = 2\pi \int_0^\pi \frac{d\sigma}{d\Omega} \sin\theta' [1 - P_1(\cos\theta')] d\theta' \ . \tag{5.5}$$

Using Rutherford's formula, k_1 reads:

$$k_1 = 4\pi b_0^2 \ln\Lambda_{ei} \ , \tag{5.6}$$

where b_0 is the *impact parameter* and $\ln\Lambda_{ei}$ the electron-ion collision Coulomb logarithm. Both quantities are defined in App. A.5. Note that the Coulomb logarithm accounts for the Debye screening [66], quantum effects [189, 192, 193] and non-ideal plasma conditions [194]. The mean diffusion angle is obtained by projecting the $l = 1$ component of f using the orthogonality of the Legendre polynomials:

$$\langle\cos\theta\rangle(s) = \int_0^{2\pi} \int_0^\pi f(\theta, s) P_1(\cos(\theta)) \sin\theta \mathrm{d}\theta \mathrm{d}\psi = \exp\left[-\int_0^s k_1(s) ds\right] \ . \tag{5.7}$$

Assuming that the particles in the beam propagate along straight lines in the z direction, the energy loss rate reads:

$$\frac{d\varepsilon}{dz} = -\frac{1}{\langle\cos\theta\rangle(s)} S_e(\varepsilon) \ , \tag{5.8}$$

where S_e is the electron stopping power. Compared to the CSDA formulation, additional energy loss is accounted for by the *angular diffusion* in the transverse direction to the beam propagation. This transverse energy diffusion can be viewed as the divergence of a beam, which thickness Δ relates to the mean diffusion angle:

$$\frac{d\Delta}{dz} = 2\langle\tan\theta\rangle(s) = 2\frac{\sqrt{1 - \langle\cos\theta\rangle^2(s)}}{\langle\cos\theta\rangle(s)} \ . \tag{5.9}$$

The stopping power in Eq. (5.8) is defined as the energy loss per unit length:

$$S_e(\varepsilon) = -n_i \int_0^\varepsilon \varepsilon' \frac{d\sigma}{d\varepsilon'} d\varepsilon' \ . \tag{5.10}$$

It is supposed in this formula, that the particle has a sufficiently high energy so that it cannot gain more energy through collisions with the plasma particles. Because of the small electron to ion mass ratio, hot electrons propagating in a plasma are mainly slowed down by other electrons (this can be seen in Fig. 5 of [189]). The stopping power of the fast electron beam is decomposed in three contributions [195, 196]: *bound* electrons, *free* electrons and *plasmons* [189, 193, 194]. The expressions used for these stopping powers are presented in [197] and are identical to those currently implemented in the M_1 electron transport model [197, 198] used to validate this work

in Sec. 5.2.

The 2D formalism of Eqs. (5.8) and (5.9) will now be referred to as the Angular Scattering Approximation (2D-ASA, or ASA). One can use Eq. (5.8) alone in a 1D approach (called 1D-ASA), then the HE beam energy decrease due to the angular scattering is accounted for via the $< \cos\theta >^{-1}$ term only. The 1D-ASA is as straightforward to implement as the CSDA, because it is still ray-based and interfaces well with the GO-based algorithms. On the contrary, 2D models using the ASA must account for the lateral energy spread described by Eq. (5.9). This adaptation to 2D was done in Ref. [197] by considering electron beamlets with infinitesimal initial thickness $\Delta(0)$ and with flat transverse intensity profiles (so-called *pencil beams*). In this reference, the dose from the HE beams is computed on separate Eulerian grids and the results projected back to the original hydrodynamic Lagrangian grid. However, this approach is numerically inefficient when considering multiple electron beams or inline solvers.

We now present an adaptation of the 2D-ASA to a thick-ray-based formalism, in a multigroup framework, for HE beams of a Gaussian transverse intensity profile and HE sources of any angular distribution.

5.1.2 Implementation in the framework of thick-rays

In our approach, HE sources are computed from the parameters of Gaussian optical beamlets (the source terms are presented in Secs. 5.3 and 5.4). Therefore, we deal with hot electron sources and beams which transverse intensity profiles are also Gaussian. Consequently, instead of splitting a HE beam in many pencil beams, we can directly model a Gaussian HE beam, and make use of the efficient projection algorithms developed for PCGO beamlets. This approach considerably reduces the CPU time required for HE beam propagation and projection onto the Lagrangian mesh. We present here the implementation of this CSD formalism to 2D, transversally Gaussian hot electron beams, in a multigroup approach and considering arbitrary angular distributions.

5.1.2.1 Elementary Gaussian beamlet

The evolution equation for the Gaussian electron beam thickness w is similar to Eq. (5.9) and reads:

$$\frac{dw}{dz} = \langle \tan\theta \rangle(s) = \frac{\sqrt{1 - \langle \cos\theta \rangle^2(s)}}{\langle \cos\theta \rangle(s)} \ . \tag{5.11}$$

The electron beam axis trajectory is computed along the Lagrangian mesh using the algorithms developed for the RT method and assuming a straight ray. This is achieved by artificially setting the relative permittivity to $\epsilon = 1$. The stopping power and mean diffusion angle are computed from the hydrodynamic quantities T_e, T_i and ρ, which are interpolated continuously from the Lagrangian mesh along the ray trajectory using the same algorithms as those described in App. A.1.1.

The integration of the electron beam transport into the PCGO projection algorithm requires the definition of a beam intensity, in addition to its thickness w. As for PCGO rays (see Eq. (2.79)), we assume a Gaussian intensity profile for the electron beam energy flux q:

$$q(s,r) = q_0(s) \exp\left[-2\left(\frac{r}{w}\right)^2\right] \ , \tag{5.12}$$

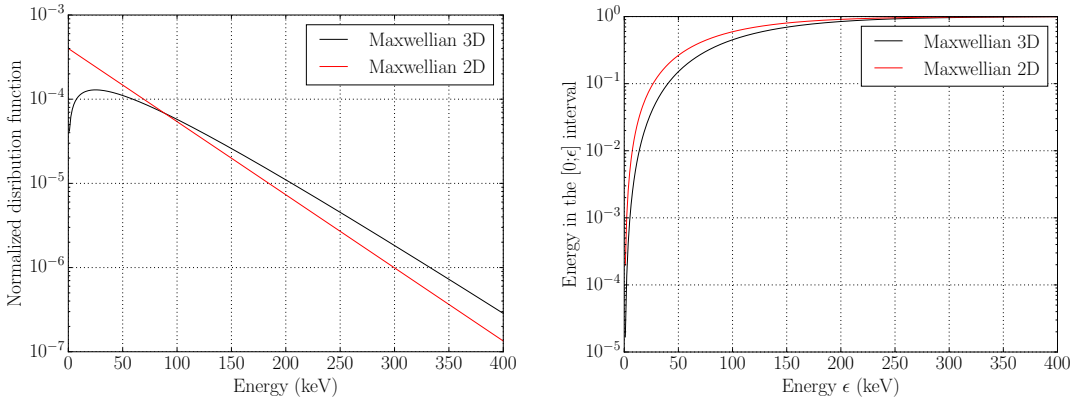

Figure 5-1 – *(color) [left] 2D and 3D Maxwellian distribution functions for the averaged energy $\langle E \rangle = 50$ keV. Both functions are normalized so as to contain the same energy flux. [right] Cumulative 2D and 3D Maxwellian distribution functions, i.e. energy flux comprised in the $[0;\varepsilon]$ interval as a function of the energy ε. Both functions converge to the same asymptotic value because they contain the same energy flux. The 2D distribution function is shown as a red (grey) line and the 3D distribution function as a black line.*

where q_0 is the beam on-axis intensity, r is the radial coordinate and s is the curvilinear coordinate. The computation of q_0 depends on the distribution function f_E for the electron beamlet. For an idealized mono-energetic beamlet, $q_0 = n_h \varepsilon_0 v_0$, with ε_0 being the initial energy of the beam, n_h being the number of electrons and v_0 being their initial velocity. This approach corresponds to the framework of the ASA (5.8), which describes mono-energetic beamlets.

5.1.2.2 Multi-group electron beams

Conversely, for the study of multigroup hot electrons beams, we define the energy distribution function:

$$f_E(\varepsilon) = \exp\left[-\frac{\varepsilon}{k_\mathrm{B} T_\mathrm{h}}\right] , \tag{5.13}$$

where T_h is the so-called *supra-thermal* electron temperature. This form of the distribution function corresponds to a Maxwellian distribution defined with two degrees of freedom in the momentum space. Note that for a 1D distribution, $f_E(\varepsilon) \propto 1/\sqrt{\varepsilon}\exp\left[-\varepsilon/k_\mathrm{B}T_\mathrm{h}\right]$, and for a 3D distribution $\propto \sqrt{\varepsilon}\exp\left[-\varepsilon/k_\mathrm{B}T_\mathrm{h}\right]$. The difference between the 2D and 3D distributions is relatively small, as it is illustrated in Fig. 5-1. For the same average energy flux, the 2D distribution function is slightly shifted toward the lower energies when compared to the 3D distribution function. The choice of the 2D function is motivated by the 2D planar framework, in which the model is implemented.

In practice, the f_E function (5.13) is approached by a discrete logarithmically-binned energy distribution function $\hat{f}_E^0(\varepsilon)$, composed of superposed beamlets of mono-energetic distribution function f_E^k:

$$\hat{f}_E^0(\varepsilon) = \sum_{k=0}^{N_g^E-1} f_E^k = \sum_{k=0}^{N_g^E-1} A_k \delta(\varepsilon - E_k) , \tag{5.14}$$

$$\log E_k = \log E_{\min} + k\left(\frac{\log E_{\max} - \log E_{\min}}{N_g^E - 1}\right) ,$$

where $E_{\min}$ and $E_{\max}$ are the energy boundaries and the A_k are normalization factors. Typically[1], $E_{\min} \simeq k_B T_h/5$ and $E_{\max} \simeq 8 k_B T_h$. The discretized energy distribution resembles a Dirac comb with logarithmic steps and converges toward f_E for $N_g^E \to \infty$. The A_k factors are obtained by imposing the power conservation per bin at $t = 0$:

$$A_k = \frac{\int_{E_{k-1/2}}^{E_{k+1/2}} \varepsilon v_e(\varepsilon) f_E(\varepsilon) d\varepsilon}{\int_0^\infty \varepsilon v_e(\varepsilon)\delta(\varepsilon - E_k) d\varepsilon} = \frac{\int_{E_{k-1/2}}^{E_{k+1/2}} \varepsilon v_e(\varepsilon) f_E(\varepsilon) d\varepsilon}{E_k v_e(E_k)} , \tag{5.15}$$

where $v_e(\varepsilon) = c\sqrt{1 - 1/\gamma_e(\varepsilon)^2}$ is the electron velocity and γ_e is the Lorentz factor. Given an initial beam power P_0^e, width w and height h, the beam electron density n_{be} reads:

$$n_{be} = \frac{P_0^e}{\sqrt{\pi/2} w h \int_{E_{\min}}^{E_{\max}} \varepsilon f_E(\varepsilon) v(\varepsilon) d\varepsilon} , \tag{5.16}$$

where $n_{be} A_k$ is the initial number density of electrons for beam k. The initial intensity for beamlet k reads:

$$q_0^k = n_{be} A_k \int_{E_{k-1/2}}^{E_{k+1/2}} \varepsilon\delta(\varepsilon - E_k) v(\varepsilon) d\varepsilon = n_{be} \int_{E_{k-1/2}}^{E_{k+1/2}} \varepsilon v_e(\varepsilon) f_E(\varepsilon) d\varepsilon . \tag{5.17}$$

5.1.2.3 Beam aperture

The mono- and multigroup HE beams described above are initialized with $< \cos\theta >= 1$, i.e. each beamlet is initially collimated. In general, LPI processes at the origin of HE beams may accelerate electrons in different directions. Considering a HE source i with an aperture Θ (defined in Fig. 5-2), a HE beam i of principal axis $\mathbf{e}_{\text{HE}}^i$ is described by N_g^S multigroup sources:

$$q^i(w, \Theta)\mathbf{e}_{\text{HE}}^i = \sum_{j=1}^{N_g^S} \mu^{ij} q^{ij}(w) \mathbf{e}_{\text{HE}}^{ij} , \tag{5.18}$$

where μ^{ij} are constant factors that define the angular distribution, and the axis of the group j $\mathbf{e}_{\text{HE}}^{ij}$ is defined as:

$$\mathbf{e}_{\text{HE}}^i . \mathbf{e}_{\text{HE}}^{ij} = \cos(\theta_j) = \cos\left(-\Theta/2 + \frac{(j-1)\Theta}{N_g^S - 1}\right) , \tag{5.19}$$

with θ_j the angle between the group j and the axis of the HE source $\mathbf{e}_{\text{HE}}^i$, defined such as $\sum_{j=1}^{N_g^S} \mathbf{e}_{\text{HE}}^{ij} / |\sum_{j=1}^{N_g^S} \mathbf{e}_{\text{HE}}^{ij}| = \mathbf{e}_{\text{HE}}^i$, for any N_g^S. For simplicity, the initial width of each group j is taken to be equal to that of the source. The desired angular distribution can be obtained by varying the μ^{ij} factors. For an isotropic distribution in the $[-\Theta/2; +\Theta/2]$ cone, these factors simply read:

$$\mu^{ij} = 1/N_g^S . \tag{5.20}$$

[1] For the energy boundaries considered here, the use of logarithmically-spaced bins increases the convergence rate with N_g^E of the variance of the power repartition per bin compared to linearly-spaced bins. Neither of these approaches are optimal. It might be improved by using bins with the same power per bin, i.e. a zero variance for any number of energy groups.

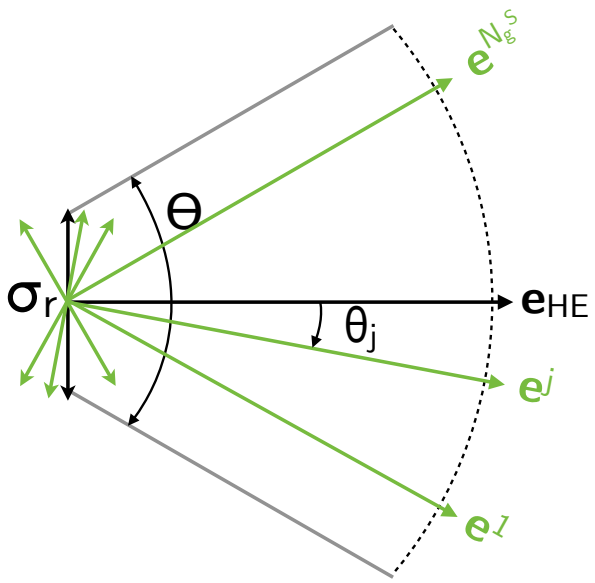

Figure 5-2 – *Definition of the angular parameters of a multigroup HE beam with a non-zero initial aperture. The HE source spatial parameter are represented in black and the discretization with initially anisotropic sources is shown in green.*

For a HE source with N_g^E energy group and N_g^S angular groups, $N_g^E \times N_g^S$ mono-energetic beamlets are required, so that this approach can be relatively costly. An assessment of the number of spatial and energy groups to properly describe a HE source of initial aperture $\Theta = \pi/4$ is conducted in Sec. 5.2.2.

5.1.2.4 Power deposition

Equations (5.7), (5.8) and (5.11) are integrated along a central ray trajectory between two mesh cells using a Runge Kutta algorithm of order 4 with an adaptative step size, in order to correctly resolve the singular behavior of w and $\mathrm{d}\varepsilon/\mathrm{dz}$ as $\langle\cos\theta\rangle$ goes to zero. Considering the integration of these equations between z and $z + dz$, the power lost by the beamlet can be expressed as:

$$\begin{aligned} P_{lost}^{z+dz} &= P^z - A_k n_{be}(w^0/w^{z+dz}))\sqrt{\frac{\pi}{2}} h w^{z+dz} \int_{E_{k-1/2}}^{E_{k+1/2}} \varepsilon\delta(\varepsilon - E_k^{z+dz}) v_e(\varepsilon) d\varepsilon \\ &= P^z - w^0\sqrt{\frac{\pi}{2}} h q_{z+dz}^k \ . \end{aligned} \tag{5.21}$$

This power loss (the deposited dose) is projected onto the Lagrangian mesh by considering linear variations of w and q between the entry and exit points of the central ray in the cell and using the PCGO algorithm for the Gaussian field projection. Comparisons with the reduced kinetic code M_1 available at Celia [199] for mono-energetic and multigroup (5.13) HE beams are presented in the following section.

5.1.2.5 Straggling and blooming

The base framework of the ASA model is that of mono-energetic HE beamlets that widen through angular diffusion in the coordinate space and slow down through both collisions and angular

Case	ρ_0 (g/cc)	T_e (eV)	T_i (eV)	E_e (keV)	P_e (PW)	Δ_x (μm)	Δ_y (μm)	N_x	N_y
Mono_1	10	1000	1000	100	1.458	80	240	80	100
Mono_2	300	1	1	2500	1.492	80	240	80	100
Multi_1	10	1000	1000	30	1.433	30	240	60	60
Multi_2	10	1000	1000	100	1.433	30	240	60	60

Table 5.1 – *Plasma and simulation parameters for the comparisons between M_1 and ASA in the constant density cases. E_e is either the HE beam energy (for a mono-energetic beam) or the HE temperature (for a multigroup beam), P_e is the HE beam power, Δ_x and Δ_y are the plasma dimensions along the x (propagation) and y (transverse) directions, N_x and N_y are the number of mesh cells in each direction.*

diffusion in the momentum space. This beam widening in the momentum space is called *blooming*. Moreover the electron slowing down is also associated with the energy spread in the direction of the beam axis (so-called *straggling*) [192]. These two effects can be included in the ASA model by considering higher orders in the distribution function for the beam, which involves the second moment of the differential angular cross section [192, 197]. 2D comparisons with the M_1 model in the case of a mono-energetic electron beam have shown a significant benefit of taking into account beam straggling and blooming, which smooth the sharp cutoff behavior characteristic of the SDA equation (5.8). However, it was shown in Ref. [197] that this significant difference in the case of a mono-energetic electron beam is greatly reduced when considering HE beams with a broad energy distribution. This is also illustrated in the following section.

5.2 Validation

The ASA model and the M_1 code are now compared in several cases relevant to ICF conditions, for mono-energetic and multigroup HE beams. The electronic M_1 [199, 198, 200] model is an angular moment approximation of the Vlasov-Fokker-Planck equation, based on entropy maximization principles, that is implemented in the CHIC code. Note that the present THETIS model is not interfaced with the M_1 model. The reason being that although the numerical cost of M_1 is much lower than that of kinetic models, it is usually limited to one beam. This is not sufficient for a direct-drive like configuration with many laser beams, where each of them may be a source of multiple hot electron beams generated by nonlinear LPIs. As such, the M_1 approach is not adequate as it is still a rather time consuming method when considering multiple electron beams.

We consider a stationary regime for M_1 and study the dependence of the dose deposition on the number of electron groups and the size of transverse inhomogeneities. Note that for simple plasma conditions, results obtained from the non-stationary M_1 model converge toward the stationary solution. For simplicity, the plasma equation of state of all cases is that of a perfect gas and the plasma is always considered to be fully ionized.

5.2.1 Constant density plasma

5.2.1.1 Mono-energetic case

We consider two cases of a DT plasma with densities of 10 and 300 g/cc, and electron beams of the energy 100 keV and 2.5 MeV. These choices are relevant to the plasma densities and HE

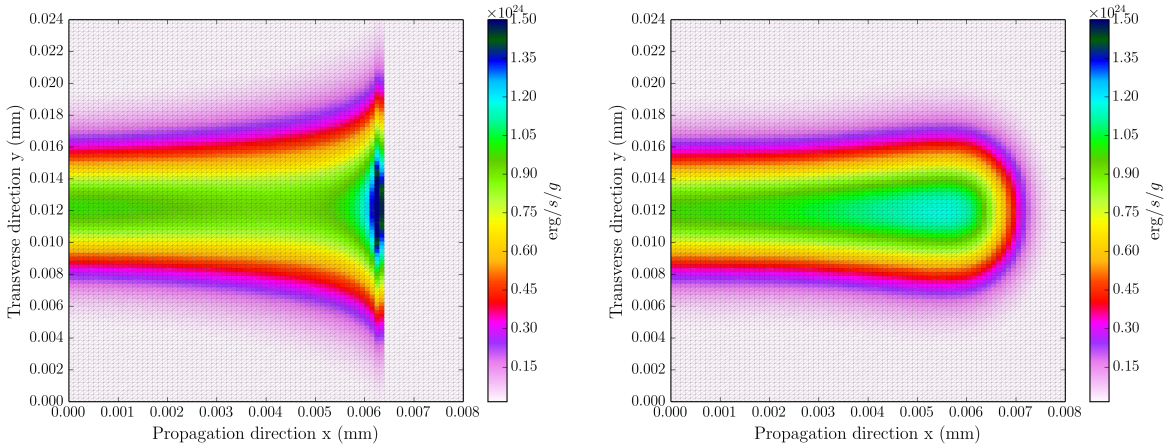

Figure 5-3 – *Spatial energy deposition field from the HE beam ($erg.s^{-1}.g^{-1}$): results from the ASA model [left] and the M_1 model [right] for the 2.5 MeV case.*

energies encountered in the Shock Ignition and Fast Ignition frameworks, respectively. Plasma and simulation parameters are summarized in Tab. 5.1 (cases Mono_1 and Mono_2).

The predicted *dose rate* (power absorbed per unit mass) for the 2.5 MeV case is presented in Fig. 5-3 and illustrates the major flaw of the ASA model in its current formulation without straggling and blooming, that is a rapid divergence of the beam at the end of its trajectory. This is quite different from the M_1 results. The difference is due to the longitudinal diffusion taken into account in M_1, but not in the ASA model. Consequently, the overall energy deposition field predicted by M_1 presents the morphology of a droplet, whereas the ASA model produces peaked profiles. Figure 5-4 represents the dose integrated along the transverse direction y as a function of the propagation direction x. For both electron energies, the ASA model produces a sharp cutoff with a maximum of energy deposition that is overestimated in value and underestimated in depth. That is particularly the case for the 100 keV beam, the difference being much less visible for the 2500 keV beam due to a smaller angular diffusion of relativistic electrons. The total energy deposited in both cases is the same for both models, while the dose distributions are different. Although there is a rather large difference in that morphology, mono-energetic beams with such sharp energy distributions are not physical and only multigroup distribution functions are considered in physical applications of the ASA model in Thetis.

We note also that our ASA model is much more computationally efficient. The computation times for the cases Mono_1 and Mono_2 are 600 s and 1200 s with M_1 while our implementation of the ASA model takes 0.2 s for both cases. Typical computation times for such cases with the standard ASA model reported in Ref. [197] (based on pencil beams and dedicated Eulerian grids) are of the order of 5 s.

5.2.1.2 Multi-group case

We now consider two cases of a DT plasma with a density 10 g/cc and exponential electron distributions (5.13) with $T_\text{h} = 30$ and 100 keV. These parameters are relevant to the Shock Ignition conditions, where the HEs generated from the SRS and TPD instabilities emitted close

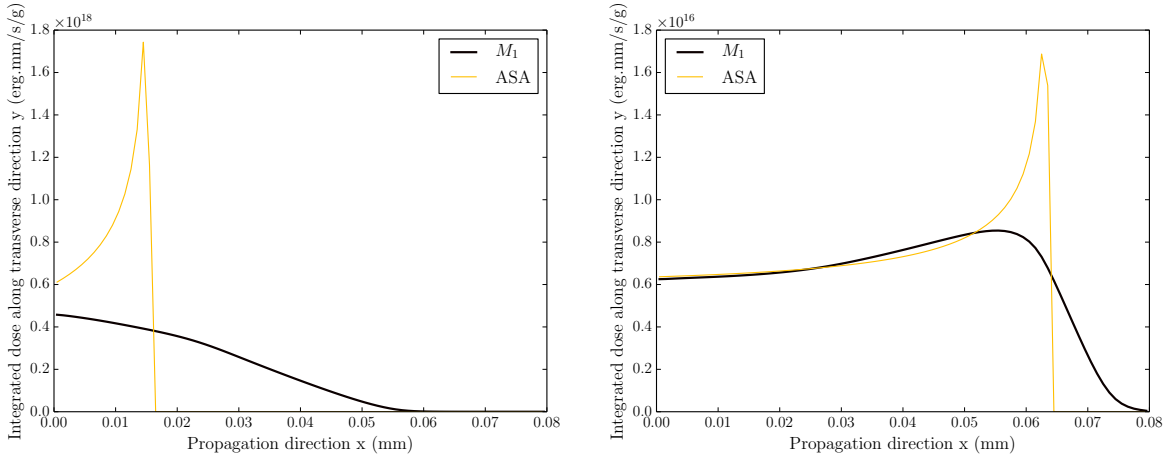

Figure 5-4 – *(color) Integrated dose along the transverse direction as a function of the propagation distance in erg.mm.s^{-1}.g^{-1} for the 100 keV [left] and 2.5 MeV [right] cases. Results from the M_1 model are presented with a thick black line and results from the ASA model with an orange (light grey) line.*

to the quarter critical density can reach these typical energies. Plasma and simulation parameters are summarized in Tab. 5.1 (cases Multi$_1$ and Multi$_2$).

The calculated doses for the multigroup cases are presented in Fig. 5-5. Contrary to the mono-energetic case, M_1 and ASA produce rather similar results. There is an overall good agreement in the morphology of the energy deposition field and the sharp features of the ASA model are smoothed by the beamlet overlaps. This smoothing is dependent on the number of beamlets chosen for ASA, as is illustrated in Fig. 5-6, which represents the dose integrated in the perpendicular direction for different number of beamlets N_g^E. For $N_g^E > 50$, the ASA model correctly predicts the dose and penetration depth of the HE beam, even at the energies in the range of tens of keV considered here, which showed a significant difference in the mono-energetic case. The sharp features of the ASA model are prominent for $N_g^E = 10$ and they progressively disappear converging to the predicted dose when increasing N_g^E. The computation times for cases Multi$_1$ and Multi$_2$ are of 680 s and 3400 s with M_1 and about 2 s with ASA using $N_g^E = 500$. We note that typical computation times for such cases with the standard ASA model presented in Ref. [197] are of the order of 15 s.

5.2.2 ICF-like density profile

We now consider more complicated plasma profiles, taken from the hydrodynamic simulation of an ICF implosion (in the HiPER baseline DT configuration [201]), at a time corresponding to the beginning of the main drive pulse. Density and temperature conditions are shown in Fig. 5-7. These profiles define the initial plasma condition along the x direction and are invariant along the y direction. We study two cases of propagation of a 60 keV multigroup HE beam ; parallel to and with an angle with respect to a density gradient, from a density close to the quarter critical density. The beam is given an initial divergence of $\Theta = 10°$ in order to mimic a source with a moderate angular spread.

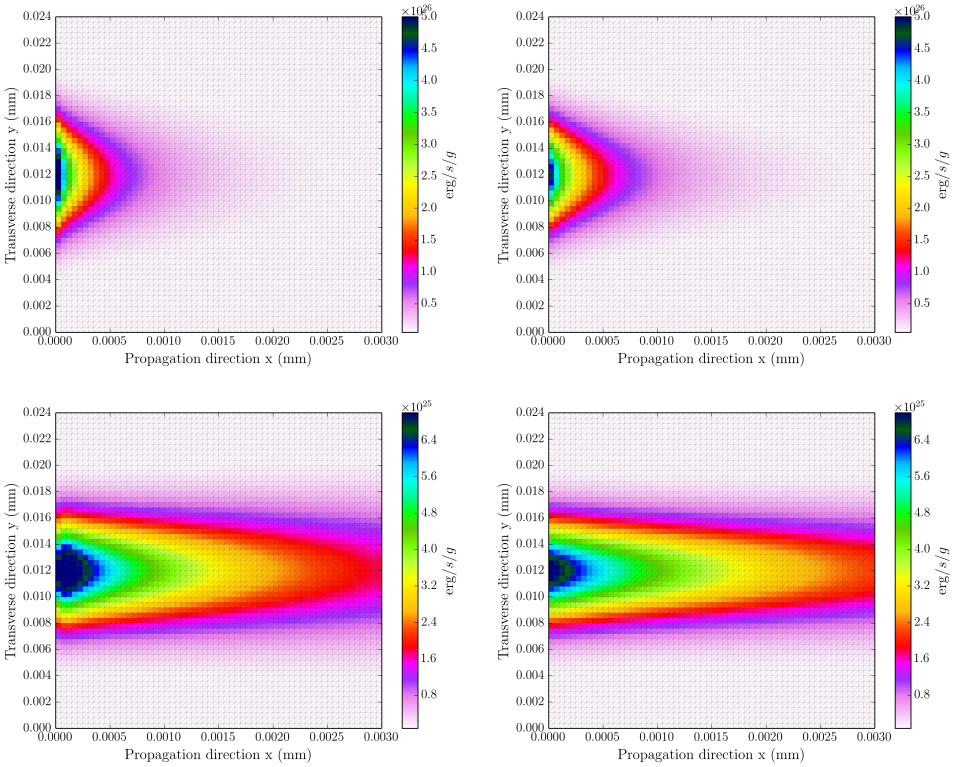

Figure 5-5 – *(color) Spatial energy deposition field from the HE beam ($erg.s^{-1}.g^{-1}$): results from the ASA model [left] and the M_1 model [right] for the 30 keV [top] and 100 keV [bottom] cases.*

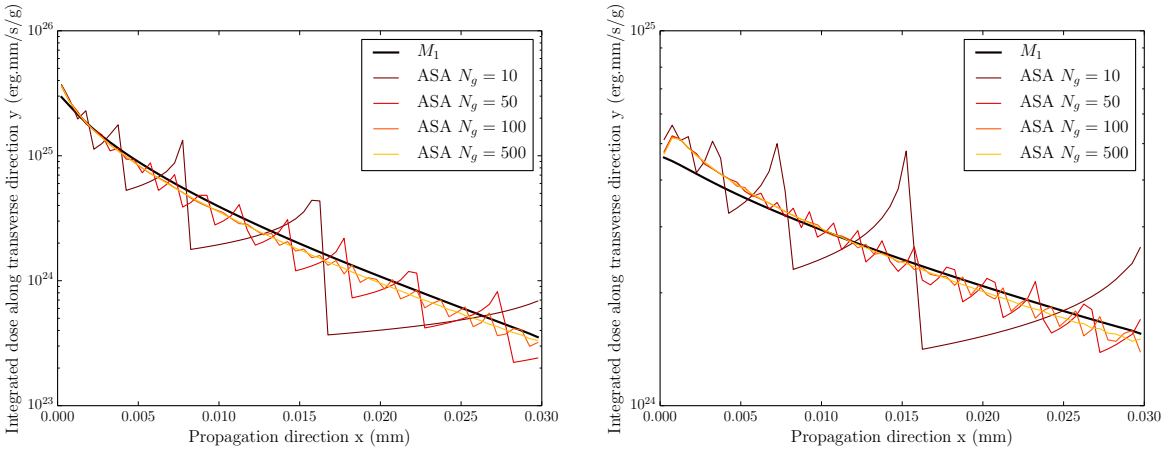

Figure 5-6 – *(color) Dose integrated along the transverse beam direction as a function of the propagation direction for the electron beams having an exponential distributions with the temperatures 30 keV [left] and 100 keV [right]. Results from the M_1 model are presented with a thick black line and results from the ASA model with colored (grey-shaded) lines for different number of groups N_g^E.*

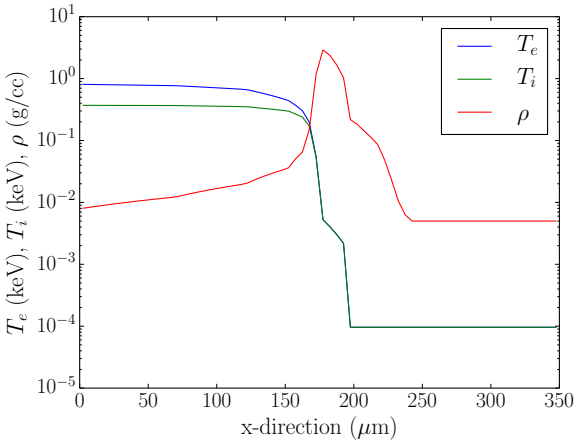

Figure 5-7 – *(color) Initial profiles for the electron temperature (blue), ion temperature (green) and density (red) along the x direction. Temperatures are expressed in keV and density in g/cc. The HE source is located at $x = 0$ where $n_e/n_c = 0.25$. Note that the density upstream of the shock (left side of the figure) has been artificially raised to 10^{-2} g/cc in order to speed up computation times with M_1.*

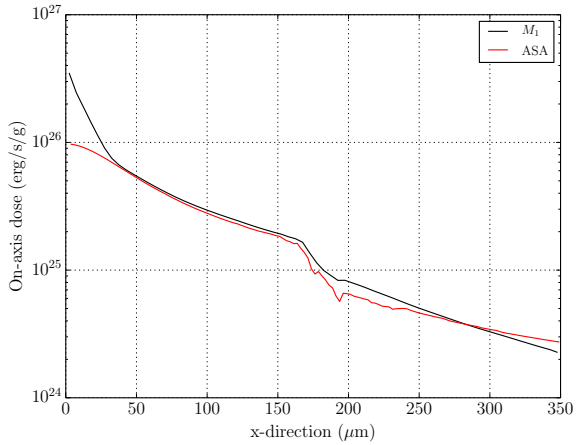

Figure 5-8 – *(color) Dose deposited by the hot electron beam along its axis in the inhomogeneous density and temperature profile. Results from the M_1 model are shown in black and results from the ASA in red.*

5.2.2.1 HE beam propagation parallel to the density gradient

Typical hot electron sources in ICF are located at the quarter critical density or at the critical density. We consider such a source at the quarter critical density, with hot electrons emitted in the direction of the density gradient. This test case provides insight on the capabilities of the ASA model in predicting the dose at the peak density and behind a shock. We compare the on-axis dose in Fig. 5-8. The energy absorbed by the plasma is similar in both models, including behind the shock. The difference in dose deposition in the first 50 μm is thought to be due to a difference in the definition of the initial conditions between the models.

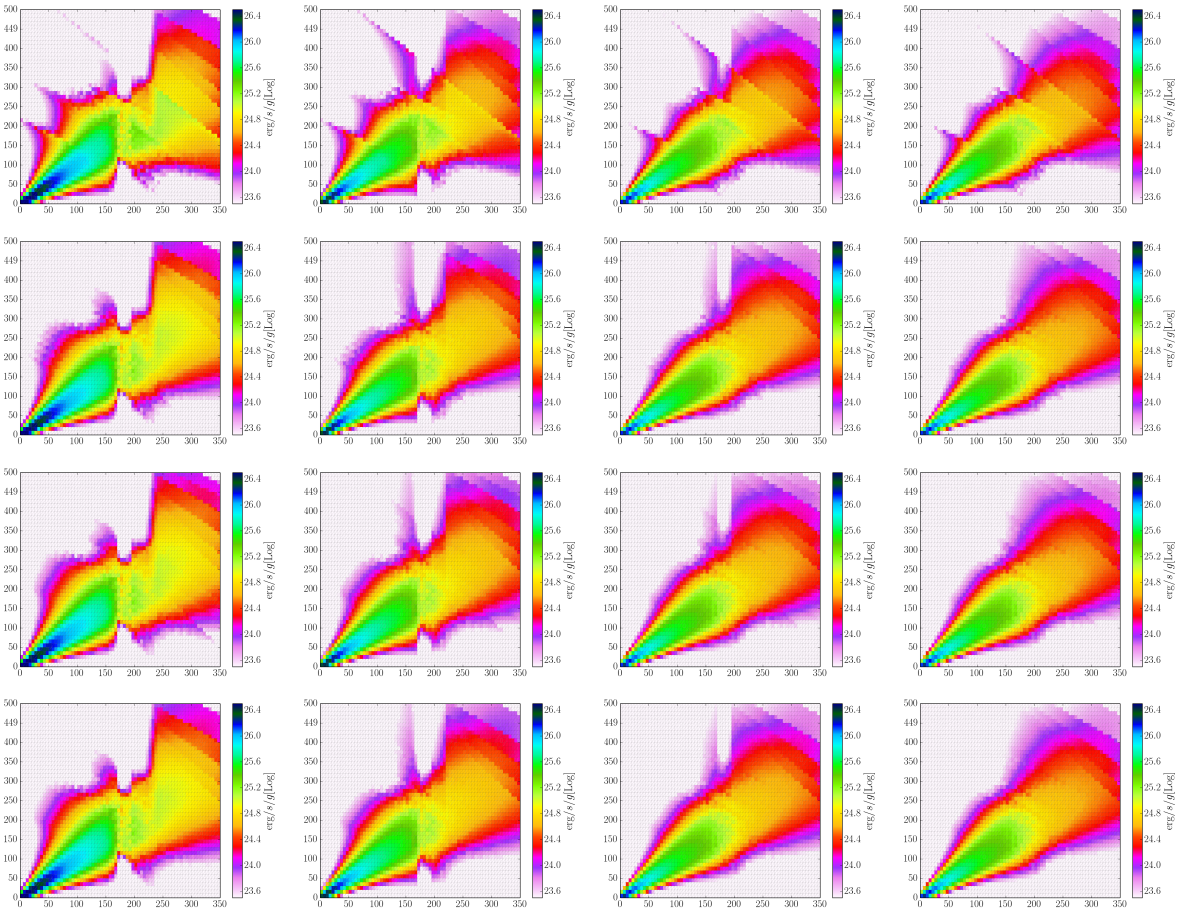

Figure 5-9 – *Dose deposited by a HE beam incident at* 45° *on a shock profile with an initial aperture* $\Theta = 10°$ *(described with* $N_g^S = 5$*), for various values of* $N_g^E \in [10, 50, 100, 1000]$ *(top to bottom) and for* $\bar{\rho} \in [1, 10, 100, 1000]$ *(left to right).* x *and* y *axis are in* μm*.*

5.2.2.2 HE beam propagation at an angle with the density gradient

It was noted in [197] that strong anisotropies of the density in the transverse direction to the HE beam propagation direction are a source of error in the ASA model. Assuming that at a constant temperature, the stopping power varies linearly with the density, the energy deposition is corrected in the orthogonal direction by the density ratio $\bar{\rho} = \rho(r)/\rho(0)$ where $\rho(0)$ is the on-axis density and $\rho(r)$ is the density at the considered point. It is suggested in Ref. [197] to set a maximum density ratio of $\bar{\rho}_{\max} = 4$, in order to avoid overestimated transverse doses. To assess the contribution of this parameter, the case of a beamlet propagating from the quarter critical density at an angle of 45° with the density gradient is now considered. We explore in Fig. 5-9 a range of parameters $N_g^E \in [10, 50, 100, 1000]$ and $\bar{\rho} \in [1, 10, 100, 1000]$ with the ASA approach, and compare the results from the M_1 model, shown 5-10 [left].

Compared to the M_1 results, it is found that $N_g^E \geq 50$ with the ASA is sufficient to reproduce a smooth dose deposition field. It is also found that the $\bar{\rho}$ parameter must not be set to a too large value, in order to avoid large precision losses in the high density region. In particular, for $\bar{\rho} \geq 100$, the ASA is not able to reproduce the cropped-beam behavior observed in the M_1

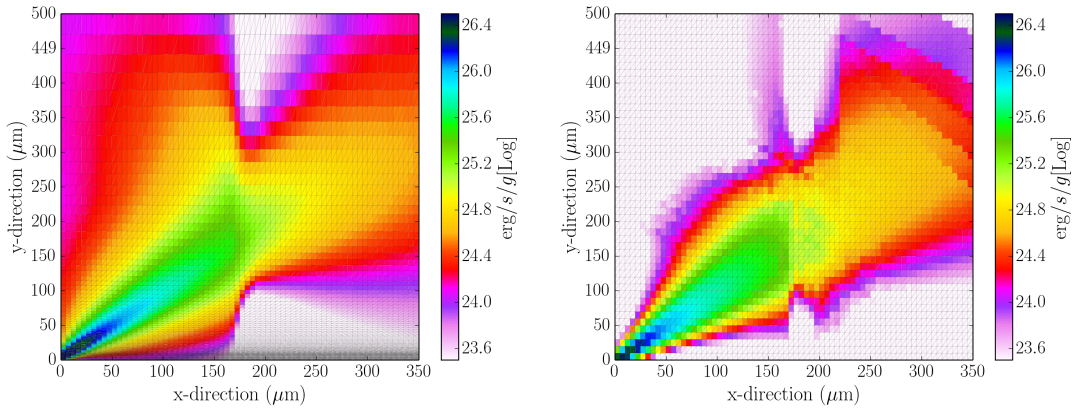

Figure 5-10 – *Dose deposited by the HE beam, results from [left] the M_1 model and from [right] PCGO+*THETIS*, with $\bar{\rho} = 10$ and $N_g^E = 50$.*

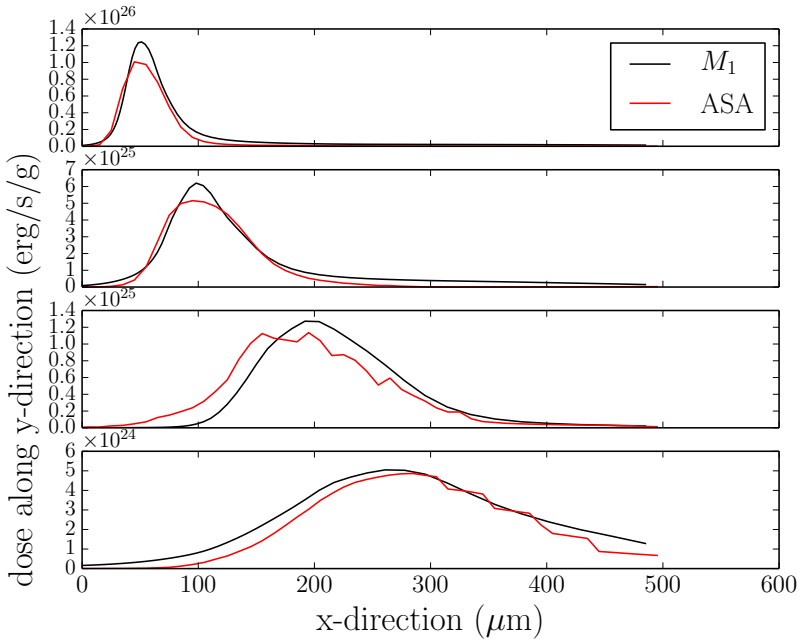

Figure 5-11 – *(color) Dose deposited by the HE beam at various depths in the y direction (see Fig. 5-10), for $y \in \{50, 100, 200, 300\}$ μm. Results from the M_1 model are indicated in black solid lines and results from the ASA in red (grey) solid lines, for $\bar{\rho} = 10$ and $N_g^E = 50$.*

simulation. On the other hand, for $\bar{\rho} = 1$, the dose field with the ASA model appears deviated due to the presence of the strong transverse inhomogeneity. The value $\bar{\rho} = 10$ is found to be a good compromise, retaining the cropped-beam features observed in the M_1 results and the HE beam directionality. In practice, we choose $N_g^E = 50$ and $\bar{\rho} = 10$ in our simulations. This particular combination is highlighted in Figs. 5-10 and 5-11. With the exception of the wings (discussed below), the ASA and M_1 models are in overall good agreement. The morphology of the dose is comparable and the regions of high plasma heating are well reproduced.

Finally, we point out that the wings of the HE beam downstream of the shock (left-hand-side

of the figure) are not well reproduced by the ASA model. This is thought to be a consequence of the initial angular distribution of the HE source, that probably differs between the M_1 and ASA approach. Notably, in the ASA model the HE source intensity as a function of the angle is constant in the $[-\Theta/2; \Theta/2]$ interval, while it decreases smoothly in the M_1 approach, in an interval larger than for the ASA initialization. This can notably be seen in Fig. 5-10 at the point of HE emission, where the whole $x = 0$ region is covered by electrons in M_1.

5.3 A Resonant Absorption model based on the thick-rays description of laser beams

Resonant Absorption occurs when an EM wave interacts with a density gradient in such a way that the wave's electric field at its turning point has a component parallel to the density gradient. This component of the electric field tunnels from the turning point to the critical density, where it is resonantly excited, thus driving an electron plasma wave and causing an additional laser absorption. Hot electrons may be accelerated by this process depending on the strength of the resonant field and the distance between the wave's turning point and the critical density. Resonant Absorption at the critical density may influence the velocity of shocks in the target, while the HE it generates are rarely a concern for the target preheat, except at very high laser intensities.

We describe below the spatial and energetic properties of hot electrons accelerated by Resonant Absorption, that serve as source parameters for the HE propagation model described in Sec. 5.1.

5.3.1 Laser energy conversion fraction

For a p-polarized electromagnetic wave incident at an angle φ (defined at the plasma-vacuum boundary) on a linear density profile of scale length L, the fraction of beam energy f_A absorbed at the critical density can be expressed as $f_A = \Phi^2(\eta_c)/2$ [61], with $\eta_c = (\omega L/c)^{2/3} \sin^2 \varphi$ and Φ being a resonance function. Based on Ref. [80], we have derived a resonance function where the decay factor of the electric field is estimated by a different interpolation function:

$$\Phi(\eta_c) \simeq 1.866 \eta_c^{1/2} \exp(-2\eta_c^{3/2}/3)/(\eta_c + 0.435)^{1/4} \ . \tag{5.22}$$

The derivation of the resonance function is rather technical and is presented separately in App. C.1, alongside comparisons to the resonance function presented in Ref. [80]. Note that compared to numerical solutions of the wave equation in a plasma with a linear density profile and PIC simulations [95], this formula captures the absorption fraction to within an error of 10% (that is corrected by re-normalization), and yields an optimal angle of $\eta_c = 0.51$ that is bracketed by the reference simulation values ($\eta_c \in [0.47; 0.53]$).

When a p-polarized PCGO beamlet propagates orthogonally to the density gradient direction, a HE beam is initialized at the critical density, parallel to the gradient direction (see Fig. 5-12). If the temperature $T_{\mathrm{h,RA}}$ of these HEs, computed with (5.23) and (5.24), is less or equal to the plasma temperature at the critical density $T_{e,\mathrm{nc}}$, this energy is deposited at the critical density. When $T_{\mathrm{h,RA}} > T_{e,\mathrm{nc}}$, we consider that 100 % of the absorption fraction f_A is converted into HEs. In any case, the power fraction f_A absorbed at the critical density or given to the electron source

is removed from the PCGO beamlet at its turning point. The wave front equation (2.72) is re-integrated from the turning point to update the downstream intensity, curvature radius and width of the PCGO beamlet. The detailed numerical implementation of Resonant Absorption into the PCGO model is presented in App. C.2.

5.3.2 Spatial parameters of the hot electron source

Resonant Absorption originates from the component of the electric field that is parallel to the density gradient. Consequently, electrons accelerated in an EPW at the critical density from this component of the electric field are ejected in the direction of the density gradient. As such, the electrons from Resonant Absorption form a parallel beam in the direction of the density gradient.

The thickness of the HE beam source is taken to be equal to the interpolated thickness of the thick ray at the turning point w_T. Results with our model are not sensitive to this approximation, as the overlap of many electron sources from many thick rays creates a rather uniform field in the transverse direction with respect to the density gradient.

5.3.3 Hot electron temperature from Resonant Absorption

Numerous experiments [36, 202, 9, 3, 203, 204, 22] have highlighted the scaling between the temperature of hot electrons produced by Resonant Absorption and the interaction parameter $I\lambda_L^2$. In the intensity regime of ICF and planar target experiments with nanosecond lasers, $I\lambda_L^2 \in [10^{13}; 10^{15}]$ Wμm^2/cm^2. In that regime, the hot electron temperature $T_{\mathrm{h,RA}}^{(1)}$ approximately scales as:

$$T_{\mathrm{h,RA}}^{(1)} = 9.369 \times 10^{-10} (I_{\mathrm{W/cm^2}} \lambda_{\mu m}^2)^{0.664} \text{ keV} . \tag{5.23}$$

We include the scaling of T_{h} at higher temperatures using the experimental law valid for $I\lambda_L^2 \in [10^{15}; 10^{17}]$ Wμm^2/cm^2:

$$T_{\mathrm{h,RA}}^{(2)} = 1.577 \times 10^{-3} (I_{\mathrm{W/cm^2}} \lambda_{\mu m}^2)^{0.247} \text{ keV} . \tag{5.24}$$

The numerical values where obtained from fits to experimental data points [202] of the suprathermal electron distribution function temperature obtained from measurements of X-ray spectra at 1.06 μm and 10.6 μm, and from measurements of ion data at 10.6 μm. These data points and fits are shown in Fig. 5-13 [left] as black symbols and black lines, respectively.

The value of the intensity used in the determination of the hot electron temperature is taken to be that of the interpolated intensity of the beam at the turning point I_T, thus accounting for collisional losses prior to the wave reaching the turning point and for refraction and diffraction processes in the density profile. Note that when T_{h} is less than the electron temperature T_e at the critical density, no electron source is created and the Resonant Absorption energy is considered to be absorbed directly at the critical density. The scaling laws defined from the experimental data are function of the vacuum intensity of the laser in the focal plane. In order to verify the consistency of our implementation of Resonant Absorption, simulation results at various values of the interaction parameter $I\lambda_L^2$ are compared to the mean hot electron temperature predicted by the experimental data, as demonstrated in the following example.

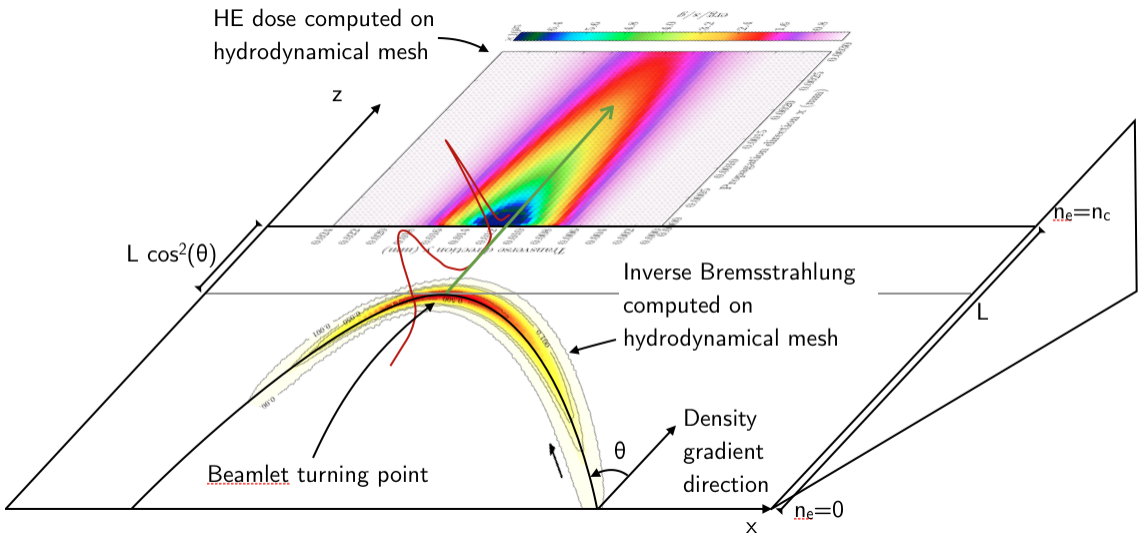

Figure 5-12 – *(color) Illustration of the numerical implementation of the laser-plasma-electron coupling in the case of Resonant Absorption, within a hydrodynamic timestep. The propagation of the PCGO beamlet is computed onto the hydrodynamic mesh. HE sources from RA are computed at the turning point of the wave, and initialized at the critical density surface. The power transferred to the HE beam is removed from the PCGO beamlet at its turning point, and the downstream phase parameters (intensity, thickness) are updated by re-integration of the wave front equation. Finally, the inverse Bremsstrahlung absorption is computed on the Lagrangian mesh, and the HE beam propagation and absorption in the plasma is computed with the ASA model.*

The simulation setup is similar to the picket pulse in shock ignition experiments that is used to set the adiabat of the shell [32]. A spherical plastic target of 470 μm radius is symmetrically irradiated by laser beams in a 100-ps Gaussian picket pulse at 351 nm wavelength. Simulations only vary by the power of the beams so that the interaction parameters $I_{\mathrm{FS}}\lambda_L^2 \in [3.85\times10^{13}; 1\times10^{14}; 2\times10^{14}; 5\times10^{14}]$ Wμm^2/cm^2 correspond to peak intensities $I_{\mathrm{FS}} \in [3.1\times10^{14}; 4.5\times10^{15}]$ W/cm^2. Realistic equation of states are used, radiative transfer computations are enabled and the inverse Bremsstrahlung absorption is included. The flux limiter is set to its usual value for these intensities in Chic, that is a sharp cutoff at $f_L = 0.04$. We measure in our simulation the hot electron temperature at the maximum of the pulse intensity, as a weighted mean:

$$\langle T_{\mathrm{h}}\rangle = \frac{\sum_{i=1}^{N_S} T_{\mathrm{h}}^i P_e^i}{\sum_{i=1}^{N_S} P_e^i}\ , \tag{5.25}$$

where T_{h}^i and P_e^i are the hot electron temperature and HE beam power of the source i, and the number of sources N_S is at most equal to the number of thick rays. For these simulations, we use 18 beams irradiating the target cylinder uniformly, with each beam being composed of 80 thick rays so that there is in the order of 1000 sources per timestep. We assume our beams to be identical to the setup at Omega when using the SG4 phaseplates at 3ω, as described in Sec. 3.3.2. The Results for the suprathermal electron temperature as a function of the interaction

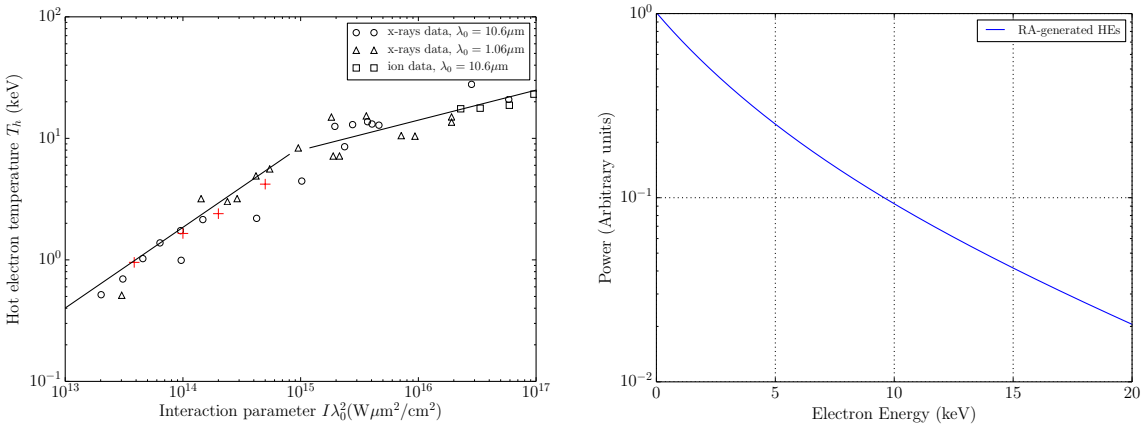

Figure 5-13 – *(color) [left] Scaling of the suprathermal electron distribution temperature T_h for the process of Resonant Absorption as a function of the interaction parameter. Black symbols are experimental data points [95] from experiments at $\lambda = 1.06$ μm and $\lambda = 10.6$ μm. Red crosses are suprathermal temperatures computed in the simulations. The two black lines are the fits for the two interaction regimes. [right] Example of an electron distribution for HEs accelerated by resonant absorption. Results are from the simulation with $I_\mathrm{FS}\lambda_L^2 = 5\times10^{14}$ $W\mu m^2/cm^2$, at the time of maximum laser intensity. The flux-weighted average temperature (5.25) is $\langle T_\mathrm{h,RA}\rangle = 3.5$ keV.*

parameter are illustrated in Fig. 5-13 [left]. We find a good agreement between the predicted temperature $\langle T_\mathrm{h}\rangle$ from the model as a whole compared to the experiments, thus validating our approach to the computation of T_h for the local HE sources. A typical energy distribution of HEs generated by Resonant Absorption as modeled in our approach is given in Fig. 5-13 [right].

5.4 Reduced HE source models from parametric instabilities

The nonlinear processes associated with parametric instabilities, described in Sec. 1.5, cannot be readily modeled at the scales of radiative hydrodynamic simulations. The mechanisms that accelerate electrons to supra-thermal energies are complex and require the use of microscopic-scale kinetic codes. Much as in the case of CBET, a reduced model of parametric instabilities (in the case of TPD and SRS) is needed. Ultimately, for the study of the couplings between plasma dynamics and hot electron dynamics, the quantities of interest are: (i) the amount of energy transferred from the laser beam to forward-propagating energetic electrons (noted F_E), (ii) their characteristic energy T_h, (iii) their direction $\mathbf{e}_\mathrm{HE}$ and angular distribution G_θ with respect to the laser drive, and eventually (iv) the amount of backscattered power R_B. Additional constraints must be considered for the consistency of the model, that are: (1) these quantities must be known at the point of emission of the HE population (usually around the $n_c/4$ region for SRS and TPD), (2) energy transferred from the EM wave to electrons or backscattered light must be accounted for consistently with respect to collisional absorption and Resonant Absorption downstream of the point of HE creation.

We present in this section an approach that yields the desired quantities while satisfying those criteria. Note that the HE source are always created from PCGO beamlets, as those carry the

information on the direction of the wavefield, and defining HE sources from PCGO beamlets allows to update the downstream intensity of the beamlets, thus obtaining a consistent coupling.

5.4.1 TPD-generated hot electrons

The Two-Plasmon Decay instability results from the coupling near the quarter-critical density of an incident transverse wave with two Electron Plasma Waves (see App. 1.5.2.3). The latter can accelerate electrons to rather high energies, although at moderate fluxes. Given an EPW of wavenumber k^{EPW}, the kinetic energy of the trapped electrons is $m_e v^2_{\mathrm{ph,EPW}}(k)/2$, where $v_{\mathrm{ph,EPW}}$ is the phase velocity of the Langmuir wave. The supra-thermal temperature T_{h} of electrons accelerated by EPWs is often approached by this kinetic energy. However, reduced PIC simulations have shown that this is incorrect in the case of TPD, where $T_{\mathrm{h,TPD}}$ is seen to be weakly correlated with $v_{\mathrm{ph}}^{\mathrm{EPW}}$, while scaling linearly with the laser intensity [205]. This was explained in Ref. [206] to be the result of a staged acceleration: thermal electrons are first trapped by Langmuir waves with a small phase velocity in lower density regions and are then accelerated by higher phase velocity waves in higher density regions. The overall picture of HE acceleration by TPD is made even more complex by considering the competition between SRS and TPD, saturation mechanisms such as pump depletion, and by other nonlinear interactions with the plasma such as cavitation. Furthermore, various experiments conducted on Omega [160] have shown the importance of *Common Wave* (CW) driven TPD on the intensity threshold and fraction of accelerated hot electrons (using 2 to 60 laser beams). They notably found that in most cases, the intensity threshold for beams with polarization smoothing was not dependent on the geometry of the beams. The resulting threshold is close to the one commonly used for a single pump wave (given by Eq. (1.163)):

$$I_{\mathrm{th,TPD}}^{\mathrm{inh,CW}} = 8.2 T_e / (L_{n_c/4,\mu m} \lambda_{L,\mu m}) \ \mathrm{PW.cm^{-2}} \ , \tag{5.26}$$

where T_e is the electron temperature in keV, $L_{n_c/4,\mu m} = n/(\partial n/\partial x)|_{n=n_c/4}$ is the density gradient scale length in μm and $\lambda_{L,\mu m}$ the laser wavelength in μm.

Given the variety of processes at play in HE acceleration by the TPD instability, we choose to model TPD-HE sources by simple phenomenological laws, with the aim of obtaining realistic hot electron temperatures, conversion fractions and spatial source parameters. The first two are determined from detailed PIC simulations conducted in plasma and laser regimes of interest to HEDP experiments, that are, plasma temperatures of the order of 1 keV and interaction parameters of the order of 10^{14} Wμm^2/cm^2. Such simulations are presented in Ref. [205], in the framework of TPD driven by a common wave excited by two beams of overlapped intensities ranging from $\eta^{\mathrm{TPD}} = I_\Sigma / I_{\mathrm{th,TPD}}^{\mathrm{inh,CW}} = 1.02$ to $\eta^{\mathrm{TPD}} = 4$ (at $\lambda_L = 351$ nm). Furthermore, we only consider the steady state stage of the interaction, which was reached in their simulation after the time τ_{std} of the order of 10 to 20 ps. This assumption of stationarity is reasonable when considering laser pulses on timescales $t \gg \tau_{\mathrm{std}}$, which correspond to the experimental configurations studied in the next chapter. More specifically, the ignitor pulse used in Shock Ignition is about 200 ps long at peak intensity, i.e. one order of magnitude larger than τ_{std}. Including the temporal dependence of the HE generation in the model requires additional developments, which are left

as future work. For conditions of overlapped laser intensity I_Σ of the order of 10^{15} W/cm^2 and temperatures of the order of the 1 keV, the asymptotic formulations of the forward supra-thermal energy flux and temperature as a function of the drive strength read [205]:

$$\mathscr{F}_{\mathrm{E}}^{\mathrm{TPD}}(\eta) = 2.6 \times 10^{-2} I_\Sigma (1 - \exp(-\sqrt{\eta - 1})) \text{ W/cm}^2 , \tag{5.27}$$

$$\mathscr{T}_{\mathrm{h,TPD}}(\eta) = 15.31 + 17.71\eta \text{ keV} , \tag{5.28}$$

which can be evaluated at $\eta = \eta^{\mathrm{TPD}}$ to obtain F_{E} and T_{h}. A typical energy distribution of HEs generated by TPD as modeled in our approach is given in Fig. 5-15.

It is important to note that these formulations are defined with respect to the total intensity field of the overlapped beamlets I_Σ. For that reason, these functions are labelled as macroscopic drive functions. Because the direction of emission of LPI-generated HEs must be related to the beamlets, that bear the notion of wave $\boldsymbol{k}$-vector, the macroscopic source functions must be translated in terms of beamlet-based HE sources. This is described in details in App. C.3.

The linear theory for the TPD instability predicts that the most favorable configuration, i.e. that maximizes the coupling constant γ_0 (see Eq. (1.158)), corresponds to the EPWs propagating at $\pi/4$ and $3\pi/4$ with respect to the pump wave. Considering the two possible configurations ($\{+\pi/4; -3\pi/4\}$ and $\{+3\pi/4; -\pi/4\}$), the EPWs are mainly generated at $\pm 45°$ from the pump wave, both forward and backward. Consequently, the most probable emission lobes for the hot electrons are at $\pm 45°$ with respect to the laser k-vector, forward and backward of the interaction region. In direct-drive ICF, as many beams compress the target and overlap, several laser beams can share a common-wave, resulting in a more complex emission profile [174]. As an example, for two beams incident at $\pm 23°$ with respect to the density gradient, the main hot electron emissions lobes are at $\pm 0°$ forward and backward, with some components still present at $\pm 45°$ forward and backward. From these observations, the spatial pattern of the HE emission is simplified as follows.

- Considering that the backward HE component propagates away from the target and in a low density plasma, backward HEs are neglected.
- Given that TPD simultaneously excite forward and backward EPWs, it is assumed that there is an equal amount of electrons accelerated in the forward and backward directions. Consequently, for a TPD-HE source i of initial power P^i_{TPD}, the power lost by the beamlet through TPD is $2P^i_{\mathrm{TPD}}$.
- Given the variety of emission lobes induces by shared pump-wave processes, TPD-generated HEs are emitted with an initial aperture $\Theta = \pi/2$ (i.e. $G_\theta^{\mathrm{TPD}} = \mathscr{G}_\theta^{\mathrm{TPD}}(\eta^{\mathrm{TPD}}) = \chi_{B(-\pi/4,\pi/4)}$) and in the direction of the beamlet $\mathbf{k}$-vector.

Moreover, because TPD does not involve backscattered light, $R_B^{\mathrm{TPD}} = \mathscr{R}_B^{\mathrm{TPD}}(\eta^{\mathrm{TPD}}) = 0$.

5.4.2 SRS-generated hot electrons

The definition of the SRS-HE source is more delicate than for TPD. As is shown in Sec. 1.5.2.1, SRS can occur below the quarter-critical density, where the SRS instability is most likely in a

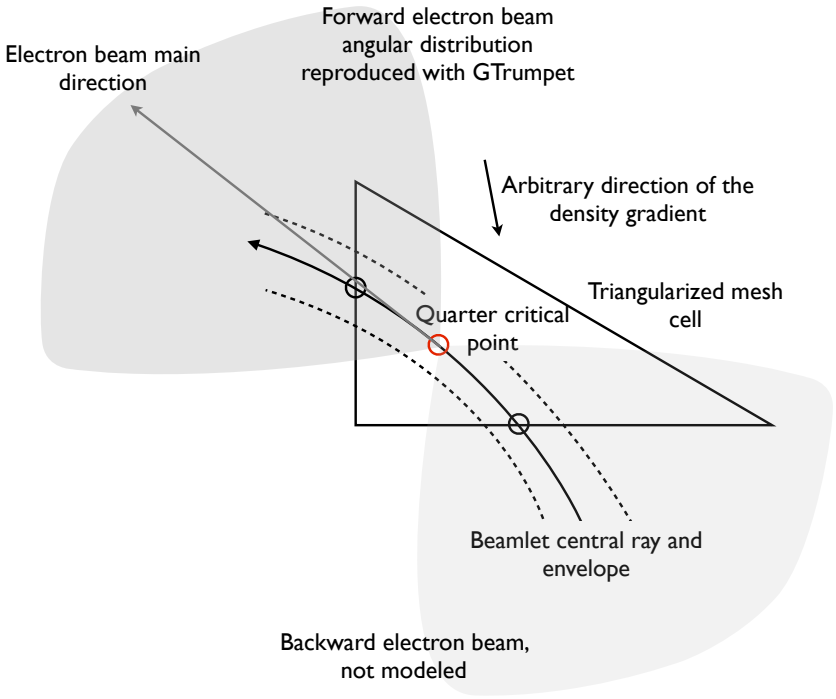

Figure 5-14 – *Schematic representation of the implementation of a hot electron source from a PCGO thick ray (case of the TPD-HE reduced model). Black circles are points where the interpolated density encloses the emission density, represented as a red circle. The initial electron source is represented as grey emission lobes. Only the forward component is propagated with the ASA model.*

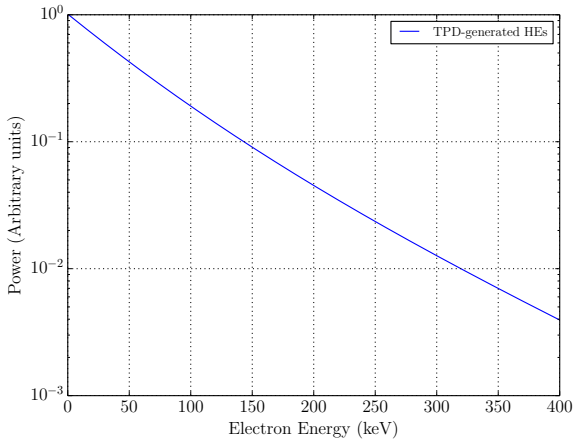

Figure 5-15 – *Example of an electron distribution for HEs accelerated by TPD. Here, the flux-weighted average temperature (5.25) is* $\langle T_{\mathrm{h,TPD}} \rangle = 60\ keV$.

convective regime, and near the quarter critical density, where it is in the absolute regime. In an inhomogeneous plasma, although it appears logical to give precedence to the absolute instability, which intensity threshold is lower, we must note that (i) SRS can become absolute below $n_c/4$ by several mechanisms, e.g. by coupling of the forward EM wave with backscattered light at $n_c/4$ [84, 85] or by local homogenization of the density profile, and (ii) experimental observations show that significant amounts of backward SRS do occur in a extended area below the quarter-critical density.

Characterization of the plasma density where the SRS is generated is usually made using the density dependence of the Raman emission [36]:

$$\lambda_{\mathrm{SRS}} = \lambda_L \left[1 - \sqrt{\frac{n_e}{n_c}(1 + 3k^2\lambda_D^2)}\right]^{-1} . \tag{5.29}$$

In most experiments, two cutoffs are observed in the Raman spectra; a small wavelength cutoff attributed to the Landau damping of the EPWs in a low density plasma, and a long wavelength cutoff corresponding to suppression of SRS in the density range between $n_c/5$ and $n_c/4$. This so-called *Raman gap* [10, 20, 207, 90, 91, 208] may be attributed to a local density profile steepening due to the ponderomotive force (although this effect may be overestimated, as suggested by recent 2D simulations [209, 210]), associated with strong EPWs from the TPD process, or to the coupling with IAWs from the SBS instability.

We can summarize the main features that a local reduced SRS model must account for.

- (I) SRS is taking place before the TPD instability (in a spatial sense) as the pump wave propagates in the plasma. Consequently, it takes precedence in the conversion of laser energy to HEs.
- (II) The SRS-HE emission being delocalized below (and up to) the quarter-critical density, the modeled HE temperature must be conservative, i.e. representative of the highest-energy HEs that can be emitted.
- (III) Regardless of micro-scale mechanisms that cannot be modeled, such as density steepening or the transition from the convective to the absolute instability below $n_c/4$, the intensity threshold must account for the most unstable configuration.
- (IV) The main direction of the scattered wave propagation observed in experiments corresponds to the backward SRS [90, 91, 92]. It is much larger compared to sidescattering [11] and forward scattering [19, 211, 212, 91].

Given these constraints, and underlining the fact that we are seeking a simple reduced model (which may be elaborated further), we propose the following approach:

- (i) The HEs are assumed to be emitted from the plasma density of $n_c/5$. This satisfies the conditions (I) and (II), and is consistent with observations of the SRS cutoff at $n_c/5$ in experiments conducted for inhomogeneous plasma that include the quarter-critical density [208]. Note that laser energy converted to SRS-HE sources depletes the beamlet and reduces the subsequent drive strength for the TPD at $n_c/4$.

- (ii) The intensity threshold for SRS is chosen to be that of the absolute instability at $n_c/4$ for the backward SRS, with the gradient scale length taken at $n_c/5$. Although this yields an artificial threshold, this hypothesis satisfies the conditions (III) and (IV), and is consistent with (i).

- (iii) The supra-thermal temperature is estimated from the phase velocity of the EPWs $v_{\mathrm{ph,EPW}}$ at $n_c/5$. Assuming that there is a gap in HE generation in the $0.2 - 0.25$ interval, and considering that $v_{\mathrm{ph,EPW}}$ for backward SRS is an increasing function of n_e/n_c, this satisfies the conditions (II) and (IV). Furthermore, this is consistent with theoretical works [213] pointing out that the energy of SRS-induced HE is indeed correlated with the phase velocity of the EPW and not with the drive intensity η^{SRS}. The absence of relation between the HE energy and the drive intensity was also observed in experiments [19, 214, 215]. Note that the working hypothesis of a SRS-HE emission at $n_c/5$ is not generic with respect to the large variety of existing LPI regimes.

- (iv) Only backscattering SRS is considered, so that HEs are emitted forward, and scattered light backward, in agreement with the condition (IV). Given the typical temperatures of SRS-HE in the interaction parameters considered here (> 30 keV), those can be considered to be emitted in the principal direction of the pump wave with $\Theta = 0$ in agreement with experimental measurements [214].

Additionally to the aforementioned points, we must choose a flux function that relates the drive strength η^{SRS} to the supra-thermal electron flux. Note that the increase in number of hot electrons as a function of η^{SRS} was highlighted in theoretical works [213]. Considering a flux function of the same form as for the TPD model (5.27), we must choose an asymptotic HE value for $\eta^{\mathrm{SRS}} \to \infty$ and a shape for the function. The asymptotic HE flux is set to 12.5% of the pump intensity, that is the maximum number of forward hot electrons that SRS can drive in a steady state [216]. This can be explained by the fact that (i) a maximum of 50 % of the pump beamlet power can be scattered, (ii) 50 % of the scattered power goes into the scattered EM wave and 50 % into the plasma wave, and (iii) 50 % of the EPW energy can be transferred to the electrons. The shape of the flux function F_e is chosen to be similar to that of TPD, and re-arranged to correspond to experimental measurements [112, 33]:

$$\mathscr{F}_{\mathrm{E}}^{\mathrm{SRS}}(\eta) = 12.5 \times 10^{-2} I_{\Sigma}(1 - \exp[-(\eta^{1/3} - 1)]) \ \mathrm{W/cm^2} \ , \tag{5.30}$$

where the power 1/3 was estimated from experimental data [20, 217]. As mentioned above, the relative intensity η^{SRS} is defined with respect to the absolute instability threshold in an inhomogeneous plasma and at the quarter critical density (see Sec. 1.5.2.1) [86, 87, 88]:

$$(I_{\mathrm{PW/cm^2}})^{\mathrm{inh}}_{\mathrm{abs,SRS}} = 102/(L^2_{\mu m}\lambda_{\mu m})^{2/3} \mathrm{PW/cm^2} \ , \tag{5.31}$$

where the characteristic density scale length $L_{\mu m} = n/\nabla n$ is computed at $n_c/5$. Under the assumptions exposed above, the HE temperature is expressed as:

$$T_{\mathrm{h,SRS}} = m_e v^2_{\mathrm{ph,EPW}}/2 \ , \tag{5.32}$$

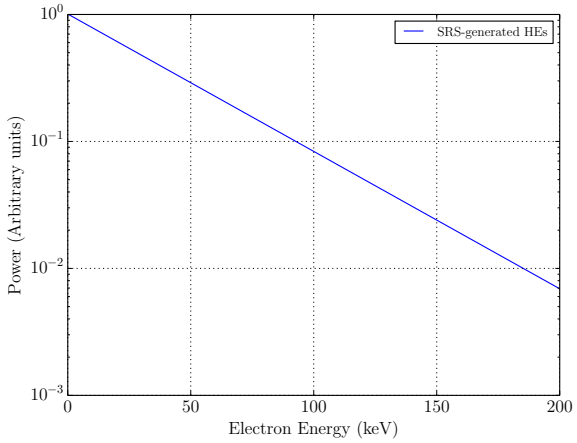

Figure 5-16 – *Example of an electron distribution for HEs accelerated by SRS. Here, the flux-weighted average temperature (5.25) is* $\langle T_{\mathrm{h,SRS}} \rangle = 40$ *keV.*

with the EPW phase velocity $v_{\mathrm{ph,EPW}} = v_{T,e}\sqrt{1+3(k_{\mathrm{pe}}\lambda_D)^2}/(k_{\mathrm{pe}}\lambda_D)$, k_{pe} being the EPW wavenumber. The frequency of backward SRS light emitted at n_e/n_c reads $\omega_{\mathrm{SRS,B}} = \omega_L(1 - \sqrt{n_e/n_c})$, so that the EPW wavenumber reads:

$$k_{\mathrm{pe}} = \frac{\omega_L}{c}\left(\frac{\omega_{\mathrm{SRS,B}}}{\omega_L}\sqrt{1-\frac{n_e}{n_c}\left(\frac{\omega_L^2}{\omega_{\mathrm{SRS,B}}^2}\right)} + \sqrt{1-\frac{n_e}{n_c}}\right) \ . \tag{5.33}$$

Given that the HE emission is fixed at $n_e/n_c = 0.2$, we obtain a simple law for the SRS-HE temperature:

$$T_{\mathrm{h,SRS}} = 34.37 + 1.5T_{e,\mathrm{keV}} \ , \tag{5.34}$$

which gives SRS-HE temperatures in the range of $[35; 42]$ keV for the typical plasma temperatures considered in this work, that is consistent with experimental observations [215, 113]. A typical energy distribution of HEs generated by SRS as modeled in our approach is given in Fig. 5-16. For a SRS-HE source i of initial power P^i_{SRS}, a forward HE beam is initialized in the direction of the pump wave with no initial angular spread. Moreover, it is considered that an equal amount of power is backscattered (i.e. $\mathscr{R}_B^{\mathrm{TPD}} = P^i_{\mathrm{SRS}}$), so that the power loss by SRS for the pump wave is $2P^i_{\mathrm{SRS}}$. This linear dependence between the laser power fraction converted into HEs F_e^{SRS} and the backscattered laser power fraction was observed in experiments, across three orders of magnitudes for [11]. Note that we have assumed for simplicity that $\mathscr{R}_B^{\mathrm{TPD}} \equiv P^i_{\mathrm{SRS}}$, while it is shown in the experiment that $\mathscr{R}_B^{\mathrm{TPD}} \approx 1.25P^i_{\mathrm{SRS}}$.

5.5 Conclusions

We have presented a novel formulation of the Laser-Plasma Interaction model at hydrodynamic scales, that couples the plasma dynamics with linear and nonlinear LPI processes, including the creation and propagation of high-energy electrons excited by parametric instabilities and collective effects. This formulation accounts for laser beam refraction and diffraction, energy absorption due to collisional and resonant processes and hot electron generation due to the

Stimulated Raman Scattering, Two-Plasmon Decay and Resonant Absorption processes. Hot electron transport and absorption by the plasma are described within the Angular Scattering Approximation, adapted to two-dimensional, transversally Gaussian, multigroup Hot Electron beams of arbitrary angular distribution. The HE transport model is compared against reference simulations using the M_1 code. The ASA model is validated for multigroup HE propagation and interaction with homogeneous and inhomogeneous plasmas, in the framework of steady-state and without accounting for quasi-static electric and magnetic fields.

We have proposed three simplified models for computing forward HE fluxes and temperatures from PCGO beamlets for the TPD, SRS and RA processes. This coupled LPI-HE model has been implemented in the Chic Lagrangian radiative hydrodynamic code, and is resolved inline, i.e. within hydrodynamic timesteps. It fully couples the characteristics of the wavefield predicted by the PCGO approach to the LPIs and the plasma dynamics. Because the energy transferred to non-collisional LPIs is substracted from the optical beamlets at their point of occurrence, the coupling between the diverse LPIs, including collisional absorption, is consistent and conserves energy.

Validation and application of the Thetis model to various experimental configurations is presented in the following Chapter, alongside an application to the Shock Ignition scheme.

Chapter 6

Physics of high-intensity laser target interactions in Shock Ignition

The PCGO and THETIS models implemented in the radiative hydrodynamic code CHIC are used to reproduce and interpret experimental measurements conducted on various laser systems and in various interaction geometries. The emphasis is put on the analysis of coupling between Hot Electron beams generated by nonlinear LPIs and the dynamics of the strongest shock that propagates into the target. The model is first validated in the case of energy absorption of short laser pulses in a solid target in Sec. 6.1. It is then tested against experimental results in the planar interaction geometry. We compare the shock timings, HE fluxes and temperatures, and reflectivity measurements in Sec. 6.2. This particular experiment is analyzed in details in order to assess the influence of LPI-generated HEs on the shock dynamics. A similar shock-timing experiment is considered in Sec. 6.3, although in a spherical geometry. The results are compared to the conclusion drawn in the case of the planar target experiment.

The comparisons to experimental data validate the model and provide insights on the role of HE generated by strong laser pulses onto the shock dynamics. Because the HE beams in THETIS are computed from both the optical PCGO model and the hydrodynamics of interaction, this approach is self-consistent and the model can be used predictively. Consequently, we consider in Sec. 6.4 two designs of a Shock Ignition target, and estimate the influence of the LPI-generated HEs on its dynamics.

6.1 Short-pulse absorption experiment on OMEGA

The THETIS model is tested in the case of laser absorption in plasmas, that is the most basic quantity that must be reproduced in hydrodynamic codes. Amongst others, laser absorption defines shock timings, which are crucial for ICF and especially for the SI scheme. Experimental measurements of laser absorption in those intensity regimes are available from experiments conducted on the OMEGA laser facility [218], where a 940 μm diameter spherical plastic target is irradiated by s and p polarized beams in two picket pulses ($\sim$ 100 ps) of 12 J and 18 J per beam, respectively (peak intensity on target $\approx 5 \times 10^{14}$ W/cm^2). The laser absorption fractions measured in the experiment, reproduced in Fig. 6-1 [left], are a laser energy conversion fraction of

$52 \pm 1.5\%$ for the first picket and $72 \pm 1.5\%$ for the second one coming 400 ps later. Hydrodynamic computations reported in Ref. [218] showed that the standard GO approach does not reproduce the correct absorption in both picket pulses simultaneously when considering a constant value of the electron thermal flux limiter f_L [219]. Notably, the absolute errors in absorption fractions are of the order of 13%. The laser absorption in the first picket pulse is underestimated when using the baseline flux limitation value of $f_L = 0.06$. Increasing the flux limiter to $f_L = 0.1$ allows to compensate this effect but it leads to over-estimation of the absorption fraction in the second picket pulse. Such discrepancies can be resolved by using time-varying flux limitation, that is tuned to the specific interaction conditions meant to be modeled. Unfortunately, such an approach masks the physical processes at play and thus hinders the predictive capability of these tools.

In that particular experiment, the LPI features two interaction regimes: the first pulse interacts with a cold target that presents steep density gradients, while the second one interacts with a warm coronal plasma surrounding the target, where density gradients are weaker. The interaction conditions of the first picket pulse are particularly prone to Resonant Absorption, as the steepness of the density gradients makes the wave tunneling to the critical density more likely. Note that the theory derived in App. C.1 for Resonant Absorption shows that plane-waves normally incident onto density gradients are not prone to RA. However, realistic beams as those modeled with PCGO and the splitting method of Sec. 3.2.2, possess wavefield components incident with an angle with respect to the density gradient (see Fig. 3-3 [top-right] for an example of a realistic beam envelope), so that RA can occur. Furthermore, the interaction with the solid target during the first picket pulse makes the description of plasma skin depth important. Both these processes are not readily described by GO methods, but are implemented in the present PCGO and Thetis models.

Hydrodynamic simulations are conducted with the HE transport and sources model (Thetis) and a *unique* flux limiter value, set to $f_L = 0.04$. Within the error bars, the correct laser absorption is reproduced for both picket pulses simultaneously: 53.5% in the first pulse (including 5% of resonant absorption) and 71.7% in the second pulse (including 1.8% of resonant absorption), as is shown in Fig. 6-1 [right]. We note that the corresponding simulations without Thetis but with PCGO only give the laser absorptions of 48.5% and 69.9%. Several conclusions can be drawn from these results:

- The Thetis model is well suited to describe the laser energy absorption and transport due to HE generation, in the case of short and relatively intense laser pulses interacting with both cold and warm plastic targets.

- Resonant Absorption may play a non-negligible role in the interaction of short pulses with steep density profiles, a common situation in laser-target experiments or in SI designs that use adiabat shaping [32]. Notably, the issues of shock timing for the shock ignition scheme may be sensitive to the Resonant Absorption.

- Even without Resonant Absorption, the PCGO model provides better results for the first picket pulse than when using GO rays. This improvement lies in the computation of the plasma skin-depth in the PCGO model and in the consistent treatment of the laser

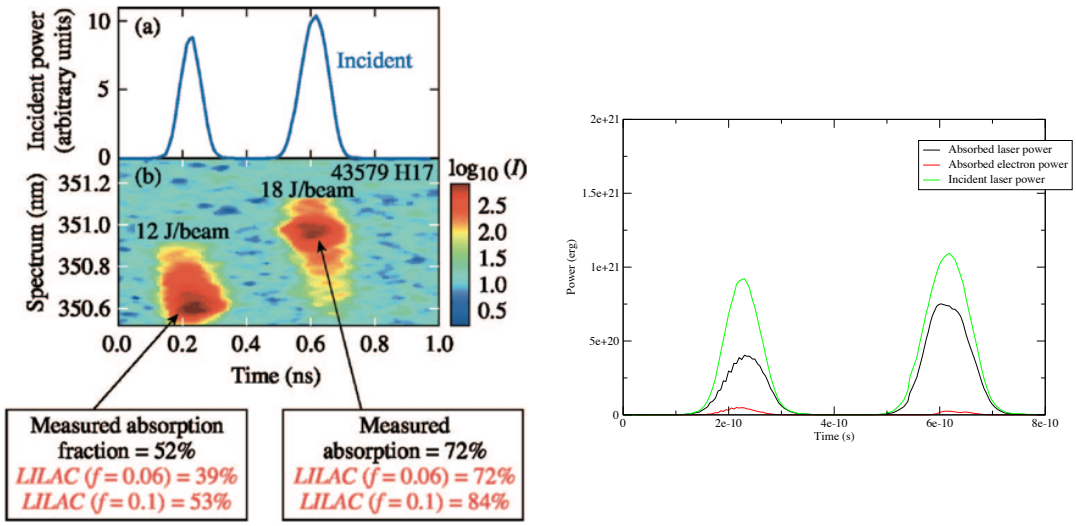

Figure 6-1 – *(color) [left] Measured absorption fraction in the experiment, for the two picket pulses separately. Values reproduced by the 1D code LILAC are shown for various values of the electron flux limiter. Figure reproduced from [218]. [right] Power absorption curves for the absorption experiment, reproduced with the LPI-HE model* THETIS. *The incident power is shown as a green line, the total absorbed power as a black line and the contribution from RA-generated hot electrons as a red line.*

diffraction.

Although the global value of the laser absorption in plasma is well reproduced in this simulation, the detailed value of the energy repartition between collisional and resonant absorption was not measured in the experiment. Therefore, the comparison is not fully conclusive and other conclusions are possible. We now present a more recent experiment which includes measurements of Hot Electron fluxes and temperatures. As such, in addition to the interpretation of the experiment, the validation of the THETIS model can be extended more precisely.

6.2 Planar Shock-timing experiment on PALS

Laser plasma configurations prone to parametric instabilities are now considered. Experimental studies of HE coupling to plasmas in ICF regimes were performed on the Prague Asterix Laser System (PALS) [33], throughout three experimental campaigns. Hydrodynamic shocks subject to LPI-generated HE fluxes were studied by combining measurements of shock breakout timing, laser absorption and HE fluxes with radiative hydrodynamic simulations. The shock timings are obtained with the Streak Optical Pyrometry diagnostic (SOP), that measures the thermal self-emission at the backside of the target (See Fig. 6-2 for the diagnostics configuration of the SOP).

As reported in Ref. [33], early 2D hydrodynamic simulations of the first two experimental campaigns (CHAl and CHCuAl targets, see below) were performed with the codes MULTI2D [220, 221], DUED [222, 223] and CHIC (using the RT model). Good agreement was found for the spatial density and temperature measured in the experiment. However, these codes were not

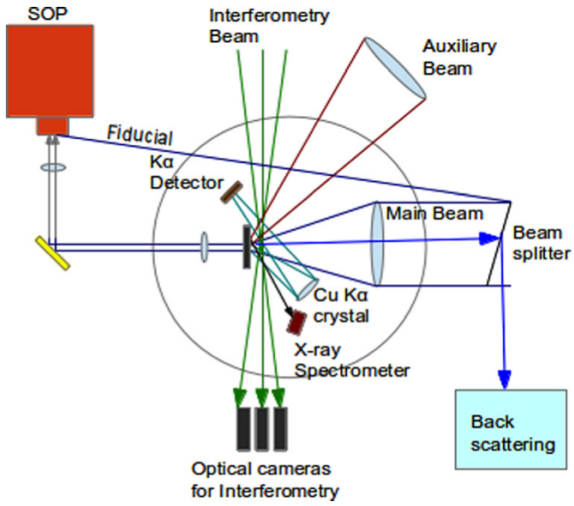

Figure 6-2 – *Schematic of the diagnostics configuration for the campaign on the CHCuAl targets.*

able to reproduce the measured shock timings, unless the laser intensity in the simulations was reduced by 50%, or by a slightly lower number if all experimental uncertainties were stretched to extreme values of 10% (e.g. focal spot size, laser energy, pulse duration...). Even with this intensity reduction, the shock chronometry at high intensities was still underestimated by up to a factor 1.8. Note that in those cases where no phase plates were used, the uncertainties on the focal spot parameters were probably high. The SBS signal in these experiments was estimated to be of a few %, and increased by a factor of 2 without phase plates. Such low reflectivities cannot account for the observed timing discrepancies.

Ultimately, the 2D hydrodynamic simulations with downscaled intensities were used to infer the ablation pressure scaling with the laser intensity, although (i) there were no convincing explanations for the significant discrepancy observed between simulations and experimental results and (ii) the effects of HEs generated by LPIs (which were present and measured) on the plasma dynamics were not accounted for. Although the HE flux estimated in the experiment from the Kα photon flux was found to be less than 1% of the incident laser energy, its impact on the plasma dynamics is not necessarily negligible. Indeed, the role of HEs on the target dynamics was evaluated in [224] using the M_1 model for HE transport in 1D geometry, with a single HE beam of fixed flux and temperature. It was found that such HE fluxes may initiate a backside target expansion, thus delaying the shock breakout time.

The three hydrocodes evoked above all rely on Ray-Tracing models to compute the laser propagation and collisional absorption in plasma. We present in this section experimental and simulation results for the SI campaigns on PALS, with particular emphasis on the latest campaign with the CHTiCu targets.

6.2.1 Experimental setup

The experiment has been conducted by an international team led by D. Batani, with the collaboration of PhD L. Antonelli and the authors of Refs. [225, 226]. The experimental setup,

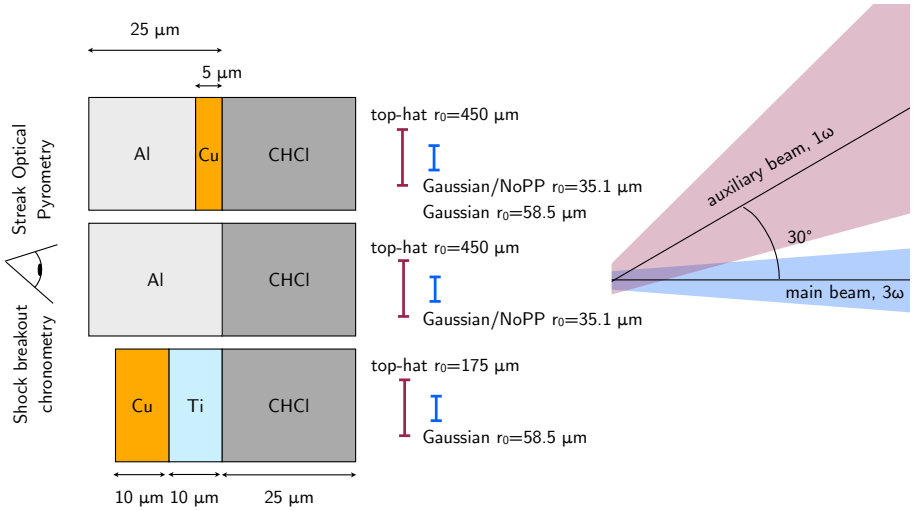

Figure 6-3 – *Simplified schematic illustration of the experimental setup for the three target types.*

that is globally unchanged across the various campaigns, involves a sequence of two laser pulses of approximately 300 ps FWHM duration: a pre-heating low intensity auxiliary beam at 1ω (λ =1315 nm, $\theta = 30°$) and a normally-incident high intensity main beam at 3ω ($I_{FS} \simeq 4 \times 10^{15}$ - 3×10^{16} W/cm^2). Various configurations of heater and interaction beams were investigated, with various multi-layered targets (See Fig. 6-3). We detail here the targets and beam configurations employed in the experiments.

6.2.1.1 Target configuration

A large variety of targets were used across the three SI campaigns on PALS. They all involved an external plastic layer, used to mimic typical ablators used in ICF targets, and various high-Z tracer layers used to measure the hot electron fluxes and temperatures through the Kα emission (See Fig. 6-2 for the diagnostics configuration of Kα diagnostics). In the experiments, three plastic thicknesses were considered (5, 10 and 25 μm) in order to estimate precisely the hot electron parameters as a function of overcoat thickness. Only the cases of the 25 μm ablator targets are considered in the simulations, as the experimental data for these targets are the most abundant. Only one target of each campaign is retained, namely; the CHAl targets, the CHCuAl targets and the CHTiCu targets (in chronological order). In all cases, the plastic is composed of C_8H_7Cl, with the Cl dopant added to allow for x-ray spectroscopy (note that the average ionization state of the warm plastic, as predicted by a Thomas-Fermi model [184, 183], is of $\langle Z \rangle \simeq 4.5$). The tracer thicknesses are, as shown in Fig. 6-3, 25 μm Al (CHAl targets), 5 μm Cu and 20 μm Al (CHCuAl targets) and 10 μm Ti and 10 μm Cu (CHTiCu targets). Considering the target manufacturing process, the uncertainties on tracer thicknesses is considered to be of 2 %, that is negligible in terms of shock timing uncertainty.

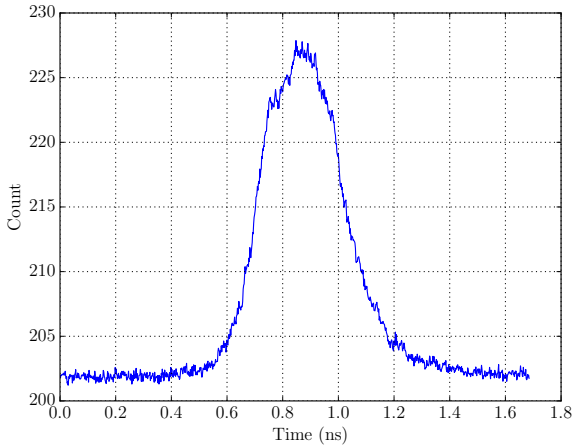

Figure 6-4 – *Temporal profile of the laser pulse (shot #46107), extracted from a slice of the fiducial data on the streak camera, as a function of time (ns) and arbitrary intensity.*

6.2.1.2 Beam configuration

PALS is a kilo-joule Iodine laser composed of two beams: a *main* beam capable of delivering up to 500 J of energy at the fundamental wavelength of 1315 nm and 250 J at 3ω, and an *auxiliary* beam that delivers up to 60 J at 1ω, both in $\sim 250-300$ ps pulses. A large intensity range was considered throughout the experiments, depending on the targets. The main pulse was fired in the preformed plasma with delays Δt with respect to the auxiliary beam; $\Delta t \in [0, 150, 300, 500, 600, 1200]$ ps. It was observed in the experiment that the shock breakout time, measured with respect to the main beam, is independent of this delay. This is also observed in our simulations, so that only the cases of a 300 ps delay are presented. We note that the low change in shock breakout timing and HE flux generation with the delays may notably be related to several points : (i) the 1ω pre-pulse is not very intense, so that the pre-plasma is rather cold and under-dense, (ii) the auxiliary beam duration and the delay between the beams are rather short, and (iii) the interaction beam being at 3ω, it penetrates much deeper into the target and the coronal plasma is less dense with respect to the main beam critical density.

The experimental pulse data used for the CHTiCu target are obtained by picking up a part of laser light from the main beam using a beam splitter, and bringing it to the streak camera as a fiducial. Because the auxiliary beam and the main beam originate from the same oscillator, it is assumed that the measured main beam pulse shape is identical to that of the auxiliary beam. The raw data from shot #46107 is shown in Fig. 6-4. Considering that this is a typical pulse for PALS, this temporal pulse shape is used for all targets and simulations. It is converted to a power (and intensity) profile using the energy and focal spot data for each target type. Note that in all cases, it is considered that 20% of this energy is lost in the wings of the beam, which extend much farther than what is defined as the "focal spot". This assumption is widely used in experiments across various laser platforms. It was notably quantified on the LIL (Ligne d'intégration Laser) and on OMEGA, where the vacuum intensity profiles are well characterized.

In all cases, the auxiliary beam is focused through a lens of focal length $F = 100$ cm and diameter $D = 15$ cm ($F_{\#} = 6.67$), and the main beam through a lens with $F = 60$ cm and

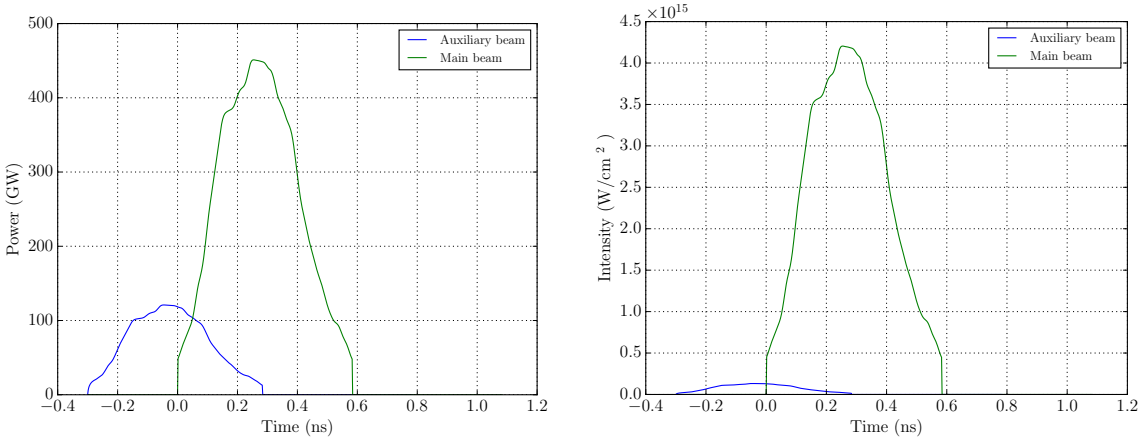

Figure 6-5 – *(color) Auxiliary and main beam pulse profiles, in [left] power (in GW), and [right] vacuum intensity in the focal plane (in W/cm^2), as a function of time (ns).*

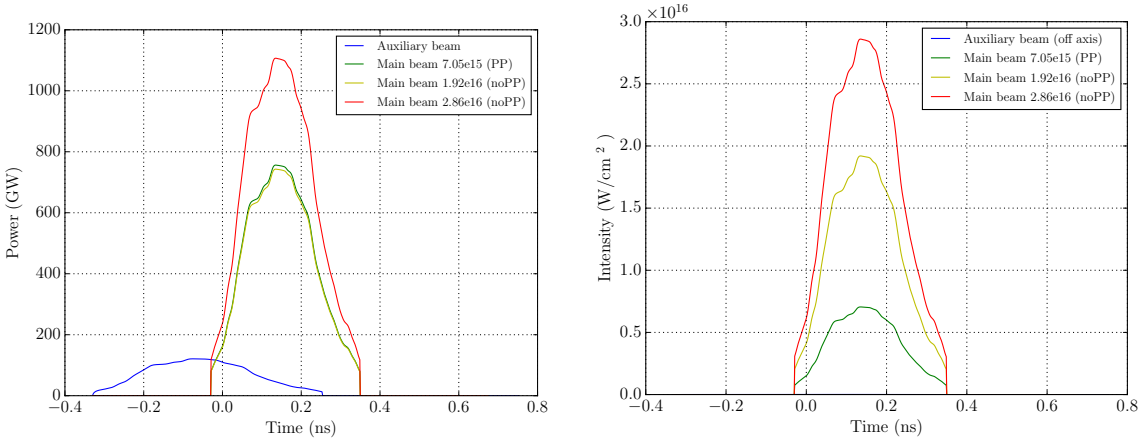

Figure 6-6 – *(color) Auxiliary and main beam pulse profiles considered for the CHAl and CHCuAl targets. [left] power profiles (in GW) and [right] vacuum intensity in the focal plane (in W/cm^2), as a function of time (ns). The auxiliary beam intensity is off scale, at $2 \times 10^{13}\, W/cm^2$.*

$D = 29$ cm ($F_\# = 2.07$). Depending on the targets, different phase plates have been used.

CHAl and CHCuAl targets The auxiliary beam was smoothed by a RPP producing a top-hat spot of 900 μm diameter, so as to produce a quasi-1D plasma expansion with respect to the main beam. For low intensity shots ($< 1 \times 10^{16}$W/cm^2), the main beam was equipped with phase plates producing a Gaussian focal spot of 100 μm FWHM ($r_0 = 58.5$ μm radius at 1/e). For high intensity shots, the phase plate was removed, thus creating a highly peaked laser profile (with intense hot spots), that is approximated by a Gaussian profile of 60 μm FWHM ($r_0 = 35.1$ μm radius at 1/e). More details about the beam parameters for these targets can be found in [225]. The detailed energy and pulse profile for each shot being unknown, we use a similar shape as shot #46107 with a 300 ps total duration (instead of 300 ps FWHM), so that $\sim$ 300 J of energy at 3ω gives close to 9×10^{15}W/cm^2 peak intensity with the phase plates and close to 3×10^{16}W/cm^2 peak intensity without the phase plates (as communicated in [225, 33]). We

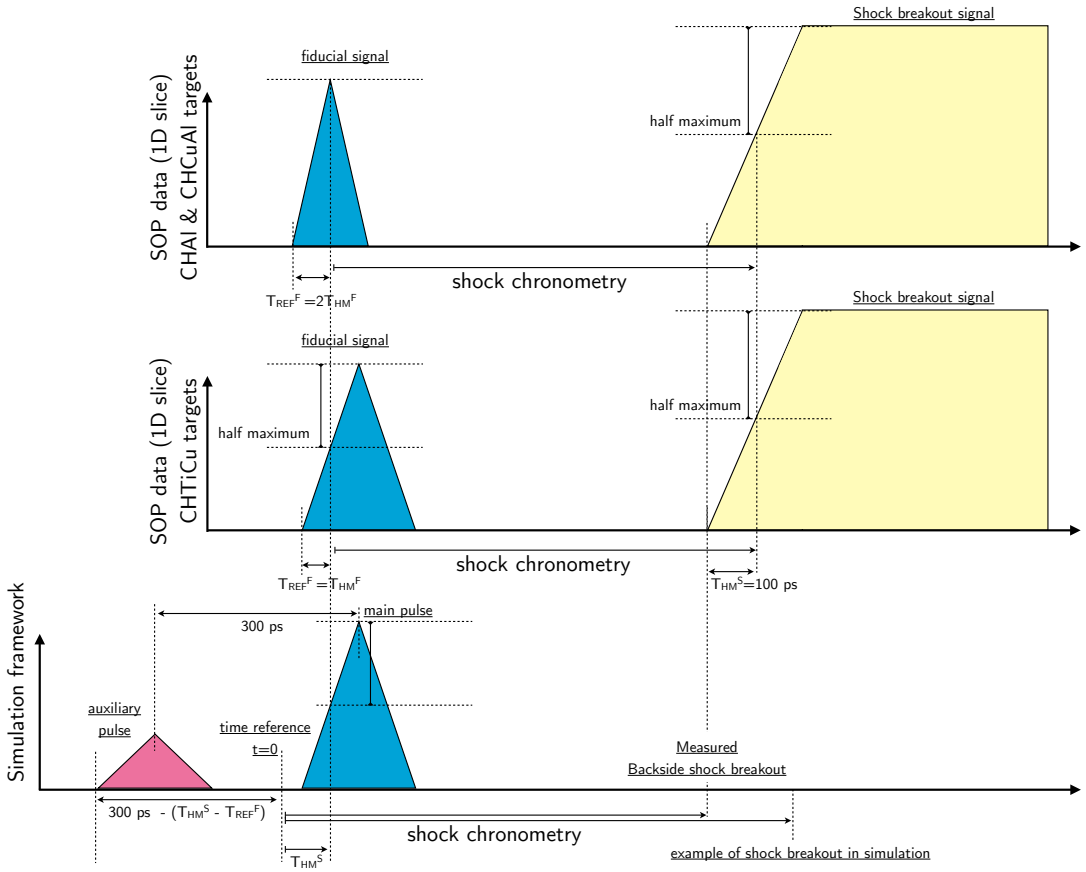

Figure 6-7 – *Schematic illustration of the definition of the shock breakout chronometry, in the convention adopted in [33] (CHAl and CHCuAl targets) and for the latest campaign (CHTiCu targets). The bottom schematic illustrates how this definition relates to the simulation framework.*

choose to study 4 different intensities; 7.06×10^{15} W/cm^2 (CHCuAl targets, with phase plate), 1.92×10^{16} W/cm^2 (CHCuAl targets, no phase plate), 2.86×10^{16} W/cm^2 (CHAl targets, no phase plate) and 4.17×10^{15} W/cm^2 (CHTiCu targets, with phase plate). The resulting pulse shapes are shown in Fig. 6-6.

The reference time $t = 0$ is defined with respect to the reference frame used for measurements of shock breakout chronometry, the latter being defined as the delay between the main pulse maximum intensity and half maximum on the SOP signal. In the simulations, it is directly the breakout time that is measured, i.e. what corresponds to the foot of the SOP signal. It was found in the SOP data that there is a 100 ps delay between the foot and the half maximum of the signal, across experiments. The time delay between the foot and the main pulse maximum is here of 130 ps. These timing considerations are illustrated in Fig. 6-7. For these targets, the resulting delay between the foot of the auxiliary pulse and the reference time is of 330 ps.

CHTiCu targets The case of the CHTiCu targets is more constrained, as the experimental data were available directly from the experimental team, and hence it is the one we discuss in most details. The auxiliary beam is smoothed by a RPP producing a top-hat spot of 350 μm diameter, that is smaller than in the previous experiments. The aim of the spot size reduction,

and hence intensity increase of the heater beam, is to create a coronal plasma with a larger gradient scale length comparable to SI conditions. The main beam is equipped with phase plates producing a Gaussian focal spot of 100 μm FWHM ($r_0 = 58.5$ μm radius at 1/e). The measured total energies for the main and auxiliary beams, averaged over the experiments for these targets, are of 193.6 ± 7.1 J and 52.0 ± 3.2 J, respectively.

Removing the background noise from the raw data, smoothing the temporal profile and normalizing the data so that the pulse contains the same energy as experimentally measured yields the power temporal profile of the main and auxiliary pulses, as shown in Fig. 6-5 [left]. Using the focal spot information given above, the vacuum focal plane intensity profiles are also obtained, as shown in Fig. 6-5 [right]. Contrary to the other targets, the shock breakout chronometry in these experiments is defined as the delay between the time of half maximum (rise side) of the main pulse and the time of half maximum on the SOP signal. For the pulse shape presented here, the half maximum rise time is of 100 ps, which is the same as the time of half maximum for the SOP signal. Consequently, for those targets, the shock breakout time can be measured between the foot of the main pulse and the foot of the SOP signal. The time axis used in the simulations (Fig. 6-5) is defined with respect to the foot of the main pulse. For these targets, the delay between the foot of the auxiliary pulse and the reference time is of 300 ps.

6.2.2 Experimental and simulation results

6.2.2.1 Additional diagnostics

The latest experimental campaign on PALS, on the CHTiCu targets, was completed by the measurements of the integrated laser reflectivity using arrays of mini calorimeters (on the 4π of the target chamber). This additional diagnostic improves the data concerning the laser absorption and better constrains hydrodynamic simulations. Reflectivity measurements were performed in separate shots, giving an averaged value of $\mathcal{R} = 25 \pm 10\%$. This value includes the reflected laser energy and the scattered SBS and SRS light. Note that the backscattered energy from the SRS is estimated to be 0.1 % in the lens cone. Furthermore, the HE population was estimated more precisely in this campaign, by reproducing the measured Kα emission from the high-Z tracers using Monte Carlo (MC) simulations of electrons propagating in a stationary target [227], with the GEANT4 and PENELOPE codes [228, 229]. For the CHTiCu target, the experimental data are reproduced with HE temperatures of 25.3 ± 7.6 keV and energy fluxes carrying 0.7 ± 0.4 % of the laser energy. These are in good agreement with other data, e.g [226] (PALS, $T_\mathrm{h} \approx 50 \pm 10$ keV, CHCuAl targets), [215] (OMEGA, $T_\mathrm{h} \approx 30$ keV), and [230] (PIC calculations, $T_\mathrm{h} = 20 - 40$ keV).

6.2.2.2 Simulation results

Simulations of the experiments for the three multilayer targets are conducted with the CHIC code using the multiscale THETIS model and compared to GO-based models, systematically using nominal experimental parameters: measured laser energy, focal spot and temporal pulse shape, and nominal target configuration. The flux limiter value was set to $f_L = 0.04$, in agreement with the absorption results obtained in Sec. 6.1. Of particular interest to this study are (i) the *shock strength* $\mathcal{S} = P_d/P_u$, that is the ratio of the downstream pressure P_d to the upstream pressure

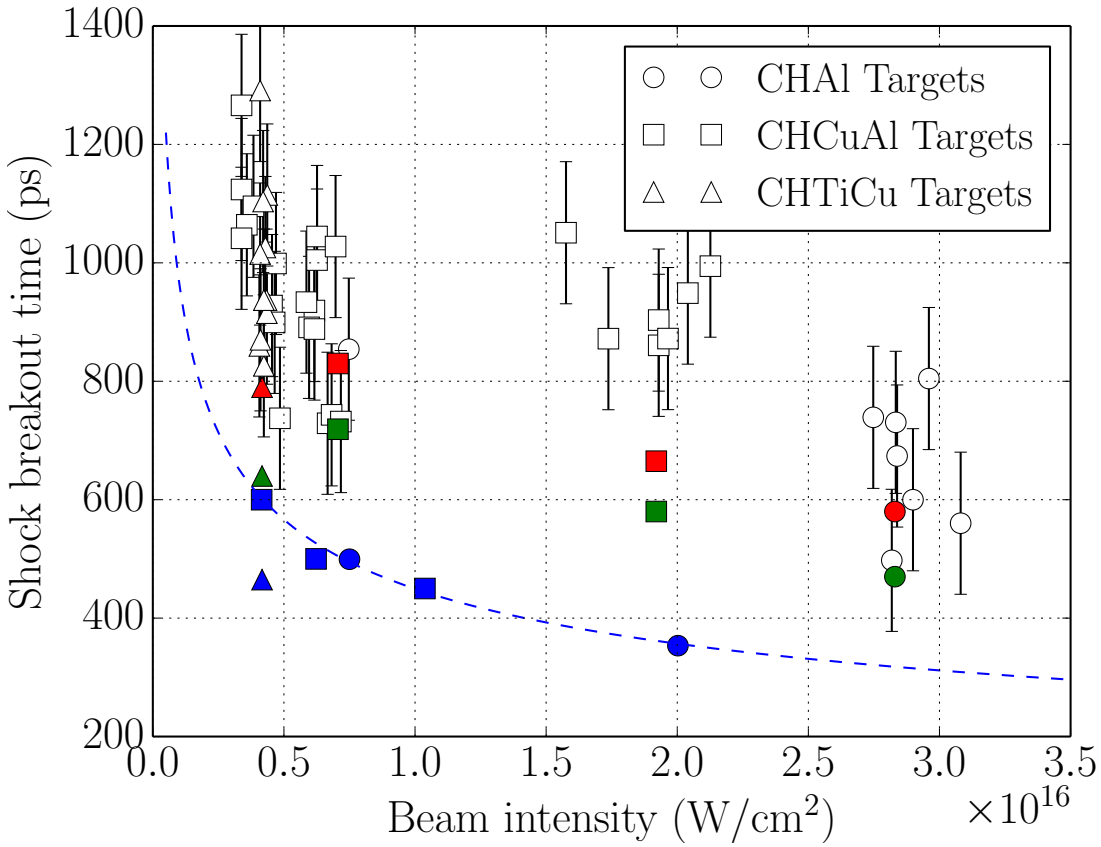

Figure 6-8 – *(color) Shock breakout times for various targets, as a function of laser intensity. Open symbols are experimental points. Colored symbols are from hydrodynamic simulations: with GO in blue [51], with the present* Thetis *model in red and with PCGO only in green. The standard scaling obtained when considering that* $P_{\text{shock}} \propto I^{2/3}$ *and* $v_{\text{shock}} \propto P^{1/2}$ *is shown as dashed blue lines. CHAl and CHCuAl targets are similar, thus following a comparable scaling.*

P_u, (ii) the plasma pressure downstream of the shock P_d and (iii) the ablation pressure $\mathcal{P}_A$. The ablation pressure is defined as the product of the ablated mass rate and the ablation velocity. It can also be compared to the plasma pressure where the material velocity in the laboratory frame is zero. We use the latter definition for simplicity, for which we consider only the plasma parameters in the vicinity of the main beam axis.

A comparison of experimental and simulation results for the shock chronometry is presented in Fig. 6-8. The x-axis corresponds to the intensity used in numerical simulations. Simulations with laser absorption modeled with the standard GO package predict a shock breakout time much shorter than the experimental timings, by up to a factor of 2.5 depending on the targets and intensities. Results from the Thetis model are significantly closer to the experimental data for all intensities and targets. This is explained by the modified target dynamics from HE preheat and by a more precise collisional absorption modeling. We discuss the processes at play by detailing the case of the CHTiCu targets, where the temporal pulse profile and laser energy are well characterized, and the experimental data contain the most precise measurements of the laser reflectivity, HE temperature and HE fluxes. The information concerning the HE fluxes and temperatures from RA, SRS and TPD, predicted by the simulation is given in Fig. 6-9.

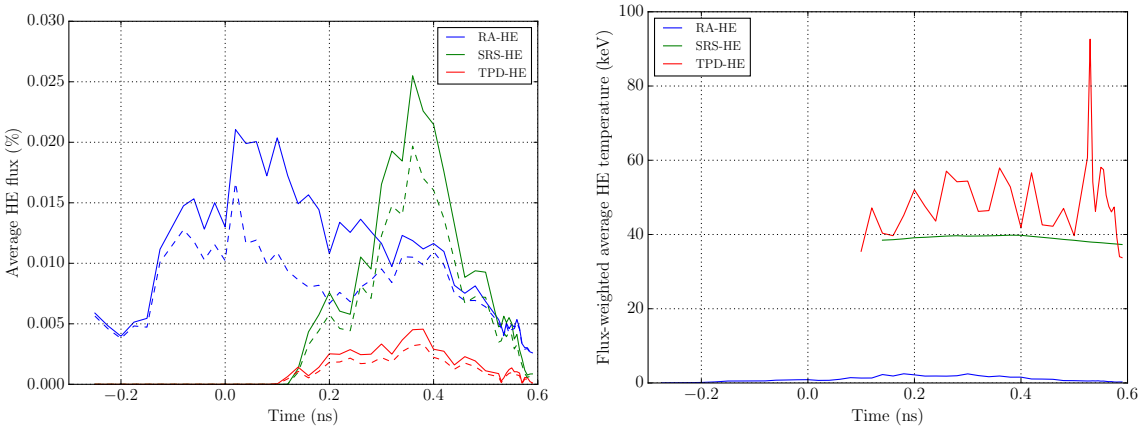

Figure 6-9 – *(color) Parameters of the HE beams predicted by* THETIS *in the simulation of the CHTiCu target. [left] Total HE fluxes for beams originating from RA, SRS and TPD processes, with emitted fluxes in solid lines and absorbed fluxes in dashed lines. [right] Suprathermal temperatures of the HE sources from RA, SRS and TPD, averaged over the sources and weighted by their respective flux.*

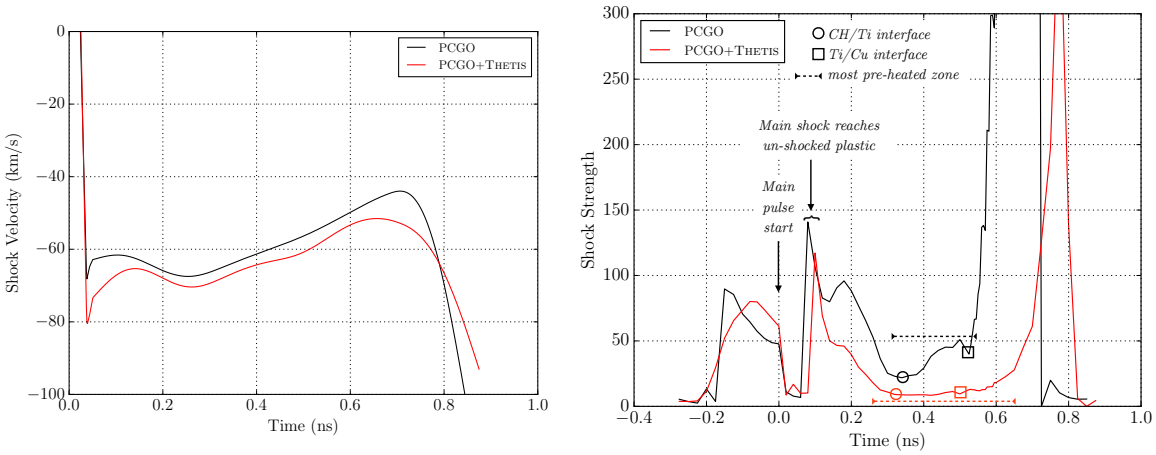

Figure 6-10 – *(color) Parameters of the shock driven by the main interaction beam, as a function of time (ns); [left] shock velocity (km/s) and [right] shock strengh. Black lines are simulations results without hot electrons and red lines with hot electrons. Negative velocities indicate that the shock is propagating toward the target's backside.*

Resonant Absorption The earliest HEs originate from the Resonant Absorption, which is seen to accelerate electrons throughout the auxiliary and main pulses, with a burst of electrons when the main beam is turned on. These low temperature HEs (a few keV at maximum) contribute at the early stage of the main pulse interaction: the resonantly absorbed energy at the critical surface increases the shock pressure and velocity, and advances the shock breakout time by 30 ps when compared to a simulation with HEs but without RA. This velocity increase can be seen in the shock velocity profiles in Fig. 6-10 [left], before the time when the SRS and TPD-HE are generated, i.e. before 0.1 ns. Furthermore, even though the shock is not far from the critical density at this time, the low-temperature RA-HE barely preheat the material in front of the shock (see Fig. 6-12), and there is no visible decrease in the shock strength, as illustrated in Fig. 6-10 [right] (in the $[0; 0.1]$ ns interval). Overall, the RA-HE fluxes are rather low (compared to

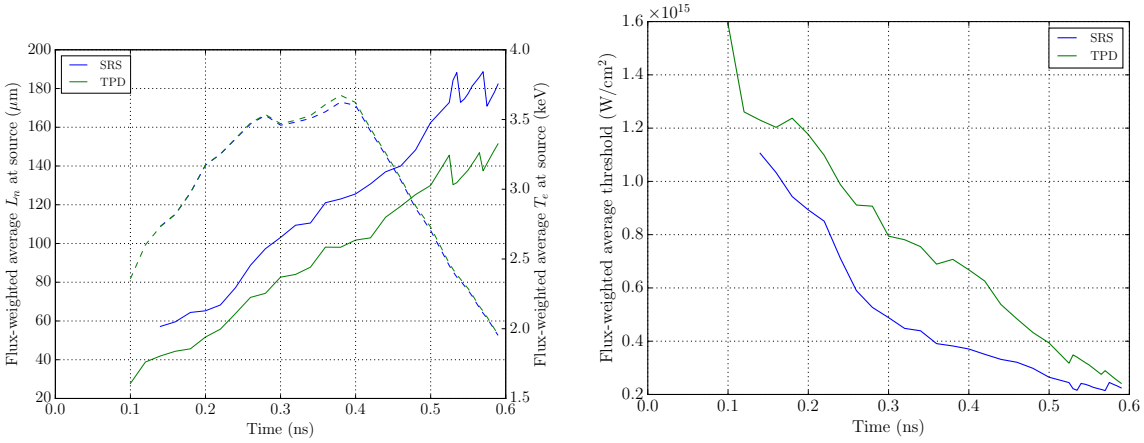

Figure 6-11 – *[left] Flux-weighed average (same formalism as in Eq. (5.25)) over the N_{HE} HE sources of the gradient scale length $\langle L_n \rangle = \sum_{i=1}^{N_{\mathrm{HE}}} P_e^i L_n^i$ (solid lines) and thermal electron temperature $\langle T_e \rangle = \sum_{i=1}^{N_{\mathrm{HE}}} P_e^i T_e^i$ (dashed lines) at the point of HE source creation. [right] Flux-weighed average over the HE sources of the local intensity thresholds for the SRS and TPD instabilities.*

typical RA-HE fluxes), that is a consequence of the main interaction beam being incident on the target at normal incidence. As in Sec. 6.1, RA can only occur from oblique rays, which are not orthogonal to the target. But the contribution of such rays is relatively low.

SRS and TPD Starting around the main pulse half maximum rise time, SRS- and TPD-HEs are generated, with higher fluxes for SRS and higher temperatures for TPD (see Fig. 6-9). Although the coronal plasma created by the auxiliary beam has a rather moderate temperature ($T_e \sim 1-2$ keV), the main beam rapidly heats it, reaching 2.5 keV when SRS and TPD thresholds are crossed and reaching a maximum of 3.5 keV around the peak of the main pulse (see the averaged plasma temperature at the point of HE emission in Fig. 6-11 [left]). We recall that the SRS and TPD thresholds for an inhomogeneous media (Eqs (5.31) and (5.26)) notably depend on the gradient scale length, and also, for the TPD threshold, on the temperature. Considering the temperatures here and considering that the gradient scale length is longer for the SRS threshold (defined at $n_c/5$) than for the TPD one (at $n_c/4$, as illustrated in Fig. 6-11 [left]), the SRS threshold is below the TPD threshold throughout the main pulse interaction, as is detailed in Fig. 6-11 [right].

These hot electron beams gradually pre-heat the bulk of the target both in front and behind of the shock to a few tens of eV, as illustrated in Fig. 6-12. The integrated average temperatures and fluxes of SRS and TPD-generated HE beams are of 40.7 keV and 1.65% of the laser energy. These values are slightly above the data modeled by the Monte-Carlo calculations, although the tracers in the target may not be sensitive enough to electron populations of higher energies: higher Z tracers such as Platinum would be required to properly assess the contribution from $\sim$ 50 keV electrons. Given the high supra-thermal temperature, a non-negligible flux of HEs reaches the rear target interface. These HEs heat the backside to several eV, thus initiating a slow plasma expansion that delays the shock breakout (see the rear target interface in Fig. 6-12).

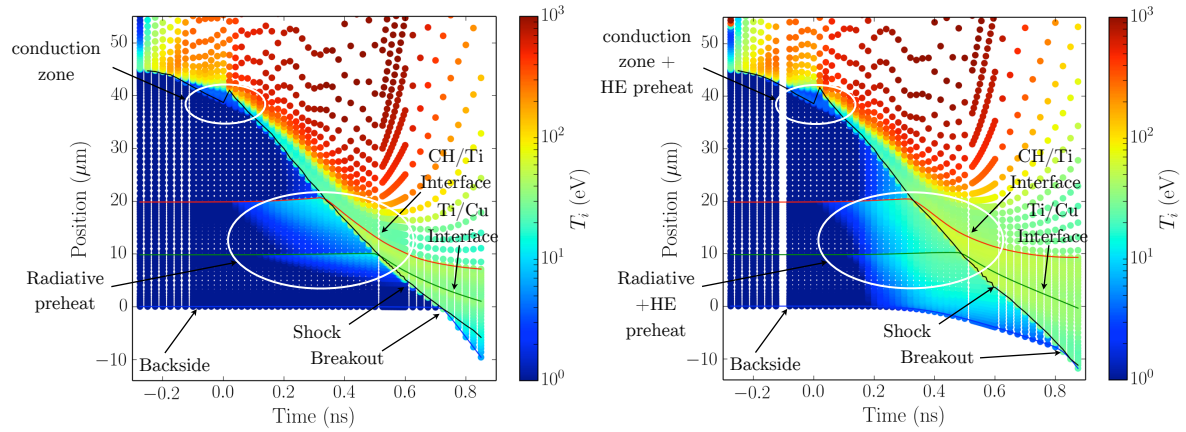

Figure 6-12 – *Log-scaled electron temperature (eV) of the CHCuAl target, as a function of time and depth in the target (along the laser axis), [left] without HEs and [right] with HEs. Similar pre-heating behaviors are observed for all targets. The solid blue line indicates the target's rear interface and the solid black line is the location of the shock. The solid green and red lines show the locations of the Cu/Ti and Ti/CHCl interfaces, respectively. Fields are averaged along the laser axis on a thickness of* ~ 20 *μm (check that)*

For that reason, simulations with PCGO and without HE fortuitously reproduce similar shock timings: the lower shock velocity is compensated by the absence of backside target expansion.

Shock dynamics The impact of target bulk preheat on the shock propagation can be evaluated from the Rankine-Hugoniot relations. For an ideal gas, the latter relate the hydrodynamic quantities across the shock:

$$\mathcal{S} = \frac{P_d}{P_u} = \frac{(\gamma+1)\rho_d - (\gamma-1)\rho_u}{(\gamma+1)\rho_u - (\gamma-1)\rho_d} \,, \tag{6.1}$$

where the subscripts u and d indicate quantities upstream and downstream of the shock, respectively. Considering a strong shock ($P_d \gg P_u$) one can obtain the well-known relation:

$$\frac{\rho_d}{\rho_u} = \frac{\gamma+1}{\gamma-1} \,, \tag{6.2}$$

where γ is the adiabatic constant. Using the mass flux conservation across the shock, the shock velocity can be related to the pressures and densities upstream and downstream of the shock:

$$\rho_u^2 u_s^2 = \frac{(P_d - P_u)\rho_d \rho_u}{\rho_d - \rho_u} \,, \tag{6.3}$$

where u_s is the shock velocity. In the limit of a strong shock, the shock velocity reads:

$$u_s = \sqrt{\frac{P_d(1+\gamma)}{2\rho_u}} \,. \tag{6.4}$$

The HE preheat in the dense tracers is slow enough that it occurs at nearly constant density, although it raises the plasma pressure. Assuming constant shock strength with and without HEs,

Eq. (6.4) shows that this pressure increase implies an increase in shock velocity. This velocity increase is observed in the simulations, which also implies that any shock strength decrease due to HEs is compensated by an increase in the post-shock pressure P_d. Note that for a homogeneous material, $\rho_d > \rho_u$ so that a mono-energetic HE beam preheats more the downstream material than the upstream material and the pressure increase du to the HEs $\Delta P_d > \Delta P_u$, so that according to (6.3) the shock velocity increases whatever the shock strength is.

The density jump across the shock $r = \rho_d/\rho_u = u_s/u_d$ can be related to the upstream plasma parameters from the equation of energy conservation across the shock, which yields:

$$r = \frac{(\gamma+1)\rho_u u_s^2}{(2\gamma P_u + (\gamma-1)\rho_u u_s^2)} \ . \tag{6.5}$$

Injecting this expression into Eq. (6.1) gives:

$$\mathcal{S} = \frac{2\rho_u u_s^2 - (\gamma-1)P_u}{(\gamma+1)P_u} \ . \tag{6.6}$$

To a first order, the local density decrease due to HE preheat is rather low ($\sim 10\%$, see Fig. 6-13 [top]) while the upstream pressure increases significantly (up to a factor 20 in the Aluminum, as illustrated in Fig. 6-13 [bottom]). Considering that the shock velocity, of the order of 60 km/s, is increased by 5% with HEs, the corresponding shock strength is reduced by a factor 5 from the preheating effect. This is the order of magnitude of what is measured in the simulation for the CHTiCu target (see Fig. 6-10 [right], in the region labelled as "most pre-heated zone"). As was noted above, the shock strength decrease and the velocity increase imply that the post-shock pressure is higher. Indeed, it is seen in the simulations that the shocked plastic pressure is about 20 Mbar higher with HEs than without, reaching up to 125 MBar.

Energy balance The integrated reflectivity found in the simulation is 28%, in good agreement with the experimental measurements of $25 \pm 10\%$. Those results using the THETIS model exhibit a significant improvement over standard GO-based approaches, simultaneously matching data from hydrodynamics, hot electrons and reflectivity measurements. Thus the model fits all constrains at the same time: the global laser absorption, the hydrodynamics of the shock and the HE preheat.

Ablation pressure The ablation pressure, shown in Fig. 6-14, reaches up to 65 MBar and does not change significantly with or without HEs. This is not surprising in this case, given that (i) the HE flux is rather low and (ii) those HE have a sufficiently high temperature to go through the ablation front, and hence contribute weakly to the ablation pressure. Furthermore, both simulations with and without HEs predict similar amounts of collisional absorption (absorption fractions are summarized in Tab. 6.1). The ablation pressure is discussed further in the following paragraphs.

Intensity scaling of the shock velocity and strength The results of all simulations (and all targets) for the laser absorption and averaged HE source parameters are reported in Tabs. 6.1 and 6.2. As expected, the LPI-HE fluxes increase with the laser intensity, the collisional absorption contribution decreases, averaged HE temperatures from TPD-HE increase and averaged SRS-HE

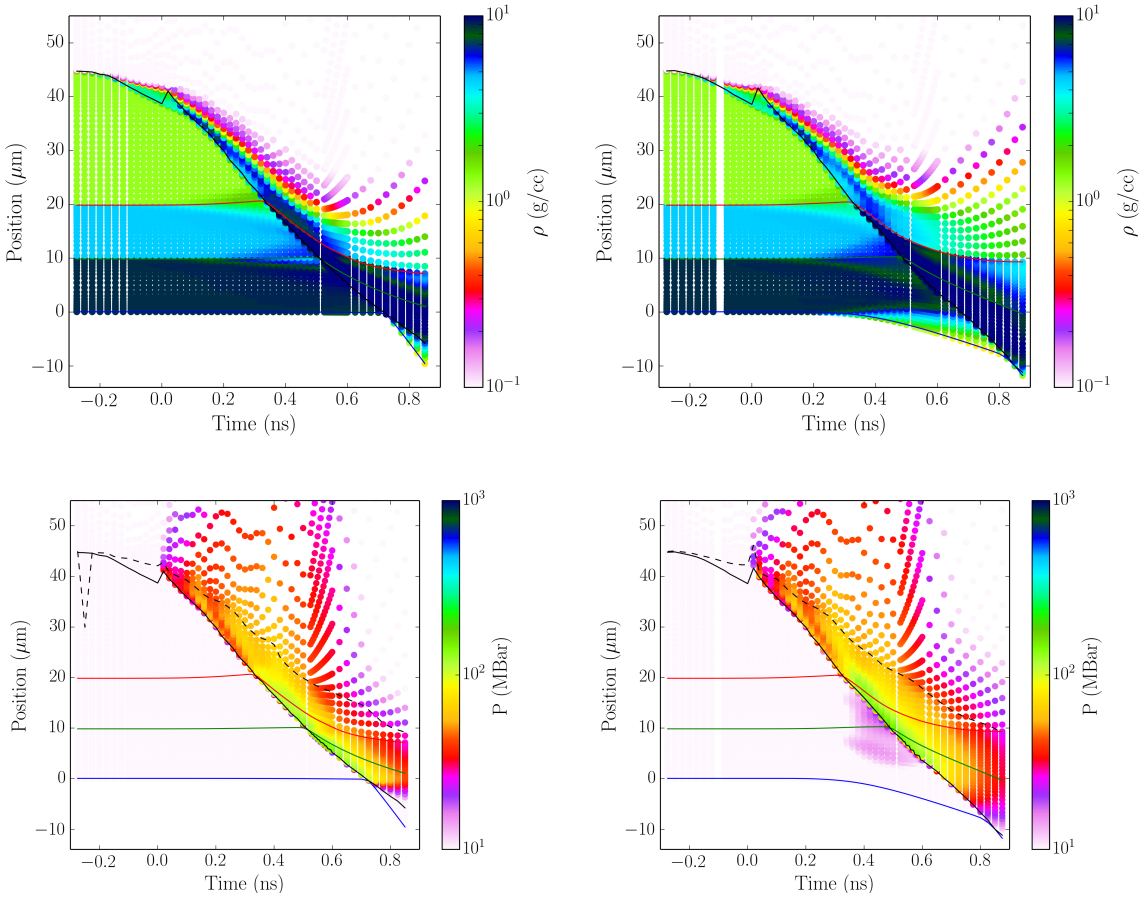

Figure 6-13 – *Log-scaled [top] density (g/cc) and [bottom] pressure (MBar) in the CHTiCu target, as a function of time and depth in the target (along the laser axis), [left] without HEs and [right] with HEs. The dashed line on the bottom figures indicate the position where the material velocity in the laboratory frame is zero, that is the point where we define the ablation pressure. Fields are averaged along the laser axis on a thickness of* ~ 20 *μm. Each dot indicates the position of a Lagrangian mesh cell.*

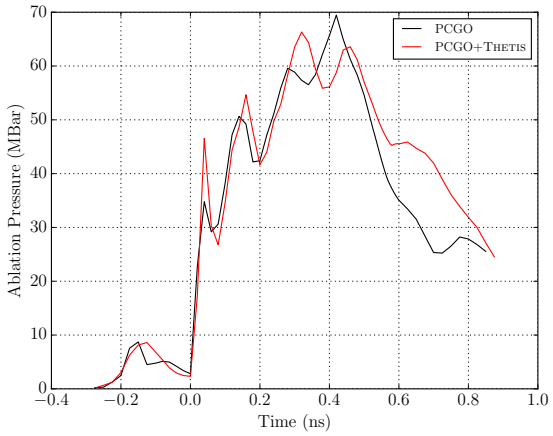

Figure 6-14 – *Ablation pressure (MBar) as a function of time (ns) for the CHTiCu target. The red solid line indicate a simulation with HEs and the black solid line a reference simulation with PCGO but without HEs.*

Target	$I_{\text{peak,W/cm}^2}$	$\mathcal{F}_{\text{RA}}$	$\mathcal{F}_{\text{TPD}}$	$\mathcal{F}_{\text{SRS}}$	$\mathcal{F}_{\text{col}}^{\text{HE}}$	$\mathcal{R}^{\text{HE}}$	$\mathcal{F}_{\text{col}}^{\text{REF}}$	$\mathcal{R}^{\text{REF}}$
CHTiCu	4.17×10^{15}	1.26 %	0.21 %	0.96 %	50.1 %	27.2 %	50.5 %	29.5 %
CHCuAl	7.05×10^{15}	1.34 %	0.37 %	1.62 %	33.1 %	43.2 %	35.0 %	45.0 %
CHCuAl	1.92×10^{16}	1.82 %	0.73 %	3.27 %	23.9 %	49.6 %	25.2 %	54.8 %
CHAl	2.86×10^{16}	1.09 %	0.95 %	4.01 %	19.4 %	53.6 %	21.5 %	58.5 %

Table 6.1 – *Repartition of the laser energy between processes, for the four intensities considered. Note that because* 20% *of the laser energy is counted in the wings of the beams and that the backward HE beams are not counted in the total reflectivity, the total on one line adds up to* $(80\% - \mathcal{F}_{\text{TPD}})$*, to the rounding error. Results [left] of the separator are for simulations with HEs, and [right] of the separator are for simulations without HEs. The various contributions are ; the laser energy converted into forward HEs (those detected by the Kα diagnostics) by processes of RA, TPD and SRS (*$\mathcal{F}_{\text{RA}}$*,* $\mathcal{F}_{\text{TPD}}$ *and* $\mathcal{F}_{\text{SRS}}$*), the laser energy converted into collisional absorption (*$\mathcal{F}_{\text{col}}^{\text{HE}}$*), and the reflected light, which includes a contribution from backward SRS equal to* $\mathcal{F}_{\text{SRS}}$*. The total laser energy reads* $\mathcal{R}^{\text{HE}} + 2\mathcal{F}_{\text{TPD}} + \mathcal{F}_{\text{SRS}} + \mathcal{F}_{\text{RA}} + \mathcal{F}_{\text{col}}^{\text{HE}} + \mathcal{F}_{\text{wings}} = 1$.

Target	$I_{\text{peak,W/cm}^2}$	$\langle T_{\text{h,RA}} \rangle$	$\langle T_{\text{h,TPD}} \rangle$	$\langle T_{\text{h,SRS}} \rangle$
CHTiCu	4.17×10^{15}	1.2 keV	47.6 keV	39.2 keV
CHCuAl	7.05×10^{15}	1.6 keV	53.3 keV	39.7 keV
CHCuAl	1.92×10^{16}	2.0 keV	64.2 keV	41.0 keV
CHAl	2.86×10^{16}	2.6 keV	69.8 keV	41.8 keV

Table 6.2 – *Averaged supra-thermal temperatures of the forward HE beams, for the four intensities considered. The contribution of each process is detailed, with HE generated from RA, TPD and SRS (*$\langle T_{\text{h,RA}} \rangle$*,* $\langle T_{\text{h,TPD}} \rangle$*, and* $\langle T_{\text{h,SRS}} \rangle$*). The brackets denote a time average of a flux-weighted average on the HE sources:* $\langle T_{\text{h}} \rangle = \int_0^{T_{\text{pulse}}} \sum_{i=1}^{N(t)} P_{\text{h}}^i(t) T_{\text{h}}^i(t) \text{d}t / \int_0^{T_{\text{pulse}}} \sum_{i=1}^{N(t)} P_{\text{h}}^i(t) \text{d}t$*, where* $P_{\text{h}}^i(t)$ *and* $T_{\text{h}}^i(t)$ *denote the power and mean energy of HE source* i *at time* t*, respectively.*

temperatures are relatively unchanged. Extending the conclusions drawn from the CHTiCu target, it is expected that the higher the HE flux and temperature, the more the shock strength will decrease and the more the shock velocity will increase. This is observed in the simulation as illustrated in Figs. 6-15 [left] and [right]. In the highest intensity case, the shock velocity in the plastic increases by up to a factor 1.4, solely from the presence of LPI-generated HEs. Similarly, the shock strength is reduced by up to a factor of 22 in the plastic. This drastic shock strength reduction is mainly caused by a significant increase of the target preheat by the SRS-HEs, that are roughly at the same temperature as in the lower intensity cases, but which flux is greatly increased.

Intensity scaling of the ablation pressure Standard ablation pressure scaling laws are usually established for steady-state regimes dominated by the inverse Bremsstrahlung absorption. Because the laser pulses used here are rather short, these laws could be out of their validity

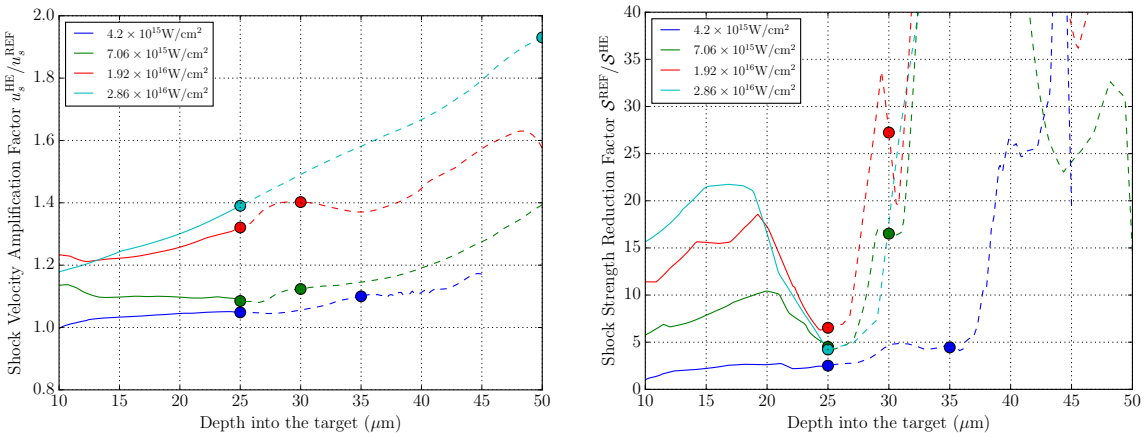

Figure 6-15 – *Modification of the shock parameters due to the presence of LPI-generated HEs. [left] Shock velocity amplification factor u_s^{HE}/u_s^{REF} and [right] shock strength reduction factor $\mathcal{S}^{REF}/\mathcal{S}^{HE}$, as a function of the shock depth into the target, for all targets and intensities. Plain lines and dashed lines indicate the approximate regions where the shock is in the CH and in the tracers, respectively. The colored circles indicate the approximate location of the CH/tracer or tracer/tracer interfaces.*

Target	$I_{peak,W/cm^2}$	$\eta_{abs,A}^{HE}$	$I_{peak,W/cm^2}^{abs,A}$	$\eta_{abs,A}^{REF}$	$I_{peak,W/cm^2}^{abs,A}$
CHTiCu	4.17×10^{15}	51.7 %	2.16×10^{15}	50.5 %	2.11×10^{15}
CHCuAl	7.05×10^{15}	34.9 %	2.46×10^{15}	35.0 %	2.46×10^{15}
CHCuAl	1.92×10^{16}	26.7 %	5.12×10^{15}	25.2 %	4.85×10^{15}
CHAl	2.86×10^{16}	21.7 %	6.21×10^{15}	21.5 %	6.14×10^{15}

Table 6.3 – *Peak absorbed intensities for all simulated targets. The absorption fraction that is considered to participate in the ablation pressure is estimated by $\eta_{abs,A} = \mathcal{F}_{RA} + \mathcal{F}_{col} + 0.25(\mathcal{F}_{SRS} + \mathcal{F}_{TPD})$. Results left of the separator are from simulations with PCGO and without HEs.*

domain. However, it can reasonably be assumed that the ablation pressure scaling remains proportional to the factor $(\eta_{abs,A} I_{15})$ to a certain power, where $\eta_{abs,A}$ is a laser absorption fraction. Considering that only the laser energy deposited in the vicinity of the critical density contributes to the ablation pressure, $\eta_{abs,A}$ includes the contributions from the collisional and Resonant Absorption, as well as the SRS and TPD absorption fractions (that is the energy deposited by SRS- and TPD-HE beams in the vicinity of the critical density and up to the ablation front). The resulting peak absorbed intensities are summarized in Tab. 6.3. The presence of LPI-HEs is expected to have a minor effect on the ablation pressure, as the $\eta_{abs,A}$ factors are rather similar between simulations with and without HEs. The ablation pressure and their amplification due to HEs are shown in Fig. 6-16, for all target types. As expected, the ablation pressure increases with the laser intensity, and the effect of HEs is rather limited. Note that the presence of tracers in the target hinders the analysis of the target dynamics, so that these conclusions are drawn for times when the shock is still in the plastic (so that no reflected shock from the plastic/tracer interface affects the ablation pressure).

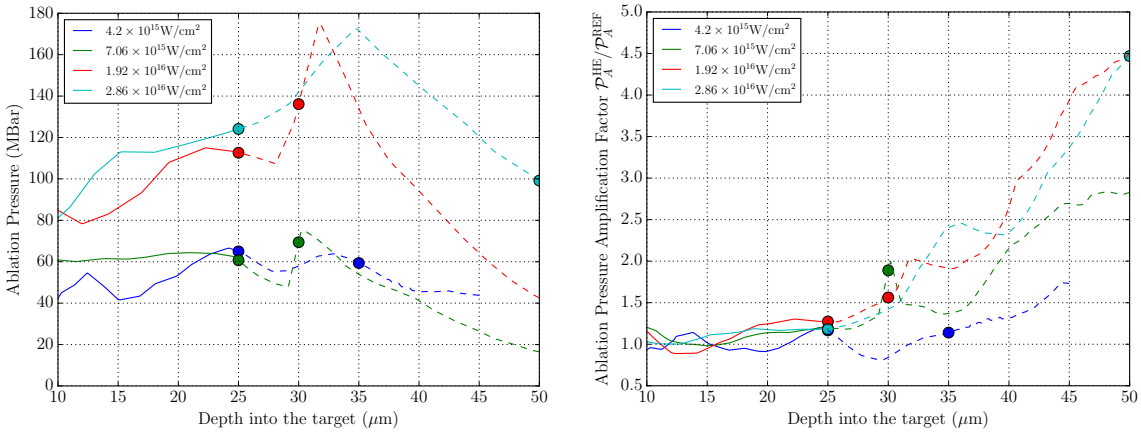

Figure 6-16 – *(color) [left] Ablation pressure across the various targets and intensities (MBar) for the cases with HEs. [right] Ablation pressure amplification factor* $\mathcal{P}_A^{\mathrm{HE}}/\mathcal{P}_A^{\mathrm{REF}}$ *induced by the presence of LPI-generated HEs. Both figures show results as a function of shock depth into the target. Plain lines and dashed lines indicate the approximate regions where the shock is in the CH and in the tracers, respectively. The colored circles indicate the approximate location of the CH/tracer or tracer/tracer interfaces.*

6.2.2.3 Summary of interpretation of the SI experiments on PALS

The Shock Ignition campaigns on PALS have allowed to measure experimentally ; shock timings, laser absorption fractions, HEs fluxes and temperatures. Detailed numerical simulation with the THETIS model have shown that the latter is able to reproduce simultaneously all experimental observables. This is a significant improvement over the capabilities of standard GO-based hydrocodes, that allows to constrain the simulation in a consistent way.

The interpretation of the experiment using the THETIS model has highlighted the role of LPI-generated HEs for short and intense laser pulses interacting with a planar target. Limiting our analysis to the plastic ablator, it is found that these HEs greatly reduce the shock strength while increasing its velocity. Both effects are a consequence of a bulk target pre-heat, that increases the upstream target pressure and temperature at almost constant density. Overall, the material pressure downstream of the shock remains higher with HEs than without, the low shock strength being compensated by the increased upstream target pressure. Because the targets considered in the experiments are short, these are almost entirely preheated. Considering an infinite CH bulk, the low strength high pressure shock would eventually reach the low pressure cold material, and acquire a much higher shock strength than without HEs. In the framework of Shock Ignition, the increase in shock velocity is not expected to be an issue, as shock timings can be experimentally determined by trial and error. However, issues of shock strength and shock pressure are crucial to the scheme. Before we can assess these effects, the THETIS model must be validated in a spherical configuration. That is the object of the following section.

6.3 Spherical Shock-timing experiment on OMEGA

6.3.1 Experimental setup

The PCGO+THETIS model is now applied for interpretation of the recent Spherical Strong-Shock (SSS) campaign realized on the OMEGA laser system in a spherical geometry [112, 113]. 60 frequency tripled beams ($\lambda_L = 351$ nm) are uniformly focused onto a spherical target of Ti-doped plastic covered by a plastic ablator. The peak overlapped intensity in the experiment reached values up to $\sim 6 \times 10^{15}$ W/cm^2. The laser pulse constituted of a 1 ns low intensity foot, followed by a 1 ns high intensity plateau. The parametric instabilities develop when the main laser pulse interacts with a warm coronal plasma, generating Hot Electrons into the target. The plasma ablation drives a strong shock, which is propagating inside the sphere and is modified by hot electrons. The shock strength was evaluated from the time of x-ray flash generated in the moment of shock collapse in the target center. Indeed, the shock converging in the target center heats a small volume of radius < 10 μm up to several hundred eV, causing the Titanium tracer to emit a short burst of x-rays. These were detected by x-ray framing cameras (XRFC) [231] and streaked x-ray spectrometers (SXS) [232]. The laser light backscattered from the target was analyzed by FABS (Full Aperture Backscatter Station), which gives time-resolved spectra in the wavelength ranges corresponding to SBS, SRS and TPD. In addition to the FABS measurements, scatter calorimeters and near-backscatter imagers were used to infer the overall energy absorption. The Hot Electron generation was characterized by the hard x-ray emission in the 10-700 keV energy range. Diagnostics for the time-resolved x-ray emission were quickly saturated at high intensities, so that only time-integrated x-ray fluxes and temperatures can reliably be inferred, using time-integrated image plate diagnostics.

Several target sizes were used, from 410 μm to 600 μm diameter. Series of shots were conducted with and without Smoothing by Spectral Dispersion. The shots without laser temporal smoothing demonstrated a significant increase of measured HE fluxes (up to a factor of 5), and a moderate increase in measured HE temperatures. As evoked in Sec. 3.1, the stationary speckles in shots without SSD are more prone to the growth of nonlinear LPIs.

Hydrodynamic simulations presented in Ref. [112] have been conducted using a CSD model to simulate HE propagation. The HEs were emitted from a plasma corona in a 2π cone with a time-varying flux and temperature prescribed from the experimental data. These parameters were not related to the laser absorption model. The simulations presented in Ref. [112] show that generation of HEs increases the shock velocity. The ablation pressure was found in the simulation by matching the shock collapse timing. It was obtained in runs without hot electrons by changing the value of the flux limiter, disregarding the detail of where the energy that drives the shock comes from. This is a severe approximation. The HEs may preheat the target both behind and beyond the shock front, and contribute to the shock dynamics in a different way than collisional laser absorption does. In particular, the previous section dedicated to the PALS experiment shows that LPI-generated HEs have a sufficient energy to propagate beyond the shock in the plastic, and that these HEs do not contribute significantly to the ablation pressure but accelerate the shock by preheating the upstream plasma. We note that the PALS and OMEGA experiments are comparable, as (i) the laser intensities are similar, and (ii) the total areal densities ρr of

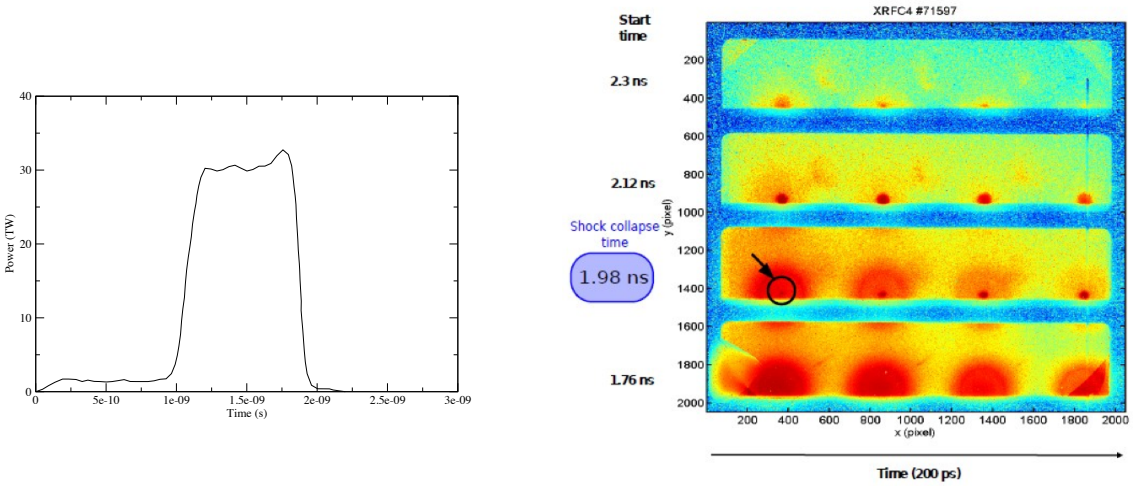

Figure 6-17 – *(color) [left] Laser pulse data and [right] XRFC data for shot #71597, showing the convergence time at 1.98 ns. [[113], W. Theobald].*

the targets are also comparable, with $\rho r \sim 16$ mg/cm^2 for the CHTiCu target on Pals and $\sim$26 mg/cm^2 for a whole radius of the spherical targets considered here. For these reasons, the conclusions presented in Ref. [112] that HEs increase the ablation pressure is disputable. We present simulation results for the SSS campaign using the Thetis model in Chic, which suggest an alternative interpretation of the collected data.

6.3.2 Simulation framework

The Spherical Strong Shock experimental campaign demonstrated the effect of SSD on the HE generation and the shock dynamics. As we have presented in Sec. 3.4, the PCGO model implemented in Chic allows to reproduce the dynamic pattern of the SSD speckles. However, the Thetis model does not account for the transient phase in the determination of fluxes and temperatures of HE sources. Therefore, our Chic simulations with the reduced SSD model and Thetis reproduce the hydrodynamic smoothing and the beam contrast of the experiment, but do not reproduce the HE flux reduction from the non-stationarity of speckles. In the present simulations, the shots without SSD were assimilated to runs with HEs and the shots with SSD to runs without HEs.

As the intensity pattern on the spherical target surface was fairly uniform, and the beams were focused to the target center, the laser-plasma interaction is modeled in 2D *mono-mode* pseudo-cylindrical geometry, whereby mono-mode we mean that only radial displacements are considered. The full configuration is that of a sphere irradiated by 60 beams with a total power P. The equivalent 2D planar configuration, only relevant to the laser module, is that of a cylinder with the mass of the sphere, irradiated by 18 beams separated by 20° (the smallest angular separation between coplanar beams on Omega) of individual intensities equal to that of one Omega beam. This approach ensures that the incident laser intensity per unit of mass is well reproduced between the 2D planar and 2D cylindrical configurations. The hydrodynamic and radiative computations are conducted in 2D-axisymmetric configuration in order to account for the convergence effects of the target density and of the shock. Note that only a 40° slice of the

	e^- transport	<-	HE	->	collisional absorption	total absorption	shock collapse time
case		$\mathcal{F}_{\text{RA}}$	$\mathcal{F}_{\text{TPD}}$	$\mathcal{F}_{\text{SRS}}$	$\mathcal{F}_{\text{col}}$	$\mathcal{F}^{\text{abs}}$	t_c
GO	$f_L = 0.03$	-	-	-	42 %	42 %	2.39 ns
GO	$f_L = 0.04$	-	-	-	45 %	45 %	2.26 ns
GO	$f_L = 0.05$	-	-	-	49 %	49 %	2.16 ns
GO	$f_L = 0.06$	-	-	-	57 %	57 %	2.07 ns
PCGO	$f_L = 0.04$	-	-	-	51.8 %	51.8 %	2.225 ns
PCGO	$f_L = 0.05$	-	-	-	56.7 %	56.7 %	2.19 ns
PCGO	non-local	-	-	-	69.5 %	69. %	1.95 ns
PCGO+THETIS	$f_L = 0.04$	1.37 %	0.78 %	5.33 %	48.43 %	55.91 %	1.98 ns
PCGO+THETIS	non-local	0.92 %	0.94 %	5.46 %	48.97 %	56.29 %	1.9 ns

Table 6.4 – *Laser energy absorption fractions obtained in various simulations. [Top] results are from simulations with the GO-based Ray Tracing model [233] and [bottom] results from the PCGO and PCGO+THETIS model. The absorbed energy fraction is defined as* $\mathcal{F}^{\text{abs}} = \mathcal{F}_{\text{TPD}} + \mathcal{F}_{\text{SRS}} + \mathcal{F}_{\text{RA}} + \mathcal{F}^{\text{HE}}_{\text{col}}$. *The total energy in the laser pulse is of 24.9 kJ. The measured experimental values are* $t_c = 1.98$ *ns and* $\mathcal{F}_{\text{abs}} = 55 \pm 5$ *%.*

cylinder is simulated, that is sufficient for computing the 2D interaction processes with PCGO and THETIS, while the rest of the sphere is reconstructed using the symmetry considerations. The details related to the pseudo-cylindrical formulation of PCGO and THETIS are given in App. B.3.

6.3.3 Experimental and simulation results

The experimental data are compared to numerical simulations. Two main constrains were imposed: reproducing the correct absorption fraction and shock collapse timing. Such simulations allow us to infer the pressure of the shock, similarly as in the PALS experiment Sec. 6.2. Early simulations with the CHIC code using the standard GO-based Ray Tracing [PhD A. Vallet [233]] have shown that it is not possible to reproduce simultaneously the absorption fraction and the shock timing without HEs, as illustrated in Tab. 6.4 [top].

The particular case of shot #71597, that is amongst the highest intensity, is studied [113]. The target is 430 μm in diameter and the plateau intensity is $\sim 5 \times 10^{15}$ W/cm^2 (the pulse data is shown in Fig. 6-17 [left]). Results from the XRFC diagnostic, shown in Fig. 6-17 [right], show that the shock reaches the target center at $t_c = 1.98$ ns. The measured integrated laser absorption is $\mathcal{F}_{\text{exp}} = 55 \pm 5\%$, with a HE energy fraction estimated at $\sim 8\%$ in the $50 - 100$ keV range (these values are averaged over all shots [113]).

We conduct various axisymmetric simulations using the target and laser pulse data with and without the LPI-HE model. The results are also compared to simulations using Geometrical Optics. The results for shock convergence timings and absorption fractions are summarized in Tab. 6.4. The simulation using the LPI-HE model yields $t_c = 1.98$ ns, with 6.11% of the laser energy converted into HEs at an average temperature of 54 keV for the TPD-HEs (varying from

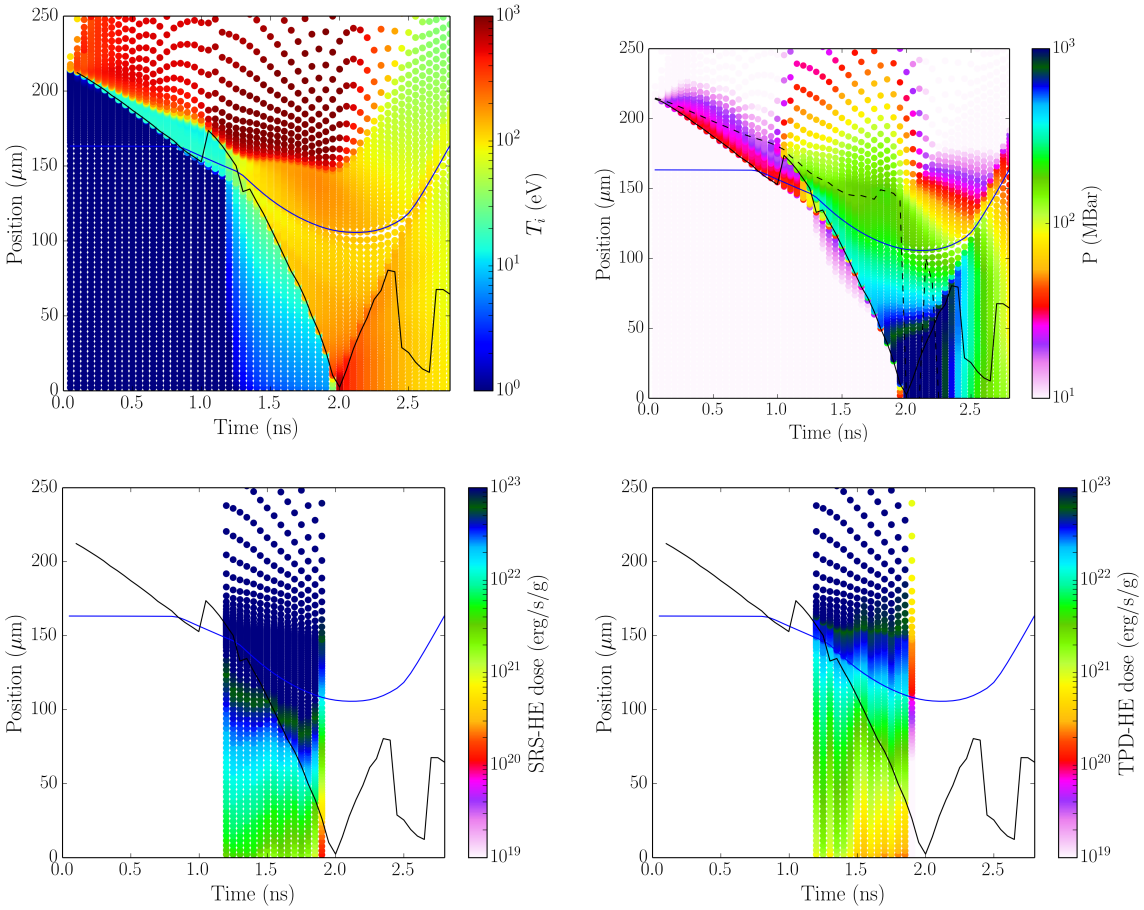

Figure 6-18 – *(color) Log-scaled [top-left] ion temperature (eV), [top-right] pressure (MBar), [bottom-left] SRS-HE dose (erg/s/g) and [right] TPD-HE dose (erg/s/g), as a function of time and target radius (the simulation being monomode, the fields presented here are identical for any cylindrical angle θ). The solid black line indicates the position of the strongest pressure discontinuity. The solid blue line indicates the position of the CH/CHTi interface. The dashed line on the [top-right] figure indicates the position where the material velocity in the laboratory frame is zero. Each dot indicates the position of a Lagrangian mesh cell.*

40 to 80 keV), 41 keV for the SRS-HEs, and an additional 1.4% of HEs produced by resonant absorption at 0.7 keV. The overall laser absorption in the simulation is of $\mathcal{F}_{\text{HE}} = 55.9\%$, with 48.4% of collisional absorption. Shock collapse timing, overall absorption, laser to hot electron conversion and supra-thermal temperatures simultaneously match the experimental data within the error bars. Results are compared to a simulation without HEs, with the flux limiter adjusted so that absorption matches the experimental data. Results using PCGO and without HEs yield an absorption fraction of $\mathcal{F}_{\text{noHE}} = 56.7\%$ with a flux limiter $f_L = 0.05$. The corresponding convergence time is $t_c = 2.19$ ns. Note that the simulation with Thetis was conducted with $f_L = 0.04$, in agreement with the results from both the absorption experiment on Omega (Sec. 6.1) and the planar target experiment on Pals (Sec. 6.2). As can be seen in Tab. 6.4, only the simulation with PCGO and HEs matches successfully the measured shock convergence timing t_c and absorption fraction. The correct shock timing may eventually be reproduced with GO

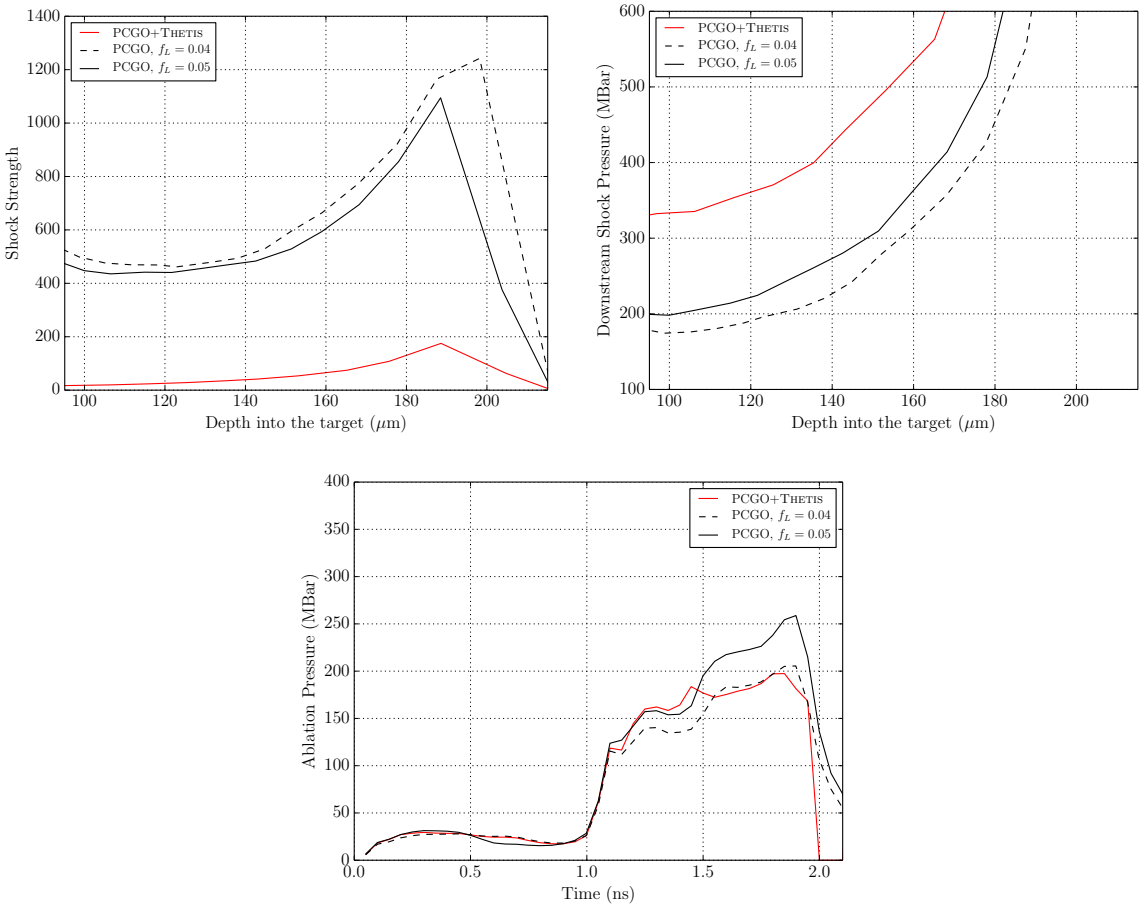

Figure 6-19 – *(color) [left] Shock strength and [right] downstream shock pressure, as a function of depth into the target (μm). The rightmost value on the abscissa corresponds to the target center (the target is 215 μm in radius). [Bottom] ablation pressure (MBar) as a function of time (ns). The plain lines are simulations with a similar absorbed energy fraction $\mathcal{F}^{\text{abs}}$ that matches the experimental measurements. The black lines are simulation results without HEs (but with PCGO) and the red lines indicate simulation results with HEs. The dashed lines indicate simulation results without HEs with the same flux limiter $f_L = 0.04$ as the simulation with HEs.*

by increasing the flux limitation above 6 %, although the absorption fraction is likely out of the experimental measurements. Simulations using PCGO without electrons and with a nonlocal flux transport model do not match the observed absorption fraction. However, simulations with PCGO and with HEs with nonlocal flux transport do reproduce a correct absorption fraction, albeit with a earlier shock timing. The use of a nonlocal transport model with a dedicated package for the very high energy electron transport (i.e. THETIS) is conceptually interesting. Furthermore, the use of nonlocal flux model is attractive as it removes the free parameter f_L from the hydrodynamic simulation. More studies on the coupling of THETIS and the nonlocal model are warranted. We now detail the results from the PCGO+THETIS simulation with $f_L = 4\%$.

Similar to the PALS campaign, it is found that the LPI-generated HEs have a sufficient temperature to heat the target upstream of the main shock, thus raising the temperature and pressure of the bulk of the material, as illustrated in Fig. 6-18. The resulting shock strength

and downstream pressure as a function of depth into the target are given in Fig. 6-19 [left] and [right]. It is found that the shock strength is significantly lower in the simulation with HEs, by a factor $\sim$ 5-10. This is easily explained considering that the preheat of the plastic can raise the temperature from $<$ 1 to 10 eV, thus increasing the pressure tenfold and decreasing the shock strength accordingly. As in the PALS campaign results, the pressure downstream of the shock is larger, here by a factor $\sim$ 1.5.

The time-evolution of the ablation pressure, defined (as in the PALS analysis) as the plasma pressure where the material velocity in the laboratory frame is zero, is illustrated in Fig. 6-19 [bottom] for all cases. At constant flux limitation, the ablation pressure is rather similar with and without HEs. Conversely, at constant energy absorbed $\mathcal{F}^{\text{abs}}$, the ablation pressure is higher without HEs, owing to the increased laser absorption in the vicinity of the critical density whereas HEs from Parametric Instabilities deposit their energy both in front and behind the ablation front. In that case, the peak ablation pressure with HEs is lower by about 20 %. This result contradicts the conclusions drawn in Ref. [112], where the contribution from HE was assumed to be confined before the ablation front.

Given the satisfying agreement obtained between the experimental data and simulation results in both the PALS and SSS campaigns, we now apply our model to the study of the highly nonlinear phase of the ignitor pulse used in Shock Ignition.

6.4 Effects of LPI-generated HEs on the ignition threshold for Shock Ignition

6.4.1 Context of the study

The Shock Ignition scheme in ICF is an alternative ignition scheme where the compression and ignition phases are separated: the target compression is conducted at a low velocity using lasers of moderate energy and the ignition is achieved at the end of the compression phase with a dedicated intense laser pulse [42, 31, 234], so-called *spike pulse*. This scheme requires overall less laser energy than hotspot ignition and is more robust to hydrodynamic instabilities. In order to obtain the required temperatures for ignition in a hotspot of $\sim$ 50 μm radius, a shock pressure of the order of 30 GBar is required. Considering the ablation pressures of the order of 150 MBar estimated in Secs. 6.2 and 6.3, the shock converging in the shell must be amplified by a factor $\sim$ 200 [235, 236]. The amplification of the shock pressure depends on (i) spherical convergence effects and (ii) the precise timing of the shock collision with the diverging shock from the laser pulse used for the compression [233]. Hydrodynamic estimates and simulations without taking into account hot electrons predict that the amplification factors of the order of 100-200 can be achieved, albeit in a narrow timing window and using laser intensities for the spike pulse of the order of 5×10^{15} - 10^{16} W/cm^2. Such laser intensities in high temperature and long scale-length plasmas are associated with strong nonlinear laser-plasma interactions, where SRS and TPD excite EPWs that drive copious amounts of Hot Electrons into the target [213, 112]. The high intensity spike is launched at a time when the imploding shell may be sufficiently dense to stop the LPI-generated HEs. In that case, it is expected that the additional energy from the HEs increases the ablation pressure. We have seen in the interpretation of the strong shock

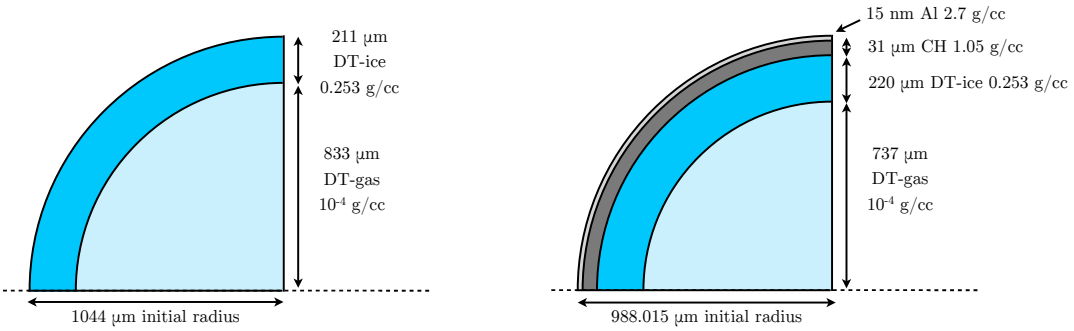

Figure 6-20 – *Schematic of the two targets considered in the study. [left] Pure-DT target from the baseline* HiPER *project. [right] SI target recently designed at* Celia*, with high yield and high safety margins with respect to the hydrodynamic instabilities.*

experiments conducted on the Pals and Omega laser systems that the HEs may actually be detrimental to both the ablation pressure and the shock strength, while reinforcing the shock pressure and velocity.

Although each of the processes involved in the compression of an ICF target or in the coupling of shock characteristics with HEs fluxes can be studied separately [237, 238, 213, 233, 51], the simultaneous study requires an integrated tool such as the one we have developed in this work. We propose in this section a preliminary study of the sensitivity of the Shock Ignition scheme to LPI-generated HEs.

6.4.2 Simulation framework

6.4.2.1 Targets and geometry

Two targets are considered: (i) the baseline pure-DT target proposed in the original HiPER project in Ref. [239] and (ii) an advanced design with increased gains and robustness to hydrodynamic instabilities, recently designed in the Celia laboratory. The latter target is more up-to-date with the current paradigms in direct-drive target design. Notably, it is imploded at a lower velocity and features a plastic ablator for the reduction of hydrodynamic instabilities and optimization of laser-target coupling. The higher-Z ablator is also expected to respond differently to the HE flux than the DT ablator. The targets are detailed in Fig. 6-20.

Each target is studied with two series of simulations, with and without the LPI-HE coupling (Thetis model). Simulations are conducted in spherical configuration in order to account for the spherical convergence effects on shock amplification and shell areal densities. The laser propagation and interaction with plasma is computed in pseudo-cylindrical monomode configuration, as detailed in Sec. B.3. All simulations are conducted with the radiative transfer enabled and the Sesame Equation of States.

6.4.2.2 Laser configuration

The laser beams are in a configuration mimicking a large-scale laser facility. We have assumed lasers of wavelength $\lambda_L = 351$nm and a uniform irradiation field on the targets, with beams incident at an angle $\theta = 0$. The focusing parameters of the beams are summarized in Tab. 6.5.

Target	ϕ_F	F	r_0	n_0
pure-DT	67.5 cm	10 m	1044 μm	4
CH-DT	88 cm	5 m	876 μm	2.66

Table 6.5 – *Focusing parameters for the two targets. ϕ_F is the radius of the focusing optics, F its focal length, and the beam vacuum envelop intensity profile in its focal plane is defined as $\langle I \rangle = \langle I \rangle_0 \exp\left[-|r/r_0|^{n_0}\right]$.*

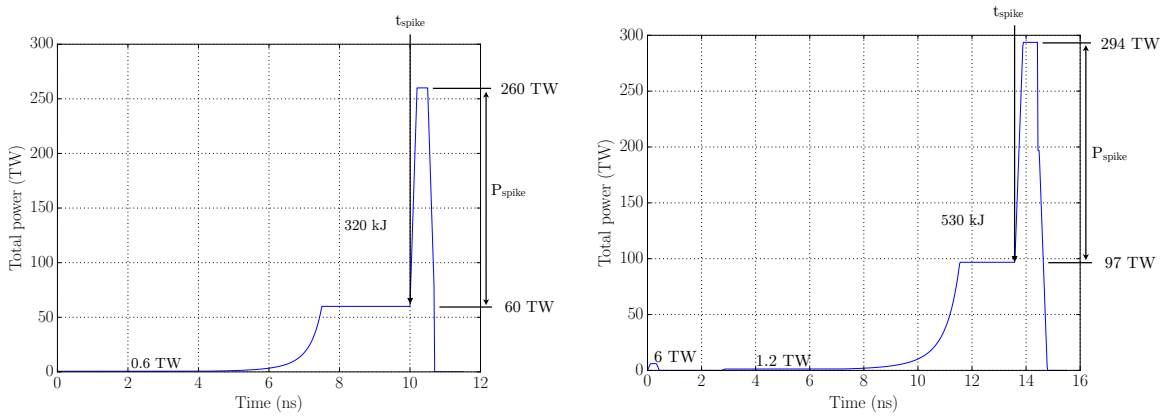

Figure 6-21 – *Total pulse power used in the baseline designs of the [left] pure-DT and [right] CH-DT targets. For simplicity, it is considered that the irradiation is symmetric on the capsule and that each beam follows the same pulse shape, with the same focusing parameters.*

Because the targets were designed in separated studies, the focusing parameters are different for the two target cases. This is not an issue for the comparison because the aim of this study is not to compare the nominal performances of the baseline and advanced target designs, but rather to assess their respective robustness to HEs. In both cases, the beams are assumed to be equipped with KPPs and the pseudo-speckle pattern is modeled with PCGO with 100 beamlets per beam.

The baseline pulse shapes for both targets are shown in Fig. 6-21. We denote by t_s the time when the ignitor pulse is launched and by P_s the peak spike power. In the pure-DT target case, the pulse rise time is 200 ps, followed by a 300 ps high intensity plateau and a 200 ps fall time. In the baseline configuration, the 200 TW ignitor pulse is launched around $t_s = 10$ ns and the ignition occurs around 11 ns, for a total invested energy of ~ 320 kJ and a yield of ~ 24 MJ. In the CH-DT target case, the heavier capsule is imploded at lower velocities using a longer pulse shape. The 200 TW ignitor pulse is launched later, around $t_s = 13.5$ ns, with a 300 ps rise time, 600 ps plateau and 300 ps fall time. The ignition occurs around 14.6 ns, with a total invested energy of the order of ~ 530 kJ and a yield of ~ 45 MJ.

6.4.3 Pure-DT target

6.4.3.1 Ignition windows

The shock ignition scheme is particularly sensitive to the timing of the strong shock launch with respect to the capsule compression, and to the timing of the shock collision inside the converging

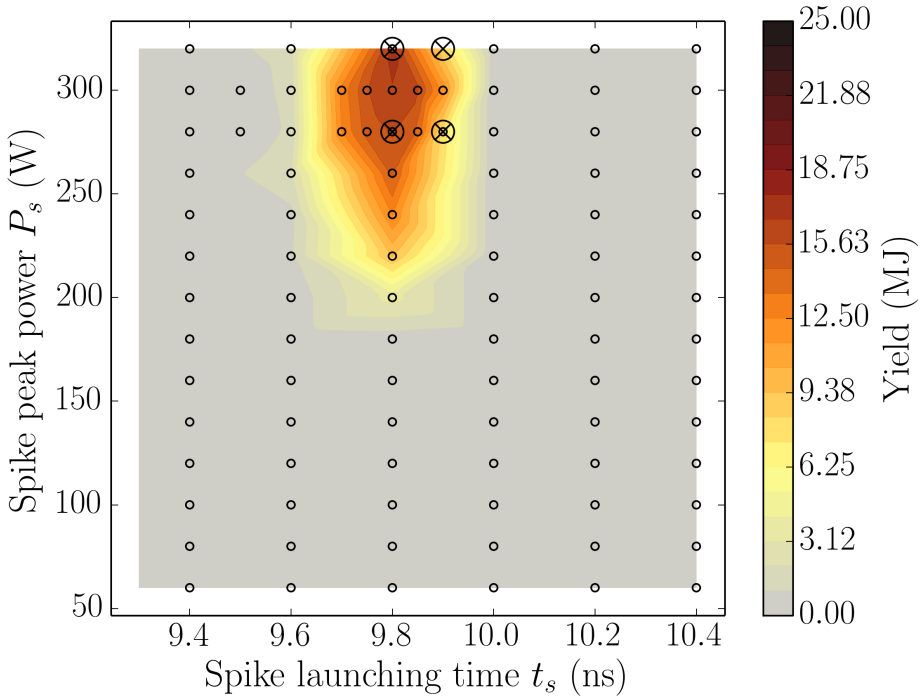

Figure 6-22 – *(color) Target gain (MJ) as a function of the spike launch time t_s and spike power P_s. Small circles indicate the points where the simulations with PCGO and without HEs were conducted. The large crossed circles represent equivalent simulations conducted with PCGO and the LPI-HE model* Thetis*, where no target ignition is attained.*

shell. These processes are particularly intricate and require extensive analysis using 1D models. In order to assess the global picture of the implosion, it is convenient to explore numerically a range of shock timings t_s and spike powers P_s around their baseline design point. Computing the target yield for each case yields the *ignition window*, it provides an information on the robustness of the target design. Given the significant modifications to shock dynamics induced by LPI-HEs, as shown in Secs. 6.3 and 6.2, it is instructive to compute these ignition windows with and without LPI-HEs.

We conduct a set of reference simulations using PCGO and without HEs, for $t_s \in \{9.4, 9.6, 9.8, 10, 10.2, 10.4\}$ ns and P_s varying in the $[60; 320]$ TW interval. These simulations are conducted with the flux limiter value of $f_L = 0.04$ used in the previous sections. The resulting ignition window is shown in Fig. 6-22. The spike launch times and target yields are in good agreement with computations realized with the RT model [234, 235]. The higher spike power obtained in our simulations (compared to what is presented in the literature) is related to the choice of a rather low flux limiter value.

Four simulations are conducted with PCGO and the LPI-generated HEs using Thetis. Anticipating that the presence of HEs should increase the shock velocity, we have chosen $t_s = \{9.8, 9.9\}$ ns, that is later than the optimal timing $t_{s,\mathrm{opt}} = 9.8$ ns. We consider two values for the spike power: $P_s = \{280, 320\}$ TW. Neither of these 4 simulations with HEs predicts the target ignition, as indicated in Fig. 6-22 by large crossed circles. We discuss the processes at play in

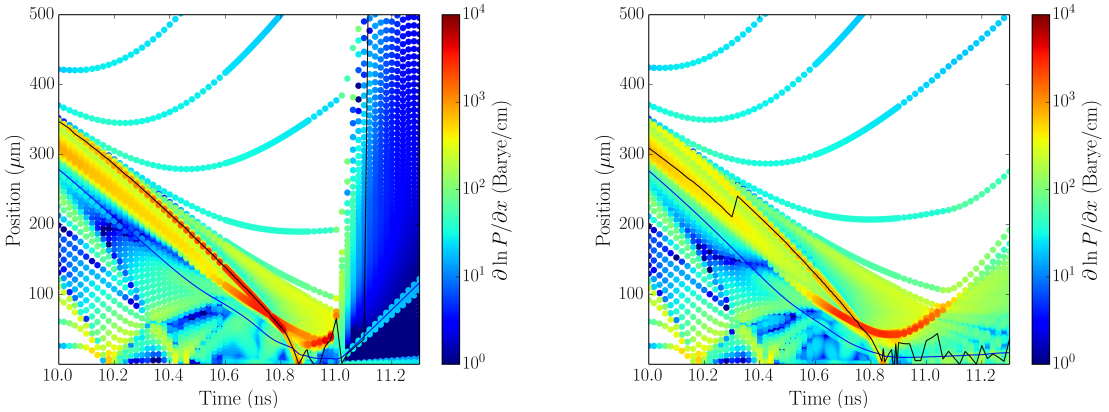

Figure 6-23 – *(color) Flow diagrams (logarithmic pressure gradient, shown in log-scale) of the targets as a function of time and radial coordinate, for the case [left] without LPI-HEs, and [right] with the LPI-HEs. The position of the strongest shock is indicated as a black line, and the position of the initial DT-ice/DT-gas interface as a blue line. Oscillations in the shock position after the shock collapse are due to the difficulty in detecting numerically the shock position. Each dot indicates the position of a Lagrangian mesh cell.*

these implosions by comparing the particular case of $t_s = 9.8$ ns and $P_s = 320$ TW, with and without LPI-generated HEs.

The global target dynamics is illustrated in Fig. 6-23, which shows the logarithmic pressure gradient as a function of the target radius and time. Several observations can be readily made from this diagram: (i) the target with LPI-HEs does not ignite, (ii) the in-flight thickness of the imploding shell increases in the case with LPI-HEs, (iii) the final convergence ratio is lower with HEs, (iv) the ignitor shock reaches the target center earlier in the case with HEs and (v) the shock strength appears higher without HEs than with HEs. We now detail these effects more precisely.

6.4.3.2 Shell preheat

In the simulations, the SRS, TPD and RA processes emit copious amounts of electrons at averaged temperatures of ~ 41 keV, 100 keV and 2.7 keV, respectively, with the total energies of ~ 1.38 %, 0.97 % and 0.33 % of the total laser energy, respectively. The time-history of the instantaneous HE fluxes (normalized to the incident laser intensity) are shown in Fig. 6-24, alongside with the corresponding HE spectra and the shell areal density $(\rho R)_{\mathrm{HE}}$ seen by the LPI-HEs, at various times. The latter is defined as:

$$(\rho R)_{\mathrm{HE}}(r) = \int_{r}^{r_{n_c/4}} \rho(r')\mathrm{d}r' \tag{6.7}$$

where $r_{n_c/4}$ is the coordinate of the quarter critical density and r is the radial coordinate. The areal density required to stop a mono-energetic electron beam of a given energy propagating in a constant density DT plasma is shown in Fig. 6-24 [bottom-right]. This panel provides an estimate of the HE energies that can be stopped by the shell. Given the HE energies involved

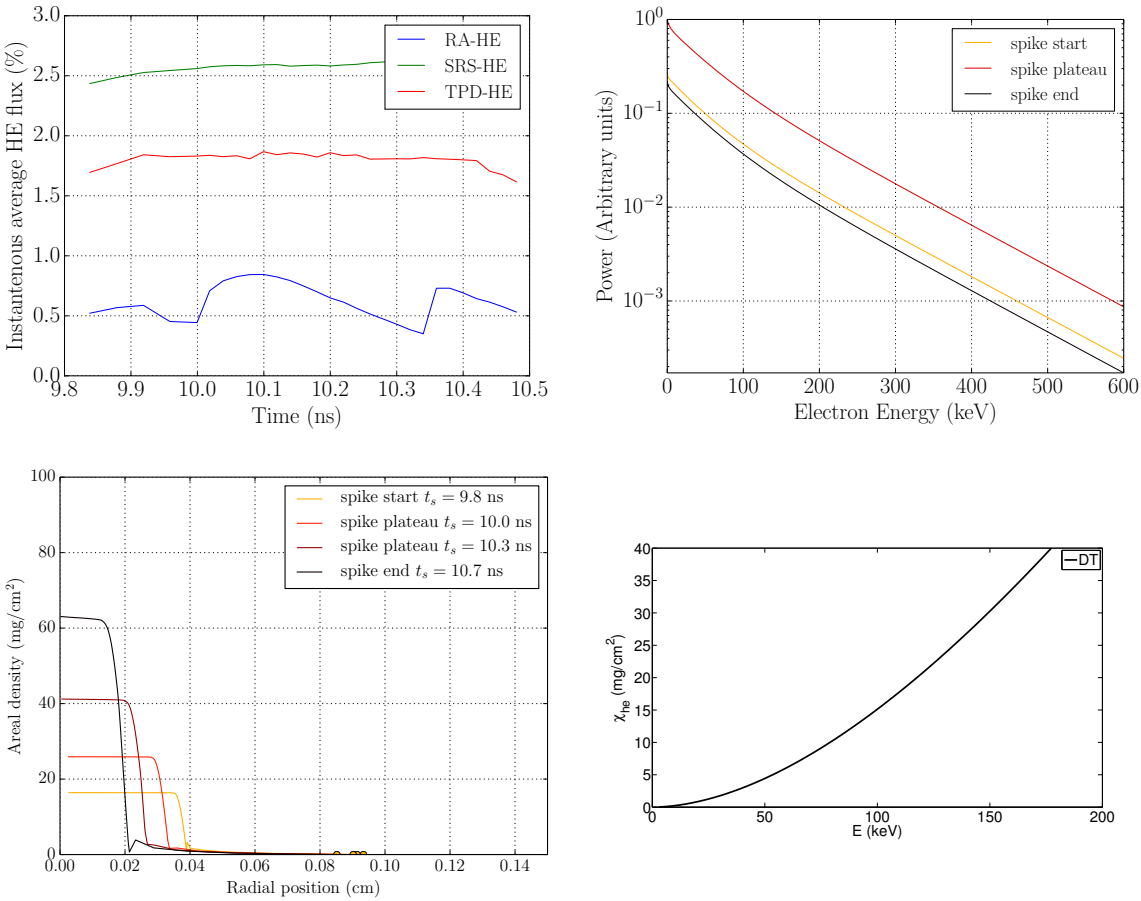

Figure 6-24 – *(color) [top-left] Flux-weighted averages (same formalism as in Eq. (5.25)) of the laser to HE instantaneous energy conversion fractions. The spectra of HEs accelerated in plasma are shown in the [top-right] panel, considering the beginning of the laser spike in orange (light grey), the plateau of the spike in red (grey) and the end of the laser spike in black. [bottom-left] Areal density $(\rho R)_{\mathrm{HE}}$ seen by the HE beams emitted at $n_c/4$, as a function of the target radius. The position of the quarter critical density is indicated by a circle. [bottom-right] Areal density required to stop a mono-energetic electron beam of a given energy propagating in a homogeneous DT plasma [240].*

here, and the shell areal densities reported in Fig. 6-24 [bottom-left], we see that the shell is not dense enough to stop the higher energies of the HE spectrum. Notably, at the begining of the spike plateau, the in-flight shell can be integrally heated by the electrons with the energies above 120 keV. Nearing the end of the plateau, the electrons with energies above 170 keV still preheat the shell. Considering the significant amount of high-energy electrons generated by the SRS and TPD, the shell is preheated in the bulk, as is shown in Fig. 6-25.

In the spherical SSS experiment, analyzed in Sec. (6.3), the target preheat occurred in a target of a quasi-uniform solid density. In the case of a SI target, the preheat occurs in a shell surrounded by lower density regions on either sides. Consequently, the pressure increase induced by the HE preheat no longer occurs at a constant density. The preheat causes an expansion of the shell, its thickness and temperature increase in-flight while its density decreases. This is

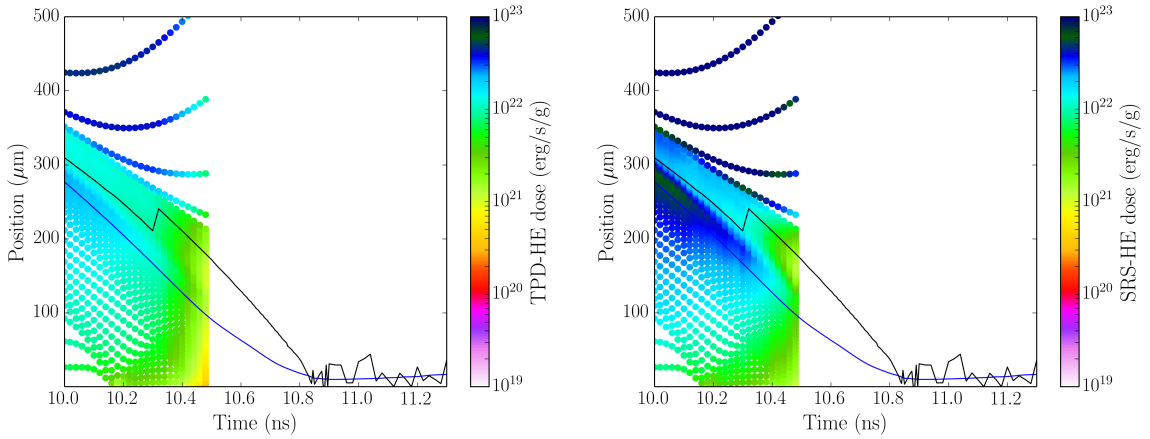

Figure 6-25 – *(color) Log-scaled dose deposited by the HE beams in plasma (erg/s/g), as a function of the target radius and time. [left] HE generated by the TPD and [right] by the SRS (the simulation being monomode, the fields presented here are identical for any cylindrical angle θ). Each dot indicates the position of a Lagrangian mesh cell.*

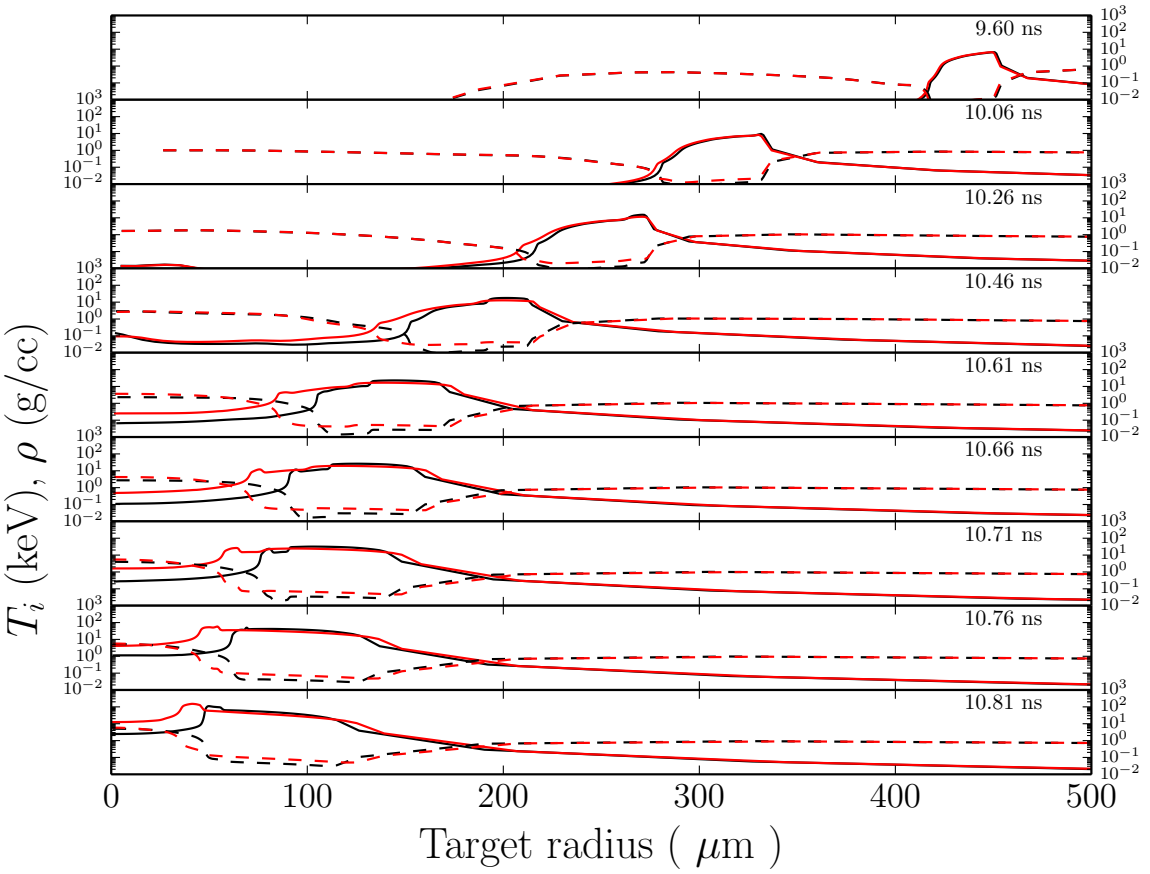

Figure 6-26 – *(color) Slices of plasma density ρ (in g/cc) indicated by plain lines, and ion temperature T_i (in keV) indicated by dashed lines, as a function of the target radii and for various times indicated on the upper-right corner of each subplot. Results from the simulation without HEs are shown in black and with HEs in red (grey).*

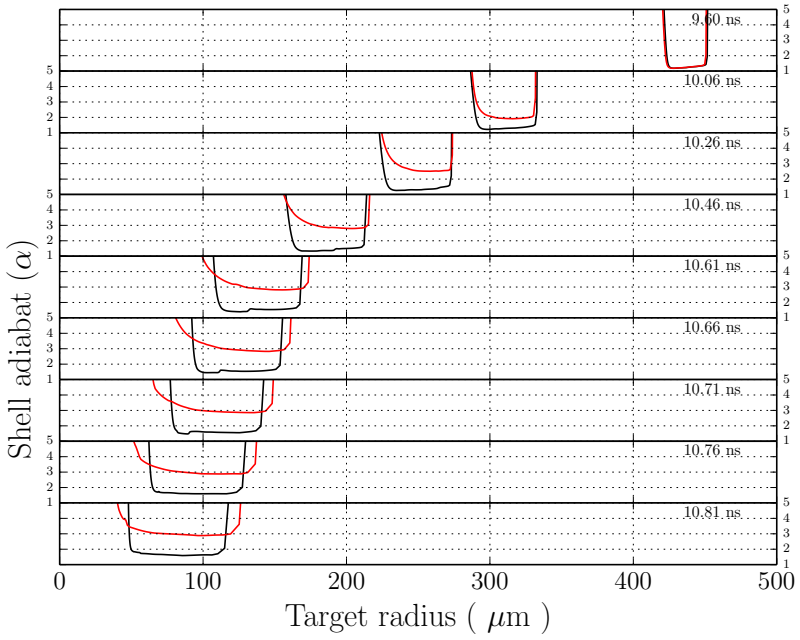

Figure 6-27 – *(color) Slices of the adiabat parameter α, as a function of the target radii and for various times indicated on the upper-right corner of each subplot. Results from the simulation without HEs are shown in black and with HEs in red (grey).*

illustrated in Fig. 6-26. The increase of the shell pressure raises its adiabat α[1] while it converges to the center, as shown in Fig. 6-27. The increase of α leads to the lower convergence ratios seen in Fig. 6-23, from $C_R \approx 833/24.1 = 34.6$ without HEs to $C_R \approx 833/30.4 = 27.4$ with HEs. It can also be noted from Fig. 6-26 that the expansion of the shell inner boundary due to the preheat can be considered as a mix of the cold shell fuel with the hot spot material. It effectively causes an increase in the density of the target center. This HE-induced hotspot mix is also discussed later in this section while considering the thermodynamic path of the hotspot.

6.4.3.3 Shock characteristics

The shock created by the high intensity ignitor pulse propagates through the preheated material while its temperate and pressure increases and its density decreases (see Fig. 6-26). The resulting pressure and temperature downstream of the shock are shown in Fig. 6-28 [top] alongside its position. We see that for a same launching time t_s, (i) the shock is faster with HEs, (ii) it reaches the hotspot with a pressure of 20 GBar for the case with HEs and 7.5 GBar for the case without HEs, and (iii) the post-shock temperature at this time is rather similar, with 5.6 keV and 5 keV for the cases with HEs and without HEs, respectively. As in the Pals and Omega experiment, the HEs significantly increase the shock pressure. This increase is not due to an increased ablation pressure, the latter being relatively equal with and without HEs as shown in Fig. 6-28 [bottom-left], but to the plasma preheat upstream of the shock. Finally, the shock strength is smaller with HEs, as shown in Fig. 6-28 [bottom-right] and in agreement with our

[1] As defined in the introduction, the shell adiabat is the ratio of its pressure to the Fermi pressure. It is a measure of the thermal agitation in the shell and of the hydrodynamic efficiency of the compression.

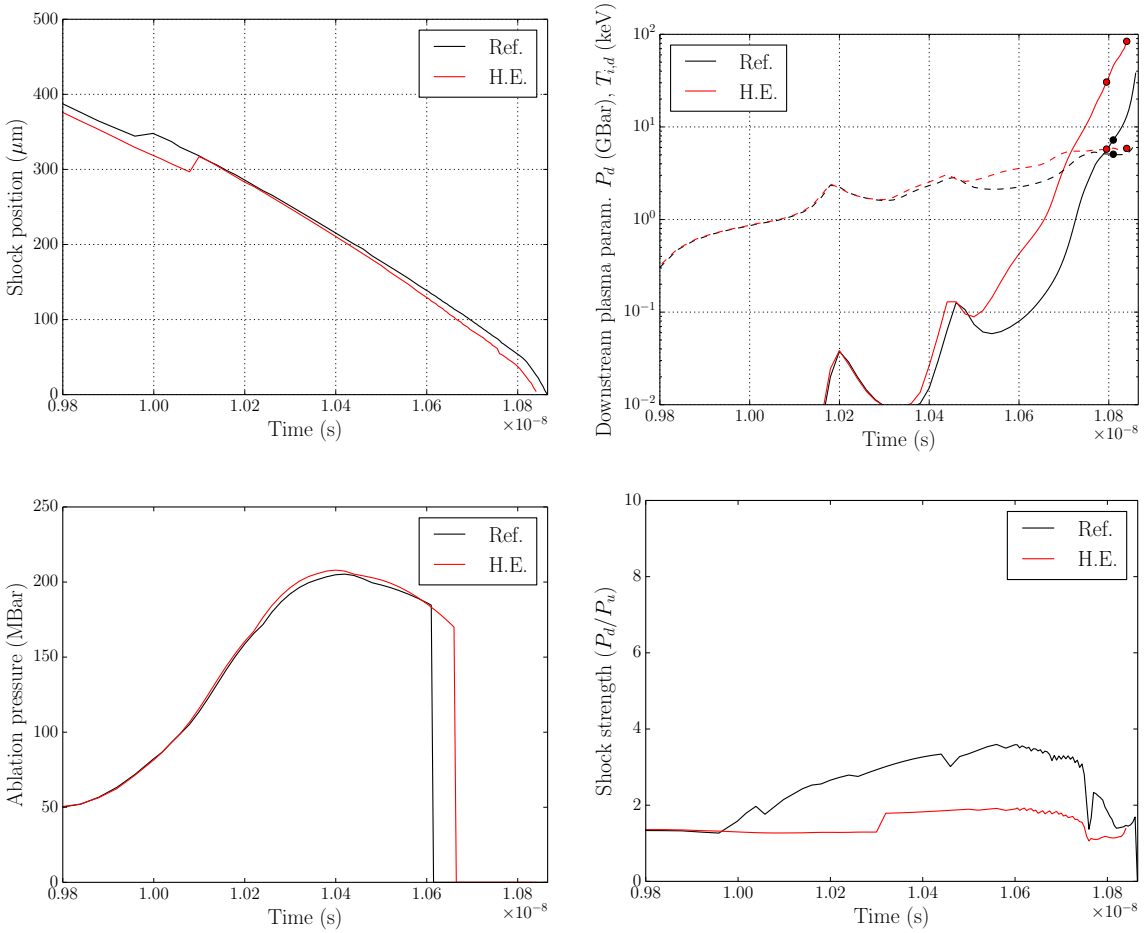

Figure 6-28 – *(color) [top-left] Position of the strongest shock in the material. The bump observed around 10 ns is due to the detection algorithm that is sensitive to the strongest pressure discontinuity. In panels showing the properties of the shock, the results shown before the time of the bump do not indicate the ignitor shock properties. [top-right] Temperature (keV) and pressure (GBar) of the shocked plasma. The plain line indicates the downstream shock pressure and the dashed lines the downstream shock temperature. For each curve, the first circle represents the time when the shock enters the hotspot, and the second circle indicates the time when the shock reaches the target center. [bottom-row] Time histories of [bottom-left] the ablation pressure and [bottom-right] the ignitor shock strength, from the time of ignitor spike launch t_s. For all panels, black and red (grey) curves indicate simulation results without and with HEs, respectively.*

previous conclusions on the strong shock experiments.

6.4.3.4 Hotspot thermodynamic path

We have seen that the ignitor shock is propagating with a larger post-shock pressure, a lower strength and a higher velocity when considering the LPI-HEs. We now assess the characteristics of the hotspot in order to determine how the shock deposits its energy and why the target does not reach the ignition. The evolution of the hotspot characteristics is assessed in a (ρR,T) diagram.

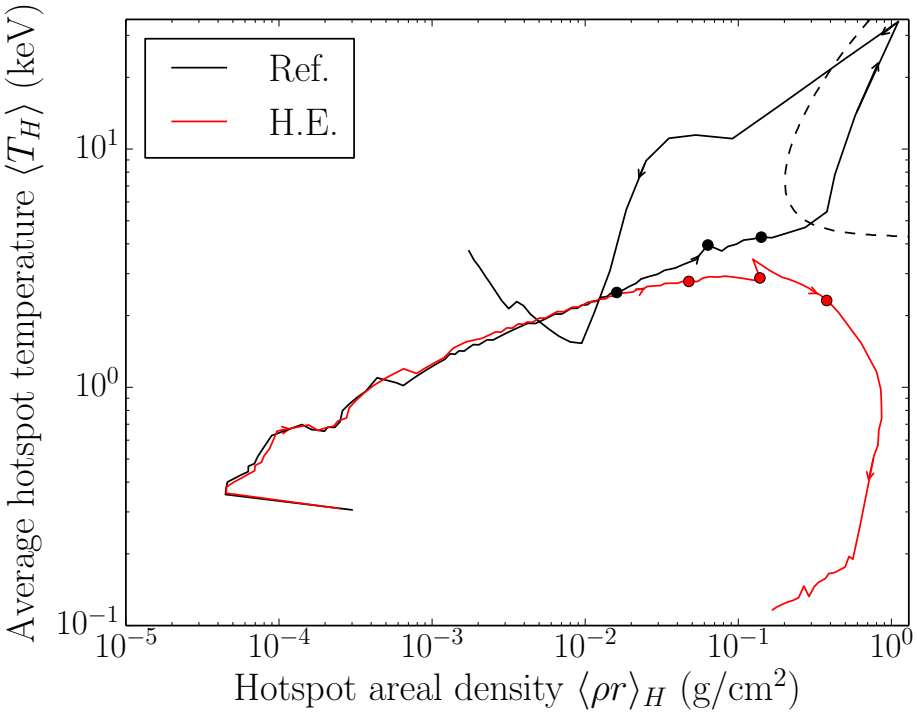

Figure 6-29 – *(color) Thermodynamic path of the hotspot, for the case without LPI-generated HEs in black and with the* Thetis *model in red (grey). The isobaric ignition curve is shown as a dashed line [234]. Arrows indicate the direction of the time-dependent evolution of the hotspot. For each curve, the first dot indicates the time when the ignitor shock enters the hotspot, the second indicates the time of shock rebound on the target center and the third is the time when the shock collides with the shell. Further shocks rebounds and collisions with the shell are not indicated.*

The hotspot averaged areal density $\langle \rho r \rangle_H$ and averaged temperature $\langle T_H \rangle$ are defined as:

$$\langle \rho r \rangle_H = \int_0^{R_H} \rho(r) \mathrm{d}r \ , \tag{6.8}$$

$$\langle T_H \rangle = 3 \int_0^{R_H} r^2 T_i(r) \mathrm{d}r / R_H^3 \ , \tag{6.9}$$

where R_H is the hotspot radius, defined as the radial coordinate r where $T_i(r) = T_i(0)/10$, with $T_i(0)$ being the ion temperature in the target center. Note that the angular coordinate does not appear here: the simulation being monomode the plasma parameters only depend on the radial position. The thermodynamic path of the hotspot for the case with and without HEs is shown in Fig. 6-29. As evoked earlier, the simulation without HEs reaches the ignition boundary (shown with a dashed line), while the simulation with HEs does not. The most notable difference is the areal density in the case with HEs that is significantly higher when the shock reaches the hotspot. This increase in hotspot density is a consequence of the effective mix with the dense shell material preheated by the HEs, as was shown in Fig. 6-26. The slight increase in temperature at this time is due to the smaller hotspot radius. For clarity, the properties of the hotspot at the time of shock entry and shock rebound are given in Tab. 6.6.

case	$\langle \rho r \rangle_H$	$\langle T_H \rangle$	$\langle \rho_H \rangle$	R_H	$\langle T_{H,e} \rangle$
no HE	0.016 g/cm^2	2.5 keV	4.63 g/cc	48.7 μm	2.05 keV
LPI-HE	0.048 g/cm^2	2.7 keV	16.93 g/cc	40.2 μm	2.53 keV
no HE	0.063 g/cm^2	3.95 keV	22.17 g/cc	30.52 μm	3.52 keV
LPI-HE	0.14 g/cm^2	2.88 keV	65.9 g/cc	33.63 μm	2.75 keV

Table 6.6 – *Summary of the properties of the hotspot when [top] the ignitor shock enters the hotspot and [bottom] the ignitor shock reaches the target center. $\langle \rho_H \rangle$ is the averaged hotspot density and $\langle T_{H,e} \rangle$ is the averaged hotspot electron temperature. Both quantities are computed using the same averaging process as for the ion temperature (6.9). Note that because of these definitions, $\langle \rho_H \rangle R_H \neq \langle \rho r \rangle_H$.*

Hotspot mass The hotspot mass M_h can be expressed as:

$$M_h = \frac{4}{3}\pi \frac{(\rho_h R_h)^3}{\rho_h^2} \approx \frac{4}{3}\pi \frac{\langle \rho r \rangle_H^3}{\langle \rho_H \rangle^2} \ . \tag{6.10}$$

Although the hotspot areal density is higher with HEs (as shown in Fig. 6-29) it also has a higher density (as seen in Fig. 6-26), so that the overall hotspot mass M_h is higher in the simulations with HEs. The time evolution of the hotspot mass is shown in Fig. 6-30, alongside the shock position and the radius of the hotspot. At the time when the shock reaches the target center, its mass is of 2.65 μg and 10.7 μg for the cases without and with HEs, respectively. The energy E_h required to bring a DT sample of mass M_f to a temperature T_h can be estimated from the expression for its internal energy [46]:

$$E_\mathrm{h} \approx 110 M_f T_h \text{ MJ} \ , \tag{6.11}$$

where M_f is expressed in g and T_h in keV. This equation shows that in order to heat the DT fuel to a given temperature (typically ~ 7 keV is required to ignite a hotspot of areal density of 0.2 g/cm^2), the increase in hotspot mass translates into an increase in required energy. Although we have seen that the shock downstream pressure is higher with HEs, it is not sufficient to ignite the hotspot of significantly increased mass (as seen in the thermodynamic diagram). Indeed, the temperature of the hotspot barely increases between the time when the shock propagates from the hotspot radius $r = R_h$ to the target center $r = 0$.

Hotspot power balance By the time the shock rebounds and reaches the shell again, the hot spot temperature has decreased. This is indicative of intense hotspot cooling, i.e. power losses are higher than the power brought in by the ignitor shock. We now assess the importance of these cooling processes. The hotspot can loose its energy either by the electron thermal conduction or by the radiative losses from the Bremsstrahlung process (with photon energies in the x-ray range). The hotspot power density $\mathcal{W}_e$ lost through electron thermal conduction can be estimated by [46]:

$$\mathcal{W}_e = 1.71 \kappa_0 \frac{T_h^{7/2}}{R_h^2} \ , \tag{6.12}$$

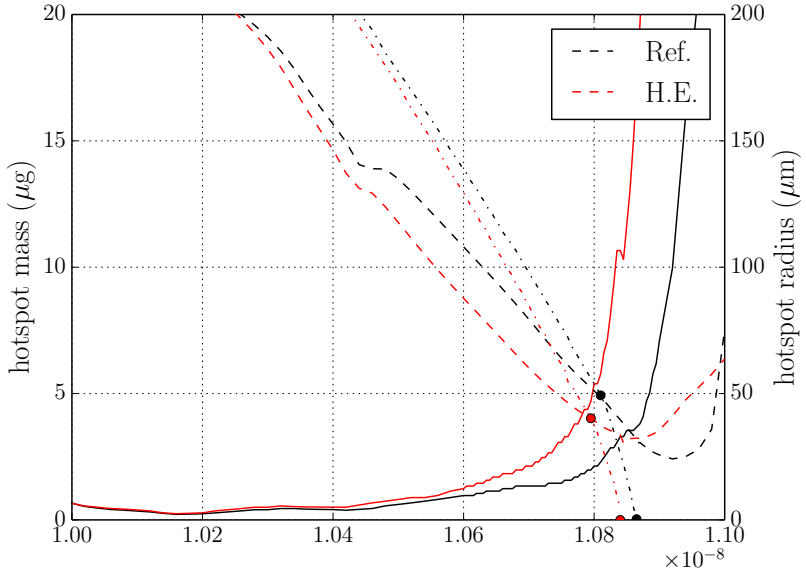

Figure 6-30 – *(color) Mass of the hotspot as a function of time, indicated as plain lines. The hotspot radius is shown as dashed lines and the shock position as dotted dashed lines. The times when the shock enters the hotspot and reaches the target center are indicated by colored circles. Data from the simulation without HEs and with HEs are shown in black and red (grey), respectively.*

where the constant value $\kappa_0 = 3 \times 10^{12}$ W/cm/keV$^{7/2}$ corresponds to the *Spitzer-Härm thermal conductivity*, R_h is expressed in cm and T_h in keV. At the time when the shock enters the hotspot and using the values given in Tab. 6.6, we find that hot electrons increase the electron conductivity losses by a factor of three, $\mathcal{W}_{e,\mathrm{HE}} \approx 3\mathcal{W}_{e,\mathrm{ref}}$. Similarly, the hotspot power density $\mathcal{W}_B$ lost through the radiative process can be estimated by [46]:

$$\mathcal{W}_B = \frac{C_B \rho_h^2 T_h^{1/2}}{m_i^2} \ , \tag{6.13}$$

where $C_B = 5.3510^{-31}$ W/cm^3/keV$^{1/2}$ is a constant, m_i is the average ion mass, T_h is expressed in keV and ρ_h in g. At the time when the shock enters the hotspot and using the values given in Tab. 6.6, we find that the radiation losses increase by a factor of 15, $\mathcal{W}_{B,\mathrm{HE}} \approx 15\mathcal{W}_{B,\mathrm{ref}}$. We can estimate the total power loss $\mathcal{W} = V_h \mathcal{W}$ using the hotspot volume $V_h = (4/3)\pi R_h^3$. We compare in Tab. 6.7 the power losses at the time when the shock enters the hotspot and reaches the target center.

The hotspot mix induced by the HE preheat of the shell and its inner side ablation leads to an increase in radiative losses by an order of magnitude. Using the value for $\mathcal{W}_{B,\mathrm{HE}}$ at the time of shock rebound and assuming a constant power loss for 30 ps, we find that the plasma looses $\sim$ 1 kJ of energy. Assuming a hotspot mass of 20 μg, we see from Eq. (6.11) that this corresponds to a temperature decrease of 0.5 keV. Even though the ignitor shock produces an enhanced downstream pressure in the case with HEs, the latter is unable to compensate for the (i) ten-fold increase in radiation losses and (ii) the additional hotspot mass that must be heated.

These conclusions explain the failure of shock ignition of the reference target and provide a

case	$\mathcal{W}_B$ (TW)	$\mathcal{W}_e$ (TW)	$\mathcal{W}_B$ (TW)	$\mathcal{W}_e$ (TW)
Ref	0.45	0.13	3.36	0.54
with HEs	3.8	0.229	35.1	0.25

Table 6.7 – *Power lost by the hotspot from the processes of Bremsstrahlung x-ray emission and electron thermal conduction. Values are given for the time when [left] the ignitor shock enters the hotspot and [right] the ignitor shock reaches the target center.*

basis for the analysis of the case of the CH-DT target.

6.4.4 CH-DT target

6.4.4.1 Ignition window

We compare the CH-DT target dynamics with and without LPI-generated HEs. The simulations without HEs are made for various spike launch times in $t_s \in [13; 13.6]$ ns and P_s varying in the $[20; 220]$ TW interval. This target was originally designed with a flux limitation f_L of 7 %. For consistency with the original design point, we now set the $f_L = 0.07$. This more "generous" flux limitation is expected to increase the laser absorption and decrease the required spike powers. Note that the spike power in the baseline design point of the CH-DT target is the same as for the pure-DT target. Given the similar target initial radii of ~ 1000 μm, the nominal intensities between the two targets are also similar, and hence the laser-plasma interaction proceeds in a comparable regime.

The reference ignition window (without HEs) is shown in Fig. 6-31 [left]. It is in reasonable agreement with the baseline computations realized in the 1D spherical geometry with the Ray-Tracing model in CHIC [Personal communication, E. Lebel, X. Ribeyre]. Minor differences are noted in terms of spike timings and powers, which are attributed to a difference in incidence

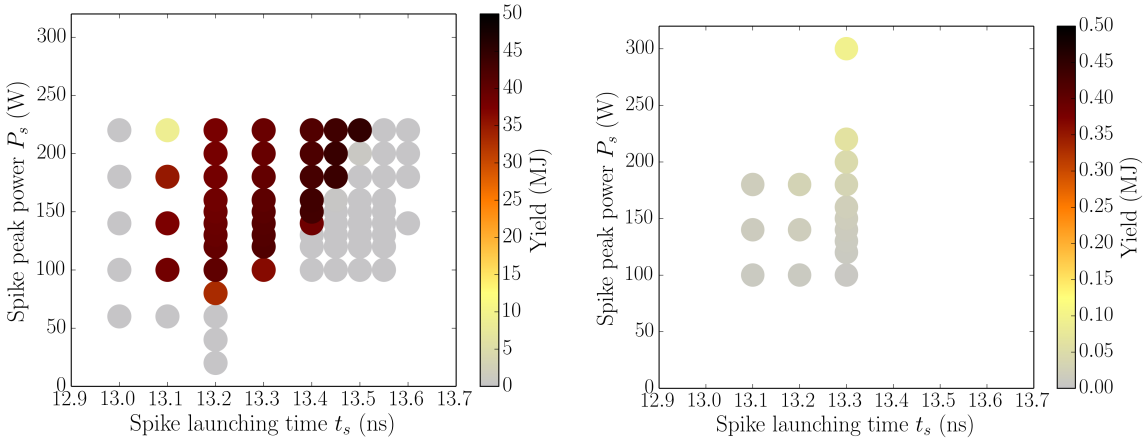

Figure 6-31 – *(color) Target gain (MJ) as a function of the spike launch time t_s and spike power P_s. Circles indicate the spike parameters where the simulations were conducted. Simulation results [left] with PCGO and [right] with PCGO and LPI-generated HEs (notice the different colorbar values).*

case	P_s	$\mathcal{F}_{\mathrm{RA}}$	$\mathcal{F}_{\mathrm{SRS}}$	$\mathcal{F}_{\mathrm{TPD}}$	$\langle T_{h,\mathrm{RA}} \rangle$	$\langle T_{h,\mathrm{SRS}} \rangle$	$\langle T_{h,\mathrm{TPD}} \rangle$
nominal	200 TW	0.12 %	1.2 %	0.94 %	1.4 keV	43 keV	98 keV
high power	300 TW	0.18 %	1.37 %	1.1 %	1.93 keV	44.5 keV	99 keV
delayed HEs	200 TW	0.11 %	1.05 %	0.84	1.5 keV	43.4 keV	98.9 keV

Table 6.8 – *Averaged parameters of the hot electrons accelerated into the target. The fluxes $\mathcal{F}$ are expressed in percent of the total incoming laser energy. At a given time, the fluxes $\mathcal{F}$ and average temperature of the HE distribution T_h are spatially averaged on all the HE sources defined by the* Thetis *model (same formalism as in Eq. (5.25)). The fluxes are then integrated over the simulation duration, and the temperatures are averaged using a mean weighted with the fluxes.*

angles chosen for the beams[2]. Simulations conducted with LPI-generated HEs using the Thetis model are presented in Fig. 6-31 [right]. As in the pure-DT case, the targets do not reach ignition. However, the yields are higher by a few orders of magnitude up to a fraction of MJ, meaning that higher amounts of fusion reaction occur despite the presence of the LPI-HEs.

In order to analyze the target dynamics, we focus on simulations conducted at the most robust shock launching time of $t_{s,\mathrm{opt}} = 13.30$ ps, that lies in the middle of the reference ignition window. For this spike timing, the spike power required to reach the ignition without HEs is of 80 TW. We study the effects of HEs by considering the particular design point of $P_s = 200$ TW. We consider three simulations with LPI-HEs and the spike launching time $t_s = 13.30$ ns: (i) a *nominal case* with $P_s = 200$ TW, (ii) a *high-power case* with $P_s = 300$ TW, and (iii) a *non-stationary case* where we consider that the nonlinear LPIs require 200 ps in order to reach a steady state, so that the 200 TW spike is launched at $t_s = 13.30$ ns and the HEs are launched at $t_{\mathrm{HE}} = t_s + \Delta t_{\mathrm{HE}} = 13.50$ ps (this particular simulation is not indicated in Fig. 6-31 [right]). The latter case may not be realistic: although a transient phase where the SRS and TPD did not accelerate HEs was observed in the SSS experiment (presented in Sec. 6.3), this delay was explained by a small overall energy and small target size, leading to steep density gradients and relatively high SRS/TPD thresholds. The scales of plasma considered here and the ignition targets are much larger, and hence much more prone to the SRS and TPD instabilities.

6.4.4.2 Hot Electron fluxes and target preheat

In the nominal simulation with $P_s = 200$ TW, the SRS, TPD and RA processes emit high energy electrons at averaged temperatures of ~ 43 keV, 98 keV and 1.4 keV, respectively, with total energies of ~ 1.2 %, 0.94 % and 0.12 % of the total laser energy, respectively. These values do not change significantly for the other cases, as reported in Tab. 6.8. The time-history of the instantaneous HE fluxes are shown in Fig. 6-32, alongside with the corresponding HE spectra and the shell areal density at various times.

The instantaneous fluxes and spectra are similar to those predicted in the pure-DT case. Compared to the latter, the shell areal density is approximately twice higher in the DT-ice,

[2]The CH-DT target was designed using the LMJ and NIF target configurations in the Polar Direct Drive geometry.

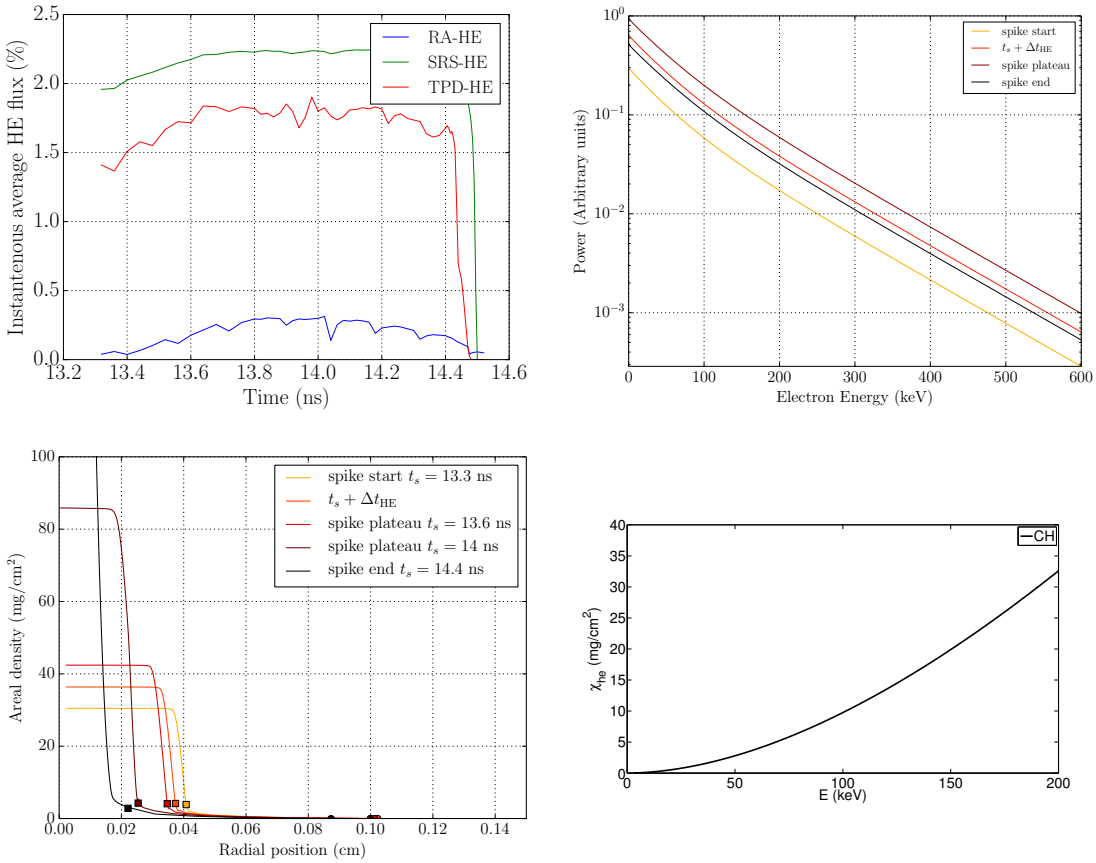

Figure 6-32 – *(color) [top-left] Flux-weighted averages (same formalism as in Eq. (5.25)) of the laser to HE energy conversion fractions. The spectra of HEs accelerated in plasma are shown in the [top-right] panel, considering the beginning of the laser spike in orange (light grey), the plateau of the spike in bright red and dark red (grey) and the end of the laser spike in black. [bottom-left] Areal density seen by the HE beams emitted at $n_c/4$, as a function of the target radius. The position of the quarter critical density is indicated by a circle. The position of the DT-ice/CH interface is indicated by a square. [bottom-right] Areal density required to stop a mono-energetic electron beam of a given energy propagating in a homogeneous CH plasma [240].*

because of the enhanced DT convergence. Although the plastic has a higher capacity to stop high energy electrons because of its higher Z (The range of mono-energetic electrons in CH is given in Fig. 6-32 [bottom-right]), the low areal density of the ablator makes it unable to stop HEs of energies larger than 50-70 keV. However, the ablator still stops a significant amount of the low energy electrons, thus partially protecting the in-flight shell. The electrons of higher energies propagate in the compressed DT-ice, which reaches areal densities of 40-100 mg/cm^2 during the laser spike plateau. This represents a capacity to stop electrons of energies lower than 170 keV at the beginning of the spike plateau. As such, this target is significantly more resistive to the LPI-generated HEs in general. The bulk of the DT-ice shell is still preheated by the higher energy electrons, but at lower fluxes: a more significant portion of the spectrum is stopped in the plastic and in the outer region of the in-flight DT shell. Note that when launching the HEs 200 ps later than the pulse start, the shell has increased in areal density by ~ 20 %.

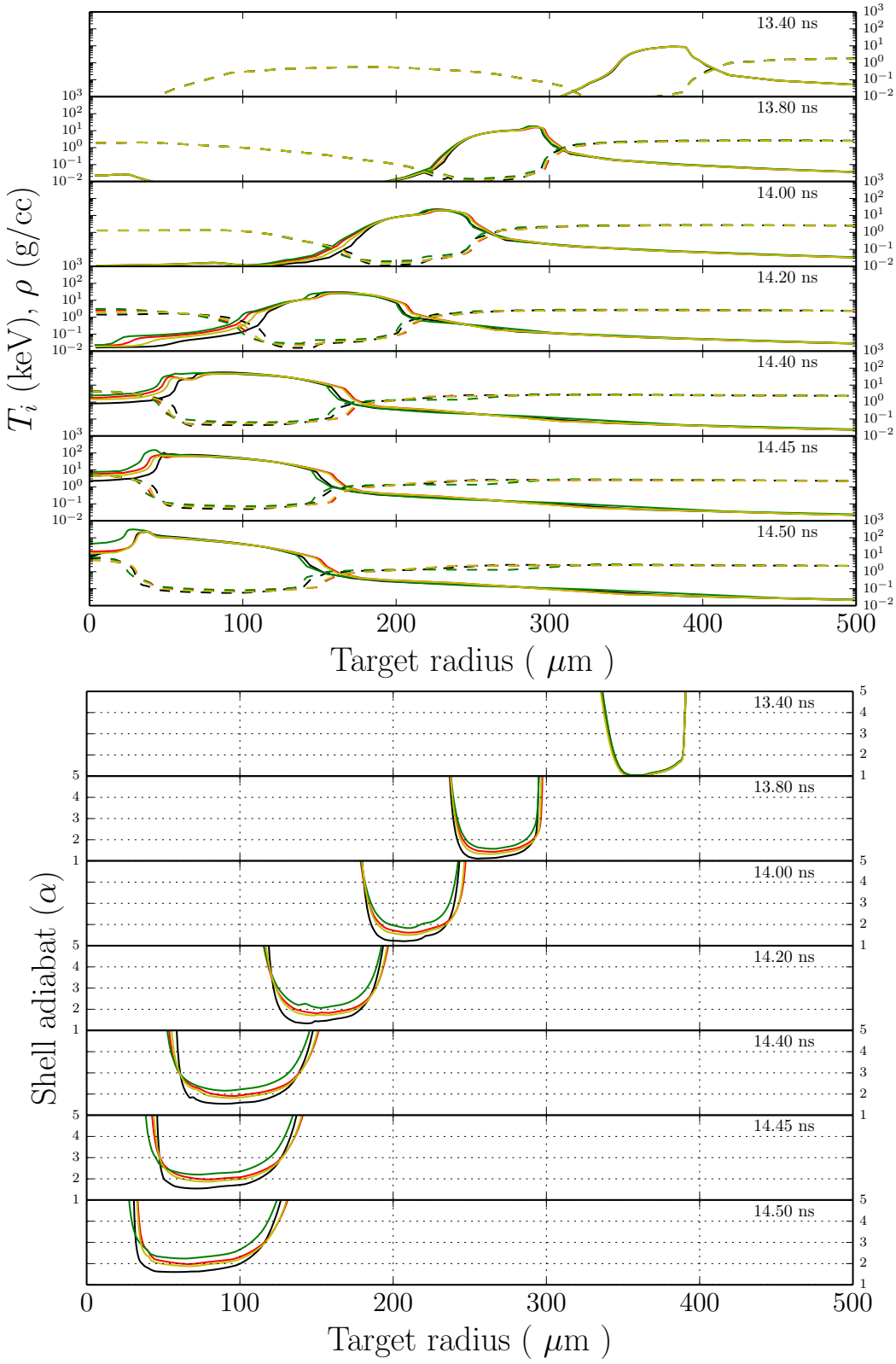

Figure 6-33 – *(color) [top] Slices of plasma density ρ (in g/cc) indicated by plain lines, and ion temperature T_i (in keV) indicated by dashed lines, and [bottom] slices of the adiabat parameter α as a function of the target radii and for various times indicated on the upper-right corner of each subplot. Results from the simulation without HEs are shown in black and with HEs as colored lines; red for the $P_s = 200$ TW case, green for the $P_s = 300$ TW case and yellow for the case with $P_s = 200$ TW with HE generation delayed by 200 ps.*

The magnitude of the DT-ice bulk preheat can be assessed in the temperature, density and adiabat parameter profiles shown in Fig. 6-33. The target dynamics in the two 200 TW cases with HEs are rather similar. In the 200 ps delay case, the target is thinner than in the non-delayed case. The hotspot mix with the dense shell material, that can be seen in Fig. 6-33 [top], is the least severe for the delayed HE case, then for the nominal case, and is the most severe for the high power case (this is most easily seen at $t = 14.20$ and 14.40 ns). Compared to the pure-DT target, the shell conserves a more cohesive structure, i.e. is closer to the reference case without HEs. This is correlated with a lower shell preheat in general than in the pure-DT case. This can notably be seen in the profiles of the adiabat parameter α shown in Fig. 6-33 [bottom]. The adiabat parameter is close to 2 at the peak convergence, lower for the delayed HE case and higher for the high power case. Even for the latter configuration, the parameter α reaches the value of 2.3, that is smaller than the value of 3 observed in the pure-DT case with HEs, which confirms that the plastic ablator did stop a significant portion of the LPI-HE spectrum.

6.4.4.3 Hotspot properties

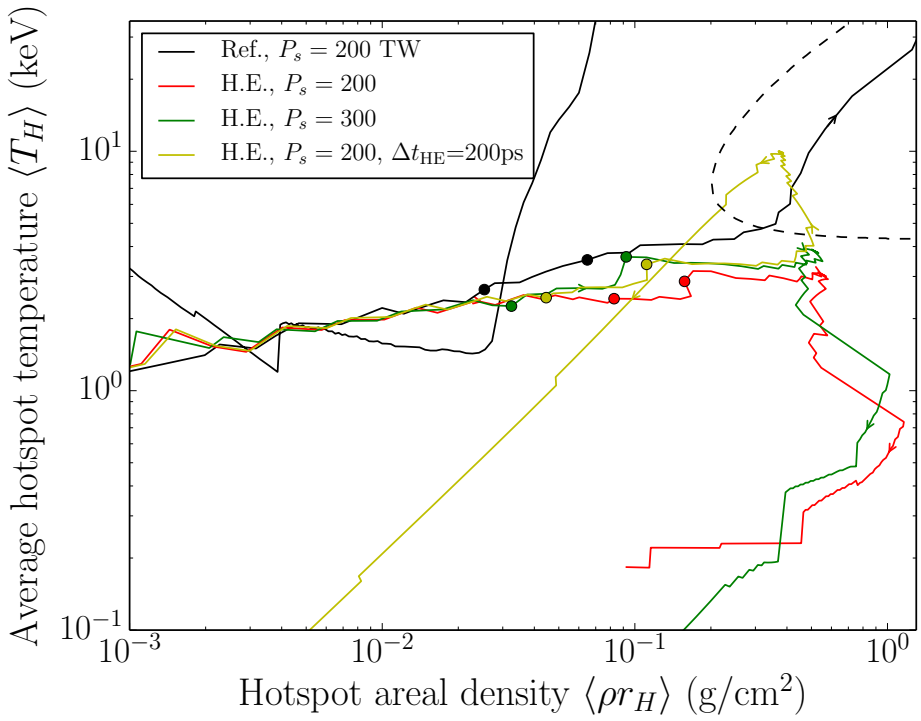

Figure 6-34 – *(color) Thermodynamic path of the hotspot, for the case without LPI-generated HEs in black and with the* Thetis *model as colored lines; red for the $P_s = 200$ TW case, green for the $P_s = 300$ TW case and yellow for the case with $P_s = 200$ TW with HE generation delayed by 200 ps. The isobaric ignition curve is shown as a dashed line [234]. Arrows indicate the direction of the time-dependent evolution of the hotspot. For each curve, the first dot indicates the time when the ignitor shock enters the hotspot and the second indicates the time of shock rebounds on the target center. Further shocks rebounds and collisions with the shell are not indicated.*

The thermodynamic path of the hotspot is shown in Fig. 6-34 for the reference case and the three cases with LPI-HEs at $t_s = 13.30$ ns. As expected from the analysis of the shell preheat, it is the case with the least hotspot mix that obtains the highest yields. Indeed, the case with 200 TW spike power and $\Delta t_{\mathrm{HE}} = 200$ ps reaches ignition, as can be clearly seen from the vertical segment of the hotspot thermodynamic trajectory. The yield in this case is of ~ 1 MJ. This is an important result, that highlights the role of the non-stationary phase of the HE generation on the target performance. Similarly, the high power case almost reaches ignition, as can be seen by the small loop in the thermodynamic path of the hotspot (the yield in that case is of ~ 0.1 MJ). This was expected given the results obtained in the pure-DT case: the shell mix causing a rapid increase in the hotspot density and mass prior to the shock convergence can be compensated by a more powerful shock arriving earlier at the target center. If the shock downstream pressure is strong enough, the mass increase is compensated (6.11), and because the shock arrives earlier it has time to rebound several times between the target center and the shell. However, the density increase still causes significant radiative losses, which are not compensated by a moderate α particle production here.

6.5 Conclusions

The Thetis model has been compared with experimental measurements in the planar and spherical geometries. The approach proposed in Ch. 5, to describe HE sources from simplified macroscopic flux functions computed from the wavefield parameters given by PCGO, gives satisfying results in terms of HE fluxes and temperatures generated by nonlinear LPIs. Moreover, a successful reproduction of shock breakout timings in the Pals and Omega experiments suggests that the angular distribution of HE beams, conditioning the dose deposited in the targets and hence the shock dynamics, is also consistent. Compared to GO-based hydrocodes, the level of agreement between experimental observables and simulation results is greatly enhanced, thus constraining the numerical simulations convincingly and allowing more precise predictions using the hydrodynamic code.

It is shown that HEs generated in the LPI regimes of interest to this study have a significant effect on the shock dynamics. Considering targets made of plastic or plastic ablator, it is notably found that typical HE beams have sufficiently high temperatures to penetrate through the dense shocked plastic and propagate in the target bulk. The HE fluxes in the considered interaction geometries are sufficient to preheat the target to the temperatures of the order of 1-10 eV, leading to a strong reduction of the shock strength. Because the target pre-heat occurs in the bulk, it has a small effect on the upstream target density. In agreement with experimental data, it is found that these shocks propagate more rapidly in the preheated material. Although the shock strength is much lower than in cases without HEs, the post-shock pressure is higher. This dynamics is of particular interest to the Shock Ignition scheme, which relies on a strong shock generated by an intense laser spike to ignite the target's hotspot. Similarly, estimating the amount of HEs generated by LPIs that reaches the target center is critical to the design of SI targets.

The model is applied to the Shock Ignition ICF scheme. We have considered a pure-DT baseline HiPER target and a more elaborate CH-DT target. Simulations of the ignition window

were conducted with the PCGO model without LPI-HEs, and with the PCGO+Thetis model. In both cases, the LPI-generated HEs are found to be detrimental to the target implosion. Although the shock downstream pressure is significantly increased with HEs, the latter have the adverse effect of causing hotspot pollution by material from the expanding preheated shell. This HE-induced hotspot mix significantly increases the hotspot mass and density before the ignitor shock reaches the hotspot. Consequently: (i) the energy required to ignite the hotspot and (ii) the radiative losses are considerably increased. We have shown that the CH-DT target is more resilient to HEs, as the plastic ablator partially shields the imploding DT from the low energy part of the HE spectrum. Using this more resilient target, it was found that the increased hotspot mass due to the preheat could be compensated by a higher spike power. In that case, the hotspot reached the border of the ignition domain. The effects of the transient phase of the HE generation from the LPI was also shown to be important. When launching the HEs 200 ps after the start of the laser spike, it was found that the shell preheat and hotspot mix were lower. Combining this effect with the increased target resilience to HEs, the ignition was reached with HEs, albeit with a modest yield of 1 MJ.

This preliminary Shock Ignition study indicates that the effects of the LPI-generated HEs on the target dynamic are significant. Considering conventional designs, the HEs may be responsible for failed target ignitions. As such, it appears necessary to include the effects of LPI-generated HEs in any realistic SI target design. Here we have highlighted the importance of the transient phase of the HE generation and their effect on the shell preheat. However, we note that the LPI-HEs may also play a role on the collision of the return shock with the ignitor shock, which was not studied here.

Chapter 7

Conclusions

This PhD thesis had several objectives.

A novel laser propagation model. Formulate a CPU-efficient and accurate laser propagation model intended for the hydrodynamic scales and suitable for the description of: (a) nonlinear LPIs, including parametric instabilities and resonant laser light absorption, (b) propagation of laser beams smoothed by optical components, and (c) linear collisional absorption by the process of inverse Bremsstrahlung.

Description of nonlinear LPIs. Develop inline models coupled to the optical module for: (a) the scattering of laser light, with emphasis on the process of Cross-Beam Energy Transfer, (b) generation and propagation of supra-thermal electrons from EPWs excited by nonlinear LPIs, and (c) which account for competition between the linear and nonlinear LPI processes.

Physics of Shock Ignition. Study of the nonlinear laser-plasma interaction in the framework of Shock Ignition, including (a) the effects of CBET on the implosion symmetry of direct-drive ICF targets and (b) the coupling between LPI-generated high energy electrons and shock dynamics.

We present here the conclusions of this work.

7.1 A novel laser propagation model

The description of nonlinear LPIs relies on the knowledge of the laser intensity in plasma. The standard approach to laser modeling at hydrodynamic scales is the Ray-Tracing model, based on a Geometrical Optics description of the wave field. In this approach, laser beams are modeled by needle-like rays damped by collisions along their propagation. This formulation describes the ray power without notion of ray intensity. Although the intensity distribution can be reconstructed based on the collisional absorption of the wavefield, the Geometrical Optics is, by design, not suited to describe the wave intensity. Therefore, we have focused our efforts on formulating a novel laser propagation model with the objective of describing more naturally the laser intensity distribution in plasma. This has been accomplished in two steps.

Paraxial Complex Geometrical Optics

We have adapted the method of Paraxial Complex Geometrical Optics to the case of plasmas. The resulting wave front equation includes information on the radius and intensity of a wave field described as a fundamental Gaussian mode in the paraxial approximation, which propagation axis is a Geometrical Optics ray. Our formulation includes the effects of collisional absorption in the underdense corona and at the critical density on the skin-depth length. This model was specially formulated for the framework of a Lagrangian hydrodynamic code, with an unstructured and irregular mesh.

The ability of GO and PCGO to model the nonlinear ponderomotive self-focusing of a laser beam was investigated. A pressure term corresponding to the ponderomotive potential was added in the hydrodynamic core, computed from the RT reconstructed intensity or from the PCGO intensity field directly. On the one hand, it was found that PCGO yields the correct ponderomotive self-focusing critical power, self-focusing distance, transverse density depletion and approaches correctly the intensity amplification. On the other hand, the RT method is unable to reproduce these quantities, as the needle-like nature of RT rays leads to artificial filamentation of the beam inside local waveguides with a size defined by the hydrodynamic mesh discretization. The vacuum diffraction modeled in the RT model by spreading the initial k-vectors of GO rays is not able to compensate the self-focusing effect, because this approach to diffraction modeling breaks down for a time-varying refractive index.

Modeling of optically smoothed beams

Second, the description of Gaussian PCGO rays was adapted to the non-Gaussian laser beams. By taking advantage of the use of Phase Plates in high-power laser systems, which effectively split laser beams in smaller beamlets, we have proposed a method for modeling large beams with many smaller PCGO beamlets pseudo-randomly focused in a region of the beam focus where the speckle radius varies slowly. This method reproduces the main features of the intensity distribution of a large beam transformed by a Phase Plate. The splitting method was compared with results from the laser propagation code Miró, in the case of the Omega SG4 beam configuration. The overlap of PCGO beamlets creates a pattern of large speckles, producing an intensity distributions and laser contrast similar to the results from Miró simulation convolved with the hydrodynamical mesh. The resulting beam contrast is similar to that of laser beams smoothed by Polarization Smoothing. Temporal-smoothing techniques have also been implemented, in the case of Smoothing by Spectral Dispersion. Comparison with theoretical estimates has demonstrated the ability of the model to reproduce the time-dependent integrated contrast of SSD-smoothed laser beams.

This model was implemented in the hydrocode Chic of the Celia laboratory. Its base formulation for 2D planar geometry has been extended to 3D geometries for specific axisymmetric configurations where spherical targets are irradiated by laser beams which focal points intersect with the rotational symmetry axis.

7.2 Description of nonlinear LPIs

Building on the novel formulation for the laser propagation, we have proposed several models to account for the nonlinear Laser-Plasma Interaction, separated in two categories: (i) the nonlinear energy transfer between crossed laser beams, arising from the light diffraction on density fluctuations excited by the ponderomotive beating of the waves, and (ii) the nonlinear coupling of the wavefield with EPWs that generate hot electron populations.

Cross-Beam Energy Transfer

Our formulation of Cross-Beam Energy Transfer relies on the discretization of the interaction region by many elementary energy exchanges between Gaussian PCGO rays, which are supposed to locally occur within a plasma of constant parameters. The ensemble of elementary energy transfer is resolved chronologically in order to be consistent. This inline model, named EYEBOLT for *ElementarY Exchange Between OpticaL Thick-rays*, has been validated against several frameworks. First, the modeling of CBET between two large beams by local energy exchanges between many beamlets has been validated in the case of a constant density, temperature and velocity plasma. Second, the EYEBOLT model has been compared to a numerical resolution of the coupled equations for the intensity of two overlapped wavefields in media presenting a linear velocity profile. Excellent agreement is found for various probe-to-pump upstream intensity ratios. Third, the EYEBOLT model has been compared to a time-dependent solution computed with the paraxial solver HARMONY, that resolves the coupled equations for the complex amplitudes of the waves. An excellent agreement of the steady-state probe beam amplification factor, beam deviation and density perturbation amplitude was found, for various probe-to-pump intensity ratios, and for intensities $I\lambda^2 \leq 10^{14}$ Wμm^2/cm^2. It was proposed that the discrepancy observed at higher intensity arose from the difference in the modeling of the wings of the wavefield, the latter being more extended in HARMONY and covering an inverse transfer resonance region. Fourth, results from the EYEBOLT model were compared to measurements of CBET gains obtained on the NOVA laser facility. A much better agreement was found compared to previous estimates obtained with analytical or paraxial models. These theoretical, numerical and experimental comparisons have provided a solid validation of our implementation of CBET based on PCGO.

Hot Electrons generated by nonlinear Laser-Plasma Interactions

The description of electrons heated to supra-thermal temperatures by nonlinear LPIs has been included into the PCGO framework. This inline model, name THETIS for *Two-dimensional Hot Electron Transport and emIssion Sources*, has two components. First, it describes the transport and energy deposition of high energy electrons in the plasma. Electron beams are modeled in the Angular Scattering Approximation, derived from the kinetic Vlasov-Fokker-Planck equation by considering the diffusion of electrons on a background of electrons and ions. Our formulation is adapted to two-dimensional, transversally Gaussian, multi-group HE beams of arbitrary angular distribution. Secondly, this transport model is interfaced with HE sources computed from the laser optical module (PCGO). Considering the case of Hot Electrons accelerated by EPWs excited by Resonant Absorption, Stimulated Raman Scattering and Two Plasmon Decay, we propose various

formulations for computing the hot electron fluxes, temperatures and angular distribution with respect to the pump wave. These formulations are based on theoretical models and analysis of the most unstable modes, experimental observation of the scattering angles and competition between processes, experimental scaling laws and Particle-In-Cell simulations. Additionally, backward propagating electrons from the TPD and backward scattered light from SRS are accounted for in the energy balance. Given the difficulty to precisely characterize LPI-generated HE fluxes in experiment, it is difficult to validate this inline coupled model with experimental data. However, the results obtained with Thetis are in good agreement with various experimental results presented in this work, in different interaction geometries and across different intensity regimes.

These inline models, also implemented in the Chic code, are consistent in terms of energy conservation. Energy transferred by CBET or to HE sources is consistently removed from the PCGO beamlet where the LPI takes place, thus affecting any further LPI process occurring downstream of the CBET or LPI-HE energy transfer. This approach naturally accounts for the competition between processes that arises from the geometrical configuration of the laser-plasma interaction.

7.3 Physics of Shock Ignition

Applications of our new integrated model were conducted in the framework of Shock Ignition ICF. We studied separately the effects of CBET and LPI-generated HEs on plasma dynamics.

Influence of CBET on direct-drive target dynamics

We applied the PCGO+Eyebolt models to the study of CBET, in the case of the laser configuration of the Omega laser facility. The beams are modeled by considering the use of the SG4 Kinoform Phase Plates, in a 2D planar geometry. We conducted full 360° simulations of a capsule implosion in which certain beams are allowed to interact through CBET, following the co-planar beam angles of the Omega chamber, of 20°, 40 °, 140° and 160°. It was found that (i) Deuterium-Tritium ablators are more prone to CBET-induced deformations than plastic ablators, (ii) the CBET decreases the laser-target coupling by displacing intensity maxima away from the critical density, thus decreasing the target convergence ratio by up to 25 %, (iii) under the beam configuration considered here, the CBET causes deformations of the target, which relative amplitude on the inner interface reaches up to 35 % for the mode 2. Conclusions on the capsule deformation were drawn for a 2D irradiation pattern. A 3D linear reconstruction of the irradiation mode shows that the mode 4 is also excited, while the excitation of the mode 2 is probably over-estimated because the CBET between non-coplanar beams is not accounted for.

Study of the LPI-generated Hot Electrons on shock dynamics

The study of HE/laser/plasma coupling was conducted with the PCGO+Thetis model. We considered several comparisons with various experiments.

- The computation of laser absorption was validated against an absorption experiment on Omega, using the PCGO+Thetis model. The experiment consisted in the consecutive

irradiation of a target with two short pulses. The first one interacts with a cold target and steep density profiles, and the second one with a warm coronal plasma and longer density profiles. Contrary to the RT-based model that must use a time-varying flux-limitation in order to reproduce the correct absorption, it was shown that our model matches the experimental data for both pulses with a fixed flux limitation. Notably, the resonant absorption contributes to the first pulse absorption, and moderately to that of the second pulse.

- The model was applied to the interpretation of a shock timing experiment conducted on the Pals laser facility. A high intensity laser beam interacts with a planar target. The ablation of the plastic layer creates a shock wave that propagates through the target and which breakout on the rear surface is measured by using a Streak Optical Pyrometry diagnostic. The HE population was inferred from the Kα emission generated by supra-thermal electrons in high-Z tracers. To a reasonable agreement, our model simultaneously matches the measurements of integrated laser reflectivity, supra-thermal electron fluxes and temperatures, and shock timings. This is a significant improvement compared to results from RT-based hydrocodes, which underestimate the shock breakout times by up to a factor of 2. It was found that the LPI-generated HEs are sufficiently energetic to penetrate through the shock and preheat the material upstream of it. Because the pre-heat occurs in the bulk of the target, it is almost isochoric. The pressure increase causes a significant shock velocity increase while also increasing the downstream pressure of the shock. Conversely, it was found that the strength of the shock, i.e. its downstream to upstream pressure ratio, is greatly reduced. Because the laser energy transferred to supra-thermal electrons is deposited both downstream and upstream of the ablation front, it was found that the ablation pressure is decreased when considering the LPI-HE processes.

- The PCGO+Thetis model was applied to a shock timing experiment in spherical geometry, conducted on Omega. A spherical target was uniformly irradiated by laser beams and the timing of shock convergence at the target center was measured. The experiment was conducted with and without Smoothing by Spectral Dispersion. In the absence of the latter, the measured HE fluxes were increased by up to a factor of 5. The LPI model with HEs was able to reproduce the shock timing measurements in the experiment without SSD. Within the error bars, the correct values for the HE flux and temperatures, laser reflectivities and shock timings were obtained. In contrast, simulations using the RT model alone in Chic were not able to reproduce the measured shock timing. As in the Pals experiment, it was found that LPI-generated HE reduce the shock strength and the ablation pressure, while increasing the downstream shock pressure and its velocity.

Influence of LPI-generated Hot Electrons on Shock Ignition target dynamics

Given the good agreement found with the new LPI model and the experimental data for interaction of intense laser pulses with planar and spherical targets, we applied the PCGO+Thetis model for the analysis of a Shock Ignition target implosion. First, we used the baseline DT-target as a starting point. Using PCGO only, we reproduced ignition curves comparable to what can be

obtained using RT-based models. Simulations using the Thetis model suggest that the HEs generated during the laser spike sufficiently preheat the bulk of the imploding shell to cause its expansion and the pollution of the hotspot with the dense shell material, before the time of shock convergence. The hotspot areal density quickly rises and the shock launched by the final laser spike is not strong enough to ignite the fusion reactions. Furthermore, the early increase in the hotspot density causes significant energy losses by the Bremsstrahlung X-ray radiation, thus rapidly cooling the hotspot. Second, we used a more advanced target design developed at the Celia laboratory, of a DT-target with a DT shell, CH ablator and Al coating. The ignition curve of simulations without HEs was compared to that of simulations with HEs. Although the targets did not reach ignition when considering the effects of LPI-HEs, the presence of the CH ablator was shown to increase the target resistance to the DT shell preheat, resulting in a decreased hotspot mix. Simulations using higher laser spike intensities suggest that the capsule could still be ignited, albeit by compensating the hotspot pollution by a shock with a much stronger downstream pressure. The timing of the LPI-HE generation also appeared to be important: a 200 ps delay in the HE generation with respect to the spike launch time was sufficient for the target to reach the ignition, although with a yield of 1 MJ only. This underlines the necessity to account for the transient period of the parametric instabilities growth.

These results have shown the importance of taking into account nonlinear processes in the design of an efficient shock ignition target. The potential applications of this model are not limited to fusion studies, and are expected to be of use for laser-target experiments in the interaction regime relevant to the instabilities considered here.

7.4 Perspectives

The perspectives of this work are numerous. We enumerate them by order of increasing complexity.

- The model in its current implementation can be used for many experimental studies. We give a few examples; (i) we presented the experimental results obtained on Pals at the wavelength of 3ω, however open questions remain for the interpretation of the data obtained at 1ω, where the results could not be reproduced with RT models, (ii) the interpretation of the spherical strong shock experiment on Omega can be extended to a recent campaign were unexpected behavior was observed when changing the ablator material, (iii) the design of Double Ablation Front experiments for Laboratory Astrophysics relies on the radiative preheating of a sample material by shocks propagating on surrounding ablators, and could be vulnerable to HE preheat, (iv) the design of a planar target experiment on the LMJ facility, that aims at measuring the effects of LPI-generated HEs on shock characteristics (the laser configuration may also be prone to CBET).

- The results presented on the Shock Ignition target design using the PCGO+Thetis model are preliminary. This subject requires a dedicated study, as it is expected that the coupling processes between the LPI-generated HEs and the shock dynamics is highly nonlinear. Notably, the details of how the HEs affect the timing of reflected shocks and their collision with the main shock remains to be explored.

- The current implementation of the parametric instabilities in Thetis is rather simple. The numerical framework being now set, there is an opportunity for adding more details to the reduced models for the parametric instabilities. Notably: (i) adding a density dependence on the SRS in order to generate a broader spectrum of HEs, (ii) implementing models for the transient phase of the instabilities, that is of particular interest for the studies related to the use of SSD and (iii) implementing a SBS reduced model. Similarly, the HE transport model based on the ASA has short-comings. Notably, it requires a significant number of energy groups in order to produce smooth energy deposition fields. This number increases even more when considering beams with an angular aperture, where the number of beamlets is multiplied by the number of spatial groups. Increased numerical efficiency could be obtained by implementing some form of straggling and blooming in the ASA model, so that less energy group would be required to achieve the same results.

- The models for electron generation and CBET are currently disjoint. There is a priori no restriction for their simultaneous use. To that end, numerical development are required. Notably, the Eyebolt model relies on a chronological ordering of the intersection stack that constantly modifies the downstream beamlet parameters. This update of the parameters must be coupled to the computation of the nonlinear LPIs in order to obtain a consistent description. This work would be considerably facilitated by tying the central-ray propagation algorithm, the energy projection algorithm, and the nonlinear LPI models directly with the resolution of the wave front equation.

- Studies of CBET in more realistic and more general laser-target configurations require to account for the energy transfer between all overlapped beams. In its current formulation, the Eyebolt model is suited for studies were an equivalent 2D planar configuration can be found. This is rarely the case, and it appears crucial to account for the CBET between non-coplanar beams. Contrary to the case of PCGO and Thetis, such calculations cannot be made in pseudo-cylindrical configurations. A 3D PCGO-based CBET model would require (i) a fully 3D implementation of PCGO and (ii) specific criteria for the crossing of PCGO rays, which will intersect in 3D through their envelop and not their centroid. Finally, the modeling of the wings of the laser beams has been shown to be of importance, and should be considered.

- In the most general laser-target configuration, the "ultimate" PCGO model based on this work would (i) be based on a 3D implementation of PCGO, preferentially in a 3D hydrodynamic code in the Cartesian coordinates, (ii) include PCGO-based CBET between the envelop of the 3D PCGO beamlets, and (iii) couple the LPI-HE generation with the CBET model.

Appendix A

PCGO implementation in a Lagrangian Hydrodynamic code

This appendix describes some of the numerical procedures devised for the implementation of PCGO in the framework of an arbitrary unstructured mesh. Note that throughout the appendix, the central ray parameter τ' is noted τ. We describe in App. A.1 the implementation of the Geometrical Optics equation, with two approaches concurrently used for the central ray in PCGO. We then detail in App. A.2 the methods employed to resolve the wave front equation for the curvature matrix of the PCGO ray. The projection of the beamlet envelope onto the mesh is described in App. A.3. It notably includes ; (i) the algorithms utilized for the efficient projection of the Gaussian electric field of PCGO beamlets onto the unstructured mesh, (ii) the neighborhood search algorithm employed to find the intersection between the mesh and the beam envelope, and (iii) the interaction of the beamlet envelope with critical density surfaces, including the description of collision absorption past the critical density on the skin depth. Integration of the wave front equation along a ray trajectory necessitates particular care to the precision of the trajectory, as discussed in App. A.1.3. Considering the assumptions made in the diverse algorithms employed here, error control on the energy conservation is ensured by a specific method, presented in App. A.4. Finally, for completeness, we give in App. A.5 the formulations of the Coulomb logarithms used throughout this work.

A.1 Geometrical Optics

The Ray-Tracing equations (Eqs. (2.25)) are Ordinary Differential Equations (ODEs) which are rather straightforward to resolve. The main difficulty lies in their efficient integration on the unstructured meshes employed in Lagrangian-hydrodynamic codes. We present two main approaches to their resolution, which are both used simultaneously in the current implementation of PCGO (as shown in Apps. A.2 and A.1.3).

A.1.1 Numerical resolution

Considering the real-valued GO trajectory equations (i.e. which only depend on the real part of the permittivity ϵ'), the ray trajectory and momentum only depend on the plasma density

n_e/n_c. In Lagrangian hydrodynamic codes, the density is defined at the center of mass of the cells. For the sake of generality, it is assumed that these cells are polygons constituted of an arbitrary number of vertices. The size of mesh cells being dictated by hydrodynamic processes only, it is not possible to directly integrate Eqs. (2.25) on the discrete Lagrangian mesh; the spatial resolution being in general insufficient. Instead, the RT equations are integrated along the continuous ray trajectory from smooth interpolations of the density field. This is achieved in several steps. First, the density field is interpolated from the center of mass of mesh cells to the nodes of the mesh. For that purpose, a widespread method is to divide a 2D linear interpolation of the squared density field to that of a 2D linear interpolation of the density field. Secondly, the mesh is *triangularized*, i.e. decomposed in elementary triangles, e.g. using Delaunay algorithms. Third, assuming that the density gradient per triangle is constant, the density at any point inside triangle i can be computed from density values known at the vertices of triangle i, $\{n_{e,i1}, n_{e,i2}, n_{e,i3}\}$, using (in 2D Cartesian geometry):

$$n_{e,i}(x,y) = a_i x \nabla_x n_e + b_i y \nabla_y n_e + c_i \ , \tag{A.1}$$

with a_i, b_i, c_i constants in triangle i that can be uniquely determined from the densities and coordinates of the 3 triangle vertices. The RT equations are integrated in triangle i by Eq. (A.1) along the ray trajecotry. This interpolation is continuous both inside a given triangle and between consecutive triangles, although it is not smooth at their junction. Typical numerical methods used for the integration of the GO equations are Runge Kutta (RK) algorithms, usually of order 4, with adaptive steps. Although RK algorithms are CPU-efficient, they loose precision for trajectories nearing the critical density. This is not an issue for simple RT-based laser propagation codes because the trajectory error is not detrimental to the precision of the collisional absorption model (presented in Sec. 2.2.2). However, this precision loss is a major issue for the integration of the wave front equation for PCGO (see Sec. 2.3.3.2). It is addressed in App. A.1.3.

A.1.2 Analytical resolution

Analytical solutions of the GO equations are easily obtained in the same framework as in Sec. A.1.1, that is for a triangularized mesh in which the density gradient is assumed to be constant. Although these solutions can be derived in cylindrical geometry for applications to 2D-axisymmetric configurations, we limit ourselves to 2D Cartesian configuration for the sake of simplicity. Starting from Eqs. (2.25) and assuming a density in triangle i of the form of Eq. (A.1), it is straightforward to derive the ray position (x,y) and velocity (v_x, v_y):

$$\begin{aligned} x(\tau) &= a_x(\tau-\tau_0)^2 + v_{x0}(\tau-\tau_0) + x_0 \ , \\ y(\tau) &= a_y(\tau-\tau_0)^2 + v_{y0}(\tau-\tau_0) + y_0 \ , \\ v_x(\tau) &= 2a_x(\tau-\tau_0) + v_{x0} \ , \\ v_y(\tau) &= 2a_y(\tau-\tau_0) + v_{y0} \ , \end{aligned} \tag{A.2}$$

where velocities are normalized to $c = 1$, and a_x and a_y are characteristic gradients in the x and y directions, defined by:

$$a_x = -\frac{1}{4n_c}\nabla_x n_e \qquad a_y = -\frac{1}{4n_c}\nabla_y n_e \ , \tag{A.3}$$

and τ is the parametric parameter of the trajectory equations, with $\tau = \tau_0$ at the entry point of triangle i. As illustrated in Fig. 2-2, for a ray propagating in a density gradient such that $a_y = 0$ and $v_{y0} \neq 0$, the ray trajectory is a parabola.

Knowing the entry point (x_0, y_0) and entry velocity (v_{x0}, v_{y0}) of a ray in a given triangle, one can find the time τ_1 at which the ray exits the triangle by searching for the intersection of the parametric curve $(x(\tau), y(\tau))$ with the triangle edges. Once τ_1 is known, the ray exit position and exit velocity can be found. This procedure requires to solve two second-order equations for each edge, each equation having 0 to 2 solutions. Cases with multiple solutions are sorted by considering that $(x(\tau_1), y(\tau_1))$ must be inside of the triangle and that $\tau_1 \neq \tau_0$. Note that the latter condition does not alway hold, as for a steep gradient aligned with the ray entry vector, the ray turns back in the triangle with $\tau_0 = \tau_1$ to within the numerical precision. Accounting for the 6 resolutions of second-order equations and the sorting of the 12 solutions, this method is usually slower than direct integration using a RK scheme (Sec. A.1.1), although the analytical solution obtained is more precise.

In general, for both the RT and PCGO methods, RK algorithms are used for the computation of trajectories. The analytical formulations presented are used in the numerical algorithms employed in the PCGO model for field projection and for the integration of the wave front equation, as is detailed in Sec. 2.3. Furthermore, the analytical formulations are of use in the correction of error committed by the RK integration of the ray trajectory, as presented below.

A.1.3 Trajectories and precision: modifications to Ray Tracing algorithms

Integration of the wave front equation in a given triangle requires the knowledge of the time spent by the ray in that triangle, that is $\Delta\tau = \tau_1 - \tau_0$. That time is found by inversion of the analytical trajectory equations (Eqs. (A.2)), from the knowledge of the entry and exit position and velocities, those being given by the trajectory computed by RK integration of the RT equations. When the density gradient in the triangle is non-zero (i.e. $a_x \neq 0$, $a_y \neq 0$), the knowledge of the velocities is sufficient and computing $\tau_1 - \tau_0$ is trivial. This timing can either be computed from the central ray coordinates on the x or y axis. Any loss of precision in ray coordinates due to the RK scheme will lead to inconsistent timings, i.e. different values of $\Delta\tau$ when computed from the x and y axis. This precision loss is higher near the critical density, and especially for rays that turn around in a triangle. In those cases, the RK integration yields exit positions and velocities that are not precise enough to compute correct values of $\Delta\tau$. In some cases, the resulting error may be large enough so that the RK integration predicts an incorrect exit edge for a ray in a triangle.

RK integration errors must be monitored in order to avoid spurious numerical behaviors in the integration of the wave front equation. For each trajectory arc computed by the RK scheme, the ray timing $\Delta\tau$ is computed from the x and y coordinates. When an inconsistency is detected, the corresponding RK step is deleted and an analytical step is conducted instead (assuming

constant density gradient, see section A.1.2). The analytical solution is then used as the next initial condition for the RK solver. This method allows to retain the CPU-efficiency of the RK scheme and obtain the numerical precision of an analytical method. The enhanced accuracy resolves numerical stability issues commonly encountered when the plasma is still cold and mesh cells are very thin in the vicinity of the critical density ($\sim 10 - 100$ nm).

A.2 Integration of the nonlinear wave front equation

The wave front equation for the curvature matrix B, Eq. (2.72), is most efficiently resolved in variations, i.e. by defining matrices P and Q such as $B = P.Q^{-1}$, which yields:

$$\frac{\mathrm{d}B}{\mathrm{d}\tau} + B^2 - \alpha_{\Re}(\tau) = \frac{\mathrm{d}P}{\mathrm{d}\tau}Q^{-1} - PQ^{-1}\frac{\mathrm{d}Q}{\mathrm{d}\tau}Q^{-1} + PQ^{-1}PQ^{-1} - \alpha_{\Re}(\tau) = 0 \ . \tag{A.4}$$

It is straightforward to see that this equation is satisfied if matrices P and Q obey:

$$\begin{aligned} \frac{\mathrm{d}P}{\mathrm{d}\tau} &= P \ , \\ \frac{\mathrm{d}Q}{\mathrm{d}\tau} &= \alpha_{\Re}(\tau)Q \ . \end{aligned} \tag{A.5}$$

The elements of matrices P and Q have meaning of derivatives of the ray normal $\boldsymbol{q}$ coordinates with respect to the ray coordinates, and derivative of the generalized momenta $\partial\psi/\partial\boldsymbol{q}$ with respect to the ray coordinates. These linear equations are integrated using an adaptative time-step Runge-Kutta scheme of order 4. Considering a central ray trajectory in triangle i, the first and second order derivatives of ϵ' must be computed for any value of $\tau \in [\tau_0, \tau_1]$. To that end, it is assumed that the density field in the vicinity of vertex k of triangle i is of the form:

$$n_e(x,y)^k = a_k + b_k x\frac{\mathrm{d}n_e}{\mathrm{d}x} + c_k y\frac{\mathrm{d}n_e}{\mathrm{d}y} + d_k x^2\frac{\mathrm{d}^2 n_e}{\mathrm{d}x^2} + e_k y^2\frac{\mathrm{d}^2 n_e}{\mathrm{d}y^2} + f_k xy\frac{\mathrm{d}^2 n_e}{\mathrm{d}x\mathrm{d}y} \ , \tag{A.6}$$

in which the free parameters are $(a_k, b_k, c_k, d_k, e_k, f_k)$. We note that these parameters could be uniquely computed from the 6 neighbors of vertex k, although this approach leads to precision losses for uneven mesh resolutions across the vertex. Consequently, the free parameters are determined by method of Singular Value Decomposition by considering 36 neighboring points, that is 3 series of neighbors around vertex k, as is illustrated in Fig. A-1. For more stability, each point is given a weight that is the inverse of its distance to the central vertex k. Once the free parameters are known, first order and second order derivatives of the density field are computed for each vertex of triangle i using Eq. (A.6), and linearly interpolated from those 3 points to any coordinate inside triangle i, as is done for the density in Sec. A.1.1. This ensure a continuous and smooth interpolation of $\alpha_{\Re}(\tau)$ along the ray trajectory for any value of τ.

To ensure numerical stability, Eqs. (A.5) are integrated along the ray trajectory with a variable step in τ that is not related to the RK integration of the trajectory equations. This is achieved by storing, for a given ray in a given triangle, only the entry coordinates and entry velocity of the ray, as well as the density gradient in the triangle. The analytical formulation for the ray trajectory and velocity as a function of τ (Eqs. (A.2)) are then used for the determination

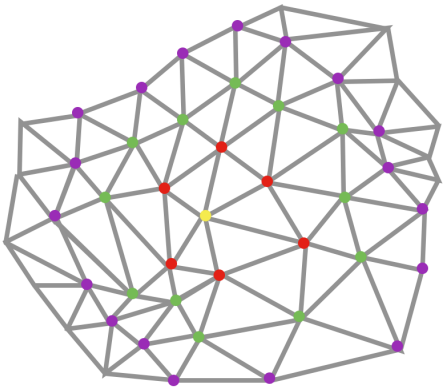

Figure A-1 – *Illustration of the triangle vertices used in the determination of first-order and second-order density gradients. The current vertex k of triangle i is shown in yellow, the first, second and third neighbors are shown in red, green and purple, respectively.*

of the density gradients transverse to the ray direction, so as to compute $\alpha_{\Re}$.

A.3 Gaussian field projection onto an unstructured Lagrangian mesh

The use of PCGO rays coupled to hydrocodes poses the problem of efficient projection of the Gaussian beam envelope onto an irregular mesh, which configuration is only determined by hydrodynamic processes. It is convenient to describe the projection technique with the problem of inverse Bremsstrahlung absorption.

Let us consider the case of a 2D planar geometry. The power P^q_{abs} deposited in the plasma by inverse Bremsstrahlung in a quadrangle q of area A_q can be written:

$$P^q_{\text{abs}} = -\iint_{A_q} \nabla \cdot \boldsymbol{I} = \iint_{A_q} \nu_{\text{IB}} \frac{\omega_p^2}{\omega_0^2} \frac{\epsilon_0}{2} |u|^2 \text{dA} \ . \tag{A.7}$$

Once again, we consider a triangularized mesh in which the density gradient is constant per triangle. We now refer to triangle j as the triangle in which the central ray is in for $\tau \in [\tau_0, \tau_1]$, coordinates at which it enters and leaves triangle j. We refer to triangle k as the triangle in which we perform the projection (e.g. energy deposition). Note that the triangles concerned by the projection can potentially represent the whole hydrodynamic grid, depending on the beam configuration.

For efficient computations, we limit the beam parameters projection to triangles which barycenter falls in the $\pm 2w$ beam envelop. The interval $[\tau_0, \tau_1]$ and the corresponding $\pm 2w$ beam envelope define a 2D surface $\mathcal{A}_j$ which intersects with the Lagrangian mesh. First, we present the criterion used to determine which triangles are "covered" by the surface $\mathcal{A}_j$.

A.3.1 Triangle selection

Fig. A-2 illustrates the selection criterion: a triangle k must be accounted for in the beam parameter projection of surface $\mathcal{A}_j$ if there is a $\tau = \tau_{jk} \in [\tau_0, \tau_1]$ at which the normal to the central ray in triangle j intersects with the barycenter of triangle k.

The barycenter of triangle k (x_k^b, y_k^b) intersects with the central ray normal at $\tau = \tau_{jk}$ when:

$$\mathbf{T}_c(\tau).\begin{pmatrix} x_k - x(\tau) \\ y_k - y(\tau) \end{pmatrix} = 0 \ , \tag{A.8}$$

where $\mathbf{T}_c(\tau)$ is the tangent vector to the central ray at τ. Using the expressions for the analytical ray trajectory given by Eqs. (A.2), this equation can be expressed as a third-order polynomial in τ:

$$\begin{aligned} -2\tau^3\left(a_x^2 + a_y^2\right) - 3\tau^2\left(a_x v_{x0} + a_y v_{y0}\right) + \\ \tau\left(2a_x\left(x_k^b - x_0\right) + 2a_y\left(y_k^b - y_0\right) - v_{x0}^2 - v_{y0}^2\right) + \\ \left(x_k^b - x_0\right)v_{x0} + \left(y_k^b - y_0\right)v_{y0} = 0 \ , \end{aligned} \tag{A.9}$$

where we have assumed $\tau_0 = 0$ for simplicity. The triangle k is considered to be covered by the envelop of the beam if $\tau_{jk} \in [0, \tau_1]$ (see Fig. A-2). It is convenient to rewrite Eq. (A.9) as:

$$c_3\tau^3 + c_2\tau^2 + c_1\tau + c_0 = 0 \ , \tag{A.10}$$

where the $\{c_0, c_1, c_2, c_3\}$ factors are readily identified from Eq. (A.9). Although this equation is straightforward to solve analytically, a few details must be highlighted. When dealing with a typical direct-drive target, mesh cells constituting the ablator and the shell are very thin. Consequently, values for τ_1, $x_k^b - x_0$ and $y_k^b - y_0$ are very small. Finding the exact solutions in this case require the use of extended quadruple precision. Furthermore, this equation yields one to three real solutions, which must be computed and examined one by one in order to determine if they are in the $[0, \tau_1]$ interval. Considering that this step, i.e. the detection of triangles for the projection, is repeated a very large number of times per iteration, it must be particularly efficient.

We consider three particular cases for solving Eq. (A.10). If $c_3\tau_1^3$ and $c_2\tau_1^2$ are very small compared to $c_1\tau_1$, the ray trajectory is almost straight. This configuration corresponds to weak (or absence of) density gradients in the cell. In that case, the general solution simply is:

$$\tau_{jk} \simeq \frac{v_{x0}(x_k^b - x_0) + v_{y0}(y_k^b - y_0)}{v_{x0}^2 + v_{y0}^2} \ . \tag{A.11}$$

When $c_3\tau_1^3$ is the only negligible term in Eq. (A.10), one must resolve a quadratic equation and rule out the solutions outside of the $[0, \tau_0]$ interval.

In the general case where no factor can be neglected, one must compute all three solutions to Eq. (A.10) and rule out the incorrect solutions. This approach is in general too numerically costly, due to the larger number of times this equation must be resolved and due to the requirement of quadruple precision. Instead, we make the assumption that the ray's parabolic trajectory is sufficiently decomposed in elementary arcs so that for a given arc, there can only be one solution

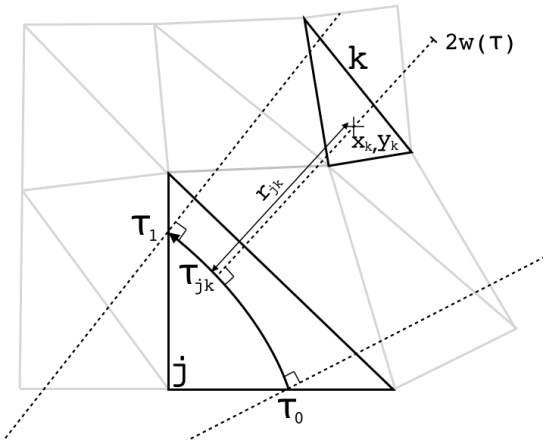

Figure A-2 – *Illustration of the selection process for a triangle k when the ray is in triangle j. The ray is illustrated for $\tau \in [\tau_0, \tau_1]$ as a curved arrow. Other triangles of the hydrodynamic grid are shown in grey. Dashed lines represent the ray normals at τ_0 and τ_1.*

of Eq. (A.10) lying in the interval $[0, \tau_1]$. We make sure this assumption is correct by introducing a splitting algorithm in the Ray Tracing step that sub-discretizes the ray trajectory as a function of its curvature. With this assumption, we can write a simple criterion to determine if there is no solution of Eq. (A.10) in $[0, \tau_1]$:

$$c_0(c_3\tau_1^3 + c_2\tau_1^2 + c_1\tau_1 + c_0) < 0 \ , \tag{A.12}$$

that is there must be a change of sign of the dot product (Eq. (A.8)) in the $[0, \tau_1]$ interval. This criterion filters the majority of cases, and the general solutions to Eq. (A.10) are only computed when it is satisfied.

A neighborhood search algorithm (see section A.3.4) allows to perform this computation on triangles neighboring j to improve performances. The distance r_{jk} from the barycenter of triangle k to the central ray in triangle j is then straigthforward to compute. The search and energy deposition are considered complete when the triangles found in the intersection of the mesh with $\mathcal{A}_|$ are at distances r_{jk} further than $\pm 2w$.

A.3.2 Integration over arbitrary triangles

The maximum power that can be deposited by the beam while the central ray is in triangle j follows from the integration of the imaginary part of the relative permittivity along the path of the central ray:

$$\begin{aligned} \Delta P^j_{\text{abs}} &= P^j_1 - P^j_0 = \sqrt{\frac{\pi}{2}}\left(I_1 w_1 - I_0 w_0\right) \\ &= \sqrt{\frac{\pi}{2}} I_0 w_0 \left(\exp\left[-2k_0 \int_{\tau_0}^{\tau_1} \epsilon_c''(\tau) d\tau\right] - 1\right) \ , \end{aligned} \tag{A.13}$$

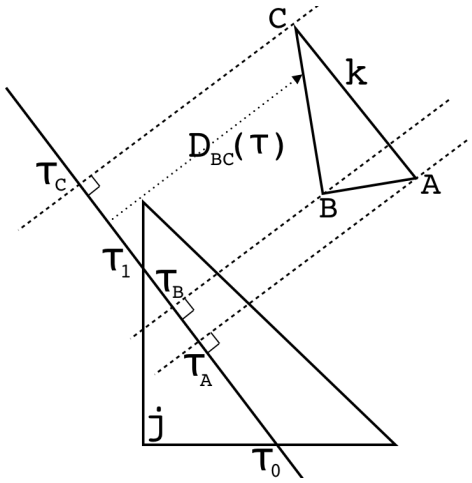

Figure A-3 – *Illustration of a triangle configuration for the integration of PCGO variables on the hydrodynamic mesh. The central ray is approximated by a straight line and crosses triangle j between τ_0 and τ_1. Dashed lines correspond to normals to the central ray at different values of τ. Distances $\mathcal{D}$ introduced in Eq. (A.15) are always taken along the ray normal, as illustrated here with $\mathcal{D}_{\mathrm{BC}}(\tau)$.*

where I designates the on-axis intensity. Subscripts 0 and 1 stand for the entrance and exit of the ray in triangle j. $\Delta P^j_{\mathrm{abs}}$ is the maximum power that can be deposited from the ray, independently of the mesh configuration. Mesh boundaries or the presence of a critical density surface can eventually crop the beam, resulting in a total power deposited in the mesh less than $\Delta P^j_{\mathrm{abs}}$. Considering a triangle k selected by the criterion defined in App. A.3.1, the power P^k_{abs} deposited by the beam reads:

$$P^k_{\mathrm{abs}} = \iint_{A_k} \nu^j_{\mathrm{IB}} \frac{\omega_p^2}{\omega_0^2} \frac{\epsilon_0}{2} |u|^2 dA \ , \tag{A.14}$$

where A_k designates the area of triangle k and we use the value of ν_{IB} from the central ray, i.e. from the triangle j, and $|u|^2 = |u_0(\tau)|^2 e^{-2r^2/w^2(\tau)}$. Note that the sum of all P^k_{abs} over selected triangles always is less or equal to $\Delta P^j_{\mathrm{abs}}$.

In order to integrate Eq. (A.14), we make the assumption that u, w and $\nu_{\mathrm{IB}} n_e/n_c$ vary linearly in $[\tau_0, \tau_1]$, between $u_0, w_0, (\nu_{\mathrm{IB}} n_e/n_c)_0$ and $u_1, w_1, (\nu_{\mathrm{IB}} n_e/n_c)_1$. This approximation remains correct as long as high gradients of laser intensity occur in regions where the mesh is reasonably refined. Once a triangle has been selected, the integration is performed over its entire surface, even if parts of the triangle lie outside of the $[\tau_0, \tau_1]$ range. This is illustrated on Fig. A-3 alongside of the notations used.

Contrary to the triangle selection algorithm detailed in App. A.3.1, we assume for the computation of P^k_{abs} that the ray trajectory between τ_0 and τ_1 is straight. Note that in order to avoid spurious behaviors related to this approximation near the critical density, where the ray curvature is large, high-curvature ray trajectories are sub-discretized in smaller arcs on which the straight line approximation is reasonable (as evoked in App. A.3.1). Given a triangle k defined by points (A,B,C), we compute the coordinates (τ_A, τ_B, τ_C) at which the ray normal intersects with the triangle points (see Fig. A-3). These values are linearly interpolated (or extrapolated) from the given values of τ_0 and τ_1 and the coordinates of the ray. We now rename (A,B,C) so

that (τ_A, τ_B, τ_C) is in ascending order. In this framework, P^k_{abs} reads:

$$P^k_{\text{abs}} = \frac{\epsilon_0\omega_0}{2}\left(\int_{\tau_A}^{\tau_B} \int_{\mathcal{D}_{AB}(\tau)}^{\mathcal{D}_{AC}(\tau)} \sqrt{\epsilon'_j(\tau)}\epsilon''_j |u|^2 \mathrm{d}q\mathrm{d}\tau + \int_{\tau_B}^{\tau_C} \int_{\mathcal{D}_{BC}(\tau)}^{\mathcal{D}_{AC}(\tau)} \sqrt{\epsilon'_j(\tau)}\epsilon''_j |u|^2 \mathrm{d}q\mathrm{d}\tau \right) , \tag{A.15}$$

where we have used $\nu^j_{\text{IB}}\omega_p^2/\omega_0^2 = \epsilon''_j\omega_0$ and $\mathcal{D}_{AB}(\tau)$ is the distance between the central ray at τ and the segment AB along the normal of the ray (this notation stands for any segment in triangle ABC). Distances $\mathcal{D}$ are linear expressions of τ by construction:

$$\mathcal{D}_{AB}(\tau) = (\mathcal{D}_B - \mathcal{D}_A)(\tau - \tau_A)/(\tau_B - \tau_A) + \mathcal{D}_A \ , \tag{A.16}$$

where $\mathcal{D}_A$ is the distance between the central ray at τ_A and the coordinates of the point A, along the ray normal. Eq. (A.15) can be simplified to:

$$P^k_{\text{abs}} = \frac{\epsilon_0\omega_0}{4}\sqrt{\frac{\pi}{2}}\Bigg[\int_{\tau_A}^{\tau_B} \sqrt{\epsilon'_j(\tau)}\epsilon''_j(\tau)|u_0(\tau)|^2 w(\tau)\left[\mathrm{Erf}\left(\frac{\sqrt{2}\mathcal{D}_{AC}(\tau)}{w(\tau)}\right) - \mathrm{Erf}\left(\frac{\sqrt{2}\mathcal{D}_{AB}(\tau)}{w(\tau)}\right)\right]\mathrm{d}\tau + \int_{\tau_B}^{\tau_C} \sqrt{\epsilon'_j(\tau)}\epsilon''_j(\tau)|u_0(\tau)|^2 w(\tau)\left[\mathrm{Erf}\left(\frac{\sqrt{2}\mathcal{D}_{AC}(\tau)}{w(\tau)}\right) - \mathrm{Erf}\left(\frac{\sqrt{2}\mathcal{D}_{BC}(\tau)}{w(\tau)}\right)\right]\mathrm{d}\tau \Bigg] , \tag{A.17}$$

with:

$$\mathcal{F}(\tau) = (\mathcal{F}(\tau_1) - \mathcal{F}(\tau_0))(\tau - \tau_0)/(\tau_1 - \tau_0) + \mathcal{F}(\tau_0) \ , \tag{A.18}$$

where $\mathcal{F}$ is either u_0, w, ϵ'_j or ϵ''_j. This expression cannot be integrated analytically for linearly varying parameters. P^k_{abs} is computed using a numerical integrator based on Romberg's method which is of a higher order than the traditional Simpson's rule [241, 242, 243].

Because the projection algorithm depends on a neighbor search algorithm, its performance in terms of CPU time depends on the relative thickness of the beam compared to the mesh resolution. In the worst case scenario (which should be avoided), the beam is as large as the entire mesh, in which case the PCGO technique is of the order of RT models. Conversely, computation of energy deposition for narrow beams (with respect to the simulation domain) is much faster with PCGO than RT. The in-between performances depend on the number of RT rays used.

A.3.3 Density correction for transverse inhomogeneities

It is assumed in Eq. (A.15) that when computing the IB absorption in a triangle i from a thick ray k propagating in triangle j, the coefficient $\sqrt{\epsilon'_j}\epsilon''_j$ is that of triangle j. In order to account for the effects of potentially strong transverse inhomogeneities in the plasma, a correction factor $\mathcal{C}^{ijk}$

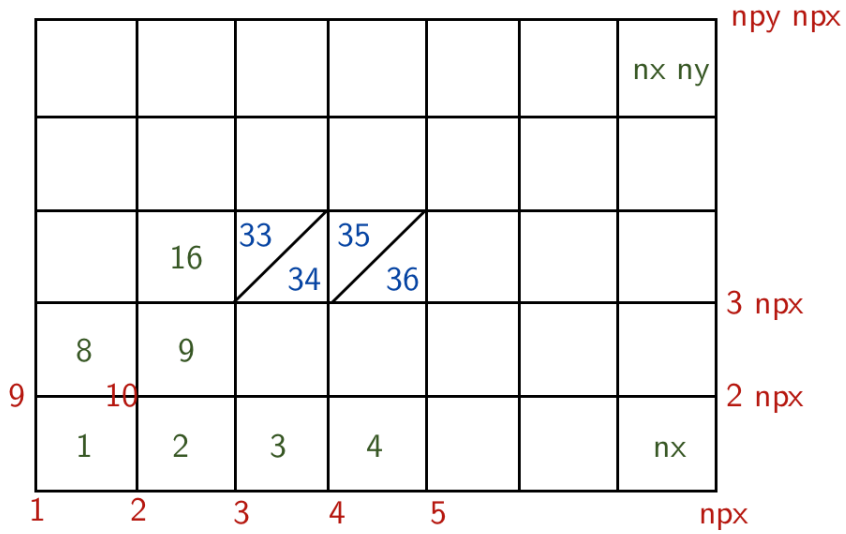

Figure A-4 – *(color) Basic topological elements of the Lagrangian mesh in* CHIC *for quadrangle cells. Node numbers are shown in red, mesh numbers in green and triangle numbers in blue.*

is added to P_{abs}^{ijk}, for subcritical triangles:

$$\mathcal{C}^{ijk} = \frac{n_e^i}{n_e^j} \frac{\sqrt{1 - n_e^i/n_c}}{\sqrt{1 - n_e^j/n_c}} \,, \tag{A.19}$$

for which the assumption remains that $\nu_{\text{IB}}^j = \nu_{\text{IB}}^i$.

A.3.4 Neighboorhood search algorithm

In order to compute the field projection from a beamlet k propagating in a triangle i, one must find the set $\{\Delta_{ki}^{\text{proj}}\}$ of triangles selected by the selection criterion (Sec. A.3.1). The straightforward approach is to compute Eq. (A.12) on the whole $m \times n$ mesh. For a simulation with N_B beams constituted of N_R beamlets each, and assuming each beamlet propagates through N_T triangles, this implies $N_c = 2 \times m \times n \times N_T \times N_R \times N_B$ computations of the numerical factors and of the third degree equation. For a 200×200 mesh with 10 beams of 100 rays each, propagating in a straight line parallel to the mesh boundary ($N_T \approx 400$), this represents 3.2×10^{10} computations of Eq. (A.12) per hydrodynamic timesteps, which is not acceptable in terms of CPU costs, even with parallel architectures. The only number that can be reduced here is $m \times n$: it is not necessary to search the whole mesh to find the suitable triangles for the projection. We describe below two neighborhood search methods that can reduce this number of operation.

A.3.4.1 Topology based method for rectangular grid

We construct the set of triangles $\{\Delta_i^o\}$ that is o quadrangles away from the quadrangle q in which triangle i is, $o = 1$ meaning direct neighboors. Following the topological numbering of mesh

quadrangles and triangles presented in Fig. A-4, $\{\Delta_i^o\}$ reads:

$$\begin{aligned}\{\Delta_i^o\} = &\{(q - oN_{px}) + \cup_{m=1}^{2o}(o-1) - (m-1)\} \\ &\cup \{(q-o) - \cup_{m=1}^{2o}(o-1)N_{px} + (m-1)N_{px}\} \\ &\cup \{(q + oN_{px}) + \cup_{m=1}^{2o}(o-1) + (m-1)\} \\ &\cup \{(q+o) + \cup_{m=1}^{2o}(o-1)N_{px} - (m-1)N_{px}\}\ ,\end{aligned} \tag{A.20}$$

where N_{px} is the number of grid points in the x direction defined in Fig. A-4, and one must then eliminate grid points outside of the mesh. The total set $\{\Delta_i^T\}$ is defined as $\{\Delta_i^T\} = \cup_{o=1,\mathrm{Max(m,n)}}\{\Delta_i^o\}$. For increasing order o, the mesh cells are increasingly farther away from the triangle i in which the beamlet centroid propagates. At any given order o, the set $\{\Delta_{ki}^o\}$ surrounds triangle i so that it is likely that Eq. (A.12) will have solutions. This is not a sufficient condition, as the selection criterion is based on triangle barycenters, although this is not an issue. When computing the field projection, the set $\{\Delta_{ki}^{\mathrm{proj}}\}$ is constructed by resolving Eq. (A.12) in sets of triangles $\{\Delta_{ki}^o\}$ of increasing order o, starting with $o = 1$. The search is stopped when either (i) triangles at a distance $\pm 2w$ along the beamlet normal have been found, or (ii) when the minimum of absolute values of distances between triangle i and triangles in $\{\Delta_{ki}^o\}$ is greater than $+2w$. The $\{\Delta_i^T\}$ ensembles must be computed for each triangles, that is $2 \times m \times n$ arrays of minimum size $2 \times m \times n$. Although this approach is memory intensive, the computation of the neighbors is only done once. Using this method, the number of computation N_c^T of the selection criterion is at least equal to N_c, and at most reduced to $N_c/(2 \times m \times n)$, depending on the thickness of the beamlet with respect to the mesh resolution.

Independently of considerations on the beamlet thickness, this method is mostly efficient for grids for which the size of the cells around the beamlet trajectory is balanced. This is rarely the case in a Lagrangian code, where, at initialization, mesh refinement is higher in a privileged direction (often perpendicular to the density gradients). It is then more advantageous to use an other criterion to construct the neighbors set.

A.3.4.2 Distance based method for rectangular, cylindrical and arbitrary grid

Instead of constructing sets of triangles concentric to a triangle i and distant by o quadrangles, we now construct the set $\{\Delta_i^D\}$ of triangles ordered in ascending distance order from triangle i (whereby distance we mean distance between barycenters). Each of the $2 \times m \times n$ $\{\Delta_i^D\}$ set is sorted using a standard Quicksort algorithm. This procedure involves the computation of $(2m \times n)^2$ L_2 norms and $2m \times n$ orderings of $2m \times n$ size arrays, so that it is rather CPU and memory intensive.

When searching through the $\{\Delta_i^D\}$ set with the selection criterion, the same stopping criteria are used as in the topology based method. Because the mesh is moving in time, this set could be recomputed at each timestep. However, the efficiency of the projection algorithm using a neighborhood based on the initial topology (that is computing $\{\Delta_i^D\}$ at the initialization only) has proven to be satisfactory. Overall, this method is more efficient than the topology based one, and is also readily applicable to any grid cell configuration, that is quadrangle, cylindrical, or polyhedral, regardless of the topological numbering of the mesh.

A.3.5 Interaction of the thick ray's envelope with the critical density: skin depth and numerical tunneling

The computation of IB absorption for subcritical triangles is conducted (Eq. (A.14)) by assuming a Gaussian profile of the field along the transverse propagation direction q. A PCGO beamlet propagating near the critical density may have a theoretical beam width larger than the distance from the central ray to the critical density, as illustrated in Fig. A-5 [left]. This situation is very common, especially when beamlets are reflected at their turning point. In those cases, the Gaussian intensity field profile is no longer correct beyond the critical density, where the field should decay exponentially. When computing the IB absorption in the overcritical triangle k from a beamlet propagation in triangle i, it is assumed that the electric field in Eq. (A.15) is of the form $|u|^2 = |u_0(\tau)|^2 \exp\left(-|r - r_c|/\delta\right)$, where $\delta = \omega_{pe}/c$ is the skin-depth at the critical density and r_c is the position of the critical density surface. Eq. (A.17) now takes the form:

$$P^k_{\text{abs}} = \frac{\delta\epsilon_0\omega_0}{4}\Bigg[\int_{\tau_A}^{\tau_B} \sqrt{\epsilon_j'(\tau)}\epsilon_j''(\tau)|u_0(\tau)|^2\left[\exp\left(\frac{\mathcal{D}_{AC}(\tau) - r_c}{\delta}\right) - \exp\left(\frac{\mathcal{D}_{AB}(\tau) - r_c}{\delta}\right)\right]\mathrm{d}\tau + \int_{\tau_B}^{\tau_C} \sqrt{\epsilon_j'(\tau)}\epsilon_j''(\tau)|u_0(\tau)|^2\left[\exp\left(\frac{\mathcal{D}_{AC}(\tau) - r_c}{\delta}\right) - \exp\left(\frac{\mathcal{D}_{BC}(\tau) - r_c}{\delta}\right)\right]\mathrm{d}\tau\Bigg] , \tag{A.21}$$

with:

$$\mathcal{F}(\tau) = (\mathcal{F}(\tau_1) - \mathcal{F}(\tau_0))(\tau - \tau_0)/(\tau_1 - \tau_0) + \mathcal{F}(\tau_0) , \tag{A.22}$$

where $\mathcal{F}$ is either u_0, ϵ_j' or ϵ_j''.

The presence of a critical density surface in the vicinity of a thick-ray may lead to an undesired effect of numerical tunneling when projecting the field, as is illustrated on Fig. A-5 [right]. This effect is not physical and must be avoided. A simple method to prevent it consists in monitoring the density of triangles in which IB deposition is computed, starting from the triangles in which the central ray propagates and outward in both directions (that is left and right, transversally from the central ray). Once a triangle which density is above the critical density has been encountered, the power deposition in that direction is stopped. Moreover, it is crucial to forbid the deposition of energy in triangles for which no vertex is subcritical. This prevents errors related to the non-continuity of the triangles selected by a selection criterion based on triangle barycenters. We note that in some very rare (and complex) cases, this control method can fail and lead to small errors in the projection. For that reason, there is an option in the code's inputs to select mesh zones on which absorption must not be computed.

A.4 Energy conservation

The methods presented in this Appendix rely on a number of approximations, numerical methods and algorithms that may not ensure preservation of the wave field energy through projection onto the Lagrangian mesh. Although many particular cases that are sources of error have

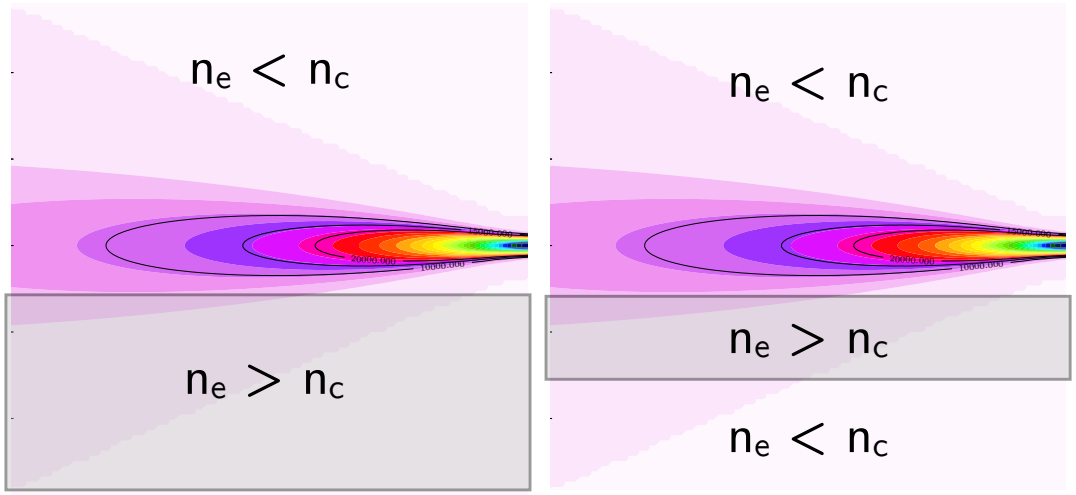

Figure A-5 – *(color) Examples of a PCGO beamlet which $\pm 2w$ envelope overlaps with a critical density surface in the plasma. The color field illustrates a Gaussian intensity profile and the grey slab is a plasma portion for which $n_e > n_c$.*

been identified and addressed separately, is it virtually impossible to account for all ray/mesh configurations that may arise and decrease the precision of the particular algorithms implemented here. For that reason, a ray-based energy conservation safeguard is implemented, as described below.

The total power absorbed in a triangle j from the field of a beamlet k which centroid is in triangle i, computed from integration of Eq. (A.14), is a scalar denoted P_j^{ik}. The total absorbed power from the contribution of beamlet k along its trajectory reads:

$$\hat{P}_{\mathrm{IB}}^k(m,n) = \sum_{i\in\{\Delta_k^{\mathrm{traj}}\}} \cup_{j\in\{\Delta_{ki}^{\mathrm{proj}}\}} P_j^{ik} \ , \tag{A.23}$$

where the quantity constructed by the union is a 2D field, and $\hat{P}_{\mathrm{IB}}^k(m,n)$ is also a field, defined on mesh numbers m and n. $\{\Delta_k^{\mathrm{traj}}\}$ is the set of triangles along the trajectory of the centroid of beamlet k and $\{\Delta_{ki}^{\mathrm{proj}}\}$ is the set of triangles selected by the selection criterion (Sec. A.3.1) for the field projection of beamlet k while its centroid is in triangle i.

The projected IB absorption field of beamlet k $\hat{P}_{\mathrm{IB}}^k(m,n)$ is uniformly renormalized by a constant factor α^k so that the final IB absorption field reads $P_{\mathrm{IB}}^k(m,n) = \alpha^k \hat{P}_{\mathrm{IB}}^k(m,n)$. The total power absorbed along the trajectory of the central ray of beamlet k is known from the integration of Eq. (2.31) (and not accounting for power variations from CBET or other nonlinear LPIs) by $P_{\mathrm{tot}}^k = P_{(\tau=\infty)}^k - P_{(\tau=0)}^k$. This quantity represents an estimate of the maximum power that can be projected from the beamlet onto the mesh, and is the power that would be deposited in the GO framework along the set $\{\Delta_k^{\mathrm{traj}}\}$. The most basic renormalization that can be used reads:

$$\alpha_{\mathrm{GO}}^k = \frac{P_{\mathrm{tot}}^k}{\sum_m \sum_n \hat{P}_{\mathrm{IB}}^k(m,n)} \ . \tag{A.24}$$

This renormalization is erroneous as it does not account for the plasma parameters in the set $\{\Delta_{ki}^{\text{proj}}\}$, that is: (i) cropped PCGO beamlets (by plasma boundaries), (ii) density variations across the beamlet normal direction (see Sec. A.3.3) and (iii) decay of the electric field at the critical density surface. α^k is computed by approaching the theoretical value of $\sum_m \sum_n \cup_{j\in\{\Delta_{ki}^{\text{proj}}\}} P_j^{ik}$ by α^{ki}:

$$\alpha^{ki} = (\tau_1 - \tau_0)|\tilde{u_0}^{ki}|^2 \tilde{\nu_{\text{IB}}^{ki}} \left(\frac{\tilde{\omega}_p^{ki}}{\omega_0^k}\right)^2 \frac{\epsilon_0}{2} \times$$
$$\left[\int_{-2\tilde{w}^{ki}}^{R_{\text{critical}}^{\text{left}}} \exp\left(-\frac{r}{\delta_{\text{left}}^{ki}}\right) \mathrm{d}r + \int_{R^{\text{left}}}^{R^{\text{right}}} \exp\left(-\frac{2r^2}{\tilde{w^{ki}}^2}\right) \mathrm{d}r + \int_{R_{\text{critical}}^{\text{right}}}^{2\tilde{w}^{ki}} \exp\left(-\frac{r}{\delta_{\text{right}}^{ki}}\right) \mathrm{d}r\right] , \quad \text{(A.25)}$$

where the quantities with a tilde ($\tilde{\nu_{\text{IB}}^{i}}$, $\tilde{u_0}^{ki}$, $\tilde{\omega}_p^{ki}$, $\tilde{w}^{ki}$) are linearly interpolated at the midpoint of the central ray trajectory k in triangle i. The transverse direction r is considered to be negative on the "left" of the beamlet centroid and positive on the "right" of the centroid. The integration boundaries read:

$$\begin{aligned} R^{\text{left}} &= \text{Max}(R_{\text{critical}}^{\text{left}}, -2\tilde{w}^{ki}) \ , \\ R^{\text{right}} &= \text{Min}(R_{\text{critical}}^{\text{right}}, 2\tilde{w}^{ki}) \ , \\ R_{\text{critical}}^{\text{left}} &= \text{Max}(r_{\text{leftC}}^{ki}, -2\tilde{w}^{ki}) \ , \\ R_{\text{critical}}^{\text{left}} &= \text{Min}(r_{\text{rightC}}^{ki}, 2\tilde{w}^{ki}) \ , \end{aligned} \quad \text{(A.26)}$$

where r_{leftC}^{ki} and r_{rightC}^{ki} are the coordinates of the critical density along the normal of the central ray k at the midpoint of its trajectory in i. The final expression for α^k reads:

$$\alpha^k = \frac{\sum_{i\in\{\Delta_k^{\text{traj}}\}} \alpha^{ki}}{\sum_m \sum_n \hat{P}_{\text{IB}}^k(m,n)} \ . \quad \text{(A.27)}$$

This formulation ensures beamlet-based energy conservation by accounting for the plasma characteristics covered by the beamlet envelope. Furthremore, because it does not depend on $P_{(\tau=\infty)}^k$, it can be used even when the central ray power variation does not uniquely depend on inverse Bremsstrahlung (that is the case when considering CBET, RAB, SRS and TPD).

A.5 Expressions for the Coulomb logarithms used in collision coefficients

For completeness, we give the expressions of the Coulomb logarithms used in the numerical codes employed here. The Coulomb logarithm is expressed as the logarithmic ratio of the maximum to minimum cutoffs of the impact parameter involved in binary elastic collisions between charged particles.

A.5.1 Electron-ion coefficient

The coulomb logarithm for electron-ion collisions reads:

$$\log \Lambda_{ei} = \max \left[\frac{1}{2} \ln \left[1 + \left(\frac{\max[\lambda_D, r_i]}{\max[b_0, \bar{\lambda_{th}}]} \right)^2 \right], 2 \right] , \tag{A.28}$$

with:

$$\begin{aligned} r_i &= \left(\frac{3}{4 n_i \pi} \right)^{1/3} , \\ b_0 &= \frac{Z e^2 (m_e + m_i)}{m_e m_i |\mathbf{v}_e - \mathbf{v}_i|^2} \approx \frac{Z e^2}{\sqrt{3 m_e k_\mathrm{B} T_e}} , \\ \lambda_{th} &= \frac{\hbar (m_e + m_i)}{m_e m_i |\mathbf{v}_e - \mathbf{v}_i|} \approx \frac{\hbar}{\sqrt{3 m_e k_\mathrm{B} T_e}} , \end{aligned}$$

where b_0 is the 90° impact parameter, λ_D is the Debye length (given in Eq. (1.34)), r_i is the inter-atomic radius [244], $\bar{\lambda_{th}}$ is the De Broglie length [245] and $\log \Lambda_{ei}$ is taken to be at least equal to 2 in order to avoid divergences with very low incident electron energies. The right-hand-side expressions were obtained assuming $|\mathbf{v}_e| \gg |\mathbf{v}_i|$ and $m_i \gg m_e$, and the average velocity of the electrons in the Maxwellian distribution function was taken to be $\langle \mathbf{v}_e \rangle = \sqrt{3 k_\mathrm{B} T_e / m_e}$.

A.5.2 Inverse Bremsstrahlung coefficient

The coulomb logarithm for inverse Bremsstrahlung reads:

$$\log \Lambda_{\mathrm{IB}} = \max \left[\frac{1}{2} \ln \left[1 + \left(\frac{\min[d_\omega, \max[\tilde{\lambda}_D, r_i]]}{\max[b_0, (1/2)\bar{\lambda_{th}}]} \right)^2 \right] - \frac{5}{4}, 2 \right] , \tag{A.29}$$

with:

$$\begin{aligned} d_\omega &= v_{T,e} / \omega_0 , \\ \tilde{\lambda}_D &= \sqrt{\frac{\epsilon_0 k_\mathrm{B} T_e}{n_e e^2} \left(1 + Z \frac{\sqrt{T_F^2 + T_e^2}}{T_i} \right)^{-1}} , \\ b_0 &= \frac{Z e^2 (m_e + m_i)}{m_e m_i |\mathbf{v}_e - \mathbf{v}_i|^2} \approx \frac{Z e^2}{\sqrt{2 m_e k_\mathrm{B} T_e}} , \\ \lambda_{th} &= \frac{\hbar (m_e + m_i)}{m_e m_i |\mathbf{v}_e - \mathbf{v}_i|} \approx \frac{\hbar}{\sqrt{2 m_e k_\mathrm{B} T_e}} , \end{aligned}$$

where $\tilde{\lambda}_D$ is the modified Debye length [244], the linear factor of 5/4 is a correction used for high Z plasmas [60], and the average velocity of the electrons in the Maxwellian distribution function was taken to be $\langle \mathbf{v}_e \rangle = \sqrt{2 k_\mathrm{B} T_e / m_e}$ [246], and T_F is the Fermi temperature:

$$T_F = \frac{\hbar^2}{2 m_e k_\mathrm{B}} (3 \pi^2 n_e)^{2/3} . \tag{A.30}$$

Appendix B

PCGO-related algorithms

B.1 Realistic beam modeling: super-Gaussian splitting

B.1.1 Splitting method

The intensity distribution computed at the virtual circle I_v^{FFT} (see Sec. 3.2.2) is approximated by a super-Gaussian intensity distribution I_v through a nonlinear least squares fit. The latter intensity distribution reads:

$$I_v = I_{0v} \exp\left[- \left| \frac{y}{r_v} \right|^{n_v} \right] \ . \tag{B.1}$$

We assume that the Gaussian distributions (beamlets) have identical widths $\hat{r_v}$ and are equally spaced in the $[-r_v; r_v]$ interval. The splitting problem then reads:

$$I_v = \sum_{k=1}^{N} I_{0v}^k \exp\left[-2 \left(\frac{y - r_v(2\frac{k-1}{N-1} - 1)}{w_v^k} \right)^2 \right] \ . \tag{B.2}$$

We define an analytical expression for I_{0v}^k:

$$\begin{aligned} I_{0v}^k &= \frac{3\hat{\mathcal{R}} I_{0v}}{N-1} \mathcal{C}_{\hat{\mathcal{R}}} \exp\left[-2 \left| 2\frac{(k-1)}{N-1} - 1 \right|^{n_v} \right] \ , \\ \mathcal{C}_{\hat{\mathcal{R}}} &= 0.53219 - \frac{3.80167 \times 10^{-3}}{\hat{\mathcal{R}}} + \frac{1.8226 \times 10^{-1}}{\hat{\mathcal{R}}^2} \ , \end{aligned} \tag{B.3}$$

where $\hat{\mathcal{R}}$ is the ratio of the beamlet radius at the virtual circle to the beam radius at the virtual circle. $\hat{\mathcal{R}}$ is computed from $\mathcal{R}$ using the beamlets Rayleigh range. The coefficients in $\mathcal{C}_{\hat{\mathcal{R}}}$ were obtained numerically by a least square fit. Defining I_v^{div} as the intensity obtained by summing the beamlets intensity profiles at the splitting coordinates, we write the mean squared error (MSE) of the decomposition as:

$$\mathrm{MSE} = \frac{1}{10 r_v} \int_{-5r_v}^{5r_v} (I_v^{\mathrm{div}}(\mathrm{r}) - I_v(\mathrm{r}))^2 d\mathrm{r} \ . \tag{B.4}$$

The MSE (see Fig. B-1) is found to decrease with increasing $\hat{\mathcal{R}}$, with small values from $\hat{\mathcal{R}} = 3$. The error is small and rather independent of n_v for values higher than 5, with the minimum

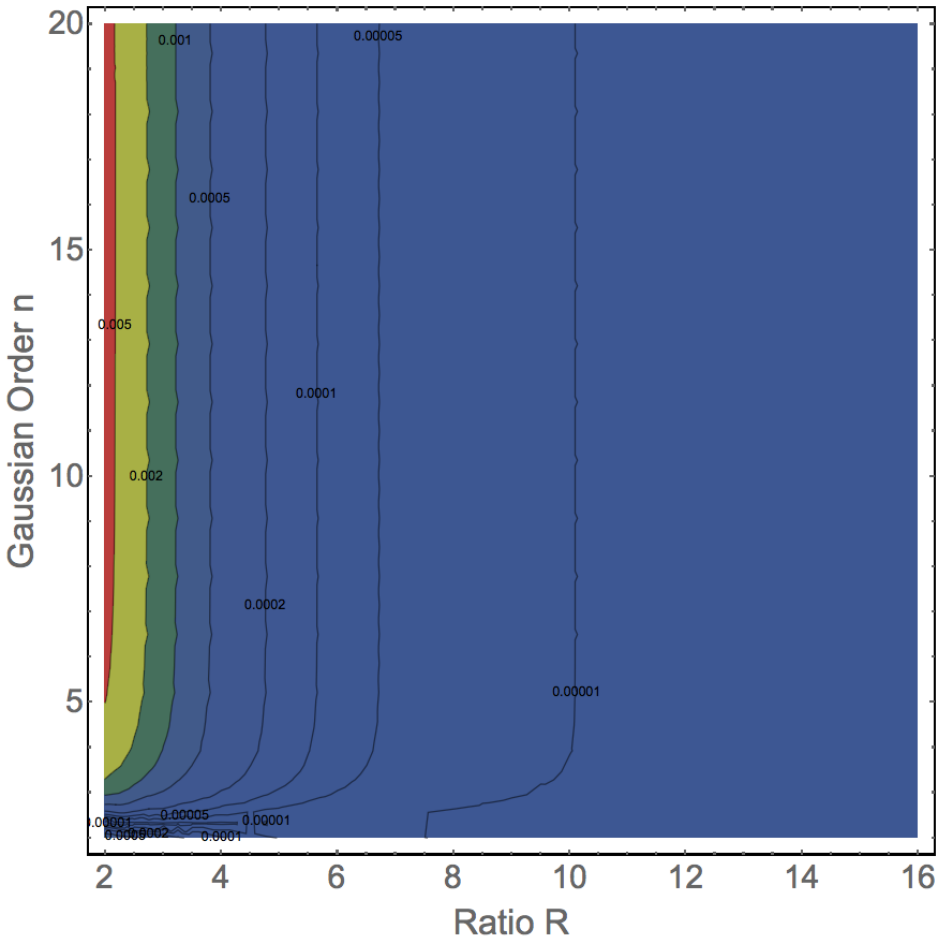

Figure B-1 – *Mean Squared Error as a function of the super-Gaussian order n_v and ratio $\mathcal{R}$, for $N = 3\hat{\mathcal{R}}$ beamlets. Red indicates higher MSE and blue lower MSE.*

being below 5. The number of beamlets used to compute the error is $N = 3\hat{\mathcal{R}}$ and constitutes an indication of the minimum number of beamlets to use. In practice, one will use much more beamlets in order to obtain a correct beam contrast in the near-field ($\sim 5N$ minimum, see Sec. 3.2.3). The value of $\hat{\mathcal{R}}$ that can be chosen has an upper limit determined by the size of the pseudo-speckles at the focal plane, which must be larger than a few wavelengths in order to satisfy the validity domain of PCGO.

B.1.2 Focusing of Gaussian beams

In this section, we detail the transformation of Gaussian beams by optical components. These results are of use for the initialization of the implementation of PCGO presented in this Appendix, in which individual Gaussian beamlets must be focused in the plasma and propagated from the virtual circle to the mesh edge.

When a Gaussian beam goes through a lens, its radius of curvature is altered by the optical component, whereas its width is unchanged, in the same way as it would for a spherical wave. The input and output curvature radii of the wave R_{in} and R_{out} can be related to the focal length f of the lens by:

$$R_{\text{out}}^{-1} = R_{\text{in}}^{-1} - f^{-1} \ , \tag{B.5}$$

which can be written in terms of the beam parameters at the lens:

$$q_{\text{out}}^{-1} = q_{\text{in}}^{-1} - f^{-1} \ , \tag{B.6}$$

where we have used $w_{\text{in}} = w_{\text{out}} = w_{\text{L}}$. Considering a parallel input beam at the lens that has an infinite curvature radius and the width w_{L}, we have $q_{\text{in}}^{-1} = -\imath\lambda/(\pi w_{\text{L}})$ and the beam parameter downstream of the lens reads:

$$q(z) = (q_{\text{out}} + z) = (-\imath\lambda/(\pi w_{\text{L}}^2) - f^{-1})^{-1} + z \ , \tag{B.7}$$

which can be rearranged to give:

$$q(z)^{-1} = \frac{(z-f) + \left(\frac{\lambda f}{\pi w_{\text{L}}^2}\right)^2 z - \imath \frac{\lambda f^2}{\pi w_{\text{L}}^2}}{(z-f)^2 + f^2\left[1 + \left(\frac{\lambda z}{\pi w_{\text{L}}^2}\right)^2\right]} \ . \tag{B.8}$$

The location of the beam waist is found by searching the point where the wavefront is flat, that is $\Re(q(z)^{-1}) = 0$:

$$z_{\text{foc}} = \frac{f}{1 + \left(\frac{\lambda f}{\pi w_{\text{L}}^2}\right)^2} \approx f \ , \tag{B.9}$$

where we have assumed $\lambda f/(\pi w_{\text{L}}^2) \ll 1$ for the last approximation. The radius of the beam at its new waist is given by $\sqrt{-\lambda/(\pi \Im(q(z_{\text{foc}})^{-1}))}$:

$$w_{\text{foc}} = \frac{\frac{\lambda f}{\pi w_{\text{L}}}}{\left[1 + \left(\frac{\lambda f}{\pi w_{\text{L}}^2}\right)^2\right]^{1/2}} \approx \frac{\lambda f}{\pi w_{\text{L}}} \ . \tag{B.10}$$

Equation (B.9) shows that in order to focus a PCGO beamlet defined at the virtual circle with a radius $\hat{w_v}$ (see Sec. 3.2.2 and App. B.1.1) an initially infinite curvature radius, one must set its curvature radius to the desired focusing distance z_{foc}. The PCGO-related validity condition (see Sec. 2.3.3.3) $w \gg \lambda$ can then be verified at the initialization from Eq. (B.10). The beam width and curvature radius at the mesh entry point are computed from the beam parameter at the virtual circle using Eqs. (2.43) and (2.44).

B.2 EYEBOLT algorithms

B.2.1 CBET: Intersection finding

In this section, we describe the algorithm used to find beams crossing points in the PCGO model. Each laser beam is modeled by a bundle of PCGO rays. We then reduce the problem of beam crossing to that of thick rays crossing. Two main assumptions are used in the model of intersection finding described below. First, we do not consider crossings between rays belonging to the same beam. A beam could theoretically exchange energy with itself through a particular configuration of speckles and a sonic flow, but this situation is ill-described in PCGO due to the nature of our

beam splitting technique (we do not model real-size speckles) and because we neglect interference. Secondly, we do not consider envelop crossings, i.e. for rays to exchange energy, they have to have their axis that intersect. In theory, beams that punctually share a part of their envelop in a plasma could exchange energy but this is a small effect. This simplification makes sense in a context where we use a large number of small rays per beam, each having a small width. When their envelops intersect with each other, but not their centers, it is likely that these rays will intersect further away, or that they are so large that their respective intensities are small.

These assumptions made, the problem of intersection finding can be reduced to two steps. Firstly, we must identify when two rays are in the same cell. We start by propagating the rays using the modified RT model. A multi-dimensional array of the cells in which rays have propagated is constructed and inspected to find the common cells and their respective rays numbers. Secondly, for each pair of rays identified in a same cell, we have to find whether they indeed intersect. In a cell (triangle), each ray coordinates are dictated by the following parametric equations (see equation (A.2)):

$$\begin{aligned} x_1(t) &= a_{x1}t^2 + v_{x01}t + x_{01} \qquad & y_1(t) &= a_{y1}t^2 + v_{y01}t + y_{01} \ , \\ x_2(s) &= a_{x2}s^2 + v_{x02}s + x_{02} \qquad & y_2(s) &= a_{y2}s^2 + v_{y02}s + y_{02} \ , \end{aligned} \tag{B.11}$$

where the subscript $1, 2$ refer to the ray numbers, and we have chosen the respective times $s_0 = 0$ and $t_0 = 0$ so that $s \in [0, s_f]$ and $t \in [0, t_f]$. Two rays will exchange energy if their respective frequencies as seen by the plasma are shifted by a precise amount, depending on the plasma parameters. This can occur with rays having the same frequency if the plasma moves with a near sonic velocity, or with rays of different frequencies. In the first case, $a_{x1} = a_{x2}$ and $a_{y1} = a_{y2}$, and in the second case, we can assume this simplification is also correct because the frequency difference between the rays is small. We then define $a_x = (a_{x1} + a_{x2})/2$ and $a_y = (a_{y1} + a_{y2})/2$. Finding the intersection point reduces to finding s_i, t_i such as:

$$\begin{aligned} a_x t_i^2 + v_{x01}t_i + x_{01} &= a_x s_i^2 + v_{x02}s_i + x_{02} \ , \\ a_y t_i^2 + v_{y01}t_i + y_{01} &= a_y s_i^2 + v_{y02}s_i + y_{02} \ , \\ s_i \in [0, s_f], t_i &\in [0, t_f] \ . \end{aligned} \tag{B.12}$$

There are two couples of solutions s_{i1}, t_{i2} and s_{i2}, t_{i2} to this set of equations (not written here for conciseness). For a significantly refined trajectory (see section A.1.3), at most one of these two couples is in the correct interval. It is worth mentioning that, similarly to the solving of equation (A.10), these solutions must be computed in extended quadruple precision in order to avoid significant numerical errors and erroneous intersection coordinates.

Once a couple of solutions s_i, t_i has been found, the intersection coordinates x_c, y_c can be computed. These coordinates are used for the interpolation of plasma quantities in the computation of the Doppler frequency shift, plasma parameters and the CBET gain.

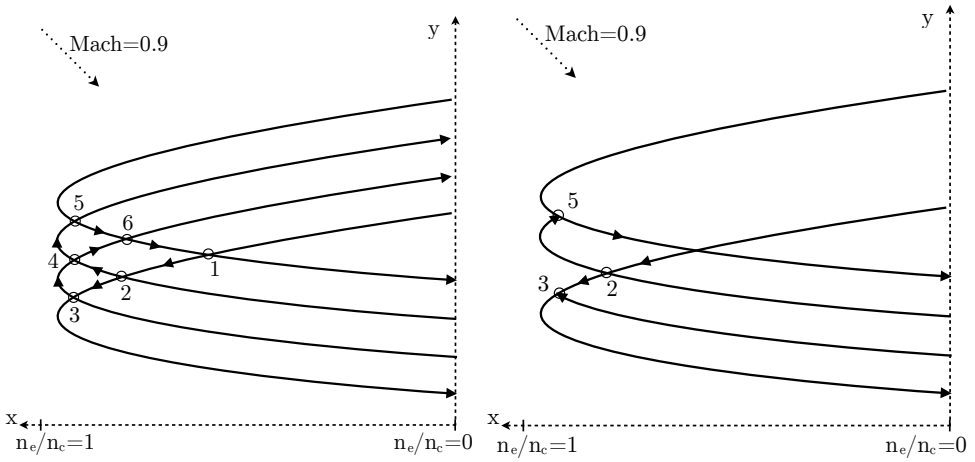

Figure B-2 – *Beamlets incident on a linear density ramp from $n_e/n_c = 0$ to $n_e/n_c = 1$ with an angle of 10°. All beamlets have the same wavelength and a Mach $M = 0.9$ flow is imposed at 45°. [left] the 6 intersections on the left have a significant and non-negligible coupling coefficient β. One can identify one 4-loop ({1;2;4;6}), two 5-loops ({1;2;3;4;6},{1;2;4;5;6}) and one 6-loop ({1;2;3;4;5;6}). The loops are analyzed in increasing degrees of complexity and the lower β node is removed. CBET in the simplified diagram [right] can now be computed by solving node 2 first and nodes 3 and 5 in any order. In that configuration, rays with upshifted frequencies in nodes 3 and 5 loses all their energy in the CBET.*

B.2.2 CBET: Intersections ordering

At each hydrodynamic timestep, the intersections between central rays of the PCGO model are identified. The resulting set of intersections is potentially large and usually reaches up to 10000 intersections in direct-drive target configurations. For the CBET model to be consistent, these energy transfers must be resolved in a chronological order with respect to each ray's propagation. For an energy transfer to be computed at a given intersection, the two rays involved must not be involved in a previous intersection, or only in previous intersections where energy transfer has already been taken into account. Once an intersection has been computed, the beamlets' energies are updated (through their intensity) and are propagated once again from the intersection to the next one by solving the wave front equations [34] in the plasma.

Considering CBET between two rays at a time, a given intersection i depends on at most two direct downstream intersections (or childs) and two direct upstream intersections (or parents). The ordering of the intersections (or nodes) starts by finding the nodes that have no parents. We define those as being the level 0. We consider a node to be ordered if all of its parents are ordered. By definition, level 0 nodes are ordered. During the solving process, we keep track of nodes for which one of two parents is ordered. Those nodes are referred to as the temporary set.

From a given level i of nodes (starting from 0), we form a set from the union of the childs of level i nodes and the temporary set. Across the nodes of this newly constructed set, we look for ordered nodes to construct the level $i + 1$. Nodes in $i + 1$ that were in the temporary set are removed. Childs of nodes in i that have not been resolved are added to the temporary set. The operation is then repeated from level $i + 1$ until the whole intersection tree has been ordered.

B.2.3 CBET: Finding and resolving loops in the intersection tree

Before applying the above algorithm to a set of nodes, one must ensure that the set can be ordered. In particular, loops in the intersection topology must be simplified for intersections to be treated in a logical order. Identifying loops is simple in principle but can be computationally challenging depending on the size of the loops and the total number of intersections. We define an intersection i as being in a loop of order n if i is in the n-th generations of its own childs (see Fig. B-2 for an example).

Loops are identified in ascending loop length order from 2 to 20. For each loop identified, the intersection for which the CBET coupling coefficient is the lowest is removed. The intersection tree is simplified before further loop-finding is applied by computing the energy exchange between the beamlets and eventually eliminating intersections containing at least one depleted beamlet.

B.3 Spherical Geometry

The PCGO and Thetis models presented in Chs. 2, 3 and 5 are formulated for a 2D planar geometry. Although a 3D spherical implosion can be approached by a 2D planar configuration as was done in Sec. 4.5 (i.e. by modeling a cylinder instead of a sphere), this approach is only suited for the study of the laser-plasma interaction in the coronal plasma. Because the mass of an imploding cylinder varies in $\propto r$ while that of an imploding sphere in $\propto r^2$, this approach is not adequate for studying the detailed shell properties at convergence. As an example, the effect of shock amplification by spherical convergence in imploding ICF targets can only be reproduced by considering 2D-axisymmetric geometries. Consequently, this approach is inadequate for the study of couplings between LPI-generated HEs and shock dynamics in the spherical geometry, which is of importance for the Shock Ignition scheme. In this section, we present a different approach to the problem, that ultimately allows to model 2D-axisymmetric implosions with the 2D planar PCGO and Thetis models.

We consider a sphere with the south-north axis oriented along the z axis, and assume that the irradiation is symmetric with respect to the equatorial plane ($x-y$ plane). Then, 2D-axisymmetric simulations can be reduced to a plane $\mathcal{P}$ that contains the target center (see Fig. B-3), assuming a rotational symmetry around z and a planar symmetry along the local r axis. Indeed, a light ray that initially propagates in the $\mathcal{P}$ plane will stay in that plane, because the density gradients transverse to $\mathcal{P}$ are symmetric by rotation around z. This means that a PCGO beamlet with the centroid lying in $\mathcal{P}$ will stay in that plane. Because all PCGO-related quantities are computed at the beamlet centroid coordinates, in that case we can describe the 2D-axisymmetric Gaussian beamlet properties from the centroid propagation in the $\mathcal{P}$ plane, with the exception of the off-plane component of the curvature matrix, which depends on the density gradients in the transverse directions to $\mathcal{P}$. In a 2D-axisymmetric framework, the transverse gradients originate only from the rotational symmetry (they vary as $1/r$), and do not carry any meaningful information on 3D deformation modes of the shell. We simplify the problem by assuming that the beamlet thickness along the off-plane axis w_2 is equal to the in-plane thickness w_1, i.e. the Gaussian beam has a circular transverse profile (that is cylindrically symmetric with respect to

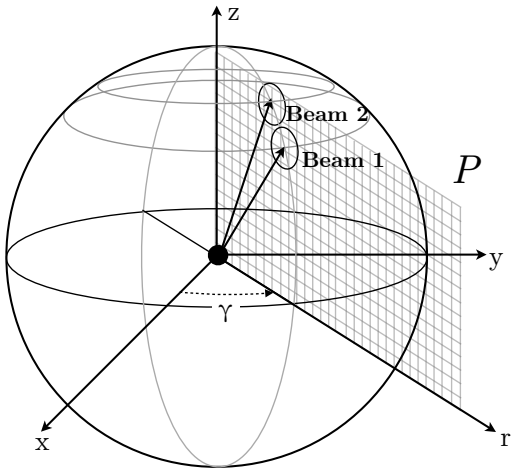

Figure B-3 – *Mesh configuration for axisymmetric simulations. The hydrodynamic equations are resolved in plane $\mathcal{P}$. z is the rotation axis and $x-y$ a symmetry plane.*

the centroid). In that framework, the transport equation (Eqs. (2.59) and (2.74)) read:

$$\begin{aligned} |\tilde{A}_0(\tau)|^2_{3\mathrm{D}} &= |\tilde{A}_0(0)|^2 \sqrt{\frac{w_{10}w_{20}}{w_1(\tau)w_2(\tau)}} \,, \\ \Longleftrightarrow |\tilde{A}_0(\tau)|_{3\mathrm{D}} &= |\tilde{A}_0(0)| \sqrt{\frac{w_0}{w(\tau)}} \,, \end{aligned} \tag{B.13}$$

which is the same expression as in the 2D framework.

According to these considerations, we consider a 2D planar laser propagation onto a target with the hydrodynamic profile being a slice of a 3D sphere (see Fig. B-3). Recalling that in hydrocodes the laser interacts with the plasma through the energy source term w_{ext}, the energy computed onto a 2D cylinder must be transformed on a 3D sphere slice. This procedure is not difficult to implement considering that in Chic, the advection equations (2.5) are resolved in 2D using the planar mass of the Lagrangian cells, while the energy diffusion equation (2.6) is resolved in a 2D-axisymmetric framework (so-called *cylindrical gemoetry*) using the real (toroidal) mass of the cells (see [115] for more details).

One caveat to this approach is the projection of PCGO beamlet properties onto the Lagrangian mesh, such as the computation of inverse Bremsstrahlung power absorbed by the plasma. In a 2D planar framework, the projection of the Gaussian field is computed onto slabs which cross-sections are the mesh cells. In a 2D-axisymmetric framework, one should compute the projection of a Gaussian field of elliptical section (or circular in our case) onto a torus which cross-sections are also the mesh cells in the plane $\mathcal{P}$. Calculation of such a volume integral represents a significant numerical development, and the problem would be much more suited to a 3D implementation in Cartesian coordinates than to the 2D-axisymmetric framework of cylindrical coordinates. The projection procedure is greatly simplified as long as one of the transverse axes of the Gaussian beamlet, $\mathbf{q}_1$ or $\mathbf{q}_2$, is orthogonal to the axis of rotational symmetry. Indeed, for a beamlet propagating in $\mathcal{P}$, because $\mathbf{q}_1$ is always in $\mathcal{P}$ and $\mathbf{q}_2$ always orthogonal to it, it is reasonable to compute projections onto the 2D planar mesh and to correct for cylindrical mass equivalence.

In Thetis, the direction of HE sources is determined from the direction of PCGO beamlets. If the latter are confined to $\mathcal{P}$, the former also lie in $\mathcal{P}$, with the exception of TPD-HE which are emitted in the full 45° forward cone, i.e. in planes that do not contain the target center. This caveat is for now neglected, for lack of a fully 3D propagation model. With that hypothesis in mind, it is straightforward to use Thetis in that configuration, because the module is tied into the PCGO projection algorithm.

Finally, although the CBET module could also be used in this configuration, it is not a consistent approach as it cannot account for energy transfers between beams propagating in different $\mathcal{P}$ planes. In this case as well, a fully 3D propagation code would be required. Note that CBET in 3D would create asymmetries in the external source term w_{ext} that could only be investigated with a fully 3D hydrodynamic code in which the axial symmetry is not assumed. Indeed, even though RT models in hydrocodes are usually 3D, their interaction with a 2D-axisymmetric code is reduced to the geometries of toroidal cells, that is, no azimuthal asymmetries can be accounted for.

In summary, the procedure proposed here consists in the following steps ;

- compute the laser plasma interaction with PCGO and Thetis in a 2D planar representation of at most a quarter of a cylinder, that represents a quarter of a meridional circle of the sphere,
- correct the source term in each cell i by the ratio of the planar mass M_i^{2Dplanar} to that of the toroidal mass M_i^{2Daxi} so that $w_{\text{ext,i}}^{\text{2Dcyl}} = w_{\text{ext,i}}^{\text{2Dplanar}} M_i^{\text{2Dcyl}} / M_i^{\text{2Dplanar}}$,
- resolve the electron-ion coupling equations in the cylindrical geometry together with the hydrodynamic and radiative equations,
- repeat that procedure at each hydrodynamic timestep.

This configuration is referred to as 2D *pseudo-cylindrical geometry*, and it is used in problems presented in Secs. 6.3 and 6.4.

Appendix C

Ray-based formulation of Hot Electron sources

C.1 Absorption fraction model for Resonant Absorption

We derive in this section a simplified theoretical model of the Resonant Absorption that allows a computation of the absorbed energy fraction from the knowledge of the density gradient length L, initial angle of the wave with the gradient φ and the wave frequency ω. Two formulations for this absorption fraction are presented and compared to numerical resolutions of the wave equation and PIC simulations.

C.1.1 *s*-polarized case

We consider a plasma with a linear density profile; $\epsilon = 1 - n_e/n_c = 1 - z/L$, and an EM wave propagating in the $y - z$ plane, incident at an angle φ with respect to the density gradient (see Fig. C-1). In that case, we have $k_x = 0$ and $\partial_x = 0$. For a s-polarized wave, $\mathbf{E}(y, z) = E_x(y, z)\mathbf{e}_x$

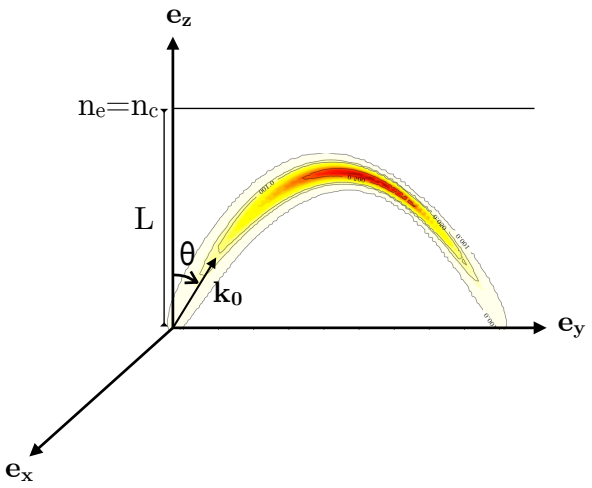

Figure C-1 – *Coordinate system and the thick ray trajectory in a plasma with a linear density profile. The wave is represented as a contour field, in the $y - z$ plane.*

and the electric field of the wave in the plasma (Eq. (1.50)) reads:

$$\frac{\partial^2 E_x}{\partial y^2} + \frac{\partial^2 E_x}{\partial z^2} + \frac{\omega^2}{c^2}\epsilon(z)E_x = 0 \ . \tag{C.1}$$

Because ϵ only depends on z, the y-dependence of the electric field is of the form $\propto \exp[\imath k_y y]$ where k_y is constant and equal to its value at $z = 0$. Geometrically, we have $k_y = (\omega/c)\sin\varphi$. Substituting for $E_x(y,z) = E(z)\exp(\imath(\omega/c)\sin\varphi y)$ in Eq. (C.1) and dividing both sides by $\exp(\imath k_y y)$ yields:

$$E(z)\frac{\omega^2}{c^2}(\epsilon(z) - \sin^2\varphi) + \frac{\mathrm{d}^2 E(z)}{\mathrm{dz}^2} = 0 \ . \tag{C.2}$$

Using the WKB approach in this equation, $E(z) \propto \exp[\imath \int k_z(z)\mathrm{d}z]$, we find that reflection of the light wave occurs for $\epsilon(z) = \sin^2\varphi$. However, the WKB approximation is not valid at the turning point. In order to estimate the field near the turning point and at the critical density (which will be useful in deriving an approximation of the resonant field in the p-polarized case), we consider an exact solution of Eq. (C.2). We define $\eta = (\omega^2/c^2 L)^{1/3}(z - L\cos^2\varphi)$ and substitute it for z in Eq. (C.2):

$$\frac{\mathrm{d}^2 E}{\mathrm{d}\eta^2} - \eta E = 0 \ . \tag{C.3}$$

Solutions of this equation are linear combinations of the Airy functions of the first kind Ai and of the second kind Bi, $E = C_1 Ai(\eta) + C_2 Bi(\eta)$. The constants C_1 and C_2 are defined from asymptotic conditions. The field must decay towards zero for $\eta \to \infty$ (that corresponds to opaque, overdense plasma), which is not the case of the Bi functions. Therefore, a solution has the form $E(\eta) = C_1 Ai$ and the constant can be found using the boundary conditions at $z = 0$, i.e. $\eta_0 = -(\omega L/c)^{2/3}\cos^2\varphi$. Assuming $|\eta_0| \gg 1$, which is satisfied for $\omega L/c \gg 1$ and incidence angles not too close to $\pi/2$, an asymptotic expression for Ai can be used:

$$Ai(\eta) = \frac{1}{\sqrt{\pi}(-\eta)^{1/4}}\cos\left(\frac{2}{3}(-\eta)^{\frac{3}{2}} - \frac{\pi}{4}\right) \ , \tag{C.4}$$

which is valid for $\eta \lesssim -1.3$. Using Euler formula for the cosine, this field can be expressed as the sum of a forward and a backward traveling wave:

$$E(z) = C_1 Ai(\eta) = C_1 \frac{1}{2\sqrt{\pi}(-\eta)^{1/4}}\left[\exp\imath\left(\frac{2}{3}(-\eta)^{3/2} - \frac{\pi}{4}\right) + \exp -\imath\left(\frac{2}{3}(-\eta)^{3/2} - \frac{\pi}{4}\right)\right] \ . \tag{C.5}$$

The first term in the square brackets represents the incident wave in the WKB expression $\int_0^z k_z \mathrm{d}z = \frac{2}{3}\left[(-\eta)^{3/2} - (-\eta_0)^{3/2}\right]$. Correspondingly, the second term represents the reflected field, so that we can rearrange (C.5) to obtain:

$$E(z) = E_{\mathrm{FS}}\left(\frac{-\eta_0}{-\eta}\right)^{1/4}\left(\exp\imath\left[\frac{2}{3}(-\eta)^{3/2} - \frac{2}{3}(-\eta_0)^{3/2}\right] + R\exp -\imath\left[\frac{2}{3}(-\eta)^{3/2} - \frac{2}{3}(-\eta_0)^{3/2}\right]\right) \ , \tag{C.6}$$

provided that:

$$C_1 = 2\sqrt{\pi}(-\eta_0)^{1/4} E_{\mathrm{FS}} \exp\left[-\frac{2}{3}\imath\frac{\omega L}{c}\cos^3\varphi + \imath\frac{\pi}{4}\right] \ , \tag{C.7}$$

where $E_{\rm FS}$ is the wave electric field at the plasma-vacuum boundary and R is the reflection coefficient. The phase term (noted $\exp \imath\phi$) in C_1 is not important for the norm of the field. The electric field then reads:

$$E_x = 2\sqrt{\pi \cos\varphi}(\omega L/c)^{1/6} E_{\rm FS} Ai(\eta) \exp\left[-\frac{2}{3}\imath\frac{\omega L}{c}\cos^3\varphi + \imath\frac{\pi}{4} + \imath\frac{\omega}{c}\sin\varphi y\right] . \tag{C.8}$$

The maximum value of E_x is achieved for $\eta = -1$ (corresponding to $z = -(c^2L/\omega^2)^{1/3} + L\cos^2\varphi$), $E_x = 1.9\sqrt{\cos\varphi}E_{\rm FS}(\omega L/c)^{1/6}$. The field at the turning point, for $\eta = 0$, reaches $E_x = 1.26\sqrt{\cos\varphi}E_{\rm FS}(\omega L/c)^{1/6}$ and then decays exponentially in the non-transparent region. The components of the magnetic field are obtained using the Faraday's law (1.48):

$$\begin{aligned} \frac{\partial E_x}{\partial z} &= B_y \imath\omega/c \ , \\ -\frac{\partial E_x}{\partial y} &= B_z \imath\omega/c \ . \end{aligned} \tag{C.9}$$

Using the expression for E_x in Eq. (C.8), the magnetic field reads:

$$\begin{aligned} B_y(y,\eta) &= -\imath\left(\frac{c}{\omega L}\right)^{\frac{1}{6}} \exp(\imath\omega/c\sin\varphi y) 2\sqrt{\pi\cos\varphi}E_{\rm FS}\mathrm{e}^{\imath\phi}\frac{\mathrm{d}Ai(\eta)}{\mathrm{d}\eta} \ , \\ B_z(y,\eta) &= -2\sqrt{\pi\cos\varphi}(\omega L/c)^{1/6}E_{\rm FS}\mathrm{e}^{\imath\phi}Ai(\eta)\sin\varphi\exp(\imath\omega/c\sin\varphi y) \ . \end{aligned} \tag{C.10}$$

The norm of the magnetic field at the turning point, i.e. $\eta = 0$, is therefore:

$$\begin{aligned} |B(y,\eta=0)| &= \left(\frac{c}{\omega L}\right)^{\frac{1}{6}} \frac{2\sqrt{\pi\cos\varphi}E_{\rm FS}}{3^{1/3}\Gamma(\frac{1}{3})}\sqrt{1+\left(\frac{\omega L}{c}\right)^{\frac{2}{3}}\frac{\Gamma(\frac{1}{3})}{3^{1/3}\Gamma(\frac{2}{3})}\sin^2\varphi} \\ &\simeq 0.92\left(\frac{c}{\omega L}\right)^{\frac{1}{6}} E_{\rm FS}\cos\varphi\sqrt{1+1.88\left(\frac{\omega L}{c}\right)^{\frac{2}{3}}\sin^2\varphi} \ , \end{aligned} \tag{C.11}$$

where Γ is the Euler Gamma function. In particular, for a wave at a normal incidence with the density gradient, we find the known expression for B at the turning point:

$$|B(\eta=0)| \simeq 0.92\left(\frac{c}{\omega L}\right)^{\frac{1}{6}} E_{\rm FS} \ . \tag{C.12}$$

It exponentially decays beyond this point.

C.1.2 *p*-polarized case

For a p-polarized wave, the electric field reads $\mathbf{E}(y,z) = E_y(y,z)\mathbf{e}_y + E_z(y,z)\mathbf{e}_z$. It is convenient here to work with the magnetic field of the wave, which has only one component $\mathbf{B}(y,z) = B_x(y,z)\mathbf{e}_x$. The wave equation for the magnetic field (1.52) projected on $\mathbf{e}_x$ reads:

$$\frac{\partial^2 B_x}{\partial y^2} + \frac{\partial^2 B_x}{\partial z^2} + \frac{\omega^2}{c^2}\epsilon(z)B_x = \frac{\partial B_x}{\partial z}\frac{\mathrm{d}\ln\epsilon}{\mathrm{d}z} \ . \tag{C.13}$$

Similarly to the electric field in the s-polarized case, $B_x(y,z)$ is expressed as:

$$B_x(y,z) = B(z)\exp(\imath k_y y) = B(z)\exp(\imath\omega/c\sin\varphi y)\ . \tag{C.14}$$

The solution for $B(z)$ can be expressed through the Airy function similarly to Eq. (C.3) if the term in the right-hand-side of Eq. (C.13) is neglected. Substituting this expression for B_x in the $\mathbf{e}_z$ component of Ampere's law yields:

$$-\frac{\partial B_x(y,z)}{\partial y} = -\imath\frac{\omega}{c}\epsilon(z)E_z(y,z)\ . \tag{C.15}$$

After differentiation and assuming $E_z(y,z) = E_z(z)\exp(\imath\omega/c\sin\varphi y)$, an expression for $E_z(z)$ is obtained:

$$E_z(z) = \sin\varphi B_x(z)/\epsilon(z)\ . \tag{C.16}$$

Even though the critical point is beyond the turning point and the field B_x decays exponentially, the value of $\epsilon \to 0$ makes the electric field large. Consequently, the electric field near the critical density reads $E_z(z) = \sin\varphi B_x(L)/\epsilon(z)$. In order to simplify the problem, it is proposed in Ref. [80] to estimate $B_x(L)$ from the B-field $|B_{c0}|$ at the turning point of the wave in the s polarized case for $\varphi = 0$ (at this angle, the B-field is at the critical density, see Eq. (C.12)). For a non-zero incidence angle, the decay of the wave from the turning point (z=$L\cos^2\varphi$) to the critical density ($z = L$) is estimated by multiplying $|B_{c0}|$ by an exponential factor $\exp -\beta$, where:

$$\beta = \int_{L\cos^2\varphi}^{L}\frac{1}{c}\sqrt{\omega_{pe}^2 - \omega^2\cos^2\varphi}\mathrm{d}z\ , \tag{C.17}$$

which yields an estimated magnetic field at the critical density, noted B_c:

$$B_c \simeq 0.92|E_{\mathrm{FS}}|\left(\frac{c}{\omega L}\right)^{1/6}\exp\left[-\frac{2\omega L\sin^3\varphi}{3c}\right]\ , \tag{C.18}$$

so that the *driver field* $E_d = B_x(L)\sin\varphi$ at the critical density ($\eta_c = (\omega L/c)^{2/3}\sin^2\varphi$) reads:

$$\begin{aligned} E_d = \sin\varphi B_c &\simeq \frac{|E_{\mathrm{FS}}|}{\sqrt{2\pi\omega L/c}}\Phi(\eta_c)\ , \\ \Phi(\eta) &= 2.3\eta^{1/2}\exp(-\frac{2\eta^{3/2}}{3})\ , \end{aligned} \tag{C.19}$$

Computing the fraction of laser energy resonantly absorbed from the above formula for Φ yields an overestimation by a factor of 1.7 [80]. We propose a different interpolation formula:

$$\Psi(\eta) \simeq \frac{1.759\eta^{1/2}}{(\eta+0.435)^{1/4}}\exp\left[-\frac{2\eta^{3/2}}{3}\right]\ , \tag{C.20}$$

that we compare to $\Phi_R = \Phi/1.7$ below. As expected, both resonance functions go to zero for $\eta \to 0$ because the component of the electric field along the gradient direction goes to zero for normal incidence. Similarly, the resonance function goes to zero for $\eta \to \infty$, as the incident wave has to tunnel through a too large distance to reach the critical surface.

Considering an EM damping rate ν^{EM}, the total absorbed energy flux Ω due to E_z can be expressed from Eq. (1.75):

$$\Omega = \int_0^\infty \nu^{\mathrm{EM}} \bar{W} = \int_0^\infty \frac{\nu^{\mathrm{EM}} \epsilon_0 |E_z|^2}{2} = \int_0^\infty \nu^{\mathrm{EM}} \epsilon_0 \frac{\sin^2 \varphi B(z)^2}{2|\epsilon(z)|^2} \mathrm{d}z \ , \tag{C.21}$$

were it was assumed that $\partial_t \bar{W} = 0$. Assuming $\nu_{\mathrm{IB}} \ll \omega$, this equation reads:

$$\frac{1}{|\epsilon(z)|^2} = \frac{1}{(1-\frac{z}{L})^2 + \left(\frac{z\nu_{\mathrm{IB}}}{L\omega}\right)^2} \simeq \frac{1}{(1-\frac{z}{L})^2 + \left(\frac{\nu_{\mathrm{IB}}}{\omega}\right)^2} \ , \tag{C.22}$$

where we have used $\nu^{\mathrm{EM}}_{\nu_{\mathrm{IB}} \ll \omega} = \nu_{\mathrm{IB}} n_e / n_c$ (Eq. (1.77)). The $1/|\epsilon|^2$ function reaches a maximum for $z = L$ proportional to ω/ν_{IB}, with a width proportional to ν_{IB}/ω. For $\nu_{\mathrm{IB}}/\omega \ll 1$, the latter function is highly peaked around the critical density. The contribution to the wave damping from the Resonant Absorption (noted Ω_{RA}) can be considered as a damping from the field resonantly excited at the critical density. The width of the resonance being narrow around $z = L$, we approximate $\sin \varphi B(z)$ by its value at the critical density E_d. Ω_{RA} then reads:

$$\Omega_{\mathrm{RA}} \simeq \frac{\epsilon_0 \nu_{\mathrm{IB}} E_d^2}{2} \int_0^\infty \frac{dz}{(1-\frac{z}{L})^2 + \left(\frac{\nu_{\mathrm{IB}}}{\omega}\right)^2} = \frac{\nu_{\mathrm{IB}} \epsilon_0 E_d^2}{2} \frac{L(\pi + 2\mathrm{arccot}(\nu_{\mathrm{IB}}/\omega))}{2\nu_{\mathrm{IB}}/\omega} \ , \tag{C.23}$$

where it was assumed that E_d is constant over the width of the resonance. We develop this expression in series using $\nu_{\mathrm{IB}}/\omega \ll 1$ to get:

$$\Omega_{\mathrm{RA}} \simeq \frac{\pi \epsilon_0 \omega L E_d^2}{2} \ . \tag{C.24}$$

Denoting the vacuum energy flux of the wave by $\bar{W}_{\mathrm{FS}} = c\epsilon_0 |E_{\mathrm{FS}}|^2/2$, the absorbed energy fraction $f_A = \Omega_{\mathrm{RA}}/\bar{W}_{FS}$ reads:

$$f_A = \frac{\pi \omega L}{c} \frac{E_d^2}{|E_{\mathrm{FS}}|^2} = \frac{F(\eta_c)^2}{2} \ , \tag{C.25}$$

where $F(\eta_c)$ is a resonance function, i.e. Φ_R for the one derived in Ref. [80] or Ψ for the one we have proposed. Figure C-2 shows a comparison of the resonance functions obtained in these simplified approaches to numerical simulations solving the wave equation in a density gradient [95] for $T_e = 2.55$ keV and $T_e = 51$ keV. Results are also compared to PIC simulations of a wave incident on a density gradient for $k_0 L = 12.5$ and $T_e = 625$ eV. Comparison of the absorption fractions f_A shows a good agreement between the simple estimates Φ_R and Ψ with the reference simulations. The latter also shows that the optimal angle for Resonant Absorption is located between $\eta_c = 0.47$ and $\eta_c = 0.53$. The resonance function we propose predicts is maximum at $\eta_c^\Psi = 0.51$, whereas the formulation from Ref. [80] yields a maximum absorption at $\eta_c^\Phi = 0.63$.

C.2 Resonant Absorption model implementation in PCGO

The model derived in Sec. C.1 gives an estimate of the EM energy absorbed at the critical density, assuming a linear density profile. In realistic simulations of planar targets or ICF implosions, density profiles could be more complicated. Consequently, the initial angle φ of the wave with

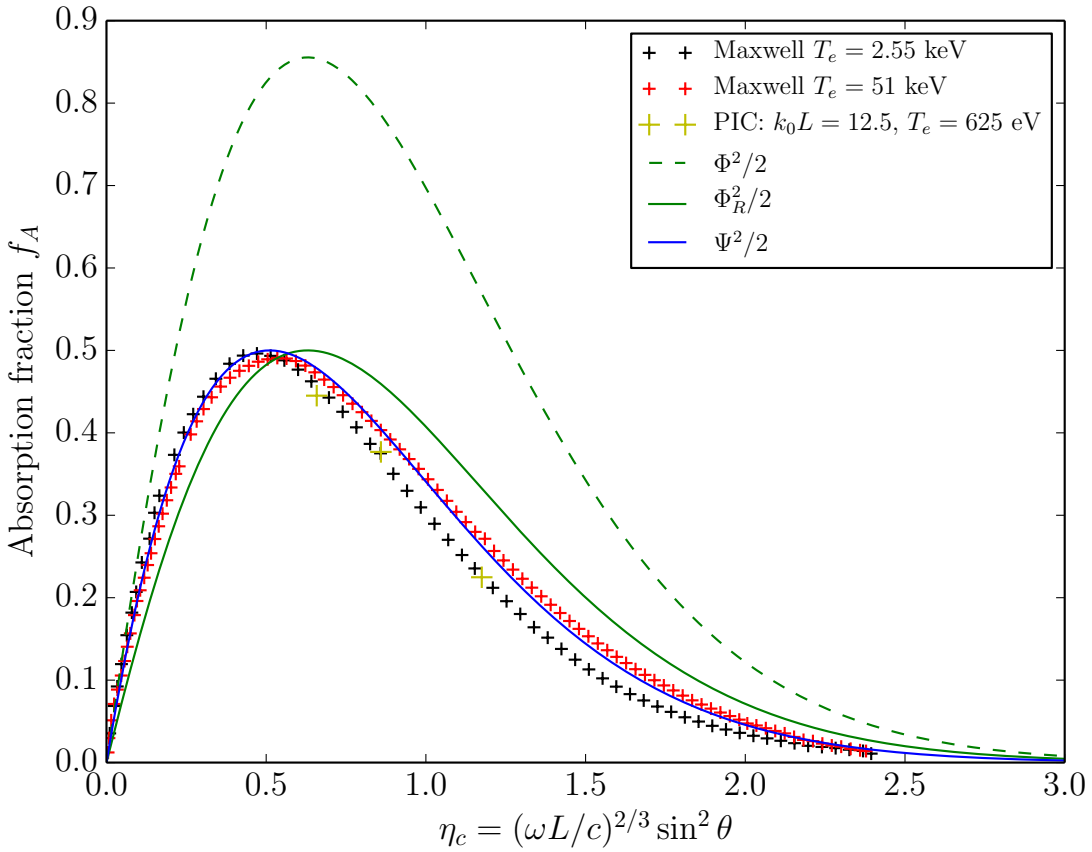

Figure C-2 – *(color) Comparison of the different absorption fractions between PIC simulations (yellow crosses, data from [95]), numerical resolution of the wave equation in plasma for two electron temperatures (black and red crosses, data from [95]) and for the two definitions of the resonance functions Φ in green and Ψ in blue.*

respect to the density gradient direction is not sufficient to characterize the entire trajectory of the wave. However, in usual implementations of GO (and PCGO), the density profile is still approximated as linear per each triangular mesh cell. Consequently, the theory derived above is adapted to the framework of a density profile that is linear by parts.

For a ray propagating in a given triangle i of density gradient length L^i, we compute the critical surface coordinate $\eta_c^i = (\omega L^i/c)^{2/3} \sin^2\varphi^i$ as if this ray had been propagating in a linear density gradient of scale length L^i from vacuum to its current position. To that end, we compute the angle φ^i that the ray would have had with the density gradient at the vacuum-plasma interface if it had been propagating in a linear density gradient of scale length L^i. The ray trajectory being analytically known per mesh triangle (see Eq. (A.2)), we can express φ^i from the x and y component of the density gradient in triangle i, noted a_x and a_y, respectively. From the Cartesian coordinate system (x, y) we define the (t, p) coordinate system with the unit vectors $\mathbf{t}$ tangent to

the density gradient and $\mathbf{p}$ parallel to it and in the opposite direction, that is:

$$\mathbf{t} = \frac{1}{\sqrt{a_x^2 + a_y^2}} \begin{pmatrix} a_y \\ -a_x \\ 0 \end{pmatrix} \qquad \mathbf{p} = \frac{-1}{\sqrt{a_x^2 + a_y^2}} \begin{pmatrix} a_x \\ a_y \\ 0 \end{pmatrix} . \tag{C.26}$$

In that coordinate system, $a_t = 0$ so that the ray velocity in the direction tangent to the density gradient reads $v_t(\tau) = v_t(0) = \sin\varphi$ where φ is the initial angle of the ray with the density gradient (see Eqs. (A.2)). In the (x, y) coordinate system, the tangential component of the ray velocity is simply $v_t(\tau) = \mathbf{v}.\mathbf{t}$, so that the initial angle with the density gradient at the vacuum-plasma interface is:

$$\varphi^i = \left| \arcsin \left(\frac{v_{x0} a_y - v_{y0} a_x}{\sqrt{a_x^2 + a_y^2}} \right) \right| , \tag{C.27}$$

where v_{x0} and v_{y0} are defined at the ray entry point of triangle i. With our notation, the density gradient scale length L^i is defined so that $n_e/n_c = z/L^i$, that is:

$$L^i = \frac{n_c}{|\nabla n_e|} = \frac{1}{4\sqrt{a_x^2 + a_y^2}} , \tag{C.28}$$

not to be mistaken for the usual definition of the scale length with $n_e/(\mathrm{d}n_e/\mathrm{d}x)$. Knowing φ_i and L_i we can compute the critical surface coordinate $\eta_c^i = (\omega L^i/c)^{2/3} \sin^2\varphi^i$ and the absorption fraction using $\Psi_R(\eta_c^i)$.

From a physical standpoint, the Resonant Absorption is mainly constituted from the contribution of the electric field at the turning point of the wave that decays to the critical density. From a discrete, ray-based perspective, this means that Resonant Absorption occurs at the turning point of the ray. In our model of Resonant Absorption, we choose to transfer energy from the thick ray to the resonance only when the ray in a given triangle is reflected, i.e. turns back with respect to the density gradient. This can be translated as a condition on the existence of $\tau \in [\tau_0, \tau_1]$ in triangle i so that the component of the ray velocity parallel to the gradient $v_p(\tau)$ reaches zero and changes sign. This is equivalent to considering that $\tau_0^p < \tau_T^p < \tau_1^p$ where τ_0^p and τ_1^p are the ray parametric coordinates in the (t, p) coordinate system, corresponding to τ_0 and τ_1, and τ_T^p is the parametric coordinate of the ray at the turning point in the (t, p) coordinate system. The component of the ray velocity parallel to the density gradient v_p reads:

$$v_p(\tau) = (\cos\varphi_p - \tau)/(2L^i) , \tag{C.29}$$

so that τ_0^p and τ_1^p read:

$$\begin{aligned} \tau_0^p &= 2L^i(-\mathbf{v}(\tau_0).\mathbf{p} + \cos\varphi^i) , \\ \tau_1^p &= 2L^i(-\mathbf{v}(\tau_1).\mathbf{p} + \cos\varphi^i) , \end{aligned} \tag{C.30}$$

and τ_T^p is found by setting $v_p(\tau) = 0$:

$$\tau_T^p = 2L^i \cos\varphi^i \ . \tag{C.31}$$

This expression allows us to compute $\eta_c^i = (\omega L^i/c)^{2/3}(1 - (\tau_T^p/(2L^i))^2)$. If $f_A(\eta_c^i)$ is non-zero, there is Resonant Absorption. Energy is taken of the thick-ray by reducing its intensity at constant width. In practice, PCGO quantities I and w are linearly interpolated from its values at τ_0 and τ_1 to the turning point coordinate to get I_T and w_T. The intensity is reduced at the turning point by $1 - f_A$ and the integration of the thick-ray parameters through the wave front equation is continued.

C.3 Definition of PCGO-based HE sources from macroscopic drive functions

Considering a Parametric Instability (PI) with an intensity threshold $I_{\text{th}}^{\text{PI}}$ and an overlap of EM waves creating an intensity field in the plasma I_Σ, one can define a macroscopic drive strength in cell i, $\eta_i^{\text{PI}} = I_{\Sigma,i}/I_{\text{th},i}^{\text{PI}}$. The global intensity field in the triangle i, computed from N thick-rays (that may not be in triangle i) reads:

$$I_{\Sigma,i} = \frac{c\epsilon_0}{2A_i} \sum_{k=1}^{N} \iint_{A_i} \sqrt{\epsilon'_k} |u_{ik}|^2 \mathrm{d}A_i \ , \tag{C.32}$$

where it is assumed here that the triangle i is subcritical for all beamlets k. The computation of this sum is not straightforward and can be achieved by means of the field projection algorithm presented in App. A.3.2.

The definition of HE sources is explicit; HE source parameters at $t + \Delta t$ are computed based on the intensity field $I_{\Sigma,i}(t)$. For that reason, the $|u_{ik}|$ term accounts for wave damping from collisional absorption, as well as the reduced intensity due to the power transfer to SRS and TPD electrons (computed at t), and the Resonant Absorption.

For $\eta_i^{\text{PI}} < 1$, it is considered that the corresponding parametric instability is absent. For $\eta_i^{\text{PI}} \geq 1$, it is considered that the parametric instability develops and that it drives hot electrons. For a given parametric instability, we define the *macroscopic source functions* $\mathscr{G}_\theta(\eta)$, $\mathscr{F}_{\text{E}}(\eta)$, $\mathscr{T}_{\text{hot}}(\eta)$ and $\mathscr{R}_B(\eta)$ (the PI superscript was dropped for clarity). These functions are used to characterize the source parameter of a given parametric instability:

$$\begin{aligned} G_{\theta,i} &= \mathscr{G}_\theta(\eta_i) \ , \\ F_{\text{E},i} &= \mathscr{F}_{\text{E}}(\eta_i) \ , \\ T_{\text{hot},i} &= \mathscr{T}_{\text{hot}}(\eta_i) \ , \\ R_{B,i} &= \mathscr{R}_B(\eta_i) \ . \end{aligned} \tag{C.33}$$

Note that for a given beamlet, $\mathbf{e}_{\text{HE}}$ is not detailed because the symmetry axis of the HE source is always taken to be the direction of the beamlet at the point of HE emission. It is now assumed that the macroscopic source functions are known (those are defined in the subsequent sections).

One must define the beamlet-based HE source parameters $\{G_{\theta,ik}, F_{\mathrm{E},ik}, T_{\mathrm{hot},ik}, R_{B,ik}\}$ (where k is a beamlet number), computed from a beamlet drive strength $\eta = \eta_{ik}$ and from the macroscopic source functions. This is a required step in order to ensure consistency and energy conservation, as evoked above in the points (1) and (2).

There are several approaches to defining η_{ik}. The most straightforward is to assume that each beamlet contributes evenly to the acceleration of electrons:

$$\begin{aligned} \eta_{ik} &= \eta_i \ , \\ F_{\mathrm{E},ik} &= \mathscr{F}_{\mathrm{E}}(\eta_{ik})/N_{B,i} \ , \\ T_{\mathrm{hot},ik} &= \mathscr{T}_{\mathrm{hot}}(\eta_{ik}) \ , \\ G_{\theta,ik} &= \mathscr{G}_{\theta}(\eta_{ik}) \ , \\ R_{B,ik} &= \mathscr{R}_{B}(\eta_{ik}) \ , \end{aligned} \tag{C.34}$$

where $N_{B,i}$ is the number of beamlets which centroid is in cell i. This approach ensures that the macroscopic HE flux is reproduced by the beamlets, that is $\sum_k F_{\mathrm{E,ik}}(\eta_{ik}) = F_{\mathrm{E,i}}(\eta_i)$. However, it does not account for the beamlet intensity statistics with respect to the direction of the HE emissions, and in certain situations $F_{\mathrm{E,i}}(\eta_{ik})/N_{B,i}$ may be larger than the beamlet local flux.

A second approach consists in mimicking the intensity statistics in the beamlet drive strength:

$$\begin{aligned} \eta_{ik} &= N_{B,i} I_{ik}^{\mathrm{int}}/I_{\mathrm{th},i} \ , \\ F_{\mathrm{E,ik}} &= \min(\mathscr{F}_{\mathrm{E}}(\eta_{ik}), \mathscr{F}_{\mathrm{E}}(\eta_i)/(N_{B,i})^{\kappa}) \ , \\ T_{\mathrm{hot},ik} &= \mathscr{T}_{\mathrm{hot}}(\eta_{ik}) \ , \\ G_{\theta,ik} &= \mathscr{G}_{\theta}(\eta_{ik}) \ , \\ R_{B,ik} &= \mathscr{R}_{B}(\eta_{ik}) \ , \end{aligned} \tag{C.35}$$

where I_{ik}^{int} is the interpolated beamlet intensity at the point of HE source creation (e.g. $n_c/4$) and κ is a free parameter. Note that $\sum_k I_{ik}^{\mathrm{int}} \neq I_{\Sigma,i}$. This approach ensures that the HE source has a statistics of HE temperatures, backscattered light, etc... that is consistent with the laser intensity statistics, and that beamlets cannot be depleted. For $\kappa = 1$, the second equation implies $\sum_k F_{\mathrm{E,ik}}(\eta_{ik}) \leq F_{\mathrm{E,i}}(\eta_i)$, so that the amount of accelerated HEs is in general underestimated with respect to the macroscopic drive function. This is compensated for by setting $\kappa = 1/2$, which is seen to give $\sum_k F_{\mathrm{E,ik}}(\eta_{ik}) \approx F_{\mathrm{E,i}}(\eta_i)$ in the simulations.

As for the Resonant Absorption model, any fraction of energy converted into hot electrons is substracted from the PCGO beamlet power at the point of emission of the electron beam. The updated PCGO beamlet parameters are re-integrated through the wave front and transport equations in order to describe the interaction consistently. The position from which electron beams is emitted is the result of an interpolation inside a mesh cell to locate the position of the emission density (e.g. $n_c/4$) along the curved ray trajectory. The ray direction defines the main axis of the emission, and the electron beam is launched from this point with the desired angular profile (see Fig. 5-14). The transverse width of the source, i.e. of each ASA beamlet, is chosen to be equal to the transverse width of the PCGO beamlet at the emission point.

Bibliography

[1] R. Fedosejevs, I. V. Tomov, N. H. Burnett, et al. "Self-steepening of the density profile of a CO2-laser-produced plasma". In: *Physical Review Letters* 39 (Oct. 1977), pp. 932–935. DOI: 10.1103/PhysRevLett.39.932.

[2] W. B. Fechner, C. L. Shepard, G. E. Busch, et al. "Analysis of plasma density profiles and thermal transport in laser-irradiated spherical targets". In: *Physics of Fluids* 27 (June 1984), pp. 1552–1560. DOI: 10.1063/1.864738.

[3] K. R. Manes, V. C. Rupert, J. M. Auerbach, et al. "Polarization and Angular Dependence of 1.06-μm Laser-Light Absorption by Planar Plasmas". In: *Phys. Rev. Lett.* 39 (5 Aug. 1977), pp. 281–284. DOI: 10.1103/PhysRevLett.39.281. URL: http://link.aps.org/doi/10.1103/PhysRevLett.39.281.

[4] R. P. Godwin, R. Sachsenmaier, and R. Sigel. "Angle-dependent reflectance of laser-produced plasmas". In: *Physical Review Letters* 39 (Nov. 1977), pp. 1198–1201. DOI: 10.1103/PhysRevLett.39.1198.

[5] J. S. Pearlman and M. K. Matzen. "Angular dependence of polarization-related laser-plasma absorption processes". In: *Physical Review Letters* 39 (July 1977), pp. 140–142. DOI: 10.1103/PhysRevLett.39.140.

[6] J. E. Balmer and T. P. Donaldson. "Resonance absorption of 1.06-micron laser radiation in laser-generated plasma". In: *Physical Review Letters* 39 (Oct. 1977), pp. 1084–1087. DOI: 10.1103/PhysRevLett.39.1084.

[7] D. M. Villeneuve, G. D. Enright, and M. C. Richardson. "Features of lateral energy transport in CO_2-laser-irradiated microdisk targets". In: *Phys. Rev. A* 27 (May 1983), pp. 2656–2662. DOI: 10.1103/PhysRevA.27.2656.

[8] D. R. Bach, D. E. Casperson, D. W. Forslund, et al. "Intensity-Dependent Absorption in 10.6-μm Laser-Illuminated Spheres". In: *Physical Review Letters* 50 (June 1983), pp. 2082–2085. DOI: 10.1103/PhysRevLett.50.2082.

[9] K. Estabrook and W. L. Kruer. "Properties of resonantly heated electron distributions". In: *Physical Review Letters* 40 (Jan. 1978), pp. 42–45. DOI: 10.1103/PhysRevLett.40.42.

[10] D. W. Phillion, E. M. Campbell, K. G. Estabrook, et al. "High-Energy Electron Production by the Raman and $2\omega_{pe}$ Instabilities in a 1.064-μm-Laser-Produced Underdense Plasma". In: *Phys. Rev. Lett.* 49 (19 Nov. 1982), pp. 1405–1408. DOI: 10.1103/PhysRevLett.49.1405. URL: http://link.aps.org/doi/10.1103/PhysRevLett.49.1405.

[11] R. P. Drake, R. E. Turner, B. F. Lasinski, et al. "Efficient Raman Sidescatter and Hot-Electron Production in Laser-Plasma Interaction Experiments". In: *Physical Review Letters* 53 (Oct. 1984), pp. 1739–1742. DOI: 10.1103/PhysRevLett.53.1739.

[12] N. H. Burnett and G. D. Enright. "Hot-electron generation and transport in high-intensity laser interaction". In: *Canadian Journal of Physics* 64 (1986), p. 920. DOI: 10.1139/p86-161.

[13] B. H. Ripin, F. C. Young, J. A. Stamper, et al. "Enhanced backscatter with a structured laser pulse". In: *Physical Review Letters* 39 (Sept. 1977), pp. 611–615. DOI: 10.1103/PhysRevLett.39.611.

[14] D. W. Phillion, W. L. Kruer, and V. C. Rupert. "Brillouin scatter in laser-produced plasmas". In: *Physical Review Letters* 39 (Dec. 1977), pp. 1529–1533. DOI: 10.1103/PhysRevLett.39.1529.

[15] A. Ng, L. Pitt, D. Salzmann, et al. "Saturation of stimulated Brillouin backscatter in CO2-laser-plasma interaction". In: *Physical Review Letters* 42 (Jan. 1979), pp. 307–311. DOI: 10.1103/PhysRevLett.42.307.

[16] F. J. Mayer, G. E. Busch, C. M. Kinzer, et al. "Measurements of short-pulse backscatter from a gas target". In: *Physical Review Letters* 44 (June 1980), pp. 1498–1501. DOI: 10.1103/PhysRevLett.44.1498.

[17] R. G. Watt, R. D. Brooks, and Z. A. Pietrzyk. "Observation of stimulated Raman backscatter from a preformed, underdense plasma". In: *Physical Review Letters* 41 (July 1978), pp. 170–173. DOI: 10.1103/PhysRevLett.41.170.

[18] J. Elazar, W. T. Toner, and E. R. Wooding. "Backscattered radiation at omega sub 0/2 from neodymium laser plasma interactions". In: *Plasma Physics* 23 (Sept. 1981), pp. 813–818. DOI: 10.1088/0032-1028/23/9/005.

[19] C. Joshi, T. Tajima, J. M. Dawson, et al. "Forward Raman instability and electron acceleration". In: *Physical Review Letters* 47 (Nov. 1981), pp. 1285–1288. DOI: 10.1103/PhysRevLett.47.1285.

[20] K. Tanaka, L. M. Goldman, W. Seka, et al. "Stimulated Raman Scattering from uv-Laser-Produced Plasmas". In: *Phys. Rev. Lett.* 48 (17 Apr. 1982), pp. 1179–1182. DOI: 10.1103/PhysRevLett.48.1179. URL: http://link.aps.org/doi/10.1103/PhysRevLett.48.1179.

[21] D. W. Phillion, D. L. Banner, E. M. Campbell, et al. "Stimulated Raman scattering in large plasmas". In: *Physics of Fluids* 25 (Aug. 1982), pp. 1434–1443. DOI: 10.1063/1.863920.

[22] D. C. Slater, Gar. E. Busch, G. Charatis, et al. "Absorption and Hot-Electron Production for 1.05 and 0.53 μm Light on Spherical Targets". In: *Phys. Rev. Lett.* 46 (18 May 1981), pp. 1199–1202. DOI: 10.1103/PhysRevLett.46.1199. URL: http://link.aps.org/doi/10.1103/PhysRevLett.46.1199.

[23] H. Nishimura, H. Azechi, K. Yamada, et al. "Experimental study of wavelength dependences of laser-plasma coupling, transport, and ablation processes". In: *Phys. Rev. A* 23 (Apr. 1981), pp. 2011–2019. DOI: 10.1103/PhysRevA.23.2011.

[24] C. Garban-Labaune, E. Fabre, C. E. Max, et al. "Effect of Laser Wavelength and Pulse Duration on Laser-Light Absorption and Back Reflection". In: *Physical Review Letters* 48 (Apr. 1982), pp. 1018–1021. DOI: 10.1103/PhysRevLett.48.1018.

[25] W. Seka, R. S. Craxton, J. Delettrez, et al. "Measurements and interpretation of the absorption of 0.35 μm laser radiation on planar targets". In: *Optics Communications* 40 (Feb. 1982), pp. 437–440. DOI: 10.1016/0030-4018(82)90049-9.

[26] T. B. Kaiser. "Laser ray tracing and power deposition on an unstructured three-dimensional grid". In: *Phys. Rev. E* 61 (Jan. 2000), p. 895. DOI: 10.1103/PhysRevE.61.895.

[27] I. V. Igumenshchev, D. H. Edgell, V. N. Goncharov, et al. "Crossed-beam energy transfer in implosion experiments on OMEGA". In: *Physics of Plasmas* 17.12, 122708 (Dec. 2010), p. 122708. DOI: 10.1063/1.3532817.

[28] A. Colaïtis, G. Duchateau, X. Ribeyre, et al. "Modeling of the cross-beam energy transfer with realistic inertial-confinement-fusion beams in a large-scale hydrocode". In: *Phys. Rev. E* 91 (1 Jan. 2015), p. 013102. DOI: 10.1103/PhysRevE.91.013102. URL: http://link.aps.org/doi/10.1103/PhysRevE.91.013102.

[29] P. Michel, L. Divol, E. A. Williams, et al. "Tuning the Implosion Symmetry of ICF Targets via Controlled Crossed-Beam Energy Transfer". In: *Physical Review Letters* 102.2, 025004 (Jan. 2009), p. 025004. DOI: 10.1103/PhysRevLett.102.025004.

[30] S. Skupsky, J. A. Marozas, R. S. Craxton, et al. "Polar direct drive on the National Ignition Facility". In: *Physics of Plasmas* 11 (May 2004), pp. 2763–2770. DOI: 10.1063/1.1689665.

[31] R. Betti, C. D. Zhou, K. S. Anderson, et al. "Shock Ignition of Thermonuclear Fuel with High Areal Density". In: *Physical Review Letters* 98.15, 155001 (Apr. 2007), p. 155001. DOI: 10.1103/PhysRevLett.98.155001.

[32] D. Batani, S. Baton, A. Casner, et al. "Physics issues for shock ignition". In: *Nuclear Fusion* 54.5 (2014), p. 054009. URL: http://stacks.iop.org/0029-5515/54/i=5/a=054009.

[33] D. Batani, L. Antonelli, S. Atzeni, et al. "Generation of high pressure shocks relevant to the shock-ignition intensity regime". In: *Physics of Plasmas* 21 (Mar. 2014), p. 032710. DOI: 10.1063/1.4869715. URL: http://dx.doi.org/10.1063/1.4869715.

[34] A. Colaïtis, G. Duchateau, P. Nicolaï, et al. "Towards modeling of nonlinear laser-plasma interactions with hydrocodes: The thick-ray approach". In: *Phys. Rev. E* 89 (3 Mar. 2014), p. 033101. DOI: 10.1103/PhysRevE.89.033101. URL: http://link.aps.org/doi/10.1103/PhysRevE.89.033101.

[35] G. Gamow. "Zur Quantentheorie des Atomkernes". In: *Zeitschrift fur Physik* 51 (Mar. 1928), pp. 204–212. DOI: 10.1007/BF01343196.

[36] D. Pesme, G. Bonnaud, M. Casanova, et al. *La fusion thermonucléaire inertielle par laser : l'interaction laser-matière part. 1, vol. 1. (French Edition)*. Synthèses. 61, Boulevard Saint-Germain: Eyrolles, 1993.

[37] John Lindl. "Development of the indirect-drive approach to inertial confinement fusion and the target physics basis for ignition and gain". In: *Physics of Plasmas* 2.11 (1995), pp. 3933–4024. DOI: 10.1063/1.871025. URL: http://scitation.aip.org/content/aip/journal/pop/2/11/10.1063/1.871025.

[38] J. Nuckolls, L. Wood, A. Thiessen, et al. "Laser Compression of Matter to Super-High Densities: Thermonuclear (CTR) Applications". In: *Nature* 239 (Sept. 1972), pp. 139–142. DOI: 10.1038/239139a0.

[39] A. W. Maschke. "Relativistic Heavy Ions for Fusion Applications". In: *IEEE Transactions on Nuclear Science* 22 (June 1975), p. 1825. DOI: 10.1109/TNS.1975.4328002.

[40] N.G. Basov, S.Yu. Gus'kov, and L.P. Feokistov. "Thermonuclear gain of ICF targets with direct heating of ignitor". English. In: *Journal of Soviet Laser Research* 13.5 (1992), pp. 396–399. ISSN: 0270-2010. DOI: 10.1007/BF01124892. URL: http://dx.doi.org/10.1007/BF01124892.

[41] M. Tabak, J. Hammer, M. E. Glinsky, et al. "Ignition and high gain with ultrapowerful lasers*". In: *Physics of Plasmas* 1 (May 1994), pp. 1626–1634. DOI: 10.1063/1.870664.

[42] V.A. Shcherbakov. "Ignition of a laser-fusion target by a focusing shock wave". In: *Sov. J. Plasma Phys. (Engl. Transl.); (United States)* 9:2 (Mar. 1983). URL: https://inis.iaea.org/search/searchsinglerecord.aspx?recordsFor=SingleRecord&RN=15034792.

[43] L. J. Perkins, R. Betti, K. N. Lafortune, et al. "Shock Ignition: A New Approach to High Gain Inertial Confinement Fusion on the National Ignition Facility". In: *Physical Review Letters* 103.4, 045004 (July 2009), p. 045004. DOI: 10.1103/PhysRevLett.103.045004.

[44] W. Seka, E. A. Williams, R. S. Craxton, et al. "Convective stimulated Raman scattering instability in UV laser plasmas". In: *Physics of Fluids (1958-1988)* 27.8 (1984), pp. 2181–2186. DOI: 10.1063/1.864844. URL: http://scitation.aip.org/content/aip/journal/pof1/27/8/10.1063/1.864844.

[45] T. Afshar-rad, L. A. Gizzi, M. Desselberger, et al. "Evidence for whole-beam self-focusing of induced spatially incoherent laser light in large underdense plasma". In: *Phys. Rev. Lett.* 68 (7 Feb. 1992), pp. 942–945. DOI: 10.1103/PhysRevLett.68.942. URL: http://link.aps.org/doi/10.1103/PhysRevLett.68.942.

[46] S. Atzeni and J. Meyer-ter Vehn. *The Physics of Inertial Fusion*. International Series of Monographs on Physics. Oxford: Oxford University Press, 2004.

[47] D. H. Froula, D. T. Michel, I. V. Igumenshchev, et al. "Laser-plasma interactions in direct-drive ignition plasmas". In: *Plasma Physics and Controlled Fusion* 54.12, 124016 (Dec. 2012), p. 124016. DOI: 10.1088/0741-3335/54/12/124016.

[48] W. L. Kruer, S. C. Wilks, B. B. Afeyan, et al. "Energy transfer between crossing laser beams". In: *Physics of Plasmas* 3 (Jan. 1996), pp. 382–385. DOI: 10.1063/1.871863.

[49] S. W. Haan, S. M. Pollaine, J. D. Lindl, et al. "Design and modeling of ignition targets for the National Ignition Facility". In: *Physics of Plasmas* 2 (June 1995), pp. 2480–2487. DOI: 10.1063/1.871209.

[50] I. V. Igumenshchev, W. Seka, D. H. Edgell, et al. "Crossed-beam energy transfer in direct-drive implosions". In: *Physics of Plasmas* 19.5, 056314 (May 2012), p. 056314. DOI: 10.1063/1.4718594.

[51] Ph. Nicolaï, J.-L. Feugeas, M. Touati, et al. "Deleterious effects of nonthermal electrons in shock ignition concept". In: *Phys. Rev. E* 89 (3 Mar. 2014), p. 033107. DOI: 10.1103/PhysRevE.89.033107. URL: http://link.aps.org/doi/10.1103/PhysRevE.89.033107.

[52] Y. A. Kravtsov. "Complex rays and complex caustics". In: *Radiophysics and Quantum Electronics* 10 (Sept. 1967), pp. 719–730. DOI: 10.1007/BF01031601.

[53] J. C. Maxwell. "A dynamical theory of the electromagnetic field". In: *Phil. Trans. R. Soc. Lond.* 155 (Jan. 1865), pp. 459–512. DOI: 10.1098/rstl.1865.0008.

[54] Oliver Heaviside. "On the Forces, Stresses, and Fluxes of Energy in the Electromagnetic Field." In: *Proceedings of the Royal Society of London* 50.302-307 (1891), pp. 126–129. DOI: 10.1098/rspl.1891.0016. eprint: http://rspl.royalsocietypublishing.org/content/50/302-307/126.full.pdf+html. URL: http://rspl.royalsocietypublishing.org/content/50/302-307/126.short.

[55] J. D. Jackson and R. F. Fox. "Classical Electrodynamics, 3rd ed." In: *American Journal of Physics* 67 (Sept. 1999), pp. 841–842. DOI: 10.1119/1.19136.

[56] I. P. Shkarofsky, T. W. Johnston, M. P. Bachynski, et al. "The Particle Kinetics of Plasmas". In: *American Journal of Physics* 35 (June 1967), pp. 551–552. DOI: 10.1119/1.1974182.

[57] J. Dawson and C. Oberman. "High-Frequency Conductivity and the Emission and Absorption Coefficients of a Fully Ionized Plasma". In: *Physics of Fluids* 5 (May 1962), pp. 517–524. DOI: 10.1063/1.1706652.

[58] T. W. Johnston and J. M. Dawson. "Correct values for high-frequency power absorption by inverse bremsstrahlung in plasmas". In: *Physics of Fluids* 16 (May 1973), pp. 722–722. DOI: 10.1063/1.1694419.

[59] L. Schlessinger and J. Wright. "Inverse-bremsstrahlung absorption rate in an intense laser field". In: *Phys. Rev. A* 20 (Nov. 1979), pp. 1934–1945. DOI: 10.1103/PhysRevA.20.1934.

[60] S. Skupsky. ""Coulomb logarithm" for inverse-bremsstrahlung laser absorption". In: *Phys. Rev. A.* 36 (Dec. 1987), pp. 5701–5712. DOI: 10.1103/PhysRevA.36.5701.

[61] V. L. Ginzburg. *The properties of Electromagnetic Waves in Plasma.* New York: Permagon, 1964.

[62] M. A. Leontovich. "A method of solution of problems of electromagnetic wave propagation along the earth's surface (in Russian)". In: *Bull. Acad. Sci. USSR, ser Phys* 8 (1 1944), p. 16.

[63] M. A. Leontovich and V. A. Fock. "Solution of the problem of propagation of electromagnetic waves along the earth's surface by the method of parabolic equations". In: *J. Phys. (Moscow)* 10 (1 1946), p. 13.

[64] C. S. Liu. "Chapter 15. Numerical Holography." In: *Acoustical Holography, Vol. 3.* Ed. by A. F. Metherell. Plenum, New York, 1971, pp. 273–293.

[65] A.V. Popov and S. A. Khozioskii. "A generalization of the parabolic equation of diffraction theory". In: *USSR Comp. Math. Math. Phys.* 17 (1977), p. 238.

[66] J. L. Delcroix. *Physique des plasmas1.* Savoirs actuels. interEditionsCNRS Editions, 1994.

[67] M. N. Rosenbluth, R. B. White, and C. S. Liu. "Temporal Evolution of a Three-Wave Parametric Instability". In: *Physical Review Letters* 31 (Nov. 1973), pp. 1190–1193. DOI: 10.1103/PhysRevLett.31.1190.

[68] G. Laval, R. Pellat, and D. Pesme. "Time behaviour of parametric instabilities in inhomogeneous plasmas". In: *Physics Letters A* 46 (Dec. 1973), pp. 281–282. DOI: 10.1016/0375-9601(73)90222-3.

[69] C. S. Liu, M. N. Rosenbluth, and R. B. White. "Raman and Brillouin scattering of electromagnetic waves in inhomogeneous plasmas". In: *Physics of Fluids* 17 (June 1974), pp. 1211–1219. DOI: 10.1063/1.1694867.

[70] A. H. Reiman, A. Bers, and D. J. Kaup. "Nonlinear Interactions of Three Wave Packets in an Inhomogeneous Medium." In: *Physical Review Letters* 39 (Sept. 1977), p. 850. DOI: 10.1103/PhysRevLett.39.850.3.

[71] A. Reiman. "Parametric decay in a finite width pump, including the effects of three-dimensional geometry and inhomogeneity". In: *Physics of Fluids* 21 (June 1978), pp. 1000–1006. DOI: 10.1063/1.862318.

[72] I. M. Gorbunov and A. N. Polianichev. "Stimulated Mandel'shtam-Brillouin scattering in an expanding plasma". In: *Zhurnal Eksperimentalnoi i Teoreticheskoi Fiziki* 74 (Feb. 1978), pp. 552–562.

[73] R. L. Berger. "Stimulated Brillouin scattering in inhomogeneous flowing plasma". In: *Physics of Fluids* 27 (July 1984), pp. 1796–1803. DOI: 10.1063/1.864791.

[74] G. Goldner and L. Friedland. "Congruent reduction in parametrically unstable space- and time-varying plasmas". In: *Physics of Fluids B* 1 (Aug. 1989), pp. 1600–1604. DOI: 10.1063/1.858938.

[75] R.J. Briggs. *Electron-stream Interaction with Plasmas \ R.J. Briggs.* Research monographs. MIT, 1964. URL: https://books.google.fr/books?id=vfvMngEACAAJ.

[76] M. N. Rosenbluth. "Parametric Instabilities in Inhomogeneous Media". In: *Phys. Rev. Lett.* 29 (9 Aug. 1972), pp. 565–567. DOI: 10.1103/PhysRevLett.29.565. URL: http://link.aps.org/doi/10.1103/PhysRevLett.29.565.

[77] C. S. Liu and M. N. Rosenbluth. "Parametric decay of electromagnetic waves into two plasmons and its consequences". In: *Physics of Fluids* 19 (July 1976), pp. 967–971. DOI: 10.1063/1.861591.

[78] J. F. Drake, P. K. Kaw, Y. C. Lee, et al. “Parametric instabilities of electromagnetic waves in plasmas”. In: *Physics of Fluids* 17 (Apr. 1974), pp. 778–785. DOI: 10.1063/1.1694789.

[79] D. W. Forslund, J. M. Kindel, and E. L. Lindman. “Plasma simulation studies of stimulated scattering processes in laser-irradiated plasmas”. In: *Physics of Fluids* 18 (Aug. 1975), pp. 1017–1030. DOI: 10.1063/1.861249.

[80] W. L. Kruer. *The Physics of Laser Plasma Interactions*. University of California, Los Angeles: Westview Press, 2003.

[81] A. D. Piliya. “Decay instability in weakly inhomogeneous plasma”. In: *Phenomena in Ionized Gases, Tenth International Conference*. Ed. by R. N. Franklin. Sept. 1971, p. 320.

[82] F. W. Perkins and J. Flick. “Parametric Instabilities in Inhomogeneous Plasmas”. In: *Physics of Fluids* 14 (Sept. 1971), pp. 2012–2018. DOI: 10.1063/1.1693711.

[83] D. Pesme, G. Laval, and R. Pellat. “Parametric Instabilities in Bounded Plasmas”. In: *Physical Review Letters* 31 (July 1973), pp. 203–206. DOI: 10.1103/PhysRevLett.31.203.

[84] P. Koch and E. A. Williams. “Absolute growth of coupled forward and backward Raman scattering in inhomogeneous plasma”. In: *Physics of Fluids* 27 (Sept. 1984), pp. 2346–2350. DOI: 10.1063/1.864890.

[85] H. C. Barr, T. J. M. Boyd, and G. A. Coutts. “Nonlocal effects and the Raman instability”. In: *Physical Review Letters* 60 (May 1988), pp. 1950–1953. DOI: 10.1103/PhysRevLett.60.1950.

[86] J. F. Drake and Y. C. Lee. “Temporally Growing Raman Backscattering Instabilities in an Inhomogeneous Plasma”. In: *Physical Review Letters* 31 (Nov. 1973), pp. 1197–1200. DOI: 10.1103/PhysRevLett.31.1197.

[87] Y. C. Lee and P. K. Kaw. “Temporal Electrostatic Instabilities in Inhomogeneous Plasmas”. In: *Physical Review Letters* 32 (Jan. 1974), pp. 135–138. DOI: 10.1103/PhysRevLett.32.135.

[88] C. S. Liu. “Parametric instabilities in an inhomogeneous unmagnetized plasma”. In: *Advances in Plasma Physics*. Ed. by A. Simon and W. B. Thompson. John Wiley and Sons, Inc., 1976, pp. 121–177.

[89] B. B. Afeyan and E. A. Williams. “Stimulated Raman sidescattering with the effects of oblique incidence”. In: *Physics of Fluids* 28 (Nov. 1985), pp. 3397–3408. DOI: 10.1063/1.865340.

[90] C. L. Shepard, J. A. Tarvin, R. L. Berger, et al. “Raman scattering in experiments with planar Au targets irradiated with 0.53 μm laser light”. In: *Physics of Fluids* 29 (Feb. 1986), pp. 583–593. DOI: 10.1063/1.865449.

[91] J. A. Tarvin, G. E. Busch, E. F. Gabl, et al. “Laser and plasma conditions at the onset of Raman scattering in an underdense plasma”. In: *Laser and Particle Beams* 4 (Nov. 1986), p. 461. DOI: 10.1017/S0263034600002147.

[92] H. Figueroa, C. Joshi, H. Azechi, et al. “Stimulated Raman scattering, two-plasmon decay, and hot electron generation from underdense plasmas at 0.35 μm”. In: *Physics of Fluids* 27 (July 1984), pp. 1887–1896. DOI: 10.1063/1.864801.

[93] L. M. Gorbunov. “Perturbation of a Medium by a Field of a Strong Electromagnetic Wave”. In: *Soviet Journal of Experimental and Theoretical Physics* 28 (June 1969), p. 1220.

[94] A. A. Galeev, G. Laval, T. M. O’Neil, et al. “Parametric Back Scattering of a Linear Electromagnetic Wave in a Plasma”. In: *Soviet Journal of Experimental and Theoretical Physics Letters* 17 (Jan. 1973), p. 35.

[95] D. W. Forslund, J. M. Kindel, Kenneth Lee, et al. "Theory and simulation of resonant absorption in a hot plasma". In: *Phys. Rev. A* 11 (2 Feb. 1975), pp. 679–683. DOI: 10.1103/PhysRevA.11.679. URL: http://link.aps.org/doi/10.1103/PhysRevA.11.679.

[96] M. Bornatici. "Parametric backscattering and absorptive instabilities in homogeneous unmagnetized plasmas". In: *Journal of Plasma Physics* 14 (Aug. 1975), pp. 105–120. DOI: 10.1017/S0022377800025563.

[97] K. Tanaka, B. Boswell, R. S. Craxton, et al. "Brillouin scattering, two-plasmon decay, and self-focusing in underdense ultraviolet laser-produced plasmas". In: *Physics of Fluids* 28 (Sept. 1985), pp. 2910–2914. DOI: 10.1063/1.865211.

[98] H. Figueroa, C. Joshi, and C. E. Clayton. "Experimental studies of Raman scattering from foam targets using a 0.35 μm laser beam". In: *Physics of Fluids* 30 (Feb. 1987), pp. 586–592. DOI: 10.1063/1.866357.

[99] M. V. Goldman. "Parametric plasmon-photon interaction : Part I. Threshold for amplification of plasmons". In: *Annals of Physics* 38 (June 1966), pp. 95–116. DOI: 10.1016/0003-4916(66)90252-1.

[100] E. A. Jackson. "Parametric Effects of Radiation on a Plasma". In: *Physical Review* 153 (Jan. 1967), pp. 235–244. DOI: 10.1103/PhysRev.153.235.

[101] A. Simon, R. W. Short, E. A. Williams, et al. "On the inhomogeneous two-plasmon instability". In: *Physics of Fluids* 26 (Oct. 1983), pp. 3107–3118. DOI: 10.1063/1.864037.

[102] D. K. Bradley, J. A. Delettrez, and C. P. Verdon. "Measurements of the effect of laser beam smoothing on direct-drive inertial-confinement-fusion capsule implosions". In: *Phys. Rev. Lett.* 68 (18 May 1992), pp. 2774–2777. DOI: 10.1103/PhysRevLett.68.2774. URL: http://link.aps.org/doi/10.1103/PhysRevLett.68.2774.

[103] J. Delettrez, D. K. Bradley, and C. P. Verdon. "The role of the Rayleigh-Taylor instability in laser-driven burnthrough experiments". In: *Physics of Plasmas* 1.7 (1994), pp. 2342–2349. DOI: 10.1063/1.870631. URL: http://scitation.aip.org/content/aip/journal/pop/1/7/10.1063/1.870631.

[104] J. D. Kilkenny, S. G. Glendinning, S. W. Haan, et al. "A review of the ablative stabilization of the Rayleigh-Taylor instability in regimes relevant to inertial confinement fusion". In: *Physics of Plasmas* 1.5 (1994), pp. 1379–1389. DOI: 10.1063/1.870688. URL: http://scitation.aip.org/content/aip/journal/pop/1/5/10.1063/1.870688.

[105] R. Epstein. "Reduction of time-averaged irradiation speckle nonuniformity in laser-driven plasmas due to target ablation". In: *Journal of Applied Physics* 82.5 (1997), pp. 2123–2139. DOI: 10.1063/1.366021. URL: http://scitation.aip.org/content/aip/journal/jap/82/5/10.1063/1.366021.

[106] V. A. Smalyuk, T. R. Boehly, D. K. Bradley, et al. "Saturation of the Rayleigh-Taylor Growth of Broad-Bandwidth Laser-Imposed Nonuniformities in Planar Targets". In: *Phys. Rev. Lett.* 81 (24 Dec. 1998), pp. 5342–5345. DOI: 10.1103/PhysRevLett.81.5342. URL: http://link.aps.org/doi/10.1103/PhysRevLett.81.5342.

[107] V. N. Goncharov, J. P. Knauer, P. W. McKenty, et al. "Improved performance of direct-drive inertial confinement fusion target designs with adiabat shaping using an intensity picket". In: *Physics of Plasmas* 10 (May 2003), pp. 1906–1918. DOI: 10.1063/1.1562166.

[108] S. P. Regan, J. A. Delettrez, V. N. Goncharov, et al. "Dependence of Shell Mix on Feedthrough in Direct Drive Inertial Confinement Fusion". In: *Phys. Rev. Lett.* 92 (18 May 2004), p. 185002. DOI: 10.1103/PhysRevLett.92.185002. URL: http://link.aps.org/doi/10.1103/PhysRevLett.92.185002.

[109] S. E. Bodner, D. G. Colombant, J. H. Gardner, et al. "Direct-drive laser fusion: Status and prospects". In: *Physics of Plasmas* 5 (May 1998), pp. 1901–1918. DOI: 10.1063/1.872861.

[110] J. D. Lindl. *Inertial Confinement Fusion: The Quest for Ignition and Energy Gain Using Indirect Drive*. New York: Springer-Verlag, 1998.

[111] Y. Kato, K. Mima, N. Miyanaga, et al. "Random Phasing of High-Power Lasers for Uniform Target Acceleration and Plasma-Instability Suppression". In: *Physical Review Letters* 53 (Sept. 1984), pp. 1057–1060. DOI: 10.1103/PhysRevLett.53.1057.

[112] R. Nora, W. Theobald, R. Betti, et al. "Gigabar Spherical Shock Generation on the OMEGA Laser". In: *Phys. Rev. Lett.* 114 (4 Jan. 2015), p. 045001. DOI: 10.1103/PhysRevLett.114.045001. URL: http://link.aps.org/doi/10.1103/PhysRevLett.114.045001.

[113] W. Theobald, R. Nora, W. Seka, et al. "Spherical strong-shock generation for shock-ignition inertial fusion". In: *Physics of Plasmas* 22.5, 056310 (2015), pp. –. DOI: 10.1063/1.4920956. URL: http://scitation.aip.org/content/aip/journal/pop/22/5/10.1063/1.4920956.

[114] L. Spitzer and R. Härm. "Transport Phenomena in a Completely Ionized Gas". In: *Physical Review* 89 (Mar. 1953), pp. 977–981. DOI: 10.1103/PhysRev.89.977.

[115] J. Breil, S. Galera, and P. H. Maire. "Multi-material ALE computation in inertial confinement fusion code CHIC". In: *Computers & Fluids* 46 (2011), pp. 161–167.

[116] Y. A. Kravtsov and N. Y. Zhu. *Theory of Diffraction, Heuristic Approaches*. Alpha Science Series on Wave Phenomena. Oxford, U.K.: Alpha Science International LTD., 2010.

[117] J. B. Keller. "Geometrical Theory of Diffraction". In: *J. Opt. Soc. Am.* 52.2 (Feb. 1962), pp. 116–130. DOI: 10.1364/JOSA.52.000116. URL: http://www.osapublishing.org/abstract.cfm?URI=josa-52-2-116.

[118] G. A. Deschamps, J. F. Rippin, and P. E. Mast. *Beam tracing and applications*. Technical report (University of Illinois at Urbana-Champaign. Antenna Laboratory). Urbana, Ill.: "Dept. of Electrical Engineering, Engineering Experiment Station, University of Illinois 1964., 1964.

[119] G.A. Deschamps. "Gaussian beam as a bundle of complex rays". In: *Electronics Letters* 7.23 (Nov. 1971), pp. 684–685. ISSN: 0013-5194.

[120] J. B. Keller and W. Streifer. "Complex Rays with an Application to Gaussian Beams". In: *J. Opt. Soc. Am.* 61.1 (Jan. 1971), pp. 40–43. DOI: 10.1364/JOSA.61.000040. URL: http://www.osapublishing.org/abstract.cfm?URI=josa-61-1-40.

[121] V. M. Babich and V. F. Lazutkin. "Eigenfunctions, concentrated near closed geodesic." In: *Topics in Mathematical Physics* 2 (1968), pp. 9–18.

[122] H. Kogelnik. "On the propagation of Gaussian beams of light through lens-like media including those with a loss or gain variation." In: *Appl. Optics* 19 (1965), pp. 1562–1569.

[123] R. K. Luneburg. *Mathematical Theory of Optics*. 1964.

[124] V. Červený, V. Pretlová, and I. Pšenčik. "Computation of ray amplitudes of seismic body waves in vertically inhomogeneous media". In: *Studia Geophysica et Geodaetica* 21 (Sept. 1977), pp. 248–255. DOI: 10.1007/BF01613252.

[125] M. M. Popov. "On a method of computation of geometrical spreading in inhomogeneous media containing interfaces". In: *Dokl. Akad. Nauk SSSR* 237 (1977), pp. 1059–1062.

[126] V. Červený and J. Vaněk. "Expansion of a plane wave into Gaussian beams". In: *Studia Geophysica et Geodaetica* 26 (June 1982), pp. 120–131. DOI: 10.1007/BF01582305.

[127] V. Červený, J. Janský, and J. Vaněk. "Ray amplitudes of seismic body waves in inhomogeneous radially symmetric media". In: *Studia Geophysica et Geodaetica* 27 (Mar. 1983), pp. 9–18. DOI: 10.1007/BF01630743.

[128] G. V. Pereverzev. "Paraxial WKB solution of a scalar wave equation." In: *Rev. Plasma Phys.Phys. Fluids* 19 (1996), pp. 1–48.

[129] E. Poli, G. V. Pereverzev, and A. G. Peeters. "Paraxial Gaussian wave beam propagation in an anisotropic inhomogeneous plasma". In: *Physics of Plasmas* 6 (Jan. 1999), pp. 5–11. DOI: 10.1063/1.873254.

[130] E. Poli, A. G. Peeters, and G. V. Pereverzev. "Boundary conditions for a Gaussian wave beam". In: *Physics of Plasmas* 8 (Oct. 2001), pp. 4325–4330. DOI: 10.1063/1.1401116.

[131] Y. A. Kravtsov and P. Berczynski. "Gaussian beams in inhomogeneous media: A review". In: *Studia Geophysica et Geodaetica* 51 (Jan. 2007), pp. 1–36. DOI: 10.1007/s11200-007-0002-y.

[132] E. Mazzucato. "Propagation of a Gaussian beam in a nonhomogeneous plasma". In: *Phys. PlasmasRev. Plasma Phys.* 1 (1997).

[133] M.M. Popov. "Eigen-oscillations of multi-mirrors resonators." In: *Vestnik Leningradskogo Universiteta* 22 (1969), pp. 44–54.

[134] M. M. Popov. *A new method for computing wave fields in a high-frequency approximation.* Tech. rep. 1981, pp. 195–216.

[135] R. A. Egorchenkov and Y. A. Kravtsov. "Diffraction of super-gaussian beams as described by the complex geometrical optics". In: *Radiophysics and Quantum Electronics* 43 (2000).

[136] S. A. Akhmanov, A. P. Sukhorukov, and R. V. Khokhlov. "Reviews of Topical Problems: Self-Focusing and Diffraction of Light in a Nonlinear Medium". In: *Soviet Physics Uspekhi* 10 (May 1968), pp. 609–636. DOI: 10.1070/PU1968v010n05ABEH005849.

[137] P. Kaw, G. Schmidt, and T. Wilcox. "Filamentation and trapping of electromagnetic radiation in plasmas". In: *Physics of Fluids* 16 (Sept. 1973), pp. 1522–1525. DOI: 10.1063/1.1694552.

[138] C. E. Max. "Strong self-focusing due to the ponderomotive force in plasmas". In: *Physics of Fluids* 19 (Jan. 1976), pp. 74–77. DOI: 10.1063/1.861305.

[139] D. Anderson, M. Bonnedal, and M. Lisak. "SelfâĂŘtrapped cylindrical laser beams". In: *Physics of Fluids* 22.9 (1979), pp. 1838–1840. DOI: http://dx.doi.org/10.1063/1.862795. URL: http://scitation.aip.org/content/aip/journal/pof1/22/9/10.1063/1.862795.

[140] V. V. Eliseev, W. Rozmus, V. T. Tikhonchuk, et al. "Stimulated Brillouin scattering and ponderomotive self-focusing from a single laser hot spot". In: *Physics of Plasmas* 2 (May 1995), pp. 1712–1724. DOI: 10.1063/1.871319.

[141] M. Grech. "Coherence properties modifications of laser beams in ICF plasmas (in French)". PhD thesis. Université Bordeaux 1, 2007.

[142] J. A. Marozas, S. P. Regan, J. H. Kelly, et al. "Laser beam smoothing caused by the small-spatial-scale B integral". In: *J. Opt. Soc. Am. B* 19.1 (Jan. 2002), pp. 7–17. DOI: 10.1364/JOSAB.19.000007. URL: http://josab.osa.org/abstract.cfm?URI=josab-19-1-7.

[143] S. P. Regan, J. A. Marozas, J. H. Kelly, et al. "Experimental investigation of smoothing by spectral dispersion". In: *Journal of the Optical Society of America B Optical Physics* 17 (Sept. 2000), pp. 1483–1489. DOI: 10.1364/JOSAB.17.001483.

[144] G.-Z. Yang, B.-Y. Gu, B.-Z. Dong, et al. "Gerchberg-Saxton and Yang-Gu algorithms for phase retrieval in a nonunitary transform system: a comparison". In: *Appl. Opt.* 33 (Jan. 1994), pp. 209–218. DOI: 10.1364/AO.33.000209.

[145] H. A. Rose and D. F. DuBois. "Statistical properties of laser hot spots produced by a random phase plate". In: *Physics of Fluids B* 5 (Feb. 1993), pp. 590–596. DOI: 10.1063/1.860545.

[146] J. Garnier. "Statistics of the hot spots of smoothed beams produced by random phase plates revisited". In: *Physics of Plasmas* 6 (May 1999), pp. 1601–1610. DOI: 10.1063/1.873413.

[147] S. Skupsky and R. S. Craxton. "Irradiation uniformity for high-compression laser-fusion experiments". In: *Physics of Plasmas* 6.5 (1999), pp. 2157–2163. DOI: 10.1063/1.873501. URL: http://scitation.aip.org/content/aip/journal/pop/6/5/10.1063/1.873501.

[148] S. Skupsky, R. W. Short, T. Kessler, et al. "Improved laser-beam uniformity using the angular dispersion of frequency-modulated light". In: *Journal of Applied Physics* 66.8 (1989), pp. 3456–3462. DOI: 10.1063/1.344101. URL: http://scitation.aip.org/content/aip/journal/jap/66/8/10.1063/1.344101.

[149] J. E. Rothenberg. "Comparison of beam-smoothing methods for direct-drive inertial confinement fusion". In: *Journal of the Optical Society of America B Optical Physics* 14 (July 1997), pp. 1664–1671. DOI: 10.1364/JOSAB.14.001664.

[150] S. Hocquet, E. Bordenave, J.-P. Goossens, et al. "Amplitude modulation filtering of FM-to-AM conversion due to the focusing grating of LMJ". In: *Journal of Physics Conference Series* 112.3, 032016 (May 2008), p. 032016. DOI: 10.1088/1742-6596/112/3/032016.

[151] J. Garnier, L. Videau, C. Gouédard, et al. "Statistical analysis for beam smoothing and some applications". In: *J. Opt. Soc. Am. A* 14.8 (Aug. 1997), pp. 1928–1937. DOI: 10.1364/JOSAA.14.001928. URL: http://josaa.osa.org/abstract.cfm?URI=josaa-14-8-1928.

[152] S. P. Regan, J. A. Marozas, R. S. Craxton, et al. "Performance of 1-THz-bandwidth, two-dimensional smoothing by spectral dispersion and polarization smoothing of high-power, solid-state laser beams". In: *Journal of the Optical Society of America B Optical Physics* 22 (May 2005), pp. 998–1002. DOI: 10.1364/JOSAB.22.000998.

[153] J. Garnier, C. Gouédard, and L. Videau. "Propagation of a partially coherent beam under the interaction of small and large scales". In: *Optics Communications* 176 (Apr. 2000), pp. 281–297. DOI: 10.1016/S0030-4018(00)00510-1.

[154] O. Morice. "Miro: Complete modeling and software for pulse amplification and propagation in high-power laser systems". In: *Optical Engineering* 42 (June 2003), pp. 1530–1541. DOI: 10.1117/1.1574326.

[155] O. Morice, X. Ribeyre, and V. Rivoire. "Broadband computations using the Miro software". In: *Third International Conference on Solid State Lasers for Application to Inertial Confinement Fusion*. Ed. by W. H. Lowdermilk. Vol. 3492. Society of Photo-Optical Instrumentation Engineers (SPIE) Conference Series. July 1999, pp. 832–838. DOI: 10.1117/12.354200.

[156] Ph. Donnat. *MIRÒ V5e Reference Manual*. CEA Technical Report. 1998.

[157] Ph. Donnat. *MIRÒ V4 Reference Manual*. CEA Technical Report. 1998.

[158] R. L. McCrory, D. D. Meyerhofer, S. J. Loucks, et al. "Progress in direct-drive inertial confinement fusion research at the laboratory for laser energetics". English. In: *The European Physical Journal D* 44.2 (2007), pp. 233–238. ISSN: 1434-6060. DOI: 10.1140/epjd/e2006-00109-0. URL: http://dx.doi.org/10.1140/epjd/e2006-00109-0.

[159] P. Michel, L. Divol, E. A. Williams, et al. "Energy transfer between laser beams crossing in ignition hohlraums". In: *Physics of Plasmas* 16.4, 042702 (2009), pp. –. DOI: 10.1063/1.3103788. URL: http://scitation.aip.org/content/aip/journal/pop/16/4/10.1063/1.3103788.

[160] D. T. Michel, A. V. Maximov, R. W. Short, et al. "Measured hot-electron intensity thresholds quantified by a two-plasmon-decay resonant common-wave gain in various experimental configurations". In: *Physics of Plasmas* 20.5, 055703 (May 2013), p. 055703. DOI: 10.1063/1.4803090.

[161] M. Maier, W. Kaiser, and J. A. Giordmaine. "Backward Stimulated Raman Scattering". In: *Physical Review* 177 (Jan. 1969), pp. 580–599. DOI: 10.1103/PhysRev.177.580.

[162] V. P. Silin and V. T. Tikhonchuk. "Nonlinear saturation of SMBS in a rarefied nonisothermal plasma". In: *ZhETF Pisma Redaktsiiu* 34 (Oct. 1981), pp. 385–388.

[163] T. Speziale. "Stimulated Brillouin sidescattering with strong ion wave damping". In: *Physics of Fluids* 27 (Oct. 1984), pp. 2583–2585. DOI: 10.1063/1.864549.

[164] C. J. McKinstrie, J. S. Li, R. E. Giacone, et al. "Two-Dimensional analysis of the power transfer between crossed laser beams". In: *Physics of Plasmas* 3.7 (1996), pp. 2686–2692. DOI: 10.1063/1.871721. URL: http://scitation.aip.org/content/aip/journal/pop/3/7/10.1063/1.871721.

[165] J. A. Heikkinen, S. J. Karttunen, and R. R. E. Salomaa. "Dynamics of absolute Brillouin scattering in the presence of ion wave harmonics". In: *Physics Letters A* 101 (Mar. 1984), pp. 217–220. DOI: 10.1016/0375-9601(84)90383-9.

[166] J. Candy, W. Rozmus, and V. T. Tikhonchuk. "Nonlinear ion waves driven by the periodic ponderomotive force". In: *Physical Review Letters* 65 (Oct. 1990), pp. 1889–1892. DOI: 10.1103/PhysRevLett.65.1889.

[167] S. Hüller, P. Mulser, and A. M. Rubenchik. "Nonstationary stimulated Brillouin backscattering". In: *Physics of Fluids B* 3 (Dec. 1991), pp. 3339–3352. DOI: 10.1063/1.859994.

[168] S. Hüller. "Stimulated Brillouin scattering off nonlinear ion acoustic waves". In: *Physics of Fluids B* 3 (Dec. 1991), pp. 3317–3330. DOI: 10.1063/1.859764.

[169] D. Pesme, S. Hüller, J. Myatt, et al. "Laser-plasma interaction studies in the context of megajoule lasers for inertial fusion". In: *Plasma Physics and Controlled Fusion* 44.12B (2002), B53. URL: http://stacks.iop.org/0741-3335/44/i=12B/a=305.

[170] S. Hüller, P. E. Masson-Laborde, D. Pesme, et al. "Harmonic decomposition to describe the nonlinear evolution of stimulated Brillouin scattering". In: *Physics of Plasmas* 13.2, 022703 (2006), pp. –. DOI: 10.1063/1.2168403. URL: http://scitation.aip.org/content/aip/journal/pop/13/2/10.1063/1.2168403.

[171] P. Michel, L. Divol, E. Williams, et al. "Modeling energy transfer via beam crossing in NIF hohlraums". In: *APS Meeting Abstracts*. Nov. 2007, p. 6003.

[172] P. Michel, R. L. Berger, B. F. Lasinski, et al. "Laser-plasma interactions and implosion symmetry in rugby hohlraums". In: *APS Meeting Abstracts*. Oct. 2011, p. 8006.

[173] P. E. Masson-Laborde, S. Hüller, D. Pesme, et al. "Stimulated Brillouin scattering reduction induced by self-focusing for a single laser speckle interacting with an expanding plasma". In: *Physics of Plasmas* 21.3, 032703 (2014), pp. –. DOI: 10.1063/1.4867659. URL: http://scitation.aip.org/content/aip/journal/pop/21/3/10.1063/1.4867659.

[174] J. F. Myatt, J. Zhang, R. W. Short, et al. "Multiple-beam laser-plasma interactions in inertial confinement fusion". In: *Physics of Plasmas* 21.5, 055501 (2014), pp. –. DOI: 10.1063/1.4878623. URL: http://scitation.aip.org/content/aip/journal/pop/21/5/10.1063/1.4878623.

[175] P. Michel, S. H. Glenzer, L. Divol, et al. "Symmetry tuning via controlled crossed-beam energy transfer on the National Ignition Facility". In: *Physics of Plasmas* 17.5, 056305 (2010), pp. –. DOI: 10.1063/1.3325733. URL: http://scitation.aip.org/content/aip/journal/pop/17/5/10.1063/1.3325733.

[176] R. K. Kirkwood, B. B. Afeyan, W. L. Kruer, et al. "Observation of Energy Transfer between Frequency-Mismatched Laser Beams in a Large-Scale Plasma". In: *Phys. Rev. Lett.* 76 (12 Mar. 1996), pp. 2065–2068. DOI: 10.1103/PhysRevLett.76.2065. URL: http://link.aps.org/doi/10.1103/PhysRevLett.76.2065.

[177] T.R Boehly, D.L Brown, R.S Craxton, et al. "Initial performance results of the OMEGA laser system". In: *Optics Communications* 133.1-6 (1997), pp. 495 –506. ISSN: 0030-4018. DOI: 10.1016/S0030-4018(96)00325-2. URL: http://www.sciencedirect.com/science/article/pii/S0030401896003252.

[178] M. Casanova. "Convenient computational forms for the frequency and damping of electrostatic waves in an unmagnetized plasma". In: *Laser and Particle Beams* 7 (01 Feb. 1989), pp. 165–171. ISSN: 1469-803X. DOI: 10.1017/S0263034600005917. URL: http://journals.cambridge.org/article_S0263034600005917.

[179] C. J. McKinstrie, A. V. Kanaev, V. T. Tikhonchuk, et al. "Three-dimensional analysis of the power transfer between crossed laser beams". In: *Physics of Plasmas* 5.4 (1998), pp. 1142–1147. DOI: 10.1063/1.872645. URL: http://scitation.aip.org/content/aip/journal/pop/5/4/10.1063/1.872645.

[180] P. N. Brown, A. C. Hindmarsh, and L. R. Petzold. "Using Krylov Methods in the Solution of Large-Scale Differential-Algebraic Systems". In: *SIAM Journal on Scientific Computing* 15.6 (1994), pp. 1467–1488. DOI: 10.1137/0915088. eprint: http://dx.doi.org/10.1137/0915088. URL: http://dx.doi.org/10.1137/0915088.

[181] P. N. Brown, A. C. Hindmarsh, and L. R. Petzold. "Consistent Initial Condition Calculation for Differential-Algebraic Systems". In: *SIAM Journal on Scientific Computing* 19.5 (1998), pp. 1495–1512. DOI: 10.1137/S1064827595289996. eprint: http://dx.doi.org/10.1137/S1064827595289996. URL: http://dx.doi.org/10.1137/S1064827595289996.

[182] A. Hindmarsh and A. Taylor. *User Documentation for IDA: A Differential-Algebraic Equation Solver for Sequential and Parallel Computers*. Lawrence Livermore National Laboratory report, UCRL-MA-136910. 1999.

[183] L. H. Thomas. "The calculation of atomic fields". In: *Mathematical Proceedings of the Cambridge Philosophical Society* 23 (05 Jan. 1927), pp. 542–548. ISSN: 1469-8064. DOI: 10.1017/S0305004100011683. URL: http://journals.cambridge.org/article_S0305004100011683.

[184] E. Fermi. "Un metodo statistico per la determinazione di alcune priorietĹ dell'atome". In: *Rend. Accad. Naz. Lincei* 6 (1927), pp. 602–607.

[185] E. A. Williams, R. L. Berger, R. P. Drake, et al. "The frequency and damping of ion acoustic waves in hydrocarbon (CH) and two-ion-species plasmas". In: *Physics of Plasmas* 2.1 (1995), pp. 129–138. DOI: 10.1063/1.871101. URL: http://scitation.aip.org/content/aip/journal/pop/2/1/10.1063/1.871101.

[186] P. Loiseau. "Cross beam energy transfer in the framework of a Mega Joule laser system (in French)". PhD thesis. Université Paris XI, 1999.

[187] S. Yu. Gus'kov, N.N. Demchenko, A. Kasperczuk, et al. "Laser-driven ablation through fast electrons in PALS-experiment at the laser radiation intensity of 1-50 PW/cm^2". In: *Laser and Particle Beams* 32 (01 Mar. 2014), pp. 177–195. ISSN: 1469-803X. DOI: 10.1017/S0263034613000992. URL: http://journals.cambridge.org/article_S0263034613000992.

[188] M. Le Pennec, X. Ribeyre, J.-E. Ducret, et al. "New opacity measurement principle for LMJ-PETAL laser facility". In: *High Energy Density Physics* (2014), pp. –. ISSN: 1574-1818. DOI: 10.1016/j.hedp.2014.12.003. URL: http://www.sciencedirect.com/science/article/pii/S1574181814000901.

[189] C. K. Li and R. D. Petrasso. "Stopping of directed energetic electrons in high-temperature hydrogenic plasmas". In: *Phys. Rev. E* 70 (6 Dec. 2004), p. 067401. DOI: 10.1103/PhysRevE.70.067401. URL: http://link.aps.org/doi/10.1103/PhysRevE.70.067401.

[190] S. Goudsmit and J. L. Saunderson. "Multiple Scattering of Electrons". In: *Phys. Rev.* 57 (1 Jan. 1940), pp. 24–29. DOI: 10.1103/PhysRev.57.24. URL: http://link.aps.org/doi/10.1103/PhysRev.57.24.

[191] H. W. Lewis. "Multiple Scattering in an Infinite Medium". In: *Phys. Rev.* 78 (5 June 1950), pp. 526–529. DOI: 10.1103/PhysRev.78.526. URL: http://link.aps.org/doi/10.1103/PhysRev.78.526.

[192] C. K. Li and R. D. Petrasso. "Stopping, straggling, and blooming of directed energetic electrons in hydrogenic and arbitrary-Z plasmas". In: *Phys. Rev. E* 73 (1 Jan. 2006), p. 016402. DOI: 10.1103/PhysRevE.73.016402. URL: http://link.aps.org/doi/10.1103/PhysRevE.73.016402.

[193] A. A. Solodov and R. Betti. "Stopping power and range of energetic electrons in dense plasmas of fast-ignition fusion targets". In: *Physics of Plasmas* 15.4, 042707 (2008), pp. –. DOI: 10.1063/1.2903890. URL: http://scitation.aip.org/content/aip/journal/pop/15/4/10.1063/1.2903890.

[194] L. Gremillet. "Theoretical and experimental study of fast electron transport in ultra-high-intensity laser-solid interaction (in French)". PhD thesis. Ecole polytechnique, Palaiseau, 2003.

[195] H. A. Bethe. *Handbuch für Physik*. Tome 242. Julius Springer, 1933, p273.

[196] C. Møller. "Zur Theorie des Durchgangs schneller Elektronen durch Materie". In: *Annalen der Physik* 406 (1932), pp. 531–585. DOI: 10.1002/andp.19324060506.

[197] C. Regan. "Fast models for fast particles transport in the context of ICF(in French)". PhD thesis. Université Bordeaux 1, 2010. URL: http://www.theses.fr/2010BOR14138.

[198] M. Touati, J.-L. Feugeas, Ph. Nicolaï, et al. "A reduced model for relativistic electron beam transport in solids and dense plasmas". In: *New Journal of Physics* 16.7 (2014), p. 073014. URL: http://stacks.iop.org/1367-2630/16/i=7/a=073014.

[199] B. Dubroca, J.-L. Feugeas, and M. Frank. "Angular moment model for the Fokker-Planck equation". English. In: *The European Physical Journal D* 60.2 (2010), pp. 301–307. ISSN: 1434-6060. DOI: 10.1140/epjd/e2010-00190-8. URL: http://dx.doi.org/10.1140/epjd/e2010-00190-8.

[200] D. Del Sorbo, J.-L. Feugeas, P. Nicolaï, et al. "Reduced entropic model for studies of multidimensional nonlocal transport in high-energy-density plasmas". In: *Physics of Plasmas* 22.8, 082706 (Aug. 2015), p. 082706. DOI: 10.1063/1.4926824.

[201] S. Atzeni, A. Schiavi, and C. Bellei. "Targets for direct-drive fast ignition at total laser energy of 200-400 kJ". In: *Physics of Plasmas* 14.5, 052702 (May 2007), p. 052702. DOI: 10.1063/1.2716682.

[202] D. W. Forslund, J. M. Kindel, and K. Lee. "Theory of Hot-Electron Spectra at High Laser Intensity". In: *Phys. Rev. Lett.* 39 (5 Aug. 1977), pp. 284–288. DOI: 10.1103/PhysRevLett.39.284. URL: http://link.aps.org/doi/10.1103/PhysRevLett.39.284.

[203] E. Fabre and F. et al Amiranoff. In: *Plasma physics and controlled nuclear fusion research*. Vol. 38. 1980, p. 263.

[204] F. Amiranoff, R. Fabbro, E. Fabre, et al. "Experimental studies of fast electron generation in laser-produced plasmas at 1.06, 0.53 and 0.26 μm laser wavelength". In: *J. Phys. France* 43.7 (1982), pp. 1037–1042. DOI: 10.1051/jphys:019820043070103700. URL: http://dx.doi.org/10.1051/jphys:019820043070103700.

[205] H. X. Vu, D. F. DuBois, J. F. Myatt, et al. "Hot-electron production and suprathermal heat flux scaling with laser intensity from the two-plasmon decay instability". In: *Physics of Plasmas* 19.10, 102703 (2012), pp. –. DOI: 10.1063/1.4757978. URL: http://scitation.aip.org/content/aip/journal/pop/19/10/10.1063/1.4757978.

[206] R. Yan, C. Ren, J. Li, et al. "Generating energetic electrons through staged acceleration in the two-plasmon-decay instability in inertial confinement fusion". In: *Phys. Rev. Lett.* 108 (17 Apr. 2012), p. 175002. DOI: 10.1103/PhysRevLett.108.175002. URL: http://link.aps.org/doi/10.1103/PhysRevLett.108.175002.

[207] R. E. Turner, D. W. Phillion, E. M. Campbell, et al. "Time-resolved observations of stimulated Raman scattering from laser-produced plasmas". In: *Physics of Fluids* 26 (Feb. 1983), pp. 579–581. DOI: 10.1063/1.864143.

[208] C. Labaune, H. A. Baldis, E. Fabre, et al. "Backward and forward stimulated Raman scattering from thin foil targets with a 0.26 μm laser". In: *Physics of Fluids B: Plasma Physics (1989-1993)* 2.1 (1990), pp. 166–170. DOI: 10.1063/1.859572. URL: http://scitation.aip.org/content/aip/journal/pofb/2/1/10.1063/1.859572.

[209] C. Riconda, S. Weber, V. T. Tikhonchuk, et al. "Kinetic simulations of stimulated Raman backscattering and related processes for the shock-ignition approach to inertial confinement fusion". In: *Physics of Plasmas* 18.9, 092701 (Sept. 2011), p. 092701. DOI: 10.1063/1.3630937.

[210] S. Weber, C. Riconda, O. Klimo, et al. "Fast saturation of the two-plasmon-decay instability for shock-ignition conditions". In: *Phys. Rev. E* 85 (1 Jan. 2012), p. 016403. DOI: 10.1103/PhysRevE.85.016403. URL: http://link.aps.org/doi/10.1103/PhysRevE.85.016403.

[211] Labaune, C., Amiranoff, F., Matthieussent, G., et al. "Instabilité Raman avant dans un plasma homogène". In: *Rev. Phys. Appl. (Paris)* 23.9 (1988), pp. 1505–1513. DOI: 10.1051/rphysap:019880023090150500. URL: http://dx.doi.org/10.1051/rphysap:019880023090150500.

[212] R. E. Turner, K. Estabrook, R. P. Drake, et al. "Observation of forward Raman scattering in laser-produced plasmas". In: *Physical Review Letters* 57 (Oct. 1986), pp. 1725–1728. DOI: 10.1103/PhysRevLett.57.1725.

[213] O Klimo and V T Tikhonchuk. "Laser-plasma interaction studies in the context of shock ignition: the regime dominated by parametric instabilities". In: *Plasma Physics and Controlled Fusion* 55.9 (2013), p. 095002. URL: http://stacks.iop.org/0741-3335/55/i=9/a=095002.

[214] C. Rousseaux, F. Amiranoff, C. Labaune, et al. "Electrons rapides dans un plasma crée par laser (in French)". In: *Rev. Phys. Appl. (Paris)* 23.9 (1988), pp. 1515–1519. DOI: 10.1051/rphysap:019880023090151500. URL: https://hal.archives-ouvertes.fr/jpa-00245979/document.

[215] W. Theobald, R. Nora, M. Lafon, et al. "Spherical shock-ignition experiments with the 40 + 20-beam configuration on OMEGA". In: *Physics of Plasmas* 19.10, 102706 (2012), pp. –. DOI: 10.1063/1.4763556. URL: http://scitation.aip.org/content/aip/journal/pop/19/10/10.1063/1.4763556.

[216] L. Yin, B. J. Albright, H. A. Rose, et al. "Onset and saturation of backward stimulated Raman scattering of laser in trapping regime in three spatial dimensions". In: *Physics of Plasmas* 16.11, 113101 (2009), pp. –. DOI: 10.1063/1.3250928. URL: http://scitation.aip.org/content/aip/journal/pop/16/11/10.1063/1.3250928.

[217] R. K. Kirkwood, R. L. Berger, C. G. R. Geddes, et al. "Scaling of saturated stimulated Raman scattering with temperature and intensity in ignition scale plasmas". In: *Physics of Plasmas* 10 (July 2003), pp. 2948–2955. DOI: 10.1063/1.1580814.

[218] S. P. Regan, R. Epstein, V. N. Goncharov, et al. "Laser absorption, mass ablation rate, and shock heating in direct-drive inertial confinement fusion". In: *Physics of Plasmas* 14.5, 056305 (2007), pp. –. DOI: 10.1063/1.2671690. URL: http://scitation.aip.org/content/aip/journal/pop/14/5/10.1063/1.2671690.

[219] A. R. Bell, R. G. Evans, and D. J. Nicholas. "Elecron Energy Transport in Steep Temperature Gradients in Laser-Produced Plasmas". In: *Phys. Rev. Lett.* 46 (4 Jan. 1981), pp. 243–246. DOI: 10.1103/PhysRevLett.46.243. URL: http://link.aps.org/doi/10.1103/PhysRevLett.46.243.

[220] R. Ramis, R. Schmalz, and J. Meyer-Ter-Vehn. "MULTI, A computer code for one-dimensional multigroup radiation hydrodynamics". In: *Computer Physics Communications* 49 (June 1988), pp. 475–505. DOI: 10.1016/0010-4655(88)90008-2.

[221] R. Ramis, J. Meyer-ter-Vehn, and J. Ramírez. "MULTI2D - a computer code for two-dimensional radiation hydrodynamics". In: *Computer Physics Communications* 180 (June 2009), pp. 977–994. DOI: 10.1016/j.cpc.2008.12.033.

[222] S. Atzeni. "2-D Lagrangian studies of symmetry and stability of laser fusion targets". In: *Computer Physics Communications* 43 (Dec. 1986), pp. 107–124. DOI: 10.1016/0010-4655(86)90056-1.

[223] S. Atzeni, A. Schiavi, F. Califano, et al. "Fluid and kinetic simulation of inertial confinement fusion plasmas". In: *Computer Physics Communications* 169 (July 2005), pp. 153–159. DOI: 10.1016/j.cpc.2005.03.036.

[224] Ph. Nicolaï, J.-L. Feugeas, T. Nguyen-bui, et al. "Effect of nonthermal electrons on the shock formation in a laser driven plasma". In: *Physics of Plasmas* 22.4, 042705 (2015), pp. –. DOI: 10.1063/1.4917472. URL: http://scitation.aip.org/content/aip/journal/pop/22/4/10.1063/1.4917472.

[225] L. Antonelli. "Laser-plasma coupling in the shock-ignition intensity regime". In: *Acta Technica*. Vol. 56. 2011, T57–T69.

[226] L. Antonelli, M. Richetta, P. Koester, et al. "Results in shock ignition experiments at PALS: Kα generation and hot electrons study". In: *Proceedings of 39th EPS Conference & 16th Int. Congress on Plasma Physics*. 2013.

[227] K. B. Wharton, S. P. Hatchett, S. C. Wilks, et al. "Experimental Measurements of Hot Electrons Generated by Ultra-intense Laser-Plasma Interactions on Solid-Density Targets". In: *Phys. Rev. Lett.* 81 (4 July 1998), pp. 822–825. DOI: 10.1103/PhysRevLett.81.822. URL: http://link.aps.org/doi/10.1103/PhysRevLett.81.822.

[228] J. Sempau, E. Acosta, J. Baro, et al. "An algorithm for Monte Carlo simulation of coupled electron-photon transport". In: *Nuclear Instruments and Methods in Physics Research Section B: Beam Interactions with Materials and Atoms* 132.3 (1997), pp. 377 –390. ISSN: 0168-583X. DOI: 10.1016/S0168-583X(97)00414-X. URL: http://www.sciencedirect.com/science/article/pii/S0168583X9700414X.

[229] S. Agostinelli, J. Allison, K. Amako, et al. "Geant4â a simulation toolkit". In: *Nuclear Instruments and Methods in Physics Research Section A: Accelerators, Spectrometers, Detectors and Associated Equipment* 506.3 (2003), pp. 250 –303. ISSN: 0168-9002. DOI: 10.1016/S0168-9002(03)01368-8. URL: http://www.sciencedirect.com/science/article/pii/S0168900203013688.

[230] O. Klimo, S. Weber, V. T. Tikhonchuk, et al. "Particle-in-cell simulations of laser-plasma interaction for the shock ignition scenario". In: *Plasma Physics and Controlled Fusion* 52.5 (2010), p. 055013. URL: http://stacks.iop.org/0741-3335/52/i=5/a=055013.

[231] D. K. Bradley, P. M. Bell, J. D. Kilkenny, et al. "High-speed gated x-ray imaging for ICF target experiments (invited)". In: *Review of Scientific Instruments* 63.10 (1992), pp. 4813–4817. DOI: 10.1063/1.1143571. URL: http://scitation.aip.org/content/aip/journal/rsi/63/10/10.1063/1.1143571.

[232] M. Millecchia, S. P. Regan, R. E. Bahr, et al. "Streaked x-ray spectrometer having a discrete selection of Bragg geometries for Omega". In: *Review of Scientific Instruments* 83.10, 10E107 (2012), pp. –. DOI: 10.1063/1.4729501. URL: http://scitation.aip.org/content/aip/journal/rsi/83/10/10.1063/1.4729501.

[233] A. Vallet. "Hydrodynamic modeling of the shock ignition scheme for inertial confinement fusion (in French)". PhD thesis. Université Bordeaux, 2014. URL: http://www.theses.fr/s127313.

[234] X. Ribeyre, M. Lafon, G. Schurtz, et al. "Shock ignition: modelling and target design robustness". In: *Plasma Physics and Controlled Fusion* 51.12, 124030 (Dec. 2009), p. 124030. DOI: 10.1088/0741-3335/51/12/124030.

[235] X. Ribeyre, V. T. Tikhonchuk, J. Breil, et al. "Analytic criteria for shock ignition of fusion reactions in a central hot spot". In: *Physics of Plasmas* 18.10, 102702 (Oct. 2011), p. 102702. DOI: 10.1063/1.3646743.

[236] A. Vallet, X. Ribeyre, and V. Tikhonchuk. "Finite Mach number spherical shock wave, application to shock ignition". In: *Physics of Plasmas* 20.8, 082702 (Aug. 2013), p. 082702. DOI: 10.1063/1.4817292.

[237] V.G. Guderley. In: *Luftfahrtforschung* 19 (1942), pp. 302–312.

[238] S. Gus'kov, X. Ribeyre, M. Touati, et al. "Ablation Pressure Driven by an Energetic Electron Beam in a Dense Plasma". In: *Physical Review Letters* 109.25, 255004 (Dec. 2012), p. 255004. DOI: 10.1103/PhysRevLett.109.255004.

[239] S. Atzeni and G. Schurtz. "HiPER target studies: towards the design of high gain, robust, scalable direct-drive targets with advanced ignition schemes". In: *Diode-Pumped High Energy and High Power Lasers; ELI: Ultrarelativistic Laser-Matter Interactions and Petawatt Photonics; and HiPER: the European Pathway to Laser Energy*. Vol. 8080. 2011.

[240] X. Ribeyre, S. Gus'kov, J.-L. Feugeas, et al. "Dense plasma heating and Gbar shock formation by a high intensity flux of energetic electrons". In: *Physics of Plasmas* 20.6, 062705 (June 2013), p. 062705. DOI: 10.1063/1.4811473.

[241] J. Stoer and R. Bulirsch. *Introduction to Numerical Analysis*. New York: Springer-Verlag, 1980, pp. 3.4–3.5.

[242] G. Dahlquist and A. Bjorck. *Numerical Methods*. Englewood Cliffs, NJ: Prentice-Hall, 1974, pp. 7.4.1–7.4.2.

[243] A. Ralston and P. Rabinowitz. *A First Course in Numerical Analysis, 2nd ed.* New York: McGraw-Hill, 1978, pp. 4.10–2.

[244] Y. T. Lee and R. M. More. "An electron conductivity model for dense plasmas". In: *Physics of Fluids* 27 (May 1984), pp. 1273–1286. DOI: 10.1063/1.864744.

[245] L. De Broglie. *Recherche sur la théorie des quanta*. Annales de physique, 10e série, Tome 3. 1925.

[246] A. Decoster, P. A. Raviart, P. A. Markowich, et al. *Modelling of collisions*. Applied Mathematics. Gauthier-Villars : Elsevier, cop. 1998., 1997. URL: http://www.worldcat.org/search?q=no%3A758259002.

Multiscale Description of the Laser-Plasma Interaction, Application to the Physics of Shock Ignition in Inertial Confinement Fusion

Keywords: Laser-Plasma Interaction, Hydrodynamic code, nonlinear LPI processes, thick-rays, hot electrons, Cross-Beam Energy Transfer, ICF.

This manuscript presents a novel formulation of the Laser-Plasma Interaction (LPI) at hydrodynamical scales, that couples the plasma dynamics with linear and nonlinear LPI processes. The standard Ray Tracing model, based on Geometrical Optics, is not well suited for that purpose because it does not readily describe the laser intensity distribution in plasma. We propose an alternative model formulated for a Lagrangian hydrodynamic code. It is based on the ray-based Paraxial Complex Geometrical Optics (PCGO) that describes Gaussian optical beamlets. A method for modeling non-Gaussian laser beams smoothed by Phase Plates is presented, that allows to create intensity variations that reproduce the beam envelope, contrast and high-intensity statistics predicted by paraxial laser propagation codes. We propose inline reduced models for the non-linear laser-plasma interaction, in the case of the Cross-Beam Energy Transfer (CBET) and the generation of Hot Electrons (HE). The inline CBET model is validated against a time-dependent conventional paraxial electromagnetic wave propagation code, in a well-defined plasma configuration with density and velocity profiles corresponding to an inhomogeneous plasma. Good agreement is found past a transient period on the picosecond time scale, notably for the spatial distribution of density perturbations and laser intensities in the interaction region. Application of the model to a direct-drive Inertial Confinement Fusion (ICF) configuration shows that CBET significantly degrades the irradiation symmetry by amplifying low frequency modes and reducing the laser-capsule coupling efficiency, ultimately leading to large modulations of the shell areal density and lower convergence ratios. The LPI/HE model predicts the HE fluxes, temperatures, angular dispersion and direction from the laser intensity of PCGO beamlets from simplified expressions based on theoretical models and scaling laws obtained in kinetic simulations. The HE beams propagation and energy deposition in plasma is described in the angular scattering approximation, adapted to two-dimensional, transversally Gaussian, multigroup HE beams of arbitrary angular distribution. This model accounts for (i) competition for the laser energy between the various instabilities and with the linear collisional absorption, (ii) coupling between nonlinear LPIs and plasma dynamics via the high energy electron beams and (iii) loss of coupling due to backscattered Raman light. Its performance is confirmed by comparison with measurements of shock timing, laser absorption, HE fluxes and temperatures in experiments conducted on Omega and Pals laser facilities. This multiscale inline LPI-HE model is used to interpret several Shock Ignition experiments. It is found that HEs from parametric instabilities significantly increase the shock pressure and velocity in the target, while decreasing its strength and the overall ablation pressure. Applications to the high-intensity regime of shock ignition ICF suggest that HEs generated by the nonlinear LPI are nefarious to the capsule implosion in conventional target designs, as they lead to a dramatic increase in the hotspot mass and losses by Bremsstrahlung radiation. This model is readily applicable to hydrodynamic description of laser-target experiments of High Energy Density Physics, in the interaction regimes involving the above-mentioned non-linear LPI processes.

Description Multi-Echelle de l'Interaction Laser-Plasma, Application à la Physique de l'Allumage par Choc en Fusion par Confinement Inertiel

Mots-Clefs : Interaction Laser-Plasma, code Hydrodynamique, processus d'ILP non-linéaires, rayons épais, electrons chauds, échange d'énergie entre faisceaux croisés, FCI.

Ce manuscrit présente une nouvelle formulation de l'Interaction Laser-Plasma (ILP) à l'échelle hydrodynamique, qui couple la dynamique du plasma avec les processus d'ILP linéaires et non-linéaires. Le modèle standard du tracé de rayon (Ray-Tracing), basé sur l'Optique Géométrique, est peu adapté pour modéliser l'ILP non-linéaire car la distribution de l'intensité laser dans le plasma n'est pas directement disponible. Nous proposons un modèle alternatif spécifiquement formulé pour un code hydrodynamique Lagrangien, basé sur l'Optique Géométrique Complexe Paraxiale qui décrit la propagation de faisceaux Gaussiens. Cette méthode est ensuite adaptée à la description de faisceaux laser non Gaussiens, et permet de reproduire la statistique d'intensité, l'enveloppe et le contraste de faisceaux lissés par une Lame de Phase. Nous proposons des modèles en ligne pour décrire l'échange d'énergie entre faisceaux croisés (CBET) et la génération d'électrons rapides par l'ILP non-linéaire, en utilisant PCGO. Le modèle en ligne de CBET est validé par comparaison avec un code de propagation d'une onde électromagnétique paraxial conventionnel dans le cas d'un plasma inhomogène en vitesse. Un bon accord est trouvé après une période transitoire de l'ordre de la picoseconde, notamment en ce qui concerne la distribution spatiale de l'intensité laser et des perturbations de densité du plasma. Ce modèle appliqué à une configuration d'attaque directe de Fusion par Confinement Inertiel (FCI) montre que le CBET réduit le couplage laser-cible, réduit le facteur de convergence, et amplifie les modes basse fréquence de déformation de la capsule. Le modèle de génération d'électrons rapides par l'ILP non-linéaire modélise les propriétés des faisceaux d'électrons rapides, i.e. leur flux, énergie moyenne, dispersions angulaire et direction, à partir de l'intensité laser prédite par PCGO et à partir d'expressions simplifiées, basées sur des modèles théoriques et des lois d'échelles obtenues à l'aide de simulations cinétiques. La propagation et le dépôt d'énergie par les électrons rapides est décrite à partir d'une approximation de diffusion angulaire adaptée en deux dimensions, pour des faisceaux de profil transverse d'intensité Gaussien, de distribution d'énergie exponentielle et d'ouverture angulaire arbitraire. Ce modèle couplé rend compte de (i) la compétition pour l'énergie laser entre les différentes instabilités et avec l'absorption collisionnelle, (ii) le couplage entre l'ILP non-linéaire et la dynamique du plasma à travers les faisceaux d'électrons rapides, et (iii) la perte de couplage laser-plasma due à la diffusion Raman arrière. Les performances de ce modèle sont évaluées par comparaisons avec des expériences d'allumage par choc conduites sur les installations laser Omega et Pals. Ce modèle multi-échelle est ensuite utilisé pour interpréter plusieurs expériences. On trouve notamment que les électrons générés par l'ILP non-linéaire augmentent la vitesse du choc et la pression en aval de ce dernier, tout en réduisant sa force et la pression d'ablation. Une application à la phase fortement non-linéaire de l'allumage par choc en FCI suggère que ces électrons sont néfastes pour l'implosion de la capsule en ce qui concerne les cibles conventionnelles : ceux-ci causent une augmentation de la masse du point chaud et des pertes radiatives. Ce modèle peut être appliqué à la modélisation hydrodynamique des expériences laser-cible de physique des hautes densités d'énergie pour les régimes d'interaction pertinents pour les instabilités évoquées ci dessus.

université de BORDEAUX

Introduction et Conclusion de Thèse

Soumises en vue de l'obtention du diplôme de

Docteur de l'Université de Bordeaux

Université de Bordeaux, Ecole doctorale des sciences et de l'ingénieur,
Section : Astrophysique, Plasmas, Nucléaire

Description Multi-Echelle de l'Interaction Laser-Plasma, Application à la Physique de l'Allumage par Choc en Fusion par Confinement Inertiel

---

par

Arnaud Colaïtis

sous la direction de
V. Tikhonchuk
G. Duchateau
Ph. Nicolaï

Thèse soutenue le 10 November 2015 à Talence (France)
Devant le jury composé de :

Riconda, C.	Associate Professor, UPMC, LULI (France)	**Rapporteur**
Michel, P.	Staff Scientist, LLNL (United States)	**Rapporteur**
Labaune, C.	Research Director, CNRS, LULI (France)	**Prés. du Jury**
Hüller, S.	Research Director, CNRS, CPHT (France)	**Examinateur**
Bonnaud, G.	Professor, CEA-DSM, INSTN (France)	**Examinateur**
Tikhonchuk, V.	Professor, Université de Bordeaux, CELIA (France)	**Examinateur**
Duchateau, G.	Research Engineer, CEA-DAM, CELIA (France)	**Examinateur**
Nicolaï, Ph.	Research Engineer, CEA-DAM, CELIA (France)	**Examinateur**
Masson-Laborde, P.-E.	Research Engineer, CEA-DAM, DCSA (France)	**Invité**

Table des matières

Chapitre 0

Introduction

0.1 Description multi-échelle de l'interaction laser-plasma

L'interaction de faisceaux laser avec les plasmas implique une large gamme de processus physiques, de l'accélération de particules chargées à l'excitation d'ondes plasma, la génération et la saturation d'instabilités laser-plasma. La compréhension du couplage laser-plasma dans son entièreté requiert l'étude d'une grande variété de champs physiques, incluant la description de la réponse électromagnétique du plasma, la théorie de l'interaction et des instabilités onde-particule et la théorie des ondes plasma linéaires et non-linéaires. Bien que de nombreux processus de couplage laser-plasma aient été observés dans les expériences, de nombreux problèmes difficiles liés à la variétés des phénomènes mis en jeu restent à résoudre. Ceux-ci dépendent notamment de l'intensité laser et des propriétés de lissage du faisceau, des paramètres plasma locaux comme la température et les gradients de densités, et de la composition du plasma. Réciproquement, les paramètres plasma dépendent de l'interaction laser-plasma. De plus, ces couplages interagissent entre eux, ce qui donne lieu à des processus additionnels de compétition ou d'amplification. La compréhension de ce problème couplé et non linéaire à motivé de nombreuse études théoriques, numériques et expérimentales. Certains exemples notoires sont : l'identification du raidissement du gradient de densité [1, 2], les mesures de l'absorption plasma pour les lasers intenses [3, 4, 5, 6, 7, 8], la mesure expérimentale de distributions électroniques caractérisées par au moins deux températures [9, 10, 11, 12], l'identification des instabilités paramétriques de type Brillouin [13, 14, 15, 16] et Raman [17, 18, 19, 20, 21], et l'évaluation de la dépendance à la longueur d'onde des processus de couplage [22, 23, 24, 25]. Le développement des outils numériques moderne permet une étude plus complète de ces processus, et ainsi, d'investiguer divers champs physique et d'améliorer l'interprétation des expériences.

On considère l'Interaction Laser-Plasma (ILP) dans le régime des durées d'impulsion de $[0.1, 10]$ ns et pour lesquelles le *paramètre d'interaction* $I\lambda_L^2$ est dans l'intervale $[10^{13}\text{-}10^{17}]$ Wμm^2/cm^2 (I est l'intensité laser et λ_L la longueur d'onde associé, dans le vide). Ces paramètres lasers sont courants dans les expériences de Physique des Hautes Densités d'Energies, avec notamment des applications en Astrophysique de Laboratoire et en Fusion par Confinement Inertiel (FCI). La dynamique des cibles sujettes à de telles intensités sur de telles durées d'impulsion à lieu sur des échelles temporelles et spatiales de l'ordre de plusieurs nanosecondes et de plusieurs millimètres.

	Echelles spatiales (m)	Echelles temporelles (s)
Hydrodynamique	10^{-3} - plasma coronal 10^{-5} - coquille en vol 10^{-7} - chocs hydrodynamiques	
Laser	10^{-4} - tâche focale 10^{-6} - inhomogénéités laser	10^{-8} - durée d'impulsion 10^{-12} - lissage (SSD)
Résolution hydro.	$10^{-7}/10^{-4}$ Méthodes Lagrangiennes → pas variable	$10^{-15}/10^{-12}$ condition de stabilité numérique → pas variable
Eqs. de Maxwell	$10^{-8}/10^{-7}$ longueur de Debye/longueur d'onde → dans tout le plasma	10^{-16} $\frac{1}{\omega}$/période laser → dans tout le plasma

Table 1 – *Echelles temporelles et spatiales impliquées dans la description hydrodynamique des processus laser-cible pour les intensités pertinentes à cette étude.*

La description théorique de la dynamique des plasmas sur ces échelles repose sur des approches fluides, utilisant des *modèles hydrodynamiques* qui permettent d'étudier de grands volumes de plasma sur des longues durées. D'autre part, l'interaction laser-plasma non linéaire est étudiée de manière appropriée aux échelles microscopiques et mésoscopiques à l'aide de code cinétiques (*particle-in-cell* et *Fokker-Planck*) et de modèles électromagnétiques paraxiaux. La diversité des échelles mises en jeu dans la description de l'évolution de la dynamique de la cible, en incluant les processus à fine échelle de l'ILP, est illustrée sur le tableau 1.

L'état de l'art de la description de la propagation laser aux grandes échelles repose sur des modèles réduits compatibles avec les performances des ordinateurs modernes. La plus commune est celle du *Tracé de Rayon* (RT) [26], qui décrit le faisceau laser par des fagots de rayons infiniment minces qui suivent les lois de propagation de l'Optique Géométrique (GO) et qui sont caractérisés par une densité de puissance. Dans les situations où les effets collectifs et les couplages non-linéaires sont peu importants ($I\lambda_L^2 \lesssim 5 \times 10^{13}$ Wμm^2/cm^2), les méthodes basées sur l'optique géométrique sont suffisamment précises et numériquement efficaces. Elles décrivent la réfraction du laser et le chauffage du plasma par l'absorption collisionnelle. Au contraire, la modélisation de l'ILP à de plus grands paramètres d'interaction repose sur la connaissance de l'amplitude du champ électrique et de la direction du front d'onde[1], quantités qui ne sont pas directement décrites par l'optique géométrique. La physique de l'ILP linéaire et non-linéaire est alors souvent modélisée par des modifications ad-hoc du flux thermique électronique maximum ou en ajustant la balance de puissance des faisceaux lasers, de façon à reproduire les résultats expérimentaux. Ces approchent limitent la compréhension des processus physiques mis en jeu et la capacité prédictive de ces outils numériques. Afin de remédier à ces limitations, des efforts récents ont été fait afin d'inclure l'ILP non-linéaire aux échelles hydrodynamiques, notamment avec la mise au point de modèles en-ligne pour décrire l'échange d'énergie entre faisceaux croisés

1. On note que bien que la notion de direction individuelle d'un rayon existe, celle du front d'onde dans son ensemble n'est pas décrite.

(CBET) [27, 28]. Ces outils ont permis de mieux interpréter et concevoir les expériences de FCI [29] et peuvent être appliqués pour évaluer des configurations d'éclairement laser-cible plus complexes, telles que le schéma d'attaque directe polaire [30]. De la même façon, les effets sur la dynamique du plasma des faisceaux d'électrons à haute énergie générés par l'ILP non-linéaire est particulièrement importante pour les études de FCI [31, 32], les expériences de double front d'ablation à haute intensité, ou pour la conception et l'interprétation des expériences laser-cible dans le régime nanoseconde [33].

Etant donné la grande variété des configurations laser-cible qui mettent en jeu ces processus, il y a un besoin évident pour un modèle multi-échelle qui pourrait rendre compte des couplages laser-plasma linéaires et non-linéaires dans les codes hydrodynamiques, ainsi que des rétro-actions entre la propagation laser dans le plasma, la génération d'électrons de haute énergie par l'ILP non-linéaire, la propagation de ces faisceaux d'électrons et la dynamique du plasma. Cette modélisation à de grandes échelles pose des problèmes sévères liés à (i) la description précise de l'intensité laser dans le plasma, (ii) la description consistante des sources d'électrons rapides à partir du modèle de propagation laser et (iii) le transport de ces faisceaux d'électrons dans le plasma. Les deux premiers points sont liés à l'usage standard de l'optique géométrique, qui ne permet pas d'évaluer de manière robuste l'intensité laser dans le plasma [34], et le dernier point demande un modèle de propagation à l'échelle hydrodynamique qui soit à la fois robuste et rapide. L'objet de ce travail est d'aborder ces difficultés afin de formuler un modèle multi-échelle qui décrive l'ILP à l'échelle hydrodynamique, y compris son couplage avec la génération de population d'électrons rapides.

Les applications de cette formulation ont pour cadre la FCI, et plus précisément le schéma d'allumage par choc, qui est particulièrement vulnérable à l'ILP non-linéaire lors du pic d'intensité laser opérant sur une durée de ~ 500 ps. Nous présentons dans la section suivante le contexte de la FCI, et la position qu'occupe l'ILP linéaire et non-linéaire dans ce cadre. Cette section fournit les bases de la formulation des objectifs de la thèse.

0.2 L'Interaction Laser-Plasma dans le cadre de la Fusion par Confinement Inertiel

0.2.0.1 La Fusion Thermonucléaire

Les réactions de fusion s'obtiennent en rapprochant suffisamment deux noyaux chargés afin qu'ils se lie à travers la force nucléaire forte, qui est attractive et dont la portée d'interaction est de l'ordre de quelques fermi (quelques 10^{-15}m). Rapprocher les noyaux chargés à de telles distances nécessite de vaincre la force de répulsion Coulombienne, qui intéragit sur de plus longues portées que la force nucléaire forte. Bien que l'énergie cinétique nécéssaire à ce rapprochement soit de l'ordre de 300 keV (pour des réactions de Deuterium-Tritium), l'effet quantique tunnel permet d'obtenir ces réactions à de plus basses énergies [35]. La section efficace σ des réactions de fusion pour divers noyaux est montrée sur la figure 0-1 [gauche]. La réaction la plus probable à basse température est celle qui utilise le mélange D-T, pour lequel la section-efficace à 10 keV est jusqu'à deux ordres de grandeurs plus grande que pour d'autres réactifs. Cette réaction particulière s'écrit :

$$ {}^{2}_{1}\mathrm{D} + {}^{3}_{1}\mathrm{T} \rightarrow {}^{4}_{2}\mathrm{He} + \mathrm{n} + 17.6\ \mathrm{MeV}\ , \tag{1} $$

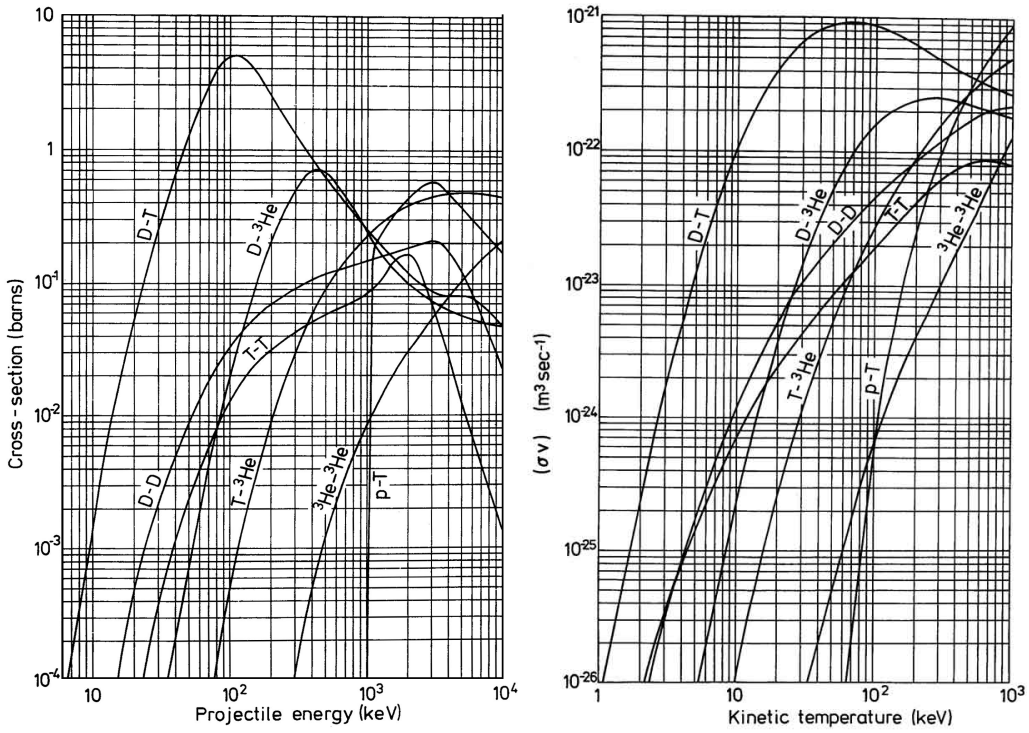

Figure 0-1 – *[gauche] Sections efficaces des réactions de fusion (en barns, i.e. $10^{-28}m^2$), en fonction de l'énergie cinétique relative moyenne entre les nucléons en keV, et [droite] réactivité des réactions de fusion (en m^3/s) en fonction de la température cinétique en keV. Figures de* http://www.kayelaby.npl.co.uk.

où les 17.6 MeV d'énergie cinétique libérés par le processus de fusion sont partagés entre la particule α (3.56 MeV) et le neutron (14.03 MeV).

Dans la région de *Gamow*, en dessous de $\sim$ 100 keV, la section efficace pour la fusion du mélange D-T augmente de façon monotone avec l'énergie cinétique des particules projectile. A ces températures, le combustible devient un plasma d'électrons et de deux espèces d'ions. En considérant un plasma à l'équilibre thermodynamique et caractérisé par une fonction de distribution Maxwellienne de température moyenne $T \simeq 10$ keV, les ions dans la queue haute énergie de la fonction de distribution sont proche du maximum de la section efficace de fusion. En intégrant sur la fonction de distribution Maxwellienne, on calcul la réactivité thermique moyenne $\langle \sigma v \rangle$ d'un plasma de fusion en fonction de sa température moyenne T, comme montré en figure 0-1 [droite]. Le chauffage du plasma permet de compenser les pertes d'énergies dans les collisions ion-ion élastiques, qui ont une section efficace bien plus grande. Cette approche où les réactions de fusion sont obtenues dans la queue haute énergie de la fonction de distribution d'un plasma chaud s'appelle *fusion thermonucléaire*. C'est l'approche de choix pour produire de grandes quantités d'énergie de fusion.

0.2.0.2 Combustion du D-T

A la température de 10 keV mentionnée précédemment, le plasma ne peut pas être confiné dans un conteneur solide ; ce dernier serait rapidement détérioré, polluant ainsi le combustible

qui refroidirait rapidement. Ainsi, ces plasmas doivent être confinés dans le vide. Cependant, les hautes températures mises en jeu impliquent aussi de hautes pressions : le plasma aura alors naturellement tendance à s'étendre et refroidir. Or, le plasma doit être confiné dans un volume donné pendant un temps suffisamment long afin d'avoir le temps de bruler la majorité du combustible. Pour un mélange équimolaire de D-T et en supposant une température constante pendant tout le confinement, la fraction de combustible brûlée F_{DT} s'écrit [36, 37] :

$$F_{\mathrm{DT}} = \frac{\langle \sigma v \rangle n_0 \tau / 2}{\langle \sigma v \rangle n_0 \tau / 2 + 1} \ , \tag{2}$$

où τ est le temps de confinement et n_0 est la densité volumique initiale des ions. Cette formule simple souligne les deux paramètres principaux de la fusion thermonucléaire ; la température T (contenue dans $\langle \sigma v \rangle$) et le produit $n_0\tau$. Afin de bruler la moitié du combustible, l'équation (2) montre que $n_0\tau$ doit être de l'ordre de $2\langle \sigma v \rangle^{-1}$. Etant donné la difficulté de maximiser simultanément n_0 et τ, le problème de la fusion peut être abordé de deux angles différents : en confinant un plasma de haute densité sur des temps courts, ou en confinant un plasma peu dense sur des temps longs (ce dernier cas étant celui de la Fusion par Confinement Magnétique).

0.2.1 La Fusion par Confinement Inertiel

Avec l'invention du laser, la possibilité de focaliser de grandes quantités d'énergies dans des petits volumes fut considérée comme un moyen d'initier les réactions de fusion. Les premières expériences ont suggérées que la configuration optimale est celle de l'irradiation d'une cible solide sphérique, la chauffant à de hautes températures tout en confinement le plasma par sa propre inertie sur de courtes durées. Cette approche est celle de la *Fusion par Confinement Inertiel* (FCI) [38].

0.2.1.1 Allumage par point chaud central

En considérant une sphère uniformément irradiée par des faisceaux lasers, on peut montrer que la fraction brûlée de combustible s'écrit [36, 37] :

$$F_{\mathrm{DT}}^{\mathrm{ICF}} = \frac{\rho r}{\rho r + (8\sqrt{\overline{m}_{\mathrm{DT}} \gamma k_{\mathrm{B}} T})/\langle \sigma v \rangle} \ , \tag{3}$$

avec γ l'indice adiabatique, k_{B} la constante de Boltzmann, $\overline{m}_{\mathrm{DT}}$ la masse moyenne des noyaux D et T et ρr la *densité surfacique* du combustible, reliée au produit $n_0\tau$ défini précédemment par $\rho r = 4\sqrt{\overline{m}_{\mathrm{DT}} \gamma k_{\mathrm{B}} T} n_0 \tau$.

Cette équation souligne que l'obtention de hautes fraction brûlées nécessite d'augmenter la densité surfacique de la cible sphérique. Etant donné que la densité surfacique d'une sphère de masse M et de rayon R varie en $\rho R = (3/(4\pi))^{1/3} M^{1/3} \rho^{2/3}$, on peut conclure que (i) augmenter la densité surfacique à masse constante requiert une augmentation de la densité ρ au dessus de celle du solide, et (ii) pour une densité surfacique donnée (i.e. pour une fraction brûlée donnée), augmenter la densité implique qu'une plus faible masse de combustible est nécessaire, et donc moins d'énergie laser doit être investie pour la chauffer à une température donnée.

L'approche actuelle de la FCI consiste à porter une faible masse de combustible à de hautes

densités et avec les bonnes propriétés thermodynamiques, tout en maintenant la symétrie de la compression et en utilisant de faibles énergies laser de façon à ce que l'énergie de fusion dépasse grandement l'énergie investie pour la compression et le chauffage du combustible.

Afin d'atteindre cet objectif, chauffer la masse entière de la sphère de D-T est inefficace car cela requiert une trop grande énergie. L'approche historique et standard de la FCI est celle de l'*allumage par point chaud central*, où seulement une petite masse de la cible est portée aux conditions nécessaires à l'initiation des réactions de fusion. Dans ce cadre, les cibles sont constituées d'une coquille sphérique de D-T contenant un gaz de D-T à basse densité. Une fois que les réactions de fusions sont démarrées dans le point chaud, les particules α générées déposent leur énergie dans la coquille dense et froide autour du point chaud, ce qui conduit à son allumage. Le chauffage du point chaud est obtenu par le travail $P\mathrm{d}V$ communiqué par la coquille en implosion. Obtenir les paramètres nécessaires à l'allumage du point chaud et de la coquille requiert de comprimer la cible à de très hautes densités, i.e. d'obtenir des facteurs de convergences de l'ordre de 30-40.

0.2.1.2 Compression de la cible par laser

L'accélération et la compression de la cible provient de l'expulsion de matériaux de la coquille ablatée par le laser à la surface externe de la cible. L'ablation laser produit une pression $\mathcal{P}_\mathrm{A}$ qui varie, en l'absence de processus anormaux d'absorption, en :

$$\mathcal{P}_\mathrm{A} = 57(\eta_\mathrm{abs} I_{15,\mathrm{W/cm^2}}/\lambda_{L,\mu m})^{2/3} \text{ Mbar} , \tag{4}$$

où η_abs est la fraction d'énergie laser absorbée, $I_{15,\mathrm{W/cm^2}}$ est l'intensité laser dans le vide en unité de 10^{15} W/cm^2, et $\lambda_{L,\mu m}$ est la longueur du laser dans le vide en μm. La pression d'ablation est approximativement égale à la pression à la densité critique ρ_c, où la lumière laser est réflechie et la vitesse plasma est égale à la vitesse acoustique c_s, de sorte que $\mathcal{P}_\mathrm{A} \approx \dot{m}_a c_s \approx \rho_c c_s^2 \propto (I/\lambda_L)^{2/3}$, où $\dot{m}_a$ est le taux de masse ablaté. Ces estimations montrent qu'augmenter la pression d'ablation et le taux de masse ablaté requiert une augmentation de l'intensité laser.

La *vitesse d'implosion* de la coquille pendant son vol libre peut être reliée au taux de masse ablaté par $U_\mathrm{imp} \approx \dot{m}_a \mathcal{A}/\rho$, où $\mathcal{A}$ est le *rapport d'aspect* de la cible en vol (rayon sur épaisseur de la coquille $R/\Delta R$) et ρ est la densité en vol de la coquille. Le rapport de convergence peut alors être exprimé par :

$$C = \frac{U_\mathrm{imp}}{\rho^{1/3}(\alpha A_F \mathcal{A})^{1/2}} = \frac{\dot{m}_a \mathcal{A}^{1/2}}{\rho^{4/3}(\alpha A_F)^{1/2}} , \tag{5}$$

où α est l'*adiabat* de la coquille, défini comme le ratio de sa pression avec la pression de Fermi $p_F = A_F \rho_s^{5/3} = 2.16\rho_s^{5/3}$ Mbar. A partir de l'équation (5), on peut voir que pour une densité initiale de la cible, obtenir des facteurs de convergence importants nécessite (i) une grande vitesse d'implosion, obtenue à travers un grand taux de masse ablaté, c'est à dire une haute pression d'ablation et donc une haute intensité laser (Eq. (4)), (ii) un faible adiabat de la coquille, c'est à dire une coquille qui reste froide durant l'implosion, i.e. la compression doit être la plus isentropique possible, et (iii) un grand rapport d'aspect. Satisfaire ces points afin d'obtenir un grand rapport de convergence n'est pas nécessairement évident. Premièrement, les hautes

intensités lasers sont néfastes à l'implosion de la coquille à cause du développement d'instabilités non-linéaires d'ILP qui peuvent conduire au préchauffage de la capsule (augmentant ainsi α) ou à des asymétries du champ laser. Deuxièmement, l'implosion de la capsule est sensible aux instabilités hydrodynamiques (comme l'Instabilité de Rayleigh Taylor (IRT)) qui naissent des défauts de surface de la capsule ou des défauts dans la symétrie de l'éclairement laser. L'IRT module le profile de densité de la capsule, ce qui peut causer sa rupture pour des déformations de longueur d'onde plus grande que l'épaisseur de la capsule. Augmenter le rapport d'aspect est alors néfaste pour la capsule, qui devient vulnérable vis à vis de l'IRT pour une plus grande plage de longueurs d'onde. Afin de diminuer la sensibilité de la capsule aux instabilités hydrodynamiques et d'augmenter le gain en énergie, des schémas d'allumage alternatifs ont été développés.

0.2.1.3 Schémas alternatifs d'allumage

L'allumage par point chaud central repose sur l'allumage du point chaud consécutif à l'assemblage de la coquille, uniquement à travers la compression de la cible par une impulsion laser de forme adéquate. Pour des implosions à faible adiabat (α de l'ordre de 2), l'énergie requise pour la compression de la cible est du même ordre de grandeur que l'énergie requise pour le chauffage du point chaud. Le principe de fonctionnement de plusieurs schémas alternatifs d'allumage est de séparer les phases de compressions et d'allumage, c'est à dire (i) d'utiliser une impulsion laser basse énergie dédiée à la compression de la cible, auquel cas le travail $P\mathrm{d}V$ communiqué plus lentement au centre de la cible n'est pas suffisant pour allumer le combustible, et (ii) utiliser une impulsion laser séparée pour allumer le point chaud. L'idée principale derrière ces schémas est de réduire l'énergie laser requise et d'augmenter la robustesse de la cible, à travers un meilleur contrôle de chacune des étapes du processus entier.

Dans le schéma d'*allumage rapide* [39, 40, 41], l'énergie additionnelle est apportée par un faisceau d'électrons ou d'ions de haute énergie, ce dernier étant créé par l'interaction d'un faisceau laser à haute énergie et haute puissance avec une cible spéciale. Etant donné la difficulté technique inhérente à l'allumage rapide, d'autres schémas alternatifs ont été développés, et notamment l'*allumage par choc* [42, 31]. Ce dernier consiste à utiliser une impulsion laser de grande intensité à la fin de la phase de compression afin de lancer un choc fort dans la cible, ainsi augmentant la pression et la température du point chaud au dessus du seuil d'allumage au moment où la coquille froide est assemblée. L'attractivité de ce schéma d'allumage repose notamment sur sa simplicité effective : les impulsions lasers requises étant disponibles dans les installations de lasers de puissance actuelles, et les cibles requises étant du même ordre de complexité que celles utilisées actuellement pour l'allumage par point chaud central [43]. En découplant les étapes de compression et de chauffage, de plus faibles énergies lasers sont nécessaires (de l'ordre de 500 kJ) pour l'obtention de gains similaires, ce qui rend l'implémentation du schéma plus facile. Cependant, utiliser une impulsion laser intense soulève de nouveaux problèmes physiques liés à la génération de flux d'électrons énergétiques et à l'amplification de chocs forts.

0.2.2 Régime d'interaction

On considère traditionnellement que le régime optimale de l'ILP pour la FCI est celui de l'absorption collisionnelle, où l'oscillation des électrons dans le champ laser chauffe le plasma

à travers leur collisions avec les ions. Ce mécanisme est préféré car (i) il permet de transférer l'énergie laser à la population thermique du plasma et (ii) il ne met pas en jeu de processus d'absorption *anormaux* qui peuvent être néfastes à l'efficacité de la compression (ceux-ci sont détaillés plus loin). La fraction d'énergie laser transmise au plasma par absorption collisionnelle dépends de la fréquence de collision électron-ion, qui elle même dépend de l'état de charge moyen des ions Z et de la densité électronique n_e. Compte tenu de la faible efficacité hydrodynamique des matériaux à fort Z (ceux-ci nécessitent plus d'énergie laser pour les ioniser et ils ont tendance à ré-émettre des rayons X qui peuvent préchauffer la cible), le régime d'interaction optimal pour la FCI est celui d'ablateurs de Z moyen, typiquement du plastique, carbone ou beryllium. L'énergie laser déposée par absorption collisionnelle est principalement localisée proche de la densité critique $n_c \propto \lambda_L^{-2}$ qui définit la densité à laquelle l'onde électromagnétique est réfléchie. Afin de maximiser le couplage du laser avec la cible solide, la densité critique doit être aussi proche que possible de la densité du solide.

En considérant l'importance de (i) coupler l'énergie laser déposée par absorption collisionnelle aussi efficacement que possible avec la cible solide et (ii) les problèmes soulevés par l'ILP non-linéaire, dont les seuils varient en $I\lambda_L^2$, la technologie de choix pour la FCI est celle des lasers de haute puissance et de courte longueur d'onde. Ainsi, les amplificateurs des lasers utilisés en sciences de la fusion sont basés sur le verre dopé au Néodyme, ce qui produit une lumière laser à la fréquence fondamentale de 1054 nm (pour les verres de phosphate). La lumière laser est ensuite triplée en fréquence avant son interaction avec la cible, à la longueur d'onde de 351 nm. Le triplement de fréquence permet d'augmenter la densité critique par un facteur 9 et de d'augmenter l'efficacité de l'absorption, la pression d'ablation (4) et les seuils des ILPs non-linéaires. Cependant, le rendement laser est relativement faible, de l'ordre de quelques %.

Lorsque le paramètre d'interaction $I\lambda_L^2$ franchi le seuil de $\sim 10^{14}$ Wμm^2/cm^2, l'ILP devient sensible à de nombreux processus de couplage entre les ondes électromagnétiques et les ondes plasma [20, 44, 45]. La plupart de ces processus additionnels, résumés sur la figure 0-2, ont un comportement non-linéaire et sont en général néfastes pour l'implosion [46, 47]. Les mécanismes dominants sont le couplage de la lumière laser avec les modes locaux du plasma ; les *ondes plasma electroniques* (EPW) (processus de *diffusion Raman stimulée* (SRS) et *décomposition en deux plasmons* (TPD)) et les *ondes acoustiques ioniques* (IAW) (processus de *diffusion Brillouin stimulée* (SBS)). En considérant les intensités lasers mises en jeu en FCI, les ILPs non-linéaires peuvent être classées en fonction de leurs effets (en général néfastes) sur l'implosion de la cible :

— Rupture de symétrie d'irradiation ;

  — Le recouvrement de faisceaux lasers dans le plasma produit des ondes acoustiques ioniques via la force pondéromotrice. Ces dernières peuvent donner lieu à l'échange d'énergie entre faisceaux à travers la diffraction des photons sur la perturbation de densité. Ce cas particulier d'interaction à trois ondes est appelée *échange d'énergie entre faisceaux croisés* (Cross-Beam Energy Transfer - CBET). Des travaux théoriques [48] ont montrés que des IAWs excitées de manière résonante pouvaient apparaitre dans le cadre de la configuration de la National Ignition Facility (NIF) [49], et en effet le CBET est maintenant utilisé pour régler la symétrie d'implosion des capsules en attaque indirecte sur le NIF [29]. La configuration d'attaque directe est aussi sensible

à l'instabilité du CBET [27, 50], qui affecte à la fois la symétrie de l'implosion et l'efficacité du couplage laser-plasma.

  - De la même manière, toute instabilité qui induit un certain degré de lumière diffusée peut conduire à des variations dans la symétrie de l'irradiation. Notamment, les instabilités SBS et SRS peuvent diffuser une large portion de la lumière laser incidente. Etant donné que l'uniformité d'irradiation requise afin d'obtenir de haut facteurs de convergences des cibles de FCI est de l'ordre de 1%, ces processus sont importants.

- Préchauffage de la cible ;
  - Toute ILP qui excite des ondes plasma électroniques à de grandes vitesses de phase peut engendrer des populations d'électrons supra-thermiques. Notamment, les instabilités de SRS et TPD peuvent conduire à la génération de faisceaux d'électrons d'énergie moyenne allant jusqu'à la centaine de keV, ce qui peut augmenter l'adiabat de la coquille et réduire le rendement hydrodynamique de l'implosion.
  - En plus du préchauffage, les populations d'électrons de haute énergie générées par l'ILP non-linéaire peuvent affecter la dynamique du plasma directement [31, 32] en altérant la propagation et la force des chocs dans la cible. Ceci est particulièrement important pour le schéma d'allumage par choc, pour lequel l'effet bénéfique ou néfaste des électrons rapides sur le choc est incertain [51].
- Pertes de couplage ;
  - En plus des effets de rupture de symétrie d'irradiation, les instabilités paramétriques génèrent des ondes diffusées et donc diminuent le couplage laser-cible. Notamment, le CBET redistribue l'énergie laser des faisceaux incidents vers les faisceaux sortants et ainsi l'intensité laser est éloignée de la densité critique.
  - Plus généralement, les grands volumes de plasma sous-dense conduisent à de grandes quantités de lumière diffusée vers l'arrière, ce qui réduit le couplage laser-cible.
- Autres ;
  - La *filamentation* du laser, qui résulte de la réfraction du faisceau dans des inhomogénéités locales de densité amplifiées par le laser focalisé via les effets thermiques et pondéromoteurs, conduit localement à de fort champs électriques et des perturbations de densités qui peuvent amplifier les autres instabilités.
  - L'*Absorption Résonante* (RA), qui résulte de l'absorption de la lumière laser via l'excitation résonante d'une onde plasma électronique à la densité critique. L'absorption résonante peut constituer une fraction significative de l'absorption laser début de l'interaction lorsque le profile de densité est très raide. Cependant, les électrons accélérés dans les EPWs générés par le champ résonant ne sont en général pas assez énergétiques pour constituer une menace de préchauffage [36].

Le développement des processus non-linéaires d'interaction est contrôlé en partie par l'utilisation de techniques de lissage spatial et temporel, qui altèrent les fluctuations d'intensité et les propriétés de cohérences des faisceaux lasers dans leur plan focal. Ces méthodes de lissage optique sont cruciales pour réduire le taux de croissances des couplages non-linéaires et pour

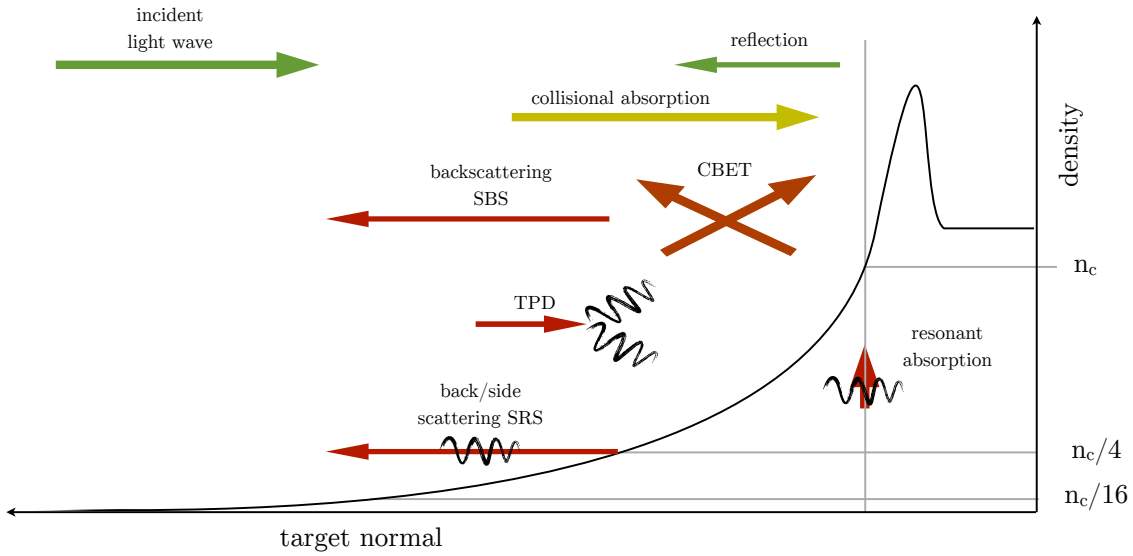

Figure 0-2 – *(couleur) Représentation schématique des processus d'ILP impliqués dans la FCI, en fonction de la densité du plasma coronal et le long de la normale à la cible. Le code couleur indique les processus linéaires en jaunes et les processus non-linéaires en rouge. Les lignes noires incurvées indiquent l'excitation d'ondes plasmas électroniques.*

mitiger les instabilités hydrodynamiques. Plus généralement, le lissage optique est très répandu dans les installations de lasers de puissance afin de contrôler les propriétés des faisceaux. Ainsi, elles constituent une partie intégrale de la description de l'ILP.

En considérant la longueur d'onde laser dans le vide de $\lambda_L = 351$ nm, l'intensité laser typique est de $\sim 5 \times 10^{14}$ W/cm^2 pendant la phase de compression de l'allumage par choc et $\sim 5 \times 10^{15}$ W/cm^2 pendant le pic d'intensité. Ces deux étapes sont susceptibles au développement des couplages non-linéaires, mais dans des régimes différents. Alors que la phase de compression est moins sensible aux problématiques de préchauffage due aux électrons rapides et aux pertes de symétrie que le schéma standard d'allumage par point chaud central, le pic d'intensité laser utilisé pour la génération du choc d'allumage se situe dans un régime d'interaction fortement non-linéaire. Pour des durées typiques de l'impulsion d'allumage de ~ 500 ps, l'ILP non-linéaire à suffisamment de temps pour se développer et (i) accélérer de grandes quantités d'électrons de hautes énergie et (ii) réduire significativement le couplage laser-cible pour la génération du choc d'allumage à travers le CBET. Bien que l'allumage par choc promesse de plus haut gains et une meilleur robustesse comparé à l'allumage par point chaud central, la physique de l'interaction laser-plasma doit être soigneusement étudiée, particulièrement pendant le pic d'intensité laser.

0.3 Objectifs de ce travail

Le sujet de ce travail est : Description Multi-Echelle de l'Interaction Laser-Plasma, Application à la Physique de l'Allumage par Choc en Fusion par Confinement Inertiel. Il est structuré en deux parties. La première est dédiée à la description des processus de couplage de l'ILP à l'échelle hydrodynamique. Cette description est motivée par le besoin d'interpréter et de concevoir des

expériences de physique des hautes densités d'énergie en général, que ce soit d'Astrophysique de Laboratoire ou de FCI. La seconde partie de ce travail est dédiée à l'étude des conditions d'interaction typiques de la phase fortement non-linéaire du schéma d'allumage par choc. Les objectifs de la thèse sont formulés comme suit.

— Etant donné la différence d'échelle qui apparait en considérant la description de l'hydrodynamique de la cible et de la grande variété des processus d'interaction mis en jeu, nous souhaitons proposer un modèle laser qui permette de décrire la propagation laser ainsi que les couplages laser-plasma linéaires et non-linéaires aux échelles hydrodynamiques. Ce modèle laser doit : (i) être adapté pour le calcul des interactions non-linéaires, (ii) être efficace en terme de temps CPU aux grandes échelles mises en jeu et (iii) reproduire les principales caractéristiques des faisceaux lasers utilisés dans les grandes installations, y compris les techniques de lissage optique.

— Etant donné le régime d'interaction de $I\lambda_L^2 \in [10^{13}\text{-}10^{17}]$ Wμm^2/cm^2, la description de l'interaction laser-plasma non-linéaire doit rendre compte de : (i) l'accélération et le transport de faisceaux d'électrons de hautes énergies générés par les instabilités paramétriques et l'absorption résonante, (ii) la diffusion de l'énergie laser par les processus non-linéaire, en particulier l'échange d'énergie entre faisceaux croisés, et (iii) la compétition entre les différents processus de l'ILP. Avec l'objectif d'une implémentation dans un code hydrodynamique, ce modèle doit être formulée pour une approche en-ligne, c'est à dire complètement couplée avec l'hydrodynamique.

— Etant donné les deux principaux problèmes liés à l'ILP non-linéaire pour l'allumage par choc, qui sont la rupture de la symétrie d'irradiation de la cible par le CBET et le préchauffage de la cible par les électrons générés par les instabilités paramétriques, l'étude du schéma de l'allumage par choc est conduite en deux étapes : (i) l'étude du CBET et de ses effets sur l'implosion d'une cible sphérique et (ii) l'étude des effets des faisceaux d'électrons de haute énergie sur la dynamique des chocs, et comment ils affectent les conditions d'allumage d'une cible.

0.4 Organisation du manuscrit

La description du modèle multi-échelle d'interaction laser-plasma et son application à l'allumage par choc est divisée en 6 Chapitres.

Chapitre I On présente dans le Chapitre 1 la théorie linéaire de la propagation des ondes électromagnétiques (EM) dans les plasmas. L'équation d'onde monochromatique, base de la description des faisceaux lasers dans les plasmas, est dérivée à partir des équations de Maxwell. La théorie de base de la réponse électromagnétique du plasma, utilisée au long de ce travail, est introduite. Afin d'illustrer le comportement général des ondes EM dans les plasmas, on présente plusieurs solutions standard de l'équation d'onde, pertinentes pour différentes sections de ce document. En particulier, on définit le cadre de l'équation d'onde scalaire, qui est le point de départ de la plupart des modèles réduits de propagation laser utilisés pour les échelles hydrodynamiques.

Chapitre II L'approche la plus répandue pour la modélisation de la propagation laser aux échelles hydrodynamique, la technique du Tracé de Rayon basé sur l'Optique Géométrie, est introduite dans le Chapitre 2. Après une évaluation des limites du modèle RT pour la modélisation de l'interaction laser-plasma non-linéaire, nous proposons une adaptation aux plasma collisionnels et au cadre d'un code hydrodynamique Lagrangien de la méthode de l'Optique Géométrique Complex Paraxial [52] (PCGO). PCGO est une alternative permettant de décrire les champs de l'onde scalaire en remplaçant les rayons infiniment fins de l'optique géométrique par des faisceaux optiques de profil d'intensité Gaussien. Nous illustrons son utilité dans le cas de la modélisation de l'instabilité d'autofocalisation pondéromotrice.

Chapitre III Le cadre de PCGO, normalement limité à la description de faisceaux Gaussiens, est étendu dans le Chapitre 3. Les installations de lasers de haute puissance font usage Lames de Phase (PP), éléments optiques qui controlent le profile spatial de la distribution d'intensité des faisceaux. En prenant avantage de l'utilisation des lames de phase pour le lissage des faisceaux, nous présentons une méthode qui permette de reproduire des faisceaux lasers réalistes en utilisant des rayons PCGO. Nous présentons des modèles réduits additionnels qui permettent de rendre compte de divers techniques de lissage en utilisant PCGO.

Chapitre IV En se basant sur la description des faisceaux laser par PCGO, on traite deux branches de problèmes d'ILP non-linéaire. Premièrement, nous proposons dans le Chapitre 4 une modèle couplé basé sur PCGO pour modéliser le CBET aux grandes échelles hydrodynamiques. Ce modèle est validé par comparaison avec des travaux théoriques, un solveur paraxial électromagnétique, et des données expérimentales. Ce modèle est ensuite utilisé dans une étude d'une configuration typique de CBET pour la FCI en attaque directe.

Chapitre V Deuxièmement, on présente dans le Chapitre 5 un modèle couplé pour traiter l'interaction laser/plasma/électron-rapide. Nous proposons un modèle de transport pour ces électrons rapides, et présentons sa validation par comparaison avec une solution de référence. Divers modèles réduis sont proposés afin de décrire les caractéristiques de flux et d'énergie moyenne des sources d'électrons accélérés par RA, SRS et TPD. Ce modèle multi-échelle couple entièrement la description de la propagation laser, la définition des sources d'électrons rapides, et la propagation des faisceaux d'électrons rapides.

Chapitre VI Enfin, on présente dans le Chapitre 6 une validation de ce modèle par comparaison avec plusieurs expériences conduites dans diverses géométries. Etant donné le bon accord qui est observé avec les données expérimentales, la physique du couplage des électrons rapides générés par l'ILP non-linéaire avec la dynamique de la cible est étudiée. On trouve notamment que ces électrons affectent les propriétés des chocs qui se propagent dans la cible. Enfin, on applique ce modèle multi-échelle à la configuration de l'allumage par choc, afin d'estimer l'influence de ces électrons générés par l'impulsion laser d'allumage sur la dynamique de l'implosion.

Les conclusions de ce travail sont présentées dans le Chapitre 7.

Chapitre 1

Conclusions

Cette thèse avait plusieurs objectifs.

Un nouveau modèle de propagation laser. Formuler un modèle de propagation laser qui soit à la fois numériquement efficace et adapté aux échelles hydrodynamiques, et qui permette de décrire : (a) l'ILP non-linéaire, incluant notamment les instabilités paramétriques et l'absorption résonante, (b) la propagation laser de faisceaux lissés par les méthodes optiques standard des lasers de puissance, et (c) l'absorption collisionnelle par Bremsstrahlung inverse.

Description de l'ILP non-linéaire Développer un modèle couplé à l'hydrodynamique qui décrive : (a) la diffusion de la lumière laser, avec un accent sur l'échange d'énergie entre faisceaux croisés, (b) la génération et la propagation d'électrons supra-thermiques émis par les EPWs excités par l'ILP non-linéaire, et (c) la compétition pour l'énergie laser entre les divers processus.

Physique de l'allumage par choc. Etudier la phase fortement non-linéaire de l'ILP dans le cadre de l'allumage par choc, y compris (a) les effets du CBET sur la symétrie de l'implosion de cible en attaque directe, et (b) le couplage entre les électrons supra-thermiques générés par l'ILP non-linéaire avec la dynamique du choc d'allumage.

Nous présentons ici les conclusions de ce travail.

1.1 Un nouveau modèle de propagation laser

La description de l'ILP non-linéaire repose sur la connaissance de l'intensité laser dans le plasma. L'approche standard pour la modélisation de la propagation laser à l'échelle hydrodynamique repose sur le Tracé de Rayon, basé sur la théorie de l'Optique Géométrique pour décrire le champ scalaire. Dans cette formulation, les faisceaux lasers sont modélisés par des fagots de rayons lumineux infiniement fins, dont la densité de puissance est amortie au cours de leur propagation par absorption collisionnelle. Cette approche permet de décrire la puissance d'un rayon sans recourir à la notion d'intensité. Bien que la distribution d'intensité dans le plasma puisse être reconstruite à partir de la connaissance de la puissance absorbée par le plasma, l'Optique Géométrique est intrinsèquement peu adaptée pour décrire l'intensité laser. Par conséquent, nous avons focalisés nos efforts sur la formulation d'un nouveau modèle de propagation avec pour objectif de décrire

plus naturellement la distribution de l'intensité laser dans le plasma. Ceci à été accompli en deux étapes.

Optique Géométrique Complexe Paraxiale

Nous avons adapté la méthode de l'Optique Géométrique Complexe Paraxiale au cas des plasmas chauds. L'équation obtenue pour le front d'onde inclue les informations sur le rayon et l'intensité du champ, décrit comme le mode fondamental Gaussien dans l'approximation paraxiale, avec comme axe de propagation un rayon d'optique géométrique. Notre formulation inclue les effets de l'absorption collisionnelle pour le plasma de couronne sous-dense et à la densité critique sur l'épaisseur de peau. Ce modèle a été spécifiquement formulé pour le cadre d'un code hydrodynamique Lagrangien, dont le maillage est non-régulier et non-structuré.

La capacité des méthodes GO et PCGO à modéliser l'effet non-linéaire d'autofocalisation pondéromotrice d'un faisceau laser a été étudiée. Un terme de pression correspondant au potentiel pondéromoteur à été ajouté dans le module hydrodynamique, soit à partir de l'intensité reconstruite pour RT ou à partir du champ d'intensité directement pour PCGO. D'une part, nous avons trouvé que PCGO permet d'obtenir la bonnes puissance critique, distance d'autofocalisation, déplétion de densité transverse, et permet d'estimer correctement l'amplification de l'intensité. D'autre part, le modèle RT n'a pas été capable de reproduire ces quantités. Notamment, la nature discrète des rayons RT conduit à la filamentation artificielle du faisceau dans des guides d'onde locaux dont l'échelle est uniquement déterminée par la résolution hydrodynamique. Le modèle de diffraction du modèle RT, qui consiste à étaler les vecteurs d'ondes initiaux des rayons lumineux, n'est pas capable de compenser l'autofocalisation : le modèle de diffraction n'est en effet valable que dans le vide où dans un plasma de densité uniforme et constante dans le temps.

Modélisation des faisceaux lissés

Deuxièmement, la description des faisceaux Gaussiens PCGO a été adaptée aux faisceaux lasers non Gaussiens. En prenant avantage de l'usage de Lames de Phase dans les lasers de puissance, qui découpent les faisceaux lasers en de multiples sous-faisceaux de petite taille, nous avons proposé une méthode pour modéliser de grands faisceaux laser en utilisant un grand nombre de faisceaux PCGO focalisés pseudo-aléatoirement dans une région proche du plan focal où le rayon des speckles varie lentement. Cette méthode reproduit les principales caractéristiques de la distribution d'intensité d'un grand faisceau laser lissé par Lame de Phase KPP ou RPP. Cette méthode de découpage a été comparée avec des résultats numériques du code de propagation Miró, dans le cas de la configuration SG4 de l'installation Omega. La superposition des faisceaux Gaussiens créé un motif de speckles larges, produisant une distribution d'intensité laser et un contraste similaire aux résultats de la simulation Miró convolués avec le maillage hydrodynamique. Le contraste laser ainsi modélisé est similaire à ceux des faisceaux lasers utilisant le Lissage par Polarisation. Une méthode de lissage temporel a aussi été implémenté : le Lissage par Dispersion Spectrale (SSD). Des comparaisons avec des estimations théoriques ont permis de démontrer la capacité du modèle à reproduire la dépendance temporelle du contraste de faisceaux lasers lissés par SSD.

Ce modèle a été implémenté dans le code hydrodynamique radiatif CHIC du laboratoire CELIA. Sa formulation de base en géométrie 2D plane a été étendue aux géométries 3D pour des cas axi-symétriques spécifiques, où la cible sphérique est irradiée par des faisceaux dont les point focaux croisent l'axe de symétrie par rotation.

1.2 Description de l'ILP non-linéaire

En se basant sur la nouvelle formulation de propagation laser, nous avons proposé différents modèles qui permettent de prendre en compte l'interaction laser-plasma non-linéaire. Nous avons séparé celle-ci en deux catégories : (i) le transfer d'énergie non-linéaire entre faisceaux croisés, qui résulte de la diffraction de la lumière laser sur des fluctuations de densités excitées par le battement pondéromoteur des ondes superposées, et (ii) le couplage non-linéaire du champ laser avec les ondes plasma électroniques qui génèrent des populations d'électrons supra-thermiques.

Echange d'énergie entre faisceaux croisés

Notre formulation de l'échange d'énergie entre faisceaux croisés repose sur la discrétsation de la zone d'interaction par de nombreux transferts d'énergie élémentaires entre faisceaux PCGO Gaussiens, pour lesquels les paramètres plasma locaux sont supposés uniformes. L'ensemble des échanges d'énergie est résolu chronologiquement afin de préserver la cohérence du modèle. Ce modèle entièrement couplé à l'hydrodynamique, nommé EYEBOLT pour *ElementarY Exchange Between OpticaL Thick-rays*, a été validé à l'aide de plusieurs références. Premièrement, nous avons évalué l'approche du modèle elle-même, qui consiste à modéliser l'échange d'énergie entre deux grand faisceaux lasers par de multiples échanges d'énergie entre faisceaux élémentaires. Cette approche a été validée dans le cadre d'un plasma de densité, température et vitesse uniforme. Deuxièmement, le modèle EYEBOLT a été comparé à une résolution numérique des équations couplées qui décrivent l'intensité de deux faisceaux lasers croisés dans un plasma, dans le cas d'un plasma présentant une variation linéaire de vitesse. Un excellent accord a été trouvé pour une large gamme de rapports d'intensités pompe-sonde. Troisièmement, le modèle EYEBOLT a été comparé à une solution dépendante du temps calculée par le code paraxial HARMONY, qui résout les équations couplées pour les amplitudes complexes des ondes lasers. Un excellent accord a été observé pour les facteurs d'amplifications de la sonde en régime stationnaire, la déviation des faisceaux et les amplitudes des perturbations de densités, ceci pour une grande gamme de rapport d'intensité pompe-sonde et pour des intensités $I\lambda^2 \leq 10^{14}$ Wμm^2/cm^2. Nous avons supposés que le moins bon accord observé aux plus hautes intensités est une conséquence de la modélisation plus restreinte des ailes des faisceaux dans PCGO que dans l'approche de HARMONY. Dans ce dernier, les ailes couvrent plus largement une région du plasma où la résonance est inverse pour le transfert d'énergie. Quatrièmement, les résultats du modèle EYEBOLT ont été comparés à des mesures expérimentales de CBET obtenues sur l'installation laser NOVA. L'accord observé constitue une grande amélioration comparé aux estimations précédentes obtenues avec des modèles analytiques. Ces comparaisons théoriques, numériques et expérimentales constituent une base solide pour la validation de notre implémentation du CBET basé sur PCGO.

Electrons rapides générés par les ILPs non-linéaires

La description des électrons chauffés à des températures supra-thermiques par les ILPs non-linéaires a été incluse dans le cadre de PCGO. Ce modèle couplé à l'hydrodynamique, nommé Thetis pour *Two-dimensional Hot Electron Transport and emIssion Sources*, possède deux composantes. Premièrement, il décrit le transport et le dépôt d'énergie des faisceaux d'électrons rapides dans le plasma. Les faisceaux d'électrons sont modélisés dans l'approximation de diffusion angulaire, dérivée de l'équation cinétique de Vlasov-Fokker-Planck en considérant la diffusion des électrons sur un plasma d'électrons et d'ions. Notre formulation est adaptée aux géométries 2D planes, pour des faisceaux d'électrons de profil d'intensité transverse Gaussien, de distribution d'énergie exponentielle et d'ouverture angulaire arbitraire. Deuxièmement, ce modèle de transport est interfacé avec des sources d'électrons calculées par le modèle optique (PCGO). En considérant les cas d'électrons rapides générés par l'Absorption Résonante, la Diffusion Raman Stimulée et la Décomposition en Deux Plasmons, nous avons proposé des modèles réduits permettant de calculer les flux des électrons rapides ainsi générés, ainsi que leur énergie moyenne et distribution angulaire par rapport à l'onde de pompe. Ces formulations sont basées sur des modèles théoriques et l'analyse des modes les plus instables, des observations expérimentales des angles de diffusion et de la compétition entre les processus non-linéaires, des lois d'échelles expérimentales et des simulations cinétiques de type PIC. De plus, l'émission des électrons vers l'arrière du TPD et la diffusion vers l'arrière de la lumière par le SRS sont pris en compte dans le bilan d'énergie. Etant donné la difficulté à caractériser précisément dans les expériences les flux d'électrons générés par l'ILP non-linéaire, il est difficile de valider ce modèle couplé avec des données expérimentales. Cependant, les résultats obtenus avec Thetis sont en bon accord avec divers résultats expérimentaux présentés dans ce travail, dans des géométries et des régimes d'interaction différents.

Ces modèles entièrement couplés à l'hydrodynamique, implémentés dans le code Chic, sont cohérents en terme de conservation d'énergie. L'énergie transférée par le CBET ou aux sources d'électrons rapides est systématiquement soustraite du rayon PCGO lorsque l'ILP a lieu, ce qui affecte les autres processus d'ILP qui ont lieu en aval du CBET ou du transfert aux faisceaux d'électrons. Cette approche prends naturellement en compte la compétition entre les processus, qui découle de la configuration géométrique de l'interaction laser-plasma.

1.3 Physique de l'allumage par choc

Nous avons appliqué notre nouveau modèle dans le cadre de l'allumage par choc en FCI. Nous avons étudié séparément les effets du CBET et des électrons rapides sur la dynamique du plasma.

Influence du CBET sur la dynamique d'une cible en attaque directe

Nous avons appliqué le modèle PCGO+Eyebolt à l'étude du CBET, dans le cas de la configuration laser de la chambre d'expérience Omega. Les faisceaux sont modélisés en supposant l'usage des Lames de Phase KPP SG4, dans une configuration 2D plane. Nous simulons l'implosion d'une capsule (cylindre) sur les 360°, en autorisant seulement certains faisceaux à échanger de l'énergie à travers le CBET. Ces faisceaux sont identifiés en considérant les ports co-planaires

de la chambre d'Omega, aux angles de 20°, 40°, 140° et 160°. Nous avons trouvé que (i) les cibles à ablateur de D-T sont plus sensibles aux déformations induites par le CBET que pour les ablateurs C-H, (ii) le CBET décroit le facteur de convergence de la cible jusqu'à 25 % en éloignant les maxima d'intensité laser de la densité critique et (iii) pour cette configuration, le CBET provoque des déformations de la cible dont l'amplitude relative à l'interface interne de la coquille atteint jusqu'à 35 % pour le mode 2. Ces conclusions sur les déformations de la cible ont été étendues pour un cas 3D en effectuant une reconstruction linéaire des modes. Nous avons trouvé que le mode 4 était aussi excité, et que le mode 2 est probablement sur-estimé dans notre modèle car le CBET entre faisceau non-coplanaires n'est pas pris en compte.

Etude des électrons rapides générés par l'ILP non-linéaire sur la dynamique des chocs

L'étude du couplage laser/plasma/électrons rapides a été effectué avec le modèle PCGO+Thetis. Nous avons considéré plusieurs comparaisons avec diverses expériences.

— Le calcul de l'absorption laser a été validé avec une expérience d'absorption conduite sur Omega, en utilisant le modèle PCGO+Thetis. L'expérience consistait à irradier une cible par deux impulsions lasers successives. La première interagi avec une cible froide aux gradients de densités très raides, et la seconde avec un plasma coronal plus chaud et des gradients de densités plus longs. Contrairement aux modèles basé sur le RT, qui doivent utiliser une variation temporelle de la limitation du flux thermique électronique maximale afin de reproduire l'absorption laser correcte, nous avons montré que notre modèle reproduit les données expérimentales pour les deux impulsions simultanément, avec une valeur fixe de la limitation de flux. Notamment, l'absorption résonante contribue à l'absorption de la première impulsion, et plus modérément à la seconde.

— La modèle a été appliqué à l'interprétation d'expériences de mesures de temps de débouchés de choc conduites sur l'installation laser Pals. Un faisceau laser de haute intensité interagit avec une cible plane. L'ablation de la couche de plastique créé une onde de choc qui se propage dans la cible, et dont le temps de débouché à l'arrière est mesuré en utilisant une technique de pyrométrie (Streak Optical Pyrometry). La population électronique supra-thermique est déduite à partir de la mesure de l'émission Kα généré par les électrons rapides dans les traceurs de haut Z. Un accord raisonnable est trouvé entre le modèle et les expériences, à la fois pour la réflectivité laser intégrée, les flux et températures des électrons supra-thermiques, et les temps de débouché de choc. Ceci constitue une amélioration significative comparé aux résultats des modèles basés sur l'Optique Géométrique, qui sous-estiment les temps de débouchés jusqu'à un facteur 2. Nous avons trouvé qu'une partie des électrons générés par les ILPs non-linéaires sont suffisamment rapides pour passer à travers le choc et préchauffer la cible en amont. Ce préchauffage est quasiment isochore car il a lieu en masse dans la cible. L'augmentation de pression associée augmente significativement la vitesse et la pression avale du choc. A l'inverse, la force du choc, c'est à dire le rapport de la pression aval sur la pression amont, est grandement réduite. Etant donné que l'énergie laser transmise aux électrons rapide est déposée à la fois en amont et en aval du front d'ablation, la pression d'ablation résultante est plus faible qu'en ne considérant pas cette interaction non-linéaire.

— Le modèle PCGO+Thetis a été appliqué à une expérience de mesure de temps de convergence de choc en géométrie sphérique, conduite sur Omega. Une cible sphérique est uniformément irradié par des faisceaux laser et le temps convergence du choc au centre est mesurée à travers le flash de rayons X associé. L'expérience a été conduite avec et sans lissage par dispersion spectrale. En son absence, les flux d'électrons rapides ont augmentés d'un facteur 5. Le modèle avec les électrons a reproduit avec succès les flux et températures mesurées dans l'expérience, ainsi que la réflectivité laser et le temps de convergence du choc. Comme dans l'expérience sur Pals, nous avons trouvé que les électrons générés par l'ILP non-linéaire réduisent la force du choc et la pression d'ablation, tout en augmentant la pression avale au choc et sa vitesse.

Influence des électrons rapides générés par les ILPs non-linéaires sur la dynamique d'une cible d'allumage par choc

Au vu du bon accord observé entre notre modèle et les mesures expérimentales pour l'interaction de faisceaux lasers intenses avec les cibles planes et sphériques, nous avons appliqué le modèle PCGO+Thetis à l'analyse d'implosion de cible pour l'allumage par choc. Premièrement, nous avons utilisé la configuration de base de la cible tout-DT du projet HiPER. En utilisant PCGO uniquement, nous reproduisons des fenêtres d'allumage comparables à celles obtenues en utilisant les modèles RT en 1D. Les simulations avec le modèle Thetis suggèrent que les électrons rapides générés durant le pic d'intensité laser préchauffent suffisamment la cible en vol pour causer l'expansion de la coquille et la pollution du point chaud par du plasma de coquille dense, avant la convergence finale de la cible. La densité surfacique du point chaud augmente alors rapidement et le choc d'allumage n'est plus assez fort pour initier les réactions de fusion. De plus, l'augmentation de la densité du point chaud tôt dans l'implosion augmente les pertes radiative par rayonnement X, ce qui le refroidit rapidement. Deuxièmement, nous avons utilisé une configuration de cible plus récente et développée au laboratoire Celia : une cible de DT avec un ablateur CH et une couche d'Aluminium. Les fenêtres d'allumage de nos simulations avec PCGO sont comparées avec et sans l'interaction non-linéaire. Les cas avec électrons rapides n'atteignent pas l'allumage, bien que la présence de l'ablateur plastique renforce la tenue de la coquille au flux d'électron rapide et réduise la pollution du point chaud. Des simulations avec une plus haute intensité laser suggèrent que la capsule puisse être allumée, en compensant l'augmentation de masse du point chaud par un choc d'allumage plus fort. L'importance du moment auquel les électrons de l'ILP non linéaire sont générés a été soulignée : un délais de 200 ps entre le pic d'intensité et la génération des électrons permettant à la cible CH-DT d'atteindre l'allumage, bien qu'avec un gain de 1 MJ seulement. Il apparait donc comme important de bien étudier la phase transitoire de la croissance des instabilités paramétriques, bien qu'elle soit ici probablement plus courte que 200 ps au vu de la grande taille du plasma.

Ces résultats démontrent l'importance de prendre en compte les processus d'interaction non-linéaire dans la conception d'une cible d'allumage par choc efficace et réaliste. Les applications potentielles de ce modèle ne sont pas limitées aux études de fusion, et sont utiles à l'études des expériences laser-cible dans les régimes d'interaction pertinents aux instabilités considérées ici.

1.4 Perspectives

Les perspectives de ce travail sont nombreuses. On les énumère par ordre croissant de complexité.

— L'implémentation actuelle du modèle peut être utilisée pour de nombreuses études expérimentales. Nous donnons quelques exemples ; (i) nous avons présenté les résultats obtenus sur Pals pour la fréquence sur cible de 3ω, cependant des questions ouvertes se posent pour l'interprétation des résultats obtenus à 1ω, où les résultats ne sont pas reproduits par les modèles RT, (ii) l'interprétation de l'expérience de temps de convergence de choc sur Omega peut être étendue à une campagne récente où des comportements différents des cibles ont été observés en fonction de l'ablateur utilisé, (iii) la conception des expériences d'astrophysique de laboratoire par Double Front d'Ablation reposent sur le préchauffage radiatif d'un échantillon de matière qui pourrait être vulnérable aux électrons rapides de l'ILP non-linéaire, ou encore (iv) la conception d'expériences en configuration plane sur le LMJ, où on cherche à mesurer les effets des électrons générés par l'ILP non-linéaire sur les caractéristiques des chocs (cette configuration pourrait aussi être sujette au CBET).

— Les résultats présentés pour l'allumage par choc en utilisant le modèle PCGO+Thetis sont préliminaires. Ce sujet requiert une étude dédiée, notamment en considérant que les processus de couplage entre les électrons rapides des ILPs et la dynamique de la cible sont non-linéaires. Les détails de l'influence des électrons sur la dynamique des réflections et collision des chocs dans la coquille peuvent aussi être explorés.

— L'implémentation actuelle des instabilités paramétriques dans Thetis est relativement simple. Le cadre numérique étant maintenant en place, il y a une opportunité pour ajouter plus de détails aux modèles réduits pour ces instabilités. Notamment : (i) ajouter une dépendance à la densité au SRS afin de générer un spectre plus large d'électrons, (ii) implémenter des modèles pour la phase non-stationnaire des instabilités, ce qui est particulièrement intéressants pour les études liées au lissage temporel, et (iii) implémenter un modèle réduit de SBS. De façon similaire, le transport des électrons basé sur l'approximation de diffusion angulaire possède certains défauts. Notamment, cette méthode demande un grand nombre de groupes en énergie afin de produire des dépôts de dose satisfaisants. Ce nombre augmente encore plus en considérant des faisceaux avec une ouverture angulaire, où le nombre de sous-faisceaux est multiplié par le nombre de groupes en espace. Une efficacité numérique accrue pourrait être obtenue en ajoutant les phénomènes de straggling et blooming au modèle, de façon à ce que moins de groupes en énergie soient requis pour obtenir les mêmes résultats.

— Les modèles pour la génération d'électrons et le CBET sont actuellement disjoints. A priori, il n'y a pas de restriction pour leur usage simultané. A cette fin, des développements numériques additionels sont nécessaires. Notamment, le modèle Eyebolt repose sur un classement chronologique des intersections qui permet de modifier les paramètres avals aux croisements. Cette mise à jour des paramètres doit être couplée au calcul de l'ILP non-linéaire afin d'avoir une description cohérente. Ce travail serait considérablement facilité en unissant les algorithmes de propagation du rayon central, de dépôt d'énergie, et des modèles de l'ILP non-linéaire directement dans la résolution de l'équation du front d'onde.

— Les études du CBET dans des configurations d'interaction plus réalistes et plus générales requierent de prendre en compte le transfert d'énergie entre tout les faisceaux. Dans sa formulation actuelle, le modèle Eyebolt est adapté à des études où une configuration équivalente 2D plane existe, ce qui est rarement le cas. Il apparait donc crucial de prendre en compte le CBET entre faisceaux non coplanaires. Contrairement au modèle Thetis, ces calculs ne peuvent pas être effectués en configuration pseudo-cylindrique. Une formulation 3D du CBET nécéssite : (i) une implémentation 3D de PCGO et (ii) des critères spécifiques pour l'intersection des enveloppes des rayons PCGO en 3D. Enfin, la modélisation des ailes des faisceaux laser à été démontrée comme étant importante pour le CBET, et doit être considérée.

— Dans la configuration laser-cible la plus général, le modèle "ultime" basé sur PCGO et ce travail (i) serait basé sur une implémentation 3D de PCGO, de préférence avec un code hydrodynamique 3D en coordonnées cartésiennes, (ii) inclurait le transfert d'énergie entre faisceaux PCGO se croisant seulement via leur enveloppe, et (iii) couplerait la génération d'électrons avec le CBET.

Bibliographie

[1] R. Fedosejevs, I. V. Tomov, N. H. Burnett et al. "Self-steepening of the density profile of a CO2-laser-produced plasma". In : *Physical Review Letters* 39 (oct. 1977), p. 932–935. doi : 10.1103/PhysRevLett.39.932.

[2] W. B. Fechner, C. L. Shepard, G. E. Busch et al. "Analysis of plasma density profiles and thermal transport in laser-irradiated spherical targets". In : *Physics of Fluids* 27 (juin 1984), p. 1552–1560. doi : 10.1063/1.864738.

[3] K. R. Manes, V. C. Rupert, J. M. Auerbach et al. "Polarization and Angular Dependence of 1.06-μm Laser-Light Absorption by Planar Plasmas". In : *Phys. Rev. Lett.* 39 (5 août 1977), p. 281–284. doi : 10.1103/PhysRevLett.39.281. url : http://link.aps.org/doi/10.1103/PhysRevLett.39.281.

[4] R. P. Godwin, R. Sachsenmaier et R. Sigel. "Angle-dependent reflectance of laser-produced plasmas". In : *Physical Review Letters* 39 (nov. 1977), p. 1198–1201. doi : 10.1103/PhysRevLett.39.1198.

[5] J. S. Pearlman et M. K. Matzen. "Angular dependence of polarization-related laser-plasma absorption processes". In : *Physical Review Letters* 39 (juil. 1977), p. 140–142. doi : 10.1103/PhysRevLett.39.140.

[6] J. E. Balmer et T. P. Donaldson. "Resonance absorption of 1.06-micron laser radiation in laser-generated plasma". In : *Physical Review Letters* 39 (oct. 1977), p. 1084–1087. doi : 10.1103/PhysRevLett.39.1084.

[7] D. M. Villeneuve, G. D. Enright et M. C. Richardson. "Features of lateral energy transport in CO_2-laser-irradiated microdisk targets". In : *Phys. Rev. A* 27 (mai 1983), p. 2656–2662. doi : 10.1103/PhysRevA.27.2656.

[8] D. R. Bach, D. E. Casperson, D. W. Forslund et al. "Intensity-Dependent Absorption in 10.6-μm Laser-Illuminated Spheres". In : *Physical Review Letters* 50 (juin 1983), p. 2082–2085. doi : 10.1103/PhysRevLett.50.2082.

[9] K. Estabrook et W. L. Kruer. "Properties of resonantly heated electron distributions". In : *Physical Review Letters* 40 (jan. 1978), p. 42–45. doi : 10.1103/PhysRevLett.40.42.

[10] D. W. Phillion, E. M. Campbell, K. G. Estabrook et al. "High-Energy Electron Production by the Raman and $2\omega_{pe}$ Instabilities in a 1.064-μm-Laser-Produced Underdense Plasma". In : *Phys. Rev. Lett.* 49 (19 nov. 1982), p. 1405–1408. doi : 10.1103/PhysRevLett.49.1405. url : http://link.aps.org/doi/10.1103/PhysRevLett.49.1405.

[11] R. P. Drake, R. E. Turner, B. F. Lasinski et al. "Efficient Raman Sidescatter and Hot-Electron Production in Laser-Plasma Interaction Experiments". In : *Physical Review Letters* 53 (oct. 1984), p. 1739–1742. doi : 10.1103/PhysRevLett.53.1739.

[12] N. H. Burnett et G. D. Enright. "Hot-electron generation and transport in high-intensity laser interaction". In : *Canadian Journal of Physics* 64 (1986), p. 920. doi : 10.1139/p86-161.

[13] B. H. Ripin, F. C. Young, J. A. Stamper et al. “Enhanced backscatter with a structured laser pulse”. In : *Physical Review Letters* 39 (sept. 1977), p. 611–615. doi : 10.1103/PhysRevLett.39.611.

[14] D. W. Phillion, W. L. Kruer et V. C. Rupert. “Brillouin scatter in laser-produced plasmas”. In : *Physical Review Letters* 39 (déc. 1977), p. 1529–1533. doi : 10.1103/PhysRevLett.39.1529.

[15] A. Ng, L. Pitt, D. Salzmann et al. “Saturation of stimulated Brillouin backscatter in CO2-laser-plasma interaction”. In : *Physical Review Letters* 42 (jan. 1979), p. 307–311. doi : 10.1103/PhysRevLett.42.307.

[16] F. J. Mayer, G. E. Busch, C. M. Kinzer et al. “Measurements of short-pulse backscatter from a gas target”. In : *Physical Review Letters* 44 (juin 1980), p. 1498–1501. doi : 10.1103/PhysRevLett.44.1498.

[17] R. G. Watt, R. D. Brooks et Z. A. Pietrzyk. “Observation of stimulated Raman backscatter from a preformed, underdense plasma”. In : *Physical Review Letters* 41 (juil. 1978), p. 170–173. doi : 10.1103/PhysRevLett.41.170.

[18] J. Elazar, W. T. Toner et E. R. Wooding. “Backscattered radiation at omega sub 0/2 from neodymium laser plasma interactions”. In : *Plasma Physics* 23 (sept. 1981), p. 813–818. doi : 10.1088/0032-1028/23/9/005.

[19] C. Joshi, T. Tajima, J. M. Dawson et al. “Forward Raman instability and electron acceleration”. In : *Physical Review Letters* 47 (nov. 1981), p. 1285–1288. doi : 10.1103/PhysRevLett.47.1285.

[20] K. Tanaka, L. M. Goldman, W. Seka et al. “Stimulated Raman Scattering from uv-Laser-Produced Plasmas”. In : *Phys. Rev. Lett.* 48 (17 avr. 1982), p. 1179–1182. doi : 10.1103/PhysRevLett.48.1179. url : http://link.aps.org/doi/10.1103/PhysRevLett.48.1179.

[21] D. W. Phillion, D. L. Banner, E. M. Campbell et al. “Stimulated Raman scattering in large plasmas”. In : *Physics of Fluids* 25 (août 1982), p. 1434–1443. doi : 10.1063/1.863920.

[22] D. C. Slater, Gar. E. Busch, G. Charatis et al. “Absorption and Hot-Electron Production for 1.05 and 0.53 μm Light on Spherical Targets”. In : *Phys. Rev. Lett.* 46 (18 mai 1981), p. 1199–1202. doi : 10.1103/PhysRevLett.46.1199. url : http://link.aps.org/doi/10.1103/PhysRevLett.46.1199.

[23] H. Nishimura, H. Azechi, K. Yamada et al. “Experimental study of wavelength dependences of laser-plasma coupling, transport, and ablation processes”. In : *Phys. Rev. A* 23 (avr. 1981), p. 2011–2019. doi : 10.1103/PhysRevA.23.2011.

[24] C. Garban-Labaune, E. Fabre, C. E. Max et al. “Effect of Laser Wavelength and Pulse Duration on Laser-Light Absorption and Back Reflection”. In : *Physical Review Letters* 48 (avr. 1982), p. 1018–1021. doi : 10.1103/PhysRevLett.48.1018.

[25] W. Seka, R. S. Craxton, J. Delettrez et al. “Measurements and interpretation of the absorption of 0.35 μm laser radiation on planar targets”. In : *Optics Communications* 40 (fév. 1982), p. 437–440. doi : 10.1016/0030-4018(82)90049-9.

[26] T. B. Kaiser. “Laser ray tracing and power deposition on an unstructured three-dimensional grid”. In : *Phys. Rev. E* 61 (jan. 2000), p. 895. doi : 10.1103/PhysRevE.61.895.

[27] I. V. Igumenshchev, D. H. Edgell, V. N. Goncharov et al. “Crossed-beam energy transfer in implosion experiments on OMEGA”. In : *Physics of Plasmas* 17.12, 122708 (déc. 2010), p. 122708. doi : 10.1063/1.3532817.

[28] A. Colaïtis, G. Duchateau, X. Ribeyre et al. “Modeling of the cross-beam energy transfer with realistic inertial-confinement-fusion beams in a large-scale hydrocode”. In : *Phys. Rev. E* 91 (1 jan. 2015), p. 013102. doi : 10.1103/PhysRevE.91.013102. url : http://link.aps.org/doi/10.1103/PhysRevE.91.013102.

[29] P. Michel, L. Divol, E. A. Williams et al. “Tuning the Implosion Symmetry of ICF Targets via Controlled Crossed-Beam Energy Transfer”. In : *Physical Review Letters* 102.2, 025004 (jan. 2009), p. 025004. doi : 10.1103/PhysRevLett.102.025004.

[30] S. Skupsky, J. A. Marozas, R. S. Craxton et al. “Polar direct drive on the National Ignition Facility”. In : *Physics of Plasmas* 11 (mai 2004), p. 2763–2770. doi : 10.1063/1.1689665.

[31] R. Betti, C. D. Zhou, K. S. Anderson et al. “Shock Ignition of Thermonuclear Fuel with High Areal Density”. In : *Physical Review Letters* 98.15, 155001 (avr. 2007), p. 155001. doi : 10.1103/PhysRevLett.98.155001.

[32] D. Batani, S. Baton, A. Casner et al. “Physics issues for shock ignition”. In : *Nuclear Fusion* 54.5 (2014), p. 054009. url : http://stacks.iop.org/0029-5515/54/i=5/a=054009.

[33] D. Batani, L. Antonelli, S. Atzeni et al. “Generation of high pressure shocks relevant to the shock-ignition intensity regime”. In : *Physics of Plasmas* 21 (mar. 2014), p. 032710. doi : 10.1063/1.4869715. url : http://dx.doi.org/10.1063/1.4869715.

[34] A. Colaïtis, G. Duchateau, P. Nicolaï et al. “Towards modeling of nonlinear laser-plasma interactions with hydrocodes : The thick-ray approach”. In : *Phys. Rev. E* 89 (3 mar. 2014), p. 033101. doi : 10.1103/PhysRevE.89.033101. url : http://link.aps.org/doi/10.1103/PhysRevE.89.033101.

[35] G. Gamow. “Zur Quantentheorie des Atomkernes”. In : *Zeitschrift fur Physik* 51 (mar. 1928), p. 204–212. doi : 10.1007/BF01343196.

[36] L. Bergé, G. Bonnaud, M. Casanova et al. *La fusion thermonucléaire inertielle par laser : l’interaction laser-matière part. 1, vol. 1. (French Edition)*. Synthèses. 61, Boulevard Saint-Germain : Eyrolles, 1993.

[37] John Lindl. “Development of the indirect-drive approach to inertial confinement fusion and the target physics basis for ignition and gain”. In : *Physics of Plasmas* 2.11 (1995), p. 3933–4024. doi : 10.1063/1.871025. url : http://scitation.aip.org/content/aip/journal/pop/2/11/10.1063/1.871025.

[38] J. Nuckolls, L. Wood, A. Thiessen et al. “Laser Compression of Matter to Super-High Densities : Thermonuclear (CTR) Applications”. In : *Nature* 239 (sept. 1972), p. 139–142. doi : 10.1038/239139a0.

[39] A. W. Maschke. “Relativistic Heavy Ions for Fusion Applications”. In : *IEEE Transactions on Nuclear Science* 22 (juin 1975), p. 1825. doi : 10.1109/TNS.1975.4328002.

[40] N.G. Basov, S.Yu. Gus’kov et L.P. Feokistov. “Thermonuclear gain of ICF targets with direct heating of ignitor”. English. In : *Journal of Soviet Laser Research* 13.5 (1992), p. 396–399. issn : 0270-2010. doi : 10.1007/BF01124892. url : http://dx.doi.org/10.1007/BF01124892.

[41] M. Tabak, J. Hammer, M. E. Glinsky et al. “Ignition and high gain with ultrapowerful lasers*”. In : *Physics of Plasmas* 1 (mai 1994), p. 1626–1634. doi : 10.1063/1.870664.

[42] V.A. Shcherbakov. “Ignition of a laser-fusion target by a focusing shock wave”. In : *Sov. J. Plasma Phys. (Engl. Transl.) ; (United States)* 9 :2 (mar. 1983). url : https://inis.iaea.org/search/searchsinglerecord.aspx?recordsFor=SingleRecord&RN=15034792.

[43] L. J. Perkins, R. Betti, K. N. Lafortune et al. “Shock Ignition : A New Approach to High Gain Inertial Confinement Fusion on the National Ignition Facility”. In : *Physical Review Letters* 103.4, 045004 (juil. 2009), p. 045004. doi : 10.1103/PhysRevLett.103.045004.

[44] W. Seka, E. A. Williams, R. S. Craxton et al. “Convective stimulated Raman scattering instability in UV laser plasmas”. In : *Physics of Fluids (1958-1988)* 27.8 (1984), p. 2181–2186. doi : 10.1063/1.864844. url : http://scitation.aip.org/content/aip/journal/pof1/27/8/10.1063/1.864844.

[45] T. Afshar-rad, L. A. Gizzi, M. Desselberger et al. “Evidence for whole-beam self-focusing of induced spatially incoherent laser light in large underdense plasma”. In : *Phys. Rev. Lett.* 68 (7 fév. 1992), p. 942–945. doi : 10.1103/PhysRevLett.68.942. url : http://link.aps.org/doi/10.1103/PhysRevLett.68.942.

[46] S. Atzeni et J. Meyer-ter Vehn. *The Physics of Inertial Fusion*. International Series of Monographs on Physics. Oxford : Oxford University Press, 2004.

[47] D. H. Froula, D. T. Michel, I. V. Igumenshchev et al. “Laser-plasma interactions in direct-drive ignition plasmas”. In : *Plasma Physics and Controlled Fusion* 54.12, 124016 (déc. 2012), p. 124016. doi : 10.1088/0741-3335/54/12/124016.

[48] W. L. Kruer, S. C. Wilks, B. B. Afeyan et al. “Energy transfer between crossing laser beams”. In : *Physics of Plasmas* 3 (jan. 1996), p. 382–385. doi : 10.1063/1.871863.

[49] S. W. Haan, S. M. Pollaine, J. D. Lindl et al. “Design and modeling of ignition targets for the National Ignition Facility”. In : *Physics of Plasmas* 2 (juin 1995), p. 2480–2487. doi : 10.1063/1.871209.

[50] I. V. Igumenshchev, W. Seka, D. H. Edgell et al. “Crossed-beam energy transfer in direct-drive implosions”. In : *Physics of Plasmas* 19.5, 056314 (mai 2012), p. 056314. doi : 10.1063/1.4718594.

[51] Ph. Nicolaï, J.-L. Feugeas, M. Touati et al. “Deleterious effects of nonthermal electrons in shock ignition concept”. In : *Phys. Rev. E* 89 (3 mar. 2014), p. 033107. doi : 10.1103/PhysRevE.89.033107. url : http://link.aps.org/doi/10.1103/PhysRevE.89.033107.

[52] Y. A. Kravtsov. “Complex rays and complex caustics”. In : *Radiophysics and Quantum Electronics* 10 (sept. 1967), p. 719–730. doi : 10.1007/BF01031601.

université de BORDEAUX

Résumé de Thèse

Soumis en vue de l'obtention du diplôme de

Docteur de l'Université de Bordeaux

Université de Bordeaux, Ecole doctorale des sciences et de l'ingénieur,
Section : Astrophysique, Plasmas, Nucléaire

Description Multi-Echelle de l'Intéraction Laser-Plasma, Application à la Physique de l'Allumage par Choc en Fusion par Confinement Inertiel

---

par

Arnaud Colaïtis

sous la direction de
V. Tikhonchuk
G. Duchateau
Ph. Nicolaï

Thèse soutenue le 10 November 2015 à Talence (France)
Devant le jury composé de :

Riconda, C.	Associate Professor, UPMC, LULI (France)	**Rapporteur**
Michel, P.	Staff Scientist, LLNL (United States)	**Rapporteur**
Labaune, C.	Research Director, CNRS, LULI (France)	**Prés. du Jury**
Hüller, S.	Research Director, CNRS, CPHT (France)	**Examinateur**
Bonnaud, G.	Professor, CEA-DSM, INSTN (France)	**Examinateur**
Tikhonchuk, V.	Professor, Université de Bordeaux, CELIA (France)	**Examinateur**
Duchateau, G.	Research Engineer, CEA-DAM, CELIA (France)	**Examinateur**
Nicolaï, Ph.	Research Engineer, CEA-DAM, CELIA (France)	**Examinateur**
Masson-Laborde, P.-E.	Research Engineer, CEA-DAM, DCSA (France)	**Invité**

On considère l'Interaction Laser-Plasma (ILP) dans le régime des durées d'impulsion de $[0.1, 10]$ ns et pour lesquelles le *paramètre d'interaction* $I\lambda_L^2$ est dans l'intervale $[10^{13}\text{-}10^{17}]$ Wμm^2/cm^2 (I est l'intensité laser et λ_L la longueur d'onde associé, dans le vide). Ces paramètres lasers sont courants dans les expériences de Physique des Hautes Densités d'Energies, avec notamment des applications en Astrophysique de Laboratoire et en Fusion par Confinement Inertiel (FCI). La dynamique des cibles sujettes à de telles intensités sur de telles durées d'impulsion à lieu sur des échelles temporelles et spatiales de l'ordre de plusieurs nanosecondes et de plusieurs millimètres. La description théorique de la dynamique des plasmas sur ces échelles repose sur des approches fluides, utilisant des *modèles hydrodynamiques* qui permettent d'étudier de grands volumes de plasma sur des longues durées. D'autre part, l'interaction laser-plasma non linéaire est étudiée de manière appropriée aux échelles microscopiques et mésoscopiques à l'aide de code cinétiques (*particle-in-cell* et *Fokker-Planck*) et de modèles électromagnétiques paraxiaux.

L'état de l'art de la description de la propagation laser aux grandes échelles repose sur des modèles réduits compatibles avec les performances des ordinateurs modernes. La plus commune est celle du *Tracé de Rayon* (RT) [1], qui décrit le faisceau laser par des fagots de rayons infiniment minces qui suivent les lois de propagation de l'Optique Géométrique (GO) et qui sont caractérisés par une densité de puissance. Dans les situations où les effets collectifs et les couplages non-linéaires sont peu importants ($I\lambda_L^2 \lesssim 5 \times 10^{13}$ Wμm^2/cm^2), les méthodes basées sur l'optique géométrique sont suffisamment précises et numériquement efficaces. Elles décrivent la réfraction du laser et le chauffage du plasma par l'absorption collisionnelle. Au contraire, la modélisation de l'ILP à de plus grands paramètres d'interaction repose sur la connaissance de l'amplitude du champ électrique et de la direction du front d'onde, quantités qui ne sont pas directement décrites par l'optique géométrique. La physique de l'ILP linéaire et non-linéaire est alors souvent modélisée par des modifications ad-hoc du flux thermique électronique maximum ou en ajustant la balance de puissance des faisceaux lasers, de façon à reproduire les résultats expérimentaux. Ces approchent limitent la compréhension des processus physiques mis en jeu et la capacité prédictive de ces outils numériques. Afin de remédier à ces limitations, des efforts récents ont été fait afin d'inclure l'ILP non-linéaire aux échelles hydrodynamiques, notamment avec la mise au point de modèles en-ligne pour décrire l'échange d'énergie entre faisceaux croisés (CBET) [2, 3]. Ces outils ont permis de mieux interpréter et concevoir les expériences de FCI [4] et peuvent être appliqués pour évaluer des configurations d'éclairement laser-cible plus complexes, telles que le schéma d'attaque directe polaire [5]. De la même façon, les effets sur la dynamique du plasma des faisceaux d'électrons à haute énergie générés par l'ILP non-linéaire est particulièrement importante pour les études de FCI [6, 7], les expériences de double front d'ablation à haute intensité, ou pour la conception et l'interprétation des expériences laser-cible dans le régime nanoseconde [8].

Etant donné la grande variété des configurations laser-cible qui mettent en jeu ces processus, il y a un besoin évident pour un modèle multi-échelle qui pourrait rendre compte des couplages laser-plasma linéaires et non-linéaires dans les codes hydrodynamiques, ainsi que des rétro-actions entre la propagation laser dans le plasma, la génération d'électrons de haute énergie par l'ILP non-linéaire, la propagation de ces faisceaux d'électrons et la dynamique du plasma. Cette modélisation à de grandes échelles pose des problèmes sévères liés à (i) la description précise de l'intensité laser dans le plasma, (ii) la description consistante des sources d'électrons rapides à partir du modèle de propagation laser et (iii) le transport de ces faisceaux d'électrons dans le plasma. Les deux premiers points sont liés à l'usage standard de l'optique géométrique, qui ne permet pas d'évaluer de manière robuste l'intensité laser dans le plasma [9], et le dernier point demande un modèle de propagation à l'échelle hydrodynamique qui soit à la fois robuste et rapide. L'objet de ce travail est d'aborder ces difficultés afin de formuler un modèle multi-échelle qui décrive l'ILP à l'échelle hydrodynamique, y compris son couplage avec la génération de population d'électrons rapides. Les applications de cette formulation ont pour cadre la FCI, et plus précisément le schéma d'allumage par choc, qui est particulièrement vulnérable à l'ILP non-linéaire lors du pic d'intensité laser.

Un nouveau modèle de propagation laser

La description de l'ILP non-linéaire repose sur la connaissance de l'intensité laser dans le plasma. L'approche standard pour la modélisation de la propagation laser à l'échelle hydrodynamique repose sur le Tracé de Rayon, basé sur la théorie de l'Optique Géométrique pour décrire le champ scalaire. Dans cette formulation, les faisceaux lasers sont modélisés par des fagots de rayons lumineux infiniement fins, dont la densité de puissance est amortie au cours de leur propagation par absorption collisionnelle. Cette approche permet de décrire la puissance d'un rayon sans recourir à la notion d'intensité. Bien que la distribution d'intensité dans le plasma puisse être reconstruite à partir de la connaissance de la puissance absorbée par le plasma, l'Optique Géométrique est intrinsèquement peu adaptée pour décrire l'intensité laser. Par conséquent, nous avons focalisés nos efforts sur la formulation d'un nouveau modèle de propagation avec pour objectif de décrire plus naturellement la distribution de l'intensité laser dans le plasma. Ceci à été accompli en deux étapes.

Optique Géométrique Complexe Paraxiale

Nous avons adapté la méthode de l'Optique Géométrique Complexe Paraxiale au cas des plasmas chauds. L'équation obtenue pour le front d'onde inclue les informations sur le rayon et l'intensité du champ, décrit comme le mode fondamental Gaussien dans l'approximation paraxiale, avec comme axe de propagation un rayon d'optique géométrique. Notre formulation inclue les effets de l'absorption collisionnelle pour le plasma de couronne sous-dense et à la densité critique sur l'épaisseur de peau. Ce modèle a été spécifiquement formulé pour le cadre d'un code hydrodynamique Lagrangien, dont le maillage est non-régulier et non-structuré.

La capacité des méthodes GO et PCGO à modéliser l'effet non-linéaire d'autofocalisation pondéromotrice d'un faisceau laser a été étudiée. Un terme de pression correspondant au potentiel pondéromoteur à été ajouté dans le module hydrodynamique, soit à partir de l'intensité reconstruite pour RT ou à partir du champ d'intensité directement pour PCGO. D'une part, nous avons trouvé que PCGO permet d'obtenir la bonnes puissance critique, distance d'autofocalisation, déplétion de densité transverse, et permet d'estimer correctement l'amplification de l'intensité. D'autre part, le modèle RT n'a pas été capable de reproduire ces quantités. Notamment, la nature discrète des rayons RT conduit à la filamentation artificielle du faisceau dans des guides d'onde locaux dont l'échelle est uniquement déterminée par la résolution hydrodynamique. Le modèle de diffraction du modèle RT, qui consiste à étaler les vecteurs d'ondes initiaux des rayons lumineux, n'est pas capable de compenser l'autofocalisation : le modèle de diffraction n'est en effet valable que dans le vide où dans un plasma de densité uniforme et constante dans le temps.

Modélisation des faisceaux lissés

Deuxièmement, la description des faisceaux Gaussiens PCGO a été adaptée aux faisceaux lasers non Gaussiens. En prenant avantage de l'usage de Lames de Phase dans les lasers de puissance, qui découpent les faisceaux lasers en de multiples sous-faisceaux de petite taille, nous avons proposé une méthode pour modéliser de grands faisceaux laser en utilisant un grand nombre de faisceaux PCGO focalisés pseudo-aléatoirement dans une région proche du plan focal où le rayon des speckles varie lentement. Cette méthode reproduit les principales caractéristiques de la distribution d'intensité d'un grand faisceau laser lissé par Lame de Phase KPP ou RPP. Cette méthode de découpage a été comparée avec des résultats numériques du code de propagation Miró, dans le cas de la configuration SG4 de l'installation Omega. La superposition des faisceaux Gaussiens créé un motif de speckles larges, produisant une distribution d'intensité laser et un contraste similaire aux résultats de la simulation Miró convolués avec le maillage hydrodynamique. Le contraste laser ainsi modélisé est similaire à ceux des faisceaux lasers utilisant le Lissage par Polarisation. Une méthode de lissage temporel a aussi été implémenté : le Lissage par Dispersion

Spectrale (SSD). Des comparaisons avec des estimations théoriques ont permis de démontrer la capacité du modèle à reproduire la dépendance temporelle du contraste de faisceaux lasers lissés par SSD.

Ce modèle a été implémenté dans le code hydrodynamique radiatif CHIC du laboratoire CELIA. Sa formulation de base en géométrie 2D plane a été étendue aux géométries 3D pour des cas axi-symétriques spécifiques, où la cible sphérique est irradiée par des faisceaux dont les point focaux croisent l'axe de symétrie par rotation.

Description de l'ILP non-linéaire

En se basant sur la nouvelle formulation de propagation laser, nous avons proposé différents modèles qui permettent de prendre en compte l'interaction laser-plasma non-linéaire. Nous avons séparé celle-ci en deux catégories : (i) le transfer d'énergie non-linéaire entre faisceaux croisés, qui résulte de la diffraction de la lumière laser sur des fluctuations de densités excitées par le battement pondéromoteur des ondes superposées, et (ii) le couplage non-linéaire du champ laser avec les ondes plasma électroniques qui génèrent des populations d'électrons supra-thermiques.

Echange d'énergie entre faisceaux croisés

Notre formulation de l'échange d'énergie entre faisceaux croisés repose sur la discrétsation de la zone d'interaction par de nombreux transferts d'énergie élémentaires entre faisceaux PCGO Gaussiens, pour lesquels les paramètres plasma locaux sont supposés uniformes. L'ensemble des échanges d'énergie est résolu chronologiquement afin de préserver la cohérence du modèle. Ce modèle entièrement couplé à l'hydrodynamique, nommé EYEBOLT pour *ElementarY Exchange Between OpticaL Thick-rays*, a été validé à l'aide de plusieurs références. Premièrement, nous avons évalué l'approche du modèle elle-même, qui consiste à modéliser l'échange d'énergie entre deux grand faisceaux lasers par de multiples échanges d'énergie entre faisceaux élémentaires. Cette approche a été validée dans le cadre d'un plasma de densité, température et vitesse uniforme. Deuxièmement, le modèle EYEBOLT a été comparé à une résolution numérique des équations couplées qui décrivent l'intensité de deux faisceaux lasers croisés dans un plasma, dans le cas d'un plasma présentant une variation linéaire de vitesse. Un excellent accord a été trouvé pour une large gamme de rapports d'intensités pompe-sonde. Troisièmement, le modèle EYEBOLT a été comparé à une solution dépendante du temps calculée par le code paraxial HARMONY, qui résout les équations couplées pour les amplitudes complexes des ondes lasers. Un excellent accord a été observé pour les facteurs d'amplifications de la sonde en régime stationnaire, la déviation des faisceaux et les amplitudes des perturbations de densités, ceci pour une grande gamme de rapport d'intensité pompe-sonde et pour des intensités $I\lambda^2 \leq 10^{14}$ Wμm^2/cm^2. Nous avons supposés que le moins bon accord observé aux plus hautes intensités est une conséquence de la modélisation plus restreinte des ailes des faisceaux dans PCGO que dans l'approche de HARMONY. Dans ce dernier, les ailes couvrent plus largement une région du plasma où la résonance est inverse pour le transfert d'énergie. Quatrièmement, les résultats du modèle EYEBOLT ont été comparés à des mesures expérimentales de CBET obtenues sur l'installation laser NOVA. L'accord observé constitue une grande amélioration comparé aux estimations précédentes obtenues avec des modèles analytiques. Ces comparaisons théoriques, numériques et expérimentales constituent une base solide pour la validation de notre implémentation du CBET basé sur PCGO.

Electrons rapides générés par les ILPs non-linéaires

La description des électrons chauffés à des températures supra-thermiques par les ILPs non-linéaires a été incluse dans le cadre de PCGO. Ce modèle couplé à l'hydrodynamique, nommé THETIS pour *Two-dimensional Hot Electron Transport and emIssion Sources*, possède deux

composantes. Premièrement, il décrit le transport et le dépôt d'énergie des faisceaux d'électrons rapides dans le plasma. Les faisceaux d'électrons sont modélisés dans l'approximation de diffusion angulaire, dérivée de l'équation cinétique de Vlasov-Fokker-Planck en considérant la diffusion des électrons sur un plasma d'électrons et d'ions. Notre formulation est adaptée aux géométries 2D planes, pour des faisceaux d'électrons de profil d'intensité transverse Gaussien, de distribution d'énergie exponentielle et d'ouverture angulaire arbitraire. Deuxièmement, ce modèle de transport est interfacé avec des sources d'électrons calculées par le modèle optique (PCGO). En considérant les cas d'électrons rapides générés par l'Absorption Résonante, la Diffusion Raman Stimulée et la Décomposition en Deux Plasmons, nous avons proposé des modèles réduits permettant de calculer les flux des électrons rapides ainsi générés, ainsi que leur énergie moyenne et distribution angulaire par rapport à l'onde de pompe. Ces formulations sont basées sur des modèles théoriques et l'analyse des modes les plus instables, des observations expérimentales des angles de diffusion et de la compétition entre les processus non-linéaires, des lois d'échelles expérimentales et des simulations cinétiques de type PIC. De plus, l'émission des électrons vers l'arrière du TPD et la diffusion vers l'arrière de la lumière par le SRS sont pris en compte dans le bilan d'énergie. Etant donné la difficulté à caractériser précisément dans les expériences les flux d'électrons générés par l'ILP non-linéaire, il est difficile de valider ce modèle couplé avec des données expérimentales. Cependant, les résultats obtenus avec Thetis sont en bon accord avec divers résultats expérimentaux présentés dans ce travail, dans des géométries et des régimes d'interaction différents.

Ces modèles entièrement couplés à l'hydrodynamique, implémentés dans le code Chic, sont cohérents en terme de conservation d'énergie. L'énergie transférée par le CBET ou aux sources d'électrons rapides est systématiquement soustraite du rayon PCGO lorsque l'ILP a lieu, ce qui affecte les autres processus d'ILP qui ont lieu en aval du CBET ou du transfert aux faisceaux d'électrons. Cette approche prends naturellement en compte la compétition entre les processus, qui découle de la configuration géométrique de l'interaction laser-plasma.

Physique de l'allumage par choc

Nous avons appliqué notre nouveau modèle dans le cadre de l'allumage par choc en FCI. Nous avons étudié séparément les effets du CBET et des électrons rapides sur la dynamique du plasma.

Influence du CBET sur la dynamique d'une cible en attaque directe

Nous avons appliqué le modèle PCGO+Eyebolt à l'étude du CBET, dans le cas de la configuration laser de la chambre d'expérience Omega. Les faisceaux sont modélisés en supposant l'usage des Lames de Phase KPP SG4, dans une configuration 2D plane. Nous simulons l'implosion d'une capsule (cylindre) sur les 360°, en autorisant seulement certains faisceaux à échanger de l'énergie à travers le CBET. Ces faisceaux sont identifiés en considérant les ports co-planaires de la chambre d'Omega, aux angles de 20°, 40°, 140° et 160°. Nous avons trouvé que (i) les cibles à ablateur de D-T sont plus sensibles aux déformations induites par le CBET que pour les ablateurs C-H, (ii) le CBET décroit le facteur de convergence de la cible jusqu'à 25 % en éloignant les maxima d'intensité laser de la densité critique et (iii) pour cette configuration, le CBET provoque des déformations de la cible dont l'amplitude relative à l'interface interne de la coquille atteint jusqu'à 35 % pour le mode 2. Ces conclusions sur les déformations de la cible ont été étendues pour un cas 3D en effectuant une reconstruction linéaire des modes. Nous avons trouvé que le mode 4 était aussi excité, et que le mode 2 est probablement sur-estimé dans notre modèle car le CBET entre faisceau non-coplanaires n'est pas pris en compte.

Etude des électrons rapides générés par l'ILP non-linéaire sur la dynamique des chocs

L'étude du couplage laser/plasma/électrons rapides a été effectué avec le modèle PCGO+Thetis. Nous avons considéré plusieurs comparaisons avec diverses expériences.

— Le calcul de l'absorption laser a été validé avec une expérience d'absorption conduite sur Omega, en utilisant le modèle PCGO+Thetis. L'expérience consistait à irradier une cible par deux impulsions lasers successives. La première interagi avec une cible froide aux gradients de densités très raides, et la seconde avec un plasma coronal plus chaud et des gradients de densités plus longs. Contrairement aux modèles basé sur le RT, qui doivent utiliser une variation temporelle de la limitation du flux thermique électronique maximale afin de reproduire l'absorption laser correcte, nous avons montré que notre modèle reproduit les données expérimentales pour les deux impulsions simultanément, avec une valeur fixe de la limitation de flux. Notamment, l'absorption résonante contribue à l'absorption de la première impulsion, et plus modérément à la seconde.

— La modèle a été appliqué à l'interprétation d'expériences de mesures de temps de débouchés de choc conduites sur l'installation laser Pals. Un faisceau laser de haute intensité interagit avec une cible plane. L'ablation de la couche de plastique créé une onde de choc qui se propage dans la cible, et dont le temps de débouché à l'arrière est mesuré en utilisant une technique de pyrométrie (Streak Optical Pyrometry). La population électronique supra-thermique est déduite à partir de la mesure de l'émission Kα généré par les électrons rapides dans les traceurs de haut Z. Un accord raisonnable est trouvé entre le modèle et les expériences, à la fois pour la réflectivité laser intégrée, les flux et températures des électrons supra-thermiques, et les temps de débouché de choc. Ceci constitue une amélioration significative comparé aux résultats des modèles basés sur l'Optique Géométrique, qui sous-estiment les temps de débouchés jusqu'à un facteur 2. Nous avons trouvé qu'une partie des électrons générés par les ILPs non-linéaires sont suffisamment rapides pour passer à travers le choc et préchauffer la cible en amont. Ce préchauffage est quasiment isochore car il a lieu en masse dans la cible. L'augmentation de pression associée augmente significativement la vitesse et la pression avale du choc. A l'inverse, la force du choc, c'est à dire le rapport de la pression aval sur la pression amont, est grandement réduite. Etant donné que l'énergie laser transmise aux électrons rapide est déposée à la fois en amont et en aval du front d'ablation, la pression d'ablation résultante est plus faible qu'en ne considérant pas cette interaction non-linéaire.

— Le modèle PCGO+Thetis a été appliqué à une expérience de mesure de temps de convergence de choc en géométrie sphérique, conduite sur Omega. Une cible sphérique est uniformément irradié par des faisceaux laser et le temps convergence du choc au centre est mesurée à travers le flash de rayons X associé. L'expérience a été conduite avec et sans lissage par dispersion spectrale. En son absence, les flux d'électrons rapides ont augmentés d'un facteur 5. Le modèle avec les électrons a reproduit avec succès les flux et températures mesurées dans l'expérience, ainsi que la réflectivité laser et le temps de convergence du choc. Comme dans l'expérience sur Pals, nous avons trouvé que les électrons générés par l'ILP non-linéaire réduisent la force du choc et la pression d'ablation, tout en augmentant la pression avale au choc et sa vitesse.

Influence des électrons rapides générés par les ILPs non-linéaires sur la dynamique d'une cible d'allumage par choc

Au vu du bon accord observé entre notre modèle et les mesures expérimentales pour l'interaction de faisceaux lasers intenses avec les cibles planes et sphériques, nous avons appliqué le modèle PCGO+Thetis à l'analyse d'implosion de cible pour l'allumage par choc. Premièrement, nous avons utilisé la configuration de base de la cible tout-DT du projet HiPER. En utilisant PCGO uniquement, nous reproduisons des fenêtres d'allumage comparables à celles obtenues en utilisant les modèles RT en 1D. Les simulations avec le modèle Thetis suggèrent que les

électrons rapides générés durant le pic d'intensité laser préchauffent suffisamment la cible en vol pour causer l'expansion de la coquille et la pollution du point chaud par du plasma de coquille dense, avant la convergence finale de la cible. La densité surfacique du point chaud augmente alors rapidement et le choc d'allumage n'est plus assez fort pour initier les réactions de fusion. De plus, l'augmentation de la densité du point chaud tôt dans l'implosion augmente les pertes radiative par rayonnement X, ce qui le refroidit rapidement. Deuxièmement, nous avons utilisé une configuration de cible plus récente et développée au laboratoire Celia : une cible de DT avec un ablateur CH et une couche d'Aluminium. Les fenêtres d'allumage de nos simulations avec PCGO sont comparées avec et sans l'interaction non-linéaire. Les cas avec électrons rapides n'atteignent pas l'allumage, bien que la présence de l'ablateur plastique renforce la tenue de la coquille au flux d'électron rapide et réduise la pollution du point chaud. Des simulations avec une plus haute intensité laser suggèrent que la capsule puisse être allumée, en compensant l'augmentation de masse du point chaud par un choc d'allumage plus fort. L'importance du moment auquel les électrons de l'ILP non linéaire sont générés a été soulignée : un délais de 200 ps entre le pic d'intensité et la génération des électrons permettant à la cible CH-DT d'atteindre l'allumage, bien qu'avec un gain de 1 MJ seulement. Il apparait donc comme important de bien étudier la phase transitoire de la croissance des instabilités paramétriques, bien qu'elle soit ici probablement plus courte que 200 ps au vu de la grande taille du plasma.

Ces résultats démontrent l'importance de prendre en compte les processus d'interaction non-linéaire dans la conception d'une cible d'allumage par choc efficace et réaliste. Les applications potentielles de ce modèle ne sont pas limitées aux études de fusion, et sont utiles à l'études des expériences laser-cible dans les régimes d'interaction pertinents aux instabilités considérées ici.

Bibliographie

[1] T. B. Kaiser. "Laser ray tracing and power deposition on an unstructured three-dimensional grid". In : *Phys. Rev. E* 61 (jan. 2000), p. 895. DOI : 10.1103/PhysRevE.61.895.

[2] I. V. Igumenshchev, D. H. Edgell, V. N. Goncharov et al. "Crossed-beam energy transfer in implosion experiments on OMEGA". In : *Physics of Plasmas* 17.12, 122708 (déc. 2010), p. 122708. DOI : 10.1063/1.3532817.

[3] A. Colaïtis, G. Duchateau, X. Ribeyre et al. "Modeling of the cross-beam energy transfer with realistic inertial-confinement-fusion beams in a large-scale hydrocode". In : *Phys. Rev. E* 91 (1 jan. 2015), p. 013102. DOI : 10.1103/PhysRevE.91.013102. URL : http://link.aps.org/doi/10.1103/PhysRevE.91.013102.

[4] P. Michel, L. Divol, E. A. Williams et al. "Tuning the Implosion Symmetry of ICF Targets via Controlled Crossed-Beam Energy Transfer". In : *Physical Review Letters* 102.2, 025004 (jan. 2009), p. 025004. DOI : 10.1103/PhysRevLett.102.025004.

[5] S. Skupsky, J. A. Marozas, R. S. Craxton et al. "Polar direct drive on the National Ignition Facility". In : *Physics of Plasmas* 11 (mai 2004), p. 2763–2770. DOI : 10.1063/1.1689665.

[6] R. Betti, C. D. Zhou, K. S. Anderson et al. "Shock Ignition of Thermonuclear Fuel with High Areal Density". In : *Physical Review Letters* 98.15, 155001 (avr. 2007), p. 155001. DOI : 10.1103/PhysRevLett.98.155001.

[7] D. Batani, S. Baton, A. Casner et al. "Physics issues for shock ignition". In : *Nuclear Fusion* 54.5 (2014), p. 054009. URL : http://stacks.iop.org/0029-5515/54/i=5/a=054009.

[8] D. Batani, L. Antonelli, S. Atzeni et al. "Generation of high pressure shocks relevant to the shock-ignition intensity regime". In : *Physics of Plasmas* 21 (mar. 2014), p. 032710. DOI : 10.1063/1.4869715. URL : http://dx.doi.org/10.1063/1.4869715.

[9] A. Colaïtis, G. Duchateau, P. Nicolaï et al. "Towards modeling of nonlinear laser-plasma interactions with hydrocodes : The thick-ray approach". In : *Phys. Rev. E* 89 (3 mar. 2014), p. 033101. DOI : 10.1103/PhysRevE.89.033101. URL : http://link.aps.org/doi/10.1103/PhysRevE.89.033101.